europhysics
conference
abstracts

24th European Physical Society Conference on

Controlled Fusion and Plasma Physics

Berchtesgaden, 9th-13th June 1997

Editors: M. Schittenhelm, R. Bartiromo and F. Wagner

Contributed Papers, Part III

Published by: The European Physical Society

Series Editor: Prof. R. Pick, Paris

Managing Editor: G. Thomas, Geneva

Volume 21A
Part III

24th European Physical Society Conference on

Controlled Fusion and Plasma Physics

Kongresshaus Berchtesgaden, Germany

9 - 13 June 1997

Editors: M. Schittenhelm, R. Bartiromo and F. Wagner

europhysics
conference
abstracts

24th European Physical Society Conference on

Controlled Fusion and Plasma Physics

Berchtesgaden, 9th-13th June 1997

Editors: M. Schittenhelm, R. Bartiromo and F. Wagner

Contributed Papers, Part III

Published by: The European Physical Society

Series Editor: Prof. R. Pick, Paris

Managing Editor: G. Thomas, Geneva

Volume 21A
Part III

EUROPHYSICS CONFERENCE ABSTRACTS is published
by the European Physical Society, ©1997

The Proceedings may be purchased from Max-Planck-Institut für Plasmaphysik, Boltzmannstrasse 2, 85748 Garching, Germany.

Preface

The 24th European Physical Society Conference on Controlled Fusion and Plasma Physics, under the auspices of the Plasma Physics Division of the European Physical Society, was hosted by the Max-Planck-Institut für Plasmaphysik Garching, Germany. Following the guidelines of the Board of the EPS Plasma Physics Division, the 1997 Conference included topics from the areas of: Tokamaks; Stellarators; Alternative Magnetic Confinement Schemes; Magnetic Confinement Theory and Modelling; Plasma Edge Physics; Plasma Heating; Current Drive and Profile Control; Diagnostics; Basic Collisionless Plasma Physics; Highly Compressed and Non Stationary Plasmas.

The scientific programme and paper selection were the responsibility of the International Programme Committee appointed by the Board of the EPS Plasma Physics Division. The Programme Committee selected 523 contributed papers (out of 651 submitted abstracts) for presentation as posters in four sessions at the meeting. Guideline for the composition of the poster session was to display the various contributions of larger teams in one session and to place teams of similar goals and interests into different sessions.

As in the past, the Proceedings are printed after the meeting, giving authors the opportunity to present their latest results in four-page papers. According to EPS Plasma Physics Division regulations, the Conference Proceedings contain the four-page papers of all those contributions for which at least one author was a registered participant at the Conference. All submitted papers satisfy this condition. 51 papers were not presented at the Conference and not submitted to the Scientific Secretary though they had originally been accepted by the Programme Committee. This caused some problems in the organisation of the poster sessions. As only in a few cases the cancellation had technical reasons, it is strongly recommended for future conferences that along with the submission of an abstract a guarantee has to be provided that an accepted paper will be presented

The four volumes of the proceedings will be mailed to all registered participants of the Conference. The papers of the 8 Review Lectures and 20 Topical Lectures will be published in a Special Issue of the journal 'Plasma Physics and Controlled Fusion', which will also be mailed to all registered participants.

M. Schittenhelm, R. Bartiromo and F. Wagner

July 1997

Programme Committee

R. Bartiromo	IGI del CNR, Italy - Chairman
E. Ascasibar	CIEMAT, Madrid, Spain
D. Gresillon	LPMI/EP, Palaiseau, France
R.D. Hazeltine	Texas University, USA
F. Hofmann	CRPP/EPFL, Lausanne, Switzerland
A. Litvak	IAP, Nizhny Novgorod, Russia
L. Stenflo	Umea University, Sweden
F. Sluijter	Eindhoven University, Netherlands
D.F.H. Start	JET Joint Undertaking, Abingdon, U. Kingdom
U. Samm	Forschungszentrum Jülich, Germany
F. Serra	Universidad Technica, Lisboa, Portugal
T. Todd	UKAEA Fusion, Abingdon, United Kingdom
F. Wagner	IPP, Garching, Germany
R. Weynants	ERM, Brussels, Belgium

Local Organising Committee

F. Wagner	Chairman
G. Zankl	Vice Chairman
M. Schittenhelm	Scientific Secretary
A. Eggeling (Ms).....	Conference Secretary
T. Geist	
H. Jahreiss	Finance Officer
Ch. Stahlberg (Ms)	
K.-H. Steuer	

Acknowledgements

The Conference Organisers gratefully acknowledge financial support from the following:

Accel Instruments GmbH
Bayerische Vereinsbank AG
Cray Research GmbH
BESTEC GmbH
European Commission
Kurdirektion Berchtesgaden
Oxford Instruments
Spinner GmbH
Max-Planck-Institut für Plasmaphysik

Contents of
Europhysics Conference Abstracts
Volume 21A (Part I - Part IV)

Index of Contributed Papers

Contributed Papers

Contents of Part I (Poster Session 1)

Contents of Part II (Poster Session 2)

Contents of Part III (Poster Session 3)

Contents of Part IV (Poster Session 4)

H-mode confinement on ASDEX Upgrade

ITER Fusion Performance Projections

D. Boucher, F. Louche[1], N. Karulin[2] and
ITER Joint Central Team and Home TEams

ITER San Diego JWS, La Jolla, USA
[1]Ecole Royale Militaire - Association Euratom / Etat Belge
[2]RRC Kurchatov Institute - Moscow - RF

A vigorous international effort has been undertaken to provide the physics information necessary to predict ITER expected fusion performances: clarify operational limits, determine scaling of key plasma parameters such as energy confinement time and finally translate this information into predictions for fusion power in ITER.
As shown in ITER Detail Design Report [1] a number of plasma quantities are needed to determine the fusion power in ITER: temperature profiles including H-mode pedestal and sawteeth activity, impurity level - determined largely by plasma facing components and the divertor - and density profiles. These quantities have been simulated using a 1-1/2 D transport code (PRETOR [1]) by adopting the following prescriptions:
- flat density profiles,
- impurity level is determined using either the simplified set: 2% Beryllium, $\tau^*_{He}/\tau_E = 10$ or the more elaborate set: 2% Beryllium, helium and Argon level determined consistently from coupling with a divertor model [1].
- edge β_T at 90% of the toroidal flux consistent with JET/DIII-D observations in ELMy H-mode operation.

The energy confinement is then specified in two different ways by using either:
- global scaling law (the normalized temperature shape being prescribed separately),
- a number of local transport models that compute the entire temperature profile with a given boundary value at 90 % of toroidal flux.

Fusion performance versus global confinement and operational limits

The global energy confinement time - represented by the HH factor (ratio: τ_E / τ_E(ITERH-97P(y)) - is varied between 0.3 to 1.5 to study its impact on the fusion power. The normalized temperature profile is fitted to the JET / DIII-D ITER demonstration discharges by an appropriate choice of normalized local transport coefficients [1].

Fig. 1 indicates the expected fusion performance in ITER as a function of the HH factor (By definition, extrapolation from present experiments corresponds to HH = 1) and for two values of the operating density: either the density is freely chosen to maximize the fusion power and maintain it at 1.5 GW - if necessary auxiliary heating up to 100MW is applied, ignited points are indicated by a thick line - or the density is restricted at the Greenwald value. The region on the right is where β_N exceeds the reference value of 2.5. The lower limit of this region indicates fusion power obtained if β_N is restricted below 2.5 while adjusting the input power to satisfy the L- to H-mode power threshold.

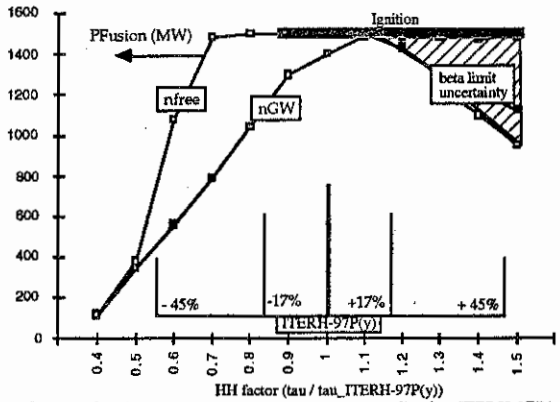

Fig. 1: Expected fusion power versus confinement normalized to ITERH-97P(y) Plasma current: 21 MA, auxiliary heating up to 100 MW.

The figure also indicates the presently estimated uncertainties on confinement. The current position of the Confinement Modeling and Database expert group is that the 95% confidence interval for the energy confinement in ITER is τ_E = 3.5 to 9s which is translated in this study as HH = 1.0 +/- 0.45. If however, a power law is the correct form for the global energy scaling law than the expected uncertainties are down to +/- 17%. Both cases are indicated in figure 1. In the lower confinement region (HH < 1.0) the expected fusion power can be significantly increased by raising the density above the Greenwald limit or by raising the plasma current as seen on fig. 2.

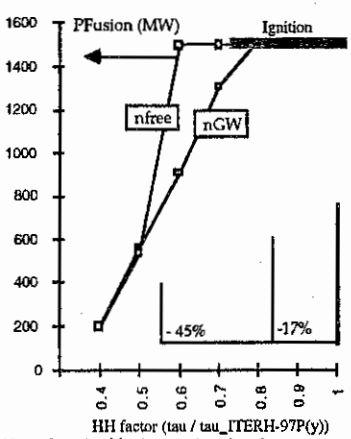

Fig. 2: The fusion power is significantly raised by increasing the plasma current to 24 MA instead of 21MA.

Within a wide range of confinement (+/- 45%) significant fusion power is achieved: 1.5 GW can be achieved if confinement is better than -40% and full ignition better than -25% compared to the reference ELMy H-mode confinement. Contingency plans such as operating above the Greenwald density and/or increasing the plasma current to 24 MA are however needed to achieve these performances under the worst confinement conditions. The possibility - compatible with the present design - to increase the amount of auxiliary heating above 100 MW is also being considered [1].

Fusion performance predicted by local transport codes

Under the auspices of the Confinement Modeling and Database expert group 9 different local transport models are being tested against experiments in view of determining their reliability - or accuracy - against ITER predictions. These models have been applied to ITER and their prediction are summarized on fig. 3:

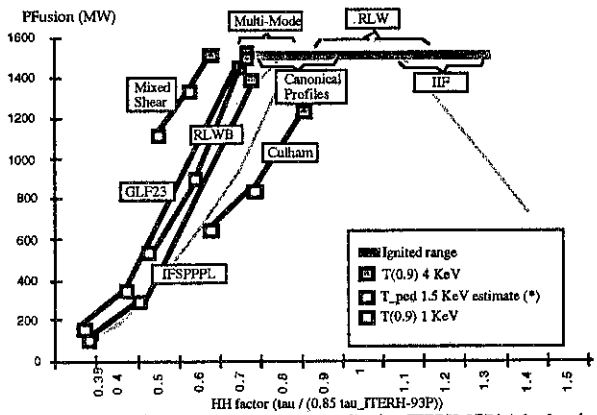

Fig. 3: Expected fusion power and global confinement normalized to ITERH-97P(y) for local transport models

It is found that the height of the edge temperature (at 90% toroidal flux surface) is the most important factor determining the fusion power (once density, etc.... and given as above). Therefore the edge temperature is varied between the very pessimistic 1 keV and the upper limit 4 keV. The reference case where the boundary is moved to the top of the H-mode pedestal at 1.5 keV is also shown (point labeled 1.5 keV estimate on the plot). The predictions at this point vary between Q~3 for IFS/PPPL and GLF23 models [3] to full ignition at 1.5 GW for the Multi-Mode, RLW and Itoh-Itoh-Fukuyama models [3] with more than 800MW with 100MW of heating for the Culham, Mixed Shear and RLWB models [3]. These cases were done at 1.5 times the Greenwald density. The spread across models is comparable but somewhat larger to the generalized confinement uncertainties given by the global scaling laws. The testing of these models against experiments is not completed and does not yet allow to distinguish convincingly among these models. However, the Multi - Mode model gives presently the best fit against the data.

Preliminary Modeling of ICRH heating

One issue common to the above studies is the need to obtain an H-mode in the first place. The power reaching the plasma edge must exceed a power threshold which is found experimentally to increase with density (except at very low density) . Simulations show that dominant ion heating is beneficial because it leads to a higher ratio Ti/Te thereby maximizing alpha heating and minimizing electron radiation. The benefit of ion heating however strongly decreases at higher densities (typically > 5 10^{19} m^{-3}) because of the stronger ion / electron collisional coupling. ICRH is a possible candidate for strong ion heating and to study this possibility, the transport code PRETOR has been interfaced with the ICRH package PION [4], which calculates the power deposition profiles and the velocity distribution function of resonating ions in a self-consistent way.

These combined codes has been used for simulating second and third harmonic tritium heating schemes in ITER Deuterium-Tritium plasmas (assuming 100 MW input power). Preliminary results have shown that the latter scenario only lead to strong ion heating at relatively high density: 65% at 9 10^{19} m^{-3}. At lower densities needed for the H-mode transition ion heating became smaller ~ 17% of total heating. It is was found that these conclusions still held even when varying the ratio $\chi i / \chi e$ from 1 to 3. Additional studies are therefore needed to refine these scenarios and optimize ion heating with ICRH.

Preliminary Evaluation of the non inductive operation

Non-inductive operation in ITER has been investigated using the ASTRA transport code which implements NBI and ECH heating and current drive systems with ITER parameters and geometry. A simplified choice of local heat and particle transport coefficients has been adopted in the study: parabolic shape is used and the coefficients are normalized to recover the global energy confinement time from H-mode global scalings. It is found that under ELMy H-mode (HH = 1) and fully non-inductive operation the total plasma current is low and typically Qth is less than 5. Therefore improved confinement with respect to the standard ELMy H-mode is required. A key candidate for improved confinement is the negative shear configuration which is associated with the formation of transport barrier and the reduction of heat transport coefficients down to neo-classical levels. If is found that a modest amount (10 MW) of NBI current drive is sufficient to control the central current profile and that about 90 MW of ECH current drive applied at r/a ~ 0.75 can drive sufficient current off axis to maintain a stable reversed shear configuration with 1.5 GW of fusion power. Further studies and optimization are needed to further quantity the fusion performances of this regime as well as its robustness against physics assumptions in particular the choice of local transport coefficients.

[1] *ITER Detailed Design Report* ITER Joint Central Team, November 1996.

[2] *Energy Confinement Scaling and the Extrapolation to ITER* J.G. Cordey et al., this conference.

[3] *Validation of 1-D Transport and Sawtooth Models for ITER* J. Connor et al., IAEA Montreal, October 96, F1-CN-64/FP-21

[4] PION code: L.-G. Eriksson, U. Willen and T. Hellsten, Nuclear Fusion 33 (1993) 1037.

L.-G. Eriksson and T. Hellsten, Physica Scripta 55 (1995) 70.

EFFECTS OF HELIUM ASH ON THE DYNAMICS OF ITER-LIKE PLASMAS

H. Bürbaumer and G. Kamelander
Austrian Research Center Seibersdorf, ÖAW-EURATOM Association
A-2444 Seibersdorf, Austria

INTRODUCTION

It is an important goal of ITER to reach ignition and to keep the plasma for periods of about 1000 seconds in an ignited state. A fully ignited regime is very difficult to maintain in a quasistationary equilibrium as a consequence of strongly interrelated processes leading to transients of power and temperature. The subject of fusion reactor dynamics research is the identification such processes and the investigation of control mechanisms to suppress or mitigate such transients. In the present paper we investigate oscillations due to helium ash identified by Ref.[1] including also spatial effects.

The thermonuclear energetic alpha particles are slowed down by collision with the bulk plasma transferring their energy to the plasma. The helium population in equilibrium with the bulk plasma becomes an impurity referred to as helium ash. The helium ash population is determined by the slowing down source and by the losses due to diffusion. The time scale of slowing down is about half a second and the ash confinement time about 50 s. If the temperature in the plasma core is increased the supply of helium particles increases also and ash accumulation takes place diluting the fuel and decreasing the reaction rate. Thus the supply due to slowing down decreases. As a consequence of diffusion the helium density decreases also reducing dilution and increasing power. This is the reason for helium oscillations.

ZERO DIMENSIONAL PHYSICAL MODEL

The physical model is based on the flux surface averaged energy equation which has been transformed into a zero dimensional equation averaging over the plasma volume

$$K_1 \frac{\partial}{\partial t}(n_{e0} + n_{i0})T_{e0} = P_\Omega + \eta_\alpha P_\alpha + P_{aux} - P_l - P_b - P_s \qquad (1)$$

where parabola profiles for density and temperature

$$n_i = n_{i0}\left(1 - x^2/a^2 - y^2/\kappa^2 a^2\right)^{\nu_n}, T = T_0\left(1 - x^2/a^2 - y^2/\kappa^2 a^2\right)^{\nu_T} \qquad (2)$$

are prescribed. $P_\Omega, P_\alpha, P_{aux}, P_L, P_b, P_s$ (Ref.. [2]) denote Ohmic power, alpha power, auxiliary power, loss power , Bremsstrahlung and synchrotron radiation. ν_T and ν_n are profile parameters, a is the minor radius, κ represents the elongation. x and y are local co-ordinates in the

plasma cross section. The fast alpha density n_α respectively the helium ash density n_{He} satisfies are modelled by the continuity equation

$$\partial n_\alpha/\partial t = S_\alpha - n_\alpha/\tau_{SD} - \nu_L n_\alpha, \quad \partial n_{He}/\partial t = n_\alpha/\tau_{SD} - n_{He}/\tau_{He}. \tag{3}$$

$S_\alpha = n_T n_D \langle \sigma_f v \rangle$ denotes the fusion source, τ_{SD} the slowing down time, ν_L the fast alpha loss factor and τ_{He} the helium confinement time. Keeping the electron density n_e constant and using the quasineutrality we express the ion density as $n_i = n_e(1 - 2n_\alpha/n_e - 2n_{He}/n_e)$.
Introducing the dilution factor $D = (1 - 2n_\alpha/n_e - 2n_{He}/n_e)^2$ we can write

$$S_\alpha = (n_e^2/4) D \langle \sigma v \rangle. \tag{4}$$

Modelling the loss power by $P_L = K_l (n_{e0} + n_{i0})/\tau_E$ and using the ITER89-P scaling

$$\tau_E^{ITER89P} = 0.048 H I_p^{0.85} R_0^{1.2} a^{0.3} \kappa^{0.5} n_{20}^{0.1} B_T^{0.3} A_i^{0.5} / P^{0.5}, \tag{5}$$

with $P = P_{aux} + P_\alpha$, we find that eqs.(1) to (5) constitute a non-linear system.
Investigating a subignited plasma near to ignition we have combined this plasma model with a control system based on modulation of auxiliary power [2] reacting with a delay time τ_d in the order of magnitude of about 0.1 s.

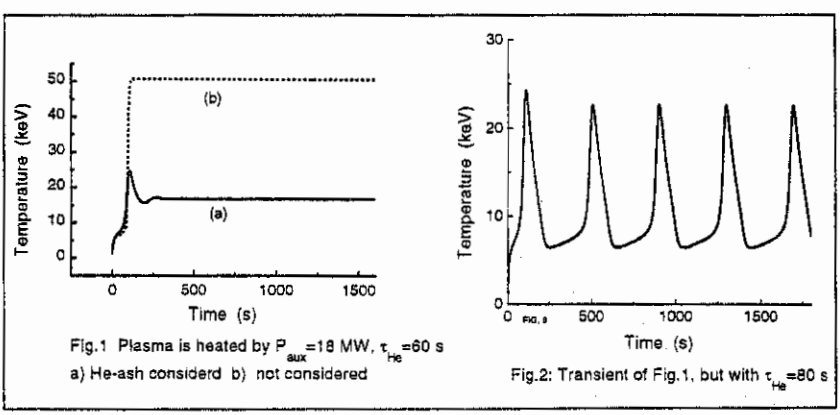

Fig.1 Plasma is heated by P_{aux}=18 MW, τ_{He}=60 s
a) He-ash considerd b) not considered

Fig.2: Transient of Fig.1, but with τ_{He}=80 s

We find that the plasma evolution depends critically on τ_{He}. From experimental evidence it is known that this parameter is 5 to 20 times of τ_E. Assuming τ_E=60 s we show the evolution of

an ITER-like plasma (R_0 =6m, a=2.15m, B_0 =4.85T, I_p =22 MA, κ =2, $n_e = 10^{20}$ m^{-3}), which is heated without control by 18MW (Fig.1). The temperature peak is a consequence of the helium effect. Repeating the simulation with τ_{He} =80 s we obtain oscillations which are just weakly damped (Fig.2).

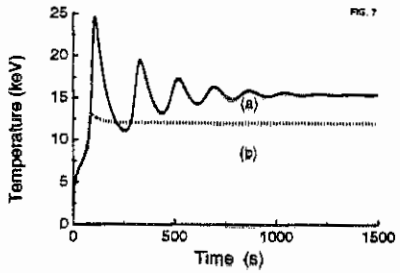

Fig.3: Transient of Fig.1, but with τ_{He} =70 s
a) without control b) with control

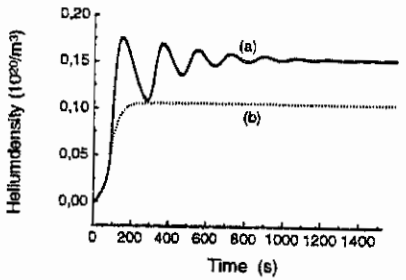

Fig.4: Transient of Fig.3, He-ash density
a) without control b) with control

Next we present a simulation with τ_{He} =70s (Figs.3 and 4). The full line shows the temperature for the uncontrolled plasma (like Figs.1 and 2). Again we find oscillations which are unacceptable for reactor operation. However if the plasma is controlled by modulating the auxiliary power as proposed by Ref.[2] the oscillations are considerably mitigated (dotted line). It is concluded that helium induces oscillations can be satisfactorily controlled by the feedback control system [2]. Of course other control systems like density control could be used.

ONE DIMENSIONAL SIMULATIONS

The simulations presented above neglect spacial effects. Keeping τ_{He} and n_e as constant are oversimplifications. For this reason we investigated the helium ash problem modificating the wellknown one-dimensional JETTO-code [3]. This code is based on the solution of the flux surface averaged transport equations retaining thus also 2D-informations. In opposition to the zero dimensional code with τ_{He} and the confinement time scaling law as input, JETTO is equipped with transport models. τ_{He} and τ_E are calculated. In our calculations we used the REBUT-Lallia transport law [4]. The distribution function of the fusion alphas is obtained by solving a kinetic equation by means of a multigroup procedure (30 groups). The slowest group is taken as helim ash and treated as an impurity

In the actual paper we present the first simulations with our modified JETTO-code. The simulations have been performed using the same tokamak parameters as for the zero dimensional case without control. We start with a parabolic density profile with the central electron density $1.3\times10^{20}\,m^{-3}$. After the Ohmic phase the plasma has been heated with 30 MW. The Figs.4 to 7 show some results.

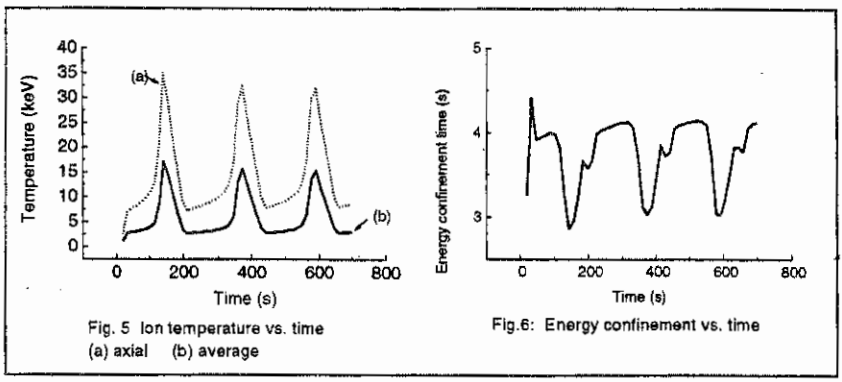

Fig. 5 Ion temperature vs. time
(a) axial (b) average

Fig.6: Energy confinement vs. time

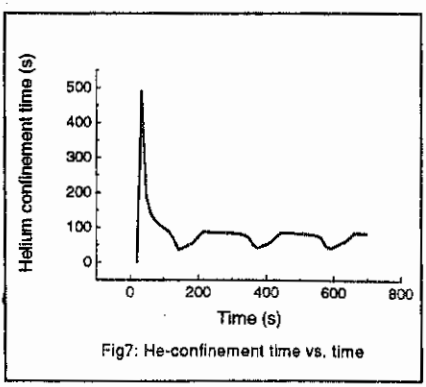

Fig7: He-confinement time vs. time

CONCLUSION

The possibility of helium induced oscillations dangerous to reactor performance are predicted by simulations under realistic conditions. For quantitative results more reliable transport models are necessary. The suppression or mitigation of such transients by means of a control system seems possible and will be the subject of further research.

References

[1] Sigmar, D.J., Wiesing, F., PFC/JA-95-48 (1995)
[2] Chaniotakis, E.A., Sigmar, D.J., Nucl. Fusion, Vol. 33, No. 6 (1993)
[3] Cenacchi, G., Taroni, A., A free-boundary plasma transport code, JET-IR(88)03
[4] Rebut, P.H., Lallia, P.P., Watkins L.L., in Plasma Physics and Controlled Nuclear Fusion Research (Proc. 12th Int. Conf. Nice, 1988) Vol.2, IAEA, Vienna (1988) 191.

An Analysis of the H-mode Threshold in ITER

The ITER H-mode Threshold Database Working Group
presented by **J A Snipes***

**MIT Plasma Science and Fusion Center, Cambridge, MA USA*

Introduction Attempts have been made for several years to accurately predict the threshold power required to achieve H-mode in ITER [1-2]. These studies have concentrated on regression fits to global quantities, with the line averaged density, toroidal field, major radius, aspect ratio, and elongation as the dominant terms. This paper extends these analyses to the most recent ITER H-mode Threshold Database DB2.2, which includes more than 5000 time slice records each with 156 variables from Alcator C-Mod, ASDEX-Upgrade, Compass, DIII-D, JET, JFT-2M, JT-60U, and TCV. In addition, more than 600 records of older data are included from the previous DB2 version of the database from ASDEX and PBX-M. The new database includes global quantities as well as local edge temperature and density measurements at the 90% and 95% flux surfaces under a variety of plasma conditions including ohmic, ICRF, and neutral beam heating. More attempts have been made to reduce the scatter in the data from many tokamaks with very different first wall properties to try to reduce the uncertainty in the threshold power predicted for ITER. The main reasons for scatter in the data vary for different machines including the step size of the input power, the change in stored energy, and neutral particle effects. Recent work suggests that sawteeth may play an important role in the threshold and could also increase scatter in the data. The result is that there remains a large uncertainty in predicting the threshold power for ITER.

Global Analyses The threshold power required to achieve H-mode can vary by more than a factor of two within a tokamak. So, one approach is to include only H-mode threshold points that have no known reason for having an unusually high threshold power and flagging them as SELDB2 = 1111111111. Using these standard selection criteria and performing the usual n, B, and R regression on the latest dataset with equal weighting between points from all 10 tokamaks (N=518) yields (Fig. 1): $P_L = P_{in} - \frac{dW}{dt} = 0.65 \cdot \bar{n}_e^{0.93} \cdot B_T^{0.86} \cdot R^{2.15}$ (Eq. 1), where the power is in MW, the line averaged density is in units of 10^{20} m^{-3}, the toroidal field is in Tesla, and the major radius is in m. This analysis yields a predicted threshold power in ITER of P_{th}(ITER) = 139 MW, using a line averaged density of 0.5×10^{20} m^{-3}, B_T = 5.68 T, and R = 8.14 m, with a one standard deviation uncertainty interval of about 107 to 182 MW,

assuming the model is correct and the main engineering variables that influence the threshold power are included.

Alternatively, if the elongation of the plasma is included as a regression variable with the same selection criteria, the following threshold scaling is found (Fig. 2):

$$P_L = 0.42 \cdot \bar{n}_e^{0.80} \cdot B_T^{0.90} \cdot R^{1.99} \cdot \kappa^{0.76} \qquad \text{(Eq. 2)},$$

which yields a predicted threshold power for ITER of 108 MW and a one standard deviation uncertainty interval of about 78 to 151 MW. This point prediction is close to that of Takizuka [2]. If the points are weighted so that each tokamak carries equal weight, W = $1/N_j$, where N_j is the number of data points from tokamak j, the scaling becomes:

$$P_L = 0.67 \cdot \bar{n}_e^{1.07} \cdot B_T^{0.73} \cdot R^{2.17} \cdot \kappa^{0.44} \qquad \text{(Eq. 3)}.$$

With this scaling, the predicted threshold power for ITER is 131 MW with an uncertainty interval of 92 to 187 MW. Note that each of these regressions was performed as a free fit, yet all except Eq. 3 came out very close to satisfying the Kadomtsev constraint [3]. Each of these predicted thresholds falls within the 50 - 200 MW range predicted by Takizuka.

One attempt to further reduce scatter in the data has been to specify an "ITER Oriented" dataset, which includes elongations from $1.4 < \kappa < 1.8$ and safety factors from $2.8 < q_{95} < 4.0$. This severely restricts the data in the database (N=221), and eliminates ASDEX, DIII-D, PBX-M, and JFT-2M. The uncertainties do not decrease and the point predictions for equal weighting between points, 102 MW (1σ = [72 - 147] MW), or between tokamaks, 112 MW ([78-161] MW), remain in the same range as the previous scalings.

Another potentially important effect to consider is the radiated power. Due to the lack of reliable radiated power measurements from within the last closed flux surface, Compass, PBX-M, and TCV are eliminated when radiated power is subtracted from the input power. The resulting regression fit between the remaining seven machines (N=142) with W = 1/N gives $P_L - P_{rad} = 0.35\ n_e^{0.73}\ B_T^{0.94}\ R^{2.27}$, which is not very different from the expression without subtracting radiation and yields nearly the same threshold prediction for ITER of 124 MW with a larger uncertainty interval of [77 - 200] MW because of the smaller dataset and the increased uncertainty due to the inclusion of radiated power measurements.

Local Analyses Another approach to the threshold is to consider local edge measurements instead of global ones since some machines have found a dependence of the H-mode threshold on edge conditions, most notably the electron temperature. New data was added to the DB2.2 version of the threshold database including temperatures and densities at the flux

surfaces corresponding to 90% and 95% of the square root of the toroidal flux. Due to the difficulties in obtaining accurate edge temperature and density measurements, Compass and JFT-2M were eliminated from the analysis and the scatter in the data from the remaining machines leads to large uncertainties in any predictions based on the edge measurements.

Nonetheless, an attempt was made to predict the edge electron temperature at the H-mode threshold in ITER. The best fits were obtained regressing $T_e(95)$ and $T_e(90)$ as functions of toroidal field, line averaged density (statistics were poor using $n_e(95)$), q_{95}, and major radius. The results with equal weighting between points are (Figs. 3-4):

$$(N=62) \qquad T_e(95)\,(eV) = 126.38 \cdot B_T^{1.32} \cdot \bar{n}_e^{-0.5} \cdot R^{0.56} \cdot q_{95}^{-1.31} \qquad \text{(Eq. 4)}$$

$$(N=102) \qquad T_e(90)\,(eV) = 170.29 \cdot B_T^{1.02} \cdot \bar{n}_e^{-0.3} \cdot R^{0.74} \cdot q_{95}^{-0.94} \qquad \text{(Eq. 5).}$$

The predictions for ITER are then $T_e^{ITER}(95) \approx 1250$ eV, with a one standard deviation uncertainty interval of about 500 eV to 3200 eV, and $T_e^{ITER}(90) \approx 2000$ eV, with an uncertainty interval of 950 eV to 4200 eV. The L-mode gradient is then predicted to be about 6 keV/m, which is somewhat low compared to existing devices. This scaling has the same density dependence but a stronger plasma current dependence and a weaker toroidal field dependence than the recent scaling found on ASDEX-Upgrade for edge T_e in terms of edge n_e [4]. Assuming the transition is governed only by plasma physics and that atomic physics can be neglected, the criterion for a transition should have the form $\rho_*^x \cdot \nu_*^y \cdot \beta^z = \text{const.}$ [3,5] and the exponents in the edge temperature scalings should satisfy the constraint $8\alpha_n - 4\alpha_R + 5\alpha_B = 2$. Eqs. 4 and 5 do not satisfy this constraint to within an exponent of 2. So, either the assumptions are incorrect or the regression has not found the correct dependences within this limited dataset.

Conclusions Despite continued attempts to reduce the uncertainties in the prediction of the H-mode threshold power in ITER, large uncertainties remain with global predictions in the range of 50 - 200 MW. Narrowing down the selection criteria results in poorer statistics with equally large or larger uncertainties than using the full dataset. The observed variation in threshold power in existing machines must also be expected in ITER. New analysis of the edge electron temperature at the H-mode threshold predicts $T_e^{ITER}(95) \approx 1250$ eV with edge gradients on the order of 6 keV/m.

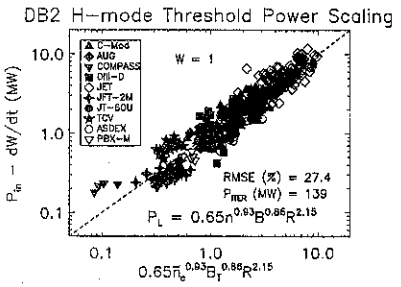

Fig. 1. Standard regression of the H-mode threshold power versus line averaged density, toroidal field, and major radius with equal weighting between points.

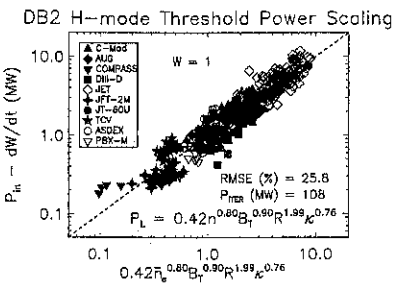

Fig. 2. H-mode threshold power regression including plasma elongation across 10 tokamaks with equal weighting between points.

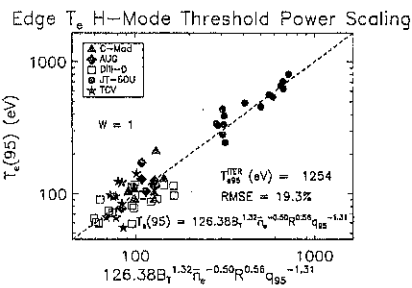

Fig. 3. Edge electron temperature regression at the 95% flux surface versus toroidal field, line averaged electron density, and edge safety factor.

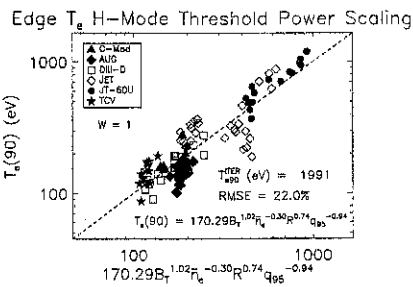

Fig. 4. Edge electron temperature regression at the 90% flux surface versus toroidal field, line averaged electron density, and edge safety factor.

References

[1] F Ryter, H-Mode Database Working Group, *Nuclear Fusion*, **36** (1996) 1217.

[2] T Takizuka, et al., in *Plasma Physics and Cont. Nucl. Fus. Res. 1996 (Proc. 16th IAEA Conf., Montreal, 1996)*, to be published.

[3] B B Kadomtsev, *Sov. J. Plasma Phys.*, **1** (1975) 295.

[4] W Suttrop, et al., to be published in *Plasma Physics and Controlled Fusion*.

[5] J W Connor and J B Taylor, *Nuclear Fusion*, **17** (1977) 1047.

BOOTSTRAP FRACTION IN TFTR, TORE SUPRA AND TEXTOR

G.T. Hoang*, **R.V. Budny**, V. Basiuk* and J. Ongena#
Princeton University, P.O. Box 451, Princeton NJ, 08543, USA
* Association Euratom-CEA, CE Cadarache, 13108 St-Lez-Durance, FRANCE
# LPP/ERM-KMS, Association Euratom-Belgian State, Brussels, BELGIUM

Advanced tokamak reactors will require a large bootstrap current, I_{boot}, in order to sustain a large fraction of the plasma current without consuming large amounts of power in current drive systems. This paper examines the bootstrap fraction, f_{boot}, for a wide variety of discharges provided from three circular cross-section tokamaks TFTR, Tore Supra, TEXTOR, with different auxiliary heating. Discharges with both monotonic and non-monotonic q-profiles are included in the dataset. An empirical scaling of f_{boot} is given, using the ratio of the peakednesses of the thermal pressure and of the total current density.

DISCHARGES STUDIED

TFTR: A dataset of more than 170 discharges was assembled to study the tritium influx and transport in discharges with D-only neutral beam injection (NBI) [1]. The neoclassical bootstrap current [2] generated by the thermal pressure is calculated using the TRANSP plasma analysis code. Measured profiles of n_e and T_e, the impurity carbon ion temperature and toroidal rotation, and, when available, the measured safety factor (q) from MSE diagnostic are inputs. The dataset includes a large range in plasma parameters:

$0.6 \le Ip[MA] \le 2.7$; $0.04 \le I_{boot}[MA] \le 1.6$; $2.8 \le q(a) \le 11$; $1.9 \le BT[T] \le 5.7$
$0.2 \le n_e(0)[10^{20}m\text{-}3] \le 1.2$; $2 \le P_{NBI}[MW] \le 35$; $1.5 \le P_{ICRH}[MW] \le 6$

Also, a wide variety of regimes is included: L-mode, supershots [3], discharges with reversed shear (RS) and enhanced reversed shear (ERS) [4], and discharges with increased-l_i [5]. High bootstrap currents are generated by peaked pressure profiles caused by strong ion heating (T_i / T_e up to 3) and/or a peaked density profile. In Fig 1, f_{boot} is plotted versus the thermal β-poloidal, β_θ. For ERS discharges a high I_{boot} is driven inside the region $r/a \le 0.4$, caused by the peaking of the pressure (due primarily to the strong increase of density profile peakedness), and the high central q (I_{boot} varies as q^2). f_{boot} of 100% and quasi-stationary ERS discharges with high f_{boot} are achieved [6]. In some ERS discharges, f_{boot} transiently surpasses 100% .

Tore Supra: The database consists of 182 time slices of more than 100 discharges using fast wave electron heating (FWEH, dipole operation [7]). Since the central FW power deposition strongly peaks the electronic temperature, more than 80% of I_{boot} are induced mainly by the T_e gradient, contrary to the TFTR regimes, T_e / T_i is up to 4. Note that the electrons are in banana collisionnality regime, and the ions in the plateau regime. The bootstrap current is determined by two ways [8, 9]:

i) a theoretical approach with a matrix formulation [10], valid in all collisionnality regimes and aspect ratios, $\varepsilon = a/R$

ii) a determination of the non-inductive current which is, for the FWEH Tore Supra cases, almost totally the bootstrap current with a method [11]

The dataset includes various plasma parameters:

$0.4 \le Ip[MA] \le 1$; $0.025 \le I_{boot}[MA] \le 0.26$; $B_T[T] = 2.2$, 2.8 and 3.4;
$3 \le q(a) \le 8.7$; $4.5 \le n_e(0)[10^{19}\ m^{-3}] \le 5.5$; $1 \le P_{FW}[MW] \le 9.4$

Most of the shots are stationary compared with the diffusion time of the current (durations of several seconds). One example has a f_{boot} of more than 40% during 5s, at $n_e(0) \approx 0.5 \times 10^{20} m^{-3}$ with PFW = 6 MW.

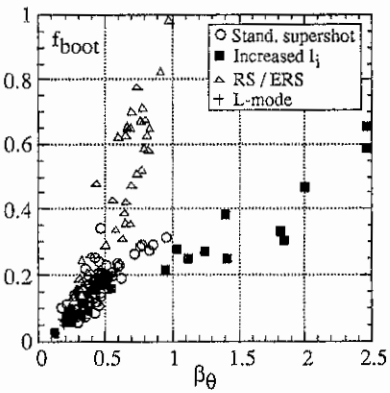

Figure 1: Boot strap current fraction versus thermal β_θ for various regimes in TFTR.

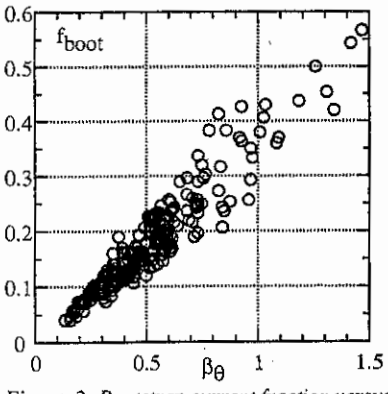

Figure 2: Bootstrap current fraction versus thermal β_θ in Tore Supra, with FWEH.

TEXTOR: 13 discharges using the combination of NBI and ICRH minority heating are included in our database. I_{boot} is dominantly generated by the density gradient.

0-D SCALING

An expression for f_{boot} has been derived in the case of simple monotonic plasma densities, temperatures, and currents [12]:

$$f_{boot} = \varepsilon^{0.5}\, \beta_\theta\, C_b \qquad \text{Eq. (1),}$$

with the function C_b depending on the peakednesses of the plasma profiles. β_θ is the ratio of the thermal plasma pressure and the magnetic pressure. For Tore Supra, the diamagnetic diagnostic gives β_θ since the electrons are directly heated by FW. For TFTR and TEXTOR, β_θ is determined by subtracting the anisotropy (calculated by TRANSP) due to fast particles from the diamagnetic poloidal-β.

An approximate fit of f_{boot} for all regimes is given by

$$f_{boot}^{fit} = 0.5\ \varepsilon^{0.5}\ \beta_\theta\ (\alpha_p / \alpha_j)^{0.5} \qquad \text{Eq. (2),}$$

where α_p is the ratio of the central and the volume-averaged values of the thermal pressure, and α_j is the ratio of the central value of the total current density and $(Ip / \pi a^2)$. Eq. (2) assumes a linear dependence of f_{boot} on β_θ . However, without this constraint, a very similar dependence on β_θ, α_p, α_j is found; f_{boot} is given by

$$f_{boot}^{fit} = 0.45\ \varepsilon^{0.5}\ \beta_\theta^{0.92}\ \alpha_p^{0.47}\ \alpha_j^{-0.45} \qquad \text{Eq. (3)}$$

In Figure 5, we compare the computed f_{boot} with f_{boot}^{fit} in Eq. (2).

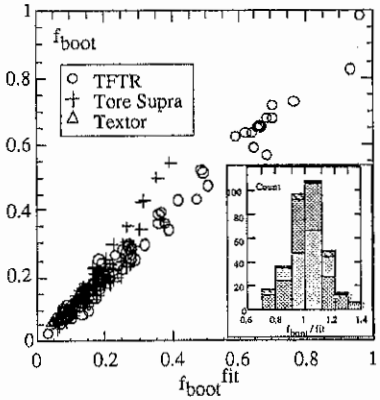

Figure 3: f_{boot} versus fit in Eq. (1)

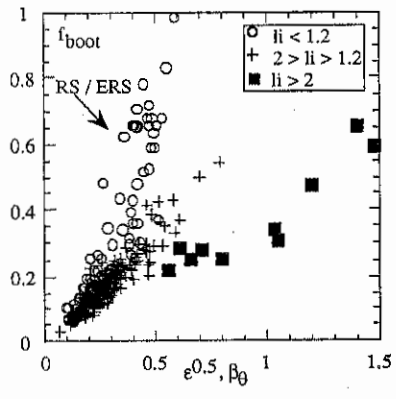

Figure 4: f_{boot} versus $\varepsilon^{0.5}\ \beta_\theta$ (TFTR, Tore Supra, and Textor)

PRESSURE AND CURRENT PROFILE DEPENDENCE

In general, when f_{boot} is relatively low, β_θ , α_p and α_j are coupled since the Ohmic current, which is still important, is linked to the pressure profile through the temperature and the density. In our database, α_p and α_j vary independently: α_p = 2-12 and α_j = 1-10. The ratio α_p / α_j varies over a large range, from 1 to 14. This allows us to study variations in these parameters separately at fixed β_θ.

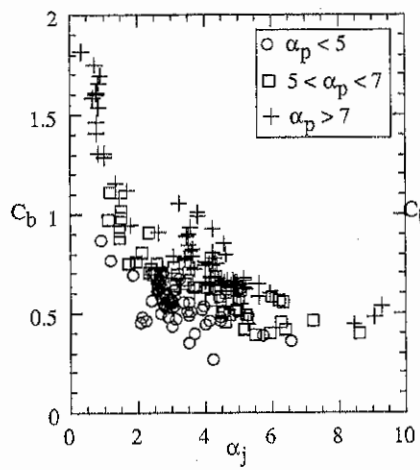

Figure 5: C_b versus α_j

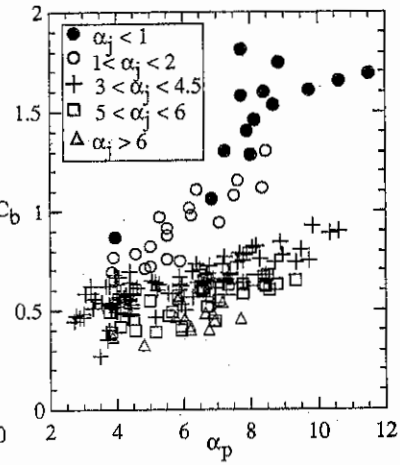

Figure 6: C_b versus α_p

In Fig 4 we plot f_{boot} as a function of the product $\varepsilon^{0.5}\ \beta_\theta$ for ranges of self inductance which characterize the peaking of the current density profile. In this figure, the discharges

with $1.2 < l_i < 1.8$ corresponds to the TFTR standard supershot and Tore Supra FWEH discharges; the $l_i > 2$ case corresponds to the discharges using special techniques for increasing l_i; and the li < 1.2 case correspond mainly to RS/ERS discharges. Fig 4 indicates that C_b in Eq. (1) has a wide variation, and depends on the current density profile. In the range of $\beta_\theta = 0.5$-1, C_b decreases, comparing to the standard discharges, with the peaked current density profiles (i.e. high-l_i, the ratio α_p / α_j decreases in this case). Contrarily, the non-monotonic profiles of the current density are favorable for high bootstrap operation: C_b significantly increases (α_p / α_j strongly increases up to 12) in the RS/ERS case.

Figure 5 shows the variation of C_b versus α_j for ranges of α_p. When the peaking factor of the current density profile increases, C_b decreases approximately as $\alpha_j^{-0.5}$. Figure 6 shows the dependence of C_b on α_p, for ranges of α_j. C_b varies approximately as $\alpha_p^{0.5}$. This weak dependence on the thermal pressure profile is due to the fact that the high gradient region is inside a small plasma volume.

SUMMARY

A large database, including a wide variety of discharges provided from TEXTOR, TFTR and Tore Supra, allows us to examine the dependence of the bootstrap fraction on the profiles of the thermal pressure and total current density, through the global parameters. The bootstrap fraction varies from 10% to 100%, with duration of a few hundred ms to several seconds.
The fraction of the bootstrap current is found to vary with the ratio of the peakedness of the total thermal pressure and current density profiles, approximately as $(\alpha_p / \alpha j)^{0.5}$. High bootstrap fractions are achieved at relatively low thermal poloidal-β (0.5–1) and high $\alpha_p / \alpha j$.

Since these two parameters are generally coupled when the plasma current is partially non-inductive, a external non-inductive source for controlling the plasma core, allowing separate control of the pressure and current density profiles could be useful for optimizing f_{boot}.

ACKNOWLEDGMENTS
We wish to thank the TEXTOR, TFTR and Tore Supra teams for results, and the U. S. Department of Energy for support under the Contract No. DE-AC02-76-CH03073.

[1] R.V. Budny, *et al.*, "Hydrogenic Species Influx ..", to be submitted to P.o. P.
[2] S.P. Hirshman and D.T. Sigmar, Nucl. Fusion, **21**, 1079 (1981).
[3] J.D. Strachan, *et al.*, Phys. Rev. Letters, **58**, 1004 (1987).
[4] F.M. Levinton, *et al.*, Phys. Rev. Letters, **75**, 4417 (1995).
[5] S.A. Sabbagh, *et al.*, Proc. 16th IAEA F1-64/AP2-17 (Montreal, 1996).
[6] G.T. Hoang, R.V. Budny, 12th Top. Conf. on RF, Savannah, USA, 1997.
[7] Equipe Tore Supra, Plasma Phys. and Controlled Nucl. Research, Suppl. **36** B 123.
[8] E.Joffrin *at al*, 22nd EPS Conference, Bournemouth 1995, Vol 19 C, part IV, p 125.
[9] V.Basiuk, *et al.*, 12th Top. Conf. on RF, Savannah, Georgia, USA, 1997.
[10] C.E. Kessel, Nuclear Fusion, **34** (9), (1994)
[11] C.Forest, *et al.*, Physics Review Letters **73**, p. 2444, 1994
[12] N.Pomphrey, PPPL-2854 (1992).

NEUTRAL BEAM INJECTION AND ROTATION IN ITER PLASMAS

R.V. Budny, G.W. Hammett, D. Mikkelsen,
Princeton University, P.O. Box 451, Princeton NJ, 08543, USA
and D. Boucher
ITER Joint Work Site, San Diego, CA, USA

Introduction - The TRANSP plasma analysis code has previously been used to study effects of high energy neutral beam injection (NBI) into ITER plasmas [1,2]. The beam current drive, heating, sawtooth mixing, and ripple loss rates were calculated for 50MW of D-NBI with an energy of 1MeV. This paper extends those studies to include a) predictions of the beam-induced toroidal rotation of the thermal plasma, b) a proposed reversed-shear (RS) mode of plasma operation with non-monotonic q_ψ, and c) the alternative of using 150keV NBI (which deposit more torque near the edge per unit power) to cause sheared toroidal rotation. We discuss the possibilities of using rotation to suppress locked modes, resistive wall modes, and turbulence.

The ITER plasmas studied are steady state cases from the ITER interim database [3] producing 1.5 GW of fusion power. All have a toroidal field of 5.7T. Two have a plasma current I_p = 21MA and monotonic q_ψ profiles with relatively flat or peaked density profiles [1,2]. The third is a preliminary RS plasma with a high bootstrap fraction, relatively low I_p = 13.5MA and low electron density. The confinement is enhanced with β_{norm} = 5 and β^*_{norm} = 7. TRANSP models the plasmas within the full poloidally-asymmetric separatrix boundary. Profiles versus the flux coordinate x (the square-root of the toroidal flux normalized to the ≈98% poloidal flux surface) are shown in Figs. 1-3.

Predictions of NBI-Induced Rotation - TRANSP has been upgraded to predict toroidal rotation velocities from the torques and a specified momentum transport coefficient χ_ϕ. Here we consider the torques on the thermal plasma caused by the NBI. In steady state, this is balanced by viscous losses. Three types of fast ion torques are normally computed by TRANSP. Examples are shown in Figs. 4-5. The JxB torque, which is the reaction of the plasma to the Stix shift [4] (and the banana-trapped analog) of the fast ions when the beam-injected neutrals are ionized, dominates at large radii. The torque of fast ion collisions with the thermal plasma dominates closer to the center. The residual torque transferred to the plasma when the fast ions become thermalized is small relative to the first two. The torque caused by the ripple loss of fast ions is also computed by TRANSP; however an additional assumption for the fraction of this torque that is absorbed by the thermal plasma must be specified. This fraction is estimated to be very small, with the rippled field reacting to most or all the momentum [5]. The ripple field computed for the 20 toroidal field coil interim design

produces small fast ion ripple losses for the monotonic q_ψ plasmas [1,6], but large losses for the RS case. Techniques using ferro-magnetic inserts in the vacuum vessel wall to reduce the ripple field have been proposed [7]. Here the ripple losses for the RS case are ignored.

The NBI is specified as 50 MW of D, injected in the direction of I_p with a tangency radius of 6.5m, from sources elevated 1.65m above the midplane. Twenty-five sources are modeled. Each source represents a rectangle of 4 x 13 beamlets in the conceptual design for the negative ion injection system. The neutral energy is assumed to be either 1MeV (interim design) for the baseline cases, or 150keV to give an extreme example of a low energy alternative. For the 1MeV case, the beam deposition is computed to peak near the plasma center, and to have a broad profile, at 1/3 the peak value, extending past x = 0.8. In steady state, the beam density is centrally peaked. The beam ion - electron heating dominates in the edge for the flat profile case.

TRANSP calculates χ_{ion} and χ_e from the assumed plasma profiles and the computed heat deposition profiles. There is considerable structure in the χ_{ion} profiles for the ITER cases, with values near x = 0.5 around 1 m^2/s for the monotonic cases. The profiles for the RS case were originally computed [3] assuming the transport is reduced, and assuming 100 MW of electron cyclotron heating and current drive instead of the 50 MW of NBI assumed here. Therefore the TRANSP does not compute a consistent χ_{ion} for this case.

In TFTR, the profile of χ_ϕ can be approximated by $\chi_\phi / \chi_{ion} \approx 1.0$ for supershots [8] and L-mode plasmas[9]. Both χ_ϕ and χ_{ion} are very low in the core of RS plasmas with enhanced confinement (ERS) [10]. For simplicity, and easy comparison of the cases, we report results assuming that χ_ϕ is constant. Results for the steady state rotation frequencies assuming χ_ϕ = 1 m^2/s for the flat case with 1MeV are shown in Fig. 4, and for the RS case with 150keV in Fig. 5. We also did runs using the more optimistic assumptions of χ_ϕ = 0.01 and 0.1 m^2/s. The results assuming 1MeV are shown in Fig. 6. For 150keV, the profiles in steady state have similar central values, but are flat to about x = 0.8, so the ω_{ExB} shear in the edge is much larger.

Implications of the Predicted Rotation Frequencies - For the RS case, the Alfven frequency is about 0.2MHz and the rotation frequency corresponding to the ion sound speed is about 5MHz in the center. Even with the optimistic assumption of χ_ϕ = 0.01 m^2/s, the thermal rotation is at a low Mach number.

Locked Modes: Whether the rotation speeds are sufficient to avoid locked modes is difficult to assess since the locked modes have several aspects. The first drags down the plasma

rotation and MHD modes to a halt. Then the stabalizing effects of a conducting structure disappear, unshielding the plasma from field imperfections, causing growth of MHD modes.

Resistive wall modes: Measurements in PBX-M indicate resistive wall modes are avoided if edge rotation frequencies are greater than few % of Alfven rotation frequency and about 10 times the inverse of the L/R time of the wall [11].

Sheared flow: The case of 150keV NBI into the RS plasma with low momentum transport (assuming $\chi_\phi = 0.01$ m^2/s) is predicted to ignite using the IFS-PPPL transport model [12] for χ_{ion} and χ_e. The computed temperature profiles become broader, and the fusion power increases. The TRANSP simulations end when the bootstrap current becomes much larger than the total plasma current. A more self-consistent simulation using $\chi_\phi \approx \chi_{ion}$ has not been done.

Conclusions - These results suggest that NBI-induced rotation could be useful for avoiding locked modes and resistive wall modes. Low energy (≈ 150keV) NBI appears useful for generating sheared flow in the edge. The sheared rotation could be used to grow RS ITER plasmas into ignition with enhanced confinement.

Work supported by US DoE Contract No. DE-AC02-76-CH03073.

References

[1] R.V.Budny, D.McCune, M.H.Redi, *et al.*, Phys. of Plasmas **3**, p. 4583 (1996).
[2] R.V.Budny, G.-Y.Fu, N.N.Gorelenkov, J.Manickam, *et al.*, Proceedings of the 23rd European Physical Society, Kiev, **1**, 55 (Petit-Lancy, 1996).
[3] Available on the internet at http://picard.iterus.org.
[4] T.H. Stix, Plasma Physics **14**, 367 (1972).
[5] R.White, private communication
[6] M.H.Redi, R.J. Goldston, R.B.White, R.V.Budny, *et al.*, Proceedings of the 23rd European Physical Society, Kiev, **1**, 71 (Petit-Lancy, 1996).
[7] M.Onozuka, Internal ITER project memarandum, March 5, 1997.
[8] S.D.Scott, P.H.Diamond, R.J.Fonck, *et al.*, Phys. Rev. Letters, **64**, 531 (1990).
[9] S.D.Scott, V.Arunasalam, C.W Barnes, *et al.*, Phys. Fluids B **2**, 1300 (1990).
[10] F.Levinton, *et al.*, Proceedings of the IAEA Conference, Montreal (1996).
[11] M.Okabayashi, N.Pomphey, J.Manickam, *et al.*, Nucl. Fusion **36**, 1167 (1996).
[12] M. Kotchenreuther, W. Dorland, M.A. Beer, *et al.*, Phys. Plasmas **2**, 2381 (1995).

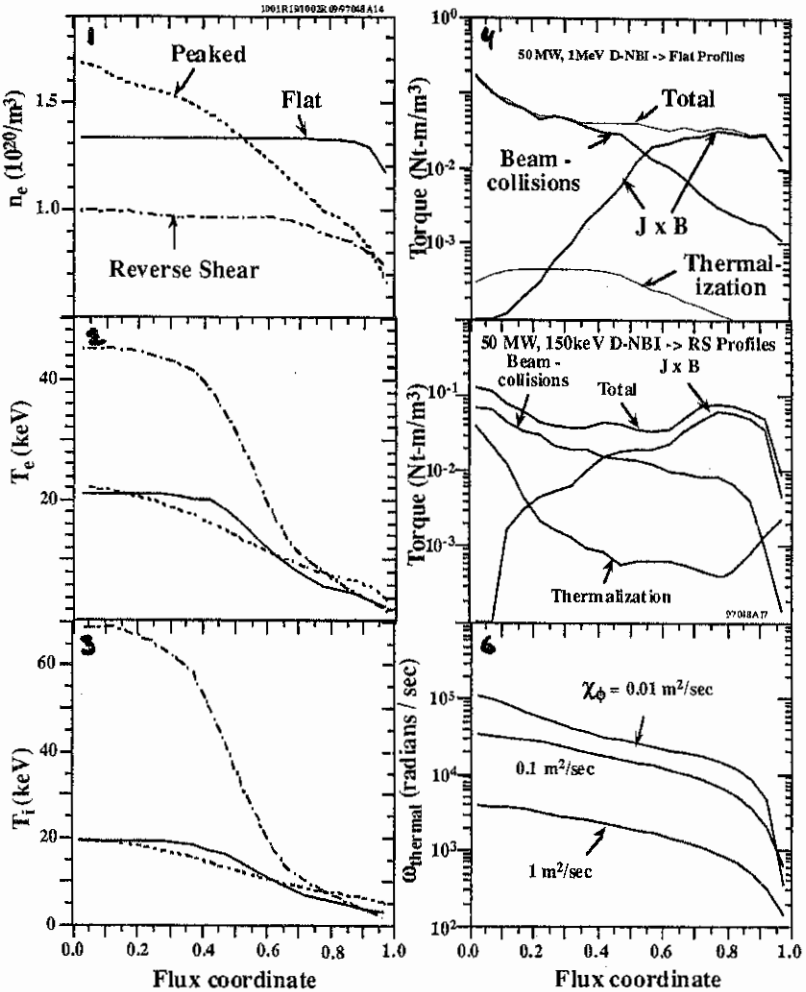

(1-3) Assumed input profiles of three ITER plasmas from the interim design database which produce 1.5 GW Fusion Power; (4-6) Predictions for 50MW D^0-NBI; (4) Torques assuming 1MeV -> Flat profile case; (5) Torques assiming 150keV -> RS case; (6) Rotation frequencies for 1MeV -> RS case assuming different values for χ_ϕ. The rotation frequencies for 150keV are broad with similar central values.

Simulation of ITER discharge rampdown by injection of impurity pellet

V. Yu. Sergeev, V. M. Timokhin, V. A. Segal and **B. V. Kuteev**
State Technical University, Politeknicheskaya 29, 195251 St. Petersburg, Russia

1. Introduction.

Use of pellet injection for the tokamak plasma quench or rampdown is widely considered [1-5]. Injection of a high-Z impurity pellet provides powerful energy losses but may stimulate runaways [2,3]. Injection of large low-Z impurity or hydrogen pellets [3] does not generate runaways but requires a large abundance of the electron density so that it may initiate or accelerate a plasma major disruption instead of mitigating it.

Here, development of the zero-dimensional model of Ref. [1] and recent results of 1D transport simulations of the ITER plasma quench by means of injection of high-Z impurity pellet alone and in combination with deuterium ones are presented.

2. Model.

The following set of 1D equations for the electron and impurity density (1), energy balance (2), Ohm's law (3) and a Maxwell equation for the toroidal electric field E (4) was solved numerically:

$$\frac{\partial n}{\partial t}+\frac{1}{r}\frac{\partial}{\partial r}(r\Gamma)=n_{imp}\frac{\partial Z_{imp}}{\partial t},\quad \frac{\partial n_{imp}}{\partial t}+\frac{1}{r}\frac{\partial}{\partial r}(r\Gamma_{imp})=0 \qquad (1)$$

$$\frac{3}{2}\frac{\partial nT}{\partial t}+\frac{1}{r}\frac{\partial}{\partial r}\left(r\left[q+\frac{5}{2}\Gamma T\right]\right)=n\left(Q_{fus}+Q_{oh}-Q_{imp}-Q_{br}\right) \qquad (2)$$

$$j=j_{ra}+\sigma E \qquad (3)$$

$$\frac{\partial j}{\partial t}=\frac{c^2}{4\pi}\frac{1}{r}\frac{\partial}{\partial r}r\frac{\partial E}{\partial r} \qquad (4)$$

Here, $n=n_{DT}+2n_{He}+Z_{imp}n_{imp}$ - electron density; $\Gamma=-D\frac{\partial n}{\partial r}-nv_p$, $\Gamma_{imp}=-D\frac{\partial n_{imp}}{\partial r}-n_{imp}v_p$ $q=-\chi\frac{\partial T}{\partial r}$ -particle, impurity and heat fluxes; Q_{fus}, Q_{oh}, Q_{br} - power of the alpha-particle heating, Ohmic heating and bremsstrahlung losses. For the impurity line radiation Q_{imp} and averaged charge of impurity ions Z_{imp}, the coronal equilibrium model [6] was used. The Alcator-like scaling for transport coefficients $\chi=10^{17}/n_e$, $D=\chi/2$ was chosen. The pinch velocity v_p was calculated to reproduce a steady state profile of the electron density for the BBP regime of ITER (R=811 cm, a=300 cm, B= 5.7 T, I_{pl}=24 MA, <T>=11 keV, $<n_e>=1\cdot10^{14}$ cm^{-3}) [7]. The equal temperature T for all plasma species were assumed. The current density j was calculated using the Spitzer conductivity law and the current produced by runaway electrons I_{run} was calculated using the Parail-Pogutse approach [8] and the 'avalanching effect' [9].

For a reason to examine the model we have simulated the task of Ref. [3] where an evolution of plasma parameters after injection of 1% Xe (uniform distribution of Xe density) into the BPP regime was considered . The simulated plasma profiles at t= 30 ms after Xe injection were similar to those obtained in Ref. [3].

3. Results of simulations and discussion.

First, we modelled the injection of one Kr pellet (1 cm size, 8 km/s velocity) into the BPP regime. The pellet ablation rate and perturbations of plasma parameters calculated using the model of Ref. [1] are shown in Fig. 1. With these initial conditions, further evolutions of plasma temperature, density and current produced by runaway electrons are shown in Fig.2. The plasma temperature quickly decreases in the region of pellet deposition. It results in displacement of the plasma current out of this region to the hot narrow region at the plasma core. The runaway current is generated nearby this region where the plasma density is not large but the temperature is small. The temporal behaviour of the total plasma thermal W_{th}, magnetic W_m energies and the runaway current I_{run} for this case are shown in Fig. 3. The thermal quench lasted about of 30 ms and then the runaway current was generated up to the plasma current value I_{pl} because no losses of runaways were taken into account in the model.

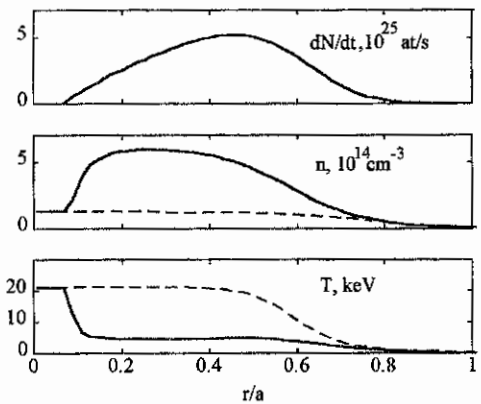

Fig. 1. Perturbations of plasma density n and temperature T (solid lines) after injection of the Kr pellet injected into the BPP regime of ITER (dashed lines).

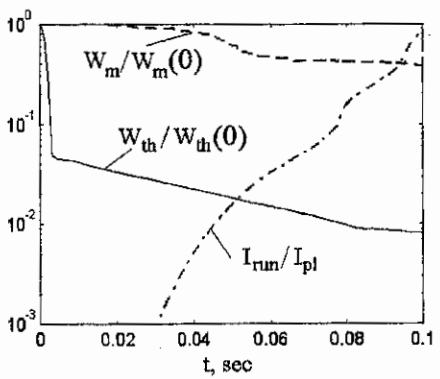

Fig.3. Behaviour of the thermal, magnetic energies and the runaway current after injection of one Kr pellet into the BPP regime.

It is known that generation of runaway can be suppressed by increase of plasma density [3]. With this goal we have modelled additional injection of several deuterium pellets (each pellet had 10 mm size and 100 m/s velocity). First deuterium pellet was injected at t = 40 ms after the injection of the Kr pellet when the runaway current was about of 1% of the total plasma current I_{pl} (see Fig. 3). This pellet deposited

deuterium into the region with runaway generation nearby the plasma centre. The temporal behaviour of the total plasma thermal W_{th}, magnetic W_m energies and the runaway current in this case are shown in Fig. 4. The first pellet suppressed runaway's generation until t= 70 ms when it started again

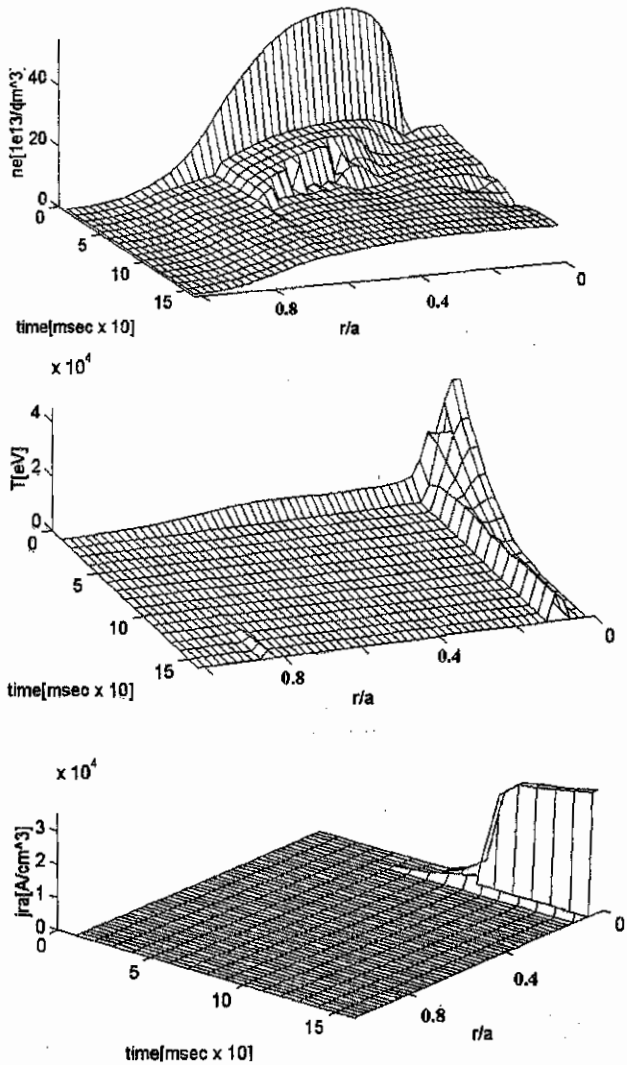

Fig.2. Behaviour of the density, temperature and density of the runaway current after injection of one Kr pellet into the BPP regime.

The second deuterium pellet was injected at this time. After these two injection, a redistribution of the plasma current profile was observed. The current density diffused to the periphery due to cooling of plasma centre by deuterium pellet injections. To initiate the current quench at the plasma periphery, the third deuterium pellet was injected at t = 250 ms. As a result, the total thermal and current quenche were occurred at about of 400 ms. The current of runaways was less then 3% of the total plasma current (see Fig. 4).

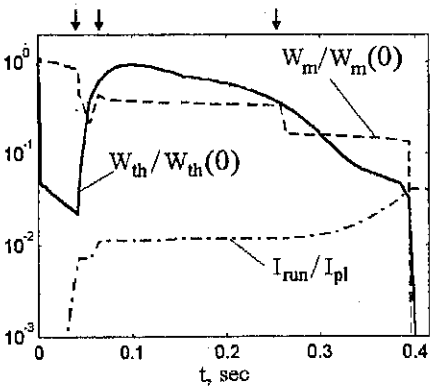

Fig.4. Behaviour of the thermal, magnetic energies and the runaway current after injection of one Kr pellet into the BPP regime and the further injection of deuterium pellet (10 mm size, 100 m/s). Times of the hydrogen pellet injections are shown by arrows.

4. Summary.

The one dimensional model for describing of the ITER plasma quench by means of injection of pellets have been developed. The results of simulation show that injection of the single Kr pellet with 10 mm size and 8 km/s velocity can provide a fast thermal quench (30 ms) before the generation of the runaway current that starts to rise near the plasma core which the pellet does not reach. In the vicinity of this zone the runaway current may grow up to the plamsa current.

Nevertheless, suppression of runaway's generation can be caused by injection of several deuterium pellets after the Kr pellet injection. For instance, we considered injection of three deuterium pellets of 10 mm size and 100 m/s velocity at 40, 70 and 250 ms after the Kr pellet injection correspondingly. This has allowed us to suppress the runaways current and to quench plasma during 0.4 s.

References.

[1] B.V. Kuteev, V.Yu. Sergeev, S. Sudo. Nucl. Fusion **35** (1995) 1167.
[2] V.Yu. Sergeev *et al.* Proc. of 23d EPS conf., Bournemouth, 1995, Part.3 p.245.
[3] S.Putvinski *et al.* To be published in the J. Nucl. Mat.
[4] G. Pautasso *et al.* To be published in the Nucl. Fus.
[5] R. Yoshino *et al.* Nucl. Fusion 33 (1996) 295
[6] R. Clark, J. Abdallah and D. Post, J. Nucl. Mat. **220** (1995) 1028.
[7] Physics and plasma operation studies. ITER Report S CA4 RE2, January 1994
[8] Parail V.V. and Pogutse O.P. in: Reviews of plasma physics, Vol.11 (Consultants Bureau, New York, 1986) p.1
[9] Jayakumar R., Fleischmann H.H. and Zweben S.J., Physics Letters A **172** (1993) 447

ITER Poloidal Field Scenario, Error Fields and Correction Coils

Y.Gribov, S.Gerasimov, P.L.Mondino, A.Portone, J.Wesley - *ITER Joint Central Team*
R.Bulmer, D.Humphreys, S.Jardin, C.Kessel, R.LaHaye, J.Leuer, L.Pearlstein-*US Home Team*
V.Belyakov, N.Doinikov, B.Mingalev, Y.Puzinovich, A.Simakov, V.Vasiliev - *RF Home Team*
H.Fugjieda, T.Shoji, K.Shinya, I.Senda - *JA Home Team*
T.Hender, B.Lloyd - *EU Home Team*

1. The ITER Poloidal Field system

The ITER Poloidal Field (PF) system will be capable of operating in three main modes: Nominal Pulse Operational Mode (21 MA, 1000 s of burn), Long Pulse Operational Mode (2000 s of burn) and "Steady-State" Operational Mode (about 10000 s of burn). Moreover the PF system will support: High Current Operational Modes (24 MA) and Low Current Operational Modes (10-15 MA for physics studies).The design of the PF system (particularly the maximum current in the PF coils and the magnetic field on them) is driven by requirements for the first mode (nominal 21 MA). For this mode the PF system must be capable of operating over a specified range of plasma pressures, characterized by a range of "beta-poloidal" ($0 \le \beta_p \le 1.2$) and current profiles, characterized by a range of internal plasma inductance ($0.7 \le l_i(3) \le 1.1$). Other scenarios should not affect peak coil currents and voltages, as well as the maximum power.

The ITER PF system as described in the Detail Design Report (DDR) issued in 1996 is reported in [1]. In 1997 the PF system was slightly modified, to allow all PF coils to use NbTi superconductor. For this purpose, the DDR coils PF2 and PF7 were each split into two coils to reduce the magnetic field on the superconductor. The other PF coils are identical to the old system. The PF coils for the Final Design Report (FDR) are shown in Fig. 1. In this system, the Central Solenoid (CS) uses Nb_3Sn superconductor, whereas the PF coils use NbTi.

Error field correction coils are also part of the ITER PF system. To avoid locked-modes (and associated disruptions) in ITER, the amplitude of the helical error field modes normal to the q=2 surface (particularly the m=2, n=1 mode, where m and n are the poloidal and toroidal wave numbers respectively) should be limited to approximately 10^{-5} relative to the toroidal magnetic field. Active correction coils are being implemented on ITER to reduce error fields to this level. To provide the mode control flexibility needed to meet presently foreseen requirements, the correction system consists of three sets of coils (see Fig. 2). It is able to reduce simultaneously three helical modes (2,1), (3,1) and (1,1).

2. Operational scenarios

The nominal inductive 21 MA mode of operation has a scenario of 7 phases lasting in total approximately 2000 s (see Fig. 3). These are: Initial Magnetization of the PF system, Plasma Initiation, Current Ramp-up, Additional Heating and Burn Ignition, Burn, Burn Termination and Current Ramp-down.

At Initial Magnetization (IM) the currents in the PF coils are determined to maximize the poloidal magnetic flux and reduce the "stray" poloidal field over the desired breakdown region at plasma formation. Its center is located at R≈10.5 m and Z≈1.5 m. At IM for the reference breakdown, the PF system produces positive magnetic flux of about 209 Wb. Current in the PF coils at IM have been chosen using a dynamic analysis of the plasma initiation to minimize the magnetic flux loss before breakdown. After Initial Magnetization, a negative voltage up to 15 V per turn is applied to the CS, a positive toroidal electric field E arises and penetrates the conducting structures in about 1-2 s. This electric field provides breakdown and plasma initiation by Townsend avalanche. To increase the "robustness" of the plasma initiation, Electron Cyclotron Heating (up to 3 MW) will be used. Delay of breakdown leads to a loss of magnetic flux available for the plasma scenario. The flux loss depends on the details of plasma initiation (e.g. value of the vertical magnetic field in the breakdown region at IM and waveforms of voltage applied to the PF coils). The maximum flux at breakdown is about 197 Wb.

At the end of the current ramp-up phase which lasts about 150 s, a full-size diverted plasma with the nominal current is obtained. Up to about 15 MA, the plasma is attached to the outer limiter and the PF system provides plasma aperture expansion consistent with the plasma current rise. This strategy avoids a flat current profile (l_i< 0.7) at X-point formation, which would require excessive currents in PF9, PF8 and PF6. Moreover, this "onion-skin" current rise strategy keeps the plasma in the stable region of the (q-l_i) plane (where q is the safety factor at the 95% flux surface). Evolution of the plasma configuration during current ramp-up is shown in Fig. 4.

When the plasma current reaches its flat top value (21 MA), additional heating power up to 100 MW will be applied for about 50 s to achieve the ignition condition. As a result, β_p will increase up to β_p=0.9. High control accuracy of the separatrix is required during this and the following phase (burn), to prevent damage of the first wall and divertor structures. Moreover, ±50 mm accuracy of the separatrix position near the Ion Cyclotron Heating & Current Drive antenna is required for effective plasma heating.

The burn duration (t_{burn}) must be about 1000 s. The resistive flux consumption $\Delta\Psi_{burn}$ depends on the plasma loop voltage V_{burn} : $\Delta\Psi_{burn} = V_{burn}\, t_{burn}$. The value of V_{burn} depends on the plasma temperature, impurity content and profiles of plasma parameters. According to present estimates, $V_{burn} \approx 0.06$ V. The value of $\Delta\Psi_{burn}$ is limited by the maximum field on the CS, which at the End of Burn (EOB) is 12.75 T. Depending on details of plasma initiation, 80-90 Wb of magnetic flux are available for burn.

At the EOB, a controlled termination of the fusion burn must be started. The plasma will be cooled in about 100 s prior to the current ramp-down to avoid large negative currents at the plasma edge. The upper limit of the ramp-down rate is determined mainly by the minimization of negative currents in the plasma boundary (to avoid too-high l_i), arising due to the negative voltage applied to plasma. Taking into account that a post-burn plasma has a longer skin penetration time than the plasma during ramp-up, the ramp-down time (about 200 s) will be longer than the ramp-up time.

Alternative scenarios are also being analyzed with the FDR PF system. As an example, Fig.5 shows magnetic configuration of the 12 MA plasma at end of the second heating phase of the reverse-shear scenario ("Steady-State" Operational Mode).

3. Error fields and correction coils

Helical error fields (m=1,2,3, n=1) in ITER are expected to arise primarily from misalignment of the current centerlines of the Toroidal Field (TF) and PF coils owing to coil manufacturing and installation and assembly positioning tolerances. The dimensional tolerance analysis of the coils taking into account anticipated deviation of the coil centerlines from the nominal position and shape, gave the following value of the error field relative to the toroidal magnetic field (5.7 T): CS and PF coils: 7×10^{-5}, TF coils: 3×10^{-5}. The error field due to TF and PF coil joggles and busbars is negligible ($\leq 10^{-5}$) in comparison with what is expected from the coils. The error field from ferromagnetic inserts in the vacuum vessel due to errors in the shape of the vacuum vessel is also negligible, if the error in the vessel shape (n=1 mode) is about 10 mm. As far as the neutral beam injectors are concerned, a combined magnetic shielding (passive and active) will be used to reduce the injectors error field in the plasma region to an acceptable level. Design of other ITER elements (e.g. a test blanket module containing ferromagnetic materials) should be such not to create an error field higher than 10^{-5}. The resultant error field from all sources in ITER has been estimated to be below about 10^{-4}.

To reduce the error field to the acceptable level (10^{-5}), a system of active correction coils will be used. The Correction Coil (CC) system consists of three sets (see Fig. 2): Top coils with maximum current 45 kA, Side coils with maximum current 150 kA and Bottom coils with maximum current 240 kA. Top and Bottom coils have four sections in each set. The side set has 8 coils with series connection of two adjacent coils. Opposite sections in each set are connected antiseries (to produce a n=1 helical component of the magnetic field). Each set has two power supplies. With the present current capacity of the coils and depending on the phase (sources) of the error field, the CC system is able to correct error fields between 8×10^{-5} to 20×10^{-5}.

Further analysis is required in the area of error field diagnostics and control algorithms.

Reference

[1] M.Huguet and the ITER Joint Central Team and Home Teams, "ITER Magnets and Plasma Control", IAEA-CN-64/F-4, 16th IAEA Fusion Energy Conference, Montreal, Canada, 7-11 October 1996.

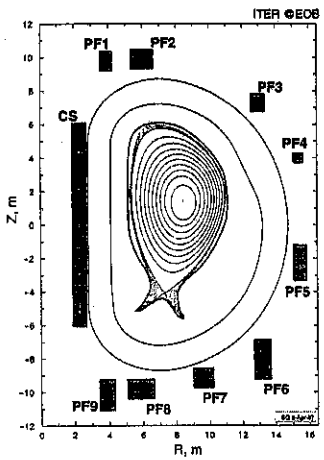

Fig. 1: ITER PF coils

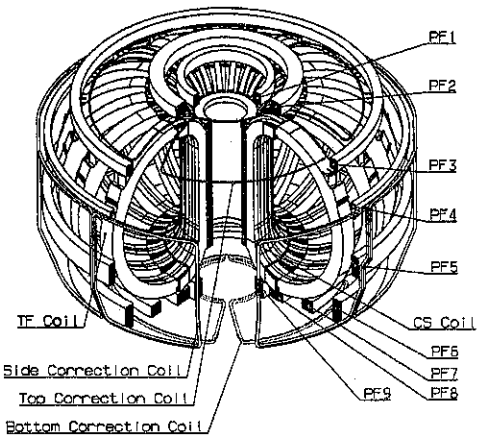

Fig. 2: ITER Correction coils

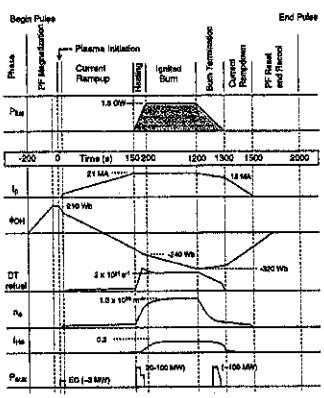

Fig. 3: Nominal 21 MA scenario

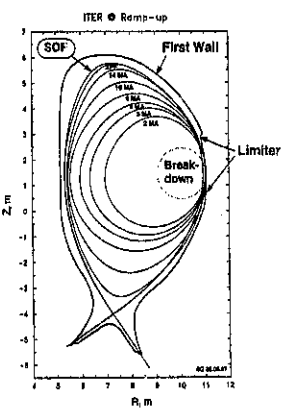

Fig. 4: Plasma current ramp-up

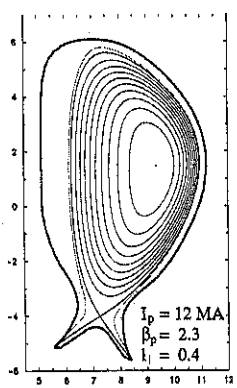

Fig. 5: Reverse-shear scenario at the end-of-heating, phase 2.

Results from 2D radiation magnetohydrodynamics calculations of the interaction of ITER disruptive plasma with the slot divertor

S. Pestchanyi[1], H. Würz[2], B. Bazylev[3], F. Kappler[2], I. Landman[1]

1 Troitsk Institute for Innovation and Fusion Research, 142092 Troitsk, Russia
2 Forschungszentrum Karlsruhe, INR, Postfach 3640, D-76021 Karlsruhe, Germany
3 Lykov Institute of Heat and Mass Transfer, Minsk, Belarus

1. Introduction

In evaluating the lifetime of ITER plasma facing components (PFC) against not normal heat loads credit is taken from the existence of a plasma shield which effectively protects the wall from excessive evaporaton [1]. The plasma shield formed from vaporized PFC material though beneficial for the PFC could become a potential threat for the tokamak because of possible penetration of the impurity ions into the central plasma [2].

For the analysis of the ITER slot divertor the 2D radiation MHD code FOREV-2 is developed. The paper describes recently performed improvements in the numerical scheme of the 2D radiation transport and in increasing the computational speed of FOREV-2 by one order of magnitude and discusses latest results of modelling of hot plasma wall interaction for the ITER slot divertor.

2. FOREV-2 code improvements

FOREV-2 based on the method of large particles [3] is a 2D-MHD code with a 2½D MHD model which takes into account that the main component of the magnetic field is in the z (toroidal) direction. FOREV-2 uses a Lagrangian and an Eulerian mesh. At the beginning of each time step the Lagrangian and the Eulerian meshes coincide. After each time step all physical values are redistributed from the Lagrangian to the fixed Eulerian mesh.

For ITER relevant conditions typically 2000 meshes with nonuniform grid for the MHD part and minimum 25 frequency group opacities for the radiation transport part are needed. With typical time step sizes of the order of 10^{-10} - 10^{-11} s those 2D calculations require extensive CPU times at workstations. For routine 2D calculations thus a drastic increase of the time step size is required. For this the characteristic Alfen velocity being inversely proportional to the density of the background plasma has to be decreased but without increase of the background density (typical value 10^{13} - 10^{14} cm^{-3}). This can be achieved by deviding the mesh space into the 2 regions with target plasma (TPR) and background plasma (BGR) and introducing in the Lagrangian time step a larger mass for the particles of the background plasma.

Despite the related decrease of the Alfen velocity in the BGR equilibration of magnetic field pressure and background plasma pressure by ion sound propagation remains much faster than comparable processes in the TPR. With this procedure computational speed increases in FOREV-2 by a factor of up to 30.

Originally in FOREV-2 a modified 2D forward reverse method (MFR) based on the assumption of isotropy of the radiation flux inside the meshes and at the mesh boundaries was used for calculation of the radiation transport. Isotropy of radiation fluxes is only valid rigorously for optically thick plasma. The plasma shield in its es-

sential parts is optically thick only for line radiation but optically thin for continuum radiation. To account for this situation and for calculation of angular dependent leakage radiation fluxes an improved version of the 2D forward reverse method (IFRM) was developed adopting and generalizing a method developed for 1D radiation transport [4]. This method uses information on the mean cosines of the radiation flux at the mesh boundaries as obtained from 2D S_N calculations [5]. As the 2D S_N method is about a factor of 20 more time consuming than the MFR method the following compromise was adopted: once per 500 time steps mean cosines are calculated with 2D S_N, new IFRM radiation fluxes are calculated once per 20 time steps.

After implementation of both improvements into FOREV-2 typical CPU times for 2D R-MHD calculations with 10000 meshes, 24 frequency groups and physical time up to 100 μs were 25 h at a RS-6000 work station. Thus now for the first time it became possible to perform routine 2D calculations with up to 70 opacity groups and to study the influence of the number of frequency groups and of Planck and Rosseland opacities on target erosion, on angular distribution of lateral leakage radiation fluxes and on side wall evaporation. Moreover the MHD expansion of the bubble of evaporated impurities in the divertor slot can be modelled.

FOREV-2 results with 2D radiation transport using MFR and IFRM are shown in Figs 1 and 2 for a perpendicular graphite target and a hot magnetized plasma of 10 MW/cm^2 with Gaußian profile of half width of 5 cm along (B_x, B_y, B_z) = (0.5 T, 0, 5 T). The computational region of 300 x 20 cm^2 was covered by 60 x 20 meshes nonuniformly distributed in x- and uniform in y-direction. Rosseland opacities with 24 frequency group optimized groups were used. With MFR lateral radiation fluxes are overestimated resulting in larger side wall erosion and in broadening of the erosion profile at the target. In total the eroded mass is a factor of 2 less for the 2D-IFRM radiation transport.

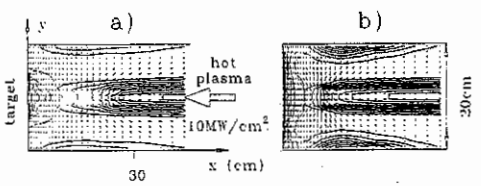

Fig.1. Comparison of density distribution and radiation flux at 100 μs a) IFRM and b) MFR.

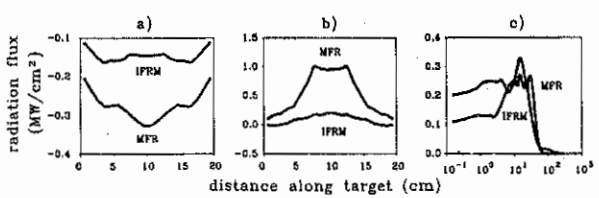

Fig.2. Comparison of radiation fluxes a) to the wall, b) x-component of radiation fluxes at 20cm from target, c) lateral radiation fluxes

3. Results of 2D modelling

3.1 Tilted targets

FOREV-2 was used to analyse the situation with targets tilted in the poloidal plane. An unsymmetrical power density pofile across the SOL was used. The power density profiles and the corresponding erosion curves are shown in Fig. 3. The differences in erosion can be understood from Fig. 4. In both cases target plasma is flowing along the tilted target in upward direction. Thus if the sharp rise of the power density is at the lower edge (Fig. 3a) then the upward flow results in a continuous depletion of plasma at the position of maximum power density and thus in higher erosion at this position.

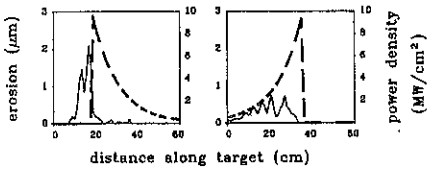

Fig.3. Power density profiles along inclined target (dotted lines) and erosion curves (solid lines).

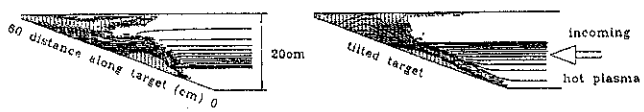

Fig.4. 2D density and plasma velocity of plasma shield at 100 μs.

3.2 Plasma shield modulation

The periodicity of the erosion profile of Fig. 3 indicates an evolving density modulation in the plasma shield triggered by an incidental density fluctuation. An analytical model describing exponential growing of the modulation amplitude due to direct heating by the impacting hot plasma was presented in [2] describing the early situation of interaction. Somewhat later after plasma shield formation erosion is determined by radiative energy transfer to the target.

Analysis of this situation shows that also in this case there is obtained an exponential growing of the modulation amplitude h(t) according to

$$h(t) = h_o \exp\left[\frac{2\pi I_p}{\rho H_{av}} B\kappa t\right]$$

with $\pi I_p = \sigma T^4$ the radiation intensity
ρ density of plasma shield
Hav specific heat of vaporization
B constant of order of 1
κ opacity for absorption

The analytic consideration, thus confirms that modulation of erosion for tilted targets and inclined impact of hot plasma exists for direct heating and radiative energy

transfer. From FOREV-2 calculations the modulation amplitude (maximum to minimum) for a tilting angle of 20° was obtained to be a factor of 5 after 100 μs. The modulation wavelength is proportional to the mean width of the plasma shield.

3.3 Impurity transport in the slot divertor

The plasmal shield ions are impurities moving upward in the ITER slot divertor towards the x-point. The MHD motion of these impurities was studied with FOREV-2 for a perpendicular and a tilted graphite target. For the incoming hot plasma a Gaussian distributed power density profile with peak power density of 1 MW/cm^2 and a half width of 5 cm was assumed. The time duration of the heat load was 40 μs. These conditions simulate a powerful ELM. Interactions of the impurity ions with the neutrals from the gaseous divertor and with the stationary SOL plasma were not taken into account in these first calculations.

The movement of the plasma shield in the (xy) plane along and across the magnetic field lines with B_x = 0.5 T and B_z = 5 T is shown in Fig. 5 for a perpendicular target at x = 0. Early in time there is an effective diffusion of cold plasma close to the target across B_z which stops the impurity expansion. After about 400 μs formation of an impurity plasma bubble of temperature below 1 eV is completed. This bubble driven by pressure gradients moves upward in the slot at velocities of about 5 x 10^5 cm/s as is seen from Fig. 6. About 1.1 ms after switching off heating the density of impurities reaches a value of 4 x 10^{15} cm^{-3} at a distance of 2 m from the target. During a time period of 0.5 ms the impurity flux at this position remains at a level of 2 x 10^{21} ions/cm^{2}s.

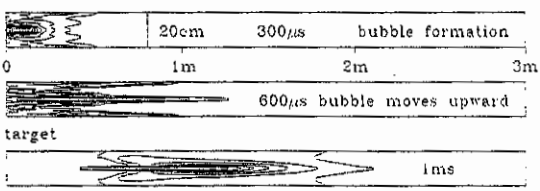

Fig.5. Time evolution of plasma density in the divertor slot showing formation of impurity bubble and its upward movement

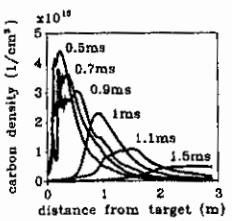

Fig.6. Time evolution of density profiles in the slot center

4. References

[1] A. Sestero, Nucl. Fusion 35+8, 1995.
[2] H. Würz et al., 19th SOFT Sept. 16 20, 1996, Lisbon Portugal.
[3] O.M. Belozerkovsky, Y.M. Davidov, "The method of large particles in gas dynamics". M. Nauka 1982 (in russian).
[4] I.V. Nemchinov, Appl. Math and Mech 34, 4 706 - 722, 1970.
[5] B. Bazylev, "The 2D S_N radiation transport code TWORAD", to be published as FZK report.

Runaway Generation during Disruptions in ITER Taking Account of Particle Trapping

M. Schittenhelm
Max-Planck-Institut für Plasmaphysik - EURATOM Association,
D-85740 Garching

Introduction: In a fusion reactor relevant plasma, like in ITER, a noticeable part of the electromagnetic energy of the plasma can be transferred to kinetic energy of runaway electrons which are generated during disruptions. In ITER, the dominating process is the runaway generation by close collisions (secondary or avalanche like generation): A runaway is scattered by a thermal electron and transfers a small part of its kinetic energy to this electron. If the transferred energy exceeds the critical energy $W_C = \frac{e^3 n_e \ln\Lambda}{4\pi\varepsilon_0^2 E}\sqrt{Z_{eff}+5}$ for runaway generation, the thermal electron will become a new runaway [1]. In general, an additional condition for the occurrence of runaways in tokamak is that the toroidal electrical field is larger than the critical field [2, 3] $E_C = \frac{e^3 n_e \ln\Lambda}{4\pi\varepsilon_0^2 m_0 c^2} \approx 0.05$ V / m for typical parameters in ITER. After a thermal quench in ITER, the electric field exceeds this critical field by two or three orders.

Secondary runaway generation: The rate for secondary generation is given by

$$\left(\frac{dN_r}{dt}\right)_{2.\,\mathrm{Gen.}} = N_r v_r n_e \sigma(W_C < \Delta W < E_{in} - W_C)$$

with the velocity v_r of the runaways (with the kinetic energy $E_{in} = (\gamma-1)m_0c^2$) and the electron scattering cross-section σ for an energy transfer $\Delta\, m_0c^2$ is given by $v_r = c\sqrt{1-\left(1+\left(\gamma^2-1\right)^{-1}\right)^{-1}}$

and $\sigma\left(\Delta_1<\Delta<\Delta_2\right) = \frac{2\pi r_e^2}{\gamma^2-1}\left[\frac{2\gamma^2}{\gamma-1-\Delta}\frac{(\gamma-1)\gamma^2}{\Delta(\gamma-1-\Delta)}+\frac{2\gamma-1}{\gamma-1}\ln\frac{\gamma-1-\Delta}{\Delta}+\Delta\right]_{\Delta_1}^{\Delta_2}$.

"Runaway trapping": Since the necessary energy transfer for runaway generation (some keV) is small compared with the kinetic energy of the scattering runaway (some 10 MeV), the scattering angle for the thermal electron in the labour frame is large and the thermal electron would become a new runaway with a perpendicular momentum much higher than its parallel momentum. Considering the formula for the scattering angle θ_2, the ratio between the perpendicular and parallel velocity is given by $\frac{v_\perp}{v_\parallel} = \tan\theta_2 = \tan\arccos\frac{(\gamma+1)\Delta}{\sqrt{\gamma^2-1}\sqrt{(\Delta+1)^2-1}}$.

Many of these new runaways are trapped and are hence not accelerated further in spite of the high loop voltage after the thermal quench. The condition for particle trapping is [4]

$$\left|v_\parallel - \frac{v_E}{\Theta}\right|^2 < 2\frac{r}{R}\left(v_\perp^2+2\left(\frac{v_E}{\Theta}\right)^2\right)\left(1-\frac{1}{c^2}\left(\frac{v_E}{\Theta}\right)^2\right) \text{ with } v_E = \frac{E}{B} \text{ and } \Theta = \frac{B_p}{B_t}.$$

Due to the relatively high electron velocity ($v_r > 0.01c$), the term v_E/Θ is very small compared to the electron velocity ($v_E/\Theta < 10^{-6}c$) and can be neglected. Hence the limit for particle trapping simplifies to the well-known result: $\frac{v_\parallel}{v_\perp} < \sqrt{2\frac{r}{R}}$.

The lowest energy transfer at which the new runaway is not trapped depends on the energy of the scattering runaway and the considered position in the plasma due to the spatial variation of the strength of the magnetic mirror.

Starting with $\frac{v_\perp}{v_\parallel} = \tan\arccos\theta_2 = \tan\arccos\frac{(\gamma+1)\Delta}{\sqrt{\gamma^2-1}\sqrt{(\Delta+1)^2-1}} = \sqrt{\frac{1}{2}\frac{R}{r}}$, the equation for the lowest energy transfer is: $\Delta_{tr} = -2 / \left(1 - \left(\frac{\sqrt{\gamma^2-1}}{(\gamma+1)} \cos\arctan\sqrt{\frac{1}{2}\frac{R}{r}} \right)^{-2} \right)$.

There are new two critical energies for the secondary generation that must be considered for the calculation of the cross-section. To get the rate for secondary runaway generation, the differential cross-section must be integrated between the lowest and the highest energy transfer that results in a new runaway. The lower boundary is the maximum of the two critical energies $\Delta_1 = \max\left(\Delta_{tr}, W_c/m_0c^2\right)$. Due to the scattering with identical particles and the resulting symmetry in the formulas, the upper boundary is the kinetic energy of the scattering electron minus the maximum of the two critical energies $\Delta_2 = \gamma - 1 - \max\left(\Delta_{tr}, W_c/m_0c^2\right)$.

The secondary generation rate at the plasma radius r is:

$$\left(\frac{dN_r}{dt}\right)_{2.\,\mathrm{Gen.}} = N_r n_e c \sqrt{\left(1+\left(\gamma^2-1\right)^{-1}\right)^{-1}}\, n_e \frac{2\pi r_e^2}{\gamma^2-1}\left[\frac{2\gamma^2}{\gamma-1-\Delta} - \frac{(\gamma-1)\gamma^2}{\Delta(\gamma-1-\Delta)} + \frac{2\gamma-1}{\gamma-1}\ln\frac{\gamma-1-\Delta}{\Delta} + \Delta\right]_{\Delta_1}^{\Delta_2}$$

To get the growth rate of the total runaway population, it is a good approximation to assume that the energy spectrum of the runaways decreases exponentially [1] like $\exp(-E_{kin}/15\mathrm{MeV})$ After the integration of the generation rate over the runaways energies with this assumption the resulting growth rate only depends on the electric field and the strength of the magnetic mirror. In Fig. 1 the results are plotted versus the minor plasma radius for the electric fields 2, 10, 40 [V/m] (dotted lines). Due to the large cross-sections for low energy transfer, large scattering angles are dominating and many of the generated runaways are trapped and are not considered in the plotted rates that strongly decrease outside the plasma centre.

The scattering of the trapped runaways with the thermal background plasma results in both a momentum loss (thermalization) and a momentum transfer from their high perpendicular momentum into parallel momentum (detrapping). If the trapped runaways leave the area of trapping, before they slow down below the critical energy, they are accelerated and become free runaways again. Under the assumption that momentum transfer to the parallel momentum is a factor two faster compared to the momentum loss to the background plasma, the generation rates are in good agreement (better than 5%) with Monte-Carlo and Fokker-Planck calculations presented in [5].The resulting growth rate is shown in Fig. 1 (solid lines). In spite of the strong detrapping the resulting growth rate shows a radial dependence and is approximately a factor two smaller at the plasma boundary compared to the centre.

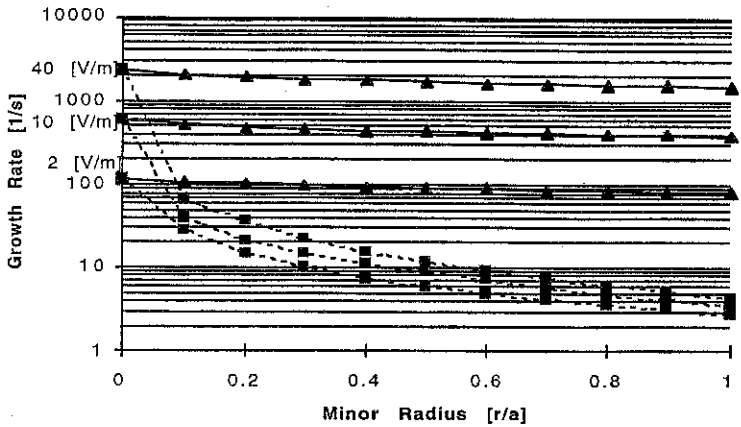

Fig. 1: The secondary generation rate vs. the normalised plasma radius. The generation rates are shown for three different electric fields. Since most runaways are generated as trapped particle, the generation rate strongly decreases outside the plasma centre (dashed line). Due to thermal scattering, most trapped runaways change their perpendicular momentum to parallel momentum before they thermalize and become free runaways again. The effective generation rate (solid line) shows an only weak radial dependence

Calculation of the resulting runaway current: For calculating the growth of the runaway population during the current quench, the following model is considered. The initial temperature profiles are fixed during the calculation. No power balance equation is considered. The initial plasma current decays according to the induction law. The initial number of runaways is zero. The Dreicer and the secondary runaway generation (presented above) are considered in the calculation. The generated runaways approximately move with the velocity of light and carry the resulting runaway current virtually without resistivity. Due to the low plasma temperature, flux diffusion must be taken into account. The numerical calculations were done with the ASTRA Code [6]. Starting with the fixed profiles of temperature and density of the background plasma as well as the initial value for the plasma current, the plasma current density, the plasma equilibrium, the resulting electric field and runaway population are calculated self-consistently. No plasma movement is considered in the calculations.

Results: The resistivity of the plasma strongly depends on the temperature and the Z_{eff}. At low resistivity the current decay needs some seconds and the resulting loop voltage is so low that the current resistively decays before a large number of runaways are generated. Considering a fast current decay due to disruption mitigation, a huge runaway population ($>10^{19}$) builds up and carries up to 100% of the initial current. A typical example is shown in Fig. 2. In case of disruption mitigation by killer pellets, a low plasma temperature of 10 eV and Z_{eff} = 5 could be assumed. In spite of the weak radial variation of the generation rate, the current density carried by the runaways after many e-foldings becomes comparable with the resistive current density in the centre although the total number of runaways is small. The loop voltage in the centre starts to break down. Due to the large flux diffusion at low temperature, the runaway current density can exceed the current density of the initial plasma current by a factor of 3 or more in the centre (Fig. 2 b). The current density in the outer regions decreases

further until the complete plasma current is carried by the runaways and the electric field breaks down in the entire plasma. Due to the strong current peaking, the central q-value quickly falls below one and reaches the stationary value of 0.23, when the current peaking saturates. The radius of the q=1 surface extends to 0.5 m (r/a=0.2). Due to the large area with q<1 (compared to the gyro-radius of the runaways), the development of instabilities should be considered in further investigations.

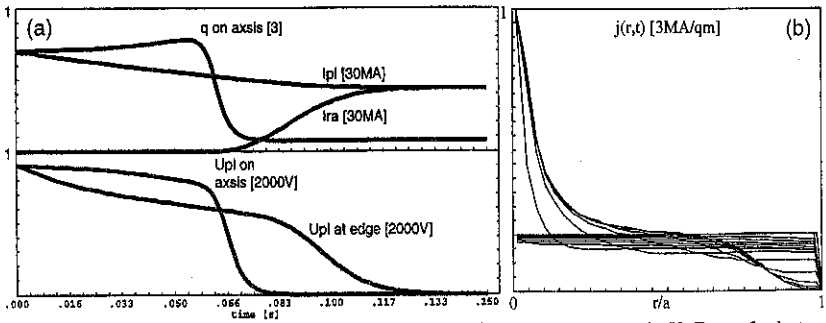

Fig. 2: Development of the runaway current I_{ra}. Electron and ion temperature are 10 eV, Z_{eff} = 5, electron density is 1.5 10^{20} m^3. The initial current is 21 MA, the resulting loop voltage is 1813 V. (a) The time histories show the total plasma current, the runaway current, the resulting q-value on the axis and the loop voltage in the centre and at the edge. (b) The total current density is plotted versus the normalised plasma radius every 10 ms. The initial profile is given by the top flat line at 0.6 MA/m^2 (in the model the current density vanishes at the limiter). The flat profiles slowly decrease like the total plasma current. After 60 ms, the strong current peaking starts for 20 ms. After 110 ms the profiles do not further change.

For an assessment of the possibility of damages to in-vessel components, the energy per thickness of the plasma layer which is scraped off and the energy spectrum of the runaway are important. The maximum of energy per layer thickness (33 MJ/m) is reached at r/a=0.7. Due to the lower volume in the centre and the small runaway density at the edge, the energy per thickness vanishes in both directions virtually linear. The maximum of the kinetic energy of a runaway is given by the balance between the accelerating electric field and the synchrotron radiation. Only a few runaways reach high energies such as up to 500 MeV. More than 75% of the runaways have energy below 30 MeV. There is a small (<10%) increase in the total energy of the runaway beam (here 45 MJ) compared to the calculation neglecting the radial dependence of the generation rate.

For a more detailed analysis of the heat load to the plasma facing components by the runaway impact, the movement and shrinking of the plasma column will be included in further the considerations.

References:

[1] Jayakumar, R., et. al., Physics Letters A 172 (1993) 447
[2] Connor, J.W., Hastie, R.J., Nucl. Fusion 15 (1975) 415
[3] Fußmann, G., Nucl. Fusion 19 (1979) 327
[4] Chiyoda, K., Sugimoto, H., Bull. Electrotechn. Lab. 43 (1979) 499
[5] Putvinski, S.V., Rosenbluth, M.N., invited paper at this conference
[6] Pereverzev, G., ASTRA: an automatic system for transport analysis in a tokamak, IPP-Report, IPP 5/42, 1991

Acknowledgement: The author would like to thanks Prof. Pereverzev for the introduction to the ASTRA-Code and for his support during the calculations.

MHD BALLOONING STABILITY OF ITER EQUILIBRIA

Yu. Igitkhanov, A.S. Kukushkin, H.P. Zehrfeld*, M. Mikhailov**, G. Strohmayer, G. Janeschitz

ITER Joint Central Team, Joint Work Site, D-85748 Garching, Germany
Max-Planck-Institute für Plasmaphysik, D-85748 Garching, Germany
* **Russian Research Centre "Kurchatov Institute", 123182, Moscow, Russia*

Introduction

In the H-mode, very steep gradients of temperature and density, and therefore pressure, occur just inside the separatrix. The pressure gradient can however be limited by the onset of ballooning modes. It is therefore necessary to examine how the stability of such modes is affected by the presence of the separatrix, the x-point and the finite edge current density of reactor-relevant current and pressure profiles. This issue is also related to the achievable density limit. Analytic stability considerations have so far been applied to circular (or slightly elongated) flux surfaces with constant poloidal field. Several analytical studies[1, 2] have shown that the features of the ideal ballooning mode are significantly modified by the presence of the x-point.

In this paper, a numerical model which takes into account the actual field geometry is developed for calculation of the marginal stability. The following scheme is implemented. The DIVA code [3] is used to calculate an ITER equilibrium for a given pressure profile. The equilibrium values of the poloidal magnetic flux $\Psi(R, z)$ are then used as an input to the CARRE grid generator [4], which creates an orthogonal grid. The latter is used to determine the values of the metric coefficients g_{ik} required in the stability equation. The ballooning equation is solved numerically along several flux surfaces near the separatrix, providing the pressure gradients corresponding to marginal stability for this equilibrium. This marginal pressure gradient is then used to calculate the next equilibrium, and so on, until the marginal pressure gradients are equal those used for the equilibrium calculation. Such a procedure, if successful, would provide the pressure profile at the plasma edge which is marginally stable against ballooning modes.

Theory Background

The theory of ballooning modes [5] allows one to calculate the stability of the plasma at a given flux surface in terms of the equilibrium quantities on this flux surface. Bishop [6,2] has used the expansion of the equilibrium quantities in powers of the distance from the separatrix, with prescribed poloidal magnetic field at the separatrix. In that case, however, the existence of global equilibrium is not guaranteed, since a continuation of the solution towards the magnetic axis could yield a singularity. Such an approach reminds one of the solution for a circular magnetic surfaces, when the shift and its derivatives are prescribed on the boundary. In reality the derivative depends on the pressure profile ower the whole plasma column and has to be

defined from the condition that the solution is finite at the magnetic axis. It has been found that there is no significant stabilising effect from the strong global shear near the separatrix, but rather that marginal stability is controlled mainly by the finite toroidal current near the separatrix. Since the net toroidal current does not enter in a straightorward way in the ballooning equation, it can affect the stability mainly through the variation of the equilibrium parameters. In order to find whether the ballooning modes limit the pressure profile we consider below the real ITER magnetic configuration instead of a simplified model.

The ballooning mode equation for marginal stability is solved in the flux co-ordinate system $\rho,\ \theta,\ \varphi$, where $\rho \equiv \psi_{norm} = (\psi - \psi_a)/(\psi_b - \psi_a)$. (ψ_a is a flux value at the axis, ψ_a at the separatrix) labels the magnetic surfaces, θ is the magnetic poloidal angle and φ is the geometric toroidal angle. In such a co-ordinate system, the ballooning equation has the form:

$$\frac{\partial}{\partial\theta}\left\{A(\theta,\theta_0,\psi,\mathrm{q})\frac{\partial\xi}{\partial\theta}\right\} + B\left(\theta,\theta_0,\psi,\left[\frac{\partial p}{\partial\psi}\right],\mathrm{q}\right)(1-\gamma) = 0 \qquad (1)$$

where:

$$A(\theta,\theta_0,\psi,\mathrm{q}) = \frac{g_{\psi\psi}}{\sqrt{g}} + C^2\frac{g_{\theta\theta}}{\sqrt{g}}\frac{1}{1+\dfrac{g_{\theta\theta}}{Q^2R^2}}; \qquad (2)$$

$$B\left(\theta,\theta_0,\psi,\frac{\partial p}{\partial\psi},\mathrm{q}\right) = \left[\frac{\partial p}{\partial\rho}\right]\frac{4\pi^2\mu_0\sqrt{g}}{R^2\left[\dfrac{\partial\psi}{\partial\rho}\right]^2}\left\{C\frac{\partial}{\partial\theta}\left(\frac{R^2}{1+\dfrac{g_{\theta\theta}}{Q^2R^2}}\right) - \frac{\left[\dfrac{\partial R^2}{\partial\psi}\right] + \dfrac{1}{Q^2}\left[\dfrac{\partial g_{\theta\theta}}{\partial\psi}\right]}{1+\dfrac{g_{\theta\theta}}{Q^2R^2}}\right\} \qquad (3)$$

$$C(\theta_0) \equiv \frac{1}{Q}\frac{\partial}{\partial\psi}\left(\frac{q(\psi)}{\left\langle\dfrac{\sqrt{g}}{R^2}\right\rangle_\theta}\int_{\theta_0}^{\theta}\left(\frac{\sqrt{g}}{R^2}\right)d\theta\right) \qquad (4)$$

Here ξ is the perturbation in ballooning space, γ is the eigenvalue (positive if unstable), p is the equilibrium pressure, $g_{\varphi\varphi} = R^2$, R is the major radius, $\langle\ldots\rangle_\theta$ indicates the averaging over θ,

$$Q \equiv q(\psi)\left(\frac{\sqrt{g}}{R^2}\right)/\left\langle\frac{\sqrt{g}}{R^2}\right\rangle_\theta \quad \text{and} \quad q(\psi) = -J(\psi)\left\langle\frac{\sqrt{g}}{R^2}\right\rangle_\theta \qquad (5)$$

$J(\psi)$ is the poloidal current. Equation (1) together with boundary conditions $\xi(\theta_{\min}) = \xi(\theta_{\max}) = 0$, $\dfrac{\partial\xi(\theta_{\min})}{\partial\theta} = \varepsilon$ and $\dfrac{\partial\xi(\theta_{\max})}{\partial\theta} = -\varepsilon$, $\varepsilon << 1$, forms an eigenvalue problem which is solved numerically.

A domain of integration of 50π in poloidal angle was found to be adequate. The most unfavourable position along the poloidal direction $\theta=\theta_0$ in the outmost boundary has been found for each magnetic surface. The growth rate has been calculated in a poloidal range $\frac{\pi}{4} \le \theta \le \pi$ for 50 points

Numerical results

Preliminary results are shown below. Several ITER equilibria with different pressure profiles were calculated using the free-boundary equilibrium code *Diva* [3]. On the basis of the external conductor system of ITER, the plasma current (I_p = 20 MA) , a value for the global beta-poloidal β_p, two profile-shape functions (one $\propto$ J'(ψ) the other $\propto$ p'(ψ)) and a prescribed position of the magnetic axis, an equilibrium is determined and its stability-relevant information put into a data interface accessible to our calculations.

The maximum eigenvalues γ are plotted versus ψ_{norm} in Fig.1 and 2 for two ITER equilibria corresponding to different profiles of the plasma pressure. ψ_{norm} varies from zero at the centre to 1 at the separatrix. Both equilibria have a finite pressure gradient at the separatrix. These equilibria prove to be stable against ballooning modes at the edge. The corresponding marginal pressure gradients are shown in Fig.3 and 4, and they are about of 50-30 times higher than the gradients used in the equilibrium calculations. Whereas the values apparently shift towards zero with an increase of pressure gradient, the marginal pressure profiles reveal no strong dependence on the pressure gradients, used in the equilibrium calculations. The Mercier criterion also indicates stability of these equilibria.

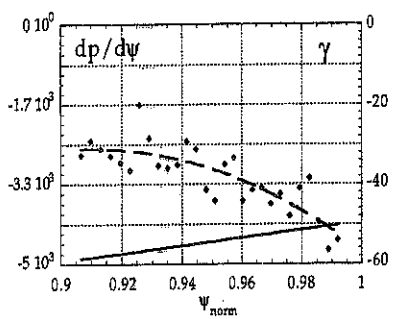

Fig. 1. Equilibrium pressure gradient and the value of γ (dashed line) for the first case.

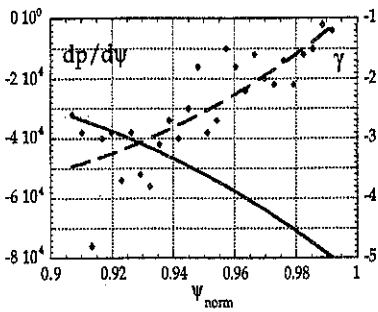

Fig. 2. The same as in Fig.1 for the second case of higher equilibrium pressure gradient

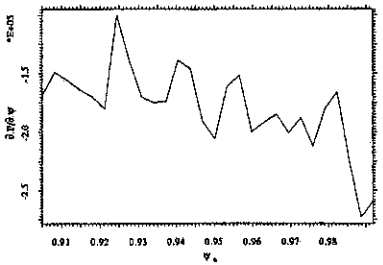

Fig. 3. Marginal pressure gradient at the edge for the first case

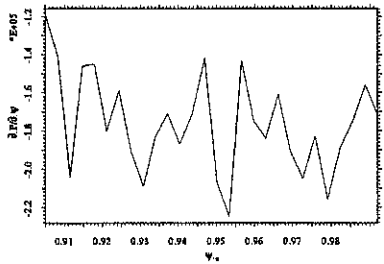

Fig. 4. The same as in Fig. 3 for the second case of higher equilibrium pressure gradient

Conclusions

The preliminary calculations show that the pressure gradient at the edge in ITER configuration is stable against the ideal high-n ballooning and Mercier type perturbation ($\beta p < 2.7$ %), and the marginal pressure gradient at the edge is insensitive to the pressure gradient used in the calculation of the equilibrium.

Acknowledgment

This report has been prepared as an account of work performed under the Agreement among the European Atomic Energy Community, the Government of Japan, the Government of the Russian Federation, and the Government of the United States of America on Cooperation in the EDA for ITER under the auspices of the International Atomic Energy Agency .

References

[1] O.Pogutse, J.Cordey, W. Kerner et al., in *EPS*, p.III-277, 1995
[2] C. Bishop, Nuclear Fusion, v.26, 8, 1986
[3] H.P.Zehrfeld, K. Grassie, Nucl. Fusion 5, 891 (1988)
[4] R. Marchand , M. Dumberry, Computer Physics Communications, 96, (1996) 232-246
[5] J.W. Connor, R.J. Hastie, J.B. Taylor, Phys. Rev. Lett. 40, 396, (1978)
D. Correa-Restrepo, Z. Naturforsch., 33a, 789, (1978)
[6] C. Bishop, P. Kirby, J.W. Connor et al, Nuclear Fusion, v.24, 1579 , 1986

ITER Operation Space in terms of T_e and N_e at the Plasma Edge

G. Janeschitz, A. Hubbard*, Yu. Igitkhanov, J. Lingertat**, T. Osborne***,
H.D. Pacher+, O.P. Pogutse**, D.E. Post, M. Shimada++, M. Sugihara, W. Suttrop+++,

ITER Joint Central Team, Joint Work Site, D-85748 Garching, Germany
** Plasma Science and Fusion Centre, MIT, Cambridge, Ma 02139, U.S.A.*
***JET Joint Undertaking, Abingdon, OX14 3EA, U.K.*
** **General Atomics, CA ..... U.S.A.*

+The NET Team , D-85748 Garching, Germany

++Jaeri, Naka, Ibaraki-ken, Japan

+++Max Planck Institut fuer Plasmaphysik, D-85748 Garching Germany

1 Introduction:

With the advent of improved diagnostic capabilities on several divertor tokamaks, it has recently become possible to define the operational space of H-mode and L-mode in terms of T_e and n_e just inside the separatrix [1], i.e. in terms of the plasma parameters at the top of the H-mode pedestal. From such a diagram we can see that the edge operational space of a particular machine is governed by 4 boundaries (Fig. 1), namely:

- The uppermost boundary divides the unstable from the stable operation space and is defined by the ballooning limit which together with the H-mode pedestal width defines a maximum pedestal temperature for a given density.
- The second boundary determines the transition between Type I and Type III ELMs. Achievement of an H-mode with good confinement requires T close to, or above this boundary, yielding a minimum edge temperature. Thus the intersection of boundary 2 with boundary 1 can be interpreted as an H-mode density limit (Hot density limit [2]).
- The third boundary determines the threshold temperature for the L to H-mode transition.
- The fourth boundary describes the temperature related to the onset of full divertor detachment leading to an X-point marfe (cold edge (L-mode) density limit [2]).

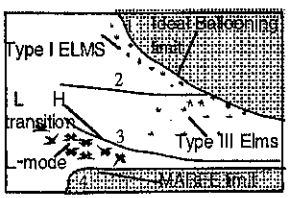

Fig. 1: Schematics of the four boundaries governing the operational space of a machine

In order to predict the operational space for ITER on the basis of edge measurements performed on different machines a theoretical expression for each boundary had to be developed and tested against the data, the width of the H-mode pedestal had to be determined and a scaling of this width to ITER had to be found.

2 Theoretical expressions for the boundaries and for the pedestal width:

Boundary 1 is assumed to be governed by the ideal ballooning limit. We thus evaluate the S-α diagram for each experiment using the analytic formulation in [3].The shear value $S \equiv \overline{\frac{r}{q}\frac{\partial q}{\partial r}}$ required for this calculation is derived from $q_{eff} = \frac{L_0^2 B_T}{2\pi\mu_0 RI}; L_0 = 2\pi a\sqrt{\frac{1+\kappa^2}{2}}$ by introducing a rather broad current density profile. The resulting average shear in the pedestal region varies between ~ 8.5 and ~ 12 depending on the machine and on B_T and I_p for the particular set of discharges. The critical pressure gradient for the onset of type I ELMs and thus for the ballooning limit has been found in several machines to depend on triangularity. In order to take this into account we multiplied "α" from our model with a function derived from a triangularity fit to the results of [4]. Multiplying this marginal pressure gradient by the pedestal width Δ gives the pressure on top of the pedestal, from which the boundary 1 can be plotted assuming a particular ratio between Ti and Te. The above current density profile was derived by adjusting it

until the ASDEX-UP Te values were reproduced with $\Delta = 2.2$ and then kept constant for all machines (for consistency) yielding the discussed shear values (limitation of analytic approach).

The pedestal width can be obtained from measurements or from an analytical expression adjusted to the boundary 1 data. The accuracy of determining Δ from measured data is quite poor in most machines and in order to extrapolate to ITER an analytical expression is needed in any case. Therefore Δ was obtained by fitting an analytic function to the boundary 1 data.

Whereas Te vs ne measured at the pedestal before a type I ELM in ASDEX and to some extent in DIII-D suggest a constant pressure and thus a constant Δ over the whole density range (Fig. 3,4), JET data are better fitted by assuming a temperature dependent Δ [5] (Fig. 5,6). In addition, when plotting the measured Δ_{exp} (tanh fit to data) from DIII-D versus the pedestal temperature a trend for Δ_{exp} to increase with Te-pedestal can be inferred (data scatter is big). We assume also that electron turbulence driven transport (Drift Alfven mode see below and [6]) is stabilised after the L-H transition over a wider range of the minor radius than the pedestal. The width of the H-mode pedestal is therefore probably governed only by the stabilisation of ion turbulence due to poloidal rotation shear (radial electric field) which is observed only over a limited width (e.g. [7]). Assuming further that this width may be related to the banana width and thus to the ion poloidal gyro radius and following the suggestion in [4] we find: $\Delta = f\sqrt{\rho_b R}$ where "f" is a scaling factor (see below) which allows extrapolation to ITER. The factor "f" was adjusted for each machine such that the resulting boundary agrees with the measured data. In addition Δ_{calc} was compared to the experimental values (within a confidence range) in the middle of the density range covered by measurements. The agreement between Δ_{calc} and the experimental values is rather good except for DIII-D where Δ_{exp} is 1 cm to 2 cm (and sometimes 3 cm) and $\Delta_{calc} \sim 4$ cm (Fig. 4) and for C-mod where Δ_{exp} is estimated to be ~8 mm while $\Delta_{calc} = 4$ mm. The differences can probably be explained for both machines with deviations of the critical pressure gradient from the ballooning limit. While DIII-D might enter second stability at the edge [8], C-mod might have gradients below the ballooning limit (no Type I ELMs). Again in order to apply a consistent approach for all machines we nevertheless assumed that the pressure gradients are governed by the ballooning limit. A more accurate evaluation of the width can only be done by sofisticated MHD code calculations (in the future).

A plot of "f" versus minor radius for the different machines is consistent with an approach of "f" to an asymptotic value around 0.275. From this plot it can also be seen that JET is already close to this value and thus ITER should have a value between JET (f=0.26) and the asymptotic limit resulting in "f_{ITER}" ~ 0.27, $\Delta_{ITER} = 9$ cm (Fig. 2). Another way of extrapolating "f" to ITER is using a non linear fit which results in "f"=0.46, $\Delta_{ITER} = 19$ cm (Fig. 2). The reason for choosing the minor radius instead of "R" for the extrapolation is that ASDEX and DIII-D have different "f" and different "a" values but the same "R". With this kind of scaling Δ_{calc} depends on the pedestal temperature and thus varies with density resulting in a boundary 1 which deviates slightly from a constant pressure curve.

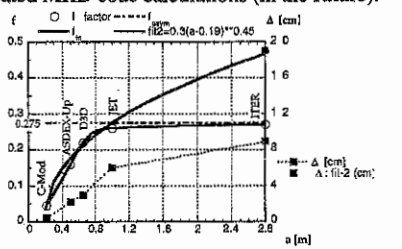

Fig. 2: Two scalings for factor "f" and of the resulting Δ versus minor radius

However, as already indicated above a nonconstant pressure seems not to be a good fit for ASDEX (Fig. 3). A tentative explanation is that due to the relatively low temperature of boundary 1 at high densities the ratio of Ti to Te might vary with density in ASDEX and possibly also somewhat in DIII-D. Thus also the critical gradient for Te will vary and counter balance the variation of Δ. We have therefore introduced a variation of the ratio r=Ti/Te from r=2 at 10^{19} m^{-3} to r=1 at $10^{20}m^{-3}$ in ASDEX and from r=1.5 to r=1 over the same density range for DIII-D. The scatter of the data would allow also for somewhat smaller variations. In the other machines including ITER we assumed that the ratio of Ti/Te is constant over the density range covered which is justified by the high pedestal temperatures found in JET (and predicted for ITER) and the high densities in C-mod. With this assumption the experimental data of all machines is fitted quite well. With the above scaling for "f", boundary 1 for ITER can then be derived.

For Boundary 2 a model is suggested by Igitkhanov and Pogutse relating the threshold temperature to a Tcrit for stabilising a flute dissipative mode which remains unstable above the threshold temperature for the drift Alfven mode (L to H transition [6]). When this expression is adjusted to ASDEX data (at the position of the pedestal), it also fits DIII-D data quite well (Fig. 3,4) but not JET (ITER) and C-mod for which a different multiplication factor which does not scale with the pedestal width would be needed. Further investigations are needed to predict the intersection point between boundary 1 and 2 and thus the H-mode density limit for ITER.

Boundary 3 is defined by the critical temperature at the position of the pedestal above which the drift Alfven mode is stabilised $T_{cr} = \left[sB\frac{I}{a^2}\right]^{f1} \frac{A^{-f2}}{n^{f3}} f_4 \Delta_{calc}$ where "f1", "f2", "f3", "f4" are weak functions of density as defined in [6]. As can be seen from Fig. 3 to 7 theory, and data agree quite well in all machines.

A qualitative physics picture of the H-mode could be that stabilisation of both electron and ion turbulence is required to establish the transport barrier. Ion turbulence is stabilised by poloidal rotation shear but during L mode Δ and the electric field are small [7] and the electron turbulence due to the drift Alfven mode may dominate transport in the edge region. When the heating power is increased the temperature at the edge increases, Δ and the electric field increase somewhat, but no large effect is expected (observed) on transport. Only when the drift Alfven mode is stabilised and thus electron transport is strongly reduced a sudden further increase of the edge (pedestal region) temperature and density becomes possible. As a result Δ and the region of electric field shear grows, increasing the width over which ion turbulence is stabilised by poloidal rotation shear. Therefore the drift Alfven mode becomes the important trigger mechanism [6] but the H-mode transport barrier develops only in the region where both electron and ion turbulence are stabilised and thus over the width defined by the poloidal rotation shear. However, confinement also improves in the core if the critical temperature gradient for ion turbulence is determined by the boundary condition (temperature) on top of the H-mode pedestal as suggested in [9].

The fourth boundary is derived from a set of analytic equations (two point model [10]) describing the onset of full divertor detachment leading to an X-point marfe (cold edge (L-mode) density limit). Calculations performed for ASDEX fit the measured data quite well and suggest that the boundary derived for ITER should be a good approximation. As can be seen from Fig. 8 the cold density limit should not pose any problems for ITER.

3 Discussion and Conclusions:

As one can see from Fig. 3 to 7 the theoretical expressions and the data agree quite well and thus give confidence for the extrapolation to ITER. The absolute values of temperature versus density for ballooning and L-H mode transition in ITER depend on the extrapolated pedestal width (Fig. 8) for which presently no theory exists and which therefore remains uncertain. However, due to the fact that these values are derived from a critical gradient times Δ, an uncertainty in the prediction of Δ only shifts the operation space temperature up and down but does not change its shape. Also results from transport codes which might use the derived expressions for calculating e.g. the H-mode power threshold (future plans) will therefore not depend strongly on the predicted width. Another important feature which can be seen from the comparison of two different triangularities (δ=0.21, δ=0.31) in JET (Fig. 5) is that discharges with higher triangularity allow H-mode operation at temperatures above Tcrit for Type III ELMs at higher density (higher H-mode density limit) pointing towards the importance of achieving reasonable high triangularity also in ITER (δ~0.25). The relatively high value of Tcrit for Type III ELMs as seen in JET (~ 3keV, BT=3.5T, Fig. 5) would result for ITER in an estimated H-mode density limit of ~ $6 \times 10^{19} m^{-3}$ at the top of the pedestal when the ratio of the two Δs is used for extrapolation. The triangularity of δ ~0.25 in ITER, higher than that of JET (δ ~0.21), might increase this value to ~ $7 \times 10^{19} m^{-3}$ implying a line average density of ~ $0.91 \times 10^{20} m^{-3}$, i.e. 11% above the Greenwald density. However due to the lack of a model for Type III ELMs the exact extrapolation and thus the H-mode density limit for ITER remains unknown.

It is a clear conclusion that the temperature on top of the H-mode pedestal is ~ 4 to 8 keV at the H-mode density limit and higher at lower densities. These values are higher by more than an order of magnitude than the value assumed in [11] ($T_{pedestal}$ = 300 eV) which was used in the model of [9] to predict a confinement for ITER well below the one obtained from the global scaling laws. If the pedestal temperatures obtained from our scaling were taken as boundary

conditions it is likely that even this model would predict adequate confinement values for ignited operation in ITER.

4 References:

[1] M. Kaufmann et al, Proc. 16th IAEA Fusion Energy Conf., paper O1-5 Montréal 1996
[2] G. Janeschitz, et. al., Proc. 16th IAEA Fusion Energy Conf., paper A1-6 Montréal 1996
[3] O. Pogutse and E. Yurchenko, *Reviews of Plasma Physics*, Vol. 11, pp. 65-148.
[4] Y. Kamada et al, Proc. 16th IAEA Fusion Energy Conf., paper A1-6 Montréal 1996
[5] J. Lingertat, et.al., this conference
[6] O.P. Pogutse, et.al. this conference
[7] R. J. Groebner, et. al., Proceedings 16th EPS Conf., Petit-Lancy, Switzerland, 1989
[8] T. Osborne, et.al., this conference
[9] M. Kotschenreuther, W. Dorland, et. al., Physics of Plasmas 2 (6) June 1995
[10] M. Sugihara et al, Proc. 12th Int. Conf. Plasma-Surface Interactions, St. Raphael 1996
[11] Glanz, Science Magazine December 1996

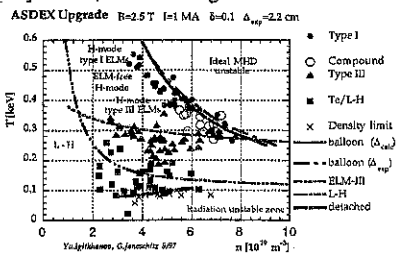

Fig.3: Operation space for ASDEX-Upgrade. The good agreement between data and theory can be seen. Type III ELM curve adjusted.

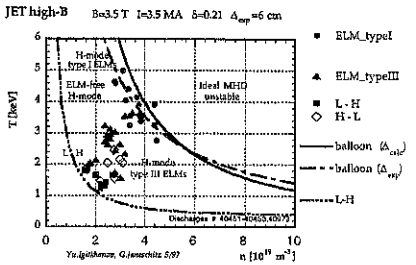

Fig. 6: The JET high field operation space shows a relatively high threshold Temperature for Type III ELMs.

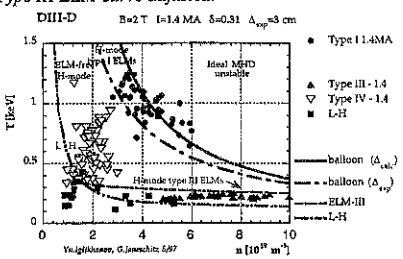

Fig. 4: Operation space for DIII-D, good agreement of data and theory except for the "Δ = 3 cm" ballooning curve (dashed).

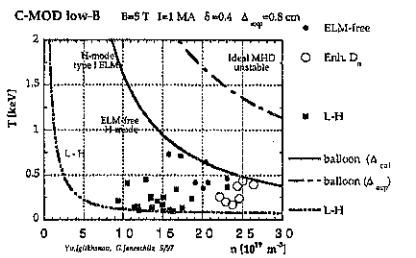

Fig. 7: C-mod operation space for BT=5T. Good agreement of theory (L-H and Δcalc ~ 4mm) and data except for the dashed curve representing Δexp = 8mm

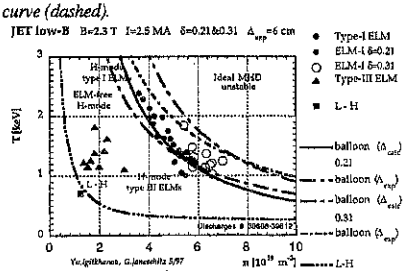

Fig. 5: JET low field operation space. The increase of the operation space (i.e. the H-mode density limit) with triangularity can be seen

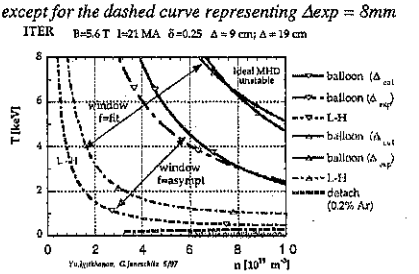

Fig. 8: ITER operation space for "f"=0.46, giving the higher temperatures, Operation space for "f"=0.27 gives T a factor two lower for ballooning and L-H

MODELLING OF WALL PUMPING, FUELLING AND ASSOCIATED DENSITY BEHAVIOUR IN TOKAMAKS

M. Sugihara, G. Federici, C. Grisolia*, Ph. Ghendrih*, T. Loarer*, H. Nakamura, Yu. Igitkhanov, G. Janeschitz, G.W.Pacher**, H.D. Pacher***, D.E. Post

ITER Joint Central Team, Joint Work Site, D-85748 Garching, Germany

** Association EURATOM-CEA sur la fusion, C.E. Cadarache, France*

***Centre canadien de fusion magnétique, Varennes, Québec, Canada*

****The NET Team , D-85748 Garching, Germany*

Introduction

Material surfaces surrounding the plasma in Tokamaks play an important role on the transient plasma density and particle balance. In fusion reactors like ITER, pumping and fuelling by walls will also affect the overall DT fuel particle balance and determine the amount of radioactive tritium in the walls. A dynamic model of the plasma and walls has been developed, which solves a time dependent coupled system of equations for 0-D plasma densities and surface and bulk concentrations for representative walls. The wall model includes both metallic and non-metallic materials. The model is applied to the density behaviour and fuelling characteristics of a long pulse discharge and transient density experiments between different configurations in Tore Supra and JT-60 . The goal is to understand the governing processes for the wall and to identify their dependencies upon the various design parameters such as operational conditions, material properties, discharge history and wall conditions.

2. Wall and Particle Balance Models and Equations

Wall and particle balance models are extension of the existing models so far developed in various groups, e.g., [1]. Five representative wall regions are considered; (1) First wall near gas puff port, (2) General first wall, (3) Limiter, (4) Divertor plate, (5) Divertor side wall.

Balance equations in implantation layer

Schematics of particle balance in each wall is shown in Fig. 1. Balance equation for the particles implanted in this layer , particles desorbed from this layer by diffusion/recombination, and particles diffusing into bulk of the wall is expressed as

$$\frac{d}{dt}N_j = \left(\Gamma_j^{in}\right) - \left(\Gamma_j^{out}\right) + A_j\left(D_j \frac{\partial}{\partial x} C_j\right)_{x=\delta} \qquad (1.1)$$

where N_j is the total particles stored in the implantation layer of the wall (j), $C_j(x)$ is the particle concentration (concentration is assumed constant in this layer, width δ). Γ_j^{in} is influx to each wall (j). Particle flux on the limiter and divertor plate Γ_j^{in} is determined by $\Gamma_j^{in}=N_p / \tau_p$. Here N_p, τ_p are total plasma particles and the particle confinement time including the recycling, respectively. Flux amplification is considered by appropriate choice of τ_p. For limiter configuration, Γ_j^{in} on the first wall is determined by some fraction of the influx on the limiter, e.g., 0.15 [1]. For divertor configuration, Γ_j^{in} on the first wall and divertor side wall are determined by the neutral density in divertor and main plasma region, respectively. Desorbed

flux from the layer Γ_j^{out} is determined by the desorption model. In the case of CFC based materials; $\Gamma_j^{out} = (N_j / N_{j,max})\Gamma_j^{in}$, where $N_{j,max}$ is maximum absorbable particles. In the case of metal wall (e.g., Be, W), $\Gamma_j^{out} = 2k_r^j (N_j)^2 / A_j \delta^2$, where k_r^j is recombination coefficient.

Diffusion into bulk materials

$$\frac{\partial}{\partial t} C_j(x) = D_j \frac{\partial^2}{\partial x^2} C_j(x) \qquad (1.2)$$

Particle balance model in plasma

$$\frac{d}{dt} N_p = \left(\Gamma_{puff}\right) - \sum_j \frac{d}{dt} N_j - \Gamma_{NET}^{co} - \Gamma_{pump} \qquad (1.3)$$

Codeposition of hydrogen

$$\Gamma_{NET}^{co} = \left[Y_D \Gamma_j^{in} - \frac{Y_D \Gamma_j^{in} f_r}{1 - f_r Y_{ss}} (1 - Y_{ss}) \right] \frac{N_j}{N_{j,\max}} \qquad (1.4)$$

where Y_D, Y_{ss}, f_r are the coefficients for hydrogen and self-sputtering and return fraction of sputtered atoms [2]. Codeposition is considered only for limiter and divertor plate. Eqs (1.1)-(1.3) are simultaneously solved with initial values adjusted for each of the problems considered.

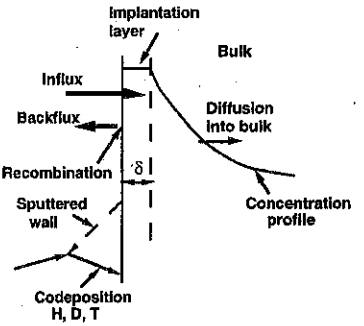

Fig. 1 Schematics of particle balance in wall.

3. Model Validations by Tore Supra and JT-60 Experiments

(1) Transition experiment from outboard limiter to inner wall in Tore Supra

Series of wall pumping experiments have been done in Tore Supra by using the transition from outer limiter to inner wall configuration without actual pumping system [3]. These shots have been performed with CFC wall materials after long hours of wall conditioning. We have selected two shots #5070 and 5080 from this series. First, initial particle contents in the walls are adjusted to obtain reasonable fit to #5070 experiment. Then, the initial contents for #5080 are somewhat increased to obtain a reasonable fit to #5080 with fixing other simulation conditions. Results of simulations are shown in Fig. 2. Fit is reasonably good only by adjusting the initial particle content in the walls. In the simulation, the increase of initial particle content between these shots are N_0(#5080) - N_0(#5070) = 1.28×10^{21} (p), where N_0 is the total initial particle content in the walls. This increment is much smaller than the total particles injected into the torus during these 10 shots, which are estimated as 2×10^{22} (p). This is consistent with the previous finding in Tore Supra [3], which concluded some reduction mechanisms of the wall-absorbed particles. By simple examination, it is shown that the particle diffusion into the bulk materials is too small to explain this reduction, unless wall temperature is very high (>1000 °K

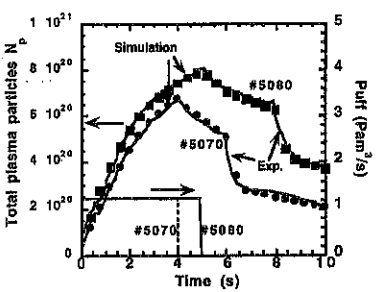

Fig. 2 Experimental density behaviour (solid lines) and simulation (closed circle, square).

is required for diffusion to be effective), which is unlikely in the experiments. Thus, most likely mechanisms for this reduction are either thermal desorption between shots (≈900 s) or surface diffusion to other part of the wall, which are not directly exposed by the particle. These speculations still need further confirmation by further detailed study. Another necessary adjustment in the simulation is τ_p. Here, $\tau_p \approx 90$ ms during gas puffing is needed and 480 ms for the rest of the period for both shots. This confinement time is consistent with that obtained by detailed study of the density decay after transition in [3]. This adjustment of τ_p need further investigation. One possible interpretation is that during density ramp-up with strong gas-puffing, density profile is flat and the flux amplification is generally high and during the density decay phase after gas-puff is stopped, density profile tends to shrink.

(2) Transition experiment from inboard limiter to outer divertor in JT-60

In JT-60, transition experiments have been done from the inboard limiter to the outer divertor with TiC coated wall [4]. Gas puff of 2 Pam^3/s was constantly injected up to 7 seconds. During transition, density decreases very rapidly due to large pumping by the divertor plate and side wall. Fuelling efficiency during the divertor phase is half of the limiter phase. Whole of these characteristic features of density behaviour are target of simulation. In order to model the particle flux on the first wall and divertor side wall, we will use the experimental results for the neutral density n_0 both in the main plasma and divertor regions as a function of main plasma density, which scales as $\langle n_e \rangle^2$ [4]. The particle flux on each wall is evaluated by $\Gamma^{in}=n_0 v_0 S_j$, where v_0, S_j are neutral velocity and wall area of (j), respectively. Result is shown in Fig. 3, where τ_p is set ≈ 80 ms throughout whole phase of the discharge. After the transition, divertor plate is saturated within ≈ 0.5 s, so that this choice of τ_p does not affect the result since the wall absorption is dominated by the first wall and side wall. Density decay after gas-puff stop is slightly slower in the experiment. This discrepancy could also be improved by reduced neutral pressure due to longer τ_p.

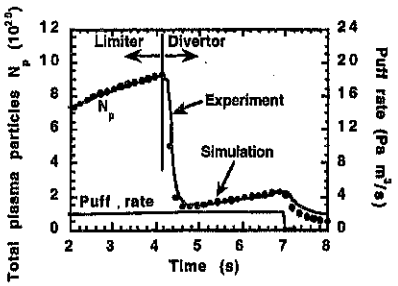

Fig. 3 Experiments (solid line) and simulation result (closed circles) for the density behaviour during limiter, transition and divertor phases in JT-60.

(3) Long pulse operation in Tore Supra

In Tore Supra, long pulse operation has been done with LHCD [5]. Plasma density has been maintained almost constant even under the continuous gas fuelling with no pumping, so that the walls absorb all of the fuelled particles. For these long pulse discharges, it is expected that some continuous absorbing mechanisms should be necessary, since the surface will be saturated during the discharge. Thus, we examine following mechanisms. (1) Enhanced diffusion into the bulk of the wall as suggested in [6], (2) Enhanced codeposition of hydrogen.

We examine the time evolution of total puffed particles when the density behaviour is reproduced. Fig. 4 shows the results for total puffed particles with and w/o appropriate enhancement of the diffusion coefficient. By choosing the appropriate initial particle content, it is possible to match the total puffed particles at the end of the discharge. However, the global time behaviour is convex upward in time, which reflect the saturation character in surface trapping. This can not been seen for a short pulse discharge (≤ 10 - 20 s), which indicate the importance of long pulse (≥ 60 s) to identify dominant effect by walls. Another mechanism of enhanced codeposition of hydrogen could also reproduce the experimental result. Required enhancement, however, are fairly large ($f_r < 0.3$ and large flux amplification τ_p<10 ms), which needs further study in experiment.

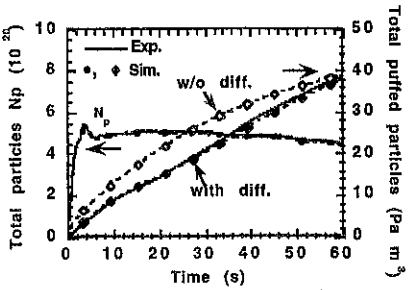

Fig. 4 Time evolution of total puffed particles for three different initial particle content in the walls when total particle (density) is matched with experiment.

Conclusions and Future R&D Needs

Dynamic wall particle interaction model is developed and applied to the experiments. The model can reproduce the density behaviour with large wall reservoir in transient experiments as well as constant wall up-take mechanisms, such as diffusion, codeposition in long pulse discharge. In addition to the wall modelling, it is identified that the modelling of the particle flux on each wall region are also important to reproduce the experimental results. This will be done by coupling the core plasma transport code with some sophisticated divertor/edge plasma models. Dedicated particle balance experiments under well controlled and diagnosed wall and plasma conditions are also essential to further develop and improve the model.

Acknowledgements

This report has been prepared as an account of work performed under the Agreement among the European Atomic Energy Community, the Government of Japan, the Government of the Russian Federation, and the Government of the United States of America on Cooperation in the EDA for ITER under the auspices of the International Atomic Energy Agency .

References

[1] J.K.Ehrenberg, JET-P(95)18.
[2] G. Federici, C.H.Wu, J. Nuclear Materials 207 (1993) 62.
[3] C. Grisolia et al., J. Nuclear Materials 196-198 (1992) 281.
[4] H. Nakamura et al., JAERI-M86-175 (1986).
[5] D. Van Houtte and Equipe Tore Supra, Nuclear Fusion 33 (1993) 137.
[6] C. Grisolia et al., Proceedings of 20th EPS, Lisboa (1993) II-595.

Effect of Light Impurities on the Divertor Performance in ITER

A.S. Kukushkin, H.D. Pacher*, D. Coster†, G. Janeschitz, D. Reiter‡, R. Schneider†

ITER Joint Central Team, Garching Joint Worksite, Garching, Germany
* The NET Team, Garching, Germany; † Max-Planck IPP, Garching, Germany;
‡ FZ Jülich, Jülich, Germany

Numerical studies of the expected performance of the ITER divertor have been carried out intensively during the last few years. Different operational regimes with divertor plasma ranging from partially attached to fully detached have been modelled [1, 2]. The results showed a possibility to maintain divertor conditions which provide simultaneously acceptable power loading on, and erosion of, the divertor components and adequate helium exhaust from the burning plasma. However, the necessary level of radiation was ensured in those calculations only by neon seeding of the edge plasma, without allowance for the intrinsic impurities, such as sputtered carbon. Thus rather high neon concentrations, 0.5% or higher were required and high values of Z_{eff} resulted at the edge of the core plasma.

The present paper shows the effect of the intrinsic light impurities on the divertor radiation. The model (B2-Eirene code package) has been elaborated to include both physical and chemical sputtering of the wall material together with a full multi-fluid description of the transport of sputtered impurities in a self-consistent way.

Effect of light impurities

At present, we use a simplified model for the chemical sputtering, assuming that the carbon atoms are sputtered by hydrogen atoms and ions with a constant yield, typically, 1%. The cross-field transport coefficients have been selected as in Ref.[1,2], $D_\perp$=0.3 m^2/s and $\kappa_\perp$= 1 m^2/s. An ITER-relevant level of helium concentration, 10% at the core boundary, has been maintained in all the calculations, and neon seeding has been added to control the power balance. In order to study the sensitivity of the result to the impurity production and radiation characteristics, two further cases have been run. The first assumes reduced yield, 0.5%, for chemical sputtering. Carbon is replaced by beryllium in the second case, artificially keeping the sputtering yield at the same 1% level.

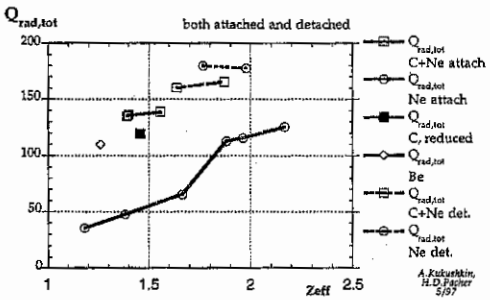

Fig. 1. Total radiated power vs. Z_{eff} at the core-edge boundary for different operational regimes (the case at Z_{eff}= 1.6, 140 MW, is the reference case)

First results show that, for similar divertor conditions and similar radiation from neutrals, higher power is radiated by impurities at lower Z_{eff} when both carbon and neon are used (see Fig. 1, curves marked C+Ne, C, and Be vs. Ne). The total power coming to the targets is reduced accordingly. With an increase of neon concentration, the plasma starts to detach from the inner target. The distribution of radiation sources along the poloidal co-ordinate is also worth noting. The radiation from the plasma edge inside the separatrix increases with Z_{eff} at the core boundary, Fig. 2, being somewhat lower in presence of carbon. The poloidal distribution of the radiation can also be represented as the poloidal integral of the power radiated between a reference point and the current position,

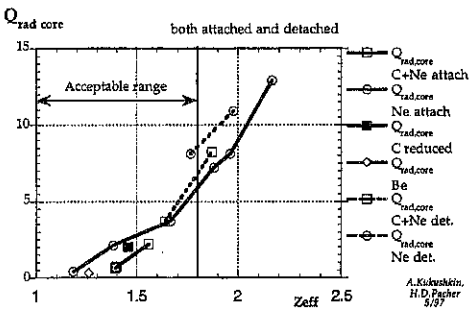

Fig. 2. Power radiated from the core edge vs. Z_{eff} for different operational regimes

$$f_{pol}(x) = \int_0^x dz \int_{r_{min}}^{r_{max}} q_{rad}(z,r)dr$$

These integrals are shown in Fig. 3 for two different cases in three separate regions: the two divertors and SOL together with plasma edge. The integrals are accumulated from targets in the divertors and clockwise from X-point in the main chamber. Fig. 3a shows f_{pol} for the semi-attached operation with sputtered carbon, whereas the profiles for the "deeply detached" case of Ref. [2] are given in Fig. 3b. For the semi-attached operation, Fig. 3a, essentially all the radiation comes from the divertors. The radiation source is somewhat peaked near the outer target, otherwise well spread out. No peak is seen near the X-point and little is radiated above the X-point. Therefore,

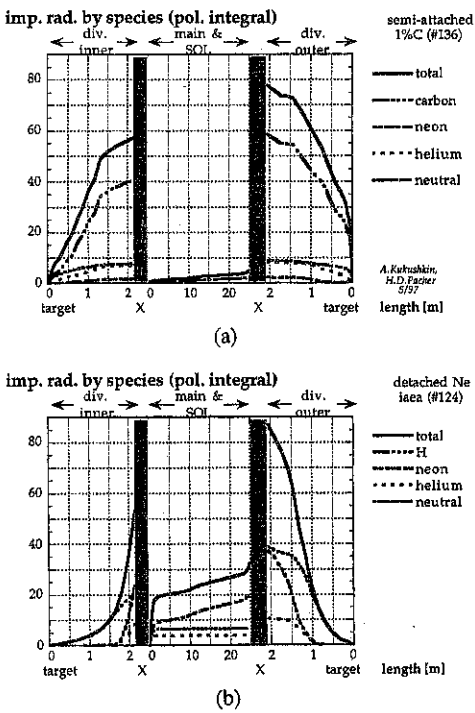

Fig. 3. Poloidal distribution of the radiated power for semi-attached (a) and deeply detached (b) operation modes

there is no trend to form a MARFE. This picture remains similar with variation of the neon seeding level up to detachment from the inner target. Only in a strongly detached case, Fig. 3b, which is not proposed for operation, is there a considerable radiation (30 MW) from above the X-point. Replacement of carbon by beryllium results in profiles similar to those with C, provided that enough Be is produced.

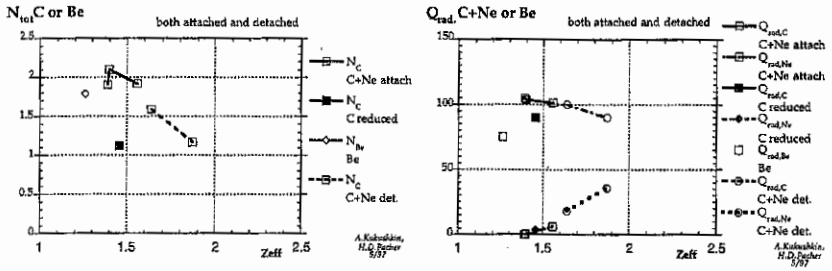

(a) (b)

Fig. 4. Variation of C (or Be) inventory (a) of, and impurity radiation (b) from, the whole edge plasma with Z_{eff} at the core-edge boundary

The relation of the carbon source to the flux of hydrogen isotopes coming to the surfaces gives rise to a self-regulation which could have a stabilising effect on the plasma detachment. When radiation from the divertor plasma increases, the particle flux to the surface decreases due to reduction of the power spent for ionisation. As a result, the carbon influx becomes lower, tending to reduce the radiation. This effect is illustrated in Fig. 4, where the carbon content and total impurity radiation are plotted versus Z_{eff} at the core.

ITER implications

The presence of the sputtered carbon in ITER has a favourable effect on the trade-off between the target loading and Z_{eff} at the core. Therefore, highly-radiating, semi-attached plasmas with peak power loads onto the targets below 5 MW/m^2 become possible even with $Z_{eff} < 1.6$ at the core boundary. This peak load appears to be rather insensitive to the specified value of the chemical sputtering yield. The radiated power, although somewhat peaked towards the outer target, is well spread out and produces loads below 1 MW/m^2, concentrated mainly in the divertor region. The total power radiated from the plasma edge and divertors can be as high as 140 MW of 200 MW entering the edge plasma for semi-

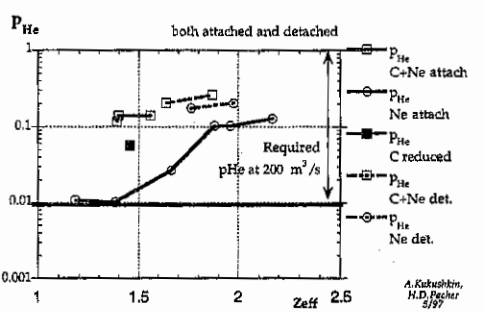

Fig. 5. Helium partial pressure at the pumping duct vs. Z_{eff} at the plasma core for different regimes

attached operation.

The conditions for helium exhaust are also acceptable for this regime, Fig. 5. There is a margin of one order of magnitude over the required minimum helium neutral pressure near the pumping duct. Moreover, a stand-alone calculation of neutral particle transport done with the Eirene code indicates favourable effect of elastic collisions between helium atoms and plasma ions (disregarded until now in coupled calculations) on the helium pumping efficiency. These collisions heat up the helium atoms thus facilitating their penetration through the divertor plasma.

Conclusions

Light (intrinsic) impurities – in a certain amount – are beneficial for the ITER divertor. They ensure higher radiation from the divertor at lower Z_{eff} at the plasma edge compared with the neon-dominated cases [1, 2]. The radiation in the divertors is weighted more towards the targets, inhibiting therefore formation of an X-point MARFE. Moreover, the impurity production by sputtering can have a self-regulating effect on the operational regime, reducing release of carbon when detachment becomes imminent.

Semi-attached operation with a realistic impurity mix can be taken as the primary option for ITER. It allows, in presence of carbon, to attain the ITER design criteria of low Z_{eff} (≤ 1.8) and low peak power load on the target (≤ 5 MW/m^2) simultaneously. The design value of 200 m^3/s for the pumping speed appears also to be adequate.

Further studies are necessary to explore the parameter space of ITER operation and to make the predictions of the divertor performance more reliable. Essential here are the model validation against experimental data from existing divertor experiments (ongoing effort) and model development which would provide a more accurate description of the divertor plasma on the long time scale of the ITER pulse.

Acknowledgement

This report has been prepared as an account of work performed under the Agreement among the European Atomic Energy Community, the Government of Japan, the Government of the Russian Federation, and the Government of the United States of America on Co-operation in the Engineering Design Activities for the International Thermonuclear Experimental Reactor ("ITER EDA Agreement") under the auspices of the International Atomic Energy Agency (IAEA).

References

1. A. Kukushkin, H.D. Pacher, et al. 12th PSI Conference, St. Raphael, 1996
2. A. Kukushkin, H. D. Pacher, et al. 16th IAEA Fusion Energy Conference, Montreal, 1996

Kinetic Simulation of Parallel Electron Transport in ITER†

O.V.Batishchev (a,b,c), A.S.Kukushkin (d), D.J.Sigmar (a)

(a) Massachusetts Institute of Technology, Cambridge, MA 02139, USA;
(b) Lodestar Research Corporation, Boulder, CO 80301, USA;
(c) Keldysh Inst. for Applied Mathematics, 125047 Moscow, Russia;
(d) ITER JCT, Garching, Germany

Introduction

We present results of Fokker-Planck modeling of the scrape-off layers (SOL) plasma with parameters accepted for design of the International Thermonuclear Experimental Reactor (ITER). Though there were attempts of hybrid BGK-hydrodynamic simulation [1], most current modeling of ITER's SOL are done using transport codes [2] entirely based on fluid theory [3], which assumes short electron Coulomb collisional mean-free path, λ, along the magnetic field in comparison with the connection length, L=300 m. The Coulomb Knudsen number, $\gamma = \lambda/L$, for ITER is usually about 0.1, which indicates that condition $\gamma \ll 1$ is valid for thermal particles, but can easily fail for the super-thermal particles due to quadratic dependence of λ on particle energy. Tail particles are known to be responsible for plasma heat conduction [4], sheath potential value [5], and plasma-neutral particles reaction rates [6].

Long mean free path nonlocal effects become particularly pronounced for detached ITER SOL plasma operation regimes which are characterized by very high gradients in plasma parameters along the magnetic field. In Fig. 1, we present calculated effective Knudsen number $\gamma = \frac{d\ln T}{dx}\lambda$ versus parallel dimension, x, for typical detached ITER plasma temperature, T, and density, n, profiles obtained using B2-EIRENE modeling.

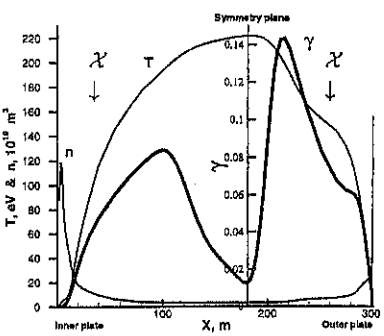

Fig.1 Plasma temperature, density and γ for ITER parameters from fluid modeling

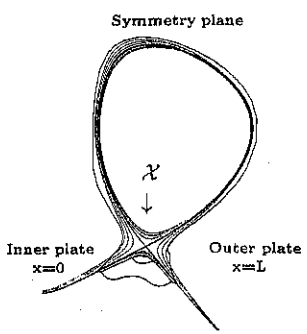

Fig.2 ITER poloidal cross-section illustrating simulation domain

Our simulation domain (and abscissa variation in Fig.1) corresponds to an open magnetic line which is close to the separatrix surface (thick line in Fig.2) and connects inner and outer plate. Symmetry plane defines the plasma stagnation point on this line.

†Work supported by U.S. Department of Energy Contract No. DE-FG02-97-ER-54392 at Lodestar and DE-FG02-91-ER-54109 at MIT

I. Linear problem

Fully kinetic simulations are performed using one-dimensional in the real space, and two-dimensional in the velocity space, adaptive Fokker-Planck code ALLA [7]. The evolution of the electron distribution function f_e is described with a simplified kinetic equation where we approximate the Coulomb term by using the Maxwellian Rosenbluth potentials φ_M and ψ_M with background T_e and n for electron-electron interactions, and the pitch-angle scattering operator (no energy exchange) for electron-ion collisions:

$$\frac{\partial f_e}{\partial t} + v\mu \frac{\partial f_e}{\partial x} - \frac{1}{v^2}\frac{\partial}{\partial v}(v^2 \mu \frac{eE_\parallel}{m_e} f_e) - \frac{1}{v}\frac{\partial}{\partial \mu}\left[(1-\mu^2)\frac{eE_\parallel}{m_e} f_e\right] = C_{ee} + C_{ei} =$$
$$L^{e/e}\left(\frac{1}{v^2}\frac{\partial}{\partial v}\left[v^2\left(\frac{\partial \varphi_M}{\partial v} f_e - \frac{\partial^2 \psi_M}{\partial v^2}\frac{\partial f_e}{\partial v}\right)\right] - \frac{\partial}{\partial \mu}\left[\frac{1-\mu^2}{v^2}\left(\frac{1}{v}\frac{\partial \psi_M}{\partial v}\frac{\partial f_e}{\partial \mu}\right)\right]\right) \qquad (1)$$
$$+ L^{e/i}\frac{\partial}{\partial \mu}\left[\frac{\mu^2-1}{v^3} n \left(\frac{\partial f_e}{\partial \mu}\right)\right],$$

here $x \in [0, L]$, $v = \sqrt{v_\parallel^2 + v_\perp^2}$ is modulus of velocity, $\mu \equiv v_\parallel / v$ is the cosine of the angle between particle velocity and x axis, $-e$ and m_e are the charge and mass of electrons, $E_\parallel$ = the parallel electric field evaluated via Braginskii approximation. and we use $L^{e/i} = L^{e/e} \approx 100 e^4/m_e$. The initial electron distribution is assumed to be a non-drifting Maxwellian with the background plasma parameters. We split simulation domain into 2 segments: with x=L corresponding to the symmetry plane, and x=0 to either inner or outer plates.

Results of the kinetic modeling are the following. In Fig.3 we present the electron parallel distribution function component directed towards the plate ($\mu = \pm 1$) at both divertors versus Maxwellian. One can se that the distribution function starts to deviate from equilibrium at energies around 10T, forming highly populated tail, which at 20T and above has roughly a temperature of the hot symmetry plane region (about 200 eV).

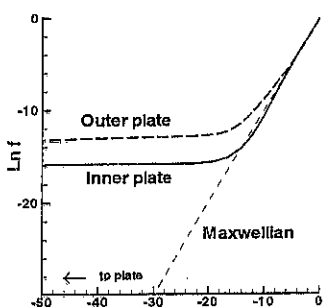

Fig.3 Downstream wing of f at both divertor plates

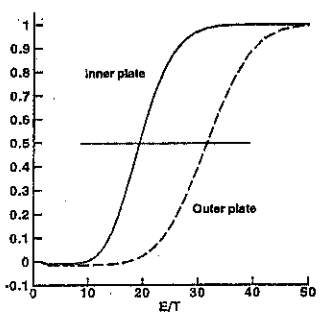

Fig.4 Normalized heat flux q(E)

In Fig.4 the normalized heat flux, $q(E)/q(\infty)$, ($q(E) = \int_{-1}^{1}\int_0^{\sqrt{E}} f_e \mu v^3 dv d\mu$), is plotted versus normalized energy, E/T. As can be seen half of the flux is carried by particles with energies higher than 20T and 30T respectively, in a contract wit Spitzer-Harm heat

flux is carried by particles in interval 4-8T [4]. Thus the strong deviation from short mean free path limit results in large departure of heat flux from Braginskii result, q_B, in downstream reason, as shown in Fig.5. In upstream region $q \approx 0.3 q_B$ because of f_e tail depletion. For the same reason electron collision rates with neutral particles can alter.

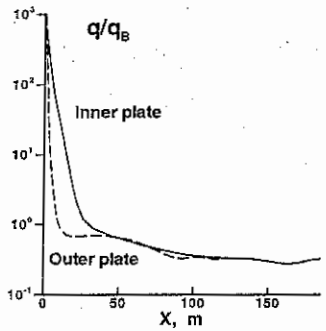

Fig.5 Heat flux to Braginskii flux ratio

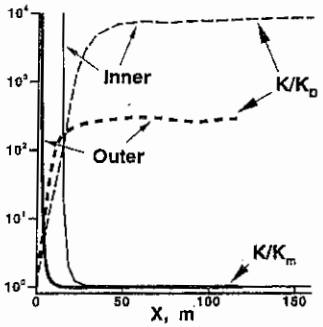

Fig.6 Ratio of ionization rate constant K to Maxwellian, K_M, and divertor value, K_D

To illustrate this in Fig.6 we present the plasma ionization rate constant $K = \int \sigma_I v f_e d\vec{v}$, normalized to Maxwellian value K_M. We see, that K many orders of magnitude exceeds K_M in the cold divertor region (T≤7eV), and it stays visible with respect to its midplane value. This indicates the possibility of high ionization rate in cold gas blanket region with high neutral density.

II. Non-linear problem

In non-linear case the actual kinetic equation solved has form given in work [8]. The Rosenbluth potentials are obtained via two coupled Poisson equations in each spatial grid node. The ambipolar electric field is obtained self-consistently from two conditions: (i) it balances parallel electron pressure and friction between electrons and ions, and (ii) suppresses charge polarization on artificially increased Debye scale λ_D/ε:

$$E_{\parallel} = \frac{m_e}{en_i} \int_{-1}^{1} \int_{0}^{\infty} v^3 \mu \left[C_{ei} - v\mu \frac{\partial f_e}{\partial x} \right] dv d\mu + \varepsilon^2 e \int_{0}^{x} \left[n_i - \int_{-1}^{1} \int_{0}^{\infty} f_e v^2 dv d\mu \right] dx' \qquad (2)$$

In addition, we simulate the whole magnetic line with two sheath boundary conditions with self-consistently obtained potential drop by using the logical sheath condition [9] (as spatial resolution $\Delta x \gg \lambda_D$). Loses of energetic electrons through the sheaths are balanced by a source of secondary electrons generatid by neutral ionization, which spatial shape is taken from the fluid modeling [2], while its total power varies self-consistently.

To obtain reasonable accuracy we used fine mesh of size $82(x)$x$257(v)$x$129(\mu)$. Along with other complications listed above this makes runs very time consuming. We were able to follow system evolution up to 10 mks (dosen electron-electron collision times measured in the symmetry plane region). The preliminary results are the followings.

Deviation of f_e was found to be as strong as in the linear case, and amplitudes of plasma-neutral reaction rates and parallel conductivity modifications with respect to Maxwellian are very close too. In Figs. 7a and 7b we plot obtained two-dimensional distribution functions near X-point (at inner plate side) and at outer divertor plate.

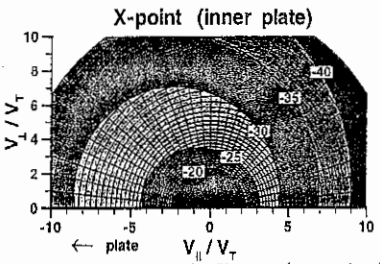

Fig.7a $\ln f_e$ *near the X-point (inner plate)*

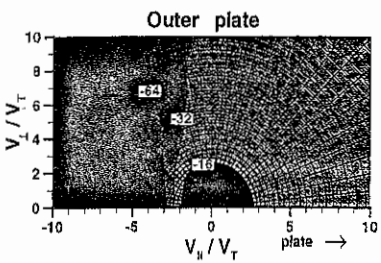

Fig.7b $\ln f_e$ *at the outer plate*

Near X-point distribution function is asymmetric, with elevated downstream (towards plate) and depleted upstream 'side', which results in 10% difference in their temperatures. Because of high plasma collisionality ($\gamma \approx 0.04$) thermal particles $E \leq T$ are perfectly maxwellized, and the difference between parallel and perpendicular temperatures is about percent. At the symmetry plane this ratio is exactly opposite. Because we are using real sheath boundary condition, which forces predominant loss of energetic particles at the plates, distribution function becomes more asymmetric as we are approaching them. In the plate vicinity (Fig.7b, where we additionally superimposed the variable v, μ grid used in the modeling) all electrons with parallel velocities bigger than $\sqrt{\Delta\Phi_f/m_e}$ (Φ_f-divertor floating potential) are absorbed. We have found increased Φ_f=3.5T and 3.7T at inner and outer plates, respectively. It can be also seen that f_e is more peaked near the plate than near X-point. Reason for this is that ionization there produces more cold secondary electrons (we assume their temperature to be 0.1 eV). Thermal core looks also less equilibrated. Note that Coulomb Knudsen number falls up to 10^{-4} in the divertor region. We also see that heat flux several times exceeds fluid results. Thermal force coefficient was found to be about -0.5 in downstream region. To be more conclusive we have to include important electron-ion Coulomb energy exchange into our model.

However, our kinetic modeling shows that combination of sharp gradients, volumetric sources of cold particles and presence of absorbing wall can cause significant departure of electron distribution function from Maxwellian even in the presence of strong Coulomb equilibration (T=1eV, n=10^{21} m^{-3}) in the ITER divertor.

References

[1] A.S. Kukushkin and A.M.Runov, *Contrib. Plasma Phys.* **34**, 204 (1994).
[2] A.S. Kukushkin et al., IAEA-CN-64/FP-27, 16th IAEA Fusion Energy Conf., Montreal, Canada, 7-11 October, 1996.
[3] S.I. Braginskii, *Reviews of Plasma Physics* (Cons. Bureau, NY) Vol. 1, 205 (1965).
[4] L. Spitzer and R. Harm, *Phys. Rev.* **89**, 977 (1953).
[5] P.S. Stangeby, *Nucl. Fusion* **33**, 1695 (1993).
[6] O.V. Batishchev et al., *Journ. Nucl. Mat.* 3042 (1997).
[7] A.A. Batishcheva et al., *Physics of Plasmas* **3**, 1634 (1996).
[8] O.V. Batishchev et al., *Physics of Plasmas* **4**, 1672 (1997).
[9] R.J. Procassini et al., *Nucl. Fusion* **30**, 2329 (1990).

Dimensional Analysis of Turbulent Transport at the Edge: the Role of Electro-Magnetic Effects in the L-H Transition

A.V.Chankin[1] and G.F.Matthews
JET Joint Undertaking, Abingdon, Oxon, OX14 3EA, UK
[1]Permanent affiliation: RSC "Kurchatov Institute", INF, Moscow, Russia

Introduction

Recent three-dimensional computations confirmed a universal role played by drift turbulence at the tokamak edge [1,2]. The turbulence is non-local and originates due to non-linear instability. It was traditionally assumed that the drift turbulence has a predominantly electrostatic nature, with MHD mechanisms located inside the separatrix. Recently, however, it has been recognised [3,4] that in high power tokamak discharges the edge plasma is sufficiently "hot" and "dense" (high T and β) for electro-magnetic effects to influence plasma transport by interacting with drift fluctuations.

The dimensional approach (see e.g. [5]), in conjunction with experimental results, provides a reasonable complement to modelling efforts. One can capitalise on the fact that both measurements and modelling reveal the typical characteristic scale length for low temperature collisional drift turbulence, namely the ion Larmor radius ρ_s. Electro-magnetic effects, by introducing new turbulence scales which fall with density/temperature, may lead to a bifurcation in the plasma transport, thereby enabling one to explain the phenomenon of the L-H transition.

Characteristic scale lengths and critical conditions for the edge transport

The radial scale of electrostatic drift fluctuations $\Delta_{fluct} \approx \pi / k_r$ is determined by the Larmor radius $\rho_s = c_s / \omega_i$ (we adopt $c_s = \sqrt{(T_e + T_i)/m_i}$ here). Typically, $k_\perp \rho_s << 1$. In addition, various mechanisms (e.g. the existence of critical gradients for instabilities) may introduce a dependence of Δ_{fluct} on $\rho^* = \rho_s / a$ (a - minor radius).

The way electro-magnetic scale should be introduced is clear from the requirement of the dimensional transformation of the equation: $\frac{\partial \mathbf{B}}{\partial t} = curl(\mathbf{V} \times \mathbf{B}) + \frac{c^2}{4\pi\sigma}\Delta\mathbf{B}$. The $curl(\mathbf{V} \times \mathbf{B})$ term of this equation is responsible for Alfvén and magneto-sonic waves. Their interaction with drift waves occurs at $\beta \approx m_e / m_i$ or even higher β ($\beta_e \equiv 4\pi n T_e / B^2 = m_e / m_i$ can be derived by equating an upper limit for parallel phase velocity of drift waves, $v_e = \sqrt{T_e / m_e}$, to Alfvén velocity $v_A = B / \sqrt{4\pi n m_i}$ [3]). A much lower threshold for β, characteristic of plasma parameters near the separatrix, is required for the $c^2\Delta\mathbf{B} / 4\pi\sigma$ term, which describes the field diffusion into the plasma, to make a strong impact on the drift turbulence (see below). Together, the $\partial\mathbf{B} / \partial t$ and $c^2\Delta\mathbf{B} / 4\pi\sigma$ terms yield the skin-depth $\Delta_{skin} = c / \sqrt{4\pi\sigma\nu}$ (ν - fluctuation frequency) for the Δ_{fluct} scale. There are two skin-depths to be considered: the *collisional* skin-depth $c / \sqrt{4\pi\sigma_{coll}\nu}$ (σ_{coll} - Spitzer

conductivity), which decreases with temperature due to $\sigma_{coll} \sim T_e^{3/2} / Z_{eff}$, and the *collisionless* skin-depth $c/\omega_{p_e} = c/\sqrt{4\pi ne^2/m_e}$ (follows from $|\sigma| = ne^2/m_e\omega$ - parallel conductivity due to electron inertia), which decreases with density. That is why at high temperature and/or density, when electro-magnetic effects become important, Δ_{fluct} should decrease, in contrast with its increase with temperature (approximately as $\rho_s \sim \sqrt{T}$) at low T. By reducing the magnitude of Δ_{fluct}, electro-magnetic effects influence transport coefficients $D_\perp$, χ_e and χ_i, so that they will reach their maxima along a certain curve in the (n_e, T) parameter space. The existence of such maxima prompts a bifurcation in the plasma transport: the L-H transition.

Which of the two skin-depths defines the size of turbulent eddies and is responsible for the magnitude of transport coefficients, depends on the collisionality. In general, since both contributions to the parallel conductivity (electron-ion collisions as well as electron inertia) are important, there must be a smooth transition between the two. For the purposes of dimensional analysis we consider the two extreme cases of high (*collisional* conductivity) and low (*collisionless* conductivity) densities. At high n_e, the important threshold is reached when $\Delta_{coll.skin}$ becomes equal to Δ_{fluct}. This equality can also be expressed as $\Delta_{fluct}^2 \nu = c^2/4\pi\sigma_{coll}$. Since the left hand side of this equation is in fact the diffusion coefficient $D_\perp$, the critical condition for the turbulence suppression by the *collisional* skin effect (the L-H transition threshold), can be formulated as:

$$D_\perp \approx c^2/4\pi\sigma_{coll} \quad . \tag{1}$$

At low densities (*collisionless* limit), for $k_r > k_\theta$ the criticality condition is:

$$\Delta_{fluct} \approx \pi c/\omega_{p_e} \quad . \tag{2}$$

Scalings for the L-H transition threshold

A number of thresholds for the L-H transition can be derived from Eqs. (1-2), depending on the particular form of scalings for Δ_{fluct} and $D_\perp$. We first consider the $\Delta_{fluct} \sim \rho_s$ ($k_\perp \rho_s = const$), or "local" scaling. The diffusion coefficient $D_\perp$ can be derived self-consistently on the assumptions:

$$D_\perp \sim \omega_{drift} \times k_r^{-2}, \quad \omega_{drift} \sim k_\theta T_e / eB\Delta_{sol}, \quad \Delta_{sol} \sim (D_\perp qR/c_s)^{1/2}, \quad k_\theta \sim k_r \sim 1/\rho_s, \tag{3}$$

Eq. (2) combined with the scaling $\Delta_{fluct} \sim \rho_s$ gives the threshold for β **(*)** (more precisely, for $\Delta_{fluct} = \pi/k_r$ the analysis gives $\beta_{crit} = (k_r\rho_s)^2 m_e/m_i$, which is significantly below the limit associated with the interaction between drift and Alfvén waves mentioned above). Eqs. (3) yield the $D_\perp \sim \frac{T_e^{2/3}(T_e+T_i)^{1/6}}{B^{2/3}} \frac{a}{(qR)^{1/2}}$ scaling which, when combined with Eq. (1), results in the following threshold parameter: $\frac{T_e^{13/8}(T_e+T_i)^{3/8}}{BZ_{eff}^{3/4}(qR)^{1/4}}$ **(a)**.

The two thresholds are schematically shown on Fig. 1. Typical separatrix parameters in medium to high density discharges fall on the *collisional* scaling provided $k_\perp \rho_s < 0.3$.

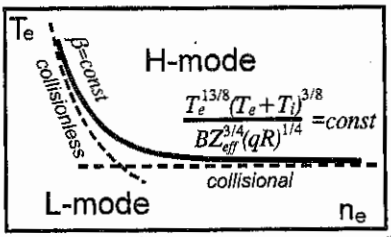

Fig. 1. H-mode operational space for local ($k_\perp \rho_s = const$) drift-type scaling with a radial fall-off length given by the density decay scaling in the SOL. Boundaries are defined by **(*)** *($\beta = const$) and* **(a)** *thresholds.*

If the SOL physics is totally ignored and the decay length Δ_{sol} in Eqs. (3) is replaced with the minor radius a, one obtains the Gyro-Bohm scaling $D_\perp \sim \frac{T_e(T_e+T_i)^{1/2}}{B^2 a}$, and Eq. (1) then yields the threshold parameter $\frac{T_e^{5/4}(T_e+T_i)^{1/4}}{BZ_{eff}^{1/2}a^{1/2}}$ **(b)**.

For the "global" scaling $\Delta_{fluct} \sim a$ ($k_\perp \rho_s \sim \rho^*$), Eq. (2) gives the threshold in $n_e a^2$ **(**)**. Eq. (1), together with Eqs. (3) in which the last dependence is replaced with $k_\theta \sim k_r \sim 1/a$, gives the threshold in $\frac{T_e^{13/6}(T_e+T_i)^{1/6}a}{BZ_{eff}^{3/2}(qR)^{1/2}}$ **(c)**. If, in addition, the SOL physics is ignored and Δ_{sol} in Eqs. (3) is replaced with a, one obtains the Bohm scaling $D_\perp \sim T_e / B$ which leads to the threshold in $T_e^{5/2} / BZ_{eff}$ **(d)**.

Finally, the scaling $D_\perp \sim \nu_{ei}\rho_s^2 q^2 R/\lambda_n$ for resistive interchange instability may be considered as an alternative to drift-type scalings. For density decay length λ_n we consider two limiting cases: $\lambda_n \sim \rho_s$ and $\lambda_n \sim a$, yielding thresholds in $(T_e+T_i)(nq^2R/B)^2$ **(e)** and $(T_e+T_i)nq^2R/aB$ **(f)** respectively.

Comparison with experiment

There is growing experimental evidence for the existance of the edge T_e threshold for the L-H transition. The threshold T_e increases with the magnetic field, but shows no strong dependence on q or $\bar{n}_e$ (the latter - only for medium to high densities, see e.g. refs. inside [4]). This is in a qualitative agreement with the threshold parameters **(a-d)**. "Global" scalings incorrectly describe the low density limit for the L-H transition: the $n_e a^2 = const$ **(**)** scaling is in a disagreement with experimental data. An observed increase in the edge T_e at low densities rather points to a critical β as being the threshold parameter [6], in line with predictions following from "local" drift-type scalings. However, an increase in the pedestal T_e prior to the L-H transition observed in experiment may also be caused by some other reasons (high Z_{eff}, locked modes etc.) and not necessarily be related to the criticality condition (2). Thresholds **(e)** and **(f)**, corresponding to resistive interchange instability seem to contradict the experiment by predicting a rather strong inverse dependence on density and safety factor and therefore should be discarded.

The critical T_e measured near the edge of the pedestal in Alcator C-Mod, ASDEX-U, DIII-D and JET prior to the L-H transition, was found to increase with toroidal field as $T_e \sim B^\alpha$, with $\alpha = 1-2$. In contrast, threshold parameters **(a-d)**, relevant to all but very low density plasmas, correspond to a fairly weak B-dependence: $T_e \sim B^\alpha$, with $\alpha < 0.7$. This discrepancy indicates that the location of the temperature measurements carried out so far (usually near the Ψ_{95} surface) does not correspond to the critical position for the onset of the L-H transition and it is the T_e near the separatrix or even inside the SOL, rather than at the edge of the pedestal, which determines the transition. This is because the SOL T_e is relatively constant (compared to the T_e in the core) owing to the $q_{e\|} \sim T_e^{7/2}$ dependence for the heat sink onto the target. The importance of the scrape-off layer as a possible source of the edge turbulence is manifested by measurements of radially increasing χ_e inside the SOL (perhaps, due to the increased collisionality, see e.g. [7]), indicating that "a complete understanding of the L-H transition will require a proper treatment of the interface between the SOL and closed flux region" [2].

Conclusions

Electro-magnetic effects introduce the skin-depth as a scale length $\lambda_\perp$ of the edge turbulence at $\beta > m_e / m_i \times (k_\perp \rho_s)^2$ (which is only the necessary condition), as opposed to $\lambda_\perp \sim \rho_s$ for the electrostatic drift turbulence at low β. As a result, transport coefficients are expected to reach maxima at sufficiently high temperature and density, thereby prompting a bifurcation in solutions for the plasma transport. The analysis is valid up to $\beta \approx m_e / m_i$ ($k_\perp \rho_s << 1$ at the edge), when the drift-Alfvén interaction occurs.

"Local" drift-type scalings for $D_\perp$ with $k_\perp \rho_s = const$ yield the threshold parameters for the L-H transition which are in a qualitative agreement with the measurements near the edge of the pedestal. However, the predicted weak dependence of the threshold T_e on B: $T_e \sim B^\alpha$ ($\alpha < 0.7$), disagrees with the strong dependence ($\alpha = 1-2$) observed near the edge of the pedestal. This discrepancy is: a) expected (the L-H threshold criterion derived must be applied near the separatrix), b) attributed to the $q_{e\|} \sim T_e^{7/2}$ dependence for the electron heat sink onto the target, which makes $T_{e,sep}$ relatively constant (compared to the T_e in the core) and c) indicates that the extreme edge (near separatrix or even SOL regions) plays a crucial role in the L-H transition.

Acknowledgements

Discussions with J.W.Connor, S.K.Erents and B.Scott are greatly appreciated.

References

[1] Scott B., Plasma Phys. Contr. Fusion 39 (1997) 471. [2] Zeiler A. et al., Phys. Plasmas 3 (1996) 2951. [3] Scott B., Camargo S., Jenko F., 16th IAEA Fusion Energy Conf., Montreal, Canada, 7-11 October 1996, paper IAEA-CN-64/DP-18. [4] Chankin A.V., to be publ. in Plasma Phys. Contr. Fusion 39 (1997) No.7. [5] Connor J.W., Taylor J.B., Nucl. Fusion 17 (1977) 1047. [6] Igitkhanov Yu.L. et al., ITER Memo. G19 MD1 96-12-12 W0.1 and S17 MD1 96-12-12 F1 (1996). [7] Erents S.K. et al., this conference.

Particle-in-Cell Simulations of Parasitic Absorption of Lower Hybrid Power in ITER

K. M. Rantamäki[1], S. J. Karttunen[2], X. Litaudon[3], D. Moreau[3] and T. J. H. Pättikangas[2]

[1]Advanced Energy Systems, Helsinki University of Technology, Association Euratom–TEKES, P. O. Box 2200, FIN-02015 HUT, Finland

[2]VTT Energy, Association Euratom–TEKES, P.O. Box 1604, FIN-02044 VTT, Finland

[3]Département de recherches sur la fusion contrôlée, Association Euratom–CEA, Centre d'études de Cadarache, Saint Paul-les-Durance, France

1 Introduction

In recent lower hybrid (LH) current drive experiments in tokamaks, generation of impurities in the grill region has been observed at Tore Supra and Tokamak de Varennes [1, 2]. A possible explanation for the impurity production is the sputtering caused by fast electrons generated by the near field of the LH grill. The grill is tuned for the low parallel refraction index $n_\parallel \simeq 2$ but the higher $n_\parallel$ values can not be avoided. These modes with high $n_\parallel$ are absorbed by electrons within a short distance of a few millimetres in front of the grill [3, 4].

In this report, the absorption mechanism described above is investigated by a self-consistent two-dimensional particle-in-cell (PIC) code XPDP2. The self-consistent PIC simulations give the key parameters of the problem: the absorbed power, the radial deposition profiles and energy spectrum of the accelerated particles close to the grill mouth. Possible consequenses for ITER are discussed.

2 PIC Model for an LH Grill

The grill parameters in the present simulations correspond to the Tore Supra launcher [5]. The main peak at $n_\parallel \simeq 1.9$ does not interact with the cold edge plasma. The grill structure generates, however, also extra peaks with higher $n_\parallel$ values. In the present simulations, the most intense extra peaks in the high $n_\parallel$ simulation correspond to $n_\parallel \simeq 9.6$ and $n_\parallel \simeq 13.5$. When the temperature is $T_e = 100$ eV, the parallel phase velocity of the mode $n_\parallel \simeq 21$, also existing in the spectrum, is $v_{ph,\parallel} \simeq 2.4 v_e$, where v_e is the thermal velocity. The density of the homogeneous plasma was $n_e = 1.0 \times 10^{18}$ m^{-3} and the magnetic field was $B = 2.78$ T.

The PIC code XPDP2 [6] used in this work, is a self-consistent electrostatic particle-in-cell code. The code is two-dimensional in space having periodic boundary conditions in the toroidal y direction and bounded in the radial x direction. The magnetic field and the grill mouth are along the y axis, and the wave is launched from the antenna in the radial x direction. In the poloidal z direction, the wave guides are assumed to be infinite.

In the periodic y direction, we have four waveguides of the width $L_{wg} = 8.5$ mm with 2 mm septa between them. An external oscillating charge density ρ_{ext} at the grill

mouth has been used to model the LH grill

$$\rho_{ext} = \rho_0 \left(1 + \epsilon \left|\frac{y - y_n}{w}\right|^{\mu}\right) \sin\left(\omega t - n\Delta\phi\right), \quad (1)$$

where y_n is the y co-ordinate in the middle on the nth waveguide. The frequency of the grill is $\nu = 3.7$ GHz, and the phase difference between the waveguides is $\Delta\phi = \pi/2$.

Two simulations have been performed. One is with a constant charge density in the waveguides, resulting in a spectrum with only small amount of energy in the high $n_\parallel$ modes. This simulation is here called the reference simulation and was obtained with $\epsilon = 0$ in Eq. (1). In the other simulation, a nonconstant charge density with very sharp peaks at the edges of the waveguides was used, i.e., $\epsilon = 3$ and $\mu = 4$. The sharp behaviour at the edges increases the amplitude of the modes with high $n_\parallel$ values. This simulation is called high $n_\parallel$ simulation.

3 Fast Electron Generation in the Near Field

Figure 1 shows the Poynting fluxes of the wave modes at time $\nu t = 8$ for the high $n_\parallel$ simulation at two locations in the radial direction. In addition to the principal mode $n_\parallel \simeq 1.9$ and an additional lower mode $n_\parallel \simeq 5.8$, the higher modes $n_\parallel \simeq 9.6$, $n_\parallel \simeq 14$ and $n_\parallel \simeq 21$ carry power into the plasma edge.

The Poynting fluxes for the reference simulation at time $\nu t = 8$ are shown in Fig. 2. In this reference simulation, there is only the mode with $n_\parallel \simeq 14$ surviving in the plasma in addition to the lower modes $n_\parallel \simeq 1.9$ and $n_\parallel \simeq 5.8$.

In Figure 3, the coupled intensity is shown for the high $n_\parallel$ simulation and the reference simulation. As can be seen in Fig. 3(a) much power is coupled to a few mm in front of the grill. In the reference simulation, the power is coupled more homogeneously and the intensity level is approximately the same as in the high $n_\parallel$ simulation further inside the plasma. The total intensity integrated over the radial length is for the high $n_\parallel$ simulation $I_{in} \simeq 38$ MW/m^2, and for the reference simulation $I_{in} \simeq 48$ MW/m^2.

The amount of intensity absorbed by the electrons per unit length is calculated as $I_{abs,e} = (\Delta E_{kin,e} - W_{kin,e})/\Delta t \Delta x A$ where $\Delta E_{kin,e}$ is the change in the kinetic energy during the time interval Δt, and $W_{kin,e}$ is the kinetic energy of the electrons due to the oscillation with the wave. $W_{kin,e}$ is obtained from an analytic model where the velocities are calculated with the help of the cold plasma conductivity tensor.

Figure 4 shows the absorption profiles in front of the grill for the high $n_\parallel$ simulation and the reference simulation. The total absorption to the electrons in the high $n_\parallel$ simulation is $I_{abs,e} = 7$ MW/m^2 which means that 18 % of the coupled power is absorbed to the electrons. As much as 56 % of this absorption takes place in the very edge of the plasma. Within 1.7 mm in front of the grill the absorbed intensity is $I_{abs,edg} = 3.9$ MW/m^2. In the reference simulation the absorption is less, only 6 %, despite of the higher coupled intensity. The total intensity absorbed to the electrons is $I_{abs,e} = 3$ MW/m^2 of which only 10 % is absorbed within the 1.7 mm at the edge plasma.

Figure 5 shows the velocity distribution of the electrons for the high $n_\parallel$ simulation in two regions of the plasma. The dashed curve is the initial thermal distribution and the solid line describes the distribution at time $\nu t = 8$. The velocity distribution closest to the grill mouths shows a fairly large tail population extending up to $v_y/v_e \simeq 6$ corresponding to maximum energies of 4 keV. The horizontal lines in Fig. 5 indicate the trapping widths of the individual modes at different $n_\parallel$ shown on the right-hand scale.

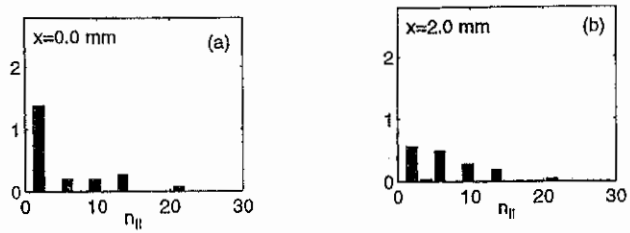

Figure 1: The power spectra in the high $n_\parallel$ simulation (a) at the plasma edge $x = 0$ mm and (b) inside the plasma at $x = 2$ mm.

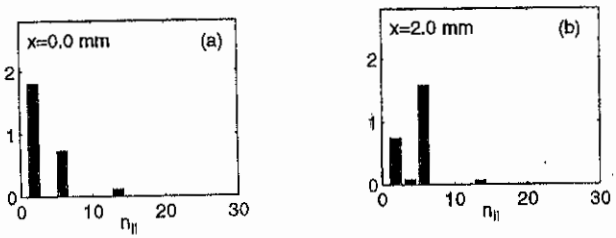

Figure 2: The power spectra in the reference simulation at (a) the plasma edge $x = 0$ mm and (b) inside the plasma at $x = 2$ mm.

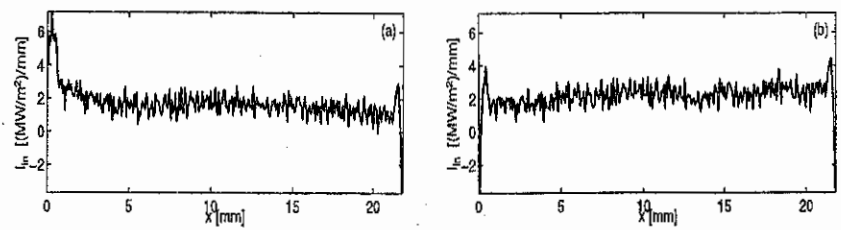

Figure 3: Coupled wave intensity versus the radial co-ordinate for (a) the high $n_\parallel$ simulation and (b) the reference simulation.

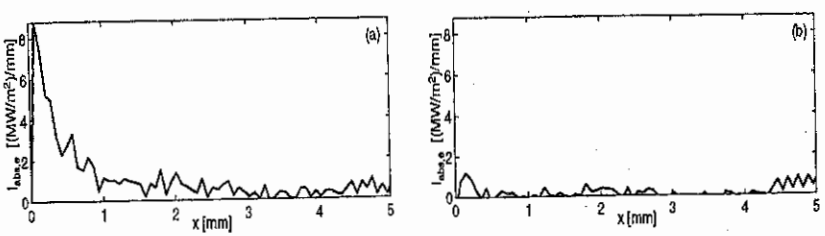

Figure 4: Absorbed wave intensity versus the radial co-ordinate for (a) the high $n_\parallel$ simulation and (b) the reference simulation.

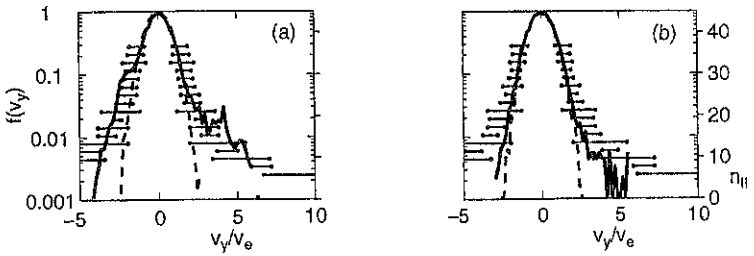

Figure 5: Parallel velocity distributions of the electrons, for the high $n_\parallel$ simulation, in the regions (a) $0 \leq x \leq 0.5$ mm, (b) 1.5 mm $\leq x \leq 2$ mm. The trapping widths of the wave modes are shown on the right-hand scale.

In the reference simulation, the overlapping of the trapping widths of the high $n_\parallel$ modes is smaller, and fast particles are no more generated. The tail population is smaller than in the high $n_\parallel$ simulation and the maximum velocities are much lower.

For ITER two 25 MW launchers are being designed but the detailed spectra of the launchers are at the moment not known. The calculations described above and the investigations of Fuchs *et al.* indicate that the amplitude and the spacing of the high $n_\parallel$ modes determine the amount of the parasitic absorption in front of the launcher. Therefore, the calculations described above can not give very accurate estimates for the parasitic absorption in ITER. A more detailed analysis would be desirable before the design of the ITER launcher is finished.

Acknowledgements: We would like to thank Dr. Alan Côte for useful discussions. We are grateful to the Plasma Theory and Simulation Group (Professor C.K. Birdsall, University of California, Berkeley) for providing us with their 2d3v PIC code XPDP2.

[1] J.H. Harris, J.T. Hogan, M. Goniche, X. Litaudon, *et al.*, Europhys. Conf. Abstr. **19C**, Part IV, 397 (1995).

[2] A. Côté, Y. Demers, P. Brooker, C. Côté, *et al.*, 16th IAEA Fusion Energy Conference, Montréal, Canada, 7–11 October 1996, paper IAEA-CN-64/EP-5.

[3] O. Dumbrajs, J.A. Heikkinen, S.J. Karttunen, T. Kiviniemi, *et al.*, 16th IAEA Fusion Energy Conference, Montréal, Canada, 7–11 October 1996, paper IAEA-CN-64/EP-9.

[4] V. Fuchs, M. Goniche, Y. Demers, *et al.*, Phys. Plasmas **3**, 4023 (1996).

[5] X. Litaudon, G. Berger-By, P. Bibet, J.P. Bizarro, *et al.*, Nucl. Fusion **32**, 1883 (1992).

[6] V. Vahedi, C.K. Birdsall, M.A. Lieberman, G. DiPeso, and T.D. Rognlien, Phys. Fluids **B 5**, 2719 (1993).

Prospects for Electron Cyclotron Current Drive Stabilization of Neoclassical Tearing Modes in ITER

F. W. Perkins[1], R. W. Harvey[2], M. Makowski[3], and M. N. Rosenbluth[1]

1. Introduction. Neoclassical islands [1-4, 6] are observed to arise at the major rational surfaces (m,n) = (2,1), (3,1), (3,2) etc. of many tokamaks. Confinement degradation and/or disruptions associated with these modes can limit β, for example in DIII-D [4]. The situation in JET [5] appears to be different. A recent review by O. Sauter [6] summarizes the physical origin of neoclassical islands that result from the loss of bootstrap current density when the pressure gradient becomes zero due to rapid parallel transport within the island.

A key feature of neoclassical islands is their slow temporal evolution — estimates suggest 10-30s for ITER [6] — which provides the opportunity to apply feedback techniques that could both increase the operational β-limit and fusion power of ITER as well as providing a technique to suppress locked modes arising from error fields. Electron Cyclotron Current Drive (ECCD) can provide current profile control [7], and is an evident candidate for modulated CD to replace the lost bootstrap current, thereby stabilizing toroidally rotating islands[8,9]. The key result of this work is a criterion on the modulated current density needed to stabilize islands. We note that the temporal modulation will suffice for rotating modes but that ECCD stabilization of locked modes will require 4 ECCD launcher ports, spaced toroidally.

2. Analysis. Our approach is a generalization of the island evolution equation as set forth in [10] , specialized to the (2,1) mode. A helical flux function is defined

$$\chi = \chi_o\left(\frac{1+\cos(2\alpha)}{2}\right) - \frac{B\hat{s}}{2q}x^2 \qquad (1)$$

and an associated nondimensional variable ψ

$$\psi = \frac{x^2}{w^2} - \left(\frac{1+\cos(2\alpha)}{2}\right) \qquad w^2 = 2q\chi_o/B\hat{s} \qquad (2)$$

where $\alpha = \theta - (\phi-\omega t)/2$, ω denotes the island rotation rate, and w the island half-width. Following standard techniques [10], the island evolution equation becomes

$$\frac{\mu_o}{\eta}\left(\frac{2\,C_1}{\pi}\right)\frac{\partial w}{\partial t} = \Delta' + \Delta'_{bs} - \Delta'_{cd} \qquad (3)$$

where

$$\Delta'_{bs} = \frac{4\,\mu_o\,Rq\,j_{bs}}{\pi\,w\,\hat{s}\,B}\,C_2 \qquad \Delta'_{cd} = \frac{4\,\mu_o\,Rq\,j_{cd}}{\pi\,w\,\hat{s}\,B}\int_{-1}^{\infty} d\psi\; W(\psi)\,J(\psi) \qquad (4)$$

[1]ITER/San Diego, 11025 North Torrey Pines Road, La Jolla, CA 92037
[2]CompX, 12839 Via Grimaldi, Del Mar, CA 92014
[3]ITER/Garching, Max-Planck-Institut fur Plasmaphysik, D-85748 Garching bei Munchen, Germany

and Δ' is the usual tearing mode stability parameter defined by the external solution and is assumed to be negative (tearing mode stability). The following flux surface average quantities enter

$$W(\psi) = \oint \frac{\cos(2\alpha)}{\sqrt{\psi + \cos^2(\alpha)}}\, d\alpha \qquad V(\psi) = \oint \frac{1}{\sqrt{\psi + \cos^2(\alpha)}}\, d\alpha \qquad (5)$$

$$J(\psi, \tau, w/w_{cd}) = \frac{1}{V(\psi)} \oint d\alpha \frac{M(\alpha,\tau)}{\sqrt{\psi + \cos^2(\alpha)}} \exp\left\{-\frac{w^2}{w_{cd}^2}\left(\psi + \cos^2(\alpha)\right)\right\} \qquad (6)$$

where $\oint$ denotes the region $-\pi<\alpha<\pi$ for $\psi>0$ and the interval where $\psi+\cos^2\alpha\geq 0$ for $-1<\psi<0$. We parameterize the modulation function $M(\alpha,\tau)$ in terms of the fractional "on" time τ, which takes on the range $0<\tau<1.0$,

$$M(\alpha, \tau) = \begin{cases} 1 & 0 < |\alpha| < \tau\pi/2 \\ 1 & \pi - \tau\pi/2 < |\alpha| < \pi \\ 0 & \tau\pi/2 < |\alpha| < \pi - \tau\pi/2 \end{cases} . \qquad (7)$$

The constants C_n are

$$C_1 = \int_{-1}^{\infty} d\psi \frac{W^2}{V} = 2.58 \qquad C_2 = \int_{-1}^{0} W\, d\psi = 2.67 \qquad (8)$$

and we note that $\int_{-1}^{\infty} d\psi\, W = 0$. We have assumed a Gaussian driven current density distribution $j_{cd} = I_{cd} \exp(-x^2/w_{cd}^2)\, (2\pi^{3/2} r\, w_{cd})^{-1}$ centered on the rational surface. The current I_{cd} is to be evaluated as if the ECCD power is on continuously. The bootstrap current density is given by j_{bs} within the island ($-1<\psi<0$) and zero outside. Since Δ'_{bs} is positive, Eq.(3) supports growing islands in the absence of ECCD which saturate when $\Delta'_{bs} = -\Delta'$.

3.Stabilization Criterion. The key observation [8] is that, in the thin island limit $w/w_{cd}\rightarrow 0$, both bootstrap and current drive contributions to Δ' have an inverse dependence on island width. It follows that one can prevent island growth when

$$K_1\, j_{cd} > j_{bs}; \qquad K_1(\tau, w/w_{cd}) = \frac{1}{C_2} \int_{-1}^{\infty} d\psi\, J(\psi, \tau, w/w_{cd})\, W(\psi) \quad . \qquad (9)$$

Figure 1 plots K_1 versus the modulation on-time τ and island width. Note that for a system continuosly on, J=1 in the thin island limit $w<<w_{cd}$, so that $K_1 = 0$. Note also that current drive effectiveness increases with island width for small islands and, for thin islands, there there is a broad maximum in effectiveness $K_1 \approx 0.68$ around $\tau \approx 0.5$. Thus, ECCD modulated 50%"on"—50%"off" can prevent the growth of neoclassical islands when

$$0.68\, j_{cd} > j_{bs} \quad . \qquad (10)$$

Of course, there must be reference signal obtained from magnetic diagnostics to select the correct phase for the modulated feedback.

4. Unmodulated ECCD. It is also of interest to ascertain what effect unmodulated ECCD power (τ=1.0) will have. In this case, no direct stabilzation can be obtained but the saturated island width will be modified according to

$$w = \frac{4\cdot\mu_o C_2 R q}{(-\Delta')\pi \hat{s} B}\left(j_{bs} - K_1 j_{cd}\right) \qquad (11)$$

Figure 2 plots K_1 for an unmodulated system as a function of island width. In this limit, K_1 achieves a maximum of $K_1 \approx 0.60$ for $w_{cd}/w \approx 0.5$-1.0. In general, K_1 depends on island size and Eq.(11) must be solved iteratively. For small-but-finite islands $w<w_{cd}$, one can evaluate $C_2K_1 = w\pi^{3/2}(2w_{cd})^{-1}$leading to the expression for the saturated island half-width

$$w = \frac{j_{bs} C_2}{\left(-\frac{\Delta'\pi \hat{s} B}{4\mu_o R q} + \frac{j_{cd}\pi^{3/2}}{2 w_{cd}}\right)} \qquad (12)$$

Equation (11) is in qualitative accord with the general observation that current drive localized near the q=2 surface can affect island saturation sizes [11]. In the other limit where current drive is concentrated into a thin layer relative to the island size, K_1 takes on the asymptotic form $K_1 = 1.55\cdot F[\Delta x/w]\cdot(w_{cd}/w)$, where Δx denotes the offset of the driven current layer from the rational surface. Figure 3 plots the function F. As expected, when Δx exceeds 75% of the island half-width, the stabilizing properties of current drive are lost.

5. Implementation. It follows that an ECCD mode stabilization system should have a modulation rate comparable to anticipated island rotation frequencies, which in ITER can be as large as 5 kHz for low-density NBI-heated discharges. The launcher design should localize current drive centered on the mode rational surface. This leads to launch configurations with off-midplane launch so that spatial focussing of the ECCD power coupled with a variable poloidal launch angle can select the flux surface for ECCD power deposition. Fig. 4 reports preliminary ray-tracing calculation which indicate that a 50 MW ECCD system for ITER can fulfill the stabilization criterion (10), given a representative boostrap current level of 0.1 MA/m^2 for ITER (see Fig. 9, ref[6]).

[1] R. Carrera, R. D. Hazeltine, M. Kotschenreuther, Phys. Fluids **29**, 899 (1986);
W. Q. Xu and J. D. Callen, Univ. of Wisconsin Report, UWPR85-5 (1985)
[2] H. Zohm, Plasma Physics and Controlled Fusion **37** A313 (1995).
[3] D. A. Gates et al (Proc. 22 Eur. Conf., Bournemouth, 1995) **19C**, Part IV, 117 (1996);
D. A. Gates et al, Report UKAEA FUS 362, Culham Laboratory, (1997)
[4] R. J. LaHaye et al., Nuclear Fusion **37** 397 (1997)
[5] JET Team (P. Thomas) (Proc. 16 IAEA Fusion Energy Conf, Montreal,1996)
paper CN-64/A3-2

[6] O. Sauter et al., Phys. Plasmas **4** 1654 (1997)
[7] R.W. Harvey et al, Nucl. Fus. 37, 69 (1997).
[8] P. Rutherford, in *Basic Physical Processes of Toroidal Fusion Plasmas,* Vol.2, 531 (1985)
[9] F. Perkins et al. (Proc. 16 IAEA Fusion Energy Conf., Montreal, 1996) paper CN-64/FP-24.
[10] R. D. Hazeltine, J. D. Meiss, *Plasma Confinement*, Adison-Wesley, Redwood City, CA, p382-386 (1992); R. Fitzpatrick, Phys. Plasmas **2** 825 (1995)
[11] A. W. Morris et al., (Proc 13 Intl. Conf. Plasma Physics and Controlled Fusion Research, Washington, D.C. 1990) Vol. 1 p 797 (1991); K. Hoshino et al., (Proc. 15 Intl. Conf. Plasma Physics and Contriolled Nuclear Fusion Research, Seville, 1994) Vol. 1, 697 (1995)

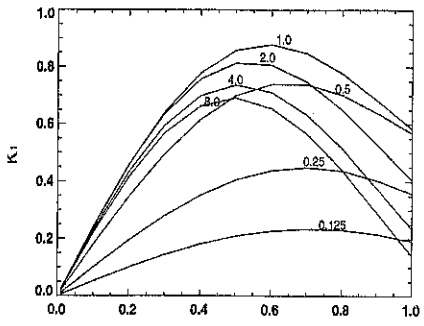

Fig. 1. K1 versus "on"-time τ for the various island widths w_{cd}/w marked on the diagram.

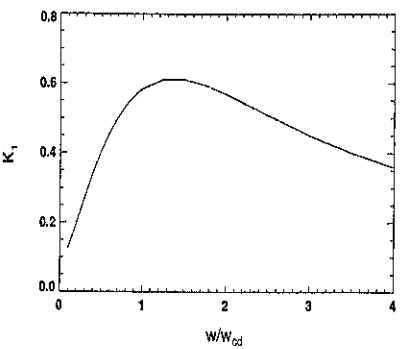

Fig. 2. K1 versus island width, for unmodulated ECCD (τ = 1.0).

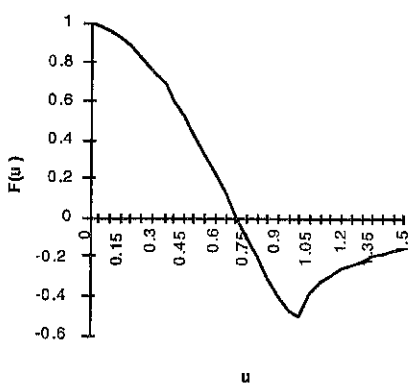

Fig. 3. F(u) versus u=Δx/w.

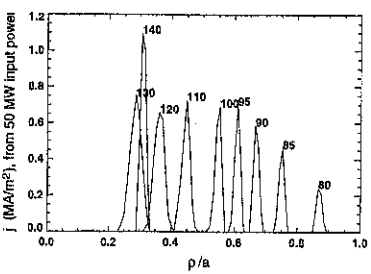

Fig. 4. Current density versus normalized radius, for 50MW input EC power at 170 GHz into an ITER plasma with flat density profile at 1.0 10^{20} /m^3, and parabolic temperature profile with central value 30 keV. The parameter marked on the curves is poloidal angle, 90 deg being straight in. Launch is from 2.5m above the midplane, with constant toroidal angle 30 deg.

ITER 2D X-ray imaging system based on the X-ray fibre optics.

A.V.Sushkov, P.V.Savrukhin, V.M.Trukhin.
RRC "Kurchatov Institute" 123182 Moscow, Russia.

1. Introduction

X-ray imaging systems are used on modern tokamaks for identification of plasma shape and position, studies of MHD modes, testing feedback systems, etc. However, hard radiation environment in ITER-like reactor devaluates traditional semiconductor detectors due to their high noise and damage induced by neutrons. This problem can be solved using radiation hardening detectors or by use of additional X-ray optics [1]. Present paper summaries initial analysis and testing of the X-ray fibre optics (Kumahov optics) and its application for ITER.

2. Principles of Kumakhov optics and laboratory testing.

Kumakhov optics [2] are based on multiple total external reflection from smooth surfaces of glass capillaries. The X-rays are reflected from glass surfaces only at very small angles of incidence. The maximum reflection angle (critical angle) for borosilicate glass may be estimates by equation:

$$\Theta_c(\text{mrad}) \cong 30/E(\text{keV}) \qquad (1)$$

where E is the energy of photons.

The necessary condition for optimal deflection efficiency is given by inequality:

$$R_c > 2d/\Theta_c^2 \qquad (2)$$

where R_c and d are the radius of curvature and diameter of the capillary. R_c = 4 m. at E = 15 keV and d = 8 μm.

Modern technology [2] allows to fabricate polycapillary fibres from borosilicate glass with channel diameter down to 1 μm and wall thickness of less than 0.1 μm.

Special testing of the prototype X-ray deflector was made using polycapillaries assembled from 250 capillaries with inner diameter 8 μm . The polycapillaries with length 220 mm are placed between source of X-ray radiation and Si(Li) detector with spectra analyser. Transmission of the polycapillaries are measured for case straight polycapillaries and polycapillaries curved with radius 6 m and 4 m (the deflection angle 2° and 3° accordingly). Results of this testing are presented in Fig 2

Laboratory testing of the 8 μm polycapillaries indicated possibility of X-ray deflection in energy range 5-35 keV for angle 2° with efficiency 2-25%. In accordance with results of this testing we propose the scheme of the ITER X-ray imaging system.

3. X-ray imaging system in ITER.

Schematic view of the X-ray imaging system based on Kumakhov optics is shown in Fig 1. The diagnostic channels are placed in ports by traditional pin hole chamber scheme with fan-like geometry. The detection channels view the plasma from the slot between blanket sections. Each detection channel has polycapillaries deflector with diameter 2 cm which deflect X-ray for the angle 2° in toroidal direction. Polycapillares placed in sealed metal tube with beryllium windows. The distance between the first wall deflector and detector for horizontal port are 1.5 m and 5 m accordingly. This allows to deflect X-rays on 17 cm from axis of incident neutrons those providing wide space for radiation shielding and insure efficient protection of the detectors from fusion neutrons.

4. Performance of the system.

The total X-ray radiation intensity on the detector are proportional $V\Omega$ (emitting volume of plasma x solid angle of detector). The relation $V\Omega_{ITER}/V\Omega_{T\text{-}10}$ are equal 2.1 and 1.35 for horizontal end vertical detectors accordingly. The intensity of X-ray radiation in ITER at least 100 times higher than in T-10 where X-ray flux is high enough for similar measurements. This allows to compensate all loses in deflector.

Experience of using gas ionisation detector in T-10 X-ray imaging system indicates that such detectors can be suitable for ITER. The gas ionisation detectors are radiation hard [3] and have high sensitivity in energy range 5-40 keV. The efficiency of proposed system with supposed gas detector (gas: CH_4 10%, Xe 90% - 30 cm; filters: Be - 5 mm, 2° deflector) as a function of photon energy and the dependence of registered X-ray intensity on Te for this system are shown in Fig 3.

Initial testing was made using 8μm polycapillaries. Additional testing of various polycapillaries is required for optimal design and improvement performance of the system. Moreover, glass fibres have low sensitivity to neutrons [2]. However, detailed testing in reactor-relevant condition is required.

5. Conclusion

1. Initial analysis of the X-ray imaging system based on Kumahov optics and laboratory testing of the polycapillaries indicates good prospects for radiation hardening X-ray diagnostic in future tokamak-reactor (ITER).

2. X-rays (5-35 keV) can be deflected for angle 2° with efficiency 2-22%. This allows to ensure efficient protection of X-ray detector from fusion neutrons.

3. X-ray transmission system is compact and requires small room in the port. Up to 150 detection channels can be easy placed in the diagnostic port that allows to have the spatial resolution down to 5 cm.

4. Real performance of the system depends from many parameters: length end diameter of capillaries, radius of curvature and deflection angle, distance between the blanket, deflectors and detectors and so on. Design of the system needs advanced testing and optimisation.

Acknowledgements

The authors gratefully acknowledge to M.A.Kumakhov and A.N.Nikitin for presented samples of polycapillares and helpful consultations and M.M.Stepanenko for help in laboratory testing of the polycapillaries.

References

1.K.W.Hill, M.Bitter, and S. von Goeler, Concepts and requirements for ITER x-ray diagnostics, *Diagnostics for Experimental Thermonuclear Fusion Reactors* Edited by P.E.Stott et all., Plenum Press, New York, 1996.

2.M.A.Kumakhov, Channelling of photons and new x-ray optics, *Nuclear Instruments and Methods in Physics Research* B48 (1990) 283-286

3.M.A.Goldman, K.W.Hill, et all., A Gridded Ionisation Chamber for Detection of X-Ray Wave Activity in Tokamak Plasmas, *Rev. Sci. Instrum.* 56, 349 (1985)

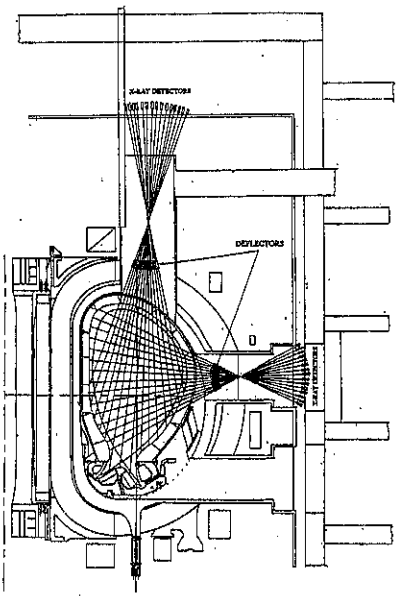

Fig. 1. Schematic view of the X-ray imaging system.

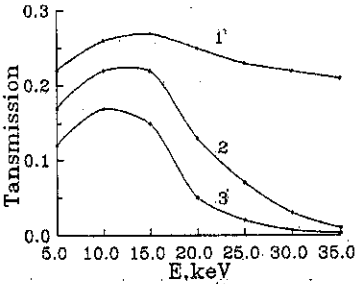

Fig. 2 The dependence of transmission of the polycapillaries on photon energy:
1. Straight polycapillaries.
2. Radius curvature 6 m
3. Radius curvature 4 m

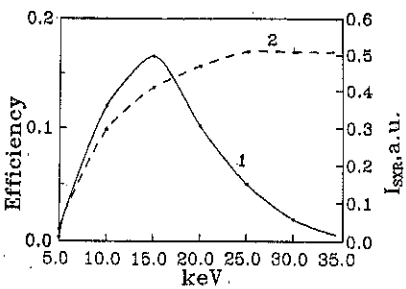

Fig. 3. 1. The efficiency of the system as function of photon energy.
2. The dependence of SXR intensity on T_e.

Compact Tokamak and Stellarator Reactors

A. J. Wootton, J. C. Wiley, P. H. Edmonds and D. W. Ross
Fusion Research Center, The University of Texas at Austin, Austin, Texas 78712, USA

We discuss the possible use of tokamaks and stellarators for thermonuclear power plants. Two approaches are presented. First we review and summarize the existing literature. Second, using simple analytic estimates, the size of the smallest power plant is derived.

Tokamaks. A survey of recent reactor designs has been completed [1,2]. In *Figure 1* the major radius R_0 of the various designs considered is plotted as a function of aspect ratio $A = R_0 / a$, with a the minor radius. To quantify 'compact' we use the machine encompassing volume V_m, the volume of the smallest cylindrical box into which the plasma will fit:

$$V_m = 2\pi\kappa R_0^3 (A+1)^2 / A^3 \qquad (1)$$

where κ is the elongation. Then the low-A Cu coil designs with large bootstrap current fraction f_{bs} are generally less compact than the normal-A superconducting designs. An exception is the pilot plant [3], marked by 'x' and labeled 'D', which assumes high f_{bs}, high confinement, large κ and large neutron wall loading Γ_n. Also, compact designs can be achieved if a very efficient current drive (η_{CD}) scheme can be used, in conjunction with a low value of safety factor q. In these TAR designs V_m is reduced by ≈ 30%. The low-A designs have approximately the same CoE as the superconducting designs [1].

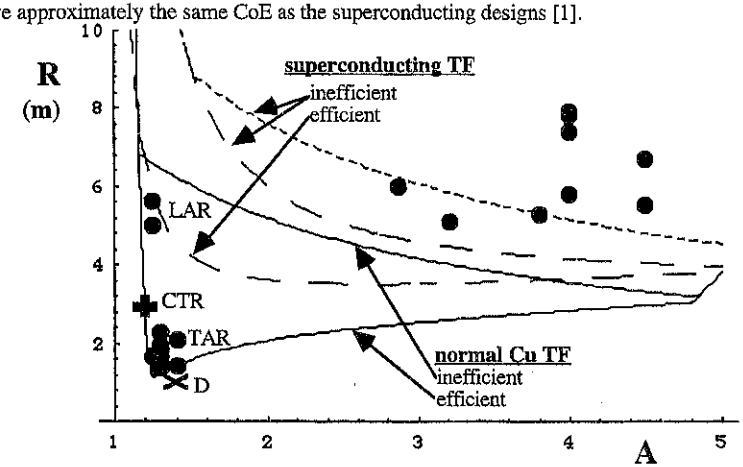

Figure 1. The solid points correspond to the results found in the published reactor studies. The lines correspond to the results of the analytic model, for both superconducting (broken line) and normal copper (solid line) TF systems, for completely efficient ($\eta_{CD} = \infty$, lower branch) and completely inefficient ($\eta_{CD} = 0$, $f_{bs} = 1$, upper branch) auxiliary current drive. The comparisons are made for $\beta_N = 3.5$, $\Gamma_n = 5x10^6$ Wm^{-2}, for both the $\eta_{CD} = 0$ (R_0 independent of recirculating power fraction χ) and for $\eta_{CD} = \infty$ with recirculating power fraction $\chi = 0.62$. Also shown as a dotted line is the superconducting $\eta_{CD} = 0$ or $f_{bs} = 1$ case with $\Gamma_n = 2x10^6$ Wm^{-2}.

An equation relating R_0 of an ignited tokamak to various parameters is required, together with constraints. The power heating the plasma is the sum of the power required to drive the plasma current, and the alpha particle power (assumed all deposited in the plasma). The power required to produce the toroidal field is accounted for. The neutron power is converted to electric power with an efficiency f_{el}. The electric power is converted to current drive and toroidal field power with specified efficiencies. The power to the grid is P_{gr}.

Details of the analysis are found in [1]. Referring to *Figure 1*, considering first the superconducting cases, then although there is a small decrease in R_0 as A is decreased in the completely efficient auxiliary current drive case, the machine encompassing volume V_m always increases as A is decreased. Considering the normal copper cases (with resistivity η), only the completely efficient ($\eta_{CD} = \infty$) auxiliary current drive case exhibits a smaller R_0 as A is decreased. The usual operational mode is restricted by Γ_n, or almost so, because of the strong dependence of the major radius on A in the beta-normal (β_N [4]) limiting cases. For $\eta_{CD} = \infty$ the functional dependence of R_0 (i.e. R_Γ) is

$$R_{\Gamma(\eta_{CD}=\infty)} \approx 3.52x10^5 \left[\frac{\eta q^2 g_2^2 \left(1+2\left(\gamma_n+\gamma_T\right)\right)}{f_{Cu} f_{el0} \chi \Gamma_n H^2 g^2 \left(1+\gamma_n+\gamma_T\right)^2} \right]^{0.36} \ln(A)^{0.64} \kappa^{-1.13} \delta^{-0.15} \qquad (2)$$

where the term [..] is the analytic dependence [1], and the dependence on geometric factors (A, κ, δ) represent a fit to the analytic solution in the parameter range relevant to the TAR designs. Parameters are: H: confinement improvement factor, δ: triangularity, $\gamma_{n,T}$ profile factors, g, g_2: fuel dilution and impurity parameters, f_{Cu}: the fraction of Cu in the TF core, χ: recirculating power fraction. For $\eta_{CD} = 0$ the functional dependence of R_0 is

$$R_{\Gamma(\eta_{CD}=0)} \approx 2.42x10^4 \left[\frac{f_{bs}^2 g_2^2 \left(1+2\left(\gamma_n+\gamma_T\right)\right)}{\Gamma_n H^4 g^2 \left(1+\gamma_n+\gamma_T\right)^2} \right]^{0.4} A^{-0.46} \kappa^{-1.18} \delta^{-0.15} \qquad (3)$$

In both cases, if κ is a decreasing function of A, then low-A benefits. At very low A either β_N or β_T becomes limiting, while at high A β_N becomes limiting (the solid lines turn up for $A \approx 5$). That is, increasing β_N at low A would allow a lower A to be accessed.

Comparing the data points for the published designs with the results of the analytic model, the low-A points, all for normal copper coils, are well described by the relevant simple model (solid lines). We conclude that there is little advantage in using low aspect ratio to obtain a more compact device (and low cost of electricity) unless either high efficiency plasma current drive and low safety factor are combined, or unless confinement, the permissible elongation and the permissible neutron wall loading increase as the aspect ratio is reduced.

Stellarators. A similar study has been performed for stellarators limited by Γ_n [5]. *Figure 2* shows the geometry of the smallest reactors, either ignited or driven, assuming either the 3-D [6] or tokamak [7] scaling relationship.

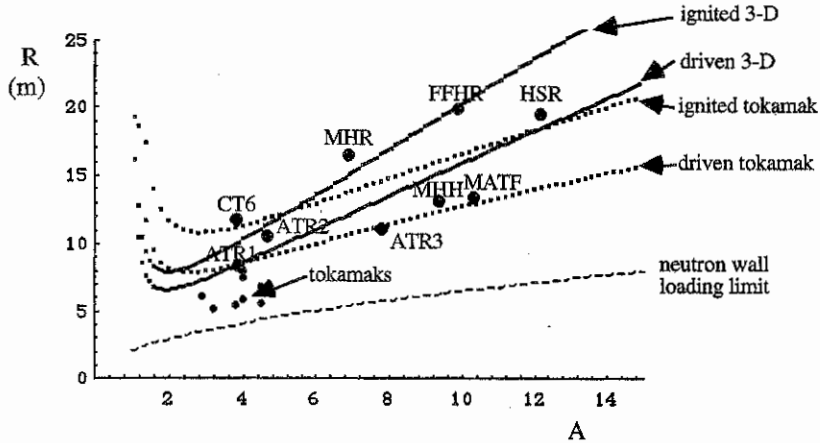

Figure 2 The major radius R as a function of as aspect ratio A of the smallest reactor, either ignited or driven, assuming either the 3-D or tokamak scaling relationship,. Also shown are the spot points for specific published studies. All published data refer to superconducting coils, with the smaller points representing tokamaks, the larger points representing stellarators (and torsatrons). The lowest line is the radius of the smallest device if only wall loading is limiting (no confinement restrictions) for a grid power of 500 MW.

For the ignited case:

$$R_i \approx 2.44x10^9 \frac{A^{1.65}}{(A-1)^{0.7}} \Gamma_n^{0.08} \xi^{-0.85} H^{-0.85} \iota^{-0.339} \overline{n}_e^{-0.43} B_{Tleg}^{-0.7} k^{-0.35} \qquad (4)$$

For the driven case:

$$R_d \approx 2.5x10^9 \frac{A^{1.65}}{(A-1)^{0.7}} \Gamma_n^{0.08} \xi^{-0.85} H^{-0.85} \iota^{-0.339} \overline{n}_e^{-0.43} B_{Tleg}^{-0.7} \zeta^{-0.35} \qquad (5)$$

Here ξ, ζ are coefficients ≈ 1, ι is the rotational transform at $r/a = 2/3$, k the fraction of alpha particles which deposit their energy in the plasma, $\overline{n}_e$ is the line-averaged particle density, B_{Tleg} is the maximum field allowed at a conductor (13 T in the examples). Also shown are the points for specific published studies. The lowest broken line represents the smallest device limited only by wall loading, so that $P_{gr} = 4\pi^2 R^2 \Gamma_n / A$, for $P_{gr} = 0.5$ GW, $\Gamma_n = 3$ MW m^{-2}.

The published 3-D cases lie approximately between the two relevant analytic curves. The published tokamak cases lie below the lowest relevant analytic curve. This is because the published tokamak case studies all use $\kappa > 1$, whereas in the analysis we have assumed $\kappa = 1$ (because of the definition of A for 3-D systems). To account for this the values of A for the tokamaks should be corrected by a multiplicative factor < 1: $A_{stellarator} / A_{tokamak} \approx \sqrt{\kappa} \approx 1.4$. Alternatively the more complete analysis should be considered [1], and then $R \approx 1/\kappa$. We conclude that the analysis can be used to approximate the A-dependence of 3-D reactor systems.

The analysis also demonstrates that significant direct alpha particle loss is not a catastrophe. Importantly, reducing A will reduce V_m of 3-D systems but not for tokamaks. This conclusion is a consequence of the differing scaling relationships used for the energy

confinement time, and thus it is crucial to perform experiments at reduced A to determine the reality.

There are three requirements that a low-A 3-D system must satisfy, in addition to those common for normal-A systems. These are:

1) The coil system must allow room for the nuclear blanket. .
2) Low-A 3-D systems must operate at larger total β values that their higher-A counterparts. Introducing plasma current has been proposed as one means to achieve this.
3) Neoclassical losses must not exceed empirical losses, or conclusions concerning reductions in size are negated. This is usually considered to imply strict optimization of the magnetic geometry. An alternative solution is to develop a partial magnetic optimization, sufficient for alpha particle confinement in the very low collisionality regime (or to accept alpha losses and develop driven systems), and to rely on E_r to ensure thermal plasma confinement.

Conclusions. Concerning tokamaks, we conclude that there is little advantage in using low A to obtain a more compact device (and low cost of electricity) unless either high efficiency plasma current drive and low safety factor are combined, or unless confinement, the permissible elongation and the permissible neutron wall loading increase as the aspect ratio is reduced. Concerning stellarators, we conclude that there is great potential for making them more compact. However either a very low effective helical ripple is implied, or radial electric fields must be effective at reducing losses. The required β are above those currently attainable.

Acknowledgments. This work was supported by the USDoE under grant DE-FG03-94ER-5421, Grant DE-FG03-95ER54296, and the Texas Atomic Energy Research Foundation.

References.

[1] A. J. Wootton, J. C. Wiley, P. H. Edmonds and D. W. Ross, "Compact Tokamak Reactors Part I (analytic results)", University of Texas at Austin Fusion Research Center Report FRCR #484, DOE/ER/542-41-163 (September 1996).

[2] J. C. Wiley, A. J. Wootton and D. W. Ross, "Compact Tokamak Reactors Part 2 (numerical results)", University of Texas at Austin Fusion Research Center Report FRCR #490, DOE/ER/542-41-169 (October 1996).

[3] R. D. Stambaugh, V. S. Chan, R. L. Miler, P. M. Anderson, C. B. Baxi, R. W. Callis, H. K. Chiu, S. C. Chiu, C. B. Forest, R. Hong, T. H. Jensen, L. L. Lao, J. A. Leuer, Y. R. Lin-Liu, M. A. Mahdavi, A. Nerem, R. Prater, P. A. Politzer, M. J. Schaffer, D. L. Sevier, T. S. Taylor, A. D. Turnbull and C. P. C. Wong, "The Spherical Torus Approach to Magnetic Fusion Development", Presented at the 16th International IAEA Fusion Energy Conference, Montreal (1996), paper F1-CN-64/G1-2.

[4] F. Troyon, R. Gruber, H. Saurenmann *et al.*, Plasma Phys. Controlled Fusion 26 209 (1984).

[5] A. J. Wootton, "Compact Stellarator Reactors", University of Texas at Austin Fusion Research Center Report FRCR #492, (January 1997).

[6] R. J. Goldston, Plasma Phys. Controlled Fusion 26 87 (1984).

[7] U. Stroth , M. Murakami, R. Dory, H. Yamada, S. Okamura, F. Sano and T. Obiki, Nuclear Fusion 36 1063 (1996).

Parameter dependence of the operating regime and performance of D-T tokamak reactors in a current-versus-size diagram

E. Rebhan, U. Vieth*

Heinrich-Heine-Universität Düsseldorf, Institut für Theoretische Physik II
Universitätsstraße 1, D-40225 Düsseldorf, Germany

* supported by DFG Graduiertenkolleg Hochtemperatur-Plasmaphysik

Abstract. On the basis of a zero-dimensional plasma model, taking into account profile effects and employing ITER scaling laws for the energy confinement time as well as semi-empirical expressions for the beta limit and the Greenwald density, the operating regime of D-T tokamak reactors in a current-versus-size diagram is determined for fixed values of the magnetic field, the aspect ratio, and the plasma elongation. The reactor performance in this regime is discussed, including sub-ignited scenarios with different amounts of auxiliary heating.

Ignition contours $\varrho = const$ in n, T-, β, T-, and β, n-diagrams. In [1, 2] burn equilibria of an ignited D-T plasma have been calculated for a zero-dimensional plasma model, self-consistently taking into account the effects of helium accumulation by assuming a transport scaling $\varrho = \tau_p/\tau_E = const$ where τ_E is the energy confinement time including transport losses only. The resulting ignition contours $\varrho = const$ are closed curves in the $n_e\tau_E T, T$-plane. The basic equations of the plasma model employed here are the alpha particle balance equation and the energy balance equation,

$$n_\alpha/\tau_p = p(2,2)\,\tfrac{1}{4}n_i^2\sigma_v(T)\,, \tag{1}$$

$$p(1,1)\,\tfrac{3}{2}n_{tot}T/\tau_E = P_\alpha + P_{aux} - P_{rad} = P \tag{2}$$

where $n_i = n_D + n_T$, $n_{tot} = 2n_i + 3n_\alpha + (Z+1)n_Z$, $P_{rad} = p(2,\tfrac{1}{2})\,[n_e n_i R_{B,1}(T) + n_e n_\alpha R_{B,2}(T)]$, $R_{B,z_j}(T) = C_B Z_j^2 T^{1/2} g_{ff}(Z_j^2/T)$, $P_\alpha = p(2,2)\,\tfrac{1}{4}n_i^2\sigma_v(T)E_\alpha$ and $n_e = n_i + 2n_\alpha + Zn_Z$ according to the requirement of quasi-neutrality. n_D and n_T are kept equal and constant by corresponding sources. The profile factors $p(x,y)$ are defined by $\langle n^x T^y\rangle = p(x,y)\langle n\rangle^x\langle T\rangle^y$ where the brackets $\langle\ \rangle$ denote volume averages and are omitted in (1)–(2). For the profiles $n = n_0(1 - r^2/a^2)^{\alpha_n}$ (same profile for the density of all species) and $T(r) = T_0(1 - r^2/a^2)^{\alpha_T}$ they are given by $p(x,y) = (1+\alpha_n)^x(1+\alpha_T)^y/(1 + x\alpha_n + y\alpha_T)$.

It is possible to express τ_E in terms of n_e and T by assuming ITER scaling laws such as ITER 89-P

$$\tau_E = 0.048\, f_H M^{0.5} I^{0.85} B^{0.2} R^{1.2} a^{0.3} \kappa^{0.5} P^{-0.5} n_e^{0.1}\,, \tag{3}$$

where f_H is the H mode enhancement factor taken to be $f_H = 2.0$ in our studies, M the isotopic mass (= 2.5 for a 50:50 D-T mixture), I the plasma current in MA, B the toroidal magnetic field in teslas, R and a the major and minor tokamak radius in meters, κ the elongation of the plasma cross section, n_e the electron density in $10^{20}\,\mathrm{m}^{-3}$, and P the net heating power in MW.

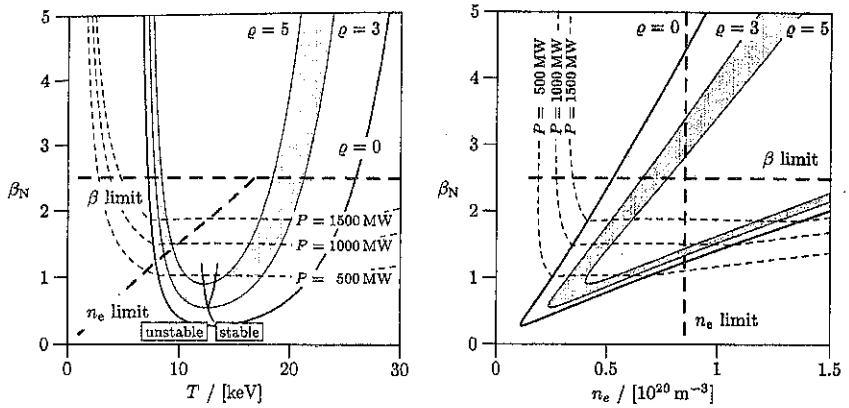

Figure 1: *Operating regime in a β, T-diagram and a β, n-diagram; $\beta = \beta_N\, I/(aB_0)$.*

Using the equilibrium equation (2), P can be expressed by $\frac{3}{2} n_{\mathrm{tot}} T/\tau_E$ and (3) rewritten as

$$\tau_E = \left(0.048\, f_{\mathrm{H}} M^{0.5} I^{0.85} B^{0.2} R^{1.2} a^{0.3} \kappa^{0.5}\right)^2 n_e^{-0.8} T^{-1.0}\,. \tag{4}$$

With this relation ignition contours can be translated from the $n_e \tau_E T, T$-plane directly into the n_e, T-plane or β, T-plane (see [3]; note, however, that in [3] the ITER scaling laws where applied to the energy confinement time $\tilde{\tau}_E$ including radiation losses while according to [4] they should, in fact, be applied to the confinement time excluding radiation losses). Fig. 1(a) shows the "ignition curve" $\varrho = 5$ in a β, T-plane — there is some uncertainty about the value of ϱ to be expected in a fusion reactor; we showed in [3] that $\varrho = 5$ is a plausible value —, the operational limits and the boundary of stability with respect to burn instabilities [3]. A similar diagram can be obtained in the n_e, T-plane. (As in all other figures, for the profiles we have assumed $\alpha_n = 0.5$ and $\alpha_T = 1$, i. e. flat density and more peaked temperature profiles.) Fig. 1(b) shows curves $\varrho = const$, $P_{\mathrm{fus}} = 5P_\alpha = const$ and the operational limits in a β, n-diagram. It is seen from this figure, that ignition is only possible in a very narrow range of these quantities which is still further limited (not shown in this diagram) by the requirement of burn stability.

Safe reactor regime in a current-versus-size diagram. Eq. (4) depends on the parameters R, a, B, κ and I, the first four of which are design parameters that are essentially fixed in a given device while I can be varied within certain limits. For B, κ, and $A = R/a$, it is quite obvious that they should be as large as possible while on the other hand they are subject to certain practical limitations. We therefore hold these quantities fixed, taking the present ITER interim design values $B = 5.7\,\mathrm{T}$, $\kappa = 1.6$, $A = 2.8$, and are left with only two free parameters I and a. The regime of possible values for these is restricted by (a) the requirement $q_a \geq 3$ where q_a is the edge safety factor, (b) the Greenwald density $n_e \leq n_{\mathrm{G}}$ where $n_{\mathrm{G}} = I[\mathrm{MA}]/(\pi a^2[\mathrm{m}])$, and (c) the Troyon beta limit $\beta \leq \beta_{\mathrm{T}}$ where $\beta_{\mathrm{T}} = g_{\mathrm{T}} I[\mathrm{MA}]/(a[\mathrm{m}]\, B_0[\mathrm{T}])$ and $g_{\mathrm{T}} = 2.5\,\%$.

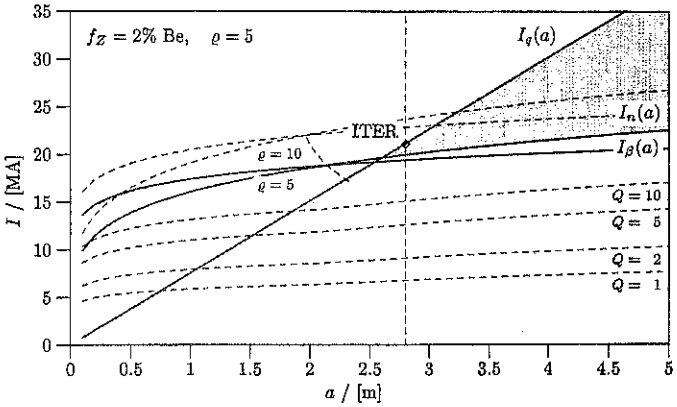

Figure 2: *Curves $I_q(a)$, $I_n(a)$, and $I_\beta(a)$ bounding the safe reactor regime in the I, a-plane for $\varrho = 5$. In the shaded area all stability conditions are satisfied.*

Using $q_a = B_0\, 2\pi a^2(1+\kappa^2)/(2\mu_0 IR)$, the first of these constraints yields the condition

$$I[\mathrm{MA}] \leq I_q(a) = \frac{5}{3}\frac{(1+\kappa^2)}{2A}\, B_0[\mathrm{T}]\, a[\mathrm{m}]\,,$$

i. e. an upper limit $I \leq I_q(a)$. In order to trace the implications of the density limit, we considered the ignition curve $\varrho = 5$ in a n_e, T-diagram. If I is too low, the ignition curve lies above the density limit and no stable plasma operation is possible. Raising I increases the Greenwald density while the ignition curve is lowered. Therefore, depending on the radius a, there exists a minimum current $I_n(a)$ such that for $I \geq I_n(a)$ a part of the ignition curve lies below the Greenwald density. Exactly the same kind of behavior is found for ignition curves in the β, T-plane in relation to the beta limit, i. e. there exists another minimum current $I_\beta(a)$ such that for $I \geq I_\beta(a)$ a part of the ignition curve lies below the beta limit.

Fig. 2 shows the three curves $I_q(a)$, $I_n(a)$ and $I_\beta(a)$ bounding the safe reactor regime for $\varrho = 5$. For safe reactor operation, I and a must be chosen in the shaded area. It is seen that the Greenwald density provides a more restrictive limitation than the beta limit. The location of the ITER device according to its present design parameters is also indicated in the figure. For sub-ignited operation with auxiliary heating, a safe operating regime can be determined in a similar way which is also shown in Fig. 2 for several values of the gain factor $Q = P_{\mathrm{fus}}/P_{\mathrm{aux}}$.

Reactor performance. An important figure of merit for the performance of a reactor is the fusion power $P_{\mathrm{fus}} = 5P_\alpha$ that can be achieved. On the ignition curve $\varrho = 5$ there is still some liberty in the choice of the operating point. In [3] we arrived at the conclusion that the optimal choice is close to the point where the plasma assumes its minimal density. In view of the fact that the density limit provides a more stringent limitation than the beta limit we have therefore chosen the point of minimal density as the optimal one. Other possible operating

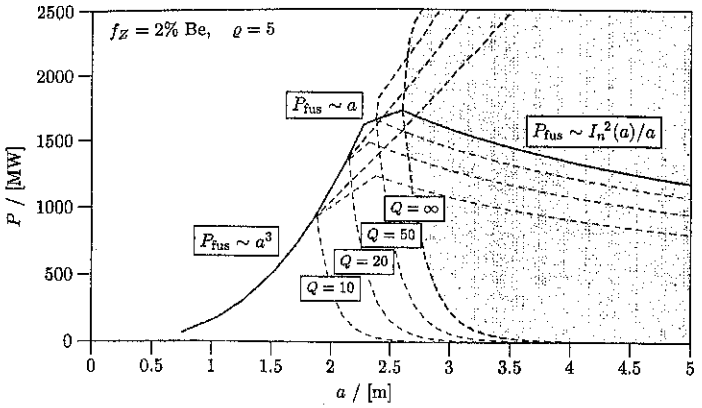

Figure 3: *Fusion power achievable in the safe reactor regime.*

points compatible with the requirement of burn stability are all points to the right of this (towards higher temperatures) but below the Greenwald density and the beta limit.

Fig. 3 shows the fusion power as a function of the plasma radius a, where B, A and κ are held fixes as explained above. At the points where the line $I = I_q(a)$ is intersected by the lower boundary of the safe reactor regime in Fig. 2 (there is only one point for each value of Q) we have either $n = n_{\rm G}$ or $\beta = \beta_{\rm T}$ and there is only a single point of operation on the curve $\varrho = 5$. The corresponding fusion power is indicated by the solid line in Fig. 3.

In the ignited regime, we have $n = n_{\rm G}$ on the lower boundary and therefore again there is only a single point of operation on the corresponding curves $\varrho = 5$. The fusion power obtained on this boundary, which corresponds to the lowest possible current $I_n(a)$ in the ignited regime, is represented by the continuation of the solid curve into the (shaded) ignited regime. If in the latter we go to the highest possible current $I_q(a)$ and take the "optimal" operating point as explained above, we obtain the fusion power on the dashed line bounding the shaded area from below. On the other hand, if for $q_a = 3$ and $\varrho = 5$ we go to the highest possible temperature that is still compatible with the density and beta limits, we obtain the fusion power on the dashed line bounding the shaded area from above. Similar lower and upper boundaries for the achievable fusion power can be obtained in the sub-ignited regime with auxiliary heating. In Fig. 3 the corresponding curves are shown for $Q = 10$, 20 and 50.

References

[1] D. Reiter, G. H. Wolf, H. Kever, Nucl. Fusion **30**, 2141–2155 (1990).

[2] E. Rebhan, U. Vieth, D. Reiter, G. H. Wolf, Nucl. Fusion **36**, 264–269 (1996).

[3] E. Rebhan, U. Vieth, Nucl. Fusion **37**, 251–270 (1997).

[4] K. Lackner, private communication

ON THE DISTRIBUTION FUNCTION OF FAST FUSION PRODUCTS IN A TOKAMAK WITH ELONGATED PLASMA

V.Ya.Goloborod'ko*, J.W.Edenstrasser**, S.N.Reznik*, **V.A.Yavorskij***

*Institute for Nuclear Research, Kiev, Ukraine
**Institute for Theoretical Physics, University of Innsbruck, Austria

Introduction

The distribution function of fast alpha particles in low current tokamaks was shown [1] to be significantly influenced by the pitch-angle scattering. However the consideration of this work was carried out for the case of circular flux surfaces. The main purpose of this report is the investigation of the effect of the pitch angle scattering on the distributions of charged fusion products confined in tokamaks with elongated flux surfaces.

Model magnetic field

We will use the model of an axisymmetric magnetic field with the elongated and shifted flux surfaces given by

$$R = R_0(r) + r\cos\chi\,; \tag{1}$$

$$z = k(r) r \sin\chi\,. \tag{2}$$

Here R and z are the spatial variables of the cylindrical coordinate system (R, z, φ); r is the flux surface radius in the equatorial plane, $z = 0$; χ is the poloidal angle; $R_0(r)$ is the major radius of a given flux surface and $k(r)$ is the elongation of the latter. It should be pointed out that the radial inhomogeneities of the flux surface shift, $\delta = dR_0/dr$, and the elongation, $l = d\ln k/d\ln r$, can significantly influence the rotational transform of the magnetic field lines. According to the Ref. [2] the safety factor, q, on the flux surface given by the Eqs. (1, 2) is determined by the following expression

$$q = q^{(0)} G(\varepsilon, \delta, l, k); \qquad q^{(0)} = \frac{J\varepsilon^2}{I}\frac{1+k^2}{2}, \tag{3}$$

where $\varepsilon = r/R_0$; $q^{(0)}$ is the safety factor in the paraxial approximation ($\varepsilon = 0$) and $\delta = l = 0$; $J = J(\psi)$ is the total (essentially external) poloidal current outside a given flux surface and $I = I(\psi)$ is the total toroidal current inside, i.e. they are the flux surface functions. G is defined by

$$G = \frac{2\left(1 - \dfrac{\mu}{1+\sqrt{1-\varepsilon^2}}\right)}{(1+k^2)(\varepsilon^2-\mu)}\left\{\frac{k^2-1+\varepsilon^2}{1-\varepsilon^2} - \frac{(k^2-1)\left(1-\dfrac{\varepsilon}{\delta}\right) - \dfrac{k^2\lambda}{2}}{\sqrt{(1-\varepsilon^2)(1-\delta^2)}} - \frac{(k^2-1+\delta^2)\dfrac{\varepsilon}{\delta} - \dfrac{k^2\lambda}{2}(1+\varepsilon\delta)}{\sqrt{(1-\varepsilon^2)(1-\delta^2)(1-\lambda)}}\right\} \tag{4}$$

Here $\lambda = -2l/(1+\sqrt{1-\delta^2})$, $\mu = (l+\varepsilon\delta)/(1+l)$. Note that $G(0, 0, 0, k) = 1$. The levels of $G = const$ for $k = 2$, A = 3 are shown in Fig. 1. It can be seen that depending of the inhomogeneities of the Shafranov shift and the elongation there is a significant increase of the safety factor. Thus, e.g., for an experimentally relevant choice of ($\delta = -0.5$, $l = 0$) one obtains $q/q^{(0)} = 1.4$.

In the case of a homogeneous elongation and a vanishing Shafranov shift the increase of the particle orbit width is given by the factor $(k+1/k)/2$, [3]. Since the above found increase of q is larger, one can conclude that δ and l are the important parameters in the description of charged fusion product confinement in tokamak plasmas. As the result the total increase of the particle orbit width is given by the factor

$$K = \frac{k + k^{-1}}{2} G(\varepsilon, \delta, l, k), \tag{5}$$

and is mainly determined by the second term of the RHS of Eq. (5). For a JET-like tokamak plasma ($k = 1.5, \varepsilon = 0.3,\ \delta = -0.5, l \cong 0$) we obtain with the help of Eq.(5) $K = 1.4$. Taking into account that the increase of the orbit width by a factor K corresponds to the effect of a decrease of the plasma current by the same factor K , one can generalize the results of the fast particle transport treatment carried out for the circular flux surfaces with plasma current I_c on the case of the elongated ones with plasma current I_{el}, where the following relationship is employed

$$I_c = \frac{2I_{el}}{k + k^{-1}} \frac{G(\varepsilon, \delta, 0, 1)}{G(\varepsilon, \delta, l, k)}. \tag{6}$$

Note, that for the case of $\varepsilon \ll 1, \delta \ll 1$ and $|l| \ll 1$

$$\frac{G(\varepsilon, \delta, 0, 1)}{G(\varepsilon, \delta, l, k)} \approx 1 - \frac{k^2 - 1}{k^2 + 1} \frac{\varepsilon^2 + \varepsilon\delta + \delta^2}{4} < 1. \tag{7}$$

Since the effect of plasma elongation is equivalent to the case of a circular plasma with reduced plasma current it means that the elongation increases the influence of the pitch-angle scattering on the alpha particle distribution function [1].

Modeling results

In the present report we examine the effect of the pitch-angle scattering of alphas on the spatial distribution of their density, on the heating profiles of electrons, P_e, and ions, P_i, and on the alpha driven bootstrap current. For this purpose we carry out the 3D Fokker-Planck modeling of the alpha particle distributions in an axisymmetric tokamak plasma with $I_c = 1.6\ MA$, aspect ratio $A = 3$ and TFTR-like plasma parameters [1] and compare them with the convective ones obtained in the absence of the pitch-angle scattering.

Fig. 2 shows the flux surface averaged radial profiles of the density of the alpha particles with energies $E \geq 0.25E_o$ and their birth source, as well as the heating profiles of electrons and ions. It should be pointed out that all profiles turn out to be monotonic, in agreement with results from TRANSP modeling in Ref. [5, 6]. On the other hand, the heating profiles for ions in the present paper are in contradiction with that obtained in Ref. [8], where nonmonotonic $P_i(\rho)$ at $r < 0.3a$ was observed. This figure does not show profiles of $P_e(\rho)$, $P_i(\rho)$ and $n(\rho)$ corresponding to the convective approximation, since their difference to the diffusive curves is less then 1%. That is in agreement with low level (<1%) of collisional alpha loss (see [7]). Finally Fig. 3 shows the flux surface averaged radial profiles of the longitudinal current driven by alphas with energies $E \geq 0.25E_o$. These profiles were obtained in both diffusive (solid lines) and convective (dashed lines) approximations. One can see that the part of the current density induced by pitch-angle scattering has a maximum in the central region of the plasma. There it is about 40% of the current calculated in the presence of slowing down only. It should be pointed out that this increase is in qualitative agreement with analytical results for alpha particle bootstrap current obtained in Refs. [4, 9] (it is greater then that of [4] and is less then predicted in [9]). The density of alpha - driven current is strongly dependent on the poloidal angle. This is confirmed by the distribution of the longitudinal

current versus major radius, represented in Fig. 4. It follows from the convective and diffusive profiles that the pitch-angle scattering affects the alpha bootstrap current mainly at the inner side of the plasma column. This effect is caused, probably, by a stronger anisotropy of the convective alpha-particle distribution at the inner side of a TFTR-like plasma.

Conclusions

The present treatment demonstrates that in an axisymmetric plasma, pitch-angle scattering has only weak influence on such global alpha particle characteristics like density or plasma heating profiles. On the other hand, from the comparison of the convective distribution function with the 3D boundary value solution we conclude that even weak pitch-angle scattering ($\nu_\perp \propto 10^{-2}\,\nu_s$, where $\nu_\perp$ and ν_s are characteristic collisional frequencies of pitch-angle scattering and slowing down, respectively) can significantly affect the fusion product distribution function (at least in the range of small pitch-angle cosines and in the vicinities of the loss-cone boundaries and the separatrix between trapped and circulating orbits). The reason for the strong influence of pitch-angle scattering is the strong pitch-angle dependence of the distribution function at the pointed out pitch-angle ranges. The elongation of the flux surfaces results in the enhancement of the pitch-angle scattering effect on the alpha particles. Evidently, as current increases the role of pitch angle scattering weakens. Distortion of the alpha particle distribution function caused by pitch-angle scattering is important for the magnitude of the alpha driven bootstrap current even in the axisymmetric limit. It is evident that this distortion should be taken into account in the investigations of alpha-driven instabilities.

Finally, note that present paper treats the minimum effect of pitch angle scattering in the phase space distribution of alpha particles in a low - current tokamak. It should be significantly enhanced by ripples of toroidal magnetic fields.

Acknowledgments

This work was supported, in part, by the Austrian ÖAW-Euratom-Association, Project P8 and Grant #2.4/176 of the Ministry of Science and Technologies of Ukraine.

References

[1] GOLOBOROD'KO, V.Ya., REZNIK S.N., YAVORSKIJ, V.A., Nucl.Fusion **37** (1997) to be published.
[2] YAVORSKIJ, V.A., Ukr. Phys. J. **41** (1995) 160.
[3] KOLESNICHENKO, Ya.I., YAVORSKIJ, V.A., Fizika Plazmy **5** (1979) 135.
[4] HSU, C.T., SHAING, K.S., GORMLEY, R.P., SIGMAR, D.J., Phys. Fluids B **4** (12) (1992) 4023.
[5] BUDNY, R.V., BELL, M.G.,BIGLARI, H., et al., Nucl. Fusion **32** (1992) 429.
[6] BUDNY, R.V., et al., Nucl. Fusion **35** (1995) 1497.
[7] GOLOBOROD'KO, V.Ya., REZNIK, S.N., YAVORSKIJ, V.A., ZWEBEN S.J., Nucl.Fusion **35** (1995) 1523.
[8] O'BRIEN, M.R., COX, M., GARDNER, C.A., ZAITSEV, F.S., Nucl. Fusion **35** (1995) 1537.
[9] GOLOBOROD'KO, V.Ya., KOLESNICHENKO, Ya.I., REZNIK, S.N., YAVORSKIJ, V.A., Fusion Technology **25** (1994) 249.

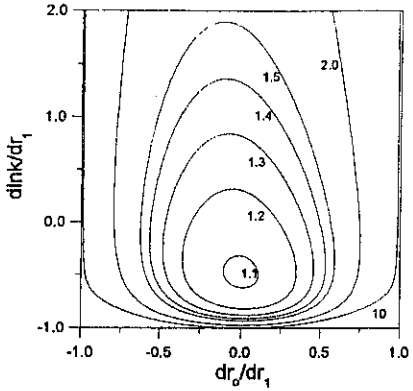

Fig.1. Levels of the safety factor, normalized by q(0) (see Eq.(3)), for the elongated flux surface (k=2) with aspect ratio A=3.

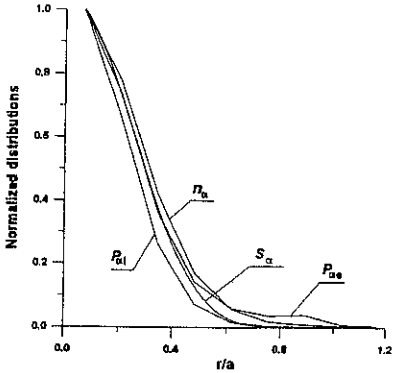

Fig.2. Radial profiles of alpha particle density and heating profiles of electrons and ions.

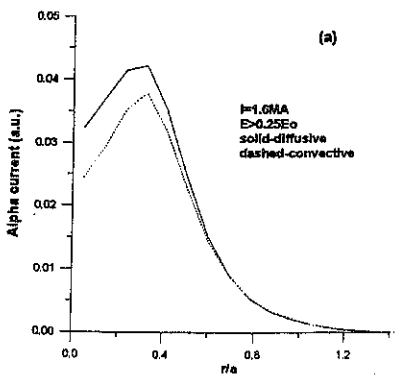

Fig.3. Distribution of longitudinal current density driven by alpha particles *vs* minor plasma radius.

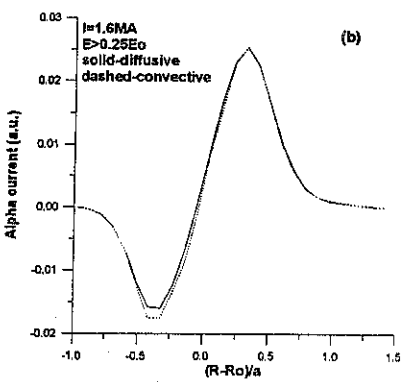

Fig.4. Distribution of longitudinal current density driven by alpha particles *vs* major plasma radius R. R_O is major radius of geometrical center of flux surface.

Simulations of Standard and High-Temperature L-mode pulses with a General Empirical Microinstability Based Transport Model

M. Marinucci[1], A.Cherubini[2], M. Erba[2], V. Parail[2], F. Romanelli[1], A. Taroni[2], G. Vlad[1]
[1]Associazione EURATOM-ENEA sulla Fusione, C.R. Frascati,
C.P. 65, 00044, Frascati, Rome, Italy
[2]JET Joint Undertaking, Abingdon, Oxon ox143EA,UK

Introduction

The theoretical determination of the transport properties in a thermonuclear plasma from first principles is still an open question. Most of the proposed transport models, relying on small scale instabilities, result in the so called gyro-Bohm expression for the transport coefficient $\chi_{gB} \approx \rho_i^2 \omega_*$, where ρ_i is the ion Larmor radius and $\omega_* \approx v_{ti}/a$ is the diamagnetic frequency (v_{ti} being the ion thermal velocity and a the minor radius). On the contrary, the presence of turbulent processes with long radial correlation length (say, $L_r \approx (a\rho_i)^{0.5}$) would result in a Bohm, rather than a gyro-Bohm transport, $\chi_B \approx \rho_i v_{ti}$. It has been shown by several experiments that both the local transport and the energy confinement time may exhibit a behaviour which, depending on the confinement regime, may be either Bohm or gyro-Bohm. On the basis of this observation, in Ref.[1] a mixed Bohm–gyro-Bohm model has been proposed, generalizing a previous Bohm model.[2] The strenght of Bohm term is related to the radial correlation lenght of the turbulence L_r. L_r in turn is realated to the strenght of the coupling of the poloidal harmonics in which a general perturbation may be decomposed in a toroidal configuration. The degree of coupling may be associated to different physical mechanisms. The model presented here relies on the simplest one, which is related to the effect of magnetic shear. Indeed, as shown in Ref.[3] if the magnetic shear parameter $s \equiv rq'/q$ (where $q(\rho)$ is the safety factor, being ρ the normalized flux coordinate) is decreased, the distance between neighbouring harmonics increases faster than the width of the mode eigenfunction, decreasing in such a way the overlap between neighbouring harmonics and, ultimately, the degree of coupling. Thus, if a large region of weak shear is obtained, a corresponding decrease of the Bohm transport is expected.

The beneficial effect of magnetic shear has been observed in several experimental conditions. A strong reduction of transport is currently observed in the central part of tokamak discharges, where magnetic shear is low, if sawteeth are suppressed. Perhaps the first experimental evidence was achieved with the pellet enhanced performance (PEP) mode in JET,[4] in which the injection of a deuterium pellet yielded a flattening of the safety factor profile inside the deposition region. Confinement enhancement with pellet injection have been reported by several tokamaks, even though usually attributed to the peaking of the density profile, rather than to changes of the safety factor profile. More recently, confinement improvement has been observed in the presence of large low or reversed shear regions produced by lower hybrid current drive or by freezing the current density profile by strong auxiliary heating during the current ramp. In the present work we will check the model against the some selected discharges of the ITER data base[5] and against the JET PEP and hot ion mode discharges.

A magnetic shear dependent transport model

Following Ref.[3] the radial correlation length in the short wavelength, moderate shear limit has been found to scale as $L_r \propto s^{-1/2}$, whereas in the long wavelength, low shear limit the radial correlation length has been found to scale as $L_r \propto e^{-1/s}$, thus vanishing very rapidly for decreasing shear. In the low shear region it is thus expected a radial correlation length which scales with the ion Larmor radius, thus giving rise to a gyro-Bohm scaling of the thermal diffusion coefficient.

According to these theoretical suggestions, a thermal diffusion coefficient can be modeled

assuming a Bohm like dependence in the radial regions where the magnetic shear is $s \geq 1$ and which vanishes with decreasing s, and a gyro-Bohm like dependence which survives where the shear $s \ll 1$.

We write the thermal diffusion coefficient as $\chi = D_B F(\rho^*, L_T^*, q, s)$, where F is a function of only dimensionless plasma quantities, $D_B(m^2/s) \equiv T_e/16eB = T_e(eV)/16B(T)$ is the Bohm diffusion coefficient, $\rho^* \equiv \rho_s/a$ and $L_T^* \equiv L_T/a$ are, respectively, the gyroradius and the characteristic length of the temperature profile both normalised to the minor radius of the plasma column a. The thermal coefficients for electrons and ions are then assumed to be:

$$\chi_{i/e} = \alpha_{B,i/e} D_B \frac{1}{L^*_{T_{i/e}}} q^2 f(s) + \alpha_{gB} D_B \rho^* \frac{1}{L^*_{T_{i/e}}} (+\chi_{neo}), \tag{1}$$

where the last term in parenthesis, containing the neoclassical ion thermal diffusion coefficient, is not included in the expression for electrons. For the shear dependent function $f(s)$ the following expression has been chosen: $f(s) = s^2/(1+|s|^3)$, if $s > 0$ and $f(s) = 0$, if $s \leq 1$. This choice respects the desired dependence of the radial correlation length $L_r \propto s^{-1/2}$ in the moderate shear limit and makes the radial correlation length vanishing for s which goes to zero. If the shear profile is flat or even 'reversed' the Bohm term of the model thermal diffusion coefficient is cut-off and the transport is made purely of the gyro-Bohm type. Finally, $\alpha_{B,e}$, $\alpha_{B,i}$ and α_{gB} are numerical coefficients used for calibration which have been tuned on a typical L-mode JET discharge and kept fixed to the following values: $\alpha_{B,e} = 8.61 \times 10^{-3}$, $\alpha_{B,i} = 3.5\alpha_{B,e}$, $\alpha_{gB} = 5.07 \times 10^{-1}$.

Transport simulations and comparison with experiments

The semi-empirical transport model described in the previous section has been inserted in the transport code JETTO in order to compare its predictions with experimental results. To better focus on the results of the thermal transport coefficient proposed, we have solved the ion and electron energy conservation equations together with the evolution of the Faraday's equation, assuming neoclassical resistivity and including the bootstrap current. Ohmic input, thermal exchange between electrons and ions, power losses via thermal diffusion are calculated self-consistently (convections losses have been neglected). The other quantities which enter in the transport equations (as, e.g., profiles of density, Z_{eff}, auxiliary power deposition, radiation power, as well as boundary conditions) have been prescribed according to the experimental database. Also the equilibrium quantities necessary to solve the transport equations have been assigned accordingly to the experimentally reconstructed equilibria. Moreover, no sawtooth model have been included in the simulations.

We present firstly a comparison of the magnetic shear dependent transport model previously described with some of the experimental results collected in the ITER Profile Database. In particular results of simulations of L-mode JET and DIII-D discharges will be considered.

For all the JET discharges analysed a good agreement with the ion experimental profiles is obtained, whereas the computed electron temperature profiles are more peaked than the experimental ones. Indeed, if a sawtooth mechanism would be included in the simulations, more flat temperature profiles would be obtained in the central region of the discharges.

Five DIII-D L-mode NB-heated discharges have been analysed, with electron density ranging from $0.4 \times 10^{20} m^{-3}$ to $1 \times 10^{20} m^{-3}$, electron temperature from $1.9 KeV$ to $3.3 KeV$, magnetic field from 1 to 2 Tesla, plasma current from $1 MA$ to $2 MA$ and with different values of ρ^*.

These discharges are well reproduced, especially the two ones at high ρ^*, whereas those at low ρ^* are somewhat understimated in the central temperature. In fig. 1-a the steady state computed temperature profiles of the shot 69627 are compared with the experimental ones. In fig. 1-b the total electron and ion thermal diffusion coefficients are shown. One can observe how the Bohm term in the central region, due to the presence of the shear function $f(s)$, tends to switch off, meanwhile the gyro-Bohm term becomes dominant.

As a second step, JET discharges which belong to enhanced confinement regimes in which there are evidence that the thermal diffusion is reduced in the central region have been analysed. A list of the principal parameters characterising the discharges are reported in Table 1. The analysis of the discharges will be performed only for the L-mode phase, before the transition to the H-mode regime. All these discharges show an improvement of the confinement in the central region of the plasma where a very low or even reversed magnetic shear is present. The improvement of the confinement is reflected in a strong thermal barrier shown on the temperature profiles between one third and half radius (in particular on the ion temperature profiles).

Table 1: JET Hot ion discharges

shot	$\langle n_e \rangle (\times 10^{20} m^{-3})$	$T_e(0)(KeV)$	$I_p(MA)$	$P_{NB,RF}(MW)$	$W_{th}^{sim}/W_{th}^{exp}$
17749	0.37	9.4	3.07	$5.(NB)+11.(RF)$	1.077
18757	0.11	9.0	3.10	$10.(NB)$	1.020
24464	0.36	4.7	3.01	$12.(NB)$	0.946
38480	0.16	13.1	2.90	$10.(NB)+10.(RF)$	0.925

Our model considerably improves the results obtained by a previous mixed Bohm–gyro-Bohm model without shear dependence.[1] In particular, the ion temperature profile is always well reproduced, being our model able to closely follow the thermal barrier shown between one third and half radius of the plasma column. The experimental electron temperature profile show a thermal barrier only on the discharge 17749 (this discharge has also a q-profile with a negative shear for $\rho < 0.4$), and in this case the result of the mixed shear-dependent model is excellent. The ion temperature is in this case slightly overestimated, even though the profile is well reproduced. Nevertheless, the general reliability of the model is brought out by the excellent agreement (shown in Table 1) between simulated and experimental total (electron plus ions) thermal energy W_{th}. In fig. 2-a the comparison between the experimental temperature profiles and the ones predicted by the mixed shear-dependent model is presented. In fig. 2-b the corresponding total electron and ion thermal diffusion coefficients are shown.

In the other discharges (which by the way, have very low shear in the central region, but a monotonic q-profile) the thermal barrier on the electron temperature profiles is not so much pronounced or even it is not present at all, whereas it tends to appear in the simulated profiles obtained using the mixed shear-dependent model which nevertheless show a very good agreement in comparison with the experimental ones. This suggest that better agreement with the experimental results could be obtained treating the shear dependence of the electrons differently from that of the ions in the thermal diffusion coefficient expressions.

Conclusions

The proposed transport model has shown capable to predict standard L-mode discharges like those contained in the ITER Profile Database. Moreover, it has succesfully employed in predicting the thermal barrier effect in presence of reversed magnetic shear in the so-called hot-ion mode and PEP discharges in JET. The results of our model are very promising in particular for these type of discharges where a previously proposed mixed transport model without a magnetic shear dependence[1] does not give satisfactory results. It has to be noted that the proposed transport model do not contain a self-consistent mechanism of 'pedestal' generation in the temperature profiles and thus no attempt to simulate H-modes discharges have been done. In conclusion, the mixed Bohm–gyro-Bohm shear dependent model seems to be very promising in simulating standard L-mode discharges and interesting new confinement regimes like the ones characterised by very low or even negative magnetic shear.

References

[1] ERBA, M., et al. Jet report JET-P(96) 10, accepted for publication in *Plasma Phys. and Contr. Fusion*

[2] TARONI, A., ERBA, M., SPRINGMANN, E., TIBONE, F., Plasma Phys. Control. Fusion **36** (1994) 1629

[3] ROMANELLI, F., ZONCA, F., Phys. Fluids B **5** (1993) 4081

[4] BALET, B., BOYD, D.A., CAMPBELL, D.J., et al., Nucl. Fusion **30** (1990) 2029

[5] CONNOR, J.W., ALEXANDER, M., ATTENBERGER, S.E., et al., in *Plasma Physics and Controlled Nuclear Fusion Research* (Proc. 16th Int. Conf. Montréal, 1996) IAEA, Vienna (1996) paper CN-64/FP-21

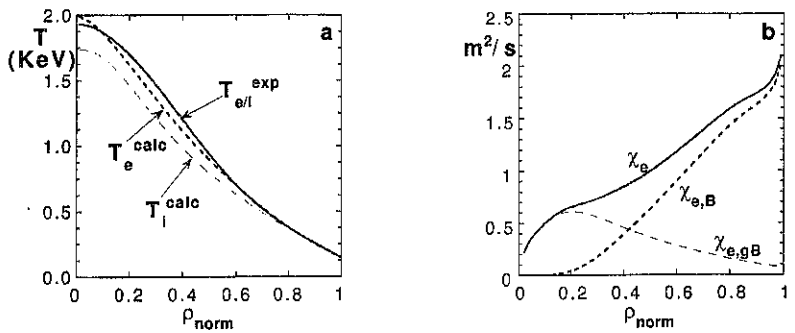

Figure 1: DIII-D discharge 69627: (a) experimental (solid line) and computed (dashed lines) electron and ion temperature profiles at $t = 2.4$ s and (b) total (solid line) electron thermal diffusivity radial profiles and Bohm and gyro-Bohm components (dashed lines) at the same time.

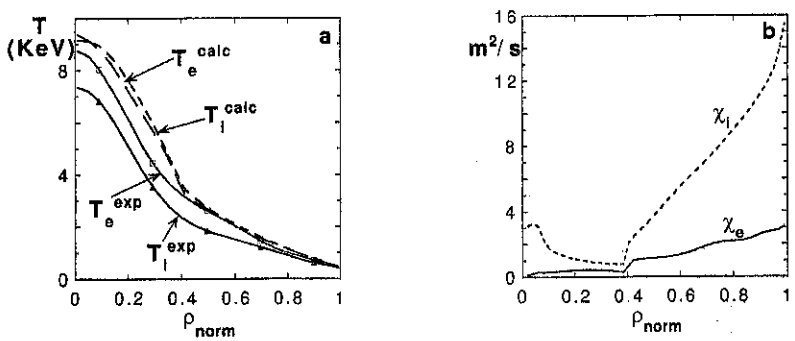

Figure 2: JET discharge 17749: (a) experimental (solid line) and computed (dashed lines) electron and ion temperature profiles at $t = 44.6$ s and (b) total electron and ion thermal diffusivity radial profiles at the same time.

THE ALFVEN DRIFT-WAVE INSTABILITY AND THE SCALING OF THE EDGE TEMPERATURE AT THE L-H TRANSITION

O. Pogutse, Yu. Igitkhanov*, W. Kerner, G. Janeschitz* and J.G. Cordey.
JET Joint Undertaking, Abingdon, Oxon., OX14 3EA, UK.
*ITER Joint Central Team, Joint Work-Site, D-85748 Garching, Germany.

ABSTRACT

The stability analysis of Alfven drift type modes leads to a threshold condition for the L-H transition. This condition yields the scaling for the edge temperature, which is in agreement with the experimental results.

1. INTRODUCTION

The measurement of the electron edge temperature T_0 and density n_0 on JET and other tokamaks suggest that there is an ideal MHD beta threshold for the onset of Giant ELM's. Furthermore, the data reveal also the existence of a second beta threshold (below the ideal ballooning limit) for the L-H transition and a third threshold for the onset of type III ELMs. These findings suggest that the Alfven drift-wave instability (ADW) plays an essential role in the edge plasma dynamics. There is strong experimental evidence that the main plasma instabilities change from ion temperature gradient modes in the plasma core to electron drift modes near the plasma edge. The stability theory gives the result that with increasing plasma pressure, the Alfven waves mix with electron drift waves and suppress the unstable long wavelength perturbations, which are dominant in the transport.

2. DISPERSION RELATION AND DIMENSIONLESS PARAMETERS

The expression for the ion density perturbation follows from the kinetic equation:

$$n_i' = \frac{e\varphi'}{T_{0i}}\left\langle\left(-1+\frac{\omega-\hat{\omega}_{*i}}{\omega-k_\parallel v_\parallel}\exp(-z)I_0(z)\right)f_{0i}(v_\parallel)\right\rangle \Rightarrow n_i' = \frac{e\varphi'}{T_{0i}}\left(-1+\frac{\omega-\hat{\omega}_{*i}}{\omega}\cdot\frac{1}{1+z}\right)n_0$$

The perturbed electron density follows from the electron hydrodynamic equations:

a) the linearised electron density equation is:

$$\omega\frac{n'_e}{n_0}-\omega_{*}\frac{e\varphi'}{T_{0e}} = k_\parallel v'_{e\parallel};$$

b) the parallel component of the electron motion equation yields:

$$\frac{T'}{T_{0e}}+\frac{n'_e}{n_0} = \frac{e\varphi'}{T_{0e}}-\frac{\omega-\omega_{*p}}{k_\parallel c}\frac{eA'_\parallel}{T_{0e}}+R\frac{v'_{\parallel e}}{v_{Te}};$$

where R are the dissipative terms $R = \dfrac{\omega+i\nu_e}{k_\parallel v_{Te}}$;

c) Ampere's law gives:

$$k_\perp^2 \delta^2 \frac{eA'_\parallel}{T_{0e}} = -\frac{cv'_{e\parallel}}{v_{Te}^2};$$

d) The temperature perturbation follows from the energy equation:

$$\left(\omega - \frac{k_\parallel^2 v_{Te}^2}{\omega + i\nu_e}\right)\frac{T'}{T_{0e}} - \omega_{*T}\frac{e\varphi'}{T_{0e}} = \frac{2}{3}k_\parallel v'_{\parallel e}.$$

From these equations the expression for the perturbed electron density is derived:

$$n'_e = n_0 \frac{\left\{\omega_* - \frac{(k_\parallel^2 v_{Te}^2 k_\perp^2 \delta^2)}{\left[\omega - \omega_{*p} + \tilde{\omega}\cdot k_\perp^2\delta^2\right]}\cdot\left[1 + \frac{2}{3}\frac{(\omega_* - (3/2)\omega_{*T})\cdot\tilde{\omega}}{\omega\tilde{\omega} - k_\parallel^2 v_{Te}^2}\right]\right\}}{\left\{\omega - \frac{(k_\parallel^2 v_{Te}^2 k_\perp^2 \delta^2)}{\left[\omega - \omega_{*p} + \tilde{\omega}\cdot k_\perp^2\delta^2\right]}\cdot\left[1 + \frac{2}{3}\frac{\omega\cdot\tilde{\omega}}{\omega\tilde{\omega} - k_\parallel^2 v_{Te}^2}\right]\right\}}\frac{e\varphi'}{T_{0e}}$$

Here $\omega_* = -(ck_y T_{0e}/eB_0)\cdot\partial\ln(n_0)/\partial x$ is the electron drift frequency for the density, $k_\parallel$ is the longitudinal wave number, $v_{Te} = (T_{0e}/m_e)^{1/2}$ is the thermal electron velocity; ν_e is the electron collision frequency and $\delta = c/\omega_{pe}$ is the collisionless skin length, $\tilde{\omega} = \omega + i\nu_e$. We define the dimensionless frequency and transverse wave number as $\Omega = \omega\cdot x_{0p}/c_s$, $k = k_\perp \rho_s$, where $c_s = (T_e/M)^{1/2}$ is the sound speed; $\rho_s = c_s/\omega_{Bi}$ is the ion Larmor radius and T_e the electron temperature. The relevent dimensionless parameters in the problem are:

$$\beta_0 = 4\pi n_0 T_{0e}/B_0^2\cdot(M/m_e), \qquad \nu = \nu_e x_0/c_s$$

$$\mu = k_\parallel v_e x_{0p}/c_s, \quad \eta_e = d\ln(T_{0e})/d\ln(n_0), \quad \tau = T_{0e}/T_{0i},$$

The quasineutrality condition $n'_e = n'_i$ yields the dispersion relation for the Alfven drift wave instability. It is an algebraic equation of fifth order with complex coefficients containing five independent parameters: $\beta_0, \nu, \mu, \eta_e, \tau$. A more detailed analysis shows that after additional renormalization:

$$\Omega_n = \Omega/\sqrt{\mu}, \quad k_n = k/\sqrt{\mu}, \quad \beta_n = \beta_0/\mu, \quad \nu_n = \nu/\sqrt{\mu},$$

the ADW instability can be characterised by only **two dimensionless parameters** the normalised plasma beta and the normalised collision frequency

$$\beta_n = \frac{\beta_0}{\mu} = \left(\frac{M_i}{m_e}\right)^{1/2}\frac{4\pi n_0 T_{0e}}{B_0^2}\frac{1}{k_{\parallel}x_{0p}}, \qquad \nu_n = \frac{\nu}{\sqrt{\mu}} = \left(\frac{M_i}{m_e}\right)^{1/4}\frac{x_{0p}^{1/2}}{\lambda_e k_\parallel^{1/2}}$$

Here x_0 characterises the pressure scale length, λ is the mean free path and $k_\parallel$ is the parallel wave number. All quantities are taken near the separatrix.

3. TRANSPORT COEFFICIENTS

The diffusion and thermalconduction coefficients for the ADW instability are evaluated as:

$$D_\perp = \frac{\chi_{gB}}{\sqrt{\mu}}\cdot\overline{\overline{\chi}}_\perp(\beta_n, \nu_{ne}), \qquad \kappa_{e\perp} = \frac{3}{2}n_e\frac{\chi_{gB}}{\sqrt{\mu}}\overline{\overline{\chi}}_\perp(\beta_n, \nu_{ne}).$$

$$\frac{\chi}{\chi} = \nu_{cr}^{1/3} \frac{\left[1 + (\nu_n / \nu_{cr})^2\right]^{1/2}}{\left[1 / \nu_{cr}^2 + (\nu_n / \nu_{cr})^{4/3}\right]^{1/2}},$$

where $\nu_{cr} = 1 / (1 + \beta_n^2)^{3/2}$ (See Fig. 1 - Fig. 2).

4. L-H THRESHOLD CRITERION

The analysis of the turbulent coefficients shows that the transport decreases for

$$\beta_n > 1 + \nu_n^{2/3}.$$

This condition yields the scaling for the edge temperature at the L -H transition. The estimate of x_0 (inside the separatrix) is derived from the assumption that the turbulent transport coefficients are continuous across the separatrix and that the convection (collisionless) or conduction (collisional) model in the SOL applies.

5. COMPARISON WITH THE EXPERIMENTS

The temperature inside the separatrix is approximated by: $T(a - \Delta x) = T_0 \cdot (1 + \Delta x / x_0)$. Then we obtain for $\nu_n > 1$:

$$T_{eV}(a - \Delta x) = 32.6 \cdot A^{-1/5} s^{3/5} n_{019}^{-3/10} B_{0T}^{3/5} I_{MA}^{3/5} a_M^{-6/5} \cdot \Delta x_{cm} \quad \text{(theory)}$$

$$T_e^{crit}(a - 2\,cm) = 145\, n_e^{-0.3\pm0.1} B_t^{0.8\pm0.1} I_p^{0.5\pm0.3}\ [eV] \quad \text{(ASDEX UP)}$$

and for $\nu_n < 1$:

$$T_{eV}(a - \Delta x) = 23.3 \cdot A^{-1/2} s\, n_{019}^{-1} B_{0T} I_{MA} a_M^{-2} \cdot \Delta x_{cm}$$

The general expression for T_{eV} reads:

$$T_{eV}(a - \Delta x) = c_T \frac{f3 \cdot A^{-0.5 f1}}{n_{019}^{f2}} \left(\frac{s \cdot B_{0T} \cdot I_{MA}}{a_M^2}\right)^{f4} \cdot \Delta x_{cm},$$

where $f1 = (1 + 2/5 \cdot \nu1) / (1 + \nu1)$, $f2 = (1 + 3/10 \cdot \nu1) / (1 + \nu1)$, $f3 = (1 + \nu1) / (1 + 7/10 \cdot \nu1)$, $f4 = (1 + 3/5 \cdot \nu1) / (1 + \nu1)$ and $\nu1 = (n_{019} / n_{cr})^{21/10}$, $n_{cr} = (B_{0T} \cdot I_{MA} / BI)^{4/7}$, $BI = c_{BI} A^{3/7} s^{-4/7} a_M^{8/7} Z_{eff}^{2/7}$. This formula contains two parameters c_T, c_{BI}. The theory gives c_T=23.3, c_{BI}=1.4. The fitting with the ASDEX experiment gives c_T=10, c_{BI}=0.7. The same values are used for all the other tokamaks too. The comparison theoretical prediction with the experimental data [ITER Internal Memo, Yu.Igitchanov at. al., No. J17MD82970423F1 (1997)] is given on Figs. 3 - 6.

6. CONCLUSIONS

The main conclusions are: **1)** the Alfven drift model predicts that the turbulent transport is suppressed when the condition: $\beta_n > 1 + \nu_n^{2/3}$ is satisfied; **2)** the transport coefficients change their dependence on plasma parameters from $\chi \sim T_0^{3/2}/n_0^{1/5}$ (for $\beta_n < \nu_n^{2/3}$) to $\chi \sim n_0^{4/13}/T_0^{20/13}$ (for $\beta_n > \nu_n^{2/3}$); **3)** the Alfven drift model predicts the edge temperature scaling in agreement with experimental findings. Furthermore, the qualitative character of the scaling depends only weakly on the SOL transport.

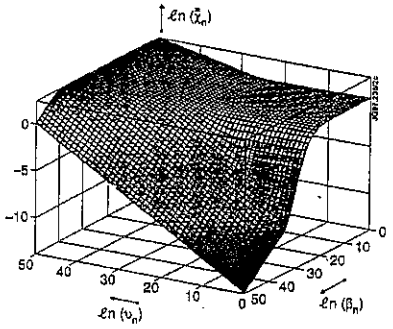

Fig. 1

Fig. 1. The dimensionless transport coefficient $\tilde{\tilde{\chi}}$.

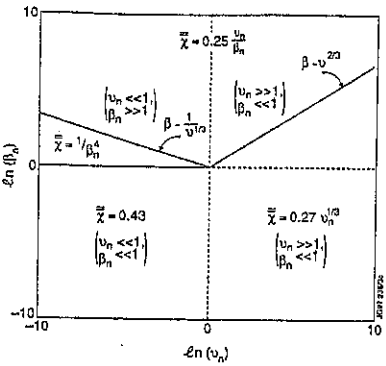

Fig. 2

Fig. 2 The asymptotic properties of $\tilde{\tilde{\chi}}$.

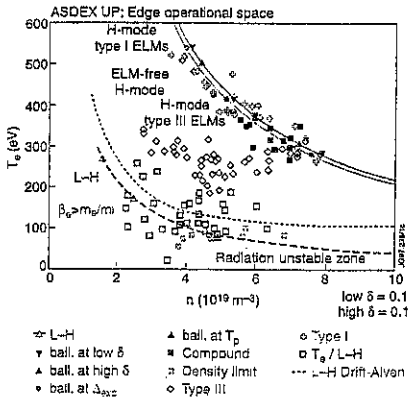

Fig. 3

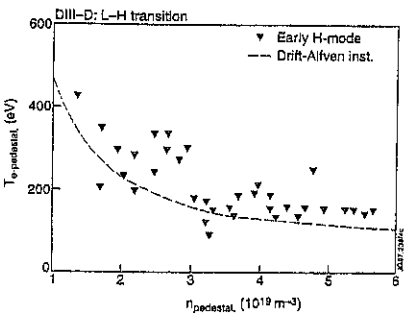

Fig. 4

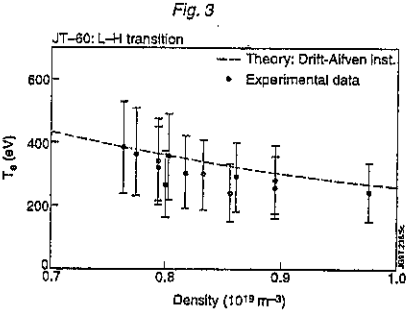

Fig. 5

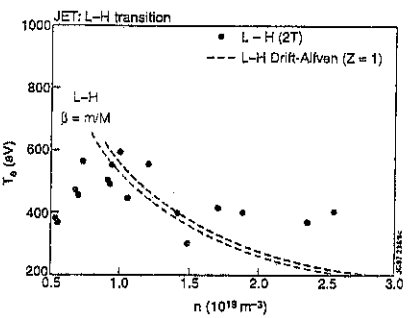

Fig. 6

Fig. 3 -6. The theoretical (dashed lines) and experimental (points) scalings of the edge temperature over edge density for different tokamaks.

ρ^* SCALING IN RADIATIVE PLASMA REGIMES

G.F.Matthews, B.Balet, J.G.Cordey, G.Fishpool, M.G.von Hellermann, L.Horton, C.Ingesson, A.Kallenbach[1], V.Parail, D.Stork, A.Taroni, G.Vlases, P.West[2], K.-D.Zastrow

JET Joint Undertaking, Abingdon, Oxforshire, OX14 3EA
[1]Max-Planck-Institut für Plasmaphysik, EURATOM Assoc., 85478 Garching, Germany
[2]General Atomics, P.O. Box 85608, San Diego, California 92186-9784, USA

INTRODUCTION

The dimensionless parameter approach to energy confinement scaling studies has put the empirical approach to predicting the energy confinement in ITER on a sound physical footing. Since the plasma geometry (shape, safety factor q_{95}), toroidal beta ($\beta \propto nT/B^2$) and collisionality ($\nu^* \propto nZ_{eff}L/T^2$) required by ITER can be achieved in current machines the standard approach used for type I ELMy H-modes [*Cordey*] is to keep these 3 dimensionless parameters fixed and scale the confinement with normalised ion gyro-radius ($\rho^* \propto T^{0.5}/BL$). To perform these ρ^* scaling experiments in JET the toroidal field was varied in the range 1-2.6T. Collisionality can be kept constant by varying $n \propto B^{4/3}$ which is achievable.

ρ^* Scaling in Radiative Regimes

Matching of the three parameters ρ^*, ν^* and β should ensure that all plasma physics phenomena, including collisional effects with Coulomb-like cross-sections are scaled correctly [*Connor*]. Lackner [*Lackner*] has shown that atomic physics effects such as radiation, charge exchange and other ion-neutral interactions of importance in the plasma edge can only be scaled when the absolute temperature, T, is also matched. In JET, detached divertor plasmas are obtained at similar values of total fractional radiated power f_{rad} and so this has been used as a closely related alternative dimensionless parameter. Using lower Z impurities (nitrogen and neon) the radiation distribution will be similar to that expected in ITER for argon. Fixing f_{rad} also avoids any confusion between changes in confinement and direct losses from within the core plasma.

Constraints

In the JET experiments [*Stork*] $q_{95}(3.1)$, $f_{rad}(\approx 60\%)$, $\beta(\approx 1.2)$ and $Z_{eff}(\approx 3)$ were kept constant. Fractional radiated power $f_{rad} = P_{rad,total}/P_{heat,total}$ can be written in terms of Z_{eff} and line averaged density n by using the multi-machine Z_{eff} scaling law [*Matthews*] given by: $Z_{eff} = 1 + 7\, f_{rad} P_{heat}/n^2 S$, where S the main plasma surface area. P_{heat} can then be substituted with an expression in terms of dimensionless parameters via an appropriate confinement scaling law: Gyro-Bohm $B\tau_E \propto \rho^{*-3}$ (~ ITER93H) or Bohm $B\tau_E \propto \rho^{*-2}$ (~ ITER89L). These relationships then imply that key parameters are constrained as follows:

Gyro-Bohm	$n \propto B^{6/7}$	$n/n_{Greenwald} \propto B^{-1/7}$	$\nu^* \propto B^{-10/7}$	$\rho^* \propto B^{-3/7}$	$P_{heat} \propto B^{12/7}$
Bohm	$n \propto B$	$n/n_{Greenwald}$ = const.	$\nu^* \propto B^{-1}$	$\rho^* \propto B^{-1/2}$	$P_{heat} \propto B^{2}$

Ideally we would find a means to keep ν^* constant and one possibility might be to allow Z_{eff} or β to vary but it turns out that the required parameter variations either do not exist or are impractical. Fortunately the ν^* dependence of both the commonly used confinement scalings is rather weak ($B\tau_{E93H} \propto \nu^{*-0.28}$, $B\tau_{E89P} \propto \nu^{*-0.12}$) so that the failure to maintain constant ν^* may have only a small effect on the results.

Scaling of global confinement

Figure 1 shows the variation of the $H_{ITER93-H}$ factor with ρ^* from the JET series of radiative ρ^* scaling series. Data have been restricted to pulses with f_{rad}>50% and multiple points have been taken from two pulses for each value of toroidal field. Also, shown are data from radiative discharges in ASDEX-Upgrade and DIII-D. All this data is consistent with a degradation with respect to the Gyro-Bohm like ITER93H scaling as ρ^* decreases. This is in contrast to the type I ELMy H-modes [*Cordey*] which are also shown.

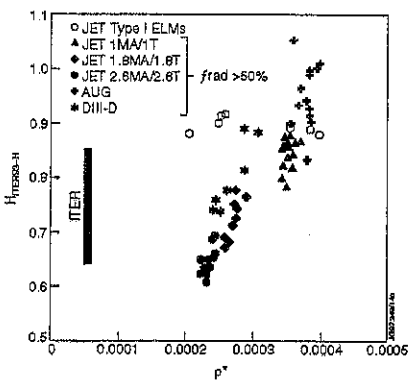

Figure 1 H_{93} vs ρ^* for H-modes with f_{rad}>0.5

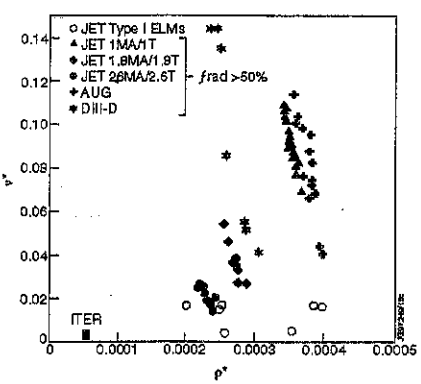

Figure 2 ρ^* vs υ^* for H-modes with f_{rad}>0.5

Figure 2 shows variation of ρ^* with ν^* for the same data. Although ν^* cannot be held constant in these discharges the existence of similar $H_{ITER93-H}$ factors for widely differing ν^* indicates that the confinement is weakly dependent on collisionality as is characteristic of existing scaling laws. There also appears to be no strong beta dependence.

Local transport analysis

Local transport analysis of JET pulses using the TRANSP code shows that the thermal diffusivity of the core ($q<2$) retains its gyro-Bohm like scaling whilst the outer region is strongly degraded. Profiles of n_e, T_e, T_i, P_e, total thermal pressure P_e+P_i and χ_{eff} (dominated by χ_i) are shown in figures 3-8. All discharges were with I_p= 2.5MA, B_T=2.5T and 12MW of NB heating. A reference unfuelled type I ELMy discharge is compared with discharges seeded with nitrogen impurity. In one of these cases (37997) the density fell due to the loss in confinement but in the other (37991) strong D_2 was used to maintain the density.

The observed decoupling of the core and edge confinement are not obviously consistent with confinement models in which the edge and core confinement are strongly linked [*Kotschenreuter*]. It is also appears different from the profile resilience reported by ASDEX-Upgrade [*Suttrop*] in which the core confinement appears to be set by the value at the top of the pedestal leading to self-similar T_e profiles.

In radiative discharges there may be a concern that the increase in χ_{eff} near the edge is merely the result of direct losses which have not been correctly accounted for in the analysis. However, tomographic inversion of the bolometric data [*Ingesson*] shows that a majority of the radiation is emitted from outside q_{95} and as a result, the derived χ_{eff} is very insensitive to the assumptions made about the radiation profile. Monte-Carlo calculations of the charge exchange losses coupled with bolometric evidence show that these losses are too small to influence the transport analysis and in any case are mainly located outside q_{95}.

CONCLUSIONS

JET experiments have been described which are a first attempt at applying the dimensionless parameter approach of discharges with ITER relevant levels of radiated power and small high frequency ELMs. Global confinement scaling appears to be Bohm like which seems to result from degradation of the cross-field transport in the region outside $q=2$. Inside this flux surface the transport is unaffected. Rigid profile consistency does not seem to be observed in either the ion or electron temperature profiles

REFERENCES

Connor J.W. and Taylor J.B, Nuclear Fusion 17 (1977) 1047
Cordey G. for the JET Team, IAEA-CN-64/AP1-2, Montreal, 1996
Ingesson C., et al., this proceedings
Lackner K., Comments on Plasma Physics and Controlled Fusion 15 (1994) 359
Kotschenreuter M. et al., IAEA-CN-64/D1-5, Montreal, 1996
Matthews G.F., et al., 12th Int. Conf. on Plasma-Surface Ints., San Raphael, 1996
Stork D. for the JET Team, IAEA-CN-64/A1-1, Montreal, 1996
Suttrop W., this conference.

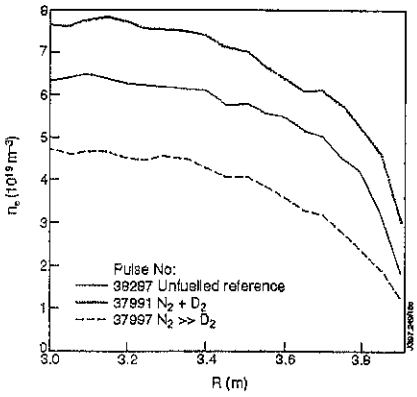

Figure 3 - Electron density profiles

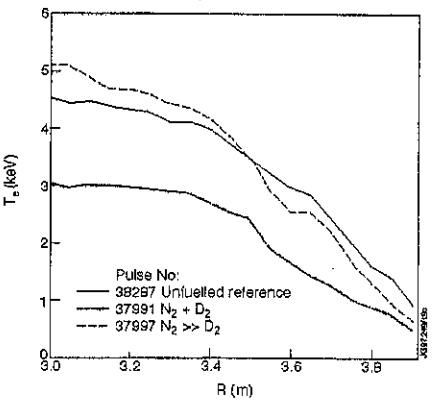

Figure 4 - Electron temperature profiles

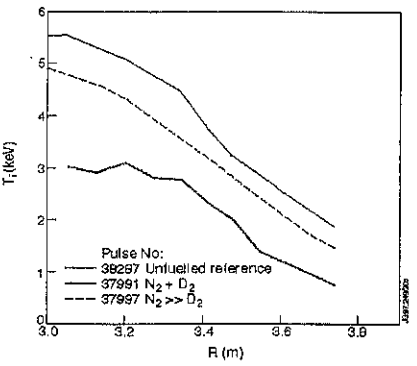

Figure 4 - Ion temperature profiles

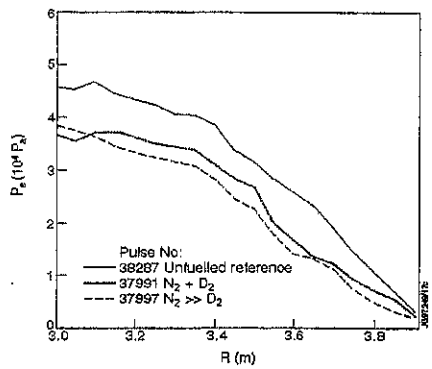

Figure 5 - Electron pressure profiles

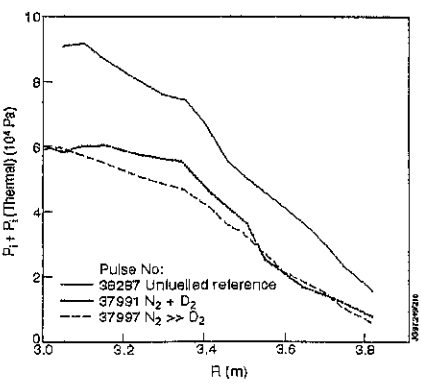

Figure 5 - Total thermal pressure profiles

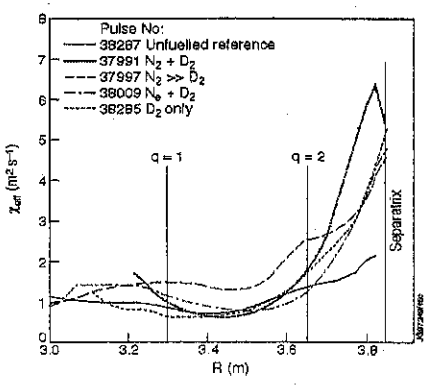

Figure 6 - χ_{eff} profiles from TRANSP

Multimachine Simulations of Divertor Pumping and its Dependency on Target Geometry and Plasma Conditions

A. Loarte[1], J.K. Ehrenberg, L.D. Horton, B. Lipschultz[2], G.F. Matthews, G. McCracken, R.D. Monk, G.D. Porter[2], G.Saibene, R. Simonini, J. Spence, A. Taroni
JET Joint Undertaking, Abingdon, Oxon., OX14 3EA, UK
[1] The NET Team, Max Planck Institut für PlasmaPhysik, Garching, Germany
[2] Plasma Fusion Centre, Massachusetts Institute of Technology, Cambridge, USA
[3] Lawrence Livermore Laboratory, Livermore, and General Atomics, San Diego, USA

1. Introduction

Understanding neutral pumping in tokamak divertors is of great importance for the design of next step divertor devices such as ITER. Neutral pumping at the divertor determines the amount of plasma convection in the SOL and the rate of Helium removal from the core plasma, which greatly influences the performance of the device.

Existing results from divertor tokamak experiments display apparently contradicting features, in particular with respect to the dependency of pumping (or neutral pressure at the pumping plenum) on the divertor geometry and proximity of the strike zone to the plenum. DIII-D shows a strong decay of the pressure (a factor of 2) in the plenum when the strike point is moved 2-3 cm from the pumping baffle [1,2] for low density H-modes and a somewhat smaller drop at high densities. However, for discharges in JET with the Mark I and Mark II divertors [3, 4, 5] and Alcator C-mod [6] a plenum neutral pressure variation of a factor of 2 is obtained only by moving the strike points over the whole divertor target (10 - 20 cm). In this paper the physical reasons behind this behaviour will be discussed in the light of results from simple models and multimachine simulations with the 2-D code EDGE2D/NIMBUS for the plasma edge [7].

2. Simple Model for the Line of Sight Neutral Flux Through a Pumping Slot

The neutral flux trough a pumping slot (which determines the pressure in the pumping plenum) is made up of two components : neutrals that arrive at the slot in the first flight after they are born at the divertor target and those that suffer multiple scattering before reaching the slot. The contribution of the first flight component to the total neutral flux will be dominated by the geometry of the divertor, i.e. the solid angle for the neutrals to reach the slot. The dependency of this first flight component on the distance from the separatrix to the pumping slot can be easily estimated under the following assumptions : a) neutrals are born with the same spatial distribution as the ion flux onto the divertor and b) neutrals emerge from the divertor target with trajectories following a cosine distribution ($\perp$ to the target) :

$$P_0^{Slot} = \int_0^b e^{-x/\lambda}\left(1 - (b-x)/\sqrt{a^2 + (b-x)^2}\right) dx \qquad (1)$$

where P_0^{Slot} is the proportion of neutrals that reach the slot in the first flight, b is the distance from the strike point to the pumping slot, a is the slot width and λ is the ion flux e-folding length at the divertor. The x axis runs along the divertor target surface and the pumping slot width, a, is projected perpendicular to the divertor target. The proportion of this first flight neutral flux component that reaches the pumping slot for several values of a and b is shown in Fig. 1. From this figure, it is clear that this component of the neutral flux is expected to decay by a factor of 2 when the strike points moves away by (1.5 - 2)λ from the slot.

3. JET-Mk I and JET-Mk II EDGE2D simulations

Following the dependencies described above, it was expected that the neutral pressure in the JET-Mk II divertor (basically a slot configuration) would depend much more critically on the strike point position that in the JET-Mk I divertor. The Mk I divertor target was made of rows of tiles separated by toroidal gaps, which lead to a weak dependency of pumping on strike point position [3,4]. However, it was found experimentally in Mk II, that the dependency of pumping on strike point position was similar (or even weaker) than in comparable experiments with the Mk I divertor [5]. Simulations with the EDGE2D/NIMBUS code, including the whole 2-D structure of the divertor and pumping chamber, have been performed to understand this unexpected behaviour, for typical ohmic and L-mode conditions (for which the experiments were performed). The results of such a comparison are shown in Figs. 2 and 3 for JET-Mk I and Mk II divertors respectively (P_{sol} = 1.2 MW, n_{sep} = 9.0 10^{18} m^{-3}, $D_\perp$ = 0.1 m^2/s, $\chi^{e,i}_\perp$ = 1.5 m^2/s). While the absolute magnitude of the neutral pressure in the Mk I divertor simulations is very dependent on the value of the effective transparency of the divertor plates to neutrals used in the code, its dependency on strike position is very weak and similar to the experiment. The Mk II simulations produce the same results despite the slot-like configuration of this divertor (according to Eq. 1, the expected distance to get a factor of 2 pressure drop for the first flight neutrals is 5 cm). This is due to the formation of a high neutral pressure region at the divertor corner between the horizontal and vertical plate regardless of the strike point position on the horizontal plate. This high neutral pressure has been seen to affect the characteristics of detachment both experimentally [8] and in B2-EIRENE simulations [9]. The physical mechanism that leads to this high pressure formation is the divertor target geometry of the Mk II divertor (see Fig. 4). The Mk II horizontal target is tilted towards the vertical plate and, therefore, neutrals that are not ionised, or lost in their first flight to the pumping slot, reach the vertical target from where they are reflected back into the divertor plasma. In this way, a high neutral density region can build up at the divertor corner, at some distance from the separatrix. These multiple scattering processes dominate the neutral flux to the pumping plenum leading to its weak dependence on the strike point position.

The sensitivity of the simulations results to several parameters have been tested, such as the effective values of the transport coefficients in the SOL ($D_\perp$= 0.02 → 0.1 m^2/s, $\chi^{e,i}_\perp$= 0.3 → 1.5 m^2/s), separatrix density (n_{sep}= 4.5 10^{18} m^{-3} → 9.0 10^{18} m^{-3}) and input power (P_{sol}= 1.2 →

4.8 MW). Although the calculated values of the neutral pressure in the pumping plenum depend strongly on the modelling assumptions, as expected, its dependency on the strike point positions is weak under most circumstances. A typical variation of less than a factor of two is found when the strike point is moved across the whole horizontal target, in agreement with the experiment.

4. DIII-D and Alcator C-mod EDGE2D simulations

A similar study with the EDGE2D/NIMBUS code has been carried out for DIII-D and Alcator C-mod. In this case, the experimental separatrix scan is simulated in the calculations by modifying the divertor target so that the pumping plenum entrance is moved with respect to the separatrix. Moreover, the detailed pumping chamber structure of these experiments is not used in the calculations, but the pressure at the plenum is assumed to be proportional to the neutral flux through a test surface located at the plenum entrance. Simulations for typical L-mode and H-mode discharges have been carried out for DIII-D (L-mode : P_{sol} = 2MW, n_{sep} = 1.0 10^{19} m^{-3}, $D_\perp$ = 0.2 m^2/s, $\chi^{e,i}_\perp$ = 2.5 m^2/s and H-mode : P_{sol} = 5MW, n_{sep} = 2.0 10^{19} m^{-3}, $D_\perp$ = 0.02 m^2/s, $\chi^{e,i}_\perp$ = 0.1 m^2/s) and for Ohmic discharges in C-mod (P_{sol} = 0.8MW, n_{sep} = 4.0 10^{19} m^{-3}, $D_\perp$ = 0.05 m^2/s, $\chi^{e,i}_\perp$ = 0.5 m^2/s). Despite the simplifications, the modelling reproduces the reported differences for the dependency of the neutral pressure at the divertor plenum. For DIII-D a very sharp decay of the plenum pressure is expected as the strike point moves away from the pumping plenum and this is found in the experiment and simulations (Fig.5). For C-mod a much weaker dependency is found both in experiment and simulations (Fig.6). While in C-mod the neutral flux to the pumping plenum is dominated by multiply scattered neutrals, in DIII-D this flux is dominated by first flight neutrals and, hence, sensitive to the solid angle accessible by the neutrals recycled from the divertor (see Fig. 5)

5. Conclusions

The differences in the reported results for the dependency of the neutral pressure in the divertor plenum on the strike point position can be understood and reproduced when the divertor pumping geometry is taken into account. While the plenum pressure in DIII-D is dominated by direct scattering of neutrals into the pumping slot, in JET and C-mod is dominated by multiply scattered neutrals. This results in a less critical dependency of divertor pumping on the exact position of the strike point, which facilitates the achievement of divertor pumping in these experiments for a wide range of diverted magnetic configurations.

6. References

[1] C.C. Klepper, et al., Nucl. Fusion **33** (1993) 533.
[2] R. Maingi, et al., J. Nucl. Mat. **220-222** (1995) 320.
[3] G. Saibene et al., 22nd Eur. Conf. Control. Fus. & Plasm. Phys. Vol 19C, Part II, 121.
[4] J.K. Ehrenberg, et al., 22nd Eur. Conf. Control. Fus. & Plasm. Phys. Vol 19C, Part I, 309.
[5] The JET Team, IAEA-CN-64/A4-1, 16th IAEA Conference, Montréal, Canada, 1996.
[6] A. Niemczewski et al., Nucl. Fusion **37** (1997) 151.
[7] R. Simonini, et al., Contrib. Plasma Phys. **34** (1994) 448.
[8] R. Monk et al., 24th Eur. Conf. Cont. Fus. & Plasm. Phys., 1997, Berchtesgaden, FRG.
[9] K. Borrass et al., 24th Eur. Conf. Cont. Fus. & Plasm. Phys., 1997, Berchtesgaden, FRG.

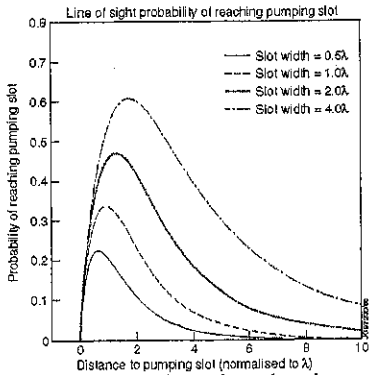

Fig. 1. Probablity of neutrals reaching the pumping slot in the first flight versus separatrix-slot distance(normalised to ion flux)

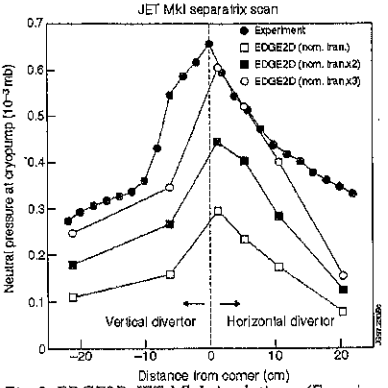

Fig. 2. EDGE2D JET-Mk I simulations. (Experiment $<n_e> = 3.1\ 10^{19}\ m^{-3}$).

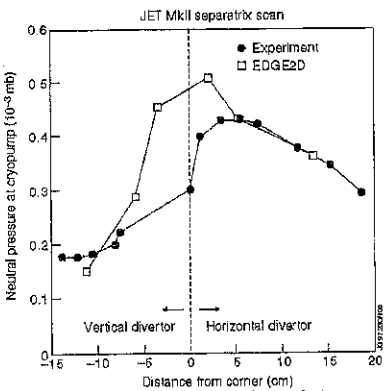

Fig. 3. EDGE2D JET-Mk II simulations. (Experiment $<n_e> = 2.1\ 10^{19}\ m^{-3}$).

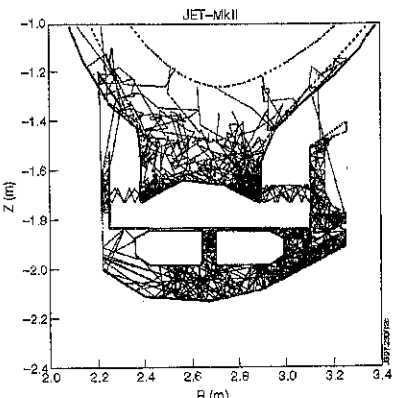

Fig. 4. Neutral trajectories in Mk II simulation.

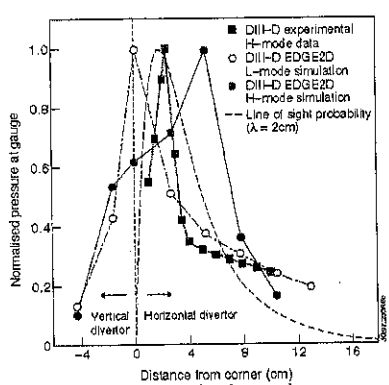

Fig. 5. DIII-D normalised neutral pressure at pumping plenum (experiment, EDGE2D and simple L.O.S. model).

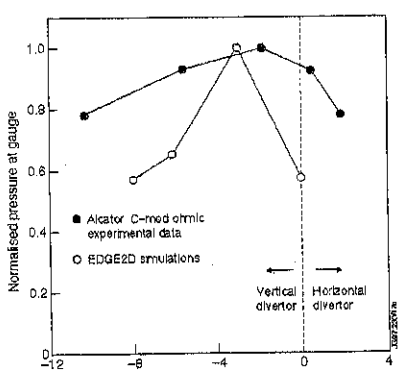

Fig. 6. C-mod normalised neutral pressure at pumping plenum (experiment and EDGE2D).

Plasma Parameters and Detachment in Divertor Simulators

T. K. Soboleva† and E. Cruz
Instituto de Ciencias Nucleares, UNAM, Mexico D.F., Mexico

S. I. Krasheninnikov† and A. Yu. Pigarov†+
MIT Plasma Science and Fusion Center, Cambridge, MA 02139, USA

Introduction. In the experiments on divertor simulators plasma with density $n_e \sim 10^{13}$ cm^{-3} streams from the source region into the long ($L_{WCh} \sim 100$ cm) working chamber where different neutral gases can be puffed in (see Fig. 1). At low neutral gas pressure in the working chamber, the plasma stream hits the target. However, with increasing gas pressure, the plasma flux onto the target, j_t, starts to decrease, and when the gas pressure exceeds some critical value ~ 10 mtorr, j_t exhibits a rather steep drop. This type of plasma behavior is observed for different working gases [1, 2]. Simplified analytical analysis of a plasma flow in simulators [3] suggests that plasma recombination can explain this experimental data and predicts a rather low electron temperature ~0.2 eV in the recombination region which seems to be in reasonable agreement with experimental findings [1]. It also predicts that molecular activated recombination (MAR), which involves ro-vibrationaly excited molecular hydrogen and is characterized by a high rate constant [3, 4] (see Fig. 2) will substantially alter plasma parameters and enhance recombination when some small amount of molecular hydrogen is puffed into the working chamber as a He/H_2 mixture. Here we discuss the results of this analytical analysis and verify them with 1D numerical modeling of plasma-neutral gas interaction (for He and He/H_2 mixture) in a divertor simulator with the parameters close to that of NAGDIS II.

Model. For a working chamber radius of about 10 cm, and a neutral gas pressure about 10 mTorr, the neutral-ion, λ_{Ni}, and neutral-neutral, λ_{NN}, mean free paths exceed the radii of the plasma stream (~ 1 cm) and working chamber, λ_{Ni}>1 cm, λ_{NN}>10 cm. Therefore, to lowest order we can assume that the neutrals are in the Knudsen transport regime and their drift velocity is small. For the same parameters, the ion-neutral mean free path $\lambda_{iN} \approx V_{Ti}/\nu_{iN} \approx V_{Ti}/(K_{iN}N)$ is smaller than L_{WCh}, where N is the neutral gas density. Therefore, the plasma flux, j, can be found from the plasma momentum balance equation written in the diffusive approximation as $j = -(dP/dx)/M\nu_{iN}$, where M is the ion mass and P is the plasma pressure. For a plasma with a temperature ~ 1-2 eV, a density ~ 3×10^{13} cm^{-3} and helium as the working gas with a pressure ≤ 10 mTorr, the main ion energy sink is due to ion-neutral interactions, while the electrons are cooling down due to electron-ion collisions [2]. For the conditions we are interested in, the ion-neutral collision frequency ν_{iN} is higher than the electron-ion energy equilibration frequency, $\nu = 2(m/M)\nu_{ei}$, where m is the electron mass, and ν_{ei} is the electron-ion collision frequency. Therefore, we can assume that the ion temperature is equal to the neutral gas temperature T_N=const., while T_e can be higher than T_N. Then, we

can write the electron energy balance and plasma continuity equations as follows:

$$\partial_x(\kappa_e\partial_x T_e) = (2/3)\nu\, n_e(T_e - T_N) + (E_{EIR}\nu_{EIR} + E_{MAR}\nu_{MAR} + E_{ion}\nu_{ion})n_e\ , \quad (1)$$

$$-\partial_x j \equiv \partial_x\left((M\nu_{iN})^{-1}\partial_x P\right) = (\nu_{EIR} + \nu_{MAR} - \nu_{ion})n_e\ , \quad (2)$$

where $\kappa_e(T_e) = 3.2 n_e T_e/m\nu_{ei} \propto (T_e)^{5/2}$ is the electron heat conduction coefficient; $\nu_{EIR} = K_{EIR} n_e$, $\nu_{MAR} = K_{MAR}[H_2]$, and $\nu_{ion} = K_{ion} N$ are the electron-ion recombination (EIR), MAR, and neutral ionization frequencies; $[H_2]$ is the molecular hydrogen density; K_{EIR} (E_{EIR}), K_{MAR} (E_{MAR}), and K_{ion} (E_{ion}) are the rate constants (effective electron energy loss) of (per) EIR, MAR, and neutral ionization. Notice that $E_{ion}>0$, while E_{EIR} and E_{MAR} (depending on plasma parameters) can positive or negative. We omit in Eq. (1) the convective part of the energy flux which is small for our case of subsonic plasma flow.

Analytical results. First we consider pure helium gas in the working chamber ($\nu_{MAR}=0$) and assume that T_e is low enough that ionization processes can be neglected. Adopting $K_{EIR} \propto (n_e)^2/(T_e)^{9/2}$ scaling one finds that for the limit of $T_e >> T_N$ and ν_{EIR}, $\nu_{MAR} << \nu$ (which allow us to neglect contributions of EIR and MAR to electron energy balance equation), Eqs. (1, 2) can be written in renormalized variables $p = P/P_*$, $\xi = x/x_*$, and $\tau = T_e/T_*$, where T_* is determined from the relation

$$\nu_{iN}\nu_{EIR}(n,T_*)(M/m)^2 = (\nu_{ei}(n,T_*))^2\ . \quad (3)$$

Notice that since $\nu_{ei}(n,T_*) \propto n$ and $\nu_{EIR}(n,T_*) \propto n^2$ there is no plasma density dependence on the left hand side of Eq. (3). For helium as a working gas at a pressure of 10 mTorr, Eq. (3) gives $T_* \approx 0.2$ eV. The asymptotic behavior of the solutions of Eqs. (1, 2) are

$$T_e(\xi) \propto |\xi|^{2/3} \qquad j \approx \text{const.}, \qquad P \propto |\xi|, \qquad (T_e > T_*,\ \xi \to -\infty) \quad (4)$$

$$T_e(\xi) \propto T_*/\ell n(\xi), \quad j \propto \xi^{-2}\left(\ell n(\xi)\right)^{-15/4}, \quad P \propto \xi^{-1}\left(\ell n(\xi)\right)^{-15/4}, \quad (T_e \le T_*,\ \xi \to \infty) \quad (5)$$

From Eqs. (4, 5) we see that the main reduction of the plasma flux j due to EIR occurs in the region with $T_e \sim T_*$. Before this region the plasma temperature drops sharply, while after it the temperature varies very slowly. The reason for this behavior is: i) the strong dependence of EIR on both plasma temperature and density, and ii) electron cooling due to electron-ion collisions. Indeed, upstream of the recombination region the temperature is higher and recombination negligible. There the plasma density is relatively large and, therefore, electron energy removal via electron-ion collisions is very efficient causing the electron temperature to drop sharply. As we approach the temperature $T_e \sim T_*$, the efficiencies of energy and particle transport, and electron cooling and plasma recombination become comparable. In this temperature range plasma recombination occurs. After the plasma recombines, the plasma density drops and electron cooling via e-i collisions becomes inefficient so the electron temperature varies slowly.

Consider the effects of MAR assuming some percentage of H_2 in the working chamber. From previous analysis we see that EIR only weakly affects the plasma parameters at $T_e > T_*$. MAR, however, reduces plasma density and slows down electron cooling via electron-ion equilibration. Analysis of Eqs. (1, 2) for $T_e > T_*$ suggests that the upstream plasma density, n_u, and temperature, T_u, play important roles in the competition between plasma cooling and

$(\nu_{MAR})_{crit}$,

$$(\nu_{MAR})_{crit} \approx \left((\nu_{ei}(n_u, T_u))^2/\nu_{iN}\right)(m/M)^2, \quad (6)$$

the electron temperature remains higher than T_*, and plasma recombines due to MAR and EIR do not play a significant role. For a helium discharge (with neutral pressure ~ 10 mTorr, T_u ~ 1-2 eV, $n_u \sim 3\times10^{13}$ cm^{-3}, and $K_{MAR} \sim 10^{-10}$cm^3/s) just a few percent of molecular hydrogen in the working chamber (recall $\nu_{MAR} = K_{MAR}[H_2]$) exceeds the critical level (6).

Numerical modeling. Analytical results discussed above are obtained using simplified of Eqs. (1, 2) including simplified models for both EIR and MAR rate constants, ignoring the effects of ionization and the boundary conditions (at the target and at the entrance into working chamber). To verify the main conclusions of analytic analysis we solve Eqs. (1, 2) numerically. The dependencies of the rate constants and related quantities of EIR, MAR, and ionization processes on T_e and n_e are calculated with the atomic data code CRAMD [4]. We take L_{WCh}=100 cm; T_N=0.1 eV; $N_{He}=5\times10^{13}$ cm^{-3} (5 mtorr pressure); specify the fraction of molecules, $\alpha_H \equiv [H_2]/N_{He}$; electron density, n_u, and temperature, T_u, at the entrance to the working chamber; and apply a sheath boundary condition at the target. For a pure helium discharge (α_H=0) we find (see Figs. 3, 4) that at relatively high (low) n_u (T_u) the electrons cool down very effectively due to electron-ion coupling [2], thereby switching EIR wich cause plasma recombination (Fig. 3). At lower (higher) n_u (T_u) electron cooling is weaker and EIR recombination occurs close to the target (Fig. 4). Although these results agree qualitatively with the physical picture of [3], they show that the electron temperature saturates (after strong plasma recombination occurs) at a higher level (~0.25-0.4 eV), than the $T_* \approx 0.2$ eV found from simplified analytical analysis, probably due to more accurate account of density and temperature dependencies of K_{EIR}, and boundary conditions. EIR is very strong in the high (low) n_u (T_u) case; therefore, adding a small amount of molecular hydrogen ($\alpha_H \le 0.1$) does not have strong impact on the plasma parameters. At low (high) n_u (T_u), where EIR is weaker, the influence of MAR can be substantial even for α_H<0.1. In agreement with physical picture of [3], MAR slows down electron cooling (due to reduction of the plasma density) and makes EIR ineffective (compare Fig. 4 and Fig. 5). The transition from EIR to MAR with increasing fraction of molecules can be seen from the dependence of electron temperature at the target, T_t, on α_H: MAR effects (Fig. 6) show up at high T_t.

Conclusions. In pure helium discharges the electron cooling due to e-i coupling can result in EIR switching on and strong plasma recombination. After recombination occurs the electron temperature saturates at ~0.25-0.4 eV. Adding a small percentage of molecular hydrogen can result in effective plasma recombination due to MAR which slows down electron cooling and turns EIR off. Numerical modeling supports, in general, the simplified analysis of Ref. 3.

Acknowledgments. Work performed under project ES104393 DGAPA-UNAM at UNAM, Mexico, and USDOE grant DE-FG02-91-ER-54109 at MIT, USA.

References

†Also at: I. V. Kurchatov Institute of Atomic Energy, Moscow, Russia.

⁺Also at: College of William and Mary, Williamsburg, VA USA.

[1] J. Park, M. Goeckner, S. Cohen, N. Ohno, N. Ezumi, and S. Takamura, to be published.

[2] N. Ohno et al., J. Nucl. Mater, **220-222**, 279 (1995).

[3] S. I. Krasheninnikov et al., Phys. Plasmas, **4**, 1638 (1997).

[4] A. Yu. Pigarov and S. I. Krasheninnikov, Phys. Lett. A, **222**, 251 (1996).

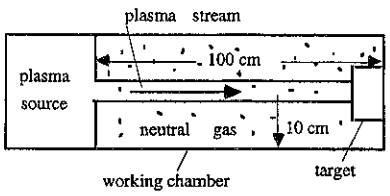

Fig. 1. *Schematic view of divertor simulator.*

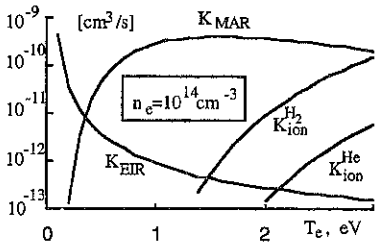

Fig. 2 *MAR, EIR, and ionization rate constants for H_e/H_2 mixture [3, 4].*

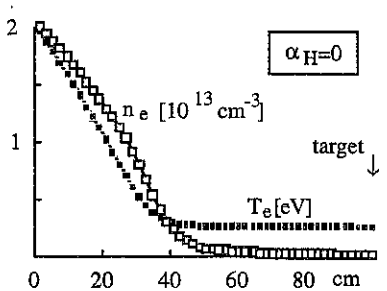

Fig. 3. *Plasma density and temperature profiles for high (low)* n_u *(*T_u*).*

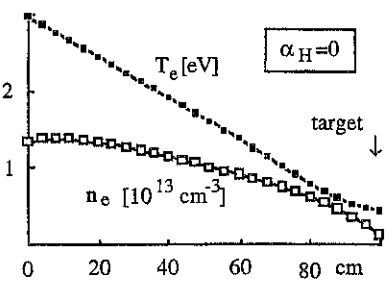

Fig. 4. *Plasma density and temperature profiles for low (high)* n_u *(*T_u*).*

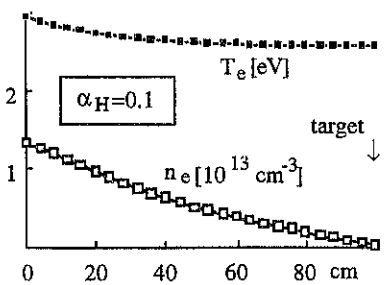

Fig. 5. *Effects of MAR on plasma density and temperature profiles for low (high)* n_u *(*T_u*).*

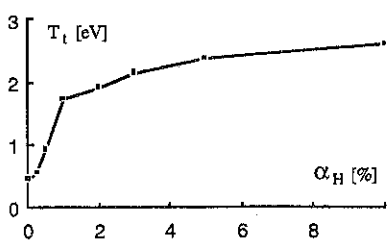

Fig. 6. *Plasma temperature at the target,* T_t*, as a function of* α_H *for low (high)* n_u *(*T_u*).*

Effect of Radial Electric Field Shear on Tokamak Transport: Flow Shear and Magnetic Field Scaling

S. H. Batha,† S. D. Scott,‡ D. R. Mikkelsen,‡ C. C. Petty,*
E. J. Synakowski,‡ G. Taylor,‡ and M. C. Zarnstorff‡
†Fusion Physics and Technology, Inc., Torrance, CA USA; ‡Princeton Plasma Physics Laboratory, Princeton, NJ USA; *General Atomics, San Diego, CA USA

I. Introduction

Numerous recent tokamak experiments using reversed magnetic shear have renewed interest in the connection between reduced energy and particle transport and large shearing rates of the radial electric field.[1,2] A simple criterion has been suggested[3] for turbulence and transport suppression. Transport is suppressed when the shearing rate, γ_{ExB}, is larger than the linear growth rate, γ_{max}, of the fastest growing mode involved in the transport. The shearing rate is defined as $\gamma_{ExB} \equiv RB_p/B_t\partial(E_r/RB_p)/\partial r$ where B_p and B_t are the poloidal and toroidal magnetic fields, respectively.[4] Force balance determines the radial electric field to be $E_r = \nabla P/nZe + V_tB_p - V_pB_t$. In plasmas with small pressure gradients, such as in L-mode discharges, the ratio $\gamma_{ExB}/\gamma_{max}$ is expected to scale as MB_p/B_t where M is the toroidal Mach number ($M = V_t/C_s$ and C_s is the ion sound speed).

Although complete turbulence suppression requires $\gamma_{ExB} \approx \gamma_{max}$, nonlinear numerical turbulence calculations have indicated that transport could be reduced even when $\gamma_{ExB} < \gamma_{max}$. Thus, shear-flow effects could potentially affect confinement in a variety of plasma regimes including L-mode and the H-mode core. For this reason, the dependence of the shearing rate on the toroidal velocity may be a concern for the validity of ρ^* and other scaling experiments that use only uni-directional beam injection. The results of those scaling experiments may be confused by a favorable scaling of transport with increased flow shear. Also, empirical expressions for the global energy confinement time, τ_E, typically do not explicitly account for rotation effects. Scalings deduced from rotating plasma experiments could be misleading for extrapolating to devices such as ITER where the external momentum input is small.

II. Experimental Results

Experiments were performed on TFTR to examine the effects of both toroidal rotation and magnetic field on transport in L-mode plasmas with monotonic q profiles. The toroidal velocity was varied by changing the net torque applied to the plasma using neutral beam heating directed in either the same (co-) or opposite (ctr-) direction to the plasma current. For the analysis presented here, the plasma rotation is assumed to track linearly with the mix of co- and ctr-injected power. More detailed analysis using measured carbon velocity profiles is in progress.

The magnetic field scaling was determined by changing simultaneously the plasma current and the toroidal field at fixed edge q.

The plasmas were formed at a major radius of 2.52 m with a minor radius of 0.87 m. The line-averaged density during the discharge was kept to a programmed level of 5.5 x 10^{19} m^{-3} (Fig. 1) by puffing deuterium gas. The plasmas were heated with 11 to 15 MW of neutral beam injection (NBI) power for two seconds. The directionality of the heating power was changed from all co- to balanced and then to all ctr- by substituting individual sources on successive discharges. The plasma current and toroidal field were either 2.0 MA and 4.8 T or 1.0 MA and 2.4 T, respectively. The confinement times were typical of L-mode discharges on TFTR, 100 - 120 ms for the high-field discharges and 50 - 90 ms for the low-field discharges. All of the discharges had sawteeth.

Global plasma performance on TFTR is critically dependent on edge conditions (edge density and particle influx). The transition from low-performance L-mode discharges to high-performance supershots is a smooth function of edge conditions. Examination of the edge density and electron temperature show that these quantities were well matched. Therefore, a variation in edge conditions was not responsible for the observed confinement variations.

The radial profiles achieved in the high-field discharges are shown in Fig. 2. The discharges were well-matched in density, beam deposition, and electron temperature profiles. Toroidal velocities between +1.5 x 10^5 and -1.0 x 10^5 m/s were obtained, corresponding to Mach numbers between +0.3 and -0.3.

It was found that global energy confinement was the highest for pure co-injection compared to balanced or pure ctr-injection, i.e., it took less co-injected power to match the same stored energy at the same line-averaged density as it took either balanced or ctr-injected power. Figure 1 shows that this was true for both high- and low-field discharges. However, to conclude that plasma rotation is favorably affecting energy confinement for co-rotation, it is necessary to

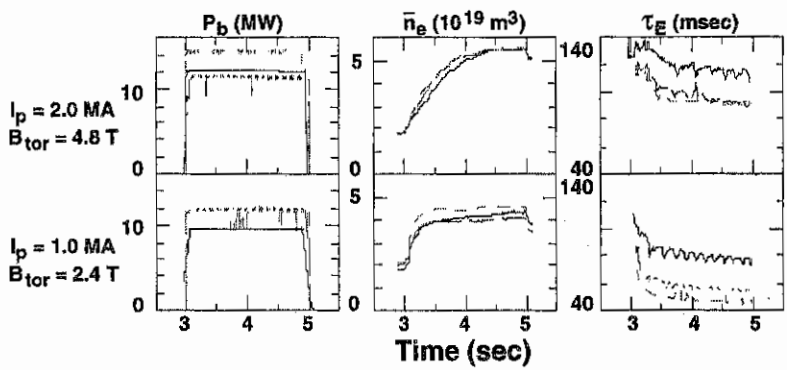

Figure 1. Energy confinement is better with co-injection for both toroidal fields. The discharges had ratios of co- to total injected neutral beam power of 1.0 (solid line), 0.4 (dashed), or 0.2 (dotted).

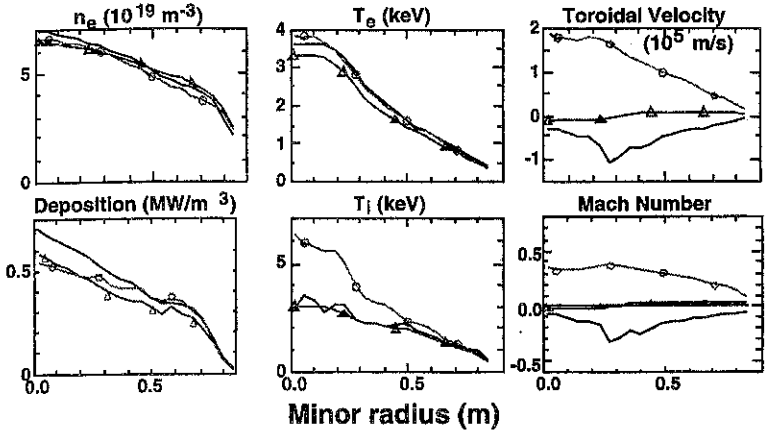

Figure 2. Profile information for the high-field discharges of Fig. 3 at 4.15 sec. The discharges had ratios of co- to total injected neutral beam power of 1.0 (o), 0.4 (Δ), or 0.2 (solid line).

include beam-orbit effects which reduce the effectiveness of ctr-injected beams. But as shown in Fig. 2, even when the orbit effects are taken into account, the co-injected plasma achieved a higher ion temperature.

Kinetic analysis shows that improvement of the ion energy transport accounts for the increase in global confinement. This is shown clearly in Fig. 3 in the elevated ion temperature 25 cm from the magnetic axis ($r \approx a/3$) for the pure co-injected plasma. There is no increase in the density or central electron temperature. The density, T_e, and T_i at the edge of the plasma showed no systematic change due to rotation.

The experimental results are summarized by Fig. 4. Both pure co- and pure ctr-injection led to improved global confinement compared to balanced injection (non-rotating plasmas). The figure of merit is the energy confinement time compared to standard L-mode scaling. Confinement is improved by 20% for the high-field discharges and by 50% for low-field discharges. Simple models of flow-shear stabilization would suggest that the effects of rotation

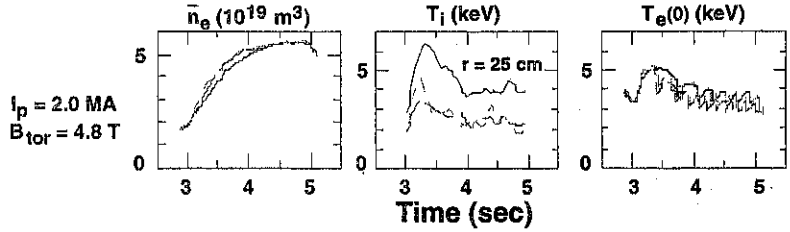

Figure 3. The core ion temperature increases greatly with co-injection. There is little effect on the electron temperature. The discharges had ratios of co- to total injected neutral beam power of 1.0 (solid line), 0.4 (dashed), or 0.2 (dotted).

should be symmetric with respect to co- or ctr-rotation. The data, however, clearly show that the minimum confinement occurs for moderate values of ctr-rotation. Detailed analysis, accounting for beam-orbit effects, will modify the shape of these curves but will not affect the overall conclusion that rotation improves confinement.

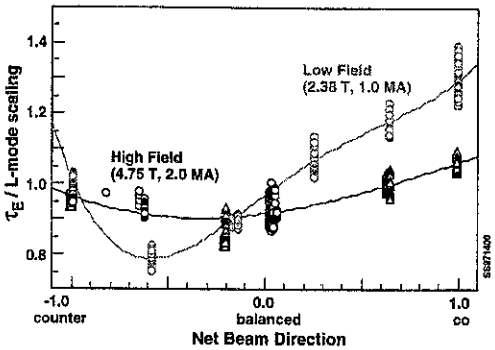

Figure 4. Both high-field (Δ) and low-field (o) data sets show that rotation improves energy confinement.

These L-mode experiments were limited to rotation velocities of Mach ±0.3. Mach numbers up to +0.8 and -0.6 have been produced in supershot discharges which have large pressure gradients, $T_i >> T_e$, and peaked density profiles. The co-injection discharges exhibited significantly improved core ion heat confinement compared to balanced or ctr-injection, with local χ_i (r=a/3) decreasing an order of magnitude in some cases. The effect on global energy confinement was masked by several classical effects of rotation on beam deposition and thermalization which made global τ_E a maximum for slight co-injection rather than pure co-injection.

III. Conclusion

The effect of rotation on global energy confinement was clearly observed in discharges with $T_i \approx T_e$ and weak pressure gradients. Increased confinement was observed for both strong co- and strong ctr-rotation. Kinetic analysis indicates that ion energy confinement was affected most by rotation. The effect was stronger at lower toroidal magnetic field ($B_t \approx 2.4$ T). Suppression of transport by radial electric field shear is supported by both of these observations.

These results suggest that shear-flow effects should be considered in the analysis of empirical global τ_E scaling and dimensionless scans for estimating τ_E in next-step tokamaks.

Work supported by the U. S. Department of Energy Contract No. DE-AC02-76-CH03073.

References

1. K. H. Burrell, *Phys. Plasmas* **4**, 1499 (1997).
2. E. J. Synakowski *et al.*, *Phys. Plasmas* **4**, 1736 (1997).
3. R. E. Waltz, G. D. Kerbel, and J. Milovich, *Phys. Plasmas* **1**, 2299 (1994).
4. T. S. Hahm and K. H. Burrell, *Phys. Plasmas* **2**, 1648 (1995).

SOL Currents for Feedback Stabilization of MHD Modes

Robert J. Goldston, Princeton Plasma Physics Laboratory

Abstract

A new technique is proposed for the stabilization of resistive wall modes and resistive tearing modes in tokamaks and other fusion devices. Time-modulated non-axisymmetric currents are driven in the scrape-off layer (SOL), with the purpose of generating a modulated poloidal field, capable of providing sufficient magnetic pressure for feedback stabilization of slowly growing MHD modes. Estimates of required currents and voltages are provided for near-term experimental tests, and for the International Thermonuclear Experimental Reactor (ITER). The requirements are found to be reasonable.

Introduction

A number of authors have considered the role of scrape-off layer (SOL) currents in magneto-hydrodynamic stability [1] Most recently, Schmidt and Jardin [2] have considered using SOL currents as a means to provide n=0 position feedback control. Here we consider the use of non-axisymmetric, time-varying SOL currents to suppress the growth of resistive-wall modes and possibly resistive tearing instabilities, through the generation of time and space varying magnetic pressure. (*All units are SI unless otherwise noted.*)

Modes to be stabilized

The basic idea of this approach is to use non-axisymmetric currents in the SOL to inject helical flux into what would otherwise be considered, from an MHD point of view, the "vacuum region" surrounding the plasma. This helical flux would be phased in such a manner as to provide a restoring force on a growing instability. For the force to be maximum, it is advantageous if the injected helical flux is contained between the plasma edge and a conducting wall or vacuum vessel. Thus it is necessary that the mode to be stabilized rotate fast compared with the resistive penetration time of a relatively nearby conducting wall. This is generally the case even for unstable resistive wall modes, in a plasma rotating at a speed too far below the Alfvén velocity for stabilization by ion-acoustic effects. For the case of unstable resistive tearing modes, even modest plasma rotation makes wall penetration times and resistive island growth times long compared with rotation speeds. The technique discussed here could, in principle, be applied to tokamaks, spheromaks, RFP's, or even FRC's.

Configuration

The proposed configuration is a toroidally segmented divertor electrode on the outer side of a single-null plasma, or on the outer top or bottom of a double-null plasma. The divertor segments (4 segments to provide control for an n=1 instability at any phase, 8 segments for an

n=2, etc.) must be independently biasable. In the single-null configuration an unsegmented inner divertor could be solidly grounded, while in the double-null case the opposite outer divertor as well as the inner divertors would be unsegmented and grounded to the vacuum vessel, as illustrated in Fig. 1. (This electrical configuration could be achieved in the absence of divertors through use of appropriately located toroidal belt limiters.) By using the divertor segments as electrodes, one can inject helical flux into the crucial region between the outer edge of the plasma and the surrounding conducting wall. Resistive links or other special techniques might be required to control breakdown between adjacent electrodes, and to provide well-defined paths for halo currents during plasma disruptions. It is possible that the best location for the electrodes would be in a region somewhat removed from the highest heat flux on the divertor plate, in order to separate the functions of flux injection and power and particle removal.

It is interesting to note that the helical flux injection pattern which comes naturally with this technique is almost ideally shaped for control of external kinks, in that the helicity of the injected flux will match nearly exactly the dominant eigenmode of the kink. For the case of the resistive tearing mode, the poloidal mode structure will not match the instability precisely, but it may be desirable in any case to tailor the structure of the feedback fields by the inclusion of higher n and/or m components to constrain the island motion and thus minimize the "phase-flip" instability.

Current requirement

The requirement for feedback power depends in a complex way on sensing capabilities, the physics of the mode to be controlled, and the frequency response and phase stability of the feedback circuit. For present purposes we will characterize the required response capability in terms of $\delta B_\theta/B_\theta$. For practical estimates of required currents and voltages, we will assume $\delta B_\theta/B_\theta \sim 5\%$. Now we consider a single helical "stripe" of current, running from the biased divertor plate, along the field lines, to the grounded plate. This stripe has, by construction, radial width l_r, poloidal width l_θ, and parallel length $l_\parallel$. The radial width, l_r, we will consider to be a control variable, depending on the SOL width and the width of the electrodes employed, but much smaller than any of the other characteristic lengths of the system. For an instability of poloidal mode number m (~ nq) we can estimate $l_\theta \sim \pi a\sqrt{\kappa}/m$, and $l_\parallel \sim \pi Rq$. This allows us to estimate δI, the current in this stripe required to achieve the desired $\delta B_\theta/B_\theta$.

$B_\theta \sim \mu_0 I_p / (2\pi a\sqrt{\kappa})$ eq (1)

$\delta B_\theta \sim \mu_0 \delta I / (2 l_\theta)$ eq (2)

giving

$\delta I / I_p \sim \delta B_\theta/(mB_\theta) \sim 1\%$ eq (3)

For a moderate-scale present-day device, operating perhaps at 750 kA, this corresponds to a "stripe" current of about 7.5kA. For ITER operating at 21 MA, this corresponds to about 200 kA per stripe.

It is interesting to ask the question as to whether this current density can be provided by simple biasing of the divertor electrodes, or if some more complex form of current injection is required. The ion saturation current will limit simple current injection at sheath voltages of over a few times the local electron temperature. We estimate for a deuterium plasma

$$j_{sat} \sim 0.6\, n_e C_s \sim 10^{-15} n_e \sqrt{T_{ev}} \qquad \text{eq (4)}$$

where we take $T = T_i \sim T_e$. The current density in the injected "stripe" is estimated at

$$\delta I / (l_r\, l_\theta) \sim I_p\, (\delta B_\theta / B_\theta) / (l_r\, a\, \pi \sqrt{\kappa}) \qquad \text{eq (5)}$$

If for the present-day experiment we estimate l_r at 0.1m, and take $a \sim 0.4$m, $\kappa \sim 2$ we find a requirement on the plasma properties at the electrode of

$$n\sqrt{T_{ev}} \sim 2\ 10^{20} \qquad \text{eq(6)}$$

which can be achieved, for example, with a density of $6\ 10^{19}$ at the divertor plate and a temperature of 10 eV. A similar estimate for ITER, using $l_r \sim 0.2$ m gives a requirement on $n\sqrt{T_{ev}}$ of $5\ 10^{20}$, which is in the range of what is expected.

There is not a great deal of extra "room" in these estimates, however, and it may be desirable for a near-term experiment to include methods to enhance the emissivity of the electrodes. One possibility might be the use of the small 1 kA current injectors recently developed for use in the MST reversed-field pinch (Ref.). 20 such injectors distributed toroidally around the device, just outside the highest heat-flux region on the divertor, would provide adequate current injection capability.

Voltage Requirements

First we estimate the resistive voltage drop along the field. The parallel Spitzer resistivity in the SOL can be estimated at

$$\eta_\parallel \sim 1.7\ 10^{-3}\, (T_{ev})^{-3/2} \qquad \text{eq (7)}$$

assuming $Z_{eff} \sim 2$, giving a voltage drop of

$$V \sim 1.7\ 10^{-3}\, (T_{ev})^{-3/2}\, (\delta B_\theta / B_\theta)\, I_p\, R\, q / (l_r\, a \sqrt{\kappa}) \qquad \text{eq (8)}$$

If we assume the electron temperature in most of the SOL for a present-day experiment is about 30eV, this gives a very reasonable 45V for the resistive drop in the present-day case, and depending on the SOL electron temperature, similar or even lower for ITER. The RMS resistive power dissipation in the SOL, counting 2 "stripes", would be ~350 kW for the near-term experiment, and ~10 MW for ITER. A similar power dissipation would be expected in the sheath, for the case of simple plate biasing.

Next we estimate the inductance of a current stripe, from an estimate of the stored poloidal field energy.

$$(1/2)\, L\, (\delta I)^2 \sim (l_r\, l_\theta\, l_\parallel)\, (\delta B_\theta)^2 / 2\, \mu_0 \qquad \text{eq (9)}$$

$L \sim (l_r\, l_{||} / l_\theta)\, \mu_0 / 4 \sim (\mu_0\, m\, R\, q\, l_r / 4\, a \sqrt{\kappa})$ eq (10)

For present-day parameters this gives $L \sim 1.3\ 10^{-6}$ H; in ITER the inductance could be perhaps twice higher. If we wanted to limit the reactive power to be no greater than 2x the resistive power, this would limit the frequency range to about 4 kHz in a present-day device, and about 50 Hz in ITER. These frequency ranges are appropriate for stabilization of resistive-wall modes and tearing modes in these devices.

Conclusion

Modulated non-axisymmetric SOL currents could provide a reasonable "actuator" for feedback control of slowing-growing MHD modes in a near-term experiment and in the ITER device. These currents have the advantage of providing a nearly ideal field pattern for control of the external kink / resistive wall mode. The n-spectrum should be optimized to limit the phase-flip instability of the tearing mode. Current, voltage, and power requirements, as well as frequency range, are all reasonable both for present-day experiments and for ITER.

References

[1] See for example "Proceedings of the IAEA Technical Meeting on Tokamak Biasing," Montreal, Canada, 1992 (IAEA, Vienna, Austria, 1993) and references therein.

[2] Schmidt, J.A., and Jardin, S.C., Bull. Am. Phys. Soc. **41**, 1435 (1996)

[3] Fiksel, G. et al., Bull. Am. Phys. Soc. **41**, 1407 (1996)

Acknowledgement

This work was supported by DOE Contract No. DE-AC02-76-CHO-3073.

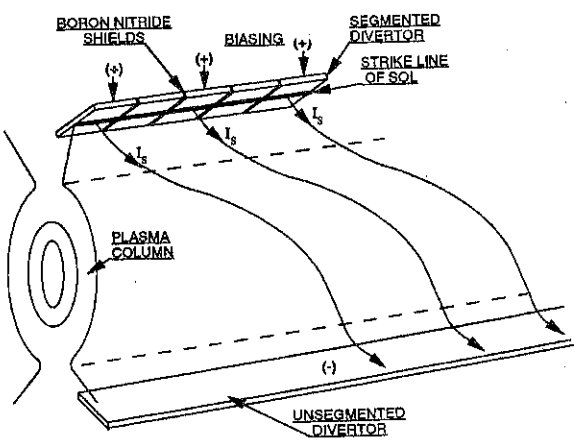

Fig. 1. Toroidally segmented divertor for feedback control of MHD modes.

Dynamics of Core Transport Barriers, Poloidal Flow, and the Radial Electric Field in TFTR Reverse Shear Plasmas

E.J. Synakowski, S.H. Batha,[a] R.E. Bell, F. Levinton,[a] E. Mazzucato, D. Newman,[b] M.G. Bell, R.V. Budny, C.E. Bush,[b] P.C. Efthimion, R.J. Fonck,[c] J.S. Kim,[c] B. LeBlanc, H. Park, A.T. Ramsey, G. Schmidt, S.D. Scott, G. Taylor, and M.C. Zarnstorff
Plasma Physics Laboratory, Princeton University, Princeton, NJ 08543, USA
[a] Fusion Physics and Technology, Torrance, California USA 90503.
[b] Oak Ridge National Laboratory, Oak Ridge, Tennessee USA 37830.
[c] University of Wisconsin, Madison, Wisconsin USA 53706

I. Introduction - The likely role of E×B shear in fluctuation suppression and transport barrier formation and relaxation in TFTR ERS plasmas has been described recently in the literature.[1,2,3] The strongest evidence comes from forced variations in the radial electric field E_r through the application of different torques with co- and counter-directed neutral beam injection in ERS plasmas. There, transport and core fluctuation levels increase when the local E×B shearing rate[4] is driven below a threshold value, but remain low when the shearing rate is above this threshold. Studies outlined here point to success in developing further understanding of the role of E_r in bifurcation phenomena. A one-dimensional transport/transition model[5] is used to examine core plasma and density fluctuation dynamics. Also, a signature of a possible trigger mechanism for ERS transitions has been identified with impurity poloidal rotation measurements made deep in the core of TFTR plasmas.

II. General Characteristics of Fluctuations at Bifurcations - Attention is paid to three basic characterisitcs of density fluctuation behavior. First, the fluctuations often exhibit a bursting character. Second, changes in the envelope of the fluctuation amplitude across a forward transition is rapid compared to the time scale for changes across a back transition. Third, during a back transition, fluctuations reappear at the outer boundary of the good confinement region before they reappear nearer the axis, suggesting that the degradation of the high confinement region begins at the boundary of this region and propagates inward.

A 1-dimensional model is used to examine these bifurcation dynamics. It consists of a time-dependent multimode transport model which is evolved in conjunction with calculations of the temporal and spatial evolution of the envelope of the fluctuation amplitudes. Importantly, E×B shear is included self-consistently. Resultant fluctuation and profile dynamics are the result of nonlinear interplay between instability growth and E×B shear suppression of the turbulence. The fluxes are evaluated self-consistently, with the calculated fluctuation levels serving as input in the transport model. The dominant instability is taken to be an ion drift-wave (η_i). The calculation uses of energy and particle source profiles evaluated with the TRANSP code for conditions similar to that of the plasmas of interest. The response of the particle and energy fluxes in the model to a given fluctuation amplitude is adjusted to reproduce the confinement characteristics of the pre-transition plasma.

The observed bursting character of the fluctuations and bifurcations to states of enhanced confinement and low fluctuation levels are anticipated in the calculations. The nonlinear quenching of fluctuations and the existence of bifurcations in the calculation hinge on a combination of a radially hollow instability drive, caused by shear reversal and peaked density profiles in the prelude, and a calculated centrally peaked beam deposition profile,

which increase pressure gradients in the region near q_{min} and nonlinearly increase the role of E×B shear through ∇p. Shown in Figure 1(b) is the calculated fluctuation amplitude at r/a = 0.25 for a reverse shear plasma with neutral beam heating power similar to that used in generating most TFTR ERS plasmas (25 MW). The bursting character of the fluctuations is the result of the nonlinear interplay between ∇p-dominated E×B shear and η_i drive. As neutral beam heating continues, the local heat flux reaches a critical value. At that point, the nonlinear dynamics between η_i drive and E×B shear suppression yield a sudden cessation of the bursting fluctuations. In the observations (Fig. 1(a)), residual fluctuations of unknown origin persist after the bifurcation; these may be related to the lack of suppression of energy flow through the electron channel. While the bursting character and bifurcation in the fluctuation behavior are reproduced in the calculation, the calculated value of the amplitude is smaller than the measured value. However, the amplitude itself is the least certain of the quantities calculated.

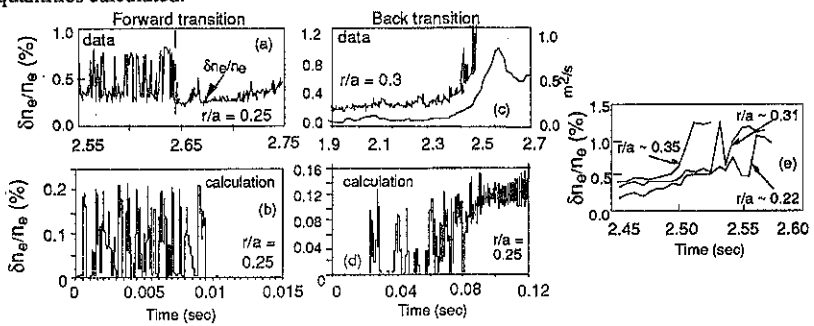

Figure 1. Measured and calculated density amplitude fluctuations. Measurements were made with reflectometry (Ref. 1). The minimum in the q profile is near r/a = 0.3 for these plasmas. (a) data, for forward transition. (b). calculation, forward transition. (c). data, back transition induced by co-injected torque. Also shown is the effective particle diffusivity D_{eff}, inferred from TRANSP. (d). calculation, back transition. The results have been smoothed over 1 ms. (e) data, back transtion, at three radii, on an expanded time scale.

The back transition was modeled by using a plasma that is already in a state of enhanced confinement, and choosing a toroidal velocity profile that reduced the E×B shearing rate to a level at which the bursting fluctuations began to occur. After the onset of the fluctuations, the pressure profiles and the E×B shearing rate were allowed to evolve self-consistently. The time scale for the return of the high fluctuation levels is of the same magnitude as that observed (Fig. 1(c,d)), and is significantly longer than that of the forward transition. In addition, the qualitative prediction[6] of the erosion of the high confinement region during a back transition from larger to smaller minor radii is seen in the reflectometry data, and is also reproduced by the calculation (Fig. 1(e)) The difference in time scales can be understood in terms of improved core confinement that is maintained by E×B shear. When ∇p dominates the determination of E_r and its gradient, E×B shear suppression during a forward transition leads to higher values of ∇p. This leads to even more effective shear suppression, resulting in a positive feedback cycle and a fast transition. For a back transition, however, loss of good confinement at the boundary of the high pressure core is impeded, not aided, by large values of ∇p. During a back transition, the receding boundary of the high

pressure core is constantly presented to the rapid transport region, yielding a high pressure gradient and shearing rate as long as there is still a reservoir of core energy to be tapped. The result is a comparatively slow fall of the shearing rate, and therefore a slower transition.

III. Measured poloidal rotation, and E_r at barrier formation and relaxation - A spectroscopic diagnostic has been designed and installed to measure the carbon poloidal rotation V_θ in the core and edge of TFTR plasmas. This high throughput system uses views that look both down and up across the path of a heating neutral beam in the core and in regions of the plasma towards the periphery without beam neutrals. This hybrid coverage will ultimately permit application of a novel inversion technique[7] for the determination of local carbon V_θ. The opposing views permit removal of the effect of the energy dependence of the excitation rate coefficient for the spectral line on the central wavelength.[8,9] .

Measurements of the chord-integrated V_θ reveal several striking features. ERS plasmas are usually, but not always, characerized by a large transient excursion of the carbon V_θ just prior to the change in confinement (Fig. 2). The rotation is opposite the ion diamagnetic drift direction, and can far exceed predictions from steady-state neoclassical theory. Pairs of reverse shear target plasmas exist between which q, n_e, T_i, T_e, carbon density, and V_ϕ profiles are, within error bars, identical. However, shortly after the start of high power heating at the same power levels, only one undergoes a V_θ excursion and transport bifurcation. The mechanism responsible for the excursion is a therefore likely to involve a highly nonlinear response to plasma conditions. In the dataset available, no excursions have been found in reverse shear plasmas without confinement transitions. Radial profiles of the chord-integrated V_θ indicate that the precursor activity is localized near the region that ultimately becomes the transport barrier region (Fig. 3), and emphasize how well localized the region of sheared V_θ is. This location is near the minimum in the q profile, as measured with the Motional Stark Effect diagnostic. Since this excursion precedes strong deviations in other plasma quantities, its change potentially represents the change in the plasma E_r at that location. In fact, preliminary MSE measurements of changes in E_r from the same plasma nearly parallel the temporal and spatial behavior of V_θ. The proof-of-principle of this technique has been demonstrated on a shot-to-shot basis,[10] and recent improvements in the system permit measurements of E_r in a single discharge. The similarity in the temporal behavior of V_θ and E_r suggests that the bifurcation in confinement may have as its origin a spontaneous generation of electric field that is accompanied by an increase in poloidal flow, rather than a spontaneous poloidal spinup to which the electric field responds. If the origin were some mechanism that acted primarily on V_θ itself, the response of E_r would yield a lag with respect to V_θ on the order of the ion-ion collision time (30-50 ms). The similarity of the changes in E_r and V_θ provides confidence that use of the carbon force balance equation is a reasonable means of inferring E_r in these plasmas. Although the cause of the excursions is not known, the fact that V_θ returns to pre-excursion values after the confinement transition indicates that ERS transitions are not caused by a neoclassical poloidal viscosity bifurcation.[11] However, it is consistent with a fluctuation-driven flow generation which is teminated by the ∇p-dominated suppression. Finally, measurements across a back transition indicate that the loss of ERS confinement precedes poloidal rotation changes, consistent with

the interpretation from Refs. 2 and 3 that the start of the confinement collapse is forced by a reduction of E_r and E×B shear by co-directed V_ϕ.

This work was supported by DoE Grant Nos. DE-AC02-76-CH03073 and DE-AC05-96OR22464.

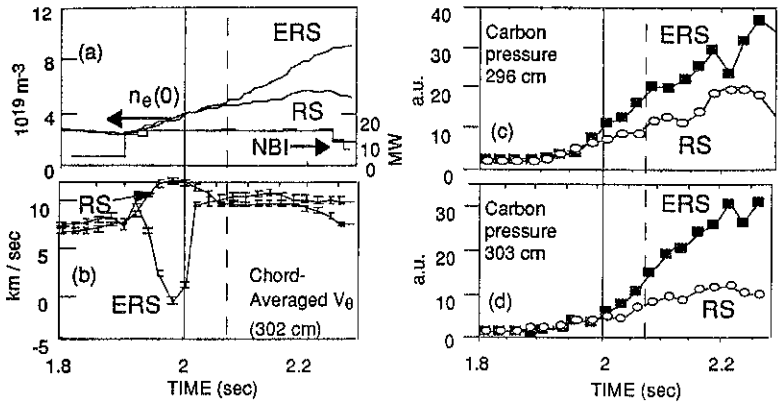

Figure 2. Time histories of various quantities in a pair of reverse shear plasmas, one with an ERS transition, and the other without. For both, B_T = 4.8 T T, and I_p = 1.6 MA. (a). the central electron density $n_e(0)$, and the neutral beam power. (b) the chord-averaged carbon poloidal rotation, at 303 cm, near q_{min}. (c). the carbon pressure, measured with CHERS. (d). same as (c), but at 303 cm.

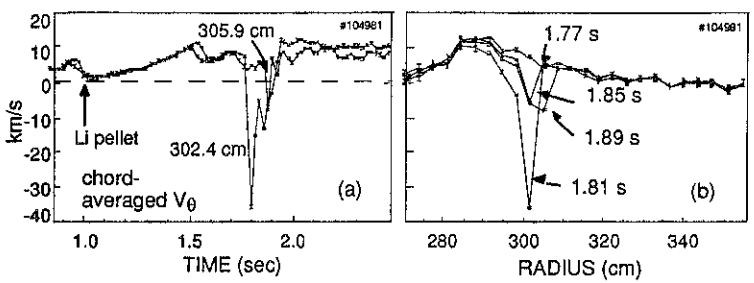

Figure 3. (a). Chord-averaged poloidal velocity for an ERS plasma with B_T = 3.4 T, I_p = 1.18 MA. (b). Radial profiles of the chord-averaged V_θ for the same plasma. The high power heating phase started at 1.7 s.

IV. References

[1] E. Mazzucato *et al.*, Phys. Rev. Lett. **77**, 3145 (1996).
[2] E.J. Synakowski *et al.*, Phys. Rev. Lett. **78**, 2972 (1997).
[3] E.J. Synakowski *et al.*, Phys. Plasmas **4**, 1736 (1997).
[4] T.S. Hahm and K. Burrell, Phys. Plasmas **2**, 1648 (1995).
[5] D. Newman *et al.*, ORNL report number ORNL/P-97/91373, submitted to Physics of Plasmas
[6] P.H. Diamond *et al.*, Phys. Rev. Lett. **78**, 1472 (1997).
[7] R.E. Bell, , Rev. Sci. Instr. **68**, 1273 (1997).
[8] R.B. Howell *et al.*, Rev. Sci. Instrum. **59**, 1521 (1988).
[9] M. von Hellermann *et al.*, Rev. Sci. Instrum. **61**, 3479 (1990).
[10] M.C. Zarnstorff *et al.*, Phys. Plasmas **4**, 1097 (1997).
[11] K. Shaing and E.C. Crume, Phys. Rev. Lett. **63**, 2369 (1989).

Alpha Particle Loss in TFTR Deuterium-Tritium Plasmas with Reversed Magnetic Shear

M. H. Redi, S. H. Batha, R. V. Budny, D. S. Darrow, F. M. Levinton, D. C. McCune, S. S. Medley, M. P. Petrov, E. Ruskov, S. von Goeler, R. B. White, M. C. Zarnstorff, S. J. Zweben and the TFTR Team
Princeton Plasma Physics Laboratory, Princeton University, Princeton, NJ 08543

1. Introduction

The confinement and loss of fusion alpha particles are examined for reversed magnetic shear plasmas in TFTR. Such plasmas, with high central q and non-monotonic q profiles can exhibit remarkably reduced energy and particle transport of the thermal ions. However, these same conditions are theoretically predicted to produce high levels of stochastic ripple loss of suprathermal particles, which may reduce the efficiency of plasma heating by the alpha particles and other heating schemes involving fast ions. This paper presents calculations of guiding-center code alpha particle orbit loss from deuterium-tritium (DT) simulations of TFTR deuterium-only experiments. They are compared to results of measurements made in DT reversed shear plasmas of both the confined alpha particle distribution and the alpha particles lost from the plasma. Large fast particle losses have also been found in reversed shear ITER simulations (up to 20%)[1,2] and from measurements of triton burnup in reversed shear experiments on JT-60U (12%)[3].

2. Guiding-Center Code Method

A new, fast, Hamiltonian-coordinate guiding center code, ORBIT[4], has been used for the simulations which makes use of a rapid accurate algorithm for the stochastic-free, confinement domain. Figure 1 shows the confinement domains for alpha particles in reversed and monotonic shear as a function of energy[5]. In the reversed shear plasma, the entire plasma is above threshold for stochastic ripple loss of trapped alpha particles at the birth energy, 3.5 MeV. All of the 33% trapped alphas are lost rapidly through unconfined orbit losses or stochastic ripple loss, as $q(r) \geq 2$ throughout the plasma. Pitch angle scattering of passing particles refills the trapped distribution and leads to continued alpha loss throughout the slowing down process.

In Table 1 are shown results for reversed shear plasmas with large major radius where toroidal magnetic field ripple is most significant. They are compared to those previously published[6] for similar experiments on TFTR but with a monotonic shear profile, at both high and low current. The predicted losses for reversed shear (~40%) are about twice the total alpha losses predicted for the high current plasma with a monotonic shear profile.

It is found that the simple renormalized Goldston, White, Boozer[7] ripple loss model[8] used in the TRANSP code for TFTR leads to alpha ripple losses in agreement with the guiding center code simulations for both the reversed shear and monotonic shear cases. The simulations show that transport due to TF ripple, for both monotonic and reversed shear q profiles, lies primarily within $r/a = 0.5$. Ripple loss is not greatest at the plasma edge, nor is there enhanced ripple broadening of the alpha profile toward minimum q in the reversed shear region. Including radially-varying collision rates or increased alpha profile peakedness does not significantly change the predicted losses. Strong synergism between collisions and ripple transport, predicted for high current, monotonic shear plasmas, is not found in reversed shear because of high first orbit loss and strong collisionless ripple diffusion.

3. Comparison with Confined Alpha Particle Data

ORBIT was used to model the observations of the pellet charge exchange diagnostic (PCX)[9]. Alpha particles with initial profiles consistent with Abel-inverted neutron profiles measured on TFTR were followed for τ_s and $2\tau_s$ in monotonic and reversed shear magnetic geometries. Because the PCX diagnostic has an observation window which detects only very deeply trapped alphas with pitch $v_{//}/v = -0.05$ at the midplane ($\theta = 0$), it was necessary to follow

a very large initial ensemble of alpha particles to obtain adequate statistics within a window of constrained pitch and poloidal angle to model the diagnostic. For simulations of PCX in monotonic shear plasmas an initial ensemble of 50,000 alphas was sufficient (as compared to 256 alphas for global estimates of alpha loss rates which takes ~4 hours Cray C90 cpu time). In reversed shear on TFTR, however, because only passing, neo-natal alphas pitch-angle scattered into trapped orbits can be seen by PCX, it was necessary to simulate ~2,000,000 alpha particles to obtain adequate statistics of ~400 alphas, within the simulated PCX window having $v_{//}/v = -0.15$ to +.05 and $|\theta| \leq 0.1$. Time dependence of the initial distributions was not modelled.

To minimize computational run time, ORBIT used the new stochastic loss algorithm and accelerated collision rates, ν_{PA} and ν_S. This method of speeding up the loss calculations gives good global loss estimates even for reversed shear equilibria. Use of conservation laws for ion energy and magnetic moment were also used to project the final orbits to $\theta = 0$ to further improve statistics. Without the rapid calculation features of the new code the simulations would not have been possible and even so are just at the edge of present computational resources.

In Figure 2 the simulated profiles are compared to PCX analysed data for monotonic and reversed shear plasmas. In monotonic shear, at one slowing down time (1.3 MeV) and at two slowing down times (0.5 MeV) the profiles are similar to those observed with PCX. The simulated profile at 0.5 MeV extends over a larger region in r/a as expected from the larger stochastic free region at lower energy.

In reversed shear two features of the PCX analysed data are distinctly different from the monotonic shear case: 1) a flat or hollow distribution at 1.71 MeV, which appears to be filled as the energy of observed alphas decreases to 1.3 MeV and 0.5 MeV; 2) a very steep profile at 0.5 MeV. The model predicts the general characteristics of alpha loss in reversed shear which clarify how a hollow profile could arise. In reversed shear no trapped alphas would be observed at 3.5 MeV, while at lower energies a peaked, flat or hollow profile can result depending on pitch angle scattering and the passing alpha distribution. The simulated profiles for reversed shear were obtained with a pitch angle scattering rate twice that of the experiment for which data is presented. 50,000 particle simulations with various collision rates indicate that agreement with PCX would be achieved with a reduction in ν_{PA}. At 0.5 MeV, ORBIT results are in good agreement with the data, showing a steep profile obtained after $2\tau_S$.

4. Lost Alpha Particle Data

Measurements of alpha loss 90 degrees below the midplane during Ip=1.6 MA RS/ERS discharges showed an alpha loss per DT neutron to be about three times larger than during standard 1.6 MA DT supershots, roughly consistent with the expected increase in first orbit loss at the vessel bottom due to the higher q(r) near the center. Measurements of alpha ripple loss to the outer midplane could not be made due to the large minor radius of the RS/ERS plasmas and the shadowing effect of the outer limiters.

5. Neutral Beam Ion Ripple Loss in Reversed Shear

DT enhanced reversed shear plasmas exhibit neutron levels a factor of 2-3 lower than expected from extrapolation of the neutron emission from DD plasmas with similar confinement. The effects of ripple diffusion of neutral beam ions and the Maxwellian tail of thermal ions on the neutron rate are being investigated. Preliminary guiding-center code simulations predict losses for tritium beams to be about the same as for deuterium beams at the same energy and pitch angle, although higher triton loss rates are expected from the reduced stochastic threshold (20% lower due to the higher Larmor radius). The TRANSP ripple loss model is being upgraded to make use of the new confinement domain algorithm and may account satisfactorily for low DT reversed shear neutron emission. The present GWB ripple loss model predicts ~20% loss of D or T beams for R=2.6m TFTR supershots[8] and in reversed shear. TRANSP simulations adjusted to match the neutron emission are found to have reduced tritium neutral beam ion heating corresponding to 20-30% additional tritium loss. TRANSP has been used to see if anomalous impurity accumulation to deplete reacting D and T ions

would reduce predicted neutron emission while retaining good confinement and agreement with measurements of the perpendicular stored energy. Simulations of RS plasmas into which short tritium beam pulses are injected show that the uncertainties in recycling and Z_{eff} are not sufficient to account for the DD/DT neutron discrepancy[10].

6. Conclusion

Simulations with a Hamiltonian coordinate guiding-center code of a reversed shear plasma in TFTR predict that alpha particle losses are near 40%, about double the total alpha losses from a comparable plasma with a monotonic shear profile[5]. In the reversed shear case, the entire plasma is above threshold for stochastic loss of trapped alpha particles at birth energy. Pitch angle scattering of passing particles refills the trapped distribution and leads to continued alpha loss throughout the slowing down process.

The simulations are in qualitative agreement with PCX confined alpha profile data for monotonic shear. In reversed shear at low energy, the ripple loss modelling and pitch angle scattering rates from DT simulations give profiles roughly consistent with PCX. At high energy agreement is less good. The simulations were based on a TFTR experiment having a pitch angle scattering rate twice that of the plasma in which the PCX data was taken. Predictions for this profile are most sensitive to the pitch angle scattering rate because of the loss of birth energy trapped alphas.

Qualitative agreement of ORBIT simulations with measurements of confined alpha profiles and alpha loss data gives confidence in the simulation method for predicting the global losses of TFTR and ITER (3-19% for some reversed shear configurations). Guiding center code simulations of neutral beam ion ripple loss and TRANSP analysis of the effects on the DT neutron emission in reversed shear are also needed. The discovery of reversed shear plasma configurations with dramatically improved transport holds promise for future applications of controlled fusion. The high losses predicted for TFTR and ITER reversed shear scenarios support new constraints on the allowed TF ripple for such reactors. The exploitation of reversed shear equilibria for reactor design will require minimal magnetic field ripple and impurity levels to reduce collisional ripple loss and to optimize alpha particle confinement and heating.

Acknowledgment

We are grateful to R. J. Hawryluk, W. M. Nevins and R. J. Goldston for their interest and encouragement. This research was supported by the U. S. Department of Energy Contract No. DE-AC02-76-CHO-3073.

* Supported by the US Dept. of Energy Contract DE-AC02-76CH03073.

[1] M. H. Redi, *et al.*, EPS, Kiev, Ukraine (1996).
[2] S. Konovalov, ITER Phys. Report, 1996.
[3] K. Tobita, *et al.*, IAEA-CN-64/A5-6, Montreal (1996).
[4] R. B. White, *et al.*, Phys. Plas. **3**, 3043 (1996).
[5] M. H. Redi, *et al.*, "Calculations of Alpha Particle Loss from Reversed Magnetic Shear in the Tokamak Fusion Test Reactor", PPPL 3239, Princeton, NJ (1997).
[6] M. H. Redi, *et al.*, Nuclear Fusion **35**, 1191 (1995).
[7] R. J. Goldston, *et al*, Phys. Rev. Lett. **47** 647 (1981).
[8] M. H. Redi, *et al.*, Nuclear Fusion **35**, 1509 (1995).
[9] R. A. Fisher, *et al*, Phys. Rev. Lett. **75** 846 (1995).
[10] E.Ruskov,*et al.*, 5th IAEA TCM on Alpha-particles in Fusion Research, JET, UK (1997).

Table 1. Guiding Center Code Alpha Losses (%) for R=2.6m TFTR Cases

	Reversed Shear (1.6 MA)	Monotonic Shear (1.8 MA)	Monotonic Shear (0.9 MA)
First Orbit	18	6	21
Delayed Particle Loss	22	17	13
Total Particle Loss	40	23	34
Total Energy Loss	38	19	32

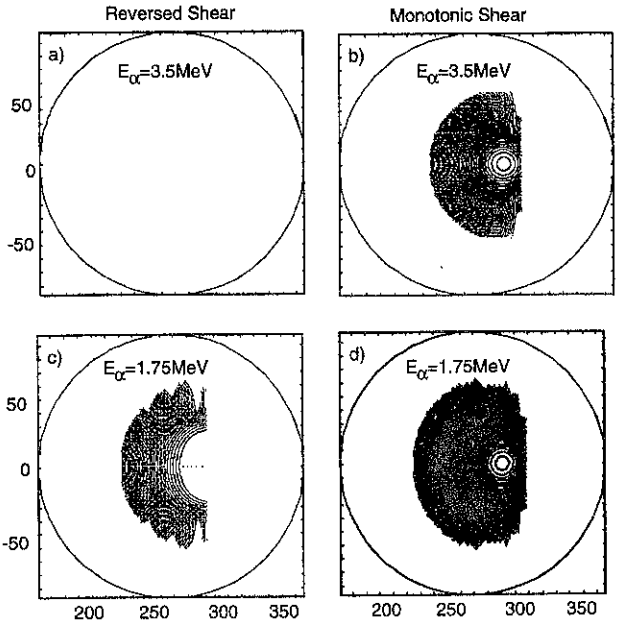

Figure 1. Confinement region for alpha particles in reversed shear (1a,1c) and monotonic shear (1b,1d) as a function of alpha energy.

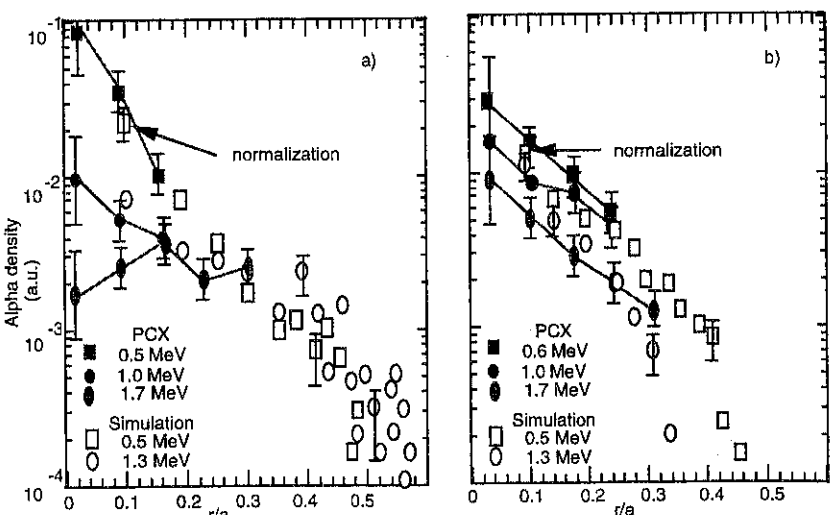

Figure 2. Analysed data from pellet charge exchange diagnostic and simulated profiles for reversed shear (2a) and monotonic (2b) plasmas as a function of alpha energy.

Experiments with Ion Bernstein Waves on TFTR

G. Schilling, R. E. Bell, S. Bernabei, C. E. Bush,* R. Cesario,**
D. A. D'Ippolito,*** G. R. Hanson,* K. W. Hill, J. C. Hosea, T. Intrator,****
B. P. LeBlanc, R. Majeski, J. R. Myra,*** R. Nazikian, M. Ono, C. K. Phillips,
J. H. Rogers, J. R. Wilson, and the TFTR Group

Princeton University Plasma Physics Laboratory, Princeton, New Jersey, USA
* Oak Ridge National Laboratory, Oak Ridge, Tennessee, USA
**Associazone EURATOM-ENEA Frascati, Italy
***Lodestar Research Corporation, Boulder, Colorado, USA
**** University of Wisconsin - Madison, Wisconsin, USA

INTRODUCTION

The control of plasma pressure and magnetic shear profiles has become increasingly important in the light of the theoretical and observed stability and transport advantages of certain profiles.[1-4] The recent phase of RF experiments in TFTR has focused on plasma heating and current drive, with the ultimate objective of internal transport barrier generation, using both directly launched and mode-converted ion Bernstein waves. The Ion Bernstein wave (IBW) possesses properties that make it attractive for heating large, hot dense plasmas.[5] A new four-strap direct launch IBW antenna was installed to investigate the coupling and localized heating characteristics in the NB heated Supershot regime and the possibility of forming a velocity shear driven transport barrier. Two of the two-strap fast wave antennas have now been replaced by four-strap versions to give better launched wave directivity and improved power handling capability for mode-converted IBW experiments.

IBW DIRECT LAUNCH TRANSPORT BARRIER

Biglari et al. [1] have suggested that externally driven ion Bernstein waves can create a large gradient in local ion motion in the wave damping region, leading to sheared plasma flow through the Reynolds stress tensor. If the flow shear is large enough, inherent fluctuations are strongly decorrelated, large amplitude growth is suppressed, and that part of transport attributable to the fluctuations is reduced. Experiments on PBX-M have demonstrated plasma core profile and transport modification through the application of direct launch IBW power,

leading to the formation of an internal transport barrier and a Core High confinement (CH) mode.[2] Theoretical estimates indicate that 1-2 MW of IBW power should suffice to form a similar barrier on TFTR.

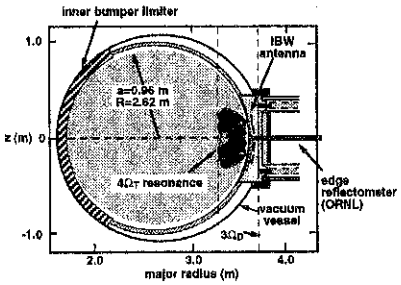

FIGURE 1. TFTR IBW launch configuration

The IBW launch and damping configuration is shown in Figure 1, left. The wave is launched from the low field side of the plasma and damps on the selected ion resonance. Two IBW direct launch scenarios have been attempted. The electron plasma wave launch, EPW, is consistent with localized ion heating on the low field side of the plasma (desired for CH mode), but is very sensitive to the edge density profile. The cold electrostatic ion cyclotron wave launch, CESICW, is less sensitive to the edge density profile due to greater power flux at the edge. [6]

A new poloidal rotation diagnostic [7] provides measurements of carbon poloidal velocity in the core plasma. A chord-averaged profile showing the change in the profile upon application of IBW power is shown in Figure 2. The change in poloidal velocity with and without IBW for two chords in Figure 3 shows the development of shear. The location of the induced shear is consistent with the IBW damping location calculated from ray tracing. The EPW launch was used for these shots, with the $3\Omega_D$ resonance at 280 cm.

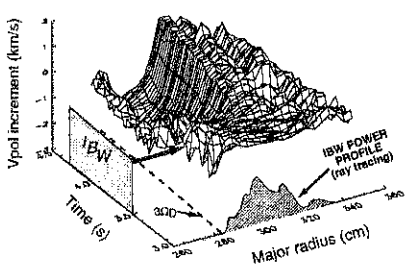

FIGURE 2. Incremental chord-averaged carbon poloidal velocity profile resulting from IBW.

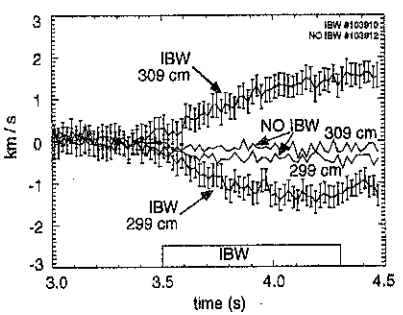

FIGURE 3. Change in carbon poloidal velocity at two different radial locations.

Within the error of temperature data for these shots, the observed velocity shear cannot be accounted for by local changes in T_i or T_e. A quantitative assessment of this shear flow and its potential for internal transport barrier formation is in progress.

We could only couple 10-40% of the rf power to the plasma core [8]; antenna power up to 1.7 MW was launched, but no more than 0.35 MW could ever be accounted for in the core. This was insufficient to form an internal transport barrier and the CH mode. Coupling was higher for $(0,0,\pi,\pi)$ antenna current phasing than for (0,0,0,0). [9] The edge density profile, as determined by the ORNL edge reflectometer, was consistent with that which was expected to provide good coupling. RF probes only sporadically measured a weak indication of parametric decay instability; they also determined that their received signal was not localized toroidally. Core microwave reflectometry at the RF fundamental detected occasional signals on the high field side of the plasma, when core ion resonances were expected to damp the waves. During CESICW launch, when the only ion resonance was on the high field side (^{3}He minority at 254 cm), core reflectometry measured the wave throughout the plasma core. Although some of the power may have been dissipated in sheaths in front of the antenna (D. A. D'Ippolito, this conference), no thermal heating was observed in the outboard limiter closest to the IBW antenna. All these measurements suggest that coupling to surface waves may have been the chief reason for our poor core performance.

MODE CONVERSION OF FAST WAVE TO IBW

As can be seen from the plot of the D-T dispersion relation, Figure 4 , strong mode conversion electron heating requires both that no ion cyclotron resonance exists between the D and T cyclotron layers and that there exists no Doppler broadening (i.e. low T_i) of ion resonances into the MC layer. Strong ion absorption is expected if an ion minority is present or T_i is high.

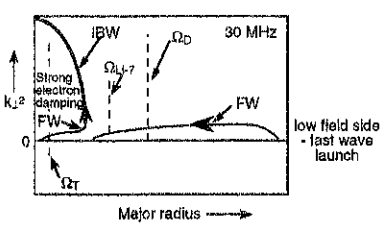

FIGURE 4. Mode conversion of the fast wave to the IBW.

During initial tests of D-T mode conversion in 1996, ^{7}Li minority absorption was believed to dominate. Natural Li metal (~93% ^{7}Li) had been used heavily for wall conditioning, and this was subsequently replaced by metal isotopically enriched to 95% ^{6}Li. With the practical

elimination of this intermediate absorbing minority, the fast wave can now propagate to the mode-conversion zone, where it either damps locally on electrons or the Doppler broadened T cyclotron resonance. Those experiments relying on Be metal as a plasma facing component will run into this same problem, with no isotopic solution since Be is 100% ^{9}Be.

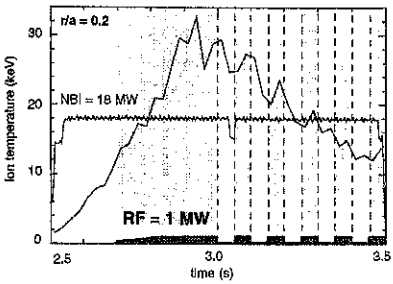

FIGURE 5. D-T mode conversion ion heating

Efficient ion heating was observed in high performance Supershots with T_i ~ 30 keV (large Doppler broadening), Figure 5, left. Efficient electron heating and current drive had been observed earlier in D-^{3}He-^{4}He MC experiments, and electron heating was regained in the present D-T experiments by lowering T_i through deliberate confinement reduction. Numerical modeling using the codes FELICE (M. Brambilla) and METS95 (D. Smithe) show 75% of the wave power damping on ions for this Supershot (T_i = 30 keV + 25% tritium beam ions, T_e = 8 keV, B_0 = 5.1 T, $n_e(0) = 4.5 \cdot 10^{19}$ m^{-3}).

REFERENCES

[1] H. Biglari, M. Ono. P. H. Diamond, and G. G. Craddock, in *Proceedings of the Ninth Topical Conference on Radio Frequency Power in Plasmas,* Charleston, SC 1991, 376-380

[2] B. LeBlanc, et al., Phys. Plasmas **2** (3), March 1995, 741-751

[3] F. M. Levinton et al., Phys. Rev. Lett. **75**, 4417 (1995)

[4] T. S. Hahm and K. H. Burrell, Phys. Plasma **2** (5), May 1995, 1648-1651

[5] M. Ono, Phys. Fluids B **5** (2), February 1993, 241-280.

[6] M. Ono, et al., to be published in *Proceedings of the Twelfth Topical Conference on Radio Frequency Power in Plasmas, Savannah, GA, April 1-3, 1997*

[7] R. E. Bell, L. E. Dudek, B. Grek, D. W. Johnson, R. W. Palladino, A. T. Ramsey, Bulletin of the American Physical Society Vol. 41, No. 7 (1996), 1378

[8] J. H. Rogers, et al., to be published in *Proceedings of the Twelfth Topical Conference on Radio Frequency Power in Plasmas, Savannah, GA, April 1-3, 1997*

[9] J. C. Hosea, et al., to be published in *Proceedings of the Twelfth Topical Conference on Radio Frequency Power in Plasmas, Savannah, GA, April 1-3, 1997*

ACKNOWLEDGMENT: Work supported by U. S. DoE contract DE-AC02-76-CH0-3073

Analysis of Radio-Frequency Sheath Interactions in TFTR

D. A. D'Ippolito and J. R. Myra
Lodestar Research Corporation, Boulder, Colorado

J. H. Rogers, K. W. Hill, J. C. Hosea, R. Majeski, G. Schilling and J. R. Wilson
Princeton Plasma Physics Laboratory, Princeton, New Jersey

G. R. Hanson, A. C. England, and J. B. Wilgen
Oak Ridge National Laboratory, Oak Ridge, Tennessee

1. Introduction

New theoretical and experimental tools are applied to the analysis of ICRF antenna-edge plasma interactions on the TFTR tokamak. New theoretical advances include development of the ANSAT (ANtenna Sheath Analysis Tool) numerical code[1] for computing the rf sheath voltage distribution for realistic antennas, and a new SOL transport model including the effects of diffusion, rf-induced $\mathbf{E} \times \mathbf{B}$ convection, and particle losses to the antenna. A novel feature of the experimental work is the use of a microwave reflectometer to measure the density profile in front of the TFTR Bay-K antenna [2]; the reflectometer viewed the plasma through a diagnostic port in the geometric center of the Faraday screen (FS), allowing a precise comparison of measured and predicted density profiles. Here we show that the measured density depression at the antenna during the rf pulse, and the measured FS-impurity (titanium) concentration in the core plasma in π phasing, are in reasonable agreement with predictions of rf antenna sheath models. The impurity influx in $\pm\pi/2$ phasing is due to a combination of the local antenna source and a non-local secondary source which grows in importance as Ti atoms are deposited on the limiters. A full discussion of this work will be presented elsewhere [3]. In this paper, we discuss two important results of this study:

(1) rf sheath-induced $\mathbf{E} \times \mathbf{B}$ convection *decreases* the density but *increases* the perpendicular plasma outflux in the vicinity of the antenna;

(2) the Ti impurity concentration on TFTR is due to a combination of a local antenna source with weak phasing dependence and a non-local source with a strong dependence on the antenna phasing and the limiter condition.

2. Convective Cell Analysis

It is often observed that the plasma density near the antenna decreases during the rf pulse, even when the density rises farther from the antenna. The reduced density is sometimes attributed to ponderomotive density expulsion, but this effect is negligible for TFTR parameters (at 1 MW, a typical $E_\parallel$ of 30 V/cm produces a ponderomotive potential of only 5 V). By contrast, sheath-driven convection [4-6] is a strong effect for TFTR antenna parameters. The spatial variation of the rectified sheath potential $\phi(x,y)$ drives rapid $\mathbf{E} \times \mathbf{B}$ convection near the antenna [4], where x,y denote the radial and poloidal directions. The convective cell (CC) eddy size is determined by the poloidal ripple of the rf $E_\parallel$ field (due to the FS-antenna box structure) and by its radial decay length. ANSAT calculations of $\phi(x,y)$ for the Bay-M antenna [1] showed that there are two radial regions of CCs: a layer of closed CCs centered on the surface tangent to the FS protection limiter, and a region of open CCs which sweep particles rapidly into the FS on a timescale of the eddy time τ_c. The closed CCs

flatten the density profile and the open CCs increase the particle loss rate. The antenna structure itself acts as a particle sink, and the rf convection depletes the density when the eddy time is shorter than the parallel flow time, $\tau_c < \tau_\parallel$ [5]. For TFTR parameters, this inequality is typically satisfied during high-power operation. The region of density depletion is comparable to the eddy size, which is dependent on rf power P_{rf} and antenna phasing (see below). All of these features agree qualitatively with the density profiles measured by the reflectometer.

For quantitative comparison, a "two-sheet" fluid model [6] was developed to solve the particle continuity equation including diffusion, flow in both directions around the CC ($\pm v_x$), particle sources, and the particle sink at the FS. This model has been applied to analyze the measured density profiles for a series of shots comparing 0 and π phasings at different values of P_{rf} [3]. For each shot, the particle source (ionization profile) is chosen to give good agreement with the ohmic density profile and is then assumed to be the same during the rf pulse. Bohm diffusion and the convective velocity profile, $v_x(x) = v_a \exp[(x - x_{FS})/L_{rf}]$, are assumed and x_{FS} denotes the radial location of the surface tangent to the FS . (The radial positions x are defined at the toroidal location corresponding to the center of the antenna.) The values of v_a and L_{rf} giving the best fit of the model to the measured density profile during the rf pulse are determined for each shot. The best-fit values of v_a and L_{rf} agree reasonably well with those calculated from rf sheath theory by the ANSAT code, indicating the self-consistency of the model. A comparison of the experimental and CC model profiles is shown in Fig. 1 for shot 84102 (0 phasing, P_{rf} = 0.5 MW). Note that the theory gives a good fit to the data for reasonable values of the parameters. The CC model reproduces the general features of a linear decay near the rf limiter at x_{RF} = 359.5 cm, depleted density in front of the antenna, and a flattened profile in the FS region ($x > x_{FS}$ = 360.7 cm). For this shot the density depletion region extends out to the rf limiter, but the size of this region is parameter dependent. The observed depletion is stronger for 0 phasing than for π phasing and increases with rf power [2,5]. The good agreement between the model and the data for this series of shots suggests that the rf power and phasing dependences are explained by the scaling of the convective velocity, $v_x \approx (c/B)(\phi/L_y)$, where $L_y^{-1} = \phi^{-1}\, d\phi(y)/dy$; the rectified sheath potential is phasing dependent and scales as $\phi \propto (P_{rf})^{0.5}$ [4].

The radial plasma flux to the antenna Γ_x can be computed from the CC model. We define $\Gamma_{oh} = \Gamma_x(x_{FS})$ and $\Gamma_{rf} = \Gamma_x(x_{FS})$ for the ohmic and rf density profiles, respectively, and plot the ratio Γ_{rf}/Γ_{oh} vs P_{rf} in Fig. 2. The curves are the theoretical predictions using the CC parameters from the ANSAT sheath analysis, and the data points are the values inferred by a least-squares fit of the CC model to the measured profiles. The closed circles and solid line denote π phasing, the open circles and large-dashed line denote 0 phasing, and the small-dashed line corresponds to 0 phasing with twice the ANSAT sheath voltage to indicate the range of uncertainty in the theory. There is good agreement between the first-principles sheath model and the data fit, suggesting that the CC model gives a good estimate of the plasma flux. We conclude from Fig. 2 that the flux Γ_x is *enhanced* by the rapid convection during the rf pulse ($\Gamma_{rf}/\Gamma_{oh} > 1$) despite the observed density depletion at the antenna. The result is an increased interaction with the antenna, which is consistent with the observation of increased impurity production during the rf pulse, as discussed in Sec. 3.

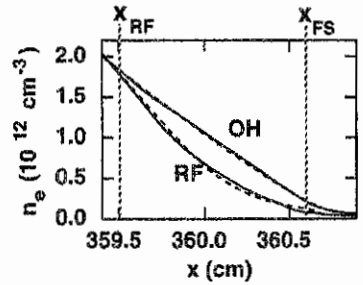

Figure 1. Best fit of the CC model (dashed lines) to the measured density profile (solid lines) during the ohmic phase and rf pulse for shot 84102 (0 phasing, 0.5 MW ICRF power).

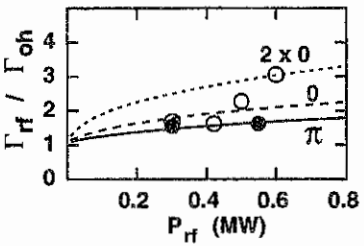

Figure 2. The rf enhancement of the radial plasma flux to the antenna vs rf power in MW for 0 and π phasing. (See text for explanation of symbols.)

3. Impurity Influx Analysis

On TFTR the only source of titanium impurities is the TiC-coated FS. The formation of rf sheaths on the antenna provides a mechanism for ion acceleration to keV energies and for rf-enhanced sputtering. The Ti influx is observed to increase by a large factor (> 40 for P_{rf} = 4 MW) when the antennas are powered. Most of the sputtered Ti atoms (90 - 95%) are screened by ionization in the SOL and are redeposited on the poloidal limiters and inner wall of TFTR, which then provide a secondary source of sputtered Ti. An analysis of the total Ti concentration in the plasma core for a series of consecutive shots in π and ±π/2 phasing and a comparison with rf-impurity models indicates that the Ti concentration in π phasing is due to the direct influx from the FS, whereas in π/2 phasing the secondary source is important and grows larger as the limiter contamination increases.

The core Ti concentration due to the direct influx from the FS, $f_{Ti}(FS)$, has been modeled using (i) the ANSAT code to calculate the average energy $E = Ze\langle\phi\rangle$ of particles striking the FS, and (ii) the measured density profiles to determine the impurity screening factor and the plasma flux to the screen (employing the CC analysis of Sec. 2). Thus, $f_{Ti}(FS) = T\,\Phi_{FS}\,\tau_p/(\langle n_e\rangle\, V_p)$, where $\tau_p \approx 0.25$ s is the measured impurity confinement time, V_p and $\langle n_e\rangle$ are the core plasma volume and average density, T is the "transmission coefficient" for Ti atoms to stream across the SOL without being ionized, $T = \exp[-\mu \int dx\, n_e(x)]$ with $\mu = \langle\sigma v\rangle/v_0$ (assumed constant), $\Phi_{FS}(\text{atoms s}^{-1}) = N_A \Gamma_\perp A_\perp Y(E)$ is the local influx of Ti atoms from the Faraday screens of all N_A antennas, $A_\perp = L_y L_z$ is the antenna area normal to the plasma outflux, and Y(E) is the sputtering yield per ion incident with energy E. The details of this modeling will be given elsewhere [3].

In Fig. 3, we plot $f_{Ti} = n_{Ti}/n_e$ vs $f_{Ti}(FS)$, where f_{Ti} is the total Ti concentration inferred from soft X-ray spectroscopy and $f_{Ti}(FS)$ is the theoretical prediction for the direct Ti influx, for selected shots in ^{3}He-^{4}He-D plasmas from the TFTR mode conversion current drive campaign. These shots were selected to compare different phasings [π (solid circles), +π/2 (open squares), and −π/2 (filled squares)] at comparable rf power for $P_{rf} \approx 3$ MW and 4 MW. The solid line denotes agreement between the direct influx theory and the experiment. The dotted lines indicate the time sequence of the shots; the 4 MW (3 MW) group began (ended) with the π-phasing shot. Note that in π phasing the Ti concentration is dominated by the direct influx, whereas in π/2 phasing at 4 MW the direct influx is a small fraction of the total,

indicating that the secondary influx from the limiters is important. The magnitude of the secondary influx is larger at high rf power and grows larger on later shots, presumably because of Ti accumulation on the limiters.

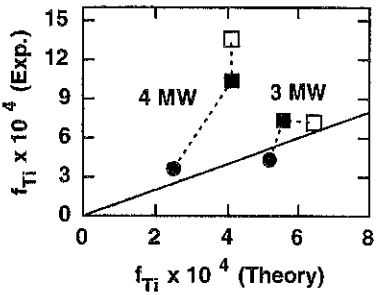

Figure 3. Comparison of the experimentally inferred Ti concentration with the theoretically predicted concentration due to the direct influx from the FS.

The most likely source of the observed phasing dependence is the $k_\parallel$-dependence of the fast wave propagation. There is significantly more power below $k_\parallel$ = 2-4 m^{-1} in $\pi/2$ phasing than in π phasing, and there are two effects associated with this low-$k_\parallel$ part of the spectrum: (i) the right-hand FW cut-off surfaces approach the plasma edge [7], allowing tunneling of the FW fields and interaction with the nearby walls and limiters, and (ii) global surface or coaxial modes are induced in the plasma edge and SOL. In both cases the interaction with the limiter may induce an $E_\parallel$ component, and a substantial "far-field" sheath voltage, $V = \int ds\, E_\parallel$, can be generated [8,9] leading to rf-induced impurity generation associated with the low-$k_\parallel$ part of the spectrum. This process may explain the phasing dependence observed in Fig. 3. The importance of low-$k_\parallel$ waves in achieving fast wave current drive suggests that more work is needed to understand and model far-field sheaths, surface waves, and other far-field rf processes.

Acknowledgements

This work was supported by the U.S. Department of Energy under Contract Nos. DE-FG03-93-ER54212, DE-FG02-97ER54392, DE-AC02-76-CH03073, and DE-AC05-84-OR21400.

References

1. J. R. Myra, D. A. D'Ippolito, and Y. L. Ho, Fusion Eng. Design **31**, 291 (1996).
2. G. R. Hanson, A. C. England, J.B. Wilgen, et al., *Eleventh Topical Conference on Radio Frequency Power in Plasmas*, AIP Conf. Proc. 355, 1995, p. 463.
3. D. A. D'Ippolito, J. R. Myra, J. H. Rogers, et al., manuscript in preparation.
4. D. A. D'Ippolito, J. R. Myra, J. Jacquinot, and M. Bures, Phys. Fluids B **5**, 3603 (1993).
5. D. A. D'Ippolito, J. R. Myra, A. C. England, et al., *Eleventh Topical Conference on Radio Frequency Power in Plasmas*, AIP Conf. Proc. 355, 1995, p. 467.
6. J. R. Myra and D. A. D'Ippolito, Phys. Plasmas **3**, 699 (1996).
7. R. Majeski, C. K. Phillips, and J. R. Wilson, Phys. Rev. Lett. **73**, 2204 (1994).
8. J. R. Myra, D. A. D'Ippolito, and M. Bures, Phys. Plasmas **1**, 2890 (1994).
9. P. E. Moroz, J. R. Myra, and D. A. D'Ippolito, *Twelfth Topical Conference on Radio Frequency Power in Plasmas*, Savannah, GA, 1997.

TRANSPORT MODEL TESTING AND COMPARISONS USING THE ITER AND DIII–D PROFILE DATABASE*

J.E. Kinsey,† R.E. Waltz, and D.P. Schissel
General Atomics, P.O. Box 85608, San Diego, California 92186-5608 USA

A fast steady-state transport code is used to test and compare several theory-based transport models including the IFS/PPPL, GLF23, Multimode, and Itoh-Itoh-Fukuyama (IIF) models. Statistics for both local and global quantities as a ratio of model to experiment are computed to assess the performance of each model against a profile database comprised of more than 50 L– and H–mode discharges. These discharges, which include parameter scans in gyroradius, collisionality, beta, plasma current, density, and power, have been obtained from the DIII–D and ITER profile databases.

I. OBJECTIVE TESTING OF TRANSPORT MODELS

In this paper we assess the performance of several theory-based transport models by comparing the predictions for the temperature profiles against experimental data from DIII–D, TFTR, and JET using the MLT transport code. We use an experimental database comprised of nearly 50 L– and H–mode discharges from the ITER and DIII–D profile databases [1]. All the models are treated equally within a single transport code using the same methodology and figures of merit to quantify the level of agreement with both global and local quantities. Using the experimental density profiles and analyzed sources, the boundary conditions are set at $\rho/a = 0.90$ for all simulations. Here, no consideration is made to test the models against data from Ohmic discharges or from plasmas in advanced operating regimes (e.g. supershots, VH–mode, reversed shear).

Included in the study are the IFS/PPPL model [2] and the more comprehensive GLF23 model [3] which are based upon gyrofluid simulations of the toroidal ion temperature gradient (ITG) mode in a three-dimensional nonlinear ballooning mode representation with extrapolated trapped electron (TEM) physics. The Multimode model [4] combines the Weiland two-dimensional ITG/TEM model with contributions from drift-resistive and kinetic ballooning modes. While its physics is not as rigorous as the gyroLandau fluid models, it has been more extensively tested in a full time-dependent transport code to successfully predict the evolution of density and temperature profiles from a wide range of discharges. All three are critical gradient models and can be characterized in terms of their "stiffness" which determines how much power flow is needed to move away from marginality. In general, the gyrofluid models tend to be very stiff while the Multmode model is moderately stiff. The IIF model [5] differs in that it is not a drift wave based transport model. It can be characterized as a current-diffusive model based upon one fluid electrostatic "inertial" MHD equation. Unlike the ITG based models, it has no threshold and, therefore, little stiffness. While testing the IIF model we found that better agreement with the database is found if the thermal diffusivities were reduced by 50%. This is justifiable since the model was not originally calibrated against a large database. All results shown here are for the recalibrated version.

*Work supported by the U.S. Department of Energy under Grant No. DE-FG03-95ER54309.
†Oak Ridge Associated Universities, Oak Ridge, Tennessee.

II. SIMULATION RESULTS AND RANKING OF MODELS

To assess the performance of each transport model, quantitative comparisons are made between the model predictions and the experimental data for both global and local quantities, Figure 1 shows that the Multimode model yields the best overall agreement with the database followed by the IFS/PPPL model (without E×B shear), IIF, and GLF23 (with E×B shear) models, respectively.

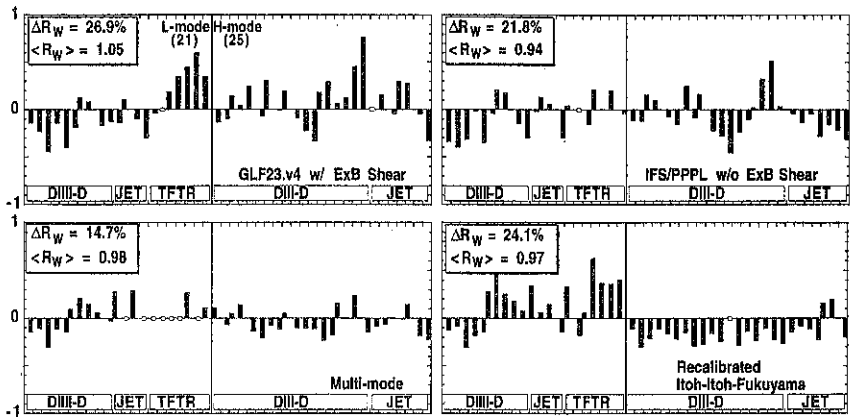

Fig. 1. Stored energy offset for the GLF23, IFS/PPPL, Multimode, and IIF models.

Here, the stored energy offset f_W, defined as W_s/W_x-1, is plotted versus discharge for each of the four transport models. The L– and H–mode results are divided left and right by a thick black line with the discharges also being conveniently grouped according to machine. Here, a positive (negative) offset indicates the model overpredicts (underpredicts) the stored energy. A hollow circleis shown when no numerical result was found for a particular discharge. In the upper left corner of each panel is the average and the root-mean-square error (rms) for the total stored energy.

Furthermore, we find that the ranking of the models is independent of the figure of merit chosen. Here, the global figures of merit include the average $\langle R_W \rangle$ and rms error ΔR_W for the total stored energy

$$\langle R_W \rangle = \sum_i \left(W_{si}/W_{xi} \right) / N \qquad \Delta R_W = \sqrt{\sum_i \left(W_{si}/W_{xi} - 1 \right)^2 / N} \tag{1}$$

where N is the total number of discharges and $W_{s,x}$ refer to the simulation and experimental stored energies, respectively. The local figures of merit include the offset f_T and rms error σ_T between the predicted and experimental temperature profiles where

$$f_T = \sum_i \left(T_s - T_x \right) \Big/ \sqrt{\sum_i T_x^2} \qquad \sigma_T = \sqrt{\sum_i \left(T_s - T_x \right)^2} \Big/ \sqrt{\sum_i T_x^2} \tag{2}$$

Table 1 shows the average and rms error for the total stored energy along with the rms error and average offset for the temperature profiles. Notice that agreement with the database gets worse when E×B shear is included in the IFS/PPPL model, but agreement improves when

included in the GLF23 model. Specifically, the offset becomes closer to unity and the average error remains essentially unchanged for the GLF23 model while the offset increases from 0.94 (too cold) to 1.20 (too hot) and the average error worsens from 22% to 37% for the IFS/PPPL model. This illustrates that the implementation of E×B shear effects is crucial and can be as important as describing the physics within the ITG model itself. In fact, it is a necessary ingredient in reproducing the experimental profiles in reversed shear discharges where models lacking E×B shear significantly underpredict the observed temperature profiles.

Table I. Rank According to Figures of Merit

	$\langle R_W \rangle$	ΔR_W	σ_{Te}	σ_{Ti}	$\langle f_{Te} \rangle$	$\langle f_{Ti} \rangle$
Multimode	0.96	0.15	0.17	0.22	–0.05	0.01
IFS-PPPL (w/o E×B)	0.94	0.22	0.28	0.26	–0.04	–0.07
IIF (recalibrated)	0.97	0.24	0.25	0.39	–0.05	–0.02
GLF23.v4 (w/ E×B)	1.05	0.27	0.32	0.34	0.02	0.03
GLF23.v4 (w/o E×B)	0.83	0.24	0.28	0.28	–0.13	–0.12
IFS-PPPL (w/ E×B)	1.20	0.37	0.53	0.34	0.17	0.08

III. SCANS IN MACHINES AND DIMENSIONLESS PARAMETERS

To test the intrinsic scaling properties of the models we examined simulations of DIII–D parameter scans within the database including H–mode scans in plasma current, heating power, and electron density. Also studied were L– and H–mode dimensionless similarity experiments where the normalized gyroradius, collisionality, and beta were systematically varied. Table II details the predicted transport confinement scalings for the DIII–D H–mode scans in plasma current (I_p varied from 0.75 to 1.5~MA at fixed P_b, n_e), neutral beam power (P_b varied from 4.7 to 13.6~MW at fixed I_p, n_e), and electron density (power changed as density varied from 2.9 to 5.4 × 10^{19} m^{-3} to keep temperature gradients fixed). All the models fail to reproduce the observed scaling in one or more of the scans.

Table II. Scaling Exponents for DIII–D Fixed Parameter Scans

	$\tau \propto I_p^{\alpha_I}, P^{\alpha_P}, n_e^{\alpha_N}$			$\tau \propto B^{\alpha_B}$		$\beta_\tau \propto \nu_*^{\alpha_1}, \beta^{\alpha_2}$			
Scan	I_p	P	n_e	ρ_*	ρ_*	ν_*	ν_*	β	β
Type	H–	H–	H–	Low-q H–	High-q H–	L–	H–	L–	H–
Exponent	α_I	α_P	α_N	α_B	α_B	α_1	α_1	α_2	α_2
Multimode	0.65	–0.59	–1.21	0.83	0.19	–0.08	–0.41	0.41	0.23
IFS-PPPL (w/o ExB)	0.89	–0.86	–1.62	0.87	0.05	–0.25	–0.42	0.32	–0.22
GLF23 (w/ ExB)	0.91	–0.73	–1.39	0.54	–0.13	–0.10	–0.14	0.47	0.03
IIF	0.56		–0.69	0.86	0.18	–0.07	–0.26	0.15	–0.09
Experiment	0.91	–0.60	–0.94	1.00	0.00	0.01	–0.23	–0.07	0.09

In H–mode plasmas a substantial portion of the stored energy is in the pedestal region. Therefore, it is of interest to test the extent in which the predicted scalings from the models result from enforcing the boundary conditions at the top of the pedestal. We find that if the pedestal temperatures are held fixed going from the low to high current discharge that the

observed linear current dependence is not reproduced. This implies that most (>70%) of the H–mode current scaling is an artifact of the changing temperatures at the top of the pedestal. In the experiment, T_e and T_i at $\rho/a = 0.9$ changed by factors of 3.5 and 1.8, respectively. For the power scan, however, we find that the experimental power scaling is reproduced when holding the boundary temperatures fixed going from the low to high power discharge suggesting that the power scaling is not determined by the pedestal boundary conditions.

Table II also describes the results for the H–mode ρ_* and L– and H–mode ν_* and β scans. Interestingly, it is found that all the models, which are intrinsically gyroBohm, follow the apparent change from gyroBohm confinement for low-q H–mode discharges to Goldston-like confinement for high-q discharges where the normalized gyroradius was varied by a factor of 1.6 holding all other dimensionless quantities fixed. With the exception of the L–mode β-scan, all the models reproduced the observed weak dependence of $B\,\tau_{tr}$ on collisionality and thermal beta in the L– and H–mode where ν_* was varied by a factor of eight in the ν_*-scans and β_{th} was varied by a factor of two in the β-scans.

IV. ITER PROJECTIONS

To test the intrinsic scaling properties of the models we examined simulations of DIII–D parameter scans within the database including H–mode scans in plasma current, heating power, and electron density. Also studied were L– and H–mode dimensionless similarity experiments where the normalized gyroradius, collisionality, and beta were systematically varied. Table II details the predicted transport confinement scalings for the DIII–D H–mode scans in plasma current (I_p varied from 0.75 to 1.5 MA at fixed P_b, n_e), neutral beam power (P_b varied from 4.7 to 13.6 MW at fixed I_p, n_e), and electron density (power changed as density varied from 2.9 to 5.4 $\times$ 10^{19} m^{-3} to keep temperature gradients fixed). All the models fail to reproduce the observed scaling in one or more of the scans.

A large uncertainty in projecting to ITER ignition is whether or not H–mode pedestal temperatures can be sustained. This is crucial because many transport models are relatively sensitive to the pedestal temperature. Comparing the predictions from the models, we see that they vary considerably from very optimistic (IIF actually exceeds β-limit) to optimistic (Multimode) to pessimistic (IFS, GLF). Figure 2 illustrates the sensitivity of the model predicted fusion power gain ($Q = 5/[P_{aux}/P_{\alpha}]$) to the pedestal temperature assuming a line-averaged density of 1.2×10^{20} m^{-3}, $\tau_{He} = 10\,\tau_E$, and $P_{aux} = 100$ MW. Typically, the Multimode model predicts ignition even for L–mode edge temperatures.

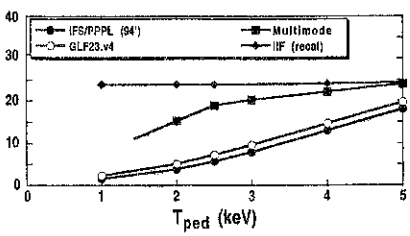

Fig. 2. Fusion energy gain versus pedestal temperature.

[1] J.W. Connor, et al., in Proc. of the 16th IAEA Fusion Energy Conf., Montreal, 1996 (International Atomic Energy Agency, Vienna, in press), paper F1-CN-64/FP-21.

[2] M. Kotschenreuther, W. Dorland, M. Beer, and G. Hammett, Phys. Plasmas **2**, 2381 (1995).

[3] R.E. Waltz, G.M. Staebler, G. Hammett, and J.P. Konings, in Proc. of the 16th IAEA Fusion Energy Conf., Montreal, 1996 (International Atomic Energy Agency, Vienna, in press), paper F1-CN-64/D1-6.

[4] J.E. Kinsey and G. Bateman, Phys. Plasmas **3**, 3344 (1996).

[5] S.I. Itoh, K. Itoh, A. Fukuyama, and M. Yagi, Phys. Rev Lett. **72**, 1200 (1994).

UNDERSTANDING TRANSPORT THROUGH DIMENSIONLESS PARAMETER SCALING EXPERIMENTS*

C.C. Petty and T.C. Luce
General Atomics, P.O. Box 85608, San Diego, California 92186-9784 USA

Introduction. The related methods of dimensional analysis, similarity, and scale invariance provide a powerful technique for analyzing physical systems. For example, the complex plasma dynamics governed by the Vlasov-Maxwell system of equations can be characterized by sets of dimensionless quantities through the application of these techniques [1,2]. Significant progress has been made recently towards predicting and understanding radial heat transport using dimensionless parameter scaling techniques. Previous experiments on the DIII–D tokamak have measured the variation of heat transport with the relative gyroradius (ρ_*) [3–6]; in this paper, the scaling of heat transport with plasma beta (β) and normalized collisionality (ν) for L–mode and H–mode plasmas on the DIII–D tokamak is reported.

Following the scale invariance approach to confinement scaling, the thermal diffusivity (χ) is assumed to depend only on local dimensionless quantities. One possible form for χ is

$$\chi = \chi_B \beta^{\alpha_\beta} \nu^{\alpha_\nu} F(\rho_*, q, R/a, \kappa, T_e/T_i, \cdots) , \qquad (1)$$

where $\chi_B = cT/eB$. By varying either β or ν while keeping the other dimensionless quantities fixed, the scaling exponents α_β and α_ν can be determined since the unknown function F remains constant. Understanding the beta and collisionality scaling of transport helps to differentiate between various proposed mechanisms of turbulent transport and allows the origin of power degradation and density scaling of confinement to be determined.

Beta Scaling of Heat Transport. Experimental results from the beta scaling of confinement should help discern the anomalous transport mechanism. Theories for which $E \times B$ transport is dominant show little enhancement or perhaps even slight reduction in transport with increasing beta, while transport models that invoke electromagnetic effects like magnetic flutter transport are generally expected to have a strong, unfavorable beta scaling. Empirically-derived scaling relations seem to favor the latter transport mechanism; the ITER-89P L–mode scaling gives $\alpha_\beta = 0.525$, whereas the ITER-93H H–mode scaling gives $\alpha_\beta = 1.235$.

In these experiments on the DIII–D tokamak, scaling of L-mode and H-mode confinement was determined for a factor-of-2 scan in beta. In order to keep ρ_*, ν, and q constant while varying β, the plasma parameters were scaled like $n \propto B^4$, $T \propto B^2$, and $I \propto B$ at fixed plasma geometry. Fast wave heating was utilized for L–mode discharges while neutral beam injection (NBI) heating was used for H–mode discharges. The global parameters for these β scans are given in Table I, which shows that the dimensionless parameters were well matched.

The energy confinement was found to depend only weakly upon beta for both the L–mode and H–mode scans. Table I shows that the normalized confinement time scaled like $B\tau_{th} \propto \beta^{-0.05\pm0.10}$ for L–mode plasmas and $B\tau_{th} \propto \beta^{0.15\pm0.13}$ for H–mode plasmas. This

*Report of work sponsored by the U.S. Department of Energy under Contract No. DE-AC03-89ER51114.

Table I: Global dimensionless parameters for β scans

	L–mode		H–mode	
Parameter	#90118	#90108	#90117	#90108
B (T)	1.63	1.91	1.62	1.93
q_{95}	3.66	3.64	3.76	3.88
$\bar{n}/B^4$	0.25	0.28	0.53	0.53
$W_{\rm th}/B^6$	5.0	5.1	15.4	16.3
$\beta_{\rm N}^{\rm th}$	0.26	0.49	0.80	1.71
$B\tau_{\rm th}$	0.166	0.161	0.229	0.257

beta dependence was much weaker than the prediction of empirically-derived scaling relations, which indicates that the (apparent) beta scalings contained in these scaling relations are not due to an actual beta dependence of heat transport.

A local transport analysis verified that the beta scaling of the thermal diffusivity for the L–mode plasmas was weak or possibly non-existent. The beta scalings of the ion and electron thermal diffusivities are plotted as a function of the normalized radius in Fig. 1. The error bars indicate that the beta scalings of χ_e and χ_i are not statistically different from each other. For H–mode plasmas, the local transport analysis found that the beta scaling for the electron fluid was weak, but a significant beta scaling was observed in the ion fluid, as shown in Fig. 2. The nearly linear, favorable beta scaling for ion transport is not explained as yet; however, any comparison of these experimental results with theoretical models should include the effect of the outward shift of the magnetic axis with increasing beta since large Shafranov shifts can stabilize trapped particle modes and reduce anomalous transport [7].

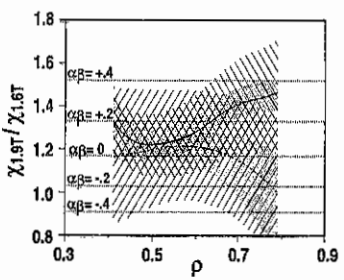

Fig. 1. Ratio of electron (solid line) and ion (dashed line) thermal diffusivities for the L–mode beta scan. The lined shading indicates the standard deviation of the random error, while the dotted shading indicates the potential effect of systematic error.

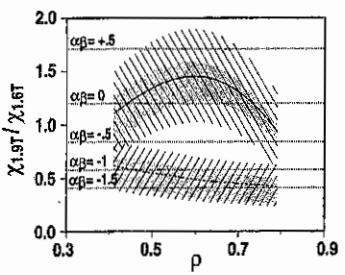

Fig. 2. Ratio of electron (solid line) and ion (dashed line) thermal diffusivities for the H–mode beta scan.

Collisionality Scaling of Heat Transport. Drift wave models of anomalous transport can generally be classified by their predicted dependence on collisionality. The thermal diffusivities for η_i and collisionless trapped electron modes are expected to have no dependence on ν, while the thermal diffusivities for the dissipative trapped particle and resistive balloon-

ing modes are expected to have strong ν scalings [8]. In addition, neoclassical transport has a linear, unfavorable ν dependence in the banana regime. Both the ITER-89P L–mode scaling and the ITER-93H H–mode scaling have the same $\nu^{-0.28}$ dependence.

In these experiments, the scaling of L–mode and H–mode confinement was determined for a factor-of-8 scan in collisionality. In order to keep ρ_*, β, and q constant while ν varied, the plasma parameters were scaled like $n \propto B^0$, $T \propto B^2$, and $I \propto B$ at fixed plasma geometry. Combined NBI and fast wave heating was used for L–mode discharges while NBI heating was utilized for H–mode discharges. The global parameters are given in Table II, which shows that the dimensionless parameters were well matched for these ν scans.

Table II: Global dimensionless parameters for ν scans

	L–mode		H–mode	
Parameter	#90765	#90753	#90768	#90740
B (T)	1.14	1.91	1.15	1.92
q_{95}	3.60	3.56	4.04	3.98
$\bar{n}B^0$	2.4	2.6	6.6	6.1
W_{th}/B^2	63	63	240	230
$\nu_{*,min}$	0.15	0.019	0.090	0.011
$B\tau_{th}$	0.128	0.123	0.180	0.406

The confinement was found to be almost independent of collisionality for L–mode plasmas, whereas a moderate ν dependence was observed for H–mode plasmas. Table II shows that the normalized confinement time scaled like $B\tau_{th} \propto \nu^{0.02\pm0.03}$ for the L–mode scan and $B\tau_{th} \propto \nu^{-0.37\pm0.05}$ for the H–mode scan. The ν dependence for H–mode plasmas was similar to that of the ITER-93H scaling, but the ν dependence for L–mode plasmas was much weaker than in the ITER-89P scaling.

The local transport analysis found that the ν scaling of the thermal diffusivity was weak for L–mode plasmas, in agreement with the global confinement scaling. This is shown in Fig. 3, where the ν scaling of the ion and electron thermal diffusivities is plotted as a function of the normalized radius. For H–mode plasmas, the local transport analysis found that the one-fluid thermal diffusivity had a moderate, unfavorable ν scaling similar to the global confinement scaling, as shown in Fig. 4. It is not yet clear if this ν scaling is present in both the electron and ion fluids. Since the anomalous transport is only 2–3 times the neoclassical level for these H–mode plasmas, the measured ν dependence may be a manifestation of the linear collisionality scaling of neoclassical transport.

Conclusions. Experiments in the DIII–D tokamak found weak beta scaling of heat transport for both L–mode and H–mode plasmas. For L–mode plasmas, the electron and ion thermal diffusivities had no measurable beta dependence and the normalized confinement time scaled like $B\tau_{th} \propto \beta^{-0.05\pm0.10}$. The confinement time for H–mode plasmas scaled like $B\tau_{th} \propto \beta^{0.15\pm0.13}$; the ions had a favorable beta scaling whereas the electrons had no measurable beta dependence. Since a strong, unfavorable beta scaling of transport was not

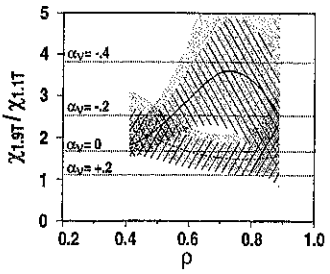

Fig. 3. Ratio of electron (solid line) and ion (dashed line) thermal diffusivities for the L–mode collisionality scan.

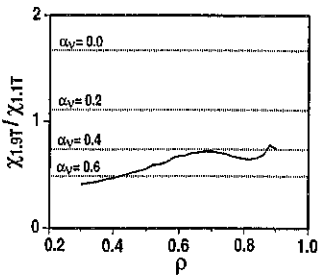

Fig. 4. Ratio of one-fluid thermal diffusivities for the H–mode collisionality scan.

observed, these experiments indicate that electromagnetic effects like magnetic flutter transport are not a significant part of the turbulent transport process.

The collisionality scaling for L–mode plasmas was also close to zero, $B\tau_{th} \propto \nu^{0.02\pm0.03}$. The ν scalings of the ion and electron thermal diffusivities were the same to within the experimental error. The lack of ν scaling, even in the plasma edge, indicates that the dissipative trapped particle and resistive ballooning modes are not significant at any radii for these L-mode plasmas [8]. For H–mode plasmas, a moderate, unfavorable ν scaling was observed in the local heat transport, with the confinement time scaling like $B\tau_{th} \propto \nu^{-0.37\pm0.05}$. This ν dependence may be a manifestation of neoclassical transport.

The parameter scalings found in these experiments are more optimistic than the present ITER scaling relations. Assuming a power law form for the scaling relation, the power degradation and density scaling of confinement are completely determined by the ρ_*, β and ν scalings. Combining the measured β and ν scalings of confinement for L–mode plasmas with Bohm-like ρ_* scaling [3], a global confinement scaling of $\tau \propto n^{0.5}P^{-0.5}$ is obtained. For H–mode plasmas, taking the measured scalings for β and ν along with gyro-Bohm-like ρ_* scaling [5,6] results in a global confinement scaling of $\tau \propto n^{0.3}P^{-0.4}$. These scaling expressions lead to a more favorable prediction of the confinement time for future ignition devices than the present ITER scaling relations such as ITER-93H.

References

[1] B.B. Kadomtsev, Sov. J. Plasma Phys. **1**, 295 (1975).
[2] J.W. Connor and J.B. Taylor, Nucl. Fusion 17, 1047 (1977).
[3] C.C. Petty *et al.*, Phys. Rev. Lett. **74**, 1763 (1995).
[4] T.C. Luce and C.C. Petty, 22nd EPS Conference, Bournemouth 1995, Vol. 19C, Part III, p. 25.
[5] C.C. Petty *et al.*, Phys. Plasmas **2**, 2342 (1995).
[6] C.C. Petty *et al.*, 23nd EPS Conference, Kiev 1996, Vol. 20C, Part I, p. 211.
[7] G. Rewoldt, W.M. Tang, and M.S. Chance, Phys. Fluids **25**, 480 (1982).
[8] J.W. Connor, Plasma Phys. and Contr. Fusion **30**, 619 (1988).

H–MODE THRESHOLD POWER SCALING AND THE ∇B DRIFT EFFECT*

T.N. Carlstrom, K.H. Burrell, R.J. Groebner, and G.M. Staebler
General Atomics, P.O. Box 85608, San Diego, CA 92186-5608

One of the largest influences on the H–mode power threshold (P_{TH}) is the direction of the ion ∇B drift relative to the X–point location, where factors of 2–3 increase in P_{TH} are observed for the ion ∇B drift away from the X–point. It is proposed that the threshold power scaling observed in single-null configurations with the ion ∇B drift toward the X-point location ($P_{TH} \sim nB$, where n is the plasma density, and B is the toroidal field) is due to the scaling of the magnitude of the ∇B drift effect. Hinton [1] and later Hinton and Staebler [2] have modeled this effect as neoclassical cross field fluxes of both heat and particles driven by poloidal temperature gradients on the open field lines in the scrape-off layer (SOL). The ∇B drift effect influences the power threshold by affecting the edge conditions needed for the L–H transition. It is not essential for the L–H transition itself since transitions are observed with either direction of B. Predictions of this model include saturation of the B scaling of P_{TH} at high field, 1/B scaling of P_{TH} with reverse B, and no B scaling of P_{TH} in balanced double-null configurations. This last prediction is consistent with the observed scaling of P_{TH} in double-null plasmas in DIII–D [3].

Neoclassical cross field fluxes

In the model by Hinton and Staebler [2], the ∇B effect is attributed to neoclassical cross field fluxes of heat and particles driven by poloidal temperature gradients on the open field lines in the SOL. In cylindrical geometry, the radial fluxes are given by:

$$q_{er} = \frac{5}{2} n_e \frac{cTe}{eB^2} \frac{B_\varphi}{r} \frac{\partial T_e}{\partial \vartheta} + q_{er}^A \tag{1}$$

$$q_{ir} = -\frac{5}{2} n_i \frac{cT_i}{eB^2} \frac{B_\varphi}{r} \frac{\partial T_i}{\partial \vartheta} + q_{ir}^A \tag{2}$$

$$\Gamma_{er} = \Gamma_{ir} = \frac{c}{eB^2} \frac{B_\varphi}{r} \left(\frac{\partial P_e}{\partial \vartheta} - e n_e \frac{\partial \Phi}{\partial \vartheta} \right) + \Gamma_r^A \tag{3}$$

where q_{er} is the radial electron heat flux, q_{ir} is the radial ion heat flux, Γ_r is the radial ambipolar particle flux, and q_{er}^A, q_{ir}^A, and Γ_r^A are the anomalous fluxes which represent all other transport processes which are not included in the Coulomb collision treatment. A diagram showing the direction of the gradients and fluxes is shown in Fig. 1. Integrating poloidally, they find that the ratio of the classical heat flux to the anomolous heat flux can be large, on the order of ~0.5 for typical scrape-off layer conditions. The direction of the poloidally integrated flux is radially inward when the ion ∇B drift direction is towards the X–point and outward when the ion ∇B drift direction is away from the X–point.

Following the work of Mahdavi *et al.* [4], we have developed a 1D heat conduction model to estimate the poloidal gradients of T_e and T_i in the SOL. These gradients are peaked near the X–point

*Work supported by the U.S. Department of Energy under Contract No. DE-AC03-89ER51114.

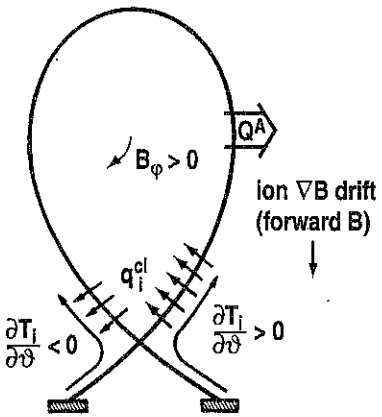

Fig. 1. Classical cross-field ion heat flux $\left(q_i^{cl}\right)$ for the ion grad-B drift towards the X–point. The anomalous energy flux (Q^A) is strongest on the outboard midplane.

region and $\partial T_i/\partial\vartheta \approx 2.5\ \partial T_e/\partial\vartheta$, consistent with experimental measurements of midplane temperatures of $T_e(0)$=80±20 eV, and $T_i(0)$=190±20 eV [5]. Assuming these gradients are the same for the inside and outside SOLs, the net cross field heat fluxes are given by the difference of 1/B on the inside and outside. Using the cylindrical approximation, this difference is given by

$$\left(\frac{B_o}{B_{out}} - \frac{B_o}{B_{in}}\right) \approx 2\varepsilon\sin\vartheta \tag{4}$$

where ε is the inverse aspect ratio.

Estimating the power flow across the separatrix due to these neoclassical cross field fluxes, we find:

$\langle q_{er}\rangle S$=0.036 MW

$\langle q_{ir}\rangle S$=–0.24 MW

$\left\langle \frac{5}{2}(T_e + T_i)\Gamma \right\rangle S$=–0.088 MW

for a net inward power of 0.26 MW. The bracket indicates a flux surface average and S is the plasma surface area. This power is comparable to the threshold power of approximately 1 MW, demonstrating that the magnitude of these neoclassical cross field fluxes can be significant with respect to aiding or inhibiting the L to H transition.

These fluxes are enhanced when the temperature near the X–point is reduced, for example, by divertor detachment. This situation can be approximated with this model by setting the X–point height equal to zero. In this case we find a net inward power of 0.64MW. This may still be an under estimate of the power due to these fluxes because we have assumed that the heat flux in the boundary layer is symmetrical for the inner and outer SOLs. Experimental observations and toroidal geometry

considerations indicate that the heat flux is higher in the outer channel and this would further increase the inward magnitude of $\langle q_{ir} \rangle$.

Another feature of this model is that it may explain the increase of P_{TH} at low density. As the density is reduced, heat flow along the boundary layer changes from being conduction limited to sheath flow limited. When this happens, the poloidal temperature gradient occurs almost entirely at the target plate. The lack of significant poloidal gradients near the core plasma reduces the neoclassical cross field fluxes and the ∇B effect is reduced.

∇B drift effect and the H–mode power threshold

The ∇B effect may be important to the L–H transition through its contribution to the edge pressure gradient from the inward radial fluxes of heat and particles. These fluxes act like a heat and particle pinch at the edge of the plasma and increase the edge pressure gradient. It is conjectured that the power threshold is actually a threshold for E_r which is related to the edge pressure gradient through the radial force balance equation [6]. By contributing to the edge pressure gradient, these fluxes reduce the power required to obtain H–mode. When the direction of the field is reversed, these fluxes act to decrease the edge pressure gradient and increase the threshold power. It is also possible that the ∇B effect could directly effect E_r through some other mechanism, but this discussion is beyond the scope of this paper.

In the present model, the cross field fluxes due to the ∇B drift effect are treated as an additional power flow across the separatrix given by

$$P_{\nabla B} \propto \varepsilon \frac{n}{r} \frac{T}{B} \frac{\partial T}{\partial \vartheta} S \tag{5}$$

where S is the plasma surface area (~rR). Depending on the direction of B, this term either adds to (ion ∇B drift toward the X–point) or subtracts from P_{SEP} to determine the threshold power for the L–H transition:

$$\left(P_{\nabla P}\right)_{TH} = P_{SEP} \pm P_{\nabla B} \tag{6}$$

where P_{SEP} is the power flowing across the separatrix and $\left(P_{\nabla P}\right)_{TH}$ is the power required to increase the pressure gradient to the threshold condition.

We do not know at present how the T and $\partial T/\partial\vartheta$ terms of $P_{\nabla B}$ scale. For a rough approximation, we assume a constant SOL pressure (nT = constant) and, equating P_{SEP} with the power flowing in the SOL, $P_{SEP} \sim KT^{5/2} \nabla T$, we approximate $\partial T/\partial\vartheta \sim P_{SEP}^{2/7}$. Using the double-null DIII–D results from [3] for $\left(P_{\nabla P}\right)_{TH}$ we then construct a scaling for P_{SEP},

$$P_{SEP}(MW) = r(m)\left(5.7 - 4.35\frac{P_{SEP}^{2/7}(MW)}{B(T)}\right) \tag{7}$$

A plot of this function is shown in Fig. 2. At sufficiently high B, P_{SEP} saturates and the B scaling no longer applies. At low B, the power goes to zero for the forward B direction. This is the region where ohmic H–mode is observed. When the second term is comparable to the first term, the scaling of P_{SEP} is roughly linear with B. In the reverse B case, the power increases at low B, and decreases at high B. Because so many different factors contribute to the scaling of $P_{\nabla B}$, it is difficult to obtain a simple scaling of P_{SEP}, and the above model should only serve as an example or guide.

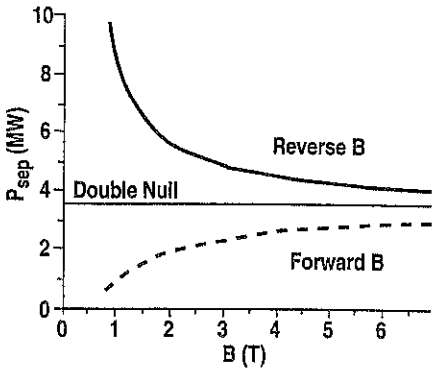

Fig. 2. Simplified scaling of P_{SEP} for both directions of B.

Conclusions

Using a simple 1D analysis of heat flow in the SOL to determine the poloidal gradient, $\partial T/\partial\vartheta$, the inward power flow across the separatrix due to neoclassical cross field fluxes is estimated. This power can be significant and it influences the H–mode power threshold, lowering it when the ion ∇B drift direction is toward the X–point, and raising it when the ion ∇B drift direction is away from the X–point. The existence of a density threshold for H–mode is also explained by this model.

A simple scaling relation of the neoclassical cross field fluxes with basic plasma parameters is developed. It shows that the B scaling of the H–mode power threshold can be explained by these neoclassical cross field fluxes. Predictions of this model include saturation of the B scaling of P_{TH} at high field, 1/B scaling of P_{TH} with reverse B, and no B scaling of P_{TH} in double-null configurations. This simple model predicts $P_{TH} \approx 12$ MW for ITER, which is far below the value of 150 MW obtained from a power law fit to the ITER threshold database [7].

[1] F.L. Hinton, Nuclear Fusion **25**, 1457 (1985).
[2] F.L. Hinton and G.M. Staebler, Nuclear Fusion **29**, 405 (1989).
[3] T.N. Carlstrom, P. Gohil, J.G. Watkins *et al.*, Plasma Physics and Controlled Fusion **36**, A147 (1994).
[4] M. Ali Mahdavi *et al.*, Physical Review Letters **47**, 1602 (1981).
[5] T.N. Carlstrom and R.J. Groebner, Physics of Plasmas **3**, 1867 (1996).
[6] K.H. Burrell *et al.*, Plasma Physics and Controlled Fusion **36**, 291 (1994).
[7] F. Ryter and the H–mode Database Working Group, Nuclear Fusion **36**, 1217 (1996).

IMPROVED ENERGY CONFINEMENT WITH NEON INJECTION IN THE DIII-D TOKAMAK*

G.M. Staebler, G.L. Jackson, W.P. West, S.L. Allen,† R.J. Groebner, M.J. Schaffer, and D.G. Whyte‡

General Atomics, P.O. Box 85608, San Diego, California, 92186-5608 USA

In this paper we will report the first direct measurements of the fully stripped neon 10^+ density profile in a plasma with enhanced energy confinement due to neon injection. This is made with a calibrated charge exchange recombination (CER) system [1]. It is found that the neon 10^+ density is peaked like the electron density with a slightly higher concentration towards the edge. The good news is that the neon 10^+ fraction is less than 1% (normalized to the electron density). The radial electric field can also be computed from the CER measurements on DIII-D. The shear in the ExB velocity is found to exceed the maximum growth rate of the ion temperature gradient (ITG) mode over part of the profile, a condition for the suppression of turbulent transport [2]. This agrees with the reduced power balance thermal diffusivities near the magnetic axis.

The phenomenon of enhanced energy confinement in tokamaks during impurity injection and auxiliary heating has been observed on several tokamaks. ISX-B had the Z-mode [3], TEXTOR the I-mode [4] and JFT-2M the IL-mode [5]. TEXTOR can get the I-mode without seeding impurities at low density, but the best performance has been with neon injection at high density and high radiated power (RI-mode) [6]. All of these enhanced confinement regimes have peaked density profiles, high auxiliary heating, high radiation, usually due to neon but other impurities have also been successful, and no sawteeth. TEXTOR has found sawtoothing RI-modes. JFT-2M has reported IL-modes with both limiters and divertors. Energy confinement times for IL-mode in JFT-2M were as good or better than the preceding ELM-free H-mode. Sawtoothing discharges with modest energy confinement improvement (1.5 times L-mode)have been observed on ASDEX-U [7] when neon injection has suppressed the H-mode. About two dozen DIII-D discharges with L-mode edges and strong neon radiation have been produced with energy confinement up to 2.0 times L-mode but most with 1.4-1.6 times L-mode. All but the highest one reported here were sawtoothing. A variety of configurations are represented, both double null and single null topologies and both ion ∇B drift toward and away from the dominant X-point. We will adopt the IL-mode terminology for these plasmas. A few discharges which returned to an H-mode edge after an IL-mode phase have been observed. In this paper we will present analysis of a plasma which obtains an energy confinement three times L-mode before sawteeth and ELMs set in returning the energy confinement to a normal H-mode level. This discharge retains the improved core confinement of the preceding IL-mode but adds on the H-mode edge barrier. This type of regime will be referred to as an IH-mode.

A single discharge with both an IL- and IH-mode phase will be analyzed in this paper. An overview of DIII-D discharge 86457 is given in Fig. 1. This was a lower single null plasma with the ion ∇B drift towards the X-point The divertor cyropump was active but the outer strike point was not located for maximizing pumping. Other parameters are: toroidal field 1.77 T, plasma current

*Work supported by U.S. Department of Energy under Contract No. DE-AC03-89ER51114 and Grant No. DE-FG03-95ER54294.

†Lawrence Livermore National Laboratory.

‡Univeristy of California, San Diego.

1.28 MA, minor radius 0.60 m, major radius 1.70 m, elongation 1.85. Neutral beam power (4.0 MW) began at 1.0 s yielding an H–mode transition 80 ms later. A neon gas puff was injected from 1.2–1.4 s and the plasma remained ELM free until a few large ELM bursts and an H to L transition occurred due to the large radiated power. Beginning at about 1.6 s the drop in stored energy halted. At this point the energy confinement time was 110 ms which is 1.2 times L–mode (ITER 89p scaling [8] including the stored energy time derivative correction to the beam plus Ohmic power). This marks the start of the IL–mode phase. The stored energy continues to climb until a transition to IH–mode at 1.92 s At 1.87 s the energy confinement has reached 234 ms. (2.0 times L–mode). During the IH–mode phase the energy confinement increases reaching a peak of 382 ms or 3.1 times L–mode at 2.1 s. The energy confinement time is above 2.5 times L–mode for most (1.94–2.2 s) of the IH–mode phase. The stored energy returns to its pre-neon puff level (energy confinement 2 times L–mode) after the onset of steady ELMs and sawteeth beyond 2.4 s. The sawteeth were delayed by the injection of one neutral beam during the current ramp-up. The safety factor (q) profile (measured with a motional stark effect diagnostic) is monotonic with positive shear but is somewhat above one at the center (see insert in Fig. 5). The profiles of the ion and electron temperature, the electron density and neon 10^+ density are shown in Fig. 2 at 1.6, 1.9 and 2.2 s. During the IL–mode phase (from 1.6 to 1.9 s) the electron and ion temperatures rise but the electron density is nearly unchanged. The neon 10^+ concentration becomes slightly hollow. After the transition to IH–mode, the electron and ion temperatures broaden as the edge density rises sharply. In the early IH–mode phase the temperatures remain more centrally peaked. The dramatic rearrangement of the neon 10^+ profile between the 1.9 and 2.2 s begins immediately after the IH–mode transition. Because of the rise in the edge electron density the neon 10^+ concentration relative to electron density is not nearly as hollow as the neon 10^+ density. The neon 10^+ concentration is more hollow in IH–mode

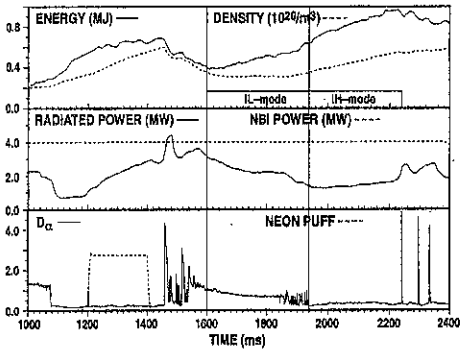

Fig. 1. DIII–D discharge 86457 overview showing stored energy, line-averaged density, total radiated power, neutral beam power, divertor D_α light, and the neon gas valve voltage.

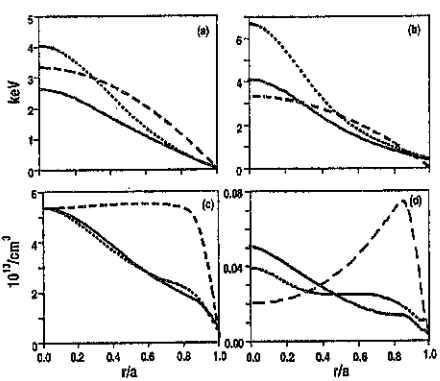

Fig. 2. Measured radial profiles of electron temperature (a), ion temperature (b) electron density (c) and neon 10^+ density (d) at three times: 1.6 s (solid), 1.9 s (dotted), 2.2 s (dashed).

than during the IL–mode phase. The measured neon 10^+ toroidal rotation profile behaves similarly to the ion temperature.

Transport analysis of this discharge has been made with the ONETWO code. Experimental profiles and EFIT equilibria were taken every 50 ms from 1.6 to 2.2 s. The profiles were then smoothed in time using a boxcar average over 150 ms intervals. The electron thermal diffusivity profiles at several times are shown in Fig. 3. The electron thermal diffusivity first falls near the center and then the reduction propagates towards the edge during the IL–mode phase. (1.6, 1.8, 1.9 s). The IH–mode phase begins with a reduction near r/a = 0.8 retaining the low central transport initially (2.1 s). Late in the IH–mode phase (2.2 s) the central electron thermal diffusivity has risen above its value at 1.6 s. The ion thermal diffusivity profiles are shown in Fig. 4 along with the ion neoclassical [9] thermal diffusivity at 2.2 s. The ion thermal diffusivity also falls near the axis first during the IL–mode phase. (1.6, 1.8, 1.9) but does not show much reduction farther out until the IH–mode phase (2.2 s) The profile at 2.1 s is the same as at 2.2 s. The persistence of a region with a power balance ion thermal diffusivity below standard neoclassical may be consistent with a revised neoclassical theory [10].

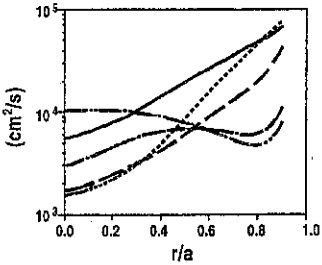

Fig. 3. Power balance electron thermal diffusivity profiles at five times: 1.6 s (solid), 1.8 s (dotted), 1.9 s (dot dashed), 2.1 s (dashed), 2.2 s (dot dot dashed).

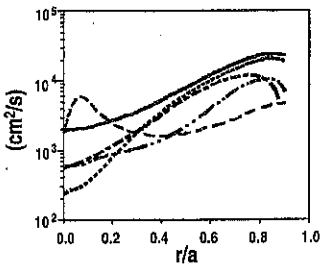

Fig. 4. Power balance ion thermal diffusivity profiles at four times: 1.6 s (solid), 1.8 s (dotted), 1.9 s (dot dashed), 2.2 s (dot dot dashed), also shown is the ion neoclassical thermal diffusivity at 2.2 s (dashed).

It has been shown theoretically that E×B velocity shear could yield core transport reduction even when the edge remains in L–mode due to high radiation [11]. In order for the E×B velocity shear to suppress transport it must exceed the maximum growth rate of the turbulent instability [2]. The measured E×B shear rate at 1.9 s and the maximum growth rate for ITG modes is shown in Fig. 5. The growth rate was computed using a comprehensive gyro-kinetic stability code in the ballooning representation [12]. The neon impurity was included in the calculation and the electrostatic approximation was used. The E×B shear exceeds the maximum growth rate in two regions, near the magnetic axis and near r/a=0.7. Both ions and electrons have reduced thermal diffusivities for r/a<0.4 which suggest that the E×B shear could contribute to the improvement in this region. However, the region near r/a=0.7 shows only a reduction in the electron thermal diffusivity at 1.9 s and there is no sign of a dramatic transport barrier with steep gradients in this region. The sharp rise in the growth rate at r/a=0.8 is due to an electron temperature gradient (ETG) mode becoming dominant over the ITG mode. The maximum growth rate for this mode is about 6 MHz at a wavenumber 100 times larger than the ITG mode. The ETG mode is stable for r/a<0.3 so it cannot affect the core but it may be preventing the E×B shear from suppressing the turbulence at r/a=0.7 by driving the ITG mode non-linearly. Even when the

E×B shear does not completely stabilize the turbulence it can reduce transport. The fact that the electron thermal diffusivity shows a broader region of reduction than the ions during the IL–mode is a unique feature of this mode compared to other enhanced core modes (NCS, VH) observed on DIII–D. It is interesting that the core particle transport does not appear to improve. Since the Thomson scattering diagnostic does not give electron density data inside of r/a=0.3 on this discharge it is possible that the density is somewhat more peaked than shown. However, the central electron cyclotron emission radiometer (which measures electron temperature) was not cut-off indicating that the central density was below 8.0×10^{13}.

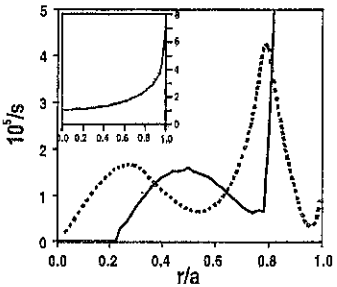

Fig. 5. Profile of the maximum ITG growth rate (solid) and measured E×B shear (dotted) at 1.9 s. Insert shows the measured safety factor profile at 1.9 s.

Both the IL–mode and the IH–mode deserve further study. IH–mode has a lower central impurity concentration and a higher confinement than IL–mode but it may not be able to achieve steady state and the particle confinement may be too good for helium ash removal. The IL–mode has a lower power flow to the divertor and peaked density profiles. It has yet to be demonstrated that E×B shear can produce a transport barrier just inside the radiating mantel as predicted [11] but E×B shear is contributing to the improved energy confinement of IL–mode.

[1] D.G. Whyte *et al.*, "Measurement and Verification of Z_{eff} Radial Profiles Using Charge Exchange Recombination Spectroscopy on DIII–D," to be submitted to Nucl. Fusion.
[2] R.E. Waltz *et al.*, Phys. Plasmas **1** (1994) 2229.
[3] E.A. Lazarus *et al.*, Nuclear Fusion **25** (1985) 135.
[4] A.M. Messiaen *et al.*, Nuclear Fusion **34** (1994) 825.
[5] M. Mori *et al.*, Nuclear Fusion **28** (1988) 1892.
[6] G. H. Wolf *et al.*, Plas. Phys. and Control. Nucl. Fusion Res., Proc. 1996 Conf. IAEA, Montreal, Canada, CN-64/02-5.
[7] J. Neuhauser *et al.*, Plas. Phys. Control. Fusion **37**(1995) A37.
[8] Yushmanov *et al.*, Nucl. Fusion **30** (1990) 1999.
[9] C.S. Chang and F. L. Hinton, Phys. Fluids **29** (1986) 3314.
[10] Z. lin *et al.*, Phys. plasmas **2** (1995) 2975.
[11] G.M. Staebler *et al.*, Plasma Phys. Control. Fusion **38** (1996) 1461.
[12] M. Kotchenreuther, Bull Am. Phys. Soc. **37** (1992) 1432.

CORE TURBULENCE AND TRANSPORT REDUCTION IN DIII–D DISCHARGES WITH WEAK OR NEGATIVE MAGNETIC SHEAR*

G.M. Staebler, C.M. Greenfield, D.P. Schissel , K.H. Burrell, T.A. Casper,† J.C. DeBoo, E.J. Doyle,‡ R.J. Fonck,◊ L.L. Lao, E.A. Lazarus,Δ G.A. Navratil,# C.L. Rettig,‡ T.L. Rhodes,‡ B.W. Rice,† H.E. St. John, B.W. Stallard,† E.J. Strait, R.E. Waltz and the DIII–D team

General Atomics, P.O. Box 85608, San Diego California, 92186-5608 U. S. A.

Core turbulence fluctuation levels have been suppressed in DIII–D discharges with weak or negative magnetic shear (NCS) near the magnetic axis. In some weak magnetic shear discharges the ion thermal transport has been reduced to neoclassical levels throughout the whole plasma. The cause of the transport reduction is investigated by calculating the stability of toroidal drift waves i.e. ion temperature gradient modes (ITG) and trapped electron modes (TE), with a comprehensive gyrokinetic linear stability code. It is found that the ITG modes and TE modes are stabilized by E×B velocity shear. The E×B velocity shear is primarily responsible for the spontaneous growth of a region of suppressed ion thermal transport. Surprisingly, the negative magnetic shear and Shafranov shift are only weak stabilizing influences for the ITG and TE modes in the DIII–D cases studied. Negative magnetic shear does eliminate the ideal magnetohydrodynamic ballooning mode instability which is a necessary access criteria for these improved core confinement regimes. Dilution of the thermal ions by fast ions from the heating beams and hot ions compared to electrons are found to be important stabilizing influences in the core.

The linear growth rates for toroidal drift waves are computed using a code written by M. Kotschenreuther [1]. This is an initial value code so it finds the most unstable mode (either ion or electron branch) at the given poloidal wavenumber. The code uses ballooning co-ordinates and has the full gyro-averaged kinetic linear response for both electrons and ions. The impurity ion species and the fast ion (from neutral beam heating) response were assumed to be adiabatic with only the effective charge (Z_{eff}) and ion dilution contributing to the growth rate calculation. The magnetic equilibrium is modeled by shifted circles (ŝ,alpha). Even though the stability code has a full electromagnetic response implemented, the ideal magnetohydrodynamic (MHD) ballooning mode limit for this model geometry is not accurate for the elongated double null DIII–D discharges. Thus, the growth rates computed for actual plasmas were done in the electrostatic approximation in order to avoid an unrealistically low MHD threshold. Parallel velocity shear was added to the original code by R.R. Dominguez and A. Brizard. Inclusion of the E×B shear in a ballooning co-ordinate code presents some technical difficulties which make a direct calculation of linear stability including E×B shear hard to interpret. It has been shown from non-linear simulations of toroidal drift wave turbulence that the turbulence quenches when the E×B shear rate is comparable to the maximum linear growth rate in the absence of E×B shear [2]. Furthermore, the saturated fluctuation intensity was found to be proportional to the net growth rate defined as the maximum growth rate minus the E×B shear rate:

*Work supported by U.S. Department of Energy under Contract Nos. DE-AC03-89ER51114, W-7405-ENG-48, and DE-AC05-96OR22464 and Grant Nos. DE-FG03-86ER53266, DE-FG02-92ER54139, and DE-FG02-89ER53297.
†Lawrence Livermore National Laboratory. ‡University of California, Los Angeles.
◊University of Wisconsin, Madison. ΔOak Ridge National Laboratory. #Columbia University.

$$\gamma_{net} = \gamma_{max} - \omega_{E\times B}, \quad \omega_{E\times B} = \frac{RB_p}{B_T}\frac{\partial}{\partial r}\left(E_r/RB_p\right) \tag{1}$$

where B_p, B_t are the poloidal and toroidal magnetic field components, R is the major radius, r the minor radius and E_r the radial electric field. This is not an exact prescription. In general there is dependence on magnetic shear and other factors [2] which can be up to a twofold variation in the coefficient of the E×B shear rate. This should be kept in mind when comparing the E×B shear rate to the maximum growth rate in the figures to follow. In all the figures in this paper the linear growth rates have been maximized with respect to the poloidal wavenumber. The maximum growth rate can sometimes have a large poloidal wavelength shift as a parameter such as density gradient length is varied. This can result in a very different stability trend for the maximum growth rate than what would be inferred from the growth rate at fixed poloidal wavenumber. The gyrokinetic stability of NCS discharges has been studied using G. Rewoldt's eigenvalue code, with similar physics included [3]. Our findings are in accord with theirs. The ion temperature gradient (ITG) and trapped electron mode (TE) are the dominant instabilities in the core of NCS plasmas [3]. The ITG branch is dominant for flat density profiles. The three main drives are the density gradient length, the temperature gradient length and the parallel velocity gradient.

Peaking the density profile excites the TE mode. The Shafranov shift (α) is included in these parameter scans through the formula

$$\alpha = 2\,\beta q^2\left(a/L_T + a/L_n\right)\,R/a \tag{2}$$

A large Shafranov shift has been proposed as the primary stabilizing mechanism in some reversed magnetic shear discharges [4]. We find that decreasing the density or temperature gradients lengths alone results in an increased maximum growth rate even though the Shafranov shift increases. However, increasing the pressure (β) is strongly stabilizing for reversed magnetic shear, as shown in Fig. 1, due to the electromagnetic coupling and the Shafranov shift. Of course, for positive magnetic shear the ideal MHD limit greatly enhances the growth rates with beta as shown in Fig. 1. Figure 1 also illustrates that there is nothing special about zero magnetic shear. Strong magnetic shear of either sign is stabilizing. But for comparable stabilization about twice as much positive magnetic shear compared to negatively magnetic shear is required. The other primary stabilizing influences found in NCS plasmas (besides β) are hot ions $T_i/T_e>1$ and fast ion dilution. The E×B shear causes a second stability of ITG and TE modes for large temperature, density or toroidal velocity shear. This is illustrated in Fig. 2. The density and temperature gradients are increased together and the E×B shear is taken to be due to the diamagnetic velocity (no toroidal momentum injection) by the formula

$$\omega_{E\times B} = \rho_i/a\left(a/L_T\right)\left(a/L_n\right) \tag{3}$$

The ion gyroradius (ρ_i) was taken to be 0.01 times the minor radius (a) in Fig. 2. The E×B shear increases faster than the maximum growth rate with the gradients so the net growth rate γ_{net} has a second stability at large gradients. The first and second stability points (zero's of γ_{net}) are distinguished by two features. Both $\omega_{E\times B}$ and γ_{max} are small at the first stable point and both are large for the second. The derivative of γ_{net} with respect to $\omega_{E\times B}$ has opposite signs at the two zeros.

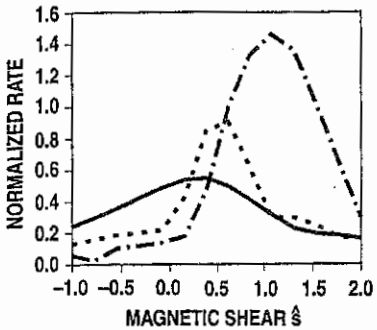

Fig. 1. Maximum growth rate vs. magnetic shear for β=0.0 (solid), β=0.005 (dashed), β=0.01 (dot-dashed). Rates are nomalized by $\left(\sqrt{T_e/m_i}\right)/a$.

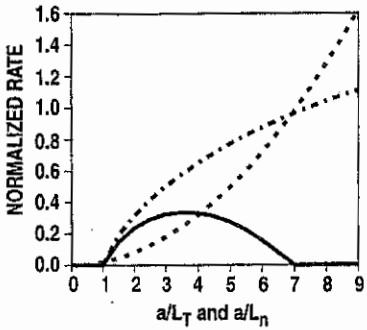

Fig. 2. γ_{net} (solid), $\omega_{E\times B}$ (dashed) and γ_{max} (dot-dashed) variation with $a/L_T=a/L_n$.

$d\gamma_{net}/d\omega_{E\times B} >$ first stable, $\quad d\gamma_{net}/d\omega_{E\times B} < 0$ second stable. (4)

This suggests a way of determining if the E×B shear has caused the stabilization of the turbulence or is just an effect of the improved confinement. If the point where γ_{net} vanishes is of the second stable type, then reducing the E×B shear would cause a return of the instability and hence the E×B shear is required for stability. If the zero of γ_{net} is of the first stable type, then increasing the E×B shear would make the toroidal drift modes unstable. An example from a DIII–D shot is shown in Fig. 3. This is a high power NCS discharge with a well established region of suppressed ion thermal transport out to r/a=0.5 [5]. The point at r/a=0.5 where $\gamma_{max}=\omega_{E\times B}$ is clearly a second stable point since γ_{net} is decreasing in the direction in which $\omega_{E\times B}$ increases. It is very typical of the dozen or so NCS discharges which have been analyzed in this way that the leading edge of the region of transport improvement is near a second stable point. This shot also shows another typical feature which is that farther into the region of improved transport, near the magnetic axis, the toroidal drift waves, in the ion gyroradius wavelength range, are linearly stable even without the E×B shear. Looking now at the low power formation phase of this same discharge in Fig. 4 we find that the region of improved confinement is smaller (r/a<0.3) [5]. The zero of γ_{net} at r/a=0.3 is ambiguous since $d\omega_{E\times B}=0$ showing that our classification scheme does not always work. The maximum growth rate was computed without the Shafranov shift to evaluate the importance of this factor in stability. As shown in Fig. 4 the maximum growth rate is only weakly affected. The maximum growth rate with the fast ion dilution removed and with $T_i=T_e$ is also shown (Shafranov shift as measured). In the center of the plasma these two effects have about the same stabilizing effect on γ_{max}. With both ion dilution and hot ions turned off the maximum growth rate exceeds the E×B shear in the center. Thus, the way in which this plasma was formed, with low target density and early neutral beam injection during the current ramp phase, greatly stabilized the plasma in the center due to the fast ion dilution and the hot ions. To a lesser extent the Shafranov shift was also stabilizing. The lower growth rate reduces the E×B shear required to initiate the transport barrier. Even after the E×B shear has formed a transport barrier, the effect of the leading edge of the barrier on the plasma within favors linear

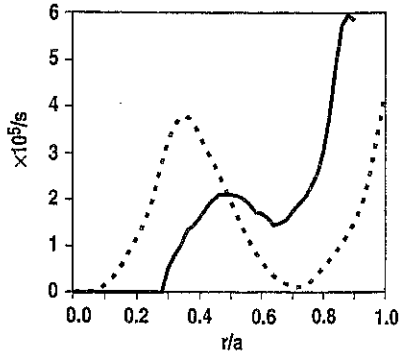

Fig. 3. γ_{max} (solid) and $\omega_{E\times B}$ (dashed) profiles for DIII–D discharge 87031 during the high power phase (1760 ms).

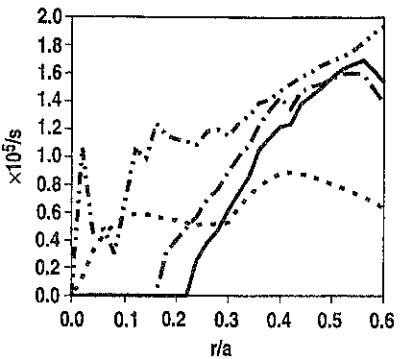

Fig. 4. γ_{max} (solid) and $\omega_{E\times B}$ (dashed) profiles for the same discharge as Fig. 3 during the low power phase (1590 ms). Also shown are γ_{max} with no Shafranov shift (α=0) (dot-dashed) and γ_{max} with T_i=T_e and no fast ion dilution (dot-dot-dashed).

stability near the axis. In many DIII–D NCS discharges the ion thermal transport improves much more than the electron thermal transport or the particle transport. This favors hot ions and fast ion dillution because the low densities and high temperatures result in a long slowing down time for the neutral beam ions. The high beta near the axis and the higher safety factor q on axis also increase the Shafranov shift behind the transport barrier initiated by the E×B shear. These stabilizing influences extend the region of reduced transport inward to the magnetic axis where the E×B shear vanishes. This extension of the suppressed transport region to the axis has been seen in modeling of internal transport barriers with E×B shear and ITG mode turbulent transport [6].

REFERENCES

[1] M. Kotschenreuther *et al.*, comput. Phys. Commun **88**, 128 (1995).

[2] R.E. Waltz *et al.*, Phys. Plasmas **1**, 2229 (1994).

[3] L.L. Lao *et al.*, Phys. Plasmas **3**, 1951 (1996).

[4] M.A. Beer and G.W. Hammett, Bull. Am. Phys. Soc. **40**, 1733 (1995).

[5] D.P. Schissel, *et al.*, Proc. 16th IAEA Fus. Eng. Conf. Montreal, October 1996, Paper F1-CN-64/A5-3.

[6] G.M. Staebler, *et al.*, Nucl. Fusion **37**, 287 (1997).

SCALING OF ELM AND H–MODE PEDESTAL CHARACTERISTICS IN ITER SHAPE DISCHARGES IN THE DIII–D TOKAMAK*

T.H. Osborne and the DIII–D H–mode Pedestal Study Group: R.J. Groebner, L.L. Lao, A.W. Leonard, R. Maingi,† R.L. Miller, G.D. Porter,‡ D.M. Thomas, and R.E. Waltz
General Atomics, P.O. Box 85608, San Diego, California 92186-9784, U.S.A.

1. Introduction

A defining feature of H–mode is the existence of a transport barrier near the plasma boundary. Although the H–mode edge transport barrier can be quite narrow (in DIII–D $\leq 2\%$ of the minor radius), the characteristics of this layer are significant in the overall plasma performance and in divertor effects.

Stiff ITG-mode turbulent transport models [1,2] predict that the core transport coefficients are reduced strongly with increasing edge temperature suggesting that ITER may require relatively high edge temperature for ignition. This result is in qualitative agreement with data from DIII–D and C-MOD [3]. On DIII–D, H-ITER93-H $\propto (T_e^{PED})^{0.55} (n_e^{PED})^{0.58}/B_T^{0.93}$, where H-ITER93-H is the energy confinement enhancement factor relative to ITER H–mode scaling, and PED refers to values at the top of the H–mode pedestal (Fig. 1). The periodic collapse of the pressure gradients associated with the H–mode transport barrier at ELMs is important not only in setting the average H–mode pedestal height, but also the short time scale of the ELM energy loss can result in large power loads to the divertor plates in ITER.

This paper primarily describes experiments in DIII–D employing discharges with ITER cross-sectional shape and aspect ratio ($L_{DIII-D}/L_{ITER} = 0.2$, where L is the length scale). In these experiments, the plasma current and toroidal field were varied by a factor of two as was the q, $3 < q_{95} < 6$, where $q_{ITER} \cong 3$. The neutral beam heating power was varied over the range $0.06 < P/S$ (MW/m^2) < 0.3, where 0.17 (IGNITION) $< P/S_{ITER} < 1.25$ (BURN), where P is the loss power, S is plasma surface area, and the density was in the range $0.2 < n_G = n/n_{GREENWALD} < 0.7$, while $n_{G-ITER} \approx 1.0$. These were gas puff fueled discharges in an open divertor configuration, with no divertor pumping, and the ∇B drift toward the x–point.

2. Scaling of H-mode Pedestal Parameters

We separated our study of the H–mode pedestal parameters into analysis of the scaling of the width of the steep pressure gradient region, which is expected to be set by turbulence suppression physics [4], and the magnitude of the gradient, which may be limited by the ELM instability [5].

*Work supported by U.S. Department of Energy Contracts DE-AC03-89ER51114, DE-AC05-96OR22464, and W-7405-ENG-48.
†Oak Ridge National Laboratory, Oak Ridge, Tennessee.
‡Lawrence Livermore National Laboratory, Livermore, California.

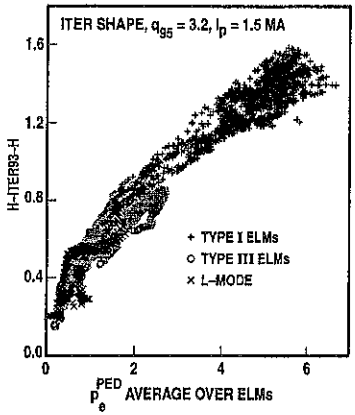

Fig. 1. H–mode energy confinement enhancement factor relative to ITER93-H–mode scaling increases with increasing H–mode pedestal pressure (kPa) averaged over ELMs.

The width of the H–mode transport barrier used in the scaling studies is determined from Thomson scattering measurements of the electron pressure profile which are fit to a hyperbolic tangent functional form in the edge region. We find that the width of the edge steep gradient region for the ion pressure generally matches that of the electrons. Parameters that were available for fitting included the electron profile parameters, and MHD equilibrium parameters which are determined from external magnetic measurements using the EFIT code. The width scaling relations presented here apply to the interval between type I ELMs; during type I ELMs the width expands greatly. Only p_e^{PED}, T_e^{PED}, and B_{pol} had significant correlation with the transport barrier width. Because of a correlation between density and plasma current, the width of the steep gradient region on the outboard midplane could be fit equally well to the edge pressure, $\delta \propto (p_e^{PED})^{0.52}/\langle B_{pol}\rangle^{0.94}$ (Fig. 2) or edge temperature, $\delta \propto (T_e^{PED})^{0.36}/\langle B_{pol}\rangle^{0.44}$. In dimensionless variables, the normalized width was equally well fit to the a power of the poloidal gyroradius, $\delta/R \propto (\rho_{POL}/R)^{0.66}$, or to the edge β_{POL}, $\delta/R \propto (\beta_{POL}^{PED})^{0.4}$. For low density type III ELMs (described in Section 2) the width is 20% to 50% larger than for type I even though p_e^{PED} and T_e^{PED} are typically signifcantly smaller. For low temperature type III ELMs the width appears to be similar to the type I case, although an explicit scaling has not been derived.

In the ITER shape discharges on DIII–D, we find that the electron pressure gradient normalized as for ballooning mode stability, $\alpha_{MHD} = 2\mu_0(dp_e/d\psi)(dV/d\psi)[V/(2\pi^2 R)]^{1/2}/4\pi^2$ before a type I ELM is relatively constant and independent of q (Fig. 3). This is in contrast to $\alpha_{CYL} = 2\mu_0(dp_e/dR)(q_{95}/B)^2 R$ which rises sharply at low s/q^2 (where s is the magnetic shear), and increases with increasing input power at high q. This behavior of α_{CYL} does not necessarily suggest second stability, instead it may be understood from the fact that $\alpha_{CYL}/\alpha_{MHD} \cong q_{95}/q_{LOCAL}$, where q_{LOCAL} is the local q on the outboard

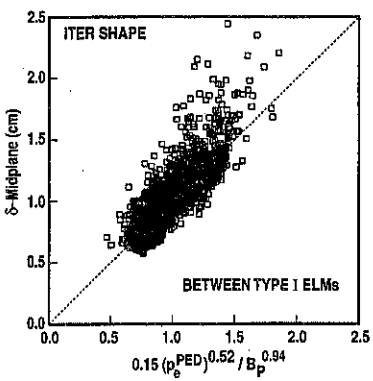

Fig. 2. Width of the H–mode steep gradient region on the outboard midplane between type I ELMs fit to powers of the electron pressure pedestal height, p_e^{PED} (kPa), and the surface averaged poloidal field B_p (T).

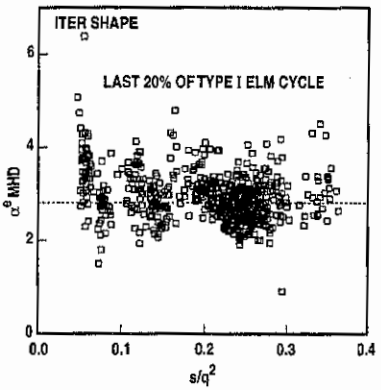

Fig. 3. Edge electron pressure gradient normalized as for ballooning mode stability just before a type I ELMs is relatively independent of s/q^2 where s is the magnetic shear.

midplane, and q_{95}/q_{LOCAL} increases with increasing β_{pol}. Using MHD equilibria determined from external magnetic measurements, we computed the stability to ideal, infinite n, ballooning modes with the BALOO [6] code. The electron pressure alone was found to be equal to or greater than the predicted first stable limit. In the few cases where the ion temperature was determined, it was similar to the electron temperature so that the experimental pressure gradient is expected to exceed the first stable limit by roughly a factor of two. Preliminary work indicates that self consistently adding the current density expected to be associated with the edge pressure gradient does not significantly change the first stable limit, however local regions of second stable access can be created in regions of high pressure gradient if the current is large enough to reduce s/q^2 below a critical value. Since s/q^2 generally decreases with increasing minor radius in these discharges, this mechanism might limit the width of the high pressure gradient region at a point where the pressure gradient is less than its peak value.

We can estimate the edge temperature in ITER by assuming type I ELMs will occur at the same α as in DIII–D at ITER q. Scaling from DIII–D discharges, $\delta/R \propto (\rho_{POL}/R)^{2/3}$ gives $T^{PED} \propto (LB_T/n_G^3)^{1/2} \approx 1$ keV for ITER [this scaling also implies $\delta \propto (L/n_G B_T)^{1/2}$, ß and $p^{PED} \propto (B_T^3/n_G L)^{1/2}$). For $\delta/R \propto (\beta_{POL}^{PED})^{1/2}$, $T^{PED} \propto (LB_T/n_G) \approx 5$ keV for ITER (and here $\delta \propto L$, and $p^{PED} \propto B_T^2$).

3. ELM Classification, Energy Loss, and Divertor Effects

Type I, II, and III ELMs [7] were observed in the ITER shape discharges on DIII–D. Type I and III ELMs appeared in distinct regions of n_e^{PED}, T_e^{PED} space (Fig 4). Type II ELMs were interspersed with type I ELMs and became more prevalent at high β_{POL} although they never replaced type I ELMs.

The energy lost from the plasma core during type I ELMs was determined from the time history of the stored energy obtained from MHD equilibrium. Data from DIII–D was combined with a few points from ASDEX-U and JET to produce a scaling for the type I ELM energy loss, $\Delta E_{ELM}/E_{TOTAL} \propto (P/S)^{-0.4} B^{-0.3}$ where P is the total input power and S is the plasma surface area, which gives $\Delta E_{ELM} \cong 26$ MJ for ITER. We can also estimate ΔE_{ELM} in ITER by assuming that the change in normalize pressure gradient, α, will be the same as that observed in DIII–D and that the pressure drops equally across the cross-section. For $\delta/R \propto (\rho_{POL}/R)^{2/3}$, $\Delta E_{ITER} \approx 7$ MJ, while for $\delta/R \propto (\beta_{POL}^{PED}/R)^{1/2}$, $\Delta E_{ITER} \approx 37$ MJ. IR camera measurements indicate that 75% to 100% of ΔE_{ELM} reaches the divertor plates on a time scale of 1–2 ms, with about twice as much going to the inboard relative to the outboard strike point.

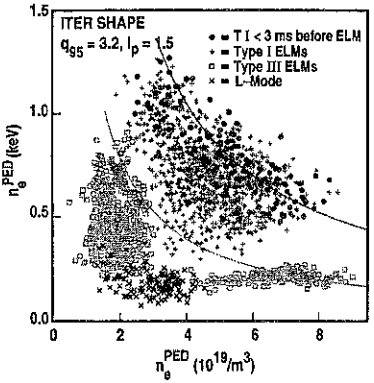

Fig. 4. Different classes of ELMs appear in distinct regions of $n-T$ space. Two different classes of type III ELMs appear at low temperature and low density (pressure gradient). Solid curves are constant pressure.

The ELM heat flux is distributed over roughly a factor of two larger area in the divertor than the steady-state heat flux. Bolometry indicates that less than about 5% of ΔE_{ELM} is radiated.

Two distinct classes of type III ELMs were identified. One class, which has been studied extensively on ASDEX-U [7], occurs below a critical edge temperature, and may be compatible with high H factor at high density where p^{PED} is comparable to that for type I ELMs. A second class of type III ELMs was identified at low density. These ELMs disappear above a critical heating power which scales as $I_p^{2.4}/n_e^2$, or, in terms of local quantities, when the edge pressure gradient is ablve a critical value which scales as I_p^2. Possibly because of this limitation on edge pressure gradient the H–mode pedestal and energy confinement is reduced in discharges with low density type III ELMs, typically $0.6 <$ H-ITER93-H < 0.9. This may be of concern since these ELMs can occur at powers near the H–mode threshold power if the density, or perhaps neutral pressure, is low enough.

4. Conclusions

We have shown a correlation between the H–mode pressure pedestal height and the energy confinement enhancement in ITER shape discharges on DIII–D which is consistent with the behavior of H in different ELM classes. The width of the steep gradient region was found to equally well fit the scalings $\delta/R \propto (\rho_{POL}/R)^{2/3}$ and $\delta/R \propto (\beta_{POL}^{PED}/R)^{1/2}$. The normalized pressure gradient α_{MHD} was found to be relatively constant just before a type I ELM. An estimate of T^{PED} for ITER gave 1 to 5 keV. We also estimate $\Delta E_{ELM} \cong 26$ MJ for ITER. We identified a distinct class of type III ELM at low density which may play a role in setting H at powers near the H–mode threshold power.

5. References

[1] M. Kotschenreuter *et al.*, Proc. 16th Int. Conf. on Plasma Phys. and Contr. Nucl. Fusion Res., Montréal (1996), IAEA-F1-CN-64/D1-5.
[2] R.E. Waltz *et al., Proc.* 16th Int. Conf. on Plasma Phys. and Contr. Nucl. Fusion Res., Montréal (1996), IAEA-F1-CN-64/D1-6.
[3] A. Hubbard *et al.*, Proc. 16th Int. Conf. on Plasma Phys. and Contr. Nucl. Fusion Res., Montréal (1996), IAEA-F1-CN-64/D1-6.
[4] K.H. Burrell *et al.*, Plasma Phys. and Contr. Fusion **34**, 1859 (1992).
[5] P. Gohil *et al.*, Phys. Rev. Lett. **61**, 1603 (1988).
[6] R.L. Miller *et al.*, Phys. Plasmas **4**, 1062 (1997).
[7] H. Zohm, Plasma Phys. and Contr. Fusion **38**, 105 (1996).

COMPARISON OF DISCHARGES WITH CORE TRANSPORT BARRIERS ON DIII-D AND JET*

T.C. Luce, B. Alper,[1] C.D. Challis,[1] G.A. Cottrell,[1] C. Gormezano,[1] C.M. Greenfield, J.C.M. deHaas,[1] G.T.A. Huysmans,[1] E.A. Lazarus,[2] D. O'Brien,[1] B.W. Rice,[3] A.C.C. Sips,[1] F.X. Söldner,[1] G.M. Staebler, E.J. Strait, T.S. Taylor, B.J.D. Tubbing,[1] A.D. Turnbull, M.R. Wade,[2] D.J. Ward,[1] and W. Zwingmann[1]
General Atomics, P.O. Box 85608, San Diego, California 92186-9784 USA

Introduction

Significant improvements in both normalized and absolute performance have been obtained in the DIII–D and JET tokamaks by optimizing the current and pressure profiles. These discharges produced the highest neutron rates in single-null plasmas in both machines (1.4 10^{16}/s for DIII–D, 5.6 10^{16}/s for JET). In DIII–D, β_N [$\beta / (I/aB)$] and H ($\tau_E/\tau_{ITER89P}$) have reached 4 simultaneously. In JET, confinement improves significantly (H up to 2.5 in L mode, up to 3 in H mode); however, MHD stability limits β to $\beta_N \leq 1.8$.

In both machines, a region of good confinement forms in the center of the discharges and moves radially outward with time at constant auxiliary power. The clearest signature of this region of good confinement is the large gradient in the ion temperature and rotation profiles. The steep gradient regions imply low transport; hence, the transition region to normal gradients is called a core transport barrier. The confinement improvement can also be seen in the electron density and, to a lesser extent, the electron temperature, but not necessarily over the same radial region. This behavior occurs while the edge parameters are typical of L mode and can persist in combination with the edge transport barrier characteristic of the H mode.

MHD Stability and Performance Limitations

The performance of both DIII–D and JET is limited by MHD stability; the maximum achieved β_N decreases with pressure peaking as seen in MHD stability calculations [1,2]. Figure 1 shows time histories of the β_N and pressure peaking for typical high performance discharges of both machines. As the transport barrier moves out with time, the pressure peaking lessens and the β_N rises. Without the reduction in pressure peaking, both machines find a disruptive limit in discharges with an L–mode edge [2,3]. The disruption on both machines typically is preceded by a rapidly growing $n=1$ mode. In DIII–D, further optimization involves initiating an H–mode transition at the proper time to avoid the disruption [4]. The subsequent edge density rise lowers the pressure peaking and allows higher β_N. The performance is limited by a variety of instabilities [3], but most commonly the limiting mode is a global mode similar to the "X event" which limits VH–modes on DIII–D and hot-ion

*Report of work sponsored by the U.S. Department of Energy under Contracts DE-AC03-89ER51114., DE-AC05-96OR22464, and W-7405-ENG-48.

[1]JET Joint Undertaking, Abingdon, Oxfordshire, U.K.

[2]Oak Ridge National Laboratory, Oak Ridge, Tennessee, U.S.A.

[3]Lawrence Livermore National Laboratory, Livermore, California, U.S.A.

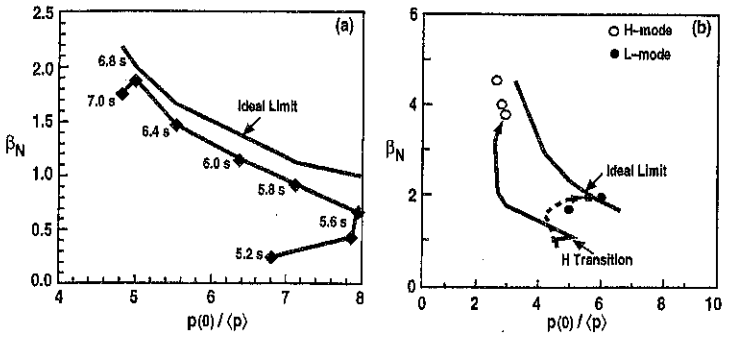

Fig. 1. Calculated β_N limit and measured β_N versus pressure peaking factor for (a) JET pulse 40847 and (b) DIII–D pulses 84736 (H mode) and 87009 (L mode). The DIII–D plot shows maximum performance times for other pulses.

modes on JET. However, $\beta_N > 4$ has been achieved. The optimization on JET has focused on real-time control of the auxiliary power to keep the plasma below the β limit with an L–mode edge. As the barrier expands, the pressure peaking drops and more power can be applied. The performance in JET with H–mode edge has not followed the favorable pattern in DIII–D. The fusion rate shows little or no improvement in JET following the H–mode transition. However, the majority of cases have an H–mode transition following an MHD event which strongly affects the rate of rise of the fusion rate. In both machines, the good core confinement reduces the loss power to the edge below the H–mode power threshold. In JET, a current ramp also raises the threshold. Thus, the discharges can stay in L mode despite a large input power. In JET, the MHD instability causes the barrier to be "leaky," raising the power flow to the edge above the H–mode threshold.

The core barrier in JET has not been observed to move past the $q = 2$ surface, and the contraction of the barrier coincides with a "soft" MHD instability. It is possible that the lower power density in JET provides insufficient drive for the barrier to pass the low order rational surfaces, while the higher power density on DIII–D allows the barrier to move past these rational surfaces to merge with the edge barrier. Experiments in DIII–D to optimize discharges in the same manner as JET are underway. The halt of the barrier expansion in JET could also be a result of differences in current profile. The inferred q profiles are quite different on DIII–D and JET. Figure 2 shows the q profiles from EFIT magnetic equilibrium reconstructions for both machines. For JET, magnetic and kinetic data are inputs to EFIT, and the mapping of ECE from both sides of the magnetic axis to magnetic coordinates is used to determine the radial position of the magnetic axis. The axis position determines $q(0)$ in this analysis. The time of the appearance of $q = 1.5$ outside the barrier in the reconstructed q profiles is coincident with a burst of MHD which limits the fusion performance. The appearance of a low-order rational surface with little magnetic or rotation shear to limit the mode width could be the cause of the barrier contraction and the H mode. This q profile evolution could also explain the observation that the H–mode transition occurs at roughly the same time

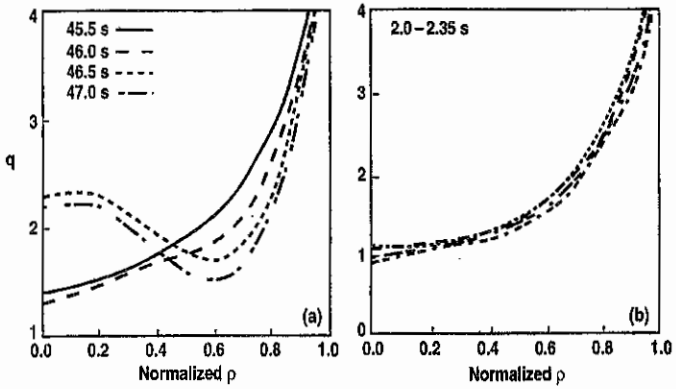

Fig. 2. Time evolution of q profiles for (a) JET pulse 40554 and (b) DIII–D pulse 88964.

independent of the discharge history. The timing of the appearance of $q = 1.5$ is controlled by the current ramp and electron temperature outside the barrier which are not closely correlated to the transport behavior inside the barrier. There are still significant questions about the q profiles shown on Fig. 2(a), especially whether the time evolution is consistent with the neoclassical Ohm's law. Calculations to check this are underway. For DIII–D, the magnetic, kinetic, and E_r-corrected MSE data are used in the EFIT reconstruction [5,6]. The profile is monotonic with $q(0) \simeq 1$ for the entire high performance phase. Bursting $m = 1/n = 1$ MHD activity is observed throughout, but there is no evidence of sawteeth. [Earlier reconstructions with magnetics only and reconstructions with uncorrected MSE data showed significantly higher $q(0)$ during the high performance phase.] The higher magnetic shear may lessen the effects of the barrier moving through such low-order rational surfaces.

Confinement

Both machines show reduction in the ion heat conduction to or below the neoclassical level inside the transport barrier. In the case of DIII–D plasmas with an H–mode edge, the good confinement region extends to the edge of the plasma and the time behavior is consistent with no conducted power in the ion channel. In JET plasmas with an L–mode edge, ion conduction is near neoclassical levels in the core and dominates the power balance outside the transport barrier [7]. The leading hypothesis to explain this behavior is that sheared $E \times B$ flows stabilize the long wavelength turbulence, leaving only neoclassical effects. Figure 3 shows a comparison of $\gamma_{E\times B}$, the measured $E \times B$ shear, with $\gamma_{\max}$ the maximum linear growth rate [8]. The DIII–D case shows that $E \times B$ shear exceeds $\gamma_{\max}$ at all radii at a time when the transport is consistent with no ion conduction across the entire plasma. The JET case, on the other hand, shows $\gamma_{\max}$ exceeds $\gamma_{E\times B}$ by a factor of 2 or more at a time when the good confinement region extends to $\rho = 0.5$. This result should be interpreted cautiously because the uncertainty in the q profile could significantly change $\gamma_{\max}$ and the $E \times B$ shear calculation assumes neoclassical poloidal rotation

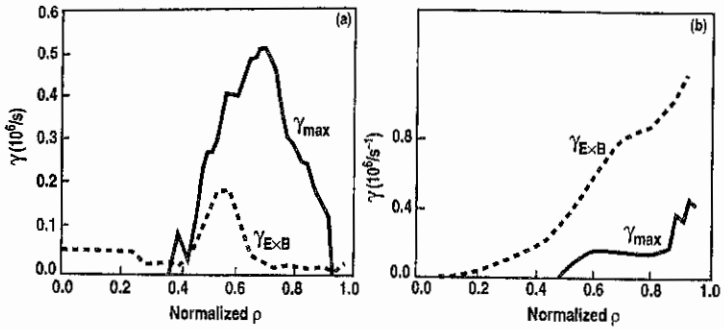

Fig. 3. Comparison of the $E\times B$ shearing rate with the maximum linear growth rate for (a) JET pulse 40554 and (b) DIII–D pulse 88964 at times near the peak performance.

in the absence of measurements. Neoclassical poloidal rotation does not model the DIII–D rotation measurements well [9]; therefore, the $E\times B$ shear may be significantly different. However, analysis of earlier times on the JET discharge show $\gamma_{max} > \gamma_{E\times B}$ by a factor of 5. Further quantitative work is necessary to draw conclusions about the consistency of the $E\times B$ stabilization hypothesis with JET data.

Conclusions

The basic phenomenology of discharges with core transport barriers is the same for DIII–D and JET. The limitations on performance in both cases are well described by MHD stability calculations. Since the discharge behavior of the two machines is so similar, it seems reasonable to apply a simple parameterization of fusion performance [10] which describes well the best performance discharges on DIII–D. The highest fusion performance shot on JET has $Q_{DD} = 3.1\ 10^{-3}$ at 3.2 MA. Scaling from the highest Q_{DD} DIII–D single-null discharge would predict $Q_{DD} = 4.2\ 10^{-3}$ for JET. Raising the plasma current to 4.0 MA would increase the projection to $6.6\ 10^{-3}$. Realization of such performance would require significant effort to develop lower q plasmas with an H–mode edge. Because the performance is so closely tied to the current profile, this class of discharges also shows significant potential for steady state if current profile control can be demonstrated.

References

[1] A.D. Turnbull *et al.*, Proc. 16th IAEA Fusion Energy Conf., Montréal, 1996.
[2] G.T.A. Huysmans *et al.*, this conference.
[3] E.J. Strait *et al.*, Phys. Plasmas **4**, 1783 (1997).
[4] E.A. Lazarus *et al.*, Phys. Rev. Lett. **77**, 2714 (1996).
[5] B.W. Rice, K.H. Burrell, L.L. Lao, Nucl. Fusion **37**, 517 (1997).
[6] B.W. Rice, this conference.
[7] G.A. Cottrell, this conference.
[8] M. Kotschenreuther, Bull. Am. Phys. Soc. **37**, 1432 (1992).
[9] G.M. Staebler, this conference.
[10] E.A. Lazarus *et al.*, Nucl. Fusion **37**, 7 (1997).

ENERGY AND PARTICLE TRANSPORT IN THE RADIATIVE DIVERTOR PLASMAS OF DIII-D*

A.W. Leonard, S.L. Allen,† N.H. Brooks, T.E. Evans, M.E. Fenstermacher,† D.N. Hill,† R.C. Isler,‡ C.J. Lasnier,† M.A. Mahdavi, R. Maingi,‡ R.A. Moyer,◊ T.W. Petrie, G.D. Porter,† M.J. Schaffer, M.R. Wade,‡ J.G. Watkins,Δ W.P. West, D.G. Whyte,◊ R.D. Wood†
General Atomics, P.O. Box 85608, San Diego, CA 92186-5608

It has been argued [1] that divertor energy transport dominated by parallel electron thermal conduction, or $q_{\|} = -\kappa T_e^{5/2} dT_e/ds_{\|}$, leads to severe localization of the intense radiating region and ultimately limits the fraction of energy flux that can be radiated before striking the divertor target. This is due to the strong $T_e^{5/2}$ dependence of electron heat conduction which results in very short spatial scales of the T_e gradient at high power densities and low temperatures where deuterium and impurities radiate most effectively. However, we have greatly exceeded this constraint on DIII-D with deuterium gas puffing which reduces the peak heat flux to the divertor plate a factor of 5 while distributing the divertor radiation over a long length as shown in Fig. 1. We find that electron thermal conduction cannot account for the measured distribution of divertor radiation and energy transport. However, plasma convection at the ion sound speed through much of the divertor is consistent with our observations.

The transport of energy parallel to the magnetic field in the scrape-off-layer (SOL) can be described by [2],

$$\frac{d}{ds}\left[-\kappa T_e^{5/2}\frac{dT_e}{ds} + nv_{\|}\left\{\frac{5}{2}(T_i + T_e) + \frac{1}{2}m_i v_{\|}^2 + I_o\right\}\right] = S_E \qquad (1)$$

where s is the parallel field line length, κ is the parallel electron thermal conductivity, T_e and T_i are the electron and ion temperatures respectively, n is the plasma density, m_i is the ion mass, $v_{\|}$ is the plasma fluid velocity parallel to the magnetic field, I_o is the atomic ionization potential (13.6 eV for a deuterium atom) and S_E represents volume sources and sinks of energy such as radiation, ionization, neutral collisions and charge-exchange. In this formulation we have combined the electron and ion energy and disregarded ion viscosity and perpendicular diffusion of energy. The first term in the energy transport equation is electron thermal conduction. The second group of terms is convection and allows transport of energy without a temperature gradient. Here we have included the ionization potential of the plasma in the convective term because we do not experimentally determine the ionization distribution, an energy sink, nor do we determine the fraction of radiation and target plate heat flux that results from plasma recombination.

To compare our radiating divertor plasmas to the energy transport described in Eq. (1), we use a divertor equilibrium with a lower X-point, as shown in Fig. 2, which allows divertor Thomson

*Work supported by U.S. Department of Energy under Contracts DE-AC03-89ER51114, W-7405-ENG-48, DE-AC05-96OR22464, DE-AC04-94AL85000 and Grant No. DE-FG03-95ER54294.
†Lawrence Livermore National Laboratory.
‡Oak Ridge National Laboratory.
◊University of California, San Diego.
ΔSandia National Laboratories.

scattering diagnostic (DTS) [3,4] measurement of the divertor plasma electron temperature and density. Sweeping the divertor plasma across the DTS measurement locations, while holding plasma conditions constant, provides 2D profiles of temperature and density. We obtain divertor data from ELMing H-mode plasmas with a plasma current, of 1.4 MA and safety factor q_{95} of ~4.2 and injected power of about 6 MW. With strong deuterium puffing, ~100 Torr-ℓ/s, we produce intense divertor radiation, shown in Fig. 2, and reduce peak divertor plate heat flux by a factor of 3–5, or a factor of 5–10 if we subtract the contribution of radiative heating of the target plate [5].

The power flowing through the outboard divertor leg is described by $\nabla \bullet q_{\|} = S_E$ where $q_{\|}$ is the parallel heat flux, the sum of conduction and convection, and S_E, the plasma volume sources and sinks of energy, is due principally to atomic radiation. For this analysis we treat the SOL below the X-point as a 1D plasma as a function of $L_{\|}$, the field line parallel distance to the divertor plate. The plasma radiation, ε ($L_{\|}$), measured by two poloidally separated bolometer arrays [6], is integrated radially through the divertor SOL to produce a 1D profile of radiation, $\varepsilon_{sol}(z)$, as a function of distance from the divertor plate. We calculate the total energy flowing in the divertor, $Q_{tot}(z)$, by starting with the divertor target heat flux measured by an IR camera and integrating the 1D radiation profile. Contributions from plasma radiation are subtracted from the target heat flux. We finally convert to energy flux density, $q_{\|}$ ($L_{\|}$), by dividing by the cross-sectional area of the SOL perpendicular to the magnetic field. The SOL area normal to the magnetic field lines is determined by the heat flux width at the divertor plate in conjunction with magnetic equilibrium measurements. The parallel path length, $L_{\|}$ is determined by mapping of a field line in the center of the SOL.

With no gas puffing we find the electron temperature profile to be consistent with conductive transport. The $q_{\|}$ profile, shown in Fig. 3(a) indicates 40 MW/m^2 flows into the outboard divertor leg below X-point with only about ~15% of it radiated before striking the divertor plate. Assuming parallel electron thermal conduction and then integrating $q_{\|} = -\kappa T_e^{5/2} dT_e/ds$ from Eq. (1) with T_e of 20 eV near the target we arrive at the conduction-fitted T_e profile as plotted in Fig. 3(a). We compare this fitted T_e profile with the T_e profile measured by DTS, averaged over the same SOL

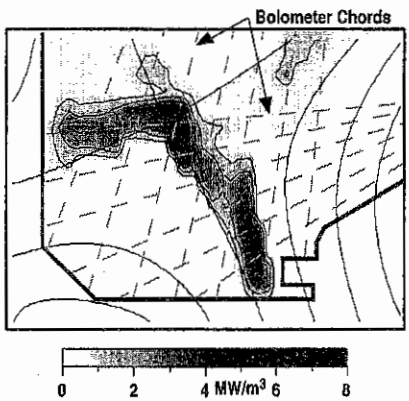

Fig. 1. The radiation profile for a radiative divertor in extended geometry in DIII-D.

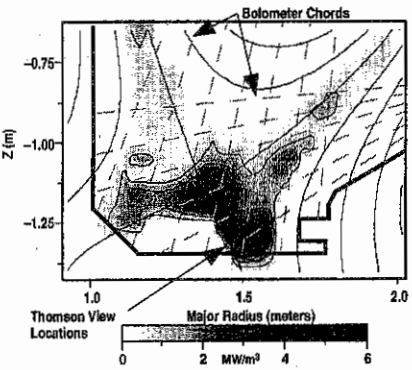

Fig. 2. The 2D radiation profile and divertor geometry for radiative plasmas used in heat transport analysis. Also shown are the bolomter view chords and the Divertor Thomson System measurement locations.

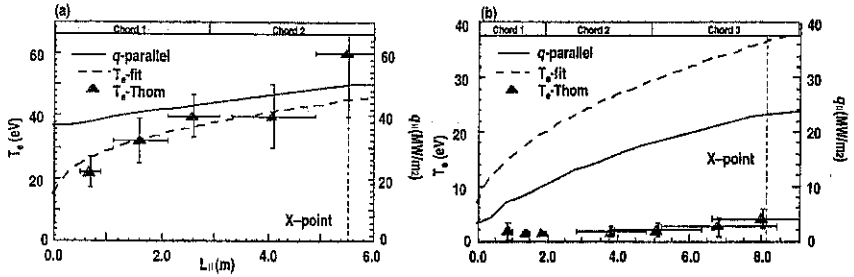

Fig. 3. The outboard divertor energy flux analysis for (a) standard ELMing H-mode and (b) radiative divertor through deuterium puffing. Shown are the energy flux profile, $q_{||}$, the fitted T_e profile for conduction dominated transport and measurements of T_e from divertor Thomson scattering measurements. Shown at the top of the graphs are the approximate view locations of the horizontal viewing bolometer chords.

width as that used in the $q_{||}$ calculation. The measured T_e, increasing from ~20 eV near the target to more than 40 eV at the X-point, is seen to be consistent with that inferred from conduction dominated energy transport.

Electron conduction cannot support the mesured energy flux in our highly radiating divertor plasmas. The energy transport in the divertor under these conditions is summarized in Fig. 3(b). Approximately 25 MW/m^2 of power flows into the divertor below the Xpoint, of which almost 85% is radiated away before reaching the divertor plate. The lower energy flux density into the divertor for the radiative case is due to a wider SOL width at the divertor plate for these plasmas and an increase in radiation above the Xpoint. The predicted T_e profile required to support the energy flux through conduction is also plotted in Fig. 2(b). Even for the modest energy flux at the divertor plate for these conditions T_e must rise above 15 eV in a relatively short parallel distance of ≤1 m, or ≤5 cm of poloidal length which is <15% of the total divertor length. The predicted T_e is in stark contrast to our DTS measurements where T_e is about 2 eV throughout the divertor. This level of T_e is able to support through conduction at most 5% of the energy flux we observe in these conditions.

Convection of plasma energy at the ion sound speed can account for our observed energy flux during these highly radiative conditions. Assuming the convection terms of Eq. (1) carry all of the energy flux we can solve for the required flow velocity using the measured profiles. The required Mach number, $c_s = \left[Zk(T_e + T_i)/m_i\right]^{1/2}$, is plotted in Fig. 4. The measured energy transport is satisfied if the plasma flows through the divertor at the ion acoustic speed before slowing as it nears the divertor target. Such an extended region of high plasma flow may follow as a consequence of T_e dropping to ~2 eV, so that the ionization mean free path is large enough (~30 cm) to shift the ionization far upstream near the X-point.

The observed radiation in the divertor is extracted from the plasma thermal energy, through electron excitation, and from the ionization potential through plasma recombination. To estimate the degree of plasma recombination we convert the inferred parallel plasma flow into particle flux, as plotted in Fig. 4. The uncertainty is large, but the data indicates that about half of the peak particle flux is lost, presumably through recombination, before reaching the divertor target.

Several other physical processes may also contribute to energy transport in the divertor, but their effects don't change the basic conslusions drawn above. In treating the SOL as 1D we have neglected

perpendicular diffusion which can widen the SOL from the X–point to the divertor. We have chosen the width of the SOL as that characteristic at the divertor plate. Because we have chosen the width of the SOL as that characteristic at the divertor plate any perpendicular diffusion may result in a more narrow upstream SOL than assumed in our analysis. This effect would lead to only a slightly greater T_e needed for conduction dominated transport due to the strong $T_e^{5/2}$ dependence of thermal conductivity. It is also possible for charge-exchange and ion-neutral collisions to carry away additional energy from the plasma. Neutrals likely contribute to our measured divertor target heat flux. Neutrals may also heat the divertor floor outside of the region of the SOL strike-point. This represents additional energy loss from the divertor plasma that we do not measure, which in turn may yield a greater $q_{\|}$ upstream than our analysis indicates. The implications of this additional loss are the same as that of perpendicular diffusion we discussed above.

Edge-localized modes (ELMs) in these plasmas may play a role in the power balance of the divertor. The bursts of energy and particles due to ELMs may temporarily heat the SOL and divertor plasma allowing more power to be conducted for a short time. Analysis of ELMs on DIII–D [7] has shown that ≤10% of the injected power is dissipated in the outboard divertor during the brief ELM pulse, representing ≤20% of the total divertor power for these radiative plasmas. Though ELMs may play a role in the dynamic behavior of the divertor they do not account for the power flow observed in the experiment. Convection is still needed to explain our observed energy transport.

We have demonstrated nearly complete dissipation of of energy flowing into the DIII–D divertor. Convection allows high power levels to be transported through regions of cold plasma such that radiative cooling and finally recombination can occur through the divertor region. The convective flow is likely created by upstream ionization due to the low T_e and ionization rate in the divertor. More work is needed before these concepts can be applied to a high power density tokamak such as ITER. The plasma upstream of the convective zone must be cooled such that ionization, which produces the convection, can occur. Finally this must be implemented in such a way that confinement in the core plasma is not degraded.

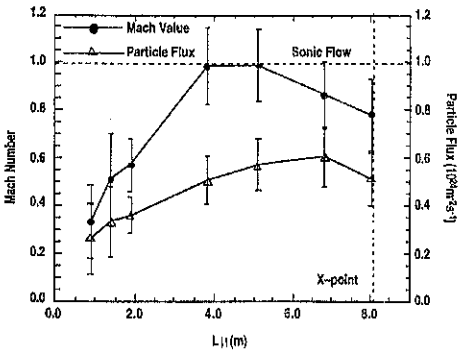

Fig. 4. The flow velocity, in Mach value, required to support the parallel energy flux through convection. Also plotted is the particle flux associated with the flow.

References

[1] K. Lackner, *et al.*, Fusion Engineering and Design **22** 107 (1993).

[2] S.I. Braginskii, "Transport Processes in a Plasma," in "Reviews of Plasma Physics," Vol 1 (M.A. Leontovich, Ed.) Consultants Bureau, New York 1965 p. 205.

[3] T.N. Carlstrom, *et al.*, Rev. Sci. Instrum. in print.

[4] S.L. Allen, *et al.*, J. Nucl. Mater., in print.

[5] T.W. Petrie, *et al.*, Nucl. Fusion **37** 321 (1997).

[6] A.W. Leonard, *et. al.*, Rev. Sci. Instrum. **66**, 1201 (1995).

[7] A.W. Leonard, *et al.*, J. Nucl. Mater., in print.

RECENT H-MODE DENSITY LIMIT EXPERIMENTS ON DIII-D*

M.A. Mahdavi, R. Maingi,† R.J. La Haye, T.C. Jernigan,† T.W. Petrie, L.R. Baylor,† A.W. Hyatt, A.W. Leonard, M. Murakami,† L.W. Owens,† R.T. Snider, R.D. Stambaugh, M.R. Wade,† J.G. Watkins,# W.P. West, D.G. Whyte,Δ R.D. Wood,◊ and The DIII-D Team
General Atomics, P.O. Box 85608, San Diego, California 92186-5608 USA

A vast body of tokamak data [1–4] is in good agreement with the empirical density limit scalings proposed by Hugill and Greenwald. These are of the form $n_{Hugill} \sim B/Rq$ and $n_{GW} \sim I_p/\pi a^2$, respectively, which differ only in the elongation dependence, roughly $(1 + \kappa^2)/2$, implicit in the definition of the safety factor q. These scalings have common puzzling features of showing no dependence on either impurity concentration or heating power, since the density limit is frequently correlated with a rapid rise of the edge radiation. Despite the resiliency of these scalings, several machines under restrictive conditions have operated at densities well above the predictions of these scalings, albeit with pellet injection and at varying degrees of confinement degradation. Furthermore, data from several machines display a weak dependence on heating power. These results cast doubt on the universal validity of both of these scalings. Nevertheless the fact remains that access to densities above Hugill-Greenwald scaling is very difficult. A number of theories [5–8] based on radiative power balance in the plasma boundary have explained some but not all features of tokamak density limit behavior, and as ITER design studies recently brought to focus, a satisfactory understanding of this phenomenon is lacking. Motivated by a need for better understanding of effects of density and fueling on tokamak plasmas in general, we have conducted a series of experiments designed to identify and isolate physical effects suspected to be directly or indirectly responsible for the density limit. The physical effects being considered include: divertor power balance, MARFE [9,10], poloidally symmetric radiative instabilities, MHD instabilities, and transport. In this paper we will first present a brief summary of the experimental results up to the writing of this paper. The remainder of the paper is devoted to a comparison of our data at the onset of the MARFE instability with predictions of theory and the implication of the results on access to densities beyond the Hugill-Greenwald limit.

Normally, in DIII-D, with either gas or pellet fueling, a density limit in the range 0.7–1.1 Greenwald limit is observed. This limit is seen following divertor detachment when the most prominent radiation zone reaches the X-point, and is attributed to the divertor power balance limit. We were able to bypass this limit [3] by lowering the SOL density relative to the line average density. This was achieved by simultaneous divertor pumping and pellet injection. The main difficulties encountered in increasing the density beyond this point were associated with deleterious effects of injection of large pellets (D = 2.7 mm, $\delta N/N \approx 30\%$), as described in the following paragraph. Once these problems were resolved, densities well above n_{GW} were accessed. As shown in Fig. 1, in H-mode plasmas densities = 1.5 × n_{GW} were

*Work supported by the U.S. Department of Energy under Contract Nos. DE-AC03-89ER51114, DE-AC05-96OR22464, DE-AC04-94AL850000, W-7405-ENG-48, and Grant No. DE-FG03-95ER54294.
†Oak Ridge National Laboratory, Oak Ridge, Tennessee.
#Sandia National Laboratories, Livermore, California.
ΔUniversity of California, San Diego, California.
◊Lawrence Livermore National Laboratory, Livermore, California.

maintained for several hundred milliseconds. In the discharge shown in Fig. 1, global energy confinement time peaked at the ITER93-H–mode scaling level before decaying due to high radiation from the plasma core. Strong attenuation of the neutral heating beam was a main contributor to the ultimate central radiation collapse. It is important to note that the density profiles in these plasmas were only moderately peaked, as the line average density was only 50% above the H–mode pedestal value a few centimeters inside the separatrix.

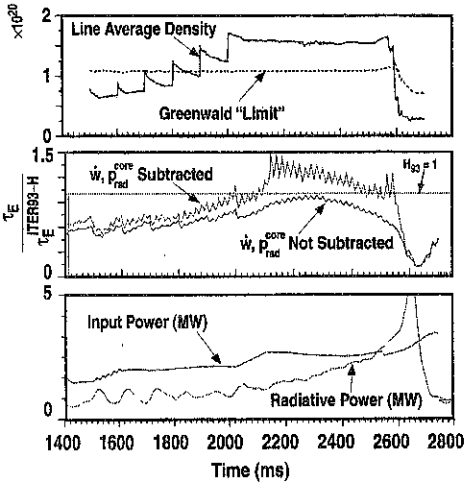

Fig. 1. H–mode confinement, $\geq \tau_E^{ITER-93H}$, at $\bar{n}_e = 1.5 n_{GW}$ is attained. Excessive radiation from plasma center degrades confinement, and ultimately leads to radiative collapse.

Pellets invariably triggered low mode number rotating MHD modes which greatly complicated access to high densities. These modes often reduced energy and particle confinement back to L–mode levels and occasionally locked and caused disruptions. Occasionally the modes continued to grow long after the pellet density perturbation had decayed away and when the current profile appeared to be stable to classical and neoclassical tearing modes. Furthermore, at times, the modes stabilized after further density increase. The initial excitation of these modes might be explained by the large adiabatic temperature perturbation at low rational surfaces; however additional physics is needed to explain their continued growth when the current profile seems to be stable. A phenomenon similar to the m=1, n=1, "snake" mode [11] is suspected, and is the subject of continuing investigation.

Several other deleterious effects of pellet fueling were observed which reduced the attainable parameter window for high density plasmas. First, spontaneous or pellet triggered ELMs expelled a large fraction of the plasma density which frequently increased the fueling demand beyond the available injection rate. This problem was mitigated only by lowering the ELM frequency through lowering the heating power relative to the plasma current, since the ELM frequency scales with P_{INJ}/I_p^2. Second, near the H–mode power threshold, pellets caused transient H-L transitions, which also caused unacceptable particle loss. This problem was avoided by lowering B_T since the power threshold scales linearly with B_T.

The MARFE condensation instability is a density dependent phenomenon which has been suspected to be the cause of the density limit in tokamaks. Figure 2 shows data from two discharges, one with $q_{95} = 9$, in which a MARFE occurred at a line density of 5×10^{19} corresponding to ~0.8 n_{GW}. The second discharge with $q_{95} = 3.2$ reached a line density of 1.8×10^{20}, corresponding to $2 \times n_{GW}$ up to the symmetric radiation limit without MARFE formation. This comparison suggests that the normally observed tokamak density limit is not due to MARFE instability. However, a closer examination shows that the same procedures

used to access high densities may have stabilized the MARFE in the high density discharge. The MARFE marginal stability condition is given by [6]:

$$\kappa_{\perp}\left(\frac{\partial^2\tilde{T}}{\partial r^2}\right)-\kappa_{\parallel}\left[\frac{\tilde{T}}{(qR)^2}\right]\cong n_e^2 T^2 \sum_I \frac{n_I}{n_e}\frac{d}{dT}\left[\frac{1}{T^2}L_I\left(T,\frac{n_0}{n_e}\right)\right]\tilde{T} \quad , \qquad (1)$$

where $\tilde{T}$ is the temperature perturbation, $L(T, n_o/n_e)$ is the radiation rate, and $\kappa_{\parallel} = (\kappa_0/Z_{eff})\, T^{5/2}$ is the Spitzer parallel conductivity. The right hand side of the equation represents the radiation destabilizing term. The left hand side terms are owing to perpendicular and parallel conduction, respectively, and are both stabilizing. We have tested the plasma parameters of the discharges of Fig. 2 against this criterion, using coronal equilibrium radiation rates from ADPAK [12]. The first term on the left was ignored, since for radial scale lengths >1 cm and $\kappa_{\perp} \cong 7 \times 10^{16}$ erg cm^{-1} eV^{-1} [13], the second term dominates. Then Eq. (1) reduces to

$$\left\{\sum_I \frac{n_e}{n_I}\left(\frac{1}{\sqrt{T}}\right)\frac{d}{dT}\left[L_I\left(T,\frac{n_o}{n_e}\right)\right]\right\}^{-1/2} \geq \left(qR\sqrt{\frac{Z_{eff}}{\kappa_o}}\right)n_e \quad \text{(for stability)} \qquad (2)$$

In Fig. 3 we have plotted the left hand side of Eq. (2) for measured impurity concentrations of 1% carbon and 0.06% oxygen. The solid curve corresponds to the coronal equilibrium [$(n_o/n_e) = 10^{-7}$]. The dashed curve incorporates the nonequilibrium effect of a uniform neutral distribution of $n_o/ne = 10^{-3}$. Modeling [14] by B2.5 and DEGAS codes show that a neutral concentration of this magnitude exists between ρ = 0.99 and $\rho = 1$ radii. Open circles in the figure represent the RHS of Eq. (2) using data for the discharge with MARFE before the MARFE formation. For this discharge, three points, ρ = 0.96–0.99, are near or inside the unstable zone. In contrast for the discharge with no MARFE formation (solid diamonds), all experimental points are well within the stable zone. Although in this analysis, the oxygen concentration is more than a factor of ten lower than that of carbon, since the oxygen radiation peak occurs at a higher temperature than carbon, oxygen is a significant contributor to instability. The stability diagram of Fig. 3 demonstrates the critical importance of boundary plasma temperature. In the temperature range of 10 to 100 eV the stability threshold increases rapidly with T_e. Above 100 eV, the temperature dependence is weak but the density ceiling in this region is high compared to normal tokamak operating densities. Thus in the divertor configuration an effective way of increasing the MARFE threshold is by increasing the separatrix temperature through SOL density control, as was done in present experiments.

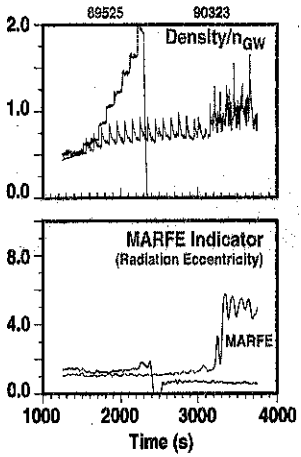

Fig. 2. Solid curve: example of high density H–mode shots with no MARFE formation [$\bar{n}_e(\max) = 1.8\times 10^{20}\,m^{-3} \cong 2\ n_{GW}$, $I_p = 1.3$ MA]. The dashed curve shows a high q L–mode edge plasma with MARFE formation at low density [$\bar{n}_e(\max) = 0.6\times 10^{20}\,m^{-3} \cong 0.8\ n_{GW}$, $I_p = 0.7$ MA].

A power law fit to the LHS of Eq. (2) shows that the local MARFE stability limit for oxygen impurity in coronal equilibrium in the 30–100 eV range scales as $n_{crit} \sim T_e^4/qR[(n_I/n_e)Z_{eff}]^{0.5}$. Now we wish to eliminate T_e in favor of n_e. We define the pressure profile factor $g(\rho)$ by $n(\rho)T(\rho) \equiv g(\rho)\langle p\rangle$. By substituting for $\langle p\rangle$ from the definition $\tau_E \equiv 1.5\langle p\rangle V/P$, where V is the plasma volume, we obtain $T(\rho) \sim g(\rho)\tau_E/Vn(\rho)$. Now using the $\tau_E = \tau_E^{ITER\text{-}89P}$ confinement scaling, we obtain a local MARFE threshold scaling of the form:

$$n_{crit}(\rho) \sim g(\rho)^{0.8}\, I_p^{0.96}\, a^{-1.9}\, \xi^{-0.11}\, P^{0.17}\, R^{0.17}\, B^{0.04}\left[\kappa^2\left(1+\kappa^2\right)\right]^{-0.22} .$$

This result with an approximate I/a^2 scaling, is remarkably insensitive to oxygen concentration and B_T, and has weak dependencies on heating power, elongation, and major radius, and might explain the origin of the Hugill-Greenwald scalings. The scaling shows that since the inner plasma has a much higher MARFE limit, the global MARFE limit can be increased by density peaking. In the divertor configuration, however, as discussed above, it is possible to maintain the separatrix temperature high and thus achieve high line average densities without density peaking.

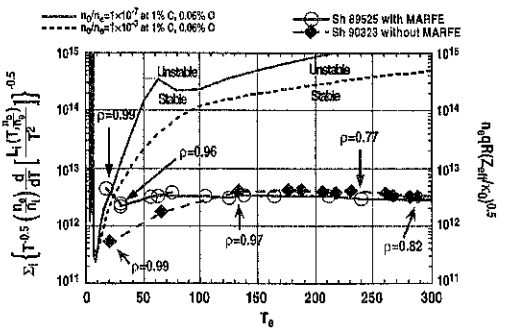

Fig. 3. Comparison of edge plasma parameters measured just inside the separatrix with the MARFE threshold criteria. The solid curve represents calculated value of LHS of Eq. (2) for coronal equilibrium. The dashed curve incorporates radiation enhancement due to a neutral concentration of $n_o/n_e = 10^{-3}$. The open circles represent the experimental values for the RHS of Eq. (2) for the discharge with MARFE formatrion, the solid diamonds correspond to the discharge that reached $n_e = 2 \times n_{GW}$ without MARFE formation.

In summary, we have demonstrated compatibility of high confinement at densities above the Hugill-Greenwald limit without strong density peaking. An explanation for the origin of Hugill and Greenwald scalings is offered which is based on the MARFE instability. We conclude that ITER, with a separatrix temperature of ≥ 150 eV, can safely access densities well above the Greenwald limit without MARFE instability.

[1] Hugill, S., Proc. 2nd Joint Varenna-Grenoble Symp., Brussels, 775 (1980).
[2] Greenwald, M., et al., Nucl. Fusion **28**, 2199 (1988).
[3] Maingi, R., et al., Phys. Plasmas 4, 1752 (1997), and references thereof.
[4] Petrie, T.W., et al., Nucl. Fusion **33**, 929 (1993).
[5] Drake, J., Phys. Fluids **30**, 8 (1987).
[6] Wesson, J.A., and Hender, T.C., Nucl. Fusion **33**, 1019 (1993).
[7] Ohyabu, N., Nucl. Fusion **19**, 1491 (1979).
[8] Borras, K., Nucl. Fusion **31**, 1035 (1991).
[9] Baker, D.R. , et al., Nucl. Fusion **22**, 807 (1982).
[10] Lipschultz, B., et al., Nucl. Fusion **22**, 977 (1984).
[11] Wesson, J.A., Plasma Physics and Controlled Fusion **37**, 337 (1995).
[12] Hulse, R., et al., Nucl. Techn./Fusion **3**, 259 (1983).
[13] Porter, G.D., et al., Phys. Plasmas **3**, 1967 (1996).

IMPACT OF EDGE CURRENT DENSITY AND PRESSURE GRADIENT ON THE STABILITY OF DIII-D HIGH PERFORMANCE DISCHARGES*

L.L. Lao, J.R. Ferron, E.J. Strait, V.S. Chan, M.S. Chu, E.A. Lazarus,† T.C. Luce, R.L. Miller, G.A. Navratil,Δ T.H. Osborne, P.A. Politzer, B.W. Rice,◊ T.S. Taylor, and A.D. Turnbull
General Atomics, P.O. Box 85608, San Diego, California 92186-5608 USA

One of the major goals of advanced tokamak research is to develop plasma configurations with good confinement and improved stability at high β. In DIII–D, various high performance configurations with H– and VH–mode edges have been produced. These include discharges with poloidal cross sections in the forms of dee and crescent shapes, single- and double-null divertors, and with various central magnetic shear profiles and current profile peakedness. All these discharges exhibit enhanced confinement in the outer plasma region which leads to a large edge pressure gradient and a large edge bootstrap current driven by this steep pressure gradient. These edge conditions often drive an instability near the edge region which can severely degrade the discharge performance [1–3]. An understanding of this edge instability is essential to sustain and enhance discharge performance.

Experimental Observations

This edge instability has been observed in DIII–D H– and VH–mode discharges with various plasma poloidal cross sections including single- and double-null divertors, dee and crescent shapes and is often preceded by a magnetic precursor with toroidal mode number $n > 1$. This is illustrated in Fig. 1. The magnetic perturbation of the precursor is localized both poloidally in the bad curvature region and toroidally with a fast growth time $\gamma^{-1} \approx 20$–150 μs and usually rotates in the electron diamagnetic drift direction. This rotational direction is consistent with a location near the plasma edge where the **E×B** drift is dominated by the diamagnetic drift associated with the large edge pressure gradient. The magnetic precursor may consist of a single pulse as shown in Fig. 1(b,d) or may be preceded by a continuous n=1 or n=2 mode in the plasma core depending on the q profiles as shown in Fig. 1(f). The instability has been observed over a wide range of normalized beta $\beta_N = 2.5$-5.0 including discharges with negative or weak central magnetic shear and high ℓ_i.

As shown in Fig. 1(a,c,e) this instability may lead to a drop in the electron temperature T_e in the plasma outer region, a slight change of T_e in the plasma outer region, or a drop of T_e across the entire plasma. Consistent with these changes in T_e, equilibrium reconstructions using magnetic measurements indicate that the plasma stored energy saturates instead of continuing to rise, when the change in T_e is slight; or decreases by 10%–12% when the drop in T_e is large. Similar changes have also been observed in the soft x-ray (SXR) measurements. In the particular discharge shown in Fig. 1(e), the decrease of plasma temperature across the

*Work supported by the U.S. Department of Energy under Contract Nos. DE-AC03-89ER51114, DE-AC05-96OR22464, W-7405-ENG-48, and Grant No. DE-FG03-95ER54294.
†Oak Ridge National Laboratory, Oak Ridge, Tennessee 37830, U.S.A.
ΔColumbia University, New York, New York 10027, U.S.A.
◊Lawrence Livermore National Laboratory, Livermore, California 94551, U.S.A.

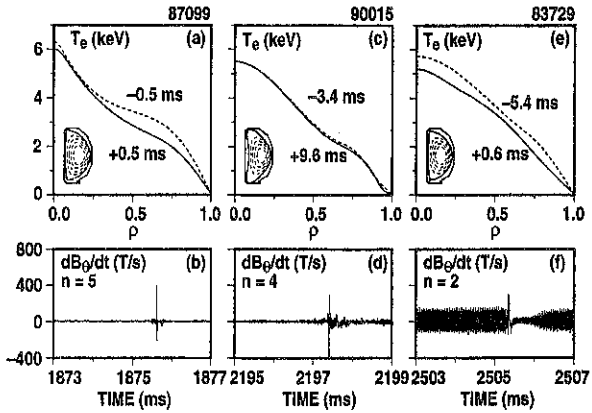

Fig. 1. Magnetic precursors and radial electron temperature profiles before (dashed) and after (solid) the edge instability.

entire plasma volume may be a result of the interaction between a continuous n=2 mode in the plasma core and the n=2 edge mode in the outer plasma region.

The attainable β values decrease when the average current density increases in the plasma outer edge region and are consistent with the previously observed operational β limit of $\beta_N \approx 4\,\ell_i$ [4,5]. This is illustrated in Fig. 2 for a group of double-null divertor discharges with plasma current I = 2–2.2 MA. Here, $\langle J\rangle_N = \langle J\rangle_{95}^{1}/\langle J\rangle_0^1$ is the average current density outside of the 95% normalized poloidal flux surface divided by the average current density across the entire plasma volume and

$$\langle J\rangle_{x_1}^{x_2} = \left[\int_{x_1}^{x_2} d\psi \oint d\ell \left(J_T/RB_p\right)\right] \Bigg/ \left[\int_{x_1}^{x_2} d\psi \oint \left(d\ell/RB_p\right)\right].$$

As shown in Fig. 2(a), discharges with high early beam injection tend to have larger $\langle J\rangle_N$ due to the slower penetration of the plasma current into the central core and have a lower β limit. Since ℓ_i is also a measurement of the distribution of the current density, this decrease of β_N with $\langle J\rangle_N$ can also be expressed as a variation with ℓ_i and is consistent with the previously observed operational β limit of $\beta_N \approx 4\ell_i$ [4,5]. This is shown in Fig. 2(b).

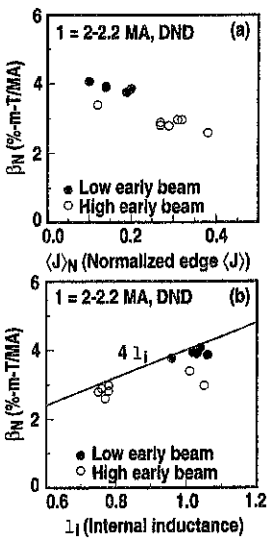

Fig. 2. Dependence of the beta limit on normalized edge current density $\langle J\rangle_N$ and ℓ_i.

Theoretical Analysis and Simulations

Near the onset of this edge instability, the discharges often have access to the second high n ideal ballooning stability regime in the plasma outer edge region but are unstable to the ballooning mode in the region near the normalized poloidal flux $\psi_N \approx 0.9$. This is illustrated in Fig. 3. As shown in Fig. 3(a,b), although the crescent and the dee shaped discharges have very different ballooning stability in the core region, near the onset of the edge instability both have access to the second ballooning stability regime in the edge region and are unstable to the ballooning mode in the region near the edge. This access to the second ballooning stability regime in the outer edge may be necessary to facilitate the development of the very steep edge pressure gradient often observed in DIII–D VH–mode discharges. Stability to the ballooning mode near the edge region $\psi_N \approx 0.9$ may play a participating role in the edge stability by further steepening the pressure gradient outside of the region. Further study is necessary to clarify the importance of the ballooning stability.

The results of ideal stability calculations are consistent with many observed features of the instability. Stability analysis using both experimental and simulated equilibria suggests the higher n modes are more unstable and both the large edge pressure gradient and high edge current density are destabilizing. This is illustrated in Fig. 4 using a sequence of simulated equilibria based on the experimental information from an actual discharge near the occurrence of this edge instability. These equilibria all have similar double-null divertor shape, q_{95} values of 5.5, ℓ_i values of 0.75, but different radial thickness of the steep pressure

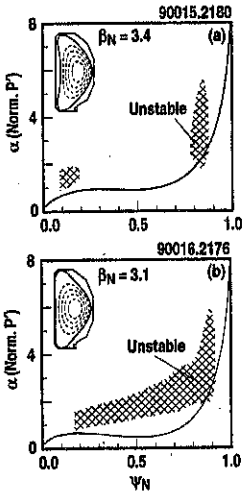

Fig. 3. Ideal ballooning stability of a crescent and a dee shaped discharge. Solid line indicates measured value.

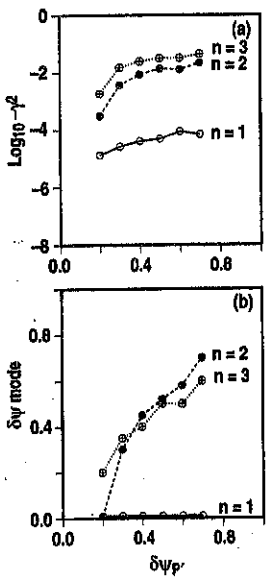

Fig. 4. Variation of growth rate and mode width with radial thickness of steep pressure gradient region.

gradient region as measured in terms of the normalized poloidal flux $\delta\psi_P$. For simplicity, the pressure gradient stream function $P'(\psi)$ is taken to have the shape of a step function with a region of small $P'(\psi)$ in the plasma core and a region of large $P'(\psi)$ in the outer edge. Both $P'(0)$ and $P'(1)$ are kept constant in the simulations. The ideal stability against the n=1,2, and 3 modes are computed using the GATO code [5] with a conducting wall at the surrounding DIII–D vacuum vessel. As shown in Fig. 4(a), the equilibria are stable to the ideal n=1 mode at all values of $\delta\psi_P$ considered but are unstable to the higher n=2 and 3 modes when $\delta\psi_P > 0.2$. Here, γ is the linear growth rate of the ideal mode. Note that both β and β_N increase with $\delta\psi_P$. Due to the finite grid size, the values of γ against the n=1 mode remain positive but small although it is stable against the n=1 mode as indicated by the radial mode structure. As shown in Fig. 4(b), the radial width of the mode $\delta\psi_{mode}$ increases with $\delta\psi_P$ which suggests that the discharge performance degradation may depend on the radial thickness of the steep pressure gradient region. Increasing $P'(1)$ tends to make the equilibria more unstable.

Summary

The performance of DIII–D high performance H– and VH–mode discharges is often limited by an edge instability which has $n > 1$. The attainable β values decrease with the average current density in the plasma outer edge region and are consistent with the previously reported operational β limit of $\beta_N \approx 4\,\ell_i$. The instability is driven primarily by the large edge pressure gradient and the large edge bootstrap current associated with the pressure gradient. The results of ideal stability calculations are consistent with many observed features of the instability and suggest that the performance degradation may depend on the radial thickness of the steep pressure gradient region. For sustainment and enhancement of the discharge performance it is essential to control the large edge pressure gradient and its radial thickness. Methods being proposed include use of external coils to produce an edge ergodic region and shaping of poloidal cross section to limit the edge second ballooning stability access, and reduce the first regime limit.

[1] Strait, .E.J.., et al., Proc. 20th EPS Conf., Lisbon, 1993, in Controlled Fusion and Plasma Physics Vol. 17C, Part I, 211 (1993).

[2] Ferron, J.R., et al., Proc. 21st EPS Conf., Montpellier, 1994, in Controlled Fusion and Plasma Physics Vol. 18B, Part I, 86 (1994)

[3] Strait, E.J., et al., Phys. Plasmas **4**, 1783 (1997).

[4] Taylor, T.S., Plasma Physics and Controlled Nuclear Fusion Research, (IAEA, Vienna, 1991), Vol. I, p. 177.

[5] Strait, E.J., et al., Proc. 18th EPS Conf., Berlin, 1991, in Controlled Fusion and Plasma Physics Vol. 15C, Part II, 105 (1991)

[6] Bernard, L.C., et al., Comput. Phys. Commun. **24**, 377 (1981).

METASTABLE BETA LIMIT IN DIII–D*

R.J. La Haye, J.D. Callen,† T.A. Gianakon,† C.C. Hegna,† L.L. Lao, C. Ren,† O. Sauter,Δ
E.J. Strait, T.S. Taylor, and H.R. Wilson◊
General Atomics, P.O. Box 85608, San Diego, California 92186-5608 USA

The long-pulse, slowly evolving single-null divertor (SND) discharges in DIII–D with H–mode, ELMs, and sawteeth are found to be limited significantly below (factor of 2) the predicted ideal limit $\beta_N = 4\,\ell_i$ by the onset of tearing modes. The tearing modes are *metastable* in that they are explained by the neoclassical bootstrap current (high β_θ) destabilization of a seed island which occurs even if $\Delta' < 0$, i.e., otherwise stable. For sufficiently high β_θ, there is a region of the modified Rutherford equation such that $dw/dt > 0$ for w larger than a threshold value; the plasma is *metastable*, awaiting the critical perturbation which is then amplified to the much larger saturated island.

Experimental results from a large number of tokamaks indicate that the high beta operational envelope of the tokamak is well defined by ideal magnetohydrodynamic (MHD) theory [1,2] and is given by $\beta(\%) \lesssim 4\ell_i I/aB$ MA/m/T for a large range of conditions. The highest beta values achieved have historically been obtained in fairly short pulse discharges, often <1–2 sawteeth periods and <1–2 energy replacement times. The maximum operational beta in single-null divertor (SND), long-pulse discharges in DIII–D with a cross-sectional shape similar to the proposed ITER tokamak (Fig. 1) is found to be limited significantly below the threshold for ideal instabilities by the onset of resistive MHD instabilities. [A hard disruptive beta limit is usually considered to be due to ideal MHD instabilities, either the n=1 kink or the n=∞ ballooning mode where n is the toroidal mode number.] The temporal evolution of a typical discharge is shown in Fig. 2; the beam power is increased gradually. There is a "soft" beta limit due to the onset of an m/n = 3/2 rotating tearing mode which saturates at an amplitude that decreases energy confinement by $\Delta\tau_E/\tau_E \approx -20\%$ [Fig. 2(b,c)] and a "hard" beta limit at slightly higher beta due to the onset of an m/n = 2/1 rotating tearing mode which grows to an amplitude that destroys the confinement and induces a disruption [Fig. 2(b,d)]. (These plasmas are neutral beam heated ELMing H–mode with sawteeth; the safety factor q_{95} is just above 3.)

An explanation of the observed experimental results is consistent with the neoclassical bootstrap current destabilization of a seed island for otherwise stable plasmas, i.e. $\Delta' < 0$ where Δ' is a measure of the free energy available from the poloidal field. For this study, Δ' is estimated from an analytical approximaton using the MHD reconstruction EFIT [3,4]. The effect of the bootstrap current is increasingly more destabilizing with increased beta poloidal β_θ as is seen from the the modified Rutherford equation for island of width w [5]

$$\left(\frac{\mu_0}{1.22\,\eta_{nc}}\right)\frac{dw}{dt} = \Delta' + a_1\varepsilon^{1/2}\beta_\theta\left(\frac{L_q}{L_p}\right)\left[\frac{w}{\left(w^2+w_d^2\right)}\right] - a_2 g(\varepsilon,\nu_i)\frac{\left(L_q/L_p\right)^2}{w^3}\rho_{\theta i}^2\beta_\theta$$

*Work supported by the U.S. Department of Energy under Contract No. DE-AC03-89ER51114 and Grant No. DE-FG02-92ER54139, and in part by the Swiss National Science Foundation and the U.K. Dept. of Trade and Industry and EURATOM.
†University of Wisconsin, Madison, Wisconsin.
ΔCRPP-EPFL, Lausanne, Switzerland.
◊UKAEA/Euratom Fusion Association, Culham, Abingdon, United Kingdom.

where the second term on the RHS is usually ($L_q/L_p > 0$) destabilizing. ($L_q \equiv q/dq/dr$ and $L_p \equiv -p/dp/dr$ with a_1 and a_2 and constants of order one.) Other MHD events such as sawteeth or ELMs usually trigger the onset of the resistive modes, supporting the idea that they are neoclassically destabilized by a seed perturbation. The neoclassical destabilization of tearing modes requires the proper conditions, i.e., high beta and low collisionality, and a seed island. The collisionality can enter (for $\Delta' < 0$) in either of two ways. In the "$\chi_\perp/\chi_\parallel$" model [6], the pressure is not equilibrated on the perturbed flux surface when perpendicular transport $\chi_\perp$ across a seed island dominates over that along the island $\chi_\parallel$, so that the critical island width w_d is an increasing function of collisionality. In the "ω_*" model [7], the toroidally enhanced ion polarization drift response of the plasma to the seed island due to inertial effects can add a stabilizing term to the modified Rutherford equation (the third term on the RHS) which dominates at small w. (Whether it is stabilizing depends on the mode frequency in the $E_r = 0$ frame, here assumed stabilizing.) It has a collisional factor $g(\varepsilon, \nu_i) = \varepsilon^{3/2}$ for $\nu_i/\varepsilon\omega_{*e} \ll 1$ and $g(\varepsilon, \nu_i) = 1$ for $\nu_i/\varepsilon\omega_{*e} \gg 1$ that can increase the critical island size a factor of 2–3. [Bootstrap current also requires $\nu_* \equiv (\nu_i/\varepsilon/\omega_{bi})$ be well below one where $\omega_{bi} = \varepsilon^{1/2}\, v_i/qR$.]

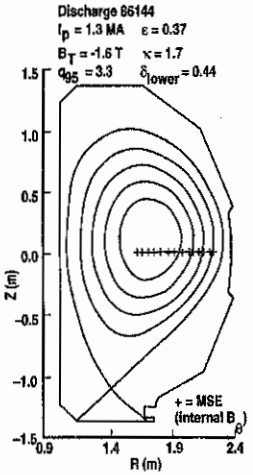

Fig. 1. Equilibrium cross section in DIII–D similar to that proposed for ITER. The 16 radial positions of the MSE diagnostic of poloidal field profile are also shown.

The ITER-like discharges in DIII–D have both sawteeth and ELM perturbations with the sawteeth period 10 to 20 times that of the ELMs. Examination of the databases of the onset of m/n=3/2 and 2/1 modes shows: (1) in 16 of 17 cases of the onset of the 3/2 mode, the mode clearly starts on a sawtooth crash with the remaining case on what may be an impurity burst, (2) the onset of the 2/1 mode is uncorrelated with a sawtooth crash but instead appears coincident with an ELM in 18 of 18 cases. For discharge #86144 of Fig. 2, as β_θ slowly increases and collisionality [here $\nu_* \equiv (\nu_i/\varepsilon)/\omega_{bi}$] decreases, a sawteeth crash induces the onset of the 3/2 mode as shown in Fig. 3(a).

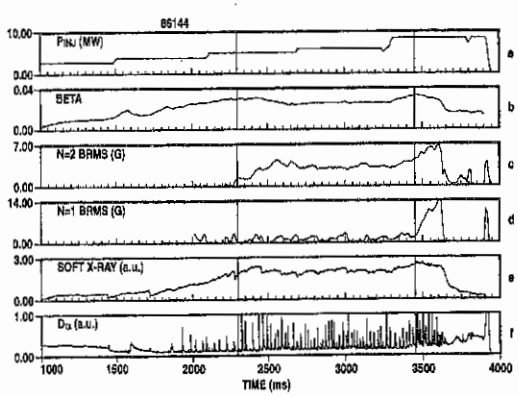

Fig. 2. Discharge #86144. (a) Injected beam power, (b) β from MHD reconstruction code EFIT, (c) rms amplitude of n = 2 rotating tearing mode (m = 3, n = 2), (d) rms amplitude of n = 1 rotating tearing mode (m = 2, n = 1), (e) central soft x-ray chord showing periodic sawteeth, and (f) D_α photodiode signal at divertor showing frequent edge localized modes. Note onset of 3/2 mode at 2250 rms and 2/1 mode at 3450 ms.

Upon further heating, β_θ again slowly rises, ν_* decreases and an ELM induces the 2/1 mode as shown in Fig. 3(b).

If $\Delta' < 0$, the neoclassical stability depends on the size of the seed perturbation w_{seed} relative to critical islands $w_d = (L_s/k\theta)^{1/2} (\chi_\perp/\chi_\parallel)^{1/4}$ and/or $w_g = [g(\varepsilon, \nu_i) (L_q/L_p)/\varepsilon^{1/2}]^{1/2} \rho_{\theta i}$. For typical DIII–D parameters $w_d \approx 0.5$ cm and $w_g \approx 2.4$ cm compared to minor radius a = 61 cm. The metastable region of the modified Rutherford equation is shown as the shaded region in Fig. 4. If a seed island w_{seed} exceeds the critical island w_{crit}, the metastable state is destabilized and w_{seed} grows to saturated size w_{sat}. Otherwise w_{seed} decays away.

As the neoclassical destabilization with beta depends on collisionality in different ways, empirical fits of critical beta for onset of 3/2 or 2/1 tearing were made to ν_*, ρ_*, etc. for as wide a range of variables as possible. The database of discharges at the onset of 3/2 tearing or 2/1 tearing scans B_T = 0.9–2.1 T at I_p = 0.65–1.5 MA with $q_{95} < 4$, $\bar{n}_{l4}$ = 0.26–0.82, with critical β = 1.73–5.16%. The radial scale lengths at q=m/n for q, T_e, and T_i at the 3/2 and 2/1 mode onsets, respectively, do not vary significantly. The H–mode core density profile is fairly flat in all cases. For the 3/2 mode onset, the mean $L_q/a = 0.55 \pm 0.05$, $L_{Te}/a = -0.39 \pm 0.06$, and $L_{Ti}/a = -0.33 \pm 0.03$. The mean Δ' using the high m approximation [4] is -9.4 ± 1.5 m^{-1}. For the 2/1 mode onset, the mean $L_q/a = 0.40 \pm 0.03$, $L_{Te}/a = -0.41 \pm 0.08$, and $L_{Ti}/a = -0.38 \pm 0.10$. The mean Δ' using the high m approximation is -8.0 ± 1.8 m^{-1}. Thus the principal experimental variables for the tearing mode destabilization are beta, collisionality, and gyroradius. A fit to $\beta_{crit} \sim \nu_*^x \rho_*^y$ was done in the spirit of dimensionless transport scaling and the dependence on the <u>local</u> parameters of the soft 3/2 tearing mode beta limit is shown in Fig. 5(a). For the 3/2 mode, the range in ν_* is only 3.1 and in ρ_* only 1.4. At low B, the 2/1 mode turns on first and the discharges disrupt. For the onset of the 2/1 mode shown in Fig. 5(b), ν_* varies a factor of 16 while ρ_* varies a factor of 1.6. The ρ_* dependence is $0 \sim 1/3$ within the uncertainty. The scaling with $\nu_i/\varepsilon\omega_{*e}$ which is more relevant for the ω^* model instead of ν_* was almost as good as for ν_*.

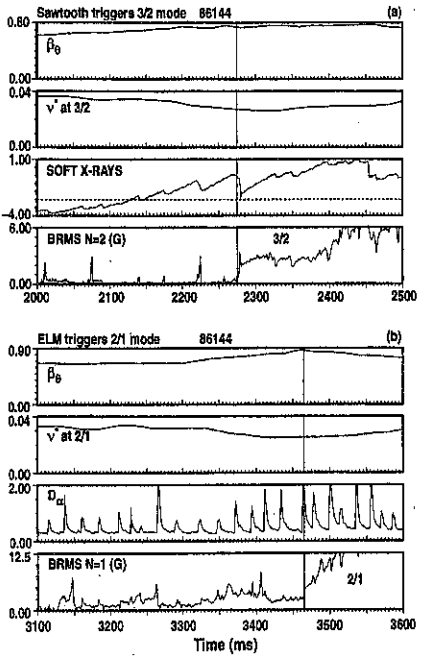

Fig. 3. (a) Correlation of a sawtooth crash (and 2/2 mode "gong") with the growth of a 3/2 tearing mode. (b) correlation of an ELM (and broad m/n "gong") with the growth of a 2/1 tearing mode.

Similar and even lower collisionality discharges in DIII–D were successfully run for 1.5 seconds at $\beta_N = 3$ without tearing modes by applying weak early beam heating in the current rampup so as to maintain $q(0) \gtrsim 1$ in the I_p flattop, with no sawteeth. Removing the sawteeth

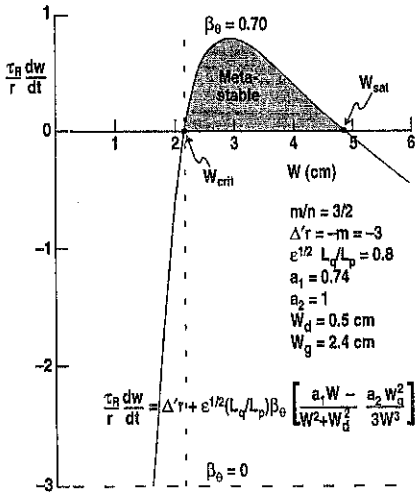

Fig. 4. Modified Rutherford equation for island growth versus island size. If seed w_s < critical size w_c, island decays. If seed w_s > critical size w_c, island grows to size w_{sat}

perturbation w_{seed} can explain avoiding the 3/2 metastable mode but surprisingly the ELMs remained large but did not destabilize the 2/1 mode.

Replacing the perturbed bootstrap current "missing" in the island O-point by radially localized ECCD has been proposed to suppress and/or stabilize the modes [8]. Experiments to evaluate this stabilization are planned for this year on DIII–D.

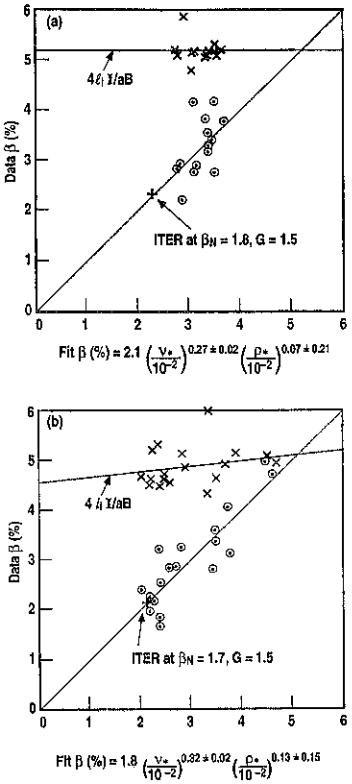

Fig. 5 (a) Onset of 3/2 tearing (⊙) in DIII–D fitted to local parameters. (b) Onset of 2/1 tearing (⊙) in DIII–D fitted to local parameters. Expected ITER beta limit is also shown (+) as well as expected ideal limit (×).

[1] Strait, E.J., et al., Phys. Plasmas **1** (1994) 1415.
[2] Strait, E.J., et al., Phys. Rev. Lett. **62** (1989) 1282.
[3] Lao, L.L., et al., Nucl. Fusion **25** (1985) 1611.
[4] Hegna, C.C. and Callen, J.D., Phys. Plasmas (1994) 2308.
[5] La Haye, R.J., et al., Proc. of the 16th IAEA Fusion Energy Conf., Montreal, 1996, to be published.
[6] Fitzpatrick, R., Phys. Plasmas **2** (1995) 825.
[7] Wilson, H.R., et al., Phys. Plasmas **3** (1995) 248.
[8] Hegna, C.C., and Callen, J.D., UW-CPTC96-7, December 1996, to be published in Phys. Plasmas.

REAL TIME EQUILIBRIUM RECONSTRUCTION FOR CONTROL OF THE DISCHARGE IN THE DIII-D TOKAMAK*

J.R. Ferron, M.L. Walker, L.L. Lao, B.G. Penaflor,
H.E. St. John, D.A. Humphreys, and J.A. Leuer
General Atomics, P.O. Box 85608, San Diego, California 92186-9784 U.S.A.

Optimum performance of a tokamak discharge requires accurate feedback control of many of the discharge parameters. For this to be possible, the values of these parameters must be accurately measured. The values of many discharge parameters, such as shape and safety factor profile, are not directly measured but can be evaluated from the available diagnostic data: magnetic field and flux measurements, for example. The most complete evaluation comes from a least squares fit of the diagnostic data to the Grad-Shafranov model that describes the force balance of the tokamak equilibrium, while allowing for a distributed current source. This full reconstruction of the equilibrium has normally been performed off-line using a computation-intensive fitting code such as EFIT [1].

This paper provides an introduction to a practical method for performing an equilibrium reconstruction in real time for arbitrary time-varying discharge shapes and current profiles. A detailed description of the algorithm is given in Ref. 2. An approximate solution to the Grad-Shafranov equilibrium relation is found which best fits the diagnostic measurements so that an equilibrium solution consistent with force balance, expressed in terms of the spatial distributions of the toroidal current density and poloidal flux, is available in real time for accurate evaluation of the discharge parameters. The algorithm is very close to that of EFIT and is executed on a time scale fast enough for control of the DIII-D tokamak.

The equilibrium reconstruction algorithm has been implemented on the digital plasma control system [3] for the DIII-D tokamak and we describe here its first application for tokamak discharge shape control. Shape identification with this reconstruction technique is robust to changes in the shape, β_p, ℓ_i, and edge current density. Relative to what is required for practical shape control, the results from the real time algorithm do not differ significantly from those of the full off-line analysis. Motional Stark Effect (MSE) diagnostic data can be included in the real time equilibrium reconstruction in order to more accurately determine the toroidal current density profile and the safety factor profile.

Shape control is implemented with the "isoflux" technique [4], in which a set of locations is specified that define the desired plasma boundary and the poloidal field coil currents are adjusted to keep the poloidal flux equal at all of these locations. This is illustrated in Fig. 1 where, for the case of a single null divertor discharge shape, the diamonds indicate the "control points," locations at which the value of the flux is controlled. Because the control is not based directly on errors in the shape, but rather on errors in the local poloidal flux value at the control points, the requirements on the equilibrium reconstruction algorithm are reduced since calculation of the plasma boundary is not necessary.

*Report of work sponsored by the U.S. Department of Energy under Contract No. DE-AC03-89ER51114.

One of the control points is chosen as the reference and the flux at the other points is controlled to be equal to the value at the reference point. For instance, for a discharge which is intended to have the boundary limited by the vessel wall, the intended point of intersection with the vessel wall is used as the reference point. In a divertor discharge the X point locations are controlled directly. The actual X point locations are determined by finding the locations where $|B_p|=0$ and the coil currents are adjusted to move the X point to the intended location. The flux at the actual X point location is then used as the reference flux

The task of the equilibrium reconstruction algorithm is to compute the distributions in the R,Z plane of the poloidal flux (ψ) and the toroidal current density (J_t) which provide a least squares best fit to the diagnostic data and which simultaneously satisfy the model given by the Grad-Shafranov equation

$$\Delta^* \psi_p = -\mu_0 R J_t(R,\psi) \ . \qquad (1)$$

The diagnostic data consist of measurements of flux and field outside the plasma, plasma current from a Rogowskii loop, internal field measurements made with the Motional Stark Effect diagnostic and current in the poloidal field shaping and Ohmic heating coils.

The full reconstruction algorithm [1] iterates the solutions for ψ and J_t until the changes in ψ between two successive iterations are small. This is illustrated in the flow chart in Fig. 2. In the figure, $(\bar{\bar{F}}\cdot\bar{R})^{-1}$ is the weighted diagnostic response matrix used to implement the least squares fit, $\bar{\psi}_N$ is the distribution of normalized flux on the computation grid which is used to form the basis functions for the least squares fit which are contained in the matrix $\bar{\bar{\Psi}}$, and $\bar{I}_p$ is the vector of values of the toroidal current on the computation grid.

In the real time version of the equilibrium reconstruction algorithm, the time consuming process of iterating to a well converged solution for a fixed set of diagnostic data is eliminated. Instead, for each new reconstruction a new set of diagnostic data is acquired, the most recent equilibrium solution is used as the starting point, and one iteration is performed. If the equilibrium is not evolving too quickly, the changes since the previous solution can be accounted for in one iteration so that the result has accuracy sufficient for discharge control. The first portion of the real time algorithm is the shape control (or "fast") computation loop in which the shape control power supply commands are generated. This shape control loop can be executed in approximately 1–2 ms because only the portion of a reconstruction iteration that generates I_p must be executed. The input to the shape control loop is the data set $\mathcal{S} = \{(\bar{\bar{F}}\cdot\bar{\bar{R}})^{-1}, \bar{\bar{\Psi}}\}$. Each time this shape control loop is executed a new set of diagnostic data is obtained but the same value of the data set $\mathcal{S}$ is reused until a new data set is prepared. The second portion of the algorithm (the "slow" loop) completes the steps required in a reconstruction iteration by preparing a new $\mathcal{S}$ data set. This involves significant computation, approximately 25 times more than the shape control loop. As part of this process, the flux vector $\bar{\psi}$ is obtained. Quantities such as the safety factor profile, poloidal beta, internal inductance, etc., which are obtained using $\bar{\psi}$, can be computed at this point.

Other modifications were made to the reconstruction algorithm in order to increase the calculation speed. In order to determine the flux at the discharge boundary, the flux at the reference control point is used. This avoids a complex boundary tracing routine. To determine the magnetic axis flux the peak value of the flux at a grid point is used. The time to

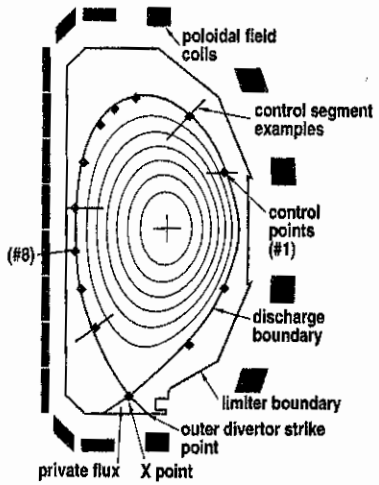

Fig. 1. *Example of a single null divertor discharge (#90291 at 2.5 s) produced using the isoflux control method in combination with real time equilibrium reconstruction. The diamonds show the locations of the control points.*

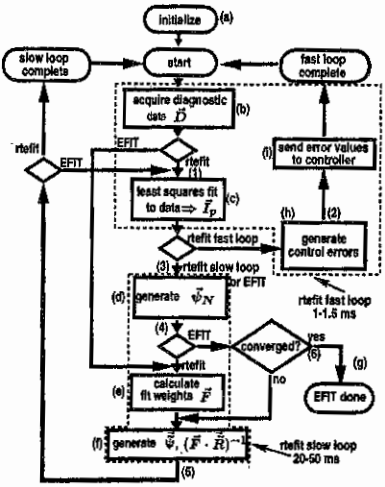

Fig. 2. *Flow chart illustraties procedure for equilibrium reconstruction calculation. Two paths through are shown, one for the full reconstruction ("EFIT") and one for the real time implementation ("rtefit"). The calculation time values shown are for the implementation in the DIII–D plasma control system.*

calculate $\mathcal{S}$ is strongly influenced by the number of fitting parameters. A direct measurement of the currents in each of the poloidal field coils is available, allowing these values to be treated as known rather than treating them as fitting parameters.'refit''

The real time equilibrium reconstruction algorithm combined with the isoflux technique has been used to control a variety of discharge shapes in the DIII–D tokamak. Some examples are the single null divertor shape shown in Fig. 1 and the various shapes shown in Fig. 3. Strike point location control, a capability essential for operation of closed divertor geometries, has also been implemented relatively easily using the isoflux technique.

Experience with DIII–D discharges controlled with the isoflux algorithm shows that the real time equilibrium reconstruction yields results with good accuracy. This is illustrated by the comparisons shown in Fig. 4 between the real time result and the result from the full equilibrium reconstruction calculated off-line. The sample discharge has a preprogrammed sweep of the X point position [Fig. 4(a) and (b)] during which the two equilibrium reconstructions agree on the X point location within a few millimeters [Fig. 4(c)]. The two computations of the flux at the control points agree to within less than 1×10^{-3}V-s/radian. To put this value in perspective, it is displayed in Fig. 4(d) and (e) for two of the control points as a distance computed from $(\psi_{\text{real time}} - \psi_{\text{EFIT}}) / (\partial\psi/\partial\ell)$ where $\psi_{\text{real time}}$ and ψ_{EFIT} are the flux values computed in real time and off-line, respectively, and the flux derivative is taken along a line between the control point and the magnetic axis. This quantity is approximately the difference in the predictions by the two calculations of the boundary location in the region

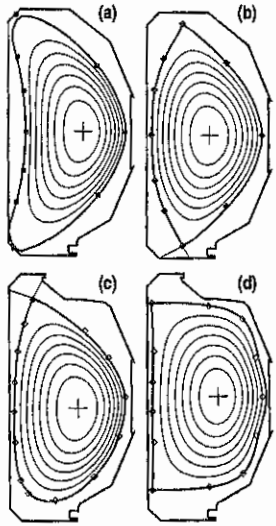

Fig. 3. Examples of discharge shapes produced in DIII–D using the isoflux control algorithm combined with the real time equilibrium reconstruction. (a) Crescent/beam shaped, (b) low triangularity double null divertor, (c) upper simple null divetor, and (d) highly "square" shaped duble null divertor.

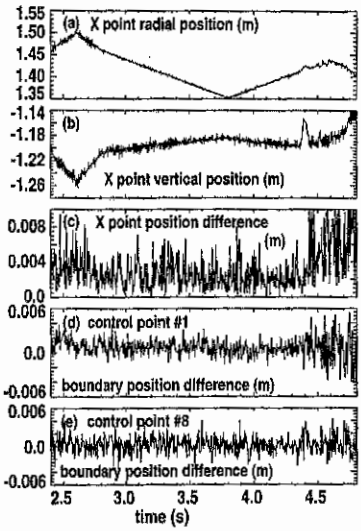

Fig. 4. Comparison of the results from the real time equilibrium reconstruction for the discharge shown in Fig. 1 to results from well-converged solutions from off-line calculations.

of the control point. Throughout the discharge, this difference is about 1 mm, small compared to the 0.62 m typical minor radius of the discharge.

In this paper, we have demonstrated that with current digital computing technology it is practical to use an algorithm that executes in real time which is nearly identical to a standard equilibrium reconstruction technique. Equilibrium parameters can be evaluated directly from a solution to the Grad-Shafranov tokamak equilibrium relation. This even allows parameters such as the safety factor profile to be evaluated in real time. The small modifications to the EFIT reconstruction algorithm described here which make the real time execution practical affect the results only on a scale of precision that is not important for practical discharge shape control.

The authors would like to thank Jim Broesch, David Baggest, Torkil Jensen, Tony Taylor, Bob Miller, and the remainder of the DIII–D team for their contributions to this work.

References

[1] L.L. Lao *et al.*, Nucl. Fusion **25**, 1611 (1985).
[2 J.R. Ferron *et al.*, "Real time equilibrium reconstruction for tokamak discharge control," General Atomics Report GA-A22586 (1997), submitted to Nuclear Fusion.
[3] J.R. Ferron, Rev. Sci. Instrum. **63**, 5464 (1992).
[4] F. Hofmann and S.C. Jardin, Nucl. Fusion **30**, 2013 (1990).

EFFECTS OF DIVERTOR GEOMETRY AND PUMPING ON PLASMA PERFORMANCE ON DIII–D*

S.L. Allen,† C.M. Greenfield, J. Boedo,# D. Colchin, ‡ M.E. Fenstermacher, † D.N. Hill,† C.J. Lasnier,† R. Lehmer,# A.W. Leonard, T.C. Luce, M.A. Mahdavi, R. Maingi,‡ R.A. Moyer,# T.W. Petrie, G.D. Porter,† B.W. Rice,† M.J. Schaffer, J.P. Smith, R.D. Stambaugh, T.S. Taylor, M.R. Wade,‡ J.G. Watkins,◊ W.P. West, R.D. Wood,† and The DIII–D Team
General Atomics, P.O. Box 85608, San Diego, California 92186-9784 USA

1. Introduction

This paper reports the status of an ongoing investigation to discern the influence of the divertor and plasma geometry on the confinement of both ELM-free and ELMing discharges in DIII–D. The ultimate goal is to achieve a high-performance core plasma which coexists with an advanced divertor plasma. The divertor plasma must reduce the heat flux to acceptable levels; the current technique disperses the heat flux over a wide area by radiation (a radiative divertor). To date, we have obtained our best performance in double-null (DN) high-triangularity ($\delta \sim 0.8$) ELM-free discharges [1]. As discussed in detail elsewhere [2], there are several advantages for both the core and divertor plasma with highly-shaped DN operation. Previous radiative-divertor experiments with D_2 injection in DN high-δ ELMing H–mode have shown that this configuration is more sensitive to gas puffing (τ decreases). Moving the X-point away from the target plate (to ~15 cm above the plate) decreases this sensitivity. Preliminary measurements also indicate that gas puffing reduces the divertor heat flux but does not reduce the plasma pressure along the field line (in contrast to detached plasmas discussed in Section 2) [3]. The up/down heat flux balance can be varied magnetically (by changing the distance between the separatrices), with a slight magnetic imbalance required to balance the heat flux [4].

The overall mission of the Radiative Divertor Project (RDP) is to install a fully pumped and baffled high-δ DN divertor. To date, however, both the DIII–D divertor diagnostics and pump were optimized for lower single-null (LSN) low-δ ($\delta \sim 0.4$) plasmas, so much of the divertor physics has been performed in LSN; these results are discussed in Section 2. As part of the first phase of the RDP, we have installed a new high-δ USN divertor baffle and pump; these results are discussed in Section 3. Both divertor and core parameters are discussed in each case.

2. Lower Single-Null (LSN), Low-δ Plasmas with Pumping

The open lower divertor pump is shown in Fig. 1. In low-δ lower single-null (LSN) open-divertor operation the cryopump can maintain the plasma density a factor of 2 below the natural density of the ELMing H–mode [5]. A rough figure-of-merit $\eta \equiv n_e\,(10^{19}\ m^{-3})/I_p$

*Work supported by the U.S. Department of Energy under Contract Nos. DE-AC03-89ER51114, W-7405-ENG-48, DE-AC05-96OR22464. and Grant No. DE-FG03-95ER54294.
†Lawrence Livermore National Laboratory, Livermore, California.
‡Oak Ridge National Laboratory, Oak Ridge, Tennessee.
◊Sandia National Laboratory, Livermore, California
#University of California, San Diego, California

(MA) is about 5–6 in the natural ELMing H–mode, and can be reduced to 2–2.5 with pumping [6]. With D_2 puffing and pumping, we have sustained radiative divertor operation with only slight degradation in confinement [7], resulting in parameters close to those desired for ITER [τ/τ(ITER-93) ~ 1, Z_{eff} ~ 1.8]. Detailed diagnostic studies [8] have shown that in the divertor: a) T_e ~1–2 eV, b) classical conduction cannot explain the heat flow along field lines at this temperature [9], c) the plasma pressure drops along the field line, and d) recombination is important close to the divertor plate. Carbon is the principle source of radiation near the X-point, with deuterium radiation dominating near the strike point.

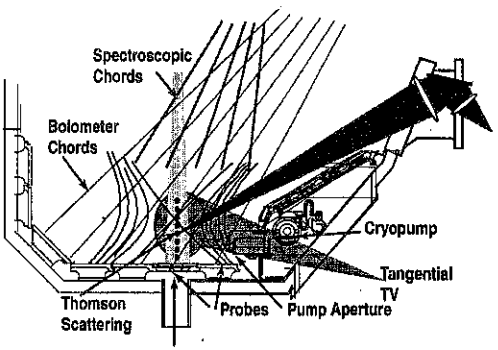

Fig. 1. The LSN low-δ divertor cryopump. There are extensive diagnostics in the lower open divertor.

Density control in non-sawtoothing ELMing H–mode shots has produced the highest performance long-pulse discharges with H_{89P} ~ 2.4 and β_N ~ 2.8 for up to 2 s, with $n_e = 5.0 \times 10^{19}$ m^{-3} and Z_{eff} ~ 1.8. Transient high performance low-δ LSN ELM-free discharges with negative or weak central magnetic shear (NCS) have also been demonstrated with the pump off [10]. A record DIII–D ion temperature of T_i ~ 25 keV was achieved with τ/τ-(ITER-89P) ~ 4 and β_n ~ 4. This represents a significant improvement over previous single-null discharges. The effectiveness of the pump in ELM-free, low δ, LSN discharges is reduced (particle exhaust ~ beam fueling rate), but reduced wall loading is still possible.

3. Upper Single-Null (USN), High-δ Plasmas with Pumping (New DIII–D Upper Divertor)

The new high-δ DIII–D divertor baffle and pump is shown in Fig. 2; the He-cooled cryopump is the same design as the lower ADP pump. Without plasma, the measured deuterium pumping speed was ~40,000 Torr ℓ/s, similar to that of the lower pump. This system has been optimized for high-δ plasmas, and has a baffle to reduce neutral flux to the plasma core. A combination of the UEDGE and DEGAS codes was used to guide the detailed design of the baffle. For a full double-null installation, the codes calculate that the core ionization should be reduced by a factor of nearly 7. The slanted baffle is water-cooled to prevent racheting of the plate temperature during a succession of plasma shots. Graphite tiles, similar to the those used on the rest of the DIII–D walls, cover the baffle. Careful attention was paid to the gas sealing of the baffle region, including installation of in-situ custom seals. New magnetic pickup coils were mounted on the plate, and these are incorporated into the EFIT shape reconstruction. Real-time EFIT (isoflux) shape control is used to position the plasma in the baffle and sweep the strike points into the pumping aperture. An IR camera views the upper divertor, along with crossed bolometer chords used for tomographic reconstructions of radiated power. Two Langmuir probes near the entrance to he pump aperture are used to measure the ion flux into the pump and an ASDEX-type gauge indicates the baffle pressure.

We have started commissioning of this system with the (unoptimized) USN plasma shown in Fig. 2. This shape has more flux-expansion than the LSN and hence the pump exhaust (and plasma density response) is less sensitive to the strikepoint location. High temperature baking, several (5–6) high power (10–12 MW) plasma shots, and glow discharge cleaning were necessary for initial conditioning of the upper divertor surfaces. Shown in Fig. 3 is a comparison of a shot with the pump warm (92044-dashed) and after the pump was cooled (92062-solid). The core density decreases and the temperature increases for the case with the pump cold. The β_N•H is similar on the two shots. The upper divertor D_α monitors and the midplane pressure (not shown also show a dramatic decrease. Even with limited initial operating time, the density control parameter η achieved has been about 2.5.

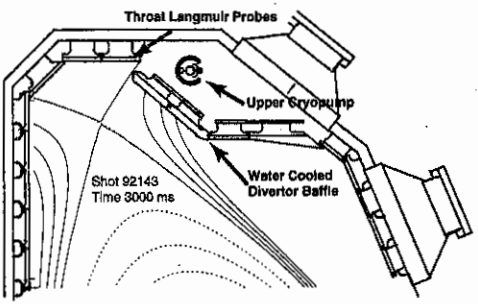

Fig. 2. USN high-δ plasma configuration in new upper DIII–D divertor.

Shown in Fig. 4 is a comparison of a pumped low-δ LSN plasma (shot 89756-dashed) with a pumped high-δ USN non-optimized plasma from the commissioning phase (92144-solid). The ELMing H–mode densities are similar at 2.5 s (although 89756 continues to decrease during the shot) and the core performance in normalized parameters β_N • H(ITER-89P) is similar. (The neutral beam power was greater on 89756, so we have compared normalized performance parameters. The ion temperature and neutron rate were higher on 89756.) As none of the tools used for optimizing the LSN discharge were used with the USN shot (e.g., neutral beam power early in the shot and a reduced target density for NCS), it seems likely that the USN discharge can be further improved with careful discharge tuning.

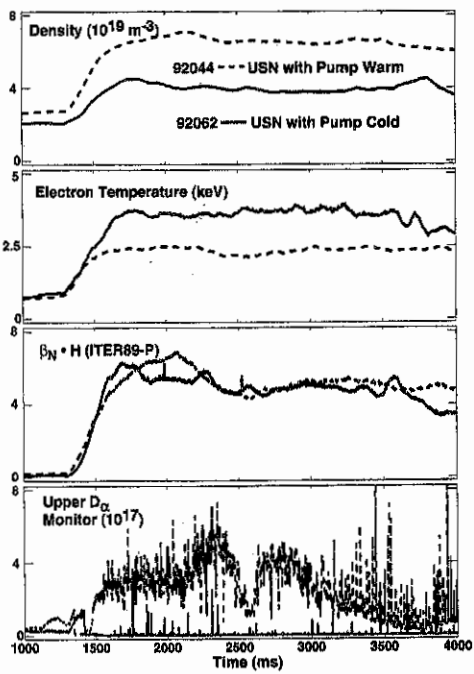

Fig. 3. Initial results showing density control with the upper divertor pump (solid-pump cold, dashed-warm).

In LSN discharges with pumping, a general observation is that there is a dependence of the plasma exhaust on the ELM frequency and size. While a detailed study of the ELM behavior in the new USN discharges has not been carried out, results so far would indicate that density control has been achieved in plasmas with relatively small ELMs at a fairly low frequency (~40 Hz). This very preliminary result will be studied more thoroughly, as we ultimately would like to achieve density control in ELM-free discharges.

We have also carried out initial experiments comparing plasma pumping and core performance with the direction of B_T, and hence the ∇B drift. This drift can influence both the core (higher H–mode threshold with ∇B away from the plate) and divertor plasmas (DIII–D heat flux data becomes more in-out symmetric with ∇B away from the plate). With the lower pump, all experiments have been carried out with the ∇B drift downward towards the divertor plate. So far, with the upper pump, we have not observed any difference in the lowest achievable density due to the direction of the ∇B drift. Subsequent analysis of the data indicates that the ∇B drift upward case is probably not fully optimized, and we will repeat this. In addition, we observe more carbon impurities and 2–4 times more radiated power (although $\beta_N \cdot H \sim 5$ and $T_i \sim 10$ keV in spite of the high impurity levels) in the ∇B upward case. As this could be a conditioning effect, these experiments will also be repeated. USN high-δ bolometer inversions indicate more radiated power on the inside/ (outside) divertor leg for ∇B upward/(downward).

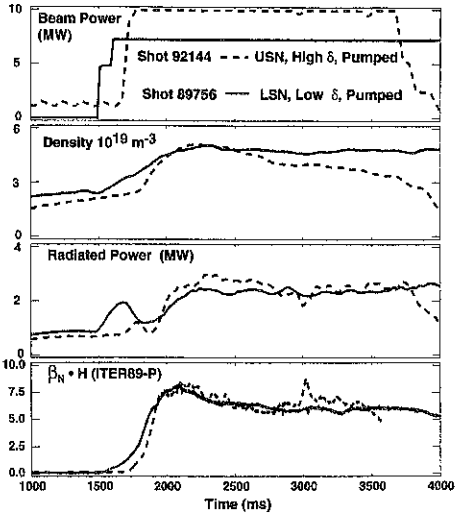

Fig. 4. Comparison of a LSN low-δ pumped discharge (dashed) with an USN pumped high-δ discharge (solid).

During the coming DIII–D experimental campaign, we will use this new hardware to optimize density control in both ELM-free and ELMing discharges.

[1] E.A. Lazarus, *et al.*, Phys. Rev. Lett. **77**, 2714 (1996).
[2] T.S. Taylor, "Advanced Tokamak Physics," *these proceedings* (review).
[3] T.W. Petrie, *et al.*, Bull. Am. Phys. Soc. **41**, 1430 (1997).
[4] C.J. Lasnier, *et al.*, "Target Plate Heat Flux in Divertor DIII–D Tokamak Discharges," submitted to Nucl. Fusion.
[5] M.A. Mahdavi, *et al.*, J. Nucl. Mater. **220–222**, 13 (1995).
[6] R. Maingi, *et al.*, Nucl. Fusion **36**, 245 (1996).
[7] T.W. Petrie, *et al.*, Nucl. Fusion **37**, 321 (1997).
[8] M.E. Fenstermacher, *et al.*, Phys. Plasmas **4**, 1761 (1997).
[9] A.W. Leonard, *et al.*, "Distributed Divertor Radiation Through Convection in DIII–D," submitted to Phys. Rev. Lett.
[10] E.J. Strait, *et al.*, in Proc. 23rd EPS. Conf., Vol. **20C**, Part III, (1996) p. 1493.

Modeling of DIII-D noble gas puff and pump experiments*

J. T. Hogan, M. Wade, R. Maingi, L. Owen
Oak Ridge National Laboratory, Oak Ridge, Tennessee, USA

M. Schaffer, P. West
General Atomics Company, San Diego, CA, USA

1. INTRODUCTION

Previous DIII-D experiments [1, 2] that induced a D^+ flow in the scrape-off layer (SOL) showed that this flow increased the divertor concentration of extrinsically injected impurities (neon, argon). These impurity fueling and exhaust (or puff and pump) experiments raise a number of modeling issues: the effect of edge-localized modes (ELMs) in regulating impurity core accumulation; the particle balance of the extrinsic impurities; the relation between divertor and plenum enrichment; and the effect of features unique to the present DIII-D Advanced Divertor configuration, specifically, the localized back-conductance of D_2 and impurities from the baffle plenum in the outboard divertor region. To aid in understanding the relations between these processes, models have been improved: for core impurity transport to include ELM effects, and for divertor models to treat helium, neon, and argon transport with DIII-D – specific configuration effects. The models have been used to analyze a series of experiments in which neon and argon were first continuously injected (in the divertor private flux region) for 1.5 s, and then exhausted by the DIII-D cryopumping system [2]. Deuterium was puffed at rates of 80 Torr L/s and 150 Torr L/s from the midplane and the divertor private region in these experiments.

2. MODEL

Core radial transport (MIST-ELM)

The suitability of H-mode confinement for reactor applications relies on the observed beneficial effect of ELMs in regulating core impurity accumulation. However, direct observation of ELM effects in reducing the particle confinement time has been made only for electron density and He^{++} profiles. In contrast, in the transport analysis of extrinsically injected impurities neon and argon, the ionization stages (NeXI, ArXVI) measured by charge exchange recombination (CER) spectroscopy are not located in the ELMing region. Thus, the MIST code [developed by R. Hulse, 3] has been modified to describe this. The ELM effect on impurities is modeled as expulsion of a predetermined fraction of all the charge state densities $n_K(\rho,t)$ for radius $\rho > \rho_{ELM}$ at a frequency (Ω_{ELM}) determined by the observed frequency of the time evolution of D_α signals. The expulsion fraction is not determined by the D_α signal, and thus becomes a fitting parameter.

Figure 1 shows results from the model of varying the assumed ELM amplitude (neon expulsion fraction) from 20% to 100% (Fig. 1a), the anomalous diffusivity (edge D_A) from 0.5 to 1 m^2/s at fixed ELM amplitude and core D_A (Fig. 1b), and the assumed radius of ELM localization from $\rho = 0.6$ to 0.85 (Fig. 1c). DIII-D discharge 86944 is shown, a case in which the ELM frequency changed from 50 Hz to 10 Hz at t = 2.75 s. Without the ELM model the transition must be modeled by varying D_A, while the fit in Fig. 1 was obtained with a fixed

This research was sponsored in part by the Office of Fusion Energy Sciences, U.S. Department of Energy, under contract DE-AC05-96OR22464 with Lockheed Martin Energy Research Corp.

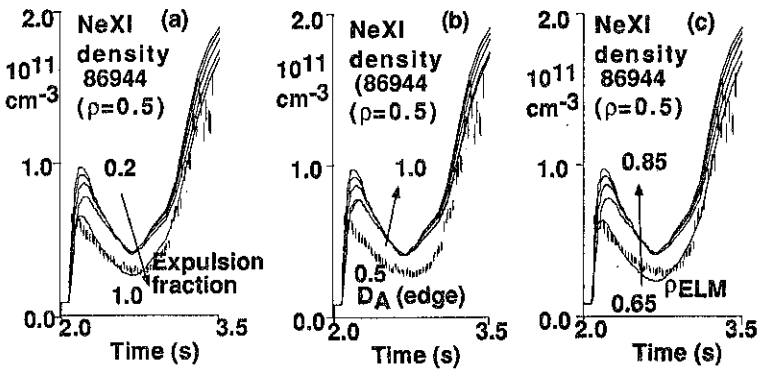

Fig. 1. Results of MIST-ELM model for DIII-D discharge 86944. Ω_{ELM} changes from 50Hz to 10Hz at t = 2.75s. A time-independent D_A is used.

D_A profile (edge value = 0.7 m^2/s). Figure 2 shows a comparison between the MIST-ELM model and CER measurement for NeXI density for DIII-D shot 89873, with 80 Torr L/s (midplane) deuterium puffing. For both neon and argon, best fits are obtained using a pinch coefficient, $c_v = 0$ (with the "MIST parametrization"), in contrast to earlier results for helium, in which $c_v = 1$ was found to be optimum. The anomalous diffusivities which result from the comparison are typically a factor of 3 lower than the diffusivities inferred from the conventional time-averaged analysis, which includes ELM effects as part of the anomalous diffusivity. For core modeling, the effective global recycling coefficient is taken to be 0.96 for both

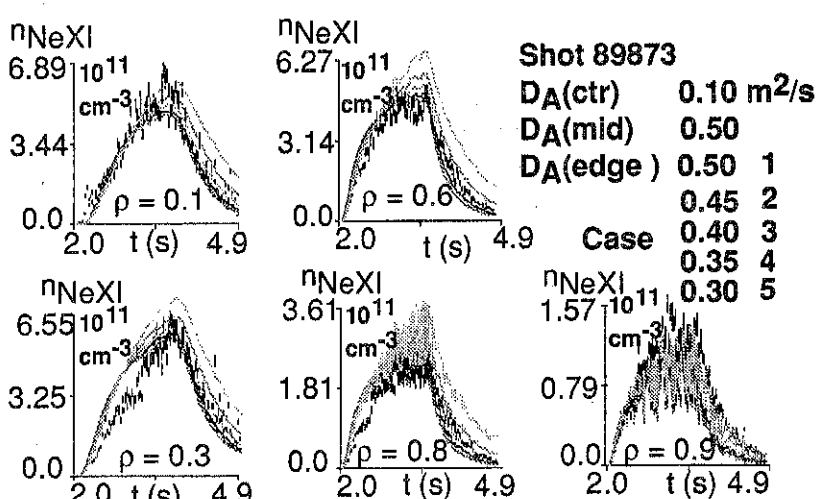

Fig. 2. Comparison of MIST-ELM model with neon fueling and exhaust experiments measured by CER spectroscopy. Sensitivity to assumed edge D_A with fixed ELM amplitude is shown.

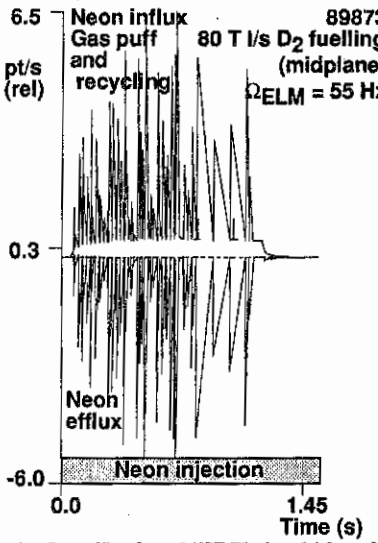

Fig. 3. Core efflux from MIST-ELM model for puff-pump case shot 89873

neon and argon, as determined by fits to the pumping decay after impurity injection is terminated.

Global particle balance

Previous analysis of DIII-D impurity fueling and exhaust experiments has shown that up to 90% of injected neon may be temporarily stored in the wall [2]. The impurity particle balance for recycling impurities has previously been analyzed in terms of multi-reservoir models with characterististic time constants [4]. The calculated core efflux from the MIST ELM model is the driving source in a global balance that describes the inventory of the noble gas impurities. The efflux of particles from the SOL from MIST serves as the influx for the divertor, plenum, and pump reservoirs. In addition, the measured neon pumping speed (which depends on the deuterium plenum pressure) is used to fix the pumping speed in the reservoir model. Figure 3 shows a typical balance as calculated from the detailed ELM model. The calculation assumes time constants $\tau_{SOL\text{-}divertor} = 0.7$ s, $\tau_{div\text{-}baffle} = \tau_{baffle\text{-}div} = 0.1$ s, and $\tau_{pump} = 0.04$ s. The neon pumping speed in DIII-D has been found to depend on D_2 plenum pressure [2], thus this calculation suggests a possible nonlinear dependence of the neon pumping rate on ELM-induced peaks in D_2 plenum pressure.

Divertor enrichment (MIST b2.5)

The divertor impurity concentration was not directly measured in these experiments, but the partial pressures of neon and argon in the baffle plenum were measured, so enrichment is described in terms of those values. The relation between divertor and plenum has been studied with a modified version of the b2 code [developed by B. Braams, 5]. The code has been run in 5- (helium), 13- (neon) and 21-species (argon) versions. A detailed model for sheath reflection of energetic impurity neutrals is included. Radial diffusivities are the same as the edge values for the MIST modeling for these discharges: $D_A = 0.7$ m^2/s, and $V_{pinch} = 0$. The ADPAK atomic physics package is included for neon/argon comparisons, and the STRAHL database is used for helium/neon comparisons. In addition, a description of the particle sources from divertor plate recycling, midplane and divertor deuterium puffing, divertor impurity puffing, and back-conductance of deuterium and impurities from the DIII-D plenum is included. These sources strongly complicate the conventional 1-D (parallel) picture of the balance between friction and ion temperature gradient forces, since there is a localized source of back-conducted D_2 (and impurities) on the outboard side of the outer strike point, near the floor. For a typical measured D_2 plenum pressure of 4 mTorr, and neon partial pressure of 0.04 mTorr, there are estimated 100 Torr L/s and 1 Torr L/s back flows for D_2 and neon,

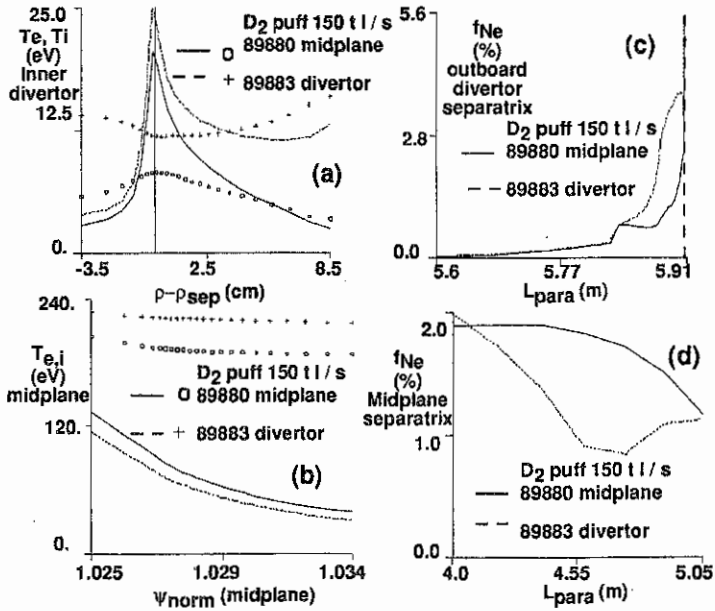

Fig. 4. MIST b2.5 model comparison of divertor / core enrichment for 150 Tl/s D_2 fueling from the midplane (89883) and divertor (89880). SOL plasma conditions are similar.

respectively, which are of the same order of magnitude as the external injection rates.

Results comparing the midplane (89883) and divertor (89880) D_2 fueling cases (150 Torr L/s) are shown in Fig. 4. Figures 4a and 4b show that the outboard midplane and inner divertor $T_{e,i}$ are similar (these compare well with Thomson scattering and Langmuir probe data, respectively). The modeled divertor plate concentrations are also similar (Fig. 4c), a result of feedback control in the experiment. However, the midplane fueling case shows a significant reduction in the neon concentration (Fig. 4d). In addition to the effects of thermal gradients and drifts, the modeling shows multiple peaks in the bulk ion density on the divertor plate which lead to impurity flows away from the bulk ion peak(s) and strongly influences retention. However, since profiles cannot yet be measured on DIII-D when the strike point is under the baffle ring, at present this is a theoretical possibility.

REFERENCES

1. M. Schaffer et al., "12th PSI," to be published in *Jour. Nucl. Mater.*
2. M. Wade et al., 1996 APS Meeting, Denver, Bull. Am. Phys. Soc. . **41**, 7 (November 1996).
3. R. Hulse, *Fusion Technology*, **3** 259 (1983).
4. A. Kallenbach et al., *Nucl. Fusion*, **35** 1231 (1995).
5. B.J. Braams, NET Report 68, EUR-FU/XII-80/87/68, January 1987.

ENERGY BALANCE, RADIATION AND STABILITY DURING RAPID PLASMA TERMINATION VIA IMPURITY PELLET INJECTIONS ON DIII–D*

D.G. Whyte,[a] T.E. Evans, A.G. Kellman, D.A. Humphreys, A.W. Hyatt, T.C. Jernigan,[b] R.L. Lee, S.L. Luckhardt,[a] P.B. Parks, M.J. Schaffer, and P.L.Taylor
General Atomics, P.O. Box 85608, San Diego, CA 92138-5608
[a]*University of California, San Diego, California.*
[b]*Oak Ridge National Laboratory, Oak Ridge, Tennessee.*

Injections of impurity "killer" pellets on DIII–D have demonstrated partial mitigation of undesirable disruption phenomena; namely reducing the convected heat loss to the wall, and the halo current's magnitude and toroidal asymmetry. However, the appearance of a runaway electron population and large magnetic fluctuations ($\tilde{B}/B_T \approx 1\%$) is coincident with the measured rapid loss of the plasma's thermal energy (≈1 MJ in 1 ms) due to impurity radiation. A numerical code is developed to simulate the impurity radiation and predict the rapid plasma cooling observed. The simulation predicts two mechanisms for the generation of runaway electrons: the "slideaway" of hot tail electrons due to rapid cooling or the transport of hot electrons into the thermally collapsed plasma due to instabilities. Pressure gradients caused by the rapid non-adiabatic cooling of the impurity are identified as the probable source of these instabilities which also lead to convective heat losses. Results of a modeling effort to optimize pellet content, impurity species and cooling time for the avoidance of instabilities and runaway electrons are shown.

1. Description of Experiment and Model

Solid impurity pellets of neon and argon are injected at the outer midplane of DIII–D (R = 1.7 m, a = 0.6 m) in an attempt to radiatively quench the plasma. Pellets have diameters of 1.8 mm or 2.7 mm, injection velocity ≈500 m/s and typically penetrate to a minor radius r of $0.2 < r/a < 0.5$. Impurity radiation is measured by a calibrated SPRED XUV survey spectrometer which provides 1 ms time resolution over the wavelength range of 100–1100 Å and has a single tangential line of sight with a tangent radius near the magnetic axis (R_{tan} = 1.8 m). Experiments have shown that the use of impurity pellets during Vertical Displacement Events (VDE) [1] reduces the convected thermal loads (measured by infrared thermography) to the divertor by up to a factor of two by increasing the fraction of initial stored energy which is radiated by the impurity. The induced poloidal halo current's magnitude and toroidal asymmetry are also reduced. Pellet injection into steady-state plasmas (i.e. pre-emptive) also show large fractions (50%–80%) of the energy radiated. However, experimental indications of runaway electron production (i.e. hard X-ray bursts, non-thermal ECE emissions) are greatly increased, especially in the case of preemptive pellet injections.

A time dependent model (Killer Pellet RADiation, KPRAD) is used to simulate the radiation and energy balance during pellet injection experiments on a given flux surface (no radial

*Work supported by the U.S. Department of Energy under Contract Nos. DE-AC03-89ER51114, DE-AC05-96OR22464, and Grant No. DE-FG03-95ER54294.

transport). The calculation first solves the ionization charge-state equilibrium for the impurity species and the subsequent radiative losses from each charge state (i.e. coronal equilibrium is not assumed). Then a new self-consistent energy balance including radiation losses, ohmic heating and collisional coupling between all species is calculated at each timestep. The new plasma solution for density and temperature is then used for the subsequent timestep's ionization balance. The code independently considers as separate species the original electrons and ions, as well as the impurity ions and the electrons contributed from their ionization. The amount of deposited pellet atoms on the flux surface is determined by using the standard pellet ablation model [2] normalized to obtain the measured penetration radius. Radiation rates for each charge state k, L_k (Wm^3) are extracted from the ADPAK [3]] atomic database. The electron density, n_e, and each charge state's density n_k are used to calculate the radiated power $P_{rad,k} = n_k\, n_e\, L_k$ (Wm^{-3}). Initial plasma parameters (n_{e0}, T_{e0}, j_0) are taken from measurements and the local current density, j, is held proportional to the measured total plasma current I_p, (i.e. $j(t) = j_0 \cdot I_p(t)/I_{p0}$). Ohmic heating power ($P_{ohmic}$) and the parallel electric field (E) are derived from Spitzer resistivity ($\eta \propto Z_{eff} T_e^{-3/2}$, $P_{ohmic} = \eta j^2$, $E = \eta j$) using the calculated electron temperature and Z_{eff}. The code predicts the time evolutions of electron and ion temperature, electron density, average charge state of impurity, total radiation, and radiation per charge state.

2. Results

The focus of this section will be the comparison of modeling results and experimental data for a preemptive radiative quench following the injection of a small (1.8 mm diam., $N_{pellet} \approx 2 \times 10^{20}$, $N_{plasma} \approx 10^{21}$, v = 390 m/s) neon pellet which penetrated to r/a ≈ 0.45. Figure 1 shows the model predicts the measured rapid decrease of the core temperature and plasma energy in ≤0.5 ms. The reason for this thermal collapse is that the high radiation rate of the low ionization stages of neon ($L_{0-7} \approx 10^{-31}$ Wm^3) and the large amount of pellet material deposited decrease the electron temperature quickly enough to inhibit ionization into or past the He-like state (two electrons), where the radiation efficiency is much lower ($L_{8-10} \approx 10^{-33}$ Wm^3). This is confirmed experimentally by the absence of any line radiation from these high charge states. The background ion temperature (T_i) and the electrons contributed from neon ionization $T_{e,Neon}$ are quickly thermalized to the main electrons through collisions and the total thermal energy of the plasma is lost to radiation. After the thermal collapse a new equilibrium is established between radiated power and the enhanced

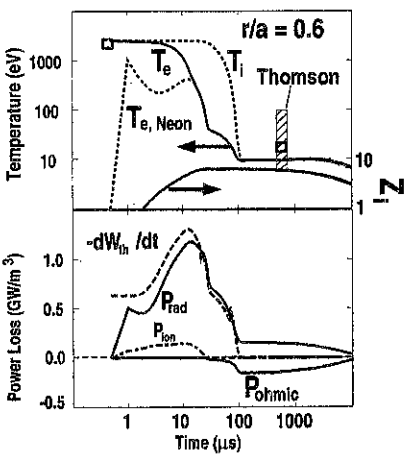

Fig. 1. Calculated T_e and average ion charge state Z_i at r/a = 0.6 vs. time after pre-emptive neon pellet passes that flux surface. Square indicates Thomson measured T_e at r/a = 0.6 and the bar the range in core T_e showing complete thermal collapse in core.

ohmic heating (from the now highly resistive plasma) and no further significant temperature decrease is expected. A comparison of the measured and calculated radiation (Fig. 2) shows good agreement in the magnitude and time behavior of the total and charge specific radiation. This indicates that indeed a large portion of the initial thermal energy is lost to radiation. Also, the significant amount of radiation well into the current quench shows that plasma magnetic energy is also being depleted via radiation. Finally, the relative increase in the radiation of the lower charge states during the current quench indicates volume recombination taking place in a very cold and dense core plasma.

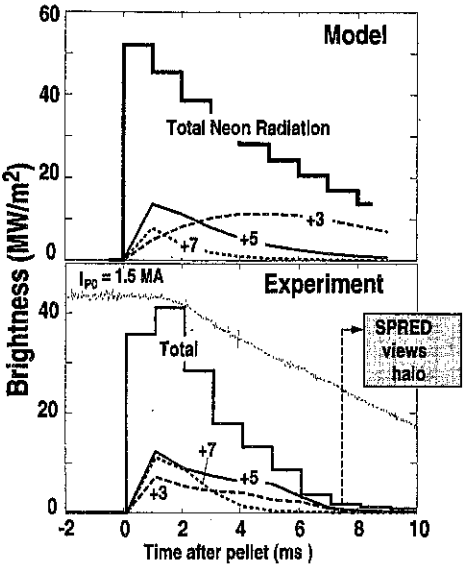

Fig. 2. Comparison of neon radiation between experiment and modeling. Experimental brightnesses of charge states are relative from resonance transitions. At t =7 ms the core plasma has moved out of SPRED's view.

The rapid thermal collapse of the plasma will cause large pressure gradients to form during the pellet ablation (Fig. 3) and drive associated instabilities (e.g. ballooning modes, etc.). The magnitude of this pressure gradient will be determined by the cooling rate of the pellet material, $\tau_{cooling}$ ($\Delta P/\Delta r \approx P_o/\Delta r \propto P_o/\tau_{cooling}$) with typical $\Delta r \approx 0.1$ m « a. This is verified experimentally (Fig. 4) by the increasing measured magnitude of n=1 modes during preemptive ablation for larger pellets and pellets made of argon ($L_{Ar} \approx 3 \cdot L_{Ne}$).

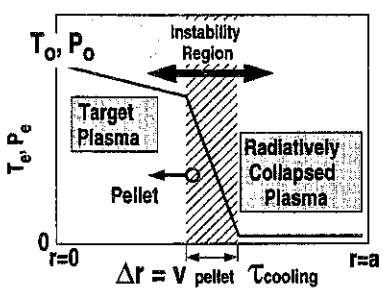

Fig. 3 Schematic of pellet moving through plasma. Rapidly cooled plasma behind pellet causes pressure gradients and instabilities.

The increased production of runaway electrons is also linked to the cooling rate (Fig. 4). This can stem from two phenomena. Figure 5 shows that a portion of the original Maxwellian tail (>12·T_e) electrons will have too weak collisional coupling to the bulk electrons and can cross over the runaway critical energy ε_{crit} which is decreasing due to the enhanced resistivity and electric field. In addition, particle transport caused by large instabilities could place $T_e > \varepsilon_{crit}$ electrons from the hot target plasma into the thermally

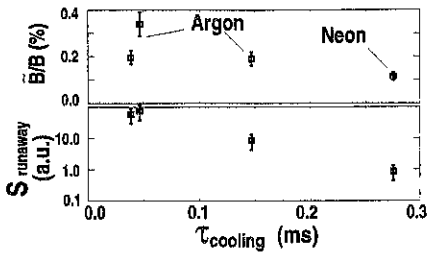

Fig. 4 Measured instability magnitude and runaway source rate increase with faster calculated cooling times. $S_{runaway}$ is obtained from time integrated non-thermal ECE emission during thermal quench.

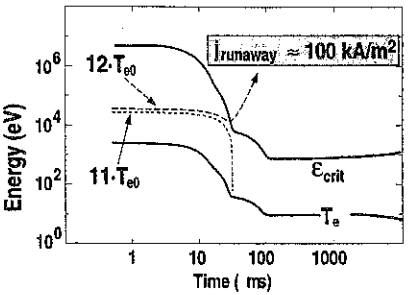

Fig. 5 Test particle calculation shows that rapid cooling can cause portion of original energetic electrons to become suprathermal and carry significant current.

collapsed plasma and also produce runaways. Both of these methods are sensitive to the cooling rate and hence agree with experimental observations.

4. Discussion

The model shows that pellet cooling is sufficient to thermally collapse the plasma over the penetration radius while simultaneously producing ∇P instabilities that cause the loss of the remaining thermal energy. A sufficiently rapid radiative loss is needed to quench the plasma, but the associated large pressure gradients from excessive cooling during the pellet ablation should be avoided since they lead to enhanced convected losses and runaways. Therefore, the pellet species must be carefully selected in order to optimize the radiative quench, since the cooling rate is primarily determined by the atomic physics of the material. Figure 6 shows the predicted response of a DIII–D plasma (T_e = 2 keV) to various amounts of pellet material and different pellet compositions. In the amount of pellet material deposited (for Ne and Ar experiments: $0.4 \le N_{dep}/N_e \le 1$), there exists a small region over which there is sufficient cooling ($W_f/W_o \le 0.2$) in a typical thermal quench time $\tau_{TQ} \approx 1$ ms, but also acceptable cooling rates [$dW/dt \cdot (\tau_{TQ}/W_0) \le 1$ are experimentally verified to not cause instabilities]. There does not exist the experimental precision to design the pellet ablation this carefully. Methane pellets however seem to exhibit the desired behavior over a large and achievable range of pellet deposition.

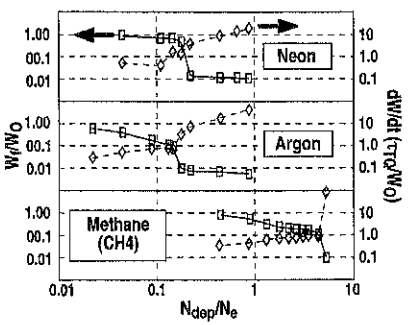

Fig. 6 Ratio of final to initial plasma thermal energy (W_f/W_0) and normalized energy loss rate vs. relative amount of deposited pellet material (N_{dep}) to local electrons (N_e).

[1] Kellman, A.G., *et al.* "Disruption Studies in DIII-D," in Proc. of the 16th IAEA Fusion Energy Conf., Montreal, Canada 1996, to be published.

[2] Kuteev, B.V., *et al.*, Nucl. Fusion **35** (1995) 1167.

[3] Hulse, R.A., *et al.*, Nucl. Technology/Fusion **3** (1983) 259.

A Study of Edge Turbulence by Phase Contrast Imaging on DIII–D

S. Coda† and M. Porkolab
Department of Physics and Plasma Fusion Center,
Massachusetts Institute of Technology, Cambridge, Mass. 02139, U.S.A.

K.H. Burrell
General Atomics, P.O. Box 85608, San Diego, CA 92186-9784, U.S.A.

1. Introduction

The DIII–D phase-contrast imaging (PCI) diagnostic measures the vertical line integrals of the density fluctuations at 16 radial locations at the outer edge of the tokamak [1]. The PCI system detects near-radial wave vectors with wave numbers in the range 1–16 cm^{-1}, with excellent radial (0.5 cm) and temporal (0.5 μs) resolution and high sensitivity ($\tilde{n} \sim 10^9$ cm^{-3}). These properties ensure good statistics for correlation analysis, resulting in a unique ability to provide time-resolved measurements of the correlation length and of the decorrelation time of the plasma turbulence.

In this paper a study of the changes occurring at the L– to H–mode transition is described, and a quantitative verification of the $\mathbf{E} \times \mathbf{B}$ shear decorrelation criterion is reported. The variations of the correlation parameters are also compared quantitatively with two available theoretical predictions. In addition, the dependence of those parameters on key plasma quantities in the L–mode phase is briefly discussed; in particular, it is shown that the random-walk turbulent diffusivity increases with input power.

2. The evolution of turbulence at the L–H transition

The reduction in the amplitude of the edge turbulence at the onset of the H mode has been widely documented in the literature [2]. Far less is known about the behaviour of the correlation properties of the turbulence, which play a key role in its ability to affect transport and are thus essential for meaningful comparisons with theory.

The L–H transition has been studied with PCI in a large variety of plasma configurations and parameters, and with different heating methods [3]. The fluctuation amplitude and the radial correlation length both decrease in the region from the last closed flux surface (LCFS) to 3–4 cm inside. The changes in the amplitude and, within the resolution of the correlation analysis (~2–3 ms), in the correlation length are simultaneous with the transition as defined by the first drop in the edge D_α emission signal. The turbulence decorrelation time is more erratic and does not change as abruptly; it is, however, generally *larger* in H mode than in L mode (see Fig. 1).

† Current address: CRPP–EPFL, CH–1015, Lausanne, Switzerland

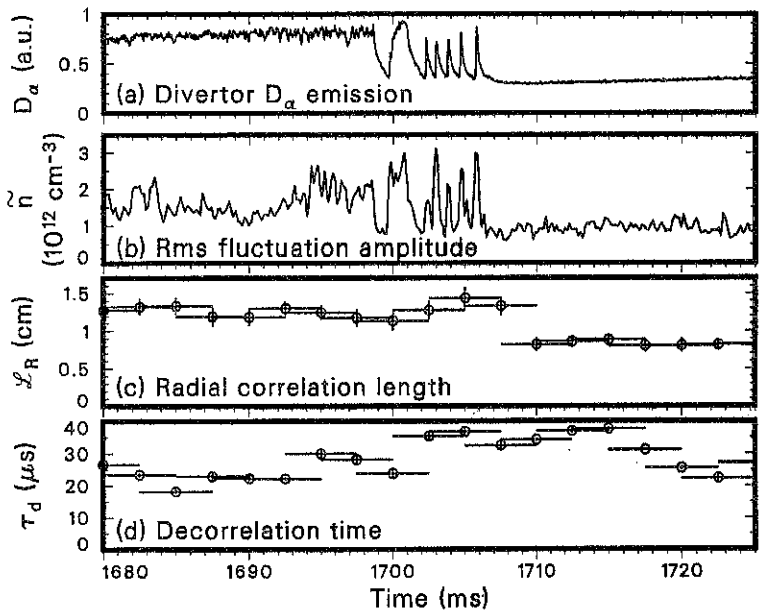

Fig. 1. Evolution of D_α emission and turbulence at the L–H transition, in a plasma with B_T=2.1 T, I_p=1.25 MA, $\bar{n}_e$=3.5×10^{13} cm^{-3}, and input neutral-beam power =6.2 MW. Measurements (b)–(d) are made with PCI in the region from the LCFS to 0.8 cm inside it.

The quenching of the turbulence is generally believed to be caused by sheared poloidal $\mathbf{E}\times\mathbf{B}$ flows inducing decorrelation between differentially rotating eddies; an increase of the shear of the radial electric field is observed to accompany and possibly precede the transition [2,4]. The canonical criterion for the H mode to occur is [5] $\omega_s > \omega_T$, where $\omega_s \equiv v'_{\mathbf{E}\times\mathbf{B}}\mathcal{L}_r/\mathcal{L}_\theta$ is the *shearing rate*, $v'_{\mathbf{E}\times\mathbf{B}}$ is the $\mathbf{E}\times\mathbf{B}$ velocity shear, $\mathcal{L}_r$ and $\mathcal{L}_\theta$ are the radial and poloidal correlation lengths respectively, and $\omega_T \equiv 1/\tau_d$ is the reciprocal of the decorrelation time in the absence of shear (L mode).

As shown above, accurate measurements of $\mathcal{L}_r$ and τ_d are provided by PCI; $v'_{\mathbf{E}\times\mathbf{B}}$ is measured by charge-exchange recombination spectroscopy [4]. In testing the shear decorrelation criterion, the largest uncertainty is introduced by $\mathcal{L}_\theta$, which we estimate from FIR scattering spectra [6]. The result of the test is shown in Fig. 2, which compares ω_s and ω_T in L and H mode. Clearly the condition $\omega_s > \omega_T$ is well satisfied in H mode, whereas the two quantities are comparable in L mode. The criterion is thus well verified.

Two theoretical predictions exist for the changes in $\mathcal{L}_r$ and τ_d occurring at the L–H transition. The Biglari–Diamond–Terry (BDT) analysis [5], carried out in cylindrical geometry, is expected to be valid in large-shear conditions; the Hahm–Burrell (HB) theory [7] includes toroidal effects but should be more applicable to a moderate-shear

case [8]. The BDT scalings are $\mathcal{L}_{rH}/\mathcal{L}_{rL} \simeq (2\omega_s\tau_{dL})^{-1/3}$ and $\tau_{dH}/\tau_{dL} \simeq (2\omega_s\tau_{dL})^{-2/3}$; the HB scalings are $\mathcal{L}_{rH}/\mathcal{L}_{rL} \simeq (1+\omega_s^2\tau_{dL}^2)^{-1/2}$ and $\tau_{dH}/\tau_{dL} \simeq 1$ (neglecting logarithmic dependencies). Here, the L and H subscripts refer to L mode and H mode, respectively.

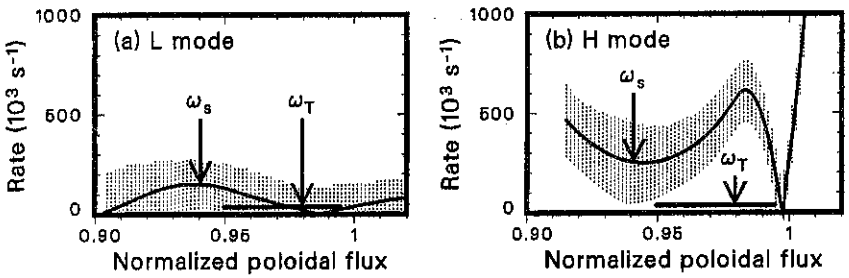

Fig. 2. Shearing rate vs. intrinsic turbulence decorrelation rate in L and H mode. The shaded areas indicate confidence intervals. The decorrelation rate is shown as a segment over the spatial range used by PCI to estimate its value. The plasma parameters are B_T=2.16 T, I_p=1.54 MA, $\bar{n}_e$=3×10^{13} cm^{-3}, input neutral-beam power = 8.5 MW.

These relations are compared with experimental values for a set of neutral-beam-heated discharges in Fig. 3. It is apparent that the BDT scaling provides a better fit to the spatial correlation data, whereas the HB scaling is a better predictor of the temporal correlation data. This mixed result probably reflects the non-self-consistent nature of both analyses, which do not consider the reaction of the turbulence on the flows. Conversely, self-consistent theories thus far have modeled the decorrelation time only in an ad-hoc manner. Additional work is thus clearly desirable on this front.

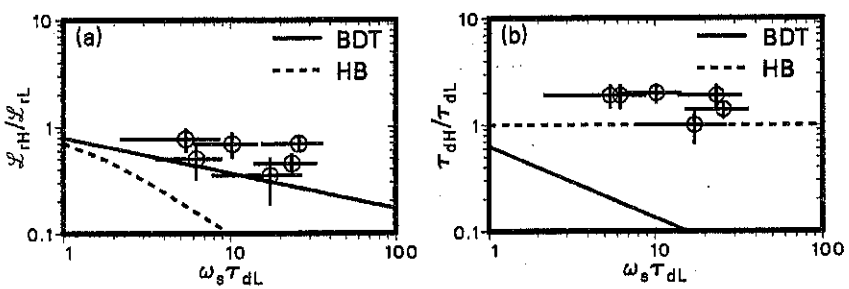

Fig. 3. Ratios of (a) radial correlation lengths and (b) decorrelation times in H and L mode, for varying shear in neutral-beam-heated discharges: PCI-measured values in the region $0.95 < \rho_n < 1.0$ (circles), BDT predictions (solid lines), and HB predictions (dashed lines).

3. Scaling of correlation length and turbulent diffusivity

A three-point scan of the input neutral-beam power in L mode, with all plasma parameters fixed, has shown that the radial correlation length increases, while the decorre-

lation time decreases, with increasing power. The random-walk diffusivity $\chi_{rw} = \mathcal{L}_r^2/\tau_d$ thus increases with power (see Fig. 4). This is in qualitative agreement with the experimental L–mode scaling of diffusivity with additional-heating power (a quantitative scaling is clearly not meaningful given the uncertainties and the limited number of points). Moreover, the magnitude of χ_{rw} is roughly of the same order as the ion diffusivity at the edge, although accurate transport analysis is problematic in this region.

In separate scans, the correlation length was also found to increase with density and to decrease with plasma current [3].

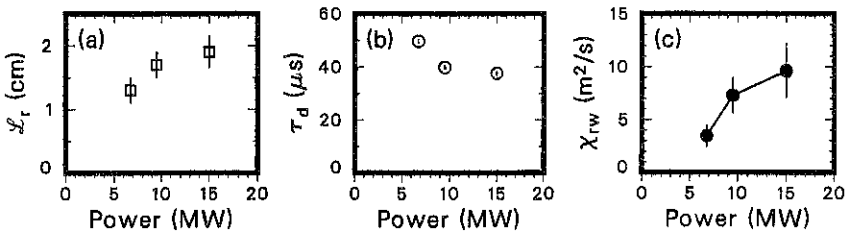

Fig. 4. (a) Radial correlation length, (b) decorrelation time, and (c) random-walk diffusivity, as a function of neutral-beam power in an L–mode plasma (B_T=2.1 T, I_p=1.35 MA, $\bar{n}_e$=4×10^{13} cm^{-3}).

Acknowledgments

We wish to thank the DIII–D team for their invaluable role in executing the experiments described in this paper. Useful discussions with Drs. T.S. Hahm, P.H. Diamond, B.A. Carreras, and R.E. Waltz are gratefully acknowledged. This work was supported by the U.S. Department of Energy under Grant No. DE-FG02-91ER54109 at MIT and Contract No. DE-AC03-89ER51114 at General Atomics.

References

[1] Coda S. and Porkolab M., *Rev. Sci. Instrum.* **66**, 454 (1995).

[2] Burrell K.H., *Plasma Phys. and Contr. Fusion* **36**, A291 (1994).

[3] Coda S., Ph.D. Thesis, M.I.T., 1997.

[4] Burrell K.H. et al., Proc. 15th Int. Conf. on Plasma Phys. and Contr. Nucl. Fusion Research, Sevilla, 1994 (IAEA, Vienna, 1995), Vol. I, p. 221.

[5] Biglari H., Diamond P.H. and Terry P.W., *Phys. Fluids B* **2**, 1 (1990).

[6] Doyle E.J. et al., Proc. 14th Int. Conf. on Plasma Phys. and Contr. Nucl. Fusion Research, Würzburg, 1992 (IAEA, Vienna, 1993), Vol. I, p. 235.

[7] Hahm T.S. and Burrell K.H., *Phys. Plasmas* **2**, 1648 (1995).

[8] Hahm T.S., private communication.

On the possible role of the impurity driven turbulence in the scrape-of layer in DIII-D double-null discharges

A.V.Nedospasov
Association " IVTAN " RAS, Izhorskaya 13/19, 127412 Moscow, Russia.

Discharges with enhanced scrape-off layer (SOL) thickness were observed in the DIII-D tokamak. The authors of these investigations pointed out that the origin of this phenomenon is not understood. In this paper a possible explanation of the enhanced SOL tickness in the DIII-D by impurity driven current-convective turbulence (ICCT) is discussed. This turbulence may occur under conditions when volume dissipation by Coulomb collisions dominats and a gradient of Z_{eff} exists.

An enhanced SOL thickness was observed in DIII-D tokamak [1]. A similar phenomenon was observed earlier in ASDEX [2,3]. In paper [4] the Kadomtsev-Pogutse-Petrov result for the ICCT diffusion coefficient D_I was rewritten in the following form:

$$D_I \approx r^{\frac{5}{2}} R^{\frac{1}{2}} \left(\frac{\mu \nu_{zi}}{T}\right)^{\frac{1}{2}} \left(\frac{E_\parallel}{B_T}\cdot\left|\frac{1}{d_z}-\frac{1}{d_n}\right|\right)^{\frac{3}{2}} F(z,z_{eff}) / \theta^2 \qquad (1)$$

Here ν_{zi} is the impurity collision frequency with main ions, μ is the reduced mass, B_T is the toroidal magnetic field, $d_{n,z}=n_{i,z}\cdot(dn_{i,z}/dr)^{-1}$ are the decay lengths of the main ions and the impurity repectively and $\vartheta=(r^2/R)\cdot dq^{-1}/dr$ is the magnetic shear.

The function $F(Z,Z_{eff})$ approaches zero for either $Z_{eff}\Rightarrow Z$ or $Z_{eff}\Rightarrow 1$, because in these limits the plasma contains only one sort of ions. It has a maximum of about 0.2 for $Z_{eff}\approx 2$. From eqn.(1) it is clear that for ICCT driven by the gradient of Z_{eff}, the radial profiles of the main ions and the impurity must be different.

The Pfirsch-Schlüter current is the main part of the longitudinal current $j_\parallel$ in the SOL. This current can be estimated according to $j_\parallel \approx e\cdot\Lambda\cdot v_s\cdot dn/dr = e\cdot n\cdot v_s\cdot\Lambda/d_n$, where v_s is the ion sound speed, Λ is the characteristic scale length depending on the limiter configuration [5]. For the case of a toroidal limiter discussed by Garbet et. al. [6],

$$\Lambda=[2\ (T_e+T_i)q/ev_sB]\ \sin[\ (\theta_1-\theta_2)/\ 2\ ] \qquad (2)$$

where Θ_1 and Θ_2 are the poloidal angles of the ends of the line of force on the limiter surface. The longitudinal electrical field $E_\parallel$ occurs due to the finite conductivity $\sigma_\parallel$ of the plasma: $E_\parallel = j_\parallel/\sigma_\parallel$. Thus, $E_\parallel$ in eqn.(1) must be replaced by:

Here, m_e and m_i are the electron and ion mass, respectively, L is the line of force length

$$E_{\parallel} = \frac{j_{\parallel}}{\sigma_{\parallel}} \simeq \frac{T_e}{e} \cdot \frac{1}{\lambda_e} \cdot \frac{\Lambda}{d_n} \cdot \sqrt{\frac{m_e}{m_i}} \qquad (3)$$

defined by intersection with limiter or divertor plates, λ_e is electron mean free path. Equations (1) and (3) describe the turbulent transport in the SOL due to impurity driven rippling instability. Using $d_n = (D_I \cdot \tau_{\parallel})^{1/2}$ and assuming $d_n \ll d_Z$ in eqn.1 we estimate the temperature dependence to follow $D_I \sim T_e^{-1/2}$. Such a dependence was found in ASDEX [2,3]. The volume dissipation by Coulomb collisions dominates when

$$\alpha = (m_e/m_i)^{1/2} L_{\parallel}/\lambda_e > 1 \qquad (4)$$

Usually the nature of edge turbulence in tokamaks is believed to be associated with the dissipation by fluctuation currents flowing through the potential sheath near the surface (so called surface dissipation or SD), i.e. when $\alpha \ll 1$. The enhanced SOL thickness in the DIII-D was observed in the double-null (DN) divertor configuration only. The analysis of the SOL plasma parameters at a radial distance of 1-3 cm from the separatrix shows that α is 2-3 times lower in SN than in DN discharges, in spite of the doublet length L: in SN $\alpha < 1$, in DN $\alpha \geq 1$. These values of α make the existence of ICCT in DN possible. According eqn.(2) the values of Λ in eqn.(3) are in a few times smaller in DN because the current along a magnetic field line changes sign in the SOL of SN configuration. Probably, this strong difference between regimes with DN and SN configuration is also important for the turbulence in SOL.

Based on the asuumption that ICCT exists in the DN SOL of DIII-D I will use a simple model. The equations for the density and the temperature of the plasma are:

$$\chi_{\perp} \frac{d^2 T_e}{d^2 x} - \frac{T_e}{\tau_t} = 0 \; ; \qquad D_{\perp} \frac{d^2 n}{d^2 x} - \frac{n}{\tau_{\parallel}} = 0 \; ; \qquad (5)$$

here $\tau_{\parallel} = L/v_S$, $\tau_t = 3\tau_{\parallel}/\gamma_0$, $\gamma_0 = q/T\Gamma_{\parallel}$, q, Γ are the density of heat and particle fluxes, respectively. The equation for the radial flux of the impurity is

$$\Gamma_{\perp} = -D_{\perp} \nabla_{\perp} n_z + n_z T v_{zi} (m_i \omega_i^2)^{-1} \left[d_n^{-1} - (Z d_z)^{-1} \right] \qquad (6)$$

Here ω_i is the gyro-frequency of the ions of the background plasma. The last term is the radial drift of the impurity due to the friction with the main ions. We are taking $m_i \ll m_z$ and $T_i \approx T_z$. Charge exchange of the impurity and ionization of the neutrals in the SOL are neglected.

The longitudinal flux is determined by the motion of the impurity in the ambipolar electric field $E_{\parallel}$ and by the friction of impurity ions with background ions:
Here v_0 is the velocity of the background ions and $l_{\parallel}$ is the distance along the magnetic field, for which we place the origin of the scale at the middle plane.

$$m_z v_\parallel \frac{dv_\parallel}{dl_\parallel} = eZE_\parallel + m_i \nu_{zi}(v_0 - v_\parallel) \qquad (7)$$

In paper [7] it was shown that for the high collision frequensies the decay length of the impurity is close to the decay length of the background plasma, i.e. the gradient of Z_{eff} tends to zero. Accordingly, in our model we may divide roughly the SOL into two regions. The first region with a relatively large decay length of the impurity is located near the separatrix. The ICCT exists in this region with $\chi \sim D_I \sim T_e^{-1/2}$. In the second region has no ICCT due to low temperatures and the "usual" turbulence by SD is present . Integrating the eqn.(5) over the radial distance from the separatrix, normalized by $x = (\chi\tau_t)^{1/2}$, with $\tau_t \sim T_e^{-1/2}$ and the boundary condition $\partial(T_e/T_0)/\partial x = 1$ for $x=0$ one can obtaine the T_e profile. The temperature tend to zero for $x \approx 1.5$. This means that in the vicinity of $x=1.5$, when the temperature becomes small, there is the boundary between the first and the second region. The density distribution in the first region calculated from eqn.(5) and with the $T_e(x)$ derived is presented in Fig.1. The boundary condition $\partial(n/n_0)/\partial x = 1$ for $x=0$ was used , because $d_n \approx d_t$. For the second region an exponential distribution of the density with the decay length $d_n \approx 1.5$ cm was used.

The qualitative agreement of the calculated curve with the the experimental one shows that ICCT and the interchange turbulence due to SD can describe the two-step profiles in the enhanced SOL of DIII-D. However, the enhanced SOL was only observed in high triangularity discharges [1]. The reason of this is not understood. May be some changing magnetic shear takes place.

It seems that the investigation of the role of the impurity driven turbulence in the SOL must be continued in theory and experiment.

Acknowledgements

I should like to thanks Dr. H.A.Claassen and Dr. U.Samm for help.

This work was supported by Deutsche Forschungsgemeinschaft and KFA Jülich.

References

[1] J.G.Watkins et.al. J.Nucl.Mater. **220-222**, 347 (1995).

[2] K.McCormick et.al, in Proceedings of the 20th European Conference on Controlled Fusion and Plasma Physics, 1993, vol.17C, PartII, p.587.

[3] M.Endler et.al., J.Nucl. Mater. **220-222**, 294 (1995).

[4] A.V.Nedospasov, Contrib. Plasma Phys. **36**, 197 (1996).

[5] A.V.Nedospasov, J. Nucl. Mater. **196-198**, 90 (1992).

[6] X.Garbet et.al. Nucl. Fusion **31**, 967 (1991).

[7] A.V.Nedospasov and G.N.Fidel'man, Sov.Plasma Phys. **14**, 675 (1988).

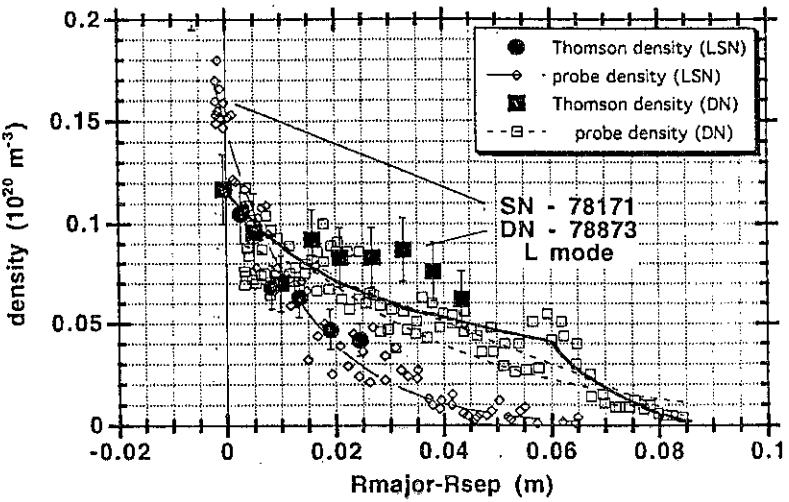

Fig.1 SOL plasma density profiles provided by Thomson scattering and Langmuir probes in DIII-D tokamak for two representative DN and SN discharges (Fig.2 from paper [1]). The calculated profile for DN is shown by upper solid line.

UEDGE Simulation of Detached Divertor Operation in DIII-D With a Chemically Sputtered Carbon Source*

G D Porter, T D Rognlien, M E Fenstermacher, D N Hill, C J Lasnier
Lawrence Livermore National Laboratory, P.O. Box 808, Livermore, CA 94550
R C Isler
Oak Ridge National Laboratory, Oak Ridge Tenn.
and the DIII-D team
General Atomics, P.O. Box 85608, San Diego, CA 92186-9784

1. Abstract

We describe the response of the scrape-off layer (SOL) plasma to variations in the intensity and geometry of an intrinsic carbon source in DIII-D. Using the multi species 2-D fluid plasma code UEDGE we find plasma modes which are similar to those seen experimentally. At high sputtering coefficient the plasma discontinuously transitions to a state in which the radiation power exceeds the input power and no steady state solution is obtained. We believe this corresponds to the MARFE (Multifaceted Asymmetric Radiation from Edge) state seen experimentally, in which the core confinement is reduced.

2. Introduction

Recent experiments in divertor physics have focused on detached operation because of the desirable low divertor heat loads. This mode is achieved by enhancing radiative power losses through injection of either additional working gas or impurity gas. Control of this mode depends in part on the ability to minimize the effect of radiation from intrinsic impurities. The dominant intrinsic impurity in DIII-D is carbon originating from carbon tiles which comprise the majority of the plasma facing surfaces. We examine the response of the divertor plasma to the intensity of carbon arising from physical sputtering at the divertor plates, and chemical sputtering from the plasma facing walls in this article. We use the 2-D multi-fluid plasma code UEDGE to simulate the behavior, and compare the simulation results with experimental measurements obtained with the extensive diagnostic set on the DIII-D tokamak.

3. Effect of intrinsic carbon impurity

Two important sources of carbon in a plasma are physical sputtering arising from an energetic ion flux impinging on a carbon surface, and chemical sputtering which forms gaseous hydrocarbon compounds when deuterium neutrals impinge on a carbon surface[1]. The response of the divertor plasma is quite different for these sources. We describe the simulation

* Work supported by U.S.DoE under LLNL contract W-7405-ENG and GA contract DE-AC03-89ER51114

results obtained for these sources in this section. In all cases, we treat each ionization state of carbon as a separate ion fluid. The impurity ions respond to the usual parallel forces: thermal and pressure gradients, and friction from plasma flow. The neutral carbon species is also treated as a fluid, with a diffusion coefficient determined by elastic scattering processes. All ion fluids are assumed to have the same local temperature. The simulation is done for a lower single null plasma with 1.3 MA current, and 3.4 MW heating power into the SOL.

3.1 Physical sputtering from the divertor plate

We simulate physically sputtered carbon by introducing a local neutral carbon flux which is proportional to the local incident flux of deuterium ions at the divertor plate. We describe the proportionality constant as the sputtering coefficient, and ignore temperature dependence. The neutral carbon arising from this source emerges from the plate in a cosine distribution, with a temperature equal to the local ion temperature. We find the plate electron temperature decreases with increasing sputtering coefficient, leading to a reduction in the ion current and saturation of the total power radiated. The neutral carbon atoms arising from plate sputtering are directed largely toward the impinging hot SOL plasma, and are reionized in the lowest temperature region near the plate. We find this geometric effect limits the power radiated from the carbon impurity to levels well below that seen in the experiment, even with sputtering coefficients which are an order of magnitude higher than expected for the 1 to 2 eV plate electron temperature obtained in the simulations. We conclude that physical sputtering is insufficient to explain the experimental results obtained in DIII-D.

3.2 Chemical sputtering off the plasma facing walls

Chemical sputtering is simulated in the UEDGE code by assuming a neutral carbon flux proportional to the local neutral deuterium flux at the walls which face the SOL plasma. As with physical sputtering, we assume the constant of proportionality is spatially constant, and refer to it as the sputtering coefficient. There are two relevant "walls" in the UEDGE simulation; the private flux wall which lies below the X-point and between the inner and outer strike points, and the outer wall which surrounds the plasma on the common flux side. Neutral carbon emerging from the private flux wall can interact with the SOL plasma up to the X-point, and thus will be injected into higher temperature regions than possible for physically sputtered carbon. We find several distinct plasma operating regimes as the sputtering coefficient is increased from zero. The electron temperature at the inner plate is below that necessary for efficient ionization of the recycling deuterium gas, but the ionization front (say the 5 eV electron temperature contour) lies very near the plate. The electron temperature at the outer plate is about 10 eV. Since the ionization front lies near the plate, the plate ion currents remain high and the plasma is attached at both plates. As the sputtering coefficient is increased carbon radiation on the inner leg moves the ionization front farther off the plate, and the ion current decreases dramatically. The ionization front moves smoothly from the plate to the X-point as the

sputtering coefficient is increased to 4×10^{-4}. The ion current to the inner leg drops approximately an order of magnitude, and the inner plasma becomes detached. The electron temperature at the outer plate remains high, for most of this range, but drops to 2 eV over the last 25% or so. This is indicative of approaching plasma detachment. The total radiated power remains below that seen in the experiment throughout this range in sputtering coefficient. Thus we see the plasma first transitions from an attached plasma to one which is detached at the inner leg, as seen previously for pure deuterium plasmas[2].

The plasma changes abruptly when the sputtering coefficient is increased to 5×10^{-4}. We follow this transition by running UEDGE in a time-dependent mode. The ionization front remains just below the X-point on the inner leg, and moves from the plate to just below the X-point on the outer leg over a period of 20 to 30 ms. As the front moves up the outer leg, the ion current decreases, detaching at both the inner and outer plates. When the ionization front reaches the X-point on the outside, it moves above the X-point on the inside, and rapid radial transport of the electron thermal energy cools the plasma on the closed flux surfaces, leading to the formation of a core MARFE. This low temperature, high density region radiates profusely, predominately from the carbon impurity. The total radiated power exceeds the heating power into the calculational domain, and we do not obtain a steady state solution. We expect operation in this mode to affect the confinement of the core plasma, and one would require a coupled core/SOL plasma code to adequately model the continued evolution of this mode.

4. Comparison with experimental results

Space limitations do not permit detailed comparison of the UEDGE simulation with all of the detailed diagnostic data available on DIII-D. We use the upstream Thomson scattering measurement of the radial electron temperature and density profiles to determine the anomalous perpendicular transport coefficients which we keep fixed at all sputtering coefficients. The density profile in the SOL matches the simulation better after detachment at the outer leg, although the radial gradient on the closed flux surfaces remains higher in the simulation than seen experimentally. We compare the simulation and experiment for two diagnostics in Figure 4-1; the total power measured by two bolometer arrays, and the electron temperature in the divertor region, obtained from the divertor Thomson scattering system. The electron temperature is measured along a vertical line extending to approximately 20 cm from the divertor plate, just outside the outer strike point. Two UEDGE simulations are shown, one with a sputtering coefficient, $Y = 3.5\times10^{-4}$, and the second with $Y=5\times10^{-4}$. The plasma is attached at the outer plate for the low sputtering coefficient, and detached and developed a core MARFE at the higher. The UEDGE solution is not at steady state for the high coefficient.

5. Discussion

The bolometer data indicates this discharge has formed a SOL MARFE rather than the core MARFE seen in the simulation. The signals from the outer SOL (channels 8, 9, and 10) remain high while those from the inner (channels 11, 12, and 13) are low. In the simulation the outer channels transition from low to high when the sputtering coefficient is increased, but the inner channels remain high. We also see the electron temperature drop to order 1 eV for the first 8 cm off the plate when the sputtering coefficient is increased, consistent with experiment. The low temperature region extends farther in the simulation than in the experiment.

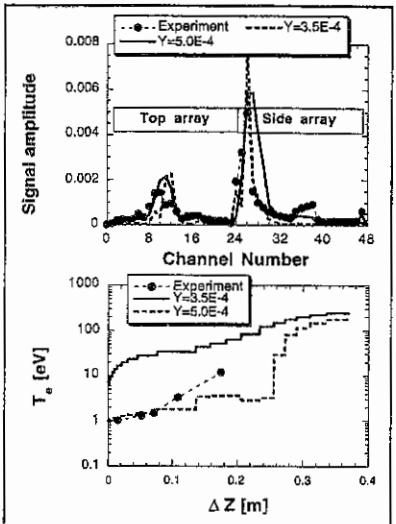

Figure 4-1 Comparison of UEDGE simulation results with experimental measurements of total radiated power (top), and electron temperature in the divertor region (bottom).

The SOL plasma modes obtained with the UEDGE simulations are similar to those seen experimentally. The plasma is frequently detached on the inner plate, especially at low heating power. Detachment at the outer plate requires enhancement of the radiated power. When attached at the outer plate, there are two dominant radiating zones; one on the inside near the X-point, and the second near the divertor plate on the outside. The radiation zone moves above the X-point when the outer leg detaches in the experiment. While the radiation zone for detached plasmas appears as a core MARFE in the simulation, it is seen as either a core MARFE or an SOL MARFE on the outside in the experiment. Experimentally, a core MARFE always forms with excessive gas injection. This suggests that the transition from a SOL MARFE to a core MARFE depends on the plasma flow, and hence on the pumping configuration of the device. The dominant pumping for the discharge simulated here is from wall pumping, a phenomena which is not well understood. Hence it is not surprising that we are unable to completely simulate a particular discharge. The similarities we obtain, however, lend confidence in the physics models of the fluid plasma.

6. References

1. Garcia-Rosales, C., J. Nucl. Mat., **211**: p. 202-214. 1994.

2. Porter, G.D., *et al.*, Phys. of Plas., 3(5): p. 1967. 1996.

THE IMPORTANCE OF THE RADIAL ELECTRIC FIELD (E_r) ON INTERPRETATION OF MOTIONAL STARK EFFECT MEASUREMENTS OF THE q PROFILE IN DIII–D HIGH-PERFORMANCE PLASMAS*

B.W. Rice,‡ L.L. Lao, K.H. Burrell, C.M. Greenfield, Y.R. Lin-Liu
General Atomics, P.O. Box 85608, San Diego, CA 92138-5608

1. Introduction

The development of enhanced confinement regimes such as negative central magnetic shear (NCS) [1,2] and VH–mode [3] illustrates the importance of the q profile and **E×B** velocity shear [4] in improving stability and confinement in tokamak plasmas. Recently, it was realized that the large values of radial electric field observed in these high performance plasmas, up to 200 kV/m in DIII–D, have an effect on the interpretation of motional Stark effect (MSE) measurements of the q profile [5,6]. It has also been shown that, with additional MSE measurements, one can extract a direct measurement of E_r in addition to the usual poloidal field measurement. During a recent vent on DIII–D, 19 additional MSE channels with new viewing angles were added (for a total of 35 channels) in order to descriminate between the neutral beam $\mathbf{v_b} \times \mathbf{B}$ electric field and the plasma E_r field. In this paper, the system upgrade will be described and initial measurements demonstrating simultaneous measurement of the q and E_r profiles will be presented.

2. MSE Measurement Geometry

The MSE measurement relies upon the splitting of the neutral beam Balmer-α line into orthogonally polarized components (σ,π) as a result of a strong electric field in the rest frame of the neutral deuterium atoms. When viewed in a direction perpendicular to **E**, the Stark components σ and π are polarized perpendicular and parallel to **E**, respectively. The total electric field in the rest frame of the neutral beam atoms traveling with velocity v_b is the sum of the motional $\mathbf{E_b} = \mathbf{v_b} \times \mathbf{B}$ field and the plasma radial electric field given by $E_r = (Z_i e n_i)^{-1} \nabla_r p_i - v_{\theta i} B_\phi + v_{\phi i} B_\theta$ where Z_i is the ion species charge, n_i the ion density, p_i the ion pressure, e is the electronic charge, and $v_{\theta i}$ and $v_{\phi i}$ are the poloidal and toroidal rotation velocities, respectively. The derivation of the relationship between the polarization angle of the Stark components and the magnetic field and E_r components is presented elsewhere [5]. Using the viewing geometry shown in Fig. 1, the polarization angle of the electric field along the line-of-sight is given by

$$\tan\gamma = \frac{A_1 B_Z + A_5 E_R}{A_2 B_\phi + A_3 B_R + A_4 B_Z + A_6 E_Z + A_7 E_R} \approx \frac{A_1 B_Z + A_5 E_R}{A_2 B_\phi} \qquad (1)$$

*This is a report of work sponsored by the U.S. Department of Energy under Contract Nos. DE-AC03-89ER51114 and W-7405-ENG-48.
‡Lawrence Livermore National Laboratory, Livermore, CA 94551 U.S.A.

where the A coefficients are viewing geometry dependent terms given by

$$A_1 = -\cos(\alpha+\Omega)$$
$$A_2 = \sin\alpha\cos\theta$$
$$A_3 = \cos\alpha\cos\theta$$
$$A_4 = \sin(\alpha+\Omega)\sin\theta$$
$$A_5 = -\cos\Omega/v_b$$
$$A_6 = -\cos\theta/v_b$$
$$A_7 = \sin\theta\sin\Omega/v_b$$

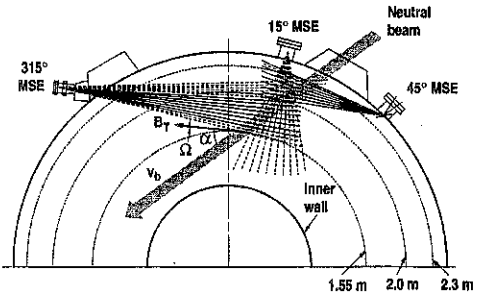

Fig. 1. Viewing geometry for 35 channel MSE system on DIII–D. The dashed lines indicate the line-of-sight of the new channels added to determine E_r.

In past analysis of MSE data, it was assumed that the E_R component in Eq. (1) could be neglected. However, in recent high-performance plasmas, the E_R term in the numerator of Eq. (1) can be up to 25% of the B_Z term and therefore must be included in the analysis. Since coefficients A_1 and A_5 vary differently depending on viewing geometry and beam velocity, we see that with two MSE systems viewing the same radial location in the plasma from different angles (A coefficients), then both the poloidal field (B_Z) and the E_R field can be determined.

An upgrade to the DIII–D MSE system has recently been completed to provide this measurement. Nineteen additional channels were added as indicated by the dashed lines-of-sight in Fig. 1, providing two different viewing angles for each location in the plasma. The hardware design for the new channels essentially duplicates that of the original system [7]. All chords are tuned to the full-energy component of the neutral beam. For the radial viewing channels, the coefficient A_5 is approximately zero, while for the tangential viewing chords $A_5 \sim 1/v_b$. Defining an effective measured vertical field as $B_{Z0} = (A_2/A_1)B_\phi \tan\gamma$ (i.e. the measured vertical field assuming E_R=0), then the radial electric field at a radius R is given by

$$E_r \approx \frac{A_1 A_1'(B_{Z0} - B_{Z0}')}{A_5 A_1' - A_1 A_5'} \qquad (2)$$

where the prime refers to the second view at a given location.

3. Experimental Results

The simultaneous measurement of the q profile and E_r profile has been tested using a recent high-triangularity discharge obtained during commissioning of the new upper divertor hardware in DIII–D (see Fig. 2). This discharge has high confinement (H=3.5) and normalized beta associated with a large E_r field, similar to VH–mode or NCS plasmas, even though the ELM-free period is relatively short. The plasma fuel is deuterium with I_p=1.6 MA and B_ϕ=2.1 T. In Fig. 2(c), the effective vertical field (assuming E_r = 0) is plotted for a tangential chord (solid line) and a radial chord (dashed line) at a radius of R~2 m. If E_r were zero, then these two curves would track one another. The separation of the two curves during the ELM-free period from 2–2.25 s is an indication of the buildup of radial electric field. Using Eq. (2),

E_r at R~2 m is calculated directly from the MSE measurements as shown in Fig. 2(d). The temporal evolution of E_r follows closely the time evolution of the plasma toroidal rotation in Fig. 2(e) obtained from charge-exchange measurements of carbon impurities. The maximum time response of the MSE E_r measurement is 1 ms with an RMS noise resolution of ~7 kV/m. The curve in Fig. 2(c) was generated using a 5 ms sliding boxcar average giving somewhat better resolution. Possible systematic errors in E_r due to spatial averaging in the radial chords and calibration are a factor of 2–3 larger than uncertainties due to noise. An additional point-of-interest in this discharge is that a locked-mode develops after the collapse in β from 2.5–3 s. During this time the the impurity rotation shows a small negative rotation. In agreement with this observation, the MSE radial electric field measurement also reverses sign during mode-locking.

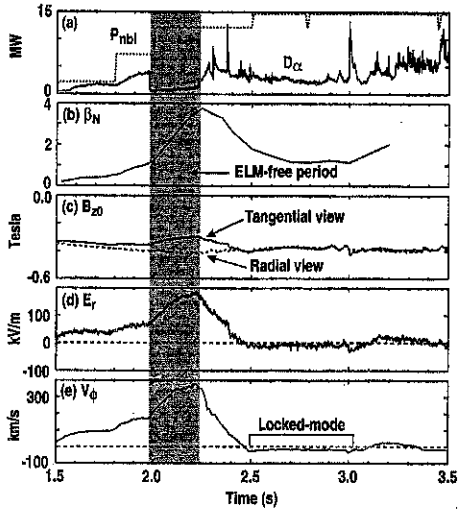

Fig. 2. Temporal evolution of discharge 92043: (a) neutral beam power and D_α emission, (b) normalized beta, (c) MSE $Bz0$ measurement, (d) local value of E_r at R=2.1 m calculated from Eq. (2), (e) CER toroidal rotation.

To determine the profile of E_r, we first examine the profiles of pitch angle and B_{Z0} shown in Fig. 3. At 1.625 s, during the low-power L–mode portion of the discharge, the effective vertical field calculated from both the tangential (circles) and radial (diamonds) systems agree, indicating almost unmeasurable levels of E_r. However, by 2.2 s the tangential and radial profiles have significantly deviated from one another indicating large E_r. The EFIT equilibrium reconstruction code [8] has been modified to fit the radial electric field from the MSE measurements in addition to determining the usual equilibrium profiles of current and pressure. Since E_r is not a flux function, the EFIT code fits the gradient of the electrostatic potential $\partial\Phi/\partial\psi$, which is related to E_r through $E_r = -\partial\Phi/\partial\psi\nabla\psi = \Phi'(RB_Z\hat{R} - RB_R\hat{Z})$. Either a polynomial or spline representation of Φ' is possible. Figure 4 shows the equilibrium reconstruction (including polynomial fit to E_r) of

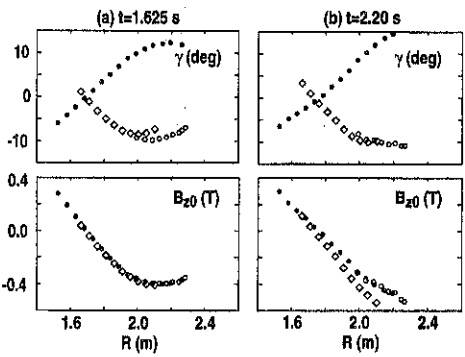

Fig. 3. Profiles MSE pitch angle and B_{Z0} measurements for two phases of discharge 92043: (a) Low-power L–mode phase with low plasma rotation and E_r field; (b) High-performance phase with peak E_r~170 kV/m.

the MSE profile data in Fig. 3 at 2.2 s. In Fig. 4(a), the B_Z data is calculated including the E_R, E_Z terms, and now shows good agreement between the tangential and radial views. The resulting q and E_r profiles are shown in Fig. 4(c) and 4(d) respectively. For comparison, the CER measurement of E_r obtained from Eq. (1) is also shown as the dashed line. The agreement between the two instruments is better than 20 kV/m over the entire plasma radius.

In addition to providing a direct local measurement of E_r, the new MSE measurements also allow the q profile to be calculated with improved accuracy. In Fig. 5, the temporal evolution of q_0 is shown, calculated from EFIT using the tangential chords only and no E_r (dashed line), versus that calculated using all MSE chords, thus including the E_r effect (solid line). The difference in q_0 is quite large, especially during the high-performance ELM-free period.

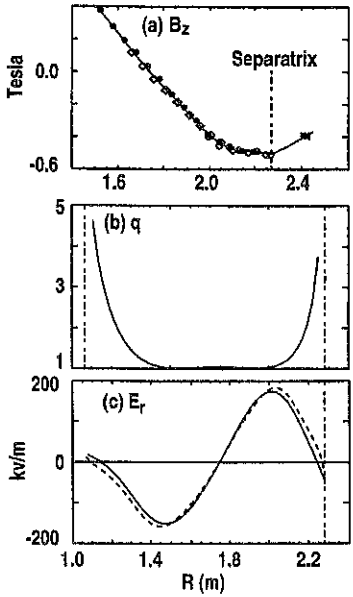

Fig. 4. EFIT equilibrium reconstruction including E_r at 2.2 s: (a) MSE B_z data ; (b) q profile; (c) E_r determined from EFIT (solid line) and CER analysis of carbon impurities (dashed line).

In conclusion, we have demonstrated on DIII–D that the MSE diagnostic can provide simultaneous measurements of the q and E_r profiles. The uncertainty in E_r due to noise is 7 kV/m or less depending on averaging, while systematic errors are currently ~2–3 times this level. Given the importance of the effect of these profiles on plasma stability and confinement, this powerful measurement should continue to guide experimentalists in achieving improved performance in tokamaks.

[1] Strait, E.J., *et al.*, Phys. Rev. Lett. **75**, 4421 (1995).

[2] Levinton, F.M., *et al.*, Phys. Rev. Lett. **75**, 4417 (1995).

[3] Jackson, G.L., *et al.*, Phys. Rev. Lett. **67**, 3098 (1991).

[4] Burrell, K.H., Phys. Plasmas **4**, 1499 (1997).

[5] Rice, B.W., *et al.*, Nucl. Fusion **37**, 517 (1997).

[6] Zarnstorff, M.C., *et al.*, Phys. Plasmas **4**, 1097 (1997).

[7] Rice, B.W., *et al.*, Rev. Sci. Instrum. **66**, 373 (1995).

[8] Lao, L.L., *et al.*, Nucl. Fusion **30**, 1035 (1990).

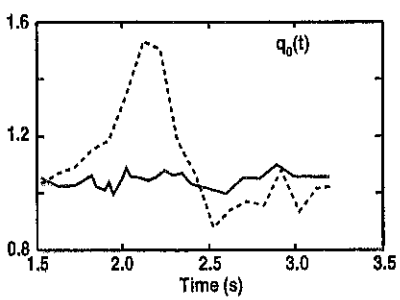

Fig. 5. Tme evolution of q (0) determined by EFIT using full MSE system including E_r (solid line) versus that obtained using only the tangential channels and no E_r (dashed line).

Current drive experiments at high density in the FTU tokamak

V. Pericoli Ridolfini, S. Cirant[1], H. Kroegler, L. Panaccione, S. Podda, P. Buratti, O. Tudisco, G. Giruzzi[2], L. Acitelli, F. Alladio, B. Angelini, M.L. Apicella, G. Apruzzese, E. Barbato, A. Bertocchi, G. Bracco, A. Bruschi[1], G. Buceti, A. Cardinali, C. Centioli, R. Cesario, S. Ciattaglia, M. Ciotti, V. Cocilovo, F. Crisanti, R. De Angelis, F. De Marco, B. Esposito, D. Frigione, L. Gabellieri, G. Gatti, E. Giovannozzi, C. Gourlan, G. Granucci[1], M. Grolli, A. Imparato, M. Leigheb, L. Lovisetto, G. Maddaluno, G. Maffia, A. Mancuso, M. Marinucci, G. Mazzitelli, P. Micozzi, F. Mirizzi, F.P. Orsitto, D. Pacella, M. Panella, L. Pieroni, G.B. Righetti, F. Romanelli, F. Santini, M. Sassi, S.E. Segre[3], A. Simonetto[1], S. Sternini, A.A. Tuccillo, F. Valente, V. Vitale, G. Vlad, V. Zanza, M. Zerbini, C. Sozzi[1]

Associazione Euratom-ENEA sulla Fusione, Centro Ricerche Frascati,
C.P. 65 - 00044 Frascati, Rome, Italy
[1]Istituto di Fisica del Plasma CNR Milano, Italy
[2]CEA Cadarache, France
[3]Dipartimento di Fisica, II Università degli Studi di Roma, Rome, Italy

LHCD experiments

Current drive (CD) studies have been performed in FTU with the 8 GHz Lower Hybrid (LH) system [1] at a power level $P_{LH} \leq 1.2$ MW, with routine high power density operation at the grill mouth (> 10 kW/cm^2). No significant impurity influx takes place for line averaged densities $\bar{n}_e > 0.4 \cdot 10^{20}$ m^{-3}. The value of the effective charge $Z_{eff,LH}$ during the LH pulse is similar to the ohmic value $Z_{eff,OH}$ at $\bar{n}_e > 1 \cdot 10^{20}$ m^{-3} ($Z_{eff,LH} \approx 1.5$), it is $Z_{eff,LH} Z_{eff,OH} \approx 0.6$ for $0.4 \cdot 10^{20} < \bar{n}_e < 0.7 \cdot 10^{20}$ m^{-3} ($Z_{eff,LH}$ between 2.2 and 2.8), whereas for $\bar{n}_e \leq 0.4 \cdot 10^{20}$ m^{-3} $Z_{eff,LH} \approx 6$, starting from $Z_{eff,OH} \approx 4.5$ [2]. In Fig 1 the relative loop voltage drop $\Delta = (V_{l,OH} - V_{l,LH})/V_{l,OH}$, which is approximately the ratio of the LH current to the total current I_{LH}/I_p is plotted versus the ratio $h = P_{LH}/(I_p \cdot \bar{n}_e \cdot R)$ [W/(A·10^{20} m^{-2})], where R is the FTU major radius. The value of h at the point where $\Delta = 1$ is the inverse of the CD efficiency η_{CD}. Data are taken in the ranges $0.3 \leq \bar{n}_e \leq 1.2 \cdot 10^{20}$ m^{-3} and $0.2 \leq P_{LH} \leq 1.1$ MW. A fit with a simple formula (dashed line), which considers the effect of the electric field on the hot electron tail [3], gives for $V_{l,LH} = 0$ a value $\eta_{CD} \approx 0.13$. Such a low value, compared e.g. with JET ($\eta_{CD} \approx 0.23$) [4], might be explained by the smaller volume averaged electron temperature $\langle T_e \rangle$ in FTU, $\langle T_e \rangle \approx 0.6$ against $\langle T_e \rangle \approx 2$ keV in JET, and by the fact that high values of I_{LH}/I_p (≥90%), have been obtained so far only for $\bar{n}_e \leq 0.4 \cdot 10^{20}$ m^{-3}, i.e. for high Z_{eff} values ($Z_{eff} > 5$. compared with $Z_{eff} \approx 1.5$ for JET). In order to quantify both effects it is convenient to consider the theoretical value of η_{CD}:

$$\eta_{CD} = \frac{124}{ln\Lambda \cdot (5 + Z_{eff})} \cdot \frac{v_{\|1}^2 - v_{\|2}^2}{c^2 \cdot ln(v_{\|1}/v_{\|2})} \qquad (1)$$

where $ln\Lambda$ is the Coulomb logarithm, $v_{\parallel 1}$,$v_{\parallel 2}$ are the low and high velocity limits of the resonant electron tail, c is the speed of light. From Eq (1) the difference in $<T_e>$ accounts for a factor ≈1.4 and the difference in Z_{eff} for a further factor of ≈1.5. The $<T_e>$ dependence comes from the assumption $v_{\parallel 1} \approx 3.5 \cdot (<T_e>/m_e)^{1/2}$, in order to assure a good LH power absorption [5], with $v_{\parallel 2}$ determined by the launched spectrum. Upon accounting for the Z_{eff} correction Eq. (1) a value of η_{CD} close to 0.2 can be estimated for Z_{eff}=1 in FTU.

The only limit on the density observed so far is imposed by the accessibility constraints on the launched LH waves. Indeed a value of I_{LH}/I_p as high as ≈0.4 (Fig. 1) is obtained for $\bar{n}_e \approx 1 \cdot 10^{20}$ m^{-3} and a central density $n_{pk} \approx 1.35 \cdot 10^{20}$ m^{-3}, with the accessibility of the LH inside half the plasma radius becoming marginal. This view is also supported by the measurements of the electron cyclotron emission from the suprathermal LH tail, shown in Fig 2. Here the radiation temperature T_{rad} normalised to $P_{LH}/\bar{n}_e$ is plotted versus density together with some code calculations [6]. The drop with $\bar{n}_e$ agrees with code predictions and the suprathermal tail feature in the spectrum is evident up to $\bar{n}_e \approx 1.32 \cdot 10^{20}$ m^{-3} with $n_{pk} \approx 1.7 \cdot 10^{20}$ m^{-3}. The lower T_{rad} observed at $\bar{n}_e \approx 1 \cdot 10^{20}$ m^{-3} when the launched peak value of the parallel refraction index $N_\parallel$ is changed from 1.52 to 2.43 and to 3.65 are also foreseen by the code if correspondingly the LH power deposition shifts radially outwards, as it is indicated by LH absorption codes.

Up to the maximum density, there is no evidence of parametric decay instabilities or strong pump broadening, which in other experiments indicate a degraded performance [7].

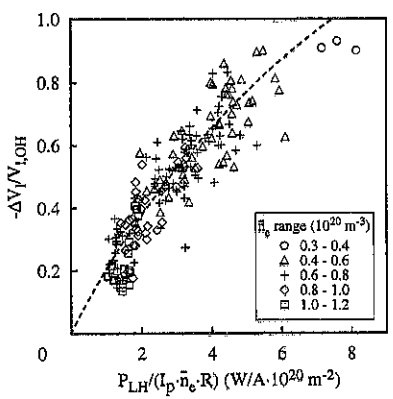

Fig 1. Plot of the relative loop voltage drop versus h (see text). Points are distinguished according to the plasma density. The full curve is a fit with the formula $(\eta_{CD}+B)*h/(1+B*h)$ [3].

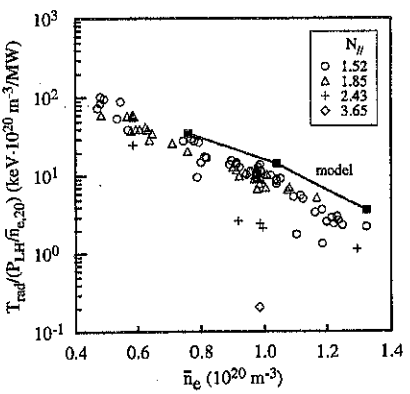

Fig 2. Radiation temperature T_{rad} [keV] of the suprathermal e-tail normalised to the power available per particle $P_{LH}/\bar{n}_e$ [MW/10^{20} m^{-3}] plotted vs the line averaged density $\bar{n}_e$. Different marks refer to different $N_\parallel$. The full line corresponds to code calculations.

Sawteeth are suppressed for densities $n_e \leq 0.6 \cdot 10^{20}$ m^{-3} but the leading quantity appears to be the LH driven current fraction. Stabilisation occurs if $I_{LH}/I_p \geq 60\%$ as illustrated in Fig. 3 where the sawtooth repetition rate τ_{st} is plotted versus h for two values of I_p. No significant shrink of the sawtooth inversion radius is observed when $I_{LH}/I_p < 60\%$. When stabilisation is attained, the m=1 MHD activity still persists and very peaked electron temperature profiles are obtained, with the central values T_{e0} reaching 5 keV. However in such a situation sawteeth reappear after a while, accompanied by a reduction of T_{e0} and by a flattening of the $T_e(r)$ profile. The analysis with a LH absorption code shows that after the temperature increase the deposition and consequently the I_{LH} profile becomes more peaked triggering the sawteeth again.

LHCD and ECH combined operation

The FTU electron cyclotron heating (ECH) system (P_{ECH}= 350 kW for 0.1 s at f=140 GHz, perpendicular injection) [8] allows to control T_e and hence to study the dependence of η_{CD} on $\langle T_e \rangle$ (Eq. (1)), as discussed in Ref. [5]. In order to reduce the effect of the parallel electric field the ECH power has been injected in a plasma close to full CD conditions, compatibly with the available LH power. Only data with the relative loop voltage drop $\Delta > 75\%$ have been considered and B_T the magnetic field was varied between 5.2 and 5.7 T in order to shift the ECH resonance region from the magnetic axis to a normalised radius r/a≈0,45 and to control the temperature profile and the onset of the sawteeth. The effect of ECH on the LH driven current is clear for

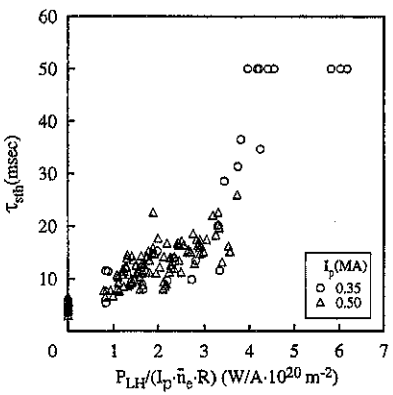

Fig 3. Sawteeth repetition rate τ_{st} versus $P_{LH}/\bar{n}_e$ [MW/10^{20} m^{-3}] for two plasma currents, I_p=0.35 and I_p=0.5 MA. Full stabilisation is obtained only for I_p=0.35 MA.

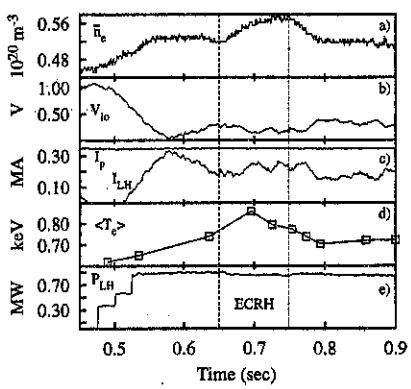

Fig 4.- Temporal evolution during combined LH+ECH injection of: a) line averaged density $\bar{n}_e$; b) loop voltage V_{loop}; c) plasma current I_p and LH driven current I_{LH}; d) volume averaged electron temperature $\langle T_e \rangle$; e) LH power P_{LH}. The vertical lines mark the ECH temporal gate

$B_T \geq 5.4$ T ($r/a \geq 0.13$). In Fig. 4 the time evolution of the most significant plasma quantities is plotted. The applied ECH power is 340 kW. The temporal shift of the decrease of the loop voltage (Fig 4b) with respect to the ECH pulse is due to the time needed to modify the temperature profile, which relaxes to the pre-LH shape within ≈ 20 msec after ECH switch off (Fig. 4d), and to the time requested to form a LH current. The magnitude of I_{LH}, which shows an increase outside the experimental error in the ECH phase, has been evaluated subtracting to the total current the ohmic contribution. This is estimated simply scaling the average conductivity in the ohmic phase by the ratio $\left\langle T_e^{1.5} \right\rangle / \left\langle T_{e,OH}^{1.5} \right\rangle$ and multiplying by the loop voltage. The increase of I_{LH} is consistent with Eq. (1), but it must be pointed out that simulations with a LH absorption code predict also an increase of the total LH absorbed power during the ECH phase. In the combined LH+ECH operation the m=1 MHD oscillation persists, and is normally enhanced in case of central ECH power deposition, whereas complete sawtooth stabilisation is attained only if the resonance region is located at $r/a > 0.3$.

Conclusions

In FTU the feasibility of current drive at high densities $\bar{n}_e > 1 \cdot 10^{20}$ m^{-3} which are of interest for ITER has been demonstrated. No apparent negative trend with density is observed, and the CD efficiency extrapolated to clean plasma conditions may reach $\eta_{CD} \approx 0.2$ [10^{20} m^{-2}·A/W]. This value could be further increased by the favourable dependence of η_{CD} with $\langle T_e \rangle$ which has been experimentally found in FTU utilising an ECH. The analysis of possible synergetic interaction between ECH and the propagation and absorption of LH waves is in progress.

REFERENCES

[1] A.A. Tuccillo et al., II Int. Workshop on Strong Microwaves in Plasmas, Nizhny Novgorod, 15-22 August 1993, **Vol. 1**, p. 47-59

[2] M.L. Apicella et al., Nucl. Fusion **37**, 381 (1997)

[3] G. Giruzzi et al., "Measurements of the hot electrical conductivity in PBX-M tokamak", to be published in Nucl. Fus.

[4] A. Ekedhal et al., Proc 23rd EPS Conf. on Plasma Phys. Controll. Fusion, Kiev, Ukraine, 24 - 28 June 1996, **V.20C**, part II, p. 969

[5] E. Barbato, ENEA REPORT RT/ERG/FUS/96/25 Centro Ricerche Frascati

[6] G. Giruzzi, Plasma Phys. Controll. Fusion **35**, A123 (1993)

[7] V. Pericoli Ridolfini et al., Nucl. Fusion **32**, 286 (1992); R. Cesario et al, ibid. p. 2127

[8] S.Cirant et al, "Long pulse ECRH experiments at 140 Ghz on FTU tokamak", Proc. of 10th Joint Workshop on ECE Emission and ECRH, Ameland (NL), April 1997

ANALYSIS OF SHEAR REVERSAL FORMATION SCENARIOS ON FTU BY LOWER HYBRID CURRENT DRIVE

E. Barbato, S. Cirant[1], F. Crisanti, L. Gabellieri, A.A.Tuccillo, G. Bracco, F.P. Orsitto, F. Alladio, L. Acitelli, B. Angelini, M.L. Apicella, G. Apruzzese, A. Bertocchi, A. Bruschi[1], G. Buceti, P. Buratti, A. Cardinali, C. Centioli, R. Cesario, S. Ciattaglia, M. Ciotti, V. Cocilovo, R. De Angelis, F. De Marco, B. Esposito, D. Frigione, G. Gatti, E. Giovannozzi, C. Gourlan, G. Granucci[1], M. Grolli, A. Imparato, H. Kroegler, M. Leigheb, L. Lovisetto, G. Maddaluno, G. Maffia, A. Mancuso, M. Marinucci, G. Mazzitelli, P. Micozzi, F. Mirizzi, D. Pacella, L. Panaccione, M. Panella, V. Pericoli Ridolfini, L. Pieroni, S. Podda, G.B. Righetti, F. Romanelli, F. Santini, M. Sassi, S.E. Segre[2], A. Simonetto[1], C. Sozzi[1], S. Sternini, O. Tudisco, F. Valente, V. Vitale, G. Vlad, V. Zanza, M. Zerbini

Associazione EURATOM-ENEA sulla Fusione, CR Frascati CP. 65, 00044 Frascati, Rome, Italy.
[1]Associazione EURATOM-ENEA-CNR, Ist.di Fisica del Plasma, Via Bassini 15, 20133 Milano, Italy
[2] Universita' Di Roma 2, Tor Vergata, Rome (Italy)

1. Introduction.

The FTU experiment at 8Ghz [1] is the only Lower Hybrid Waves (LHW) experiment, running at present, providing a Current Drive (CD) and heating data base at reactor relevant densities (~$1\times10^{20}m^{-3}$). The achievement of reversed magnetic shear configurations by partial Lower Hybrid Current Drive in fully relaxed current density conditions also represents an ITER relevant goal. Theoretically foreseen [2] shear reversal configurations have been experimentally achieved [1] in the high density FTU plasma on a time scale longer than the skin time by partial off axis LH Current Drive (LHCD) at 1 MW of power level. Experimental results are reported accompanied by a theoretical and numerical analysis of LHW power deposition and current density diffusion. Experiments are also presented of transient shear reversal configurations achieved by freezing the current density diffusion toward the plasma center during the ohmic current ramp-up phase by central Electron Cyclotron Resonant Heating (ECRH) (140GHz, 300KW, 100ms) [3] and by LHW power injection. High central electron temperature up to 9keV are obtained during the ECRH heated current ramp phase. The confinement properties of the reversal region in this condition are briefly discussed.

2. Shear reversal during the current flat-top

To study relaxed states of the current density profile "low" temperature plasmas are considered in order to make the skin time less than the LH pulse length (≤1s). In FTU it turns out $T_{e0}<1.7$ kev to have $\tau_{skin}<300$ms. In such conditions there is a large spectral gap between the parallel LHW phase velocity and the electron thermal velocity, so that first pass power absorption is expected to be small. Whatever it is the spectral gap filling mechanism, the dispersion relation and toroidal axis-symmetry impose to the launched parallel refractive index $n_{\|L}$ a maximum upshift factor [4] for each radial position, $n_{\|+}/n_{\|0}$, given by:

$$\frac{n_{\|+}(x)}{n_{\|0}} = \left[1 - x\frac{\varepsilon}{q(x)}\frac{\omega_{pe}(x)}{\omega}\right]^{-1} \qquad (1)$$

where x=r/a is the normalized minor radius, $\varepsilon=a/R_0$ the inverse aspect ratio, q the safety factor, ω_{pe} the electron plasma frequency, ω the LH frequency and $n_{\|0}=(1+\varepsilon)\, n_{\|L}$. Equation (1) also gives the spatial trapping region of all the rays with a given n_ϕ [5]. By comparing Eq. (1) with the upshift factor required for absorption, $n_{\|ELD}(x)/n_{\|0}=6.5\ T(x)^{-1/2}$, we can approximately determine the LHW power deposition region as the region where Eq. (1) and $n_{\|ELD}(x)/n_{\|0}$ overlap. Following this criterion three density region can be identified: 1) an high density region, defined as $\Gamma=\varepsilon\omega_{pe}(0)[2\omega(q(0)q(a))^{1/2}]^{-1}>1$, where deposition is expected to be central; 2) an intermediate density region, $1-n_{\|0}/n_{\|ELD}(0)<\Gamma<1$, where deposition is expected to be off axis; 3) a low density (low temperature) region ($\Gamma<1-n_{\|0}/n_{\|ELD}(0)$) where absorption is expected to be negligible. It also turns out that, in the intermediate density region, the deposition is the more peripheral the flatter are the q and density profile, as indicated by the radial position of the maximum of Eq. (1), $x_{max}^2=[q(a)/q(0)+\alpha_n]^{-1}$, becoming more peripheral for low q(a)/q(0) and α_n value. Here $\alpha_n=\ln[n_e(x)/(n(0)(1-x^2))]$ is related to the density profile peaking. This picture, based on simple arguments, is fairly well confirmed by power depositions calculations [2] based on toroidal ray-tracing and Fokker-Planck codes. In Fig. (1) an off axis deposition obtained in the intermediate density region is shown. According to such theoretical expectations, shear reversal configurations can be realized, in a low temperature plasma, by LHCD at intermediate density and by counter LHCD at high density, where, on the other hand, the runaway velocity can be well beyond the maximum velocity of fast electrons ($c/n_{\|acc}$). Resistive diffusion calculations [2], performed in the presence of all the current components, i.e. purely ohmic, purely non inductive, and cross term (hot conductivity), show that in the CD-scheme at least 40-50% of the current has to be driven at x~1/3 to get a shear reversal q profile and about 20-30% at the plasma center in the counter-CD scheme. Following these criteria two plasma targets have been selected and experimentally studied so far, suitable to undergo a shear reversal during the current flat-top by LHCD at $n_\|=1.55$ ($\Delta\phi=75°$): 1) B=4T, I_P=350kA (qa=5.5), $n_{LINE}=0.7\times10^{20}m^{-3}$, $T_e(0)$=1.6keV, 1) B=5.2T, I_P=350kA (qa=7), $n_{LINE}=0.85$-$1.2\times10^{20}m^{-3}$, $T_e(0)$=1.3keV. The latter was a preparation plasma target for central ECRH. In both cases the sawtooth activity, when present, is suppressed and Double Tearing Modes (DTM) reconnections appear later on in the discharge. A different MHD behaviour marks the two kind of discharges, as discussed in ref. [6]. In the B=4T case, the sawtooth is stabilized in 0.2-0.4 s, and, after a large MHD rearrangements of the discharge, a stable reversed configuration is achieved with a reversal radius r_s/a=0.5 and a saturated m=2 mode. Data on these discharges have already been reported elsewhere [1]. Deposition calculations for this kind of discharge give 150kA of current approximately driven between 1/3 and 1/2 of the minor radius (as shown in Fig.1) in agreement with the experimental V_{loop} drop. Resistive diffusion calculations, using such deposition as an input, give a temporal evolution of the q-profile in agreement with the q-profile reconstructed from the equilibrium data. Fig. 2a shows the

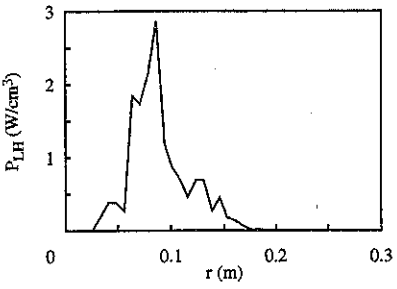

Fig. 1 - LH deposition profiles at B=4T

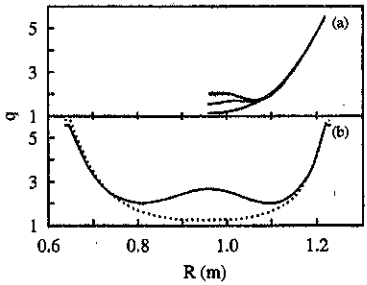

Fig. 2 - q-profile evolution a) from resistive diffusion calculation, b) from equilibrium reconstruction

calculated q-profiles 100, 300, and 500ms after the RF switch on. Fig. 2b shows the reconstructed q-profile at the sawtooth stabilization (t=0.62s) and 400ms later.

In the higher B, q(a) discharges the sawtooth is stabilized very rapidly and irregular DTM crashes appear in the discharge which does not enter in the stable regime observed in the B=4T case. The DTM inversion radius is typically located at r_s/a=0.2-0.25 thus indicating that a more central deposition profile is taking place with respect to the lower q(a) case, in agreement with the qualitative theoretical considerations given above. A density scan proved that this regime can be accessed only when density is larger than $0.85\times10^{20}m^{-3}$ while at q(a)=5.5 the density was $0.73\times10^{20}m^{-3}$. Such density values fall in the range $1-n_{||0}/n_{||ELD}(0) <\Gamma<1$. Concluding remarks are i) the LH deposition in low temperature plasmas, needed to study relaxed state of the current density profile within the RF pulse, can be controlled by a proper choice of the plasma parameters, according to theoretical expectations based on dispersion relation and axis-symmetry and confirmed by numerical deposition calculations; ii) in this way shear reversal configurations can be and, as a matter of fact , have been obtained in FTU by partial LHCD; iii) the plasma target at 5.2T has to be ameliorated lowering the q(a), thus making the off axis deposition more pronounced; a slightly off axis ECRH, rising the pressure profile, could have a stabilizing effects [6], allowing the discharge to enter the stable MHD regime found at B=4T.

3. Shear reversal during the current ramp.

Transient shear reversal configurations have been achieved by freezing the current density diffusion during the ohmic current ramp-up phase by central Electron Cyclotron Resonant Heating (ECRH). Typical plasma parameters of these discharges are: B=5.2T, dI_p/dt=5MA/s^{-1}, n_{LINE}=0.4-0.7$\times10^{20}$ m^{-3}. Very high central electron temperatures are measured by the Thomson scattering [7], in this phase (sawtooth-free) of the discharge, as shown in Fig. 3, where T_{e0}~9keV is measured. A local transport analysis gives values of χ_e around 0.2 m^2/s at the plasma center. The achievement of a shear reversal configuration is marked by DTM reconnections and by simulations of the discharge evolution that gives the q-profile time

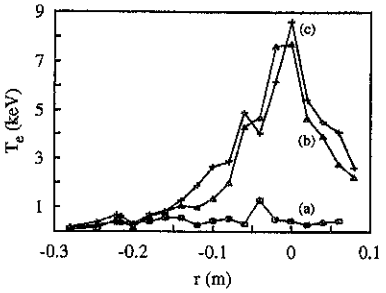

Fig. 3 - Te profile during ECRH in current ramp experiment a) t=42ms,b) t=70ms, c) t=119ms. ECRH starts at 45ms.

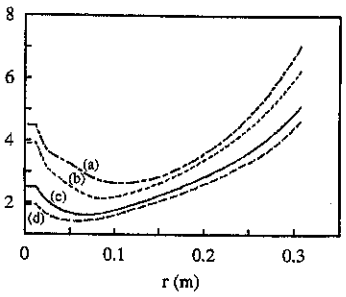

Fig. 4 - simulated q-profile time evolution in current ramp experiments a) t=65ms, b) t=75ms, c) t=95ms, d) t=105ms. ECRH starts at 60ms.

behaviour reported in Fig. 4. Uncertainties in the q-profile are connected with the used resistivity (whether Spitzer or Neoclassical) and Z_{EFF} values. In some of these discharges, at the end of the current ramp, an increase of the central electron temperature of about 1keV is observed in connection with the stabilization of an MHD mode that stops its activity when a very flat q-profile at the plasma center is established. Such temperature increase can be attributed to an improvement of the local electron confinement. Finally experiments have been done injecting LH power at the end of the current ramp on such ECR heated plasma targets, with the aim of further sustaining the shear reversal configuration. Up to now 200-400kW of LHW power has been injected at $\Delta\phi$=75-120° ($n_{||}$=1.55-2.4). Delays ranging between 30 and 100ms, on the onset of the sawtooth activity, have been observed so far. Generally the discharge without sawtooth stops in a disruption. Experiments are in progress to optimize the q-profile at the LH start in order to avoid disruptions.

References

[1] A.A Tuccillo et al., *Lower Hybrid Current Drive in FTU High Density Shear Reversed Discharges* , 12th APS Topical Conf.on RF in Plasmas, Savannah (1997)

[2] E. Barbato, ENEA Report RT/ERG/FUS/96/25

[3] S.Cirant et al., *Long pulse ECRH experiments at 140 Ghz on FTU*, Proc. of 10th Joint Workshop on ECE Emission and ECRH, Ameland (1997)

[4] E. Barbato, F Romanelli, Phys. Fluids **B2**, 2687 (1990)

[5] X. Litaudon et al., Plasma Phys. Controll. Fusion **38**, 1603 (1996)

[6] P. Buratti et al., *MHD activity in FTU plasmas with reversed magnetic shear*, this Conference

[7] Orsitto et al., Applied Optics, **34** 2712 (1995)

First Neutron Emission Profiles in FTU Plasmas

B. Esposito, L. Bertalot, P. Batistoni and M. Damiani
Associazione Euratom ENEA sulla Fusione, CRE Frascati, C.P. 65
I-0044 Frascati, Rome, Italy

1. Introduction

A six channel neutron collimator has been recently installed on the Frascati Tokamak Upgrade (FTU) to measure the 2.5 MeV DD neutron profile emission from the plasma [1]. This system, used in combination with the neutron yield monitor, has proved its capabilty of providing useful information on the ion temperature profile in the first measurements performed in ohmic and pellet-fuelled deuterium discharges during the 1996/97 FTU campaign.

The diagnostic, which can also operate as hard X-ray profile monitor, is located under the machine and is viewing the plasma radially from a vertical port (Fig.1). The camera consists of a neutron and γ-ray shielding block made of a mixture of machined polyethylene and lithium carbonate plus lead slabs. The total shield thickness is 120 cm and its weight is about 9 tons. The spatial resolution at the plasma centre is of the order of ~3 cm. The detectors, located in a shielded box, are organic liquid scintillators (NE213) coupled to photomultipliers. Pulse shape discrimination modules [2] are used to separate between γ-ray and neutrons events; the detection threshold is set at 1.8 MeV neutron energy to reject backscattered neutrons.

2. Experimental set-up

A preliminary debugging of the diagnostic has been carried out in deuterium discharges. The typical measured neutron count rate in the central channel (#3) is ~ 200 c/s at a total neutron yield rate of 2×10^{12} n/s. Although the n/γ discrimination is found to work properly (the count rate of γ-ray events being 5-10 times higher than that of neutron events in typical discharges, while the measured breakthrough of γ-ray events into neutron events is less than 0.2%) a neutron background signal, attributed to uncollimated neutrons, has been observed in all channels. A measurement of the background has been performed by inserting stainless-steel cylinders 60 cm long into the collimators channels in order to block the incoming fast neutrons and subsequently by taking data in ohmic discharges; plots of neutron count rate versus total neutron yield rate (Y_N) have been produced for all collimator channels, assuming that with the channels blocked all neutron events are due to background only. Y_N is independently measured, with an uncertainty of ~15%, by a system of six BF_3 detectors located on top of FTU [3]. The results show a linear increase of the background with the total neutron yield: this effect is particolarly strong for channels #1 and #2, probably due to the fact that a part of the shield near to these channels is missing beacause of the proximity of the diagnostic to the DCN interferometer structure. The background contribution is routinely subtracted in the final data,

but, at the moment, very large error bars are present on signals from channels #1 and #2 as the background here amounts to more than half of the total signal. After background subtraction and corrections for solid angle and detector efficiency, the raw data are transformed into line-integrated neutron emissivity (neutron brightness, in units of $ns^{-1}m^{-2}$). The efficiency of the NE213 detectors has not been directly measured, but can be obtained using the constraint that Y_N as measured by the collimator channels equals that measured by the BF_3 detectors: efficiency values of 6-8% are found.

3. Results

Data have beeen collected both for ohmic and pellet fuelled deuterium discharges with the channels unblocked. If we assume a neutron emission profile of the form $S(x) = S_0(1-x^2)^{\alpha_N}$, where x=r/a is the normalized minor radius, the neutron brightness I_N for a circular plasma can be calculated as:

$$I_N(\rho) = \frac{Y_N}{2\pi^{3/2} a R_0} \frac{\Gamma(\alpha_N + 2)}{\Gamma(\alpha_N + 3/2)} (1-\rho)^{\alpha_N + 1/2} \qquad (1);$$

here ρ is the distance (normalized to the minor radius) of a chord from the plasma and R_0 the major radius. Using eq.1 for a least square fit to the measured neutron brightness data, the neutron emissivity peaking factor, α_N, can be determined. An estimate of the ion temperature profile can be also obtained: if a functional dependance of the form $T_i(x) = T_{i0}(1-x^2)^{\alpha_T}$ is assumed for the ion temperature and the experimental electron density profile (Thomson scattering) is fitted as $n(x) = n_0(1-x^2)^{\alpha_n}$, a simple relation is found [1] between the various peaking factors: $\alpha_N = 2\alpha_n + \gamma\alpha_T$, where γ, which appears in the expression of the DD maxwellian reactivity ($\langle\sigma v\rangle_{DD} \sim T_i^{\gamma}$), ranges between 6 and 5 for 1 keV < T_i < 2 keV.

In order to improve the counting statistics, five consecutive ohmic discharges (flat top duration ~ 0.8 s) have been run with identical plasma parameters: $n_e \sim 1.2 \times 10^{20}\ m^{-3}$, $I_p = 700$ kA, $B_t = 6$ T and $Z_{eff} \sim 1.5$. Count rates near to those expected for neutron yield rates of 10^{13} n/s (for which the diagnostics has been optimized) have been obtained. Fig.2 shows the neutron brightness profile averaged over the five shots. The solid line represents the least square fit obtained assuming a neutron emissivity radial profile as described above: the derived ion temperature peaking factor is $\alpha_T = 1.33$ with $T_{i0} = 1.2$ keV.

Data from a pellet-fuelled discharge clearly show the time evolution of the neutron emission profile after the injection of a pellet at t = 0.87 s: the profile, which is initially peaked ($\alpha_N = 12$ at t = 1.0 s, see Fig. 3), becomes flatter at later times and, correspondingly, also its absolute value decreases in agreement with the time behaviour of the neutron yield monitor signal (Fig. 4). For this discharge we find, at t = 1.0 s, $\alpha_T = 1.75$ and $T_{i0} = 1.4$ keV: such values are found to agree with those of the electron temperature, indicating a good coupling between ions and electrons (peak electron density ~ $3\times 10^{20}\ m^{-3}$).

4. Conclusions

The preliminary results give confidence in the reliability of the FTU neutron collimator: the systems operates in agreement with the expected performance, with the exception of channels #1 and 2 where the signals from uncollimated neutrons overwhelm that from collimated neutrons. An additional neutron shielding is therefore necessary to fully exploit the diagnostics and work is in progress for its design.

It is foreseen that the diagnostic can routinely provide neutron emission and ion temperature profiles with error bars of ~20% and a time resolution of ~100 ms when the FTU additional heating systems (ECRH, LH and IBW) are fully operational ($Y_N > 10^{13}$ n/s).

Acknowledgments

We would like to thank E. Giovannozzi and F. Orsitto for having kindly provided the electron density data and S. Podda for his help in data reduction.

References

[1] P. Batistoni, B. Esposito, M. Martone, S. Mantovani, Rev. Sci. Instrum. **66** 4949 (1995)

[2] J. M. Adams and G. White. Nucl. Instrum. Methods **156** 459 (1978)

[3] L. Bertalot, B. Esposito, S. Podda, S. Rollet, Rev. Sci. Instrum. **63** 4554 (1992)

ch #	1	2	3	4	6	5
r (m)	-.18	-.04	.01	.06	.13	.21

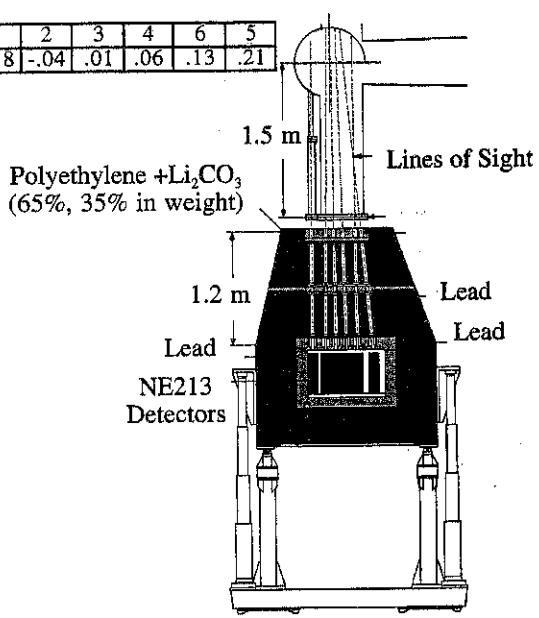

Fig.1: Schematic of the FTU neutron collimator

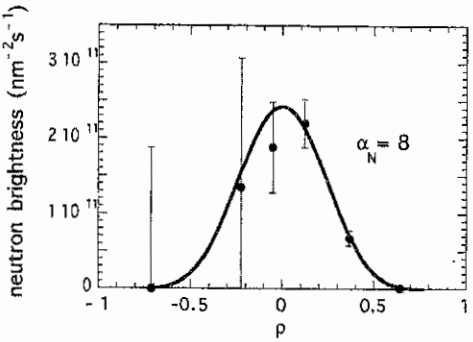

Fig.2: Neutron brightness profile in ohmic discharges (average over five discharges)

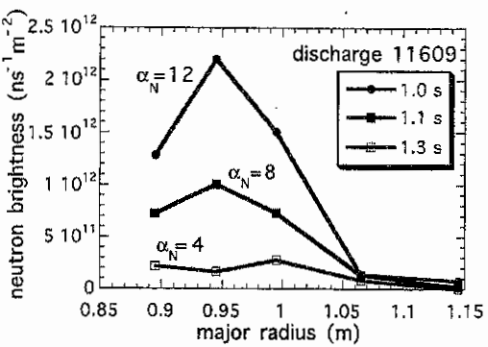

Fig.3: Neutron brightness profile after pellet injection

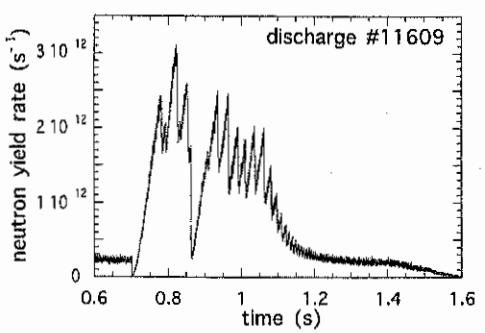

Fig.4: Neutron yield rate in pellet discharge (measured by fast scintillator cross calibrated with BF_3 detectors)

Influx of metal impurities from toroidal and poloidal limiter in FTU

G. Apruzzese, R. De Angelis, G. Gatti
Associazione EURATOM-ENEA sulla Fusione, Centro Ricerche Frascati,
C.P. 65 - 00044 Frascati, Rome, Italy

Introduction

Poloidal limiters made with different materials (inconel, W and Mo) and a Molybdenum toroidal limiter have been used on the Frascati Tokamak Upgrade (FTU) to define the last closed magnetic surface.

The study of the plasma contamination due to the inflow of metallic impurities, which occurs as a consequence of the plasma limiter interaction, is of importance in view of the possibility of using high Z materials in some region of the ITER divertor. Such a study can be conveniently performed on FTU since, in this device, the limiter thermal loads are comparable to those predicted for the ITER divertor.

Visible spectroscopy is an important diagnostic tool for studying the fluxes of impurities emitted by materials facing the plasma. In fact, it is generally possible to infer the flux of particles released by those surfaces by measuring, in the visible range, the brightness of spectral lines in the cold plasma periphery where they are mostly neutral or weakly ionised.

In this paper, the impurity influxes have been measured and compared in different operating conditions with both limiters, either in ohmic and in RF discharge.

Experimental data analysis with poloidal and toroidal limiters

The impurity flux is derived from the measurements of absolute line intensity obtained by a calibrated Optical Multichannel Analyzer spectrometer [1].

The most careful analysis is done for the molybdenum limiter since, at the moment, FTU is operating with a toroidal TZM limiter [2]. A visible spectrum, in the range of 3700-7000 Å, for a typical FTU discharge (plasma current I_p=500 kA, toroidal field B_t=6 T and line averaged electron density $\langle n_e \rangle = 0.9 \times 10^{20}$ m^{-3}) is shown in fig.1. The wavelenghts of MoI lines are: 3798.3 Å, 3864.1 Å, 3903.0 Å corresponding to the transitions from the level z^7P^o to the ground state a^7S, and 5506.5 Å, 5533.0 Å, 5570.4 Å corresponding to the transitions from the level z^5P^o to the metastable state a^5S.

To obtain the flux from the limiter, the brightness of the lines are multiplied by the ratio S/XB, i.e. the MoI number of ionisations per photon emitted (S being the ionisation rate, X the excitation rate and B the branching ratio of the observed lines). The values of S/XB are taken from the Atomic Data and Analysis Structure (ADAS) database [3]. The uncertainties on evaluating the fluxes are due, mainly, to the uncertainties on electron density and temperature: in our case, T_e = 30 eV and n_e=0.2 $\langle n_e \rangle$ are taken. The total MoI flux is composed of atoms

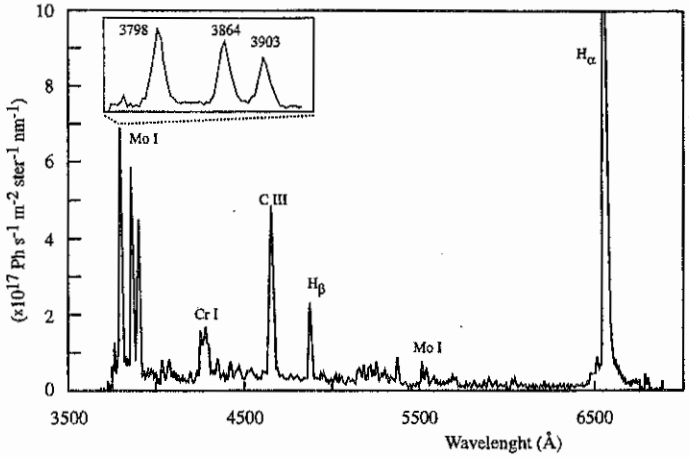

Fig.1 - Visible spectrum for a typical FTU discharge.

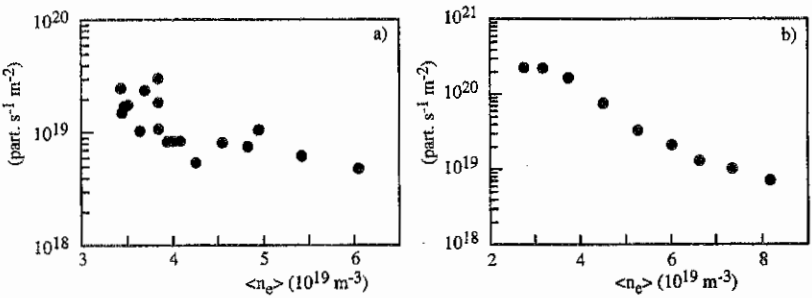

Fig.2 - Neutral Mo influx , in toroidal limiter configuration (a) and in poloidal limiter configuration (b).

released both in the ground state and in the metastable state (about 10% of the total). The first contribution to the flux is derived by the line intensity of transitions $z^7P^o \rightarrow a^7S$ and the second by the line intensity of transitions $z^5P^o \rightarrow a^5S$. In the last case, to evaluate the population of the excited level z^5P^o only from the metastable state a^5S, corrections are taken into account, as suggested by [3].

Figure 2 shows the MoI flux as a function of the electron density for a discharge with B_t=6 T and I_p=0.6 MA, in configuration of toroidal limiter and H_2 fuel (a) and in configuration of poloidal limiter and D_2 fuel (b). In both cases, the MoI flux decreases with the density until the detection limit. The MoI flux is 10 times smaller with the toroidal limiter, as expected by the ratio between the limiters' emitting surfaces. Figure 3 shows the ratio of MoI flux to the fuel

flux, derived by the brightness of H_β line intensity for case (a) and of D_γ line intensity for case (b). This ratio can be considered as an effective sputtering yield of Mo due to the hydrogen/deuterium ions impinging on the limiter surface and self-sputtering. In toroidal limiter configuration, this ratio is of the same order of magnitude as that obtained in poloidal limiter configuration.

Under certain operating conditions, at low plasma current or at high electron density, expecially during the plateau phase, the Mo flux in the discharge becomes smaller than the detection limit. The presence of Mo is observed in the stationary phase of the discharge only at very high plasma current, Ip>900 kA.

In the FTU discharges obtained with both toroidal Mo limiter and external poloidal inconel limiter, significant quantities of Cr are observed. For typical FTU discharges, the Cr behaviour is similar to that of Mo both in magnitude $\Gamma_{Cr} = 1\times10^{19}$ part. s^{-1} m^{-2}, and in temporal

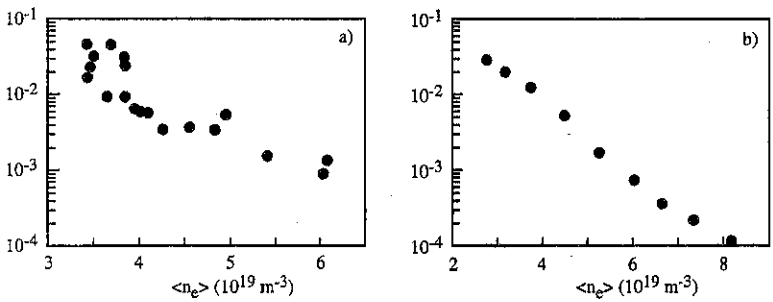

Fig.3 - The ratio of MoI flux to the fuel flux, in the same cases as fig.2.

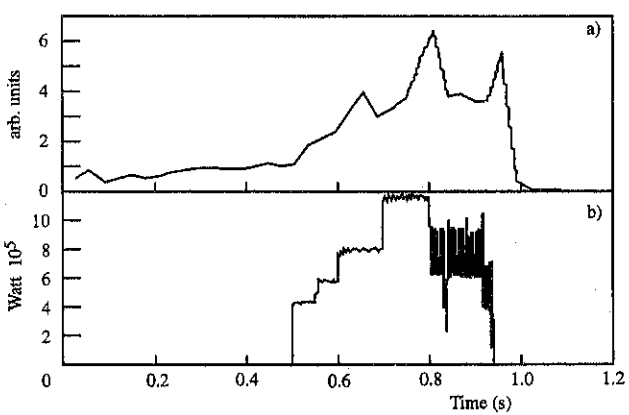

Fig.4 - Γ_{CIII} (line λ= 4647.4 Å) (a) and the coupled LH power (b) versus time.

behaviour. Cr becomes predominant in run-away discharges when the external limiter plays a fundamental role.

Even if FTU is characterised by metal impurities, there are cases where the light impurity emission becomes predominant. This happens especially during Lower Hybrid Radio Frequency injection [4], where it is observed an increment of the emission of peripherical lines of light impurities. Figure 4 shows the time behaviour of the CIII flux, measured from the visible spectra. During LH phase an increase up to a factor of 4 is observed. This increment is apparently not dependent on total power for coupled LH powers in the range 0.5 to 1.3 MW. The behaviour of carbon is in agreement with that of oxygen as observed in VUV spectra.

Conclusions

The metallic impurity flux, measured on FTU, shows a strong inverse dependence on the electron plasma density. With the poloidal inconel limiter, this dependence for Cr and Ni has been assessed experimentally over a wide range of stationary operating conditions. Mo lines have shown the same behaviour during the density rise, while they are observed in stationary phases only at high plasma current.

The Mo influx is smaller in the toroidal limiter configuration when the interaction of the plasma with the limiter is more uniformly distributed so the thermal load per unit surface is sensibly reduced. The total number of Mo atoms coming from the limiters, in both configurations, is about the same.

When operating with the inconel external poloidal limiter also, significant contribution from other metallic impurities are usually observed even if their emitting surfaces are negligible.

References

[1] I. Condrea, R. Bartiromo, G. Mazzitelli and D.H. McNeill, Proc. 14th Int. Conf. on Plasma Physics, Innsbruk,1992

[2] M.L. Apicella, G. Apruzzese, G. Bracco, et.al., Nucl. Fusion, **37**, No.3 (1997)

[3] N.R. Badnell, et al., J. Phys. B **29**, 3683 (1996)

[4] V. Pericoli et al., "Current Drive experiments at high density in the FTU tokamak", this conference

Sawtooth Stabilisation on the FTU Tokamak

P. Buratti, O. Tudisco, L.Panaccione, L. Acitelli[2], F. Alladio, B. Angelini, M.L. Apicella, G. Apruzzese, E. Barbato, A. Bertocchi, G. Bracco, A. Bruschi[1], G. Buceti, A. Cardinali, C. Centioli, R. Cesario, S. Ciattaglia, M. Ciotti, S. Cirant[1], V. Cocilovo, F. Crisanti, R. De Angelis, F. De Marco, B. Esposito, D. Frigione, L. Gabellieri, G. Gatti, E. Giovannozzi, C. Gourlan, G. Granucci[1], M. Grolli, A. Imparato, H. Kroegler, M. Leigheb, L. Lovisetto, G. Maddaluno, G. Maffia, A. Mancuso, M. Marinucci, G. Mazzitelli, P. Micozzi, F. Mirizzi, F.P. Orsitto, D. Pacella, M. Panella, V. Pericoli Ridolfini, L. Pieroni, G.B. S. Podda, Righetti, F. Romanelli, F. Santini, M. Sassi, S.E. Segre[3], A. Simonetto[1], C. Sozzi[1], S. Sternini, A.A. Tuccillo, F. Valente, V. Vitale, G. Vlad, V. Zanza, M. Zerbini

Associazione Euratom-ENEA sulla Fusione, Centro Ricerche Enegia Frascati,
C.P. 65 - 00044 Frascati, Rome, Italy
[1]Istituto di Fisica del Plasma CNR Milano, Italy
[2] ENEA Guest
[3]Dipartimento di Fisica, II Università degli Studi di Roma, Rome, Italy

Introduction

The observation of rapid, precursorless sawtooth (ST) collapses requires a trigger mechanism much faster than the progressive destabilization of a m=1 mode. This problem was first noticed for large tokamaks with strong auxiliary heating, but temperature drops occurring on a time scale of 5 μs, i.e. an order of magnitude less than the Kadomtsev reconnection time, have also been observed in FTU ohmic discharges.

In order to gain insight into the trigger mechanism, the ST modifications produced by LHCD, pellet injection [1] and ECRH have been studied on FTU.

The injection of LH waves with co-current drive suppress the ST crashes when LH power is above a threshold leaving a strong kink distortion of the plasma core with m=1. ST stabilization by LH waves has been observed in many tokamaks [2-5] always in current drive regime.

In FTU, the behaviour of nearly stabilised sawteeth is particularly interesting, in fact a kink displacement of the plasma core of the order of the q=1 surface radius, similar to that of usual sawteeth, is not followed by any collapse.

Spatial structure of precursors during ECRH

Central ECRH produced very peaked temperature profiles during the ST ramp phase. This allowed a precise determination of the spatial structure of precursor oscillations from ECE data.

Figure 1 shows the temperature profiles at the minimum and maximum of the oscillation before the ST crash and the temperature profile just after the crash. The oscillation appears in all channels within the mixing radius and it is not localized close the ST inversion radius. It turns out that the collapse can be preceded by a kink distortion with nearly constant displacement within the inversion radius. The displacement grows on a time scale much longer than that of the final temperature drop.

Another interesting feature that comes out during the ECRH sawteeth is the coexistence of two

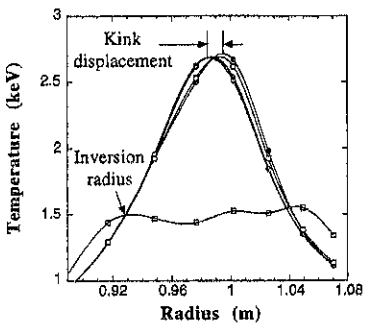

Fig. 1. Temperature profiles before and after the ST crash. Profile before crash are taken at opposite phase of precursor oscillation.

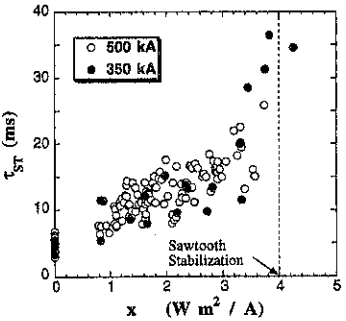

Fig. 2. *Sawtooth period vs* $x=10^{20}\ P_{LH}/(R_o\,\bar{n}_e I_p)$. *Sawteeth have been stabilized for* $x>4$

interleaved types of crashes, one with a fast time scale (~ 20 μs) and the other with a longer time scale (~100 μs) compatible with the Kadomtsev time. In the second case the slightly smaller inversion radius is filled progressively by a growing island.

Stabilization with LHCD

The ST activity of low current discharges of FTU has been stabilized by means of LH power. The effects of LH on the ST activity have been studied in a selected number of discharges that, however, are representative of the complete set of LH discharges made in FTU. Discharges with two currents (350 and 500 kA), with a density ranging from 0.3 to 1.3×10^{20} m^{-3}, and a total LH power (P_{LH}) from 0.2 to 1.2 MW have been considered. Only discharges with LH co-current drive phasing ($\Delta\phi = 75°$) have been taken into account. In fig 2, the ST period is plotted versus the normalized LH power $x=10^{20}P_{LH} / (R_o\,\bar{n}_e I_p)$, that is strictly related with the relative loop voltage drop $\Delta V_L / V_L$ [6]. No double sawteeth have been included in the plot. Sawteeth in low current discharges are stabilized for $x > 4$, that approximately correspond to a $\Delta V_L/V_L$ of about 0.6, while it is never stabilized, at the available power level, for I_p=500 kA.

Sawtooth inversion radius

The evolution of the resonant q=1 surface can be followed monitoring the ST inversion radius during the LH phase, when sawteeth are not completely stabilized. This analysis has been done in some FTU discharges using SXR line averaged emission to find the ST inversion radii. Actually, this is just an indication of the behaviour of q=1 surface and not its real position. We found that the ST inversion radius does not change significantly in all discharges we have analyzed. Figure 3 shows the time evolution of the inversion radius together with some relevant plasma quantities. The main parameters of this discharge are : I_p=500 kA, B_T = 5.2 T , $\bar{n}_e$=7.2 $\times10^{19}$ m^{-3}, P_{LH} = 1.1 MW and x= 0.33. While the ST period changes from 5 ms up to 20 ms,

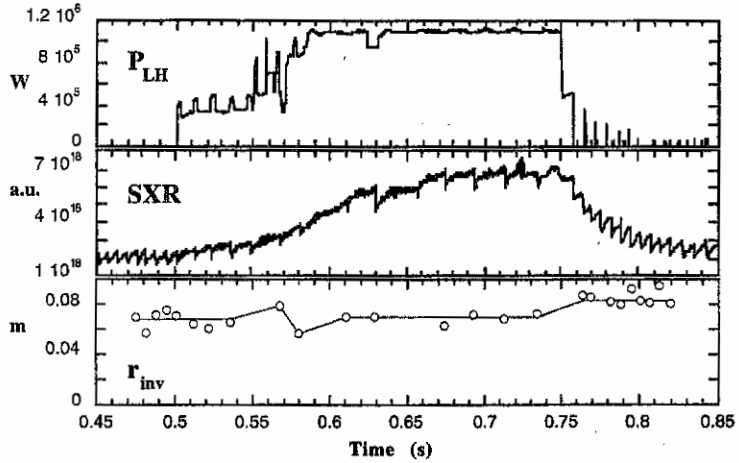

Fig. 3. Time variation of LH power (P_{LH}), central chord of soft-X ray (SXR), ST period (τ_{ST}) and inversion radius (r_{inv}). The continous line in the last plot, is the inversion radius obtained from profiles averaged at constant LH power level.

the inversion radius remains constant within 5 mm. It is worth noting that the inversion radius rises more than 1 cm when the LH power is switched off. A possible explanation can be the following: LH drives the current in the plasma core; when this source is switched off the central current decreases on the time scale of suprathermal electron confinement while the ohmic current takes some time to diffuse in, so that a transient profile broadening can occur.

In many FTU discharges with low current and density sawteeth disappear as soon as the LH is applied even at low power level. The corresponding x value is well below the threshold found before (x_{th}~4). If the power is kept at low level the ST oscillations restart after a while (50-100 msec). This behaviour is probably due again to a transient profile modification. This discharges have not been included in the plot of fig 2.

Oscillation after stabilization

Sawteeth can disappear either because the safety factor q(r) rises above 1 everywhere in the plasma or because the mechanism that triggers the ST crashes is not valid anymore. In FTU both situations are present. Most discharges show a strong m=1 oscillation after stabilization while some ones are affected by double-tearing reconnections typical of hollow q profile with minimum q>1. This latter case seems to be peculiar of plasmas target with peaked density profile and hence with an off-axis LH deposition. More details can be found in the invited paper at this conference [7].

Kink oscillations (m=1), after ST stabilization, last from one to for several hundreds of milliseconds. Usually, oscillations end during the LH power phase and sawteeth restart. This

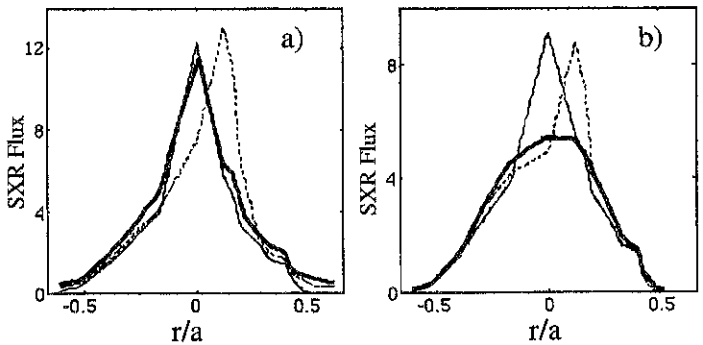

Fig.4. Line integrated soft-X ray emissivities for nearly stabilised (a) and normal (b) sawtooth. Thin lines: end of the ramp phase; dashed lines: maximum kink displacement; thick lines: end of the m=1 activity.

behaviour is analogous to that found in Alcator C [2] for high power sawteeth suppression. Before the sawteeth reappear, several burst of m=1 oscillation with the same periodicity of the successive sawteeth occurs. The SXR profiles at opposite oscillation phase are shown in fig 4a) together with the profiles of the precursor of a usual sawtooth (fig 4 b). The kink displacement in both cases is the same, but no reconnection occurs in the burst of oscillations (thick lines).

Conclusions

Sawteeth are stabilized by LH when x>4 Wm^2/A ($\Delta V_L/V_L>0.6$) for a large range of density and LH power. The q=1 radius is not modified by the LH, as it leaves the ST inversion radius unchanged; this indicates that the trigger mechanism is affected either by some fine modification of the current profile or by the presence of fast electrons. The kink displacement before ST crashes affects all the plasma within the q=1 surface as is shown in central ECRH discharges, but usually it is not seen on temperature measurements for the lack of temperature gradients. Furthermore discharges without ST crashes but with kink displacement of the order of the q=1 radius could indicate that ST crashes are not triggered by the precursor amplitude.

Reference

[1] F Alladio et al, Proc. 23rd EPS Conf. on Controll. Fusion and Plasma Phys. (Kiev,1996), paper a133, vol I, p 404.
[2] S.Knowlton, M.Porkolab, Y.Takase, Nucl Fusion **28**, 99 (1988)
[3] T.K. Chu et al, Nucl Fusion **26**, 666 (1986)
[4] F.X.Söldner, Phys. Rev. Lett. **57**, 1137 (1986)
[5] D. Moreau et al, Plasma Phys. Controll. Fusion **33**, 1621 (1991)
[6] A. A Tuccillo et al., Invited Lecture 12th APS Topical Conf. on RF in Plasmas, April 1-3 (1997) Savannah, Georgia.
[7] P.Buratti et al, invited topical lecture at this conference.

Improved confinement on FTU sustained by multiple pellet injection

D. Frigione, S. Cirant[1], E. Giovannozzi, P. Micozzi, L. Acitelli, P. Buratti, O. Tudisco, V. Zanza, F. Alladio, B. Angelini, M.L. Apicella, G. Apruzzese, E. Barbato, A. Bertocchi, G. Bracco, A. Bruschi[1], G. Buceti, A. Cardinali, C. Centioli, R. Cesario, S. Ciattaglia, M. Ciotti, V. Cocilovo, F. Crisanti, R. De Angelis, F. De Marco, B. Esposito, L. Gabellieri, G. Gatti, C. Gourlan, G. Granucci[1], M. Grolli, A. Imparato, H. Kroegler, M. Leigheb, L. Lovisetto, G. Maddaluno, G. Maffia, A. Mancuso, M. Marinucci, G. Mazzitelli, F. Mirizzi, F.P. Orsitto, D. Pacella, L. Panaccione, M. Panella, V. Pericoli Ridolfini, L. Pieroni, S. Podda, G.B. Righetti, F. Romanelli, F. Santini, M. Sassi, S.E. Segre[2], A. Simonetto[1], C. Sozzi[1], S. Sternini, A.A. Tuccillo, F. Valente, V. Vitale, G. Vlad, M. Zerbini

Associazione Euratom-ENEA sulla Fusione, Centro Ricerche Frascati,
C.P. 65 - 00044 Frascati, Rome, Italy
[1]Istituto di Fisica del Plasma CNR Milano, Italy
[2]CEA Cadarache, France
[3]Dipartimento di Fisica, II Università degli Studi di Roma, Rome, Italy

1. Introduction

Since the very early experiments on Alcator-C tokamak, it is known that pellet injection can lead to improved confinemet regimes in ohmic discharges [1]. With combined pellet injection and additional heating the so-called PEP mode (Pellet Enhanced Performance) has been obtained under transient conditions [2]. On the Frascati Tokamak Upgrade (FTU, R=0.93 m, a=0.3 m), we have extended the post-pellet enhanced confinement phase of an ohmic discharge with deep multiple pellet injection.The MHD phenomena that take place after the pellet perturbations are described together with an analysis of the transport properties of the discharge.

2. The pellet injector and the diagnostic system

On FTU [3], a pneumatic multi barrels pellet injector, built at the RISO laboratories, capable to fire up to eight pellets with a velocity of 1.5 km/s and a mass of the order of 10^{20} D atoms, is presently installed. Masses and speeds are measured by an RF cavity and two optical diodes. The ablation process lastig about 100 μs, is monitored by an H_α detector collinear with the pellet flight path. The plasma electron density is measured by a 5 chords DCN and a single central chord CO_2/HeNe interferometers: the first one, during pellet injection loses fringes while the second is able to follow very fast phenomena. A combination with the mesurements of a 10 pulses Thomson scattering system is needed for reconstructing the density profiles in the post pellet phase. The electron temperature profile is measured by an ECE Michelson interferometer and an ECE polychromator and the results are in agreement with the Thomson scattering. The radiation losses are measured by a 16 channels bolometer array and the total

radiated power is derived by assuming toroidal and poloidal symmetry when no marfe is present. The average value of the ion effective charge (Z_{eff}), is derived from the visible bremsstrahlung emission along a central chord.

3. MHD behaviour and improved performance

In low density target plasma when the pellet deposition is more peripheral, the reheating is hampered by MHD activity: a central impurity accumulation occurs, producing hollow temperature profiles, and multiple crashes associated with double tearing instability with m=2, n=1 or m=3, n=2 are observed. The sawtooth activity reappears only at high density as soon as the pre-pellet temperature and density profiles are recovered. These observations confirm the trend already outlined in a previous work with a single pellet injector [4]. In lower current discharges (500 kA, 6 T, q_ψ=6.3), the extra particle content induced by pellet injection is completely lost during the reheating phase characterized by the stabilization of the sawtooth activity. Neither the energy content nor the confinement time increase in these discharges which on the contrary are more stable against major disruptions also after the injection of a second pellet. The best performances have been obtained at q_ψ= 4.6. Figure 1 shows the case of a target sawtoothing 680 kA, 5.9T discharge with a line averaged density of 1.2×10^{20} m^{-3} and a central electron temperature of 1.5 keV. The pellet ablation takes place mainly inside the q=2 surface and extinguishes beyond the q=1 resonance as shown by the drop of the H_α emission [5] which signs the crossing of a rational surface (fig. 2) . According to the density profiles measured by the Thomson scattering before and after the pellet injection, a fast particle inward diffusion takes place after the ablation process: the central density rises up to a value 2.6 times

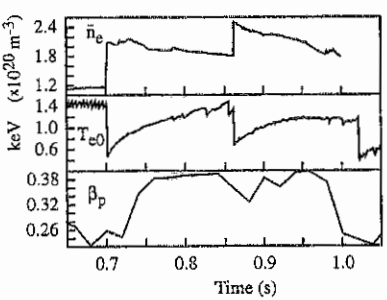

Fig. 1 - Shot 11612, 680 kA, 6 T. Temporal evolution after pellet injection. From the top: line average electron density, central electron temperature, poloidal beta.

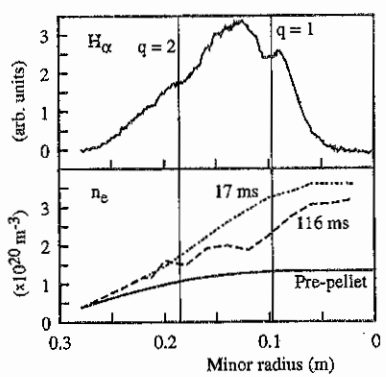

Fig. 2 - H_α emission during the ablation process and electron density profiles as measured by the Thomson scattering before and after the pellet injection.

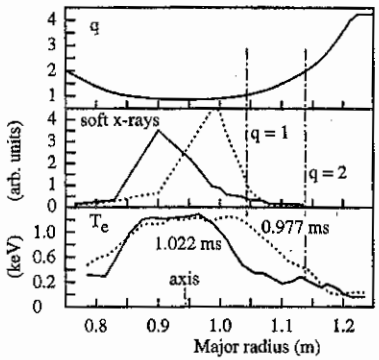

Fig. 3 - MHD activity following the second pellet. From the top: safety factor profile, X-ray emissivity showing the m=1 magnetic axis displacement, Michelson Te profiles shrinked by the growth of an m=2 island.

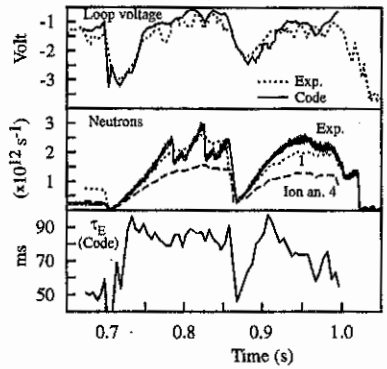

Fig. 4 - Results of the transport code compared with experimental data. From the top: loop voltage, neutron rate and global energy confinement time.

larger than the initial one and decays with a charachteristic time of the order of 300 ms in absence of any gas puffing. On the contrary, 90% of the initial central electron temperature is recovered in 100 ms. An MHD quiescent phase, lasting about 80 ms, follows the injection of the first pellet and is interrupted by sawtooth crashes occurring at a repetition time of 30-40 ms. After the second pellet, a fast m=1, n=1 activity, associated with a ±5 cm magnetic axis displacement takes place and no crashes are observed until an m=2 island develops and locks inducing the shrinking of the temperature profile (fig 3). The improved phase starts with the first pellet and lasts more than 200 ms: the central plasma pressure reaches the value of 6.4×10^4 Pa (β_p=0.4) corresponding to a global energy confinement time of 80 ms (see next section, fig 4) which is about twice the typical value observed in the saturated ohmic regime.

4. The transport code and the interpretative analysis.

In order to analyse the transport properties of the discharge in more detail, a transport code has been employed in an interpretative version. The code solves the time dependent magnetic field diffusion equation, assuming a Spitzer resistivity, and the electron and ion energy balance equations which are linearized at each time step and integrated by a finite difference method. The geometry is given by the equilibrium reconstruction: the other input data are the experimental electron density and temperature profiles, the effective charge, the toroidal magnetic field and the total plasma current. The ion plasma transport is assumed to be neoclassical multiplied by a constant anomaly factor that is adjusted in order to reproduce the

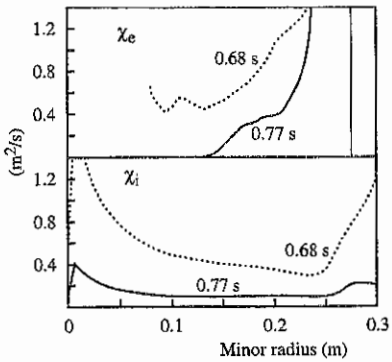

Fig. 5 - Electron and ion thermal conductivities in the pre and post pellet phase.

measured neutron emission rate. The validity of the simulation is checked also by comparing the calculated loop voltage evolution with the measured one. The initial conditions are set by the pre-pellet stationary phase. Figure 4 shows the time evolution of the calculated neutron yield, loop voltage and global energy confinement time compared with the corresponding experimental quantities. The prepellet neutron emission rate is well reproduced with an ion anomaly of 4 which, on the contrary, does not account for the strong increase following pellet injection: in this phase pure neoclassical ion losses are consistent with the experimental observation. Figure 5 shows the electron and ion conductivity profiles before and after the injection of the first pellet: in the central region the pre-pellet χ_e is not reported due to the presence of the sawtooth activity. After the pellet, both the ion and electron thermal conductivities are reduced over the whole profile: in the central region, the electron conductivity is completely quenched and transport is dominated by the ions.

5. Conclusion

We have obtained on FTU an extended improved ohmic performance sustained by repetitive deep pellet injection: the observed confinement time of 80 ms is twice the typical value of the saturated ohmic regime. The improved performance lasts for more than 200 ms and persists after the injection of a second pellet: it seems due to a good confinement of the particles deposited in the core region and to a reduction of the ion thermal conductivity over the whole discharge. The observed electron conductivity falls below the ion value in the central plasma while remains dominant outside. The growth of an m=2 island and its subsequent locking stops the improved phase: if a further pellet is injected in this conditions, a major disruption occurs. We foresee to use in the future well localised ECR heating to stabilize this mode and aim at stationary improved performance.

References

[1] M. Greenwald et al., Phys. Rev. Lett., **53** (1984) 352

[2] JET Team, Proc. 12th IAEA Conf., Nice,1988, Vol. 1, IAEA (1989) 215

[3] R. Andreani et al. Fusion Techn. **221** (1991)

[4] F. Alladio et al., Plasma Phys. Control. Fusion **35** (1993) B241-B251

[5] Pegourie, B., Dubois, M. A., Nucl. Fusion **30** (1990) 1575

Linear frequency response of reconnecting perturbations

Enzo Lazzaro[1], Lorenzo Gianoli[2], Lorenzo Valdettaro[2] and Carlo Cercignani[2]
[1] Istituto di Fisica del Plasma CNR, Assoc. ENEA-Euratom, Via Cozzi 53, Milan,Italy
[2] Dip. di Matematica, Politecnico di Milano, Piazza L. da Vinci 32, 20133 Milan, Italy

1. Introduction

The control of the nonlinear dynamics of resistive MHD modes with low poloidal and toroidal numbers m,n can be based on the electrodynamical feedback compensation of the measured perturbation by means of external quasi static (DC) or rotating (AC) helical fields with the same winding period of the mode to be controlled. A general limitation of feedback stabilization schemes that are frequency independent and operating on single modes is that the restraining action on one mode is destabilizing for another. With frequency dependent schemes multimode control can in principle be obtained but a knowledge is required of the frequency response function of the plasma under the action of the external driving perturbations. In a tokamak plasma characterized by a large Lundquist number ($S \sim 10^8$) in the zero frequency limit helical resistive perturbations appear as tearing modes localized on q rational magnetic surfaces, but at low but finite frequency $0 < \omega_0 \tau_A << 1$ there is a transformation towards Alfvĕn waves which, as shown in the following, determine the characteristics of the frequency response.

2. Boundary value problem for driven response

We formulate here a boundary value problem for externally driven magnetic field perturbations described, within the reduced MHD (RMHD) model [1, 2, 3, 4, 5], in terms of a single (m,n) helicity flux function $\Psi(r,\vartheta,\phi(t),t)$ with instantaneous phase $\phi(t)$ in a coordinate system $\{r,\vartheta = q - (n/mR)z\}$:

$$\mathbf{B} = \mathrm{Re}\nabla \times \left(\Psi(r)e^{i(m\vartheta-\phi(t))}\mathbf{e}_z\right) \tag{1}$$

and an electric drift velocity perturbation in terms of an analogous stream function:

$$\mathbf{v} = \mathrm{Re}\nabla \times \left(\Phi(r)e^{i(m\vartheta-\phi(t))}\mathbf{e}_z\right)$$

We consider a plasma with circular cross section of radius a, in absence of resistive wall. In vacuum at radius $b > a$ we model the active coils system by an ideal time varying helical surface current $I_v \cos(m\vartheta - \phi_v(t))$ with helicity ratio m/n resonant with the safety factor q at $r = r_s$ and arbitrary frequency ω_0. We consider the linearized equations for Ψ in cylindrical geometry (large R/a approximation) [5]:

$$\begin{aligned}
&\frac{\partial \Psi_1}{\partial t} - i\frac{m}{r}B_{0\vartheta}(r)\left(1-\frac{n}{m}q(r)\right)\Phi_1 = \frac{\eta_0}{\mu_0 g(r)}\nabla^2\Psi_1 \\
&-\frac{\partial \nabla^2\Phi_1}{\partial t} = -i\frac{m}{\rho_0\mu_0 r}B_{0\vartheta}(r)\left(1-\frac{n}{m}q(r)\right)\nabla^2\Psi_1 + i\frac{m}{\rho_0 r}\frac{\partial J_0}{\partial r}\Psi_1
\end{aligned} \tag{2}$$

where $g(r)$ is the slowly varying normalized profile of resistivity. The associated boundary conditions which match the external driving fields are derived from the conditions of continuity of the normal component of the magnetic field, of continuity of the tangential component of and of vanishing of the normal component of the velocity at the plasma vacuum interface, valid for a resistive plasma with vanishing current density at the edge [2]. When the system is driven by an external field (generated by saddle coils) oscillating at a given (real) frequency ω_0 the system (2) can be cast in to the general form

$$\nabla_{\perp}^2 \mathbf{u} - \underline{\underline{T}} \cdot \mathbf{u} = 0 \tag{3}$$

with $\mathbf{u}$ the dimensionless vector $\mathbf{u} = (\mathrm{Re}(\Psi_1), \mathrm{Im}(\Psi_1), \mathrm{Re}(\Phi_1), \mathrm{Im}(\Phi_1))$. Defining $x = r/a$, $\tau = t/\tau_R$, $S = \tau_R/\tau_A$. The functions

$$G(x) = \frac{m}{q(x)} - n \quad H(x) = -\frac{m}{x}\left[2x\frac{(q')^2}{q^3} - \frac{3q' + xq''}{q^2}\right]$$

are related to the q profile and the matrix $\underline{\underline{T}}$ is written:

$$\underline{\underline{T}} = \begin{bmatrix} 0 & -gS\omega & 0 & gGS \\ gS\omega & 0 & -gGS & 0 \\ \frac{H}{\omega} & -gGS & 0 & \frac{gG^2S}{\omega} \\ gGS & \frac{H}{\omega} & -\frac{gG^2S}{\omega} & 0 \end{bmatrix}$$

The structure of the matrix shows immediately that for large ω the role of the singularity at $q = m/n$ disappears. The numerical solution of the ODE system (3) has been performed with a varying step highly accurate finite difference scheme capable of taking care of the boundary layers appearing at the rational surface $(G(x) = 0)$ and at the Alfvēn resonance layers $k_{\parallel}^2 v_A^2 = \omega_0^2$ $(G(x) = \pm\omega)$. As a matter of fact, assuming mild variations of the profiles, equations (2) can be combined in to the single fourth order equation

$$\frac{i}{S}\nabla^2\left(\frac{1}{gG}\nabla^2\Psi_1\right) + \left[\nabla^2\left(\frac{\omega}{G}\Psi_1\right) - \frac{G}{\omega}\nabla^2\Psi_1\right] - \frac{H}{\omega}\Psi_1 = 0$$

which in the limit $\omega \to 0$ reduces to the tearing mode equation, but for finite ω develops at $G(x) = \pm\omega$ two boundary layers of typical width $\delta_A \sim S^{-1/3}$. These are Alfvēn waves driven in a resistive regime and appear to have a role in determining, for instance, the field reflected from the plasma, defined here in terms of the (complex) stream function $\Psi_R = \Psi_P - \Psi_V$, according to equation (1) (here Ψ_V is the external field generated by the coil in absence of plasma and Ψ_P is the plasma perturbation field in presence of external field).

3. Structure of driven perturbations and reflected field

The stream functions $\mathrm{Re}(\Psi_1)$ and the corresponding real part of the reflected field $\mathrm{Re}(\Psi_R)$ driven by external $(m = 2, n = 1)$ perturbation with resonant layer at $x \simeq 0.66$, are shown in Figs 1,2 over the interval $0 < x < 1$ (plasma), $1 < x < 1.2$ (vacuum) for a range of frequencies $10^{-10} < \omega < 10^{-3}$ and for a Lundquist number $S = 10^8$.

The rational surface shields the plasma interior from the external perturbation; as the frequency decreases the field penetration increases and the field line reconnection takes place. It is clear that at a measuring position in vacuum, say at $x \sim 1.15$ near the driving conductors the percentage of reflection is very small and without phase shift. The stream functions $\mathrm{Re}(\Psi_1)$ and the corresponding real part of reflected field $\mathrm{Re}(\Psi_R)$ driven by external $(m = 3, n = 1)$ perturbation with a resonant layer at $x \simeq 0.85$, over the interval $0 < x < 1$ (plasma), $1 < x < 1.2$ (vacuum) for the same range of frequencies and the same value of S as before are shown in Figs 3,4.

As the frequency increases reconnection at the rational surface becomes ineffective and two "wavefronts" appear at the location of the Alfvēn resonances $(G(x) = \pm\omega)$; the reflected field in this situation is affected by the outer Alfvēn wavefront (Figure 5 with $m = 2$, $n = 1$). The velocity stream function (i.e. the vortex structure) is also changed (Figure 6).

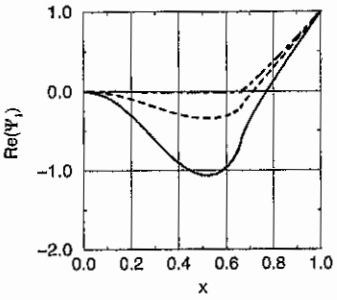

Figure 1: $\mathrm{Re}(\Psi_1)$ *vs* r/a; *mode* $m = 2, n = 1$. —:$\omega = 10^{-10}$, – – : $\omega = 10^{-4}$, – · – : $\omega = 10^{-3}$.

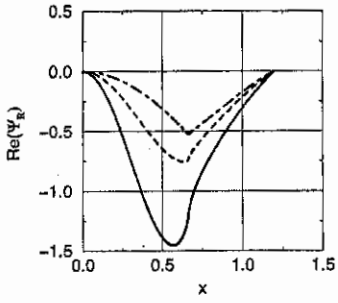

Figure 2: $\mathrm{Re}(\Psi_R)$ *vs* r/a; *mode* $m = 2$, $n = 1$.—:$\omega = 10^{-10}$, – – : $\omega = 10^{-4}$, – · – : $\omega = 10^{-3}$.

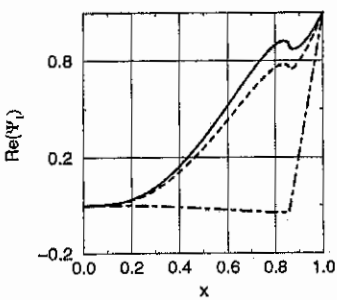

Figure 3: $\mathrm{Re}(\Psi_1)$ *vs* r/a; *mode* $m = 3, n = 1$. —:$\omega = 10^{-10}$, – – : $\omega = 2 \times 10^{-4}$, – · – : $\omega = 10^{-3}$.

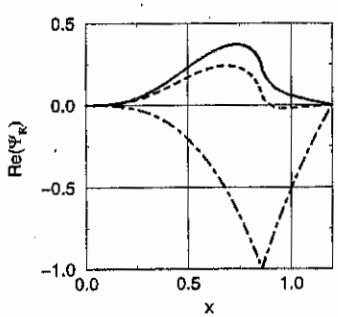

Figure 4: $\mathrm{Re}(\Psi_R)$ *vs* r/a; *mode* $m = 3$, $n = 1$.—:$\omega = 10^{-10}$, – – : $\omega = 2 \times 10^{-4}$, – · – : $\omega = 10^{-3}$.

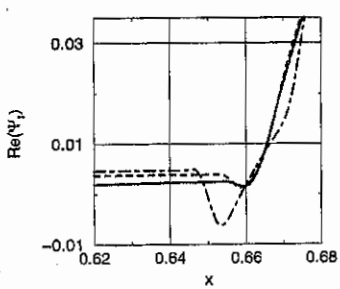

Figure 5: $\mathrm{Re}(\Psi_1)$ *vs* r/a; *mode* $m = 2$, $n = 1$.—:$\omega = 6 \times 10^{-3}$, – – : $\omega = 10^{-2}$, – · – : $\omega = 2.4 \times 10^{-2}$.

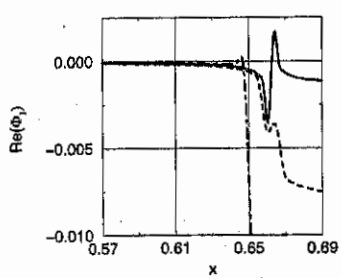

Figure 6: $\mathrm{Re}(\Phi_1)$ *vs* r/a; *mode* $m = 2, n = 1$. —:$\omega = 10^{-3}$, – – : $\omega = 6 \times 10^{-3}$, – · – : $\omega = 2.4 \times 10^{-2}$.

The frequency response for $m = 2$ and $m = 3$ modes, shown in Figs 7,8 is essentially flat in the very low frequency tearing range but it has a pole due to the excitation of the Alfvēn waves around $\omega_0 \tau_A \simeq 5 \times 10^{-2}$, for a plasma with $S = 10^8$.

This work was performed within a Task Agreement between IFP-CNR and JET; the authors are grateful to G. D'Antona, A. Santagiustina and A. Tanga for useful discussions.

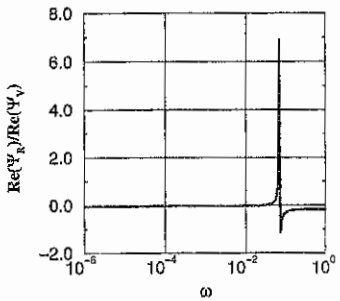

Figure 7: $\mathrm{Re}(\Psi_R)/\mathrm{Re}(\Psi_V)$ *at* $x = 1.15$ *as a function of* ω*; mode* $m = 2, n = 1$.

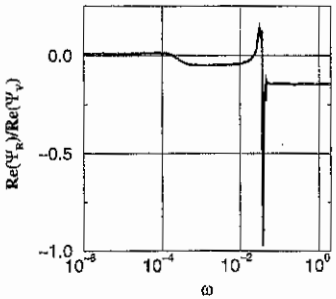

Figure 8: $\mathrm{Re}(\Psi_R)/\mathrm{Re}(\Psi_V)$ *at* $x = 1.15$ *as a function of* ω*; mode* $m = 3, n = 1$.

References

[1] H.R.Strauss. *Phys. Fluids*, 19:134, 1976.

[2] R.D. Hazeltine. *Plasma Confinement.* Addison Wesley Publ. Co.Cambridge, 1991.

[3] E. Lazzaro and M.F. Nave. *Phys. Fluids B*, 31:1623, 1988.

[4] R. Fitzpatrick, T.C. Hender, and R. Strauss. *Phys. Fluids B*, 3:644, 1991.

[5] E. Lazzaro, G. Lampis, G. Re, A.I. Smolyakov, and J. Callen. Nonlinear dynamics of externally driven magnetic islands in a tokamak plasma. In *Proceedings of the 17th Conference on Controlled Fusion and Plasma Physics, IAEA-CN-60/D-P20, vol.3, p.589 (1994)*, Vienna, 1996.

Runaway Electron Transport and Sheath Transmission Inferences from Edge Heat Flux Measurements in TEXT

K.W. Gentle, K. Schroder, D.J. Storek, and A.J. Wootton

Fusion Research Center, University of Texas at Austin, Austin, Texas 78712

An infrared camera with a special digital computer interface [1] coupled with analysis codes accounting for variable surface emissivity and temperature-dependent thermal properties in the three-dimensional heat flow equation provides heat flux measurements to the plasma-facing surfaces that can be used for novel transport measurements. Each of these effects has been found important for accurate heat flux inferences.

To observe runaway electrons, a special carbon target with a large radius of curvature was positioned in the midplane near the last closed flux surface. Top and bottom rail limiters were used for these experiments. The outward shift of the drift orbits for the energetic electrons allows them to be collected preferentially by the midplane target. Especially at low density, the contribution to the heat flux from the energetic electrons is easily distinguished from the (smaller) flux from the thermal plasma. For the TEXT tokamak ($R = 1$ m, $a = 0.27$ m, $B_T = 2$ T, 100 kA $\leq I_p \leq$ 200 kA), the electron energies are sufficiently small that the full energy is deposited within a few millimeters of path length in carbon. The heat flux measurements provide a good, local estimate of D at the edge, a crude energy spectrum for the runaways, estimates of the runaway population and confinement times, and information regarding $E_\perp$.

In general, the heat deposition on the target depends on the orbits (energy distribution function) and on radial diffusion. For conditions here, the finite Larmor orbit produces little spreading; the deposition pattern is determined by radial diffusion. By fitting the observed position and width of the pattern to a model, D may be inferred. The total power to the target gives the runaway energy flux. The energy spectrum is then constructed by pulling the target back to increasing minor radius and measuring the decrease in flux. This provides an energy filter, for only very energetic electrons have sufficient orbit shifts to reach the target without hitting the top and bottom rails. Given the energy spectrum, the energy flux can be converted to a particle flux. Furthermore, since the runaways are moving at c in a known **E**, the energy spectrum is a direct indicator of lifetimes. One can therefore estimate global confinement times and densities.

Inferences of $E_\perp$ are more difficult. Extensive measurements of electron cyclotron emission under various conditions with various antenna configurations have produced few indications of nonthermal emission as would be generated by runaways with significant $E_\perp$. Moreover, the heat deposition pattern on the target provides a bound on $E_\perp$. The helical trajectory of energetic electrons will tilt the heat deposition pattern with respect to the magnetic field line because the electrons deposit their energy along a finite path length in the carbon. A

measurable tilt is only seen at the end of the current rampdown at the conclusion of a shot, but its absence sets an upper bound on $E_\perp$ in other cases.

At a low density, 0.8 x 10^{19} m^{-3}, the heat flux to the target is dominated by runaways. For analysis, the heat flux along a line through the center of the two-dimensional pattern is plotted in Fig. 1 for several target positions. The tip is tangent to a magnetic flux surface; position is measured on the curved surface. (A displacement of 40 mm from the tip translates to only a 4 mm increment in minor radius.) Model predictions are shown in Fig. 2.

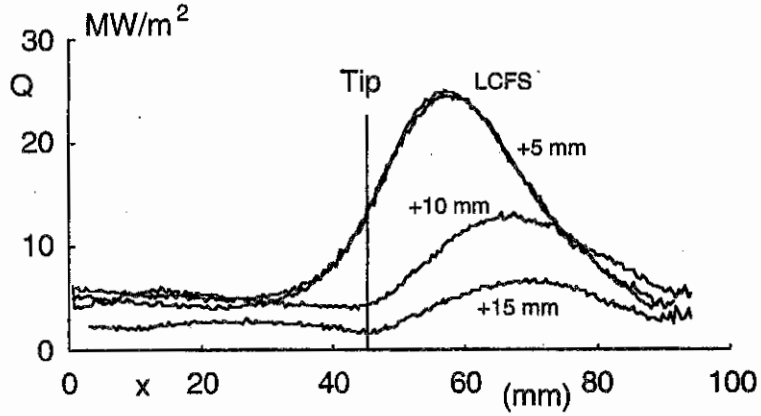

Fig. 1 Measured heat flux to a target at low density.

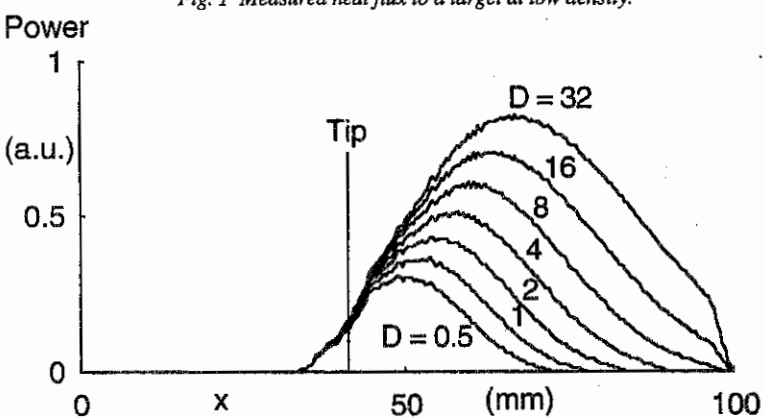

Fig. 2 Model predictions of heat flux to target as a function of D.

The displacement of the peak from the tip and the width of the peak both increase with D. The position and width of the curves at the Last Closed Flux Surface and 5 mm outside in Fig. 1 agree well with the predictions of the model for D ~ 1-2 m^2/s from Fig. 2. At higher densities, the runaway density decreases and its contribution to the heat flux to the target becomes mixed with that of the thermal plasma. After subtraction of the thermal contribution, a distribution remains that implies D ~ 2-4 m^2/s at a density of 2 x 10^{19} m^{-3}. The decrease in flux as the target is pulled away from the plasma gives a crude energy spectrum, shown in Fig. 3 for the two densities. Note that both the energies and populations of runaways decrease rapidly with increasing density. (Although the units of Fig. 3 are arbitrary, they are the same for the two densities.) These energies are well below the maximum energies confined by the magnetic fields and correspond to small fractional shifts in the drift orbits. Diffusion is the dominant loss mechanism. At low density, the energy spectrum suggests a confinement time typical of an average D ~ 1 m^2/s, whereas the higher density suggests D ~ 4 m^2/s. Although this latter value is comparable with values of χ_e for these discharges, this nevertheless poses a serious problem. The χ_e is usually presumed to arise from electrostatic fluctuations that would not affect runaway electrons. Only magnetic fluctuations would normally drive diffusion of runaway electrons. A level of magnetic fluctuations that would produce D ~ 4 m^2/s for runaways would not produce a significant χ_e for thermal electrons, but two distinct classes of turbulence may be required for electrostatic and magnetic effects.

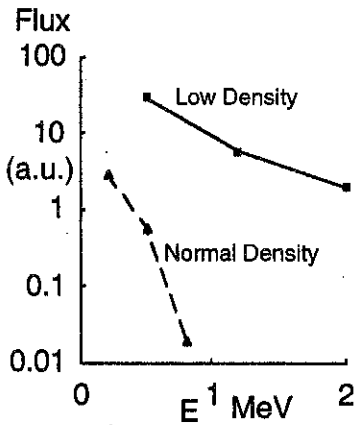

Fig 3 Energy Spectra

From these spectra and the amount of heat deposited on the target, an estimate of runaway density can be constructed. At low density, the runaway fraction is 10^{-4}, whereas at the higher density it is only 2 x 10^{-6}.

The values of $E_\perp$ are sufficiently small that they can only be bounded by these experiments. The deposition pattern implies $E_\perp < 100$ keV and $E_\perp < 0.1\ E_\parallel$. There is no evidence to support values of $E_\perp$ much greater than E at the Dreicer energy, when the electrons become collisionless and run away. The runaways in TEXT are quite definitely not subject to the processes described in ASDEX-U [2] that drive large values of $E_\perp$.

By making detailed measurements of the heat flux to divertor tiles under conditions where the edge plasma parameters are well known [3] and simple -- small gradients along field lines,

an effective sheath heat transmission coefficient can be determined and several other aspects of sheath models can be tested. Since the heat fluxes in TEXT are comparatively low, full coverage of divertor tiles is not necessary. The tiles are shaped so that field lines make angles from 88° to 60° with the surface normal. For the two-dimensional tile surface, one direction represents varying angles of incidence for flux from a single magnetic surface, and the orthogonal direction represents different flux surfaces. With careful calculation of the tile surface and plasma magnetic geometry, the heat flux from a given magnetic surface was found to vary directly with cos θ, the angle between field line and surface normal, as expected. No anomalies were found over the range of angles and plasma conditions of this experiment.

The sheath transmission coefficient, as defined by Stangeby [4], was determined by comparing the heat flux with predictions [4] based on Langmuir probe measurements of edge plasma parameters [3]. Transmission coefficients no higher than 6 are found, somewhat smaller than predicted, and values as low as 3 at higher densities are seen. The precision of this comparison is not high, however, both because of the uncertainties in absolute values of Langmuir probe measurements of density and temperature and because of magnetic uncertainties in the flux-surface position of the probe.

There is one discrepancy between heat flux measurements and probe measurements that is significant and hard to excuse, however. The radial decay length for the heat flux is significantly smaller than that implied by the decay lengths of density and temperature measured by the Langmuir probe. This is equivalent to the statement that the sheath transmission coefficient decreases with radius outside the last closed flux surface, reaching values below 1. Although absolute values are uncertain, the difference between a radial decay length of a few millimeters for the heat flux compared with values of more than twice that inferred from probes is independent of exact probe position or absolute probe accuracy.

Work supported by the U.S. Department of Energy under Grant No. DE-FG05-88ER-53267.

[1] D.J. Storek and K.W. Gentle, Rev. Sci. Instr. **67**, No. 3 (1966).

[2] B. Kurzan, K-H. Steuer, G. Fussmann, Phys. Rev. Lett. **75**, 4626 (1995).

[3] W.L. Rowan et al. (this conference).

[4] P.C. Stangeby, Phys. Fluids **27**, No. 3 (1984).

Nonlinear Dynamics of the Fishbone

J. Candy, †F. Porcelli, H.L. Berk, B.N. Breizman

Institute for Fusion Studies, University of Texas at Austin
Austin, Texas 78712, USA

†Dipartimento di Energetica, Politecnico di Torino
10129 Torino, Italy

Introduction "Fishbones" are oscillations of the $n = 1$ internal kink mode driven by resonant interaction with trapped fast ions [1] produced by neutral beam injection (NBI) or by ion-cyclotron resonance heating (ICRH). The eigenmode structure of the internal kink is dominated by the $m = 1$ component – which is nearly singular at the $q = 1$ surface.

Early fishbone measurements were obtained during low-field ($0.7\text{T} \lesssim B_0 \lesssim 1.7\,\text{T}$), NBI-heated discharges in PDX [2]. The oscillations, observed during nearly perpendicular injection of up to 7.2 MW of beam power, were characterized by bursts of $\lesssim 1$ ms, with repetition time on the order of a few milliseconds. Remarkably, a significant fraction of the beam heating power (20 % – 40 %) was lost in some cases.

In JET NBI and ICRF-heated discharges, fishbone bursts are routinely seen in ECE and SXR emission, as well as magnetic signals. Each burst – composed of many fishbone oscillations in the kHz range – typically lasts for a few ms, and repeats over a longer interval of a few tens of ms. An important difference between PDX and JET fishbones is the fast ion loss fraction: unlike PDX, the larger, higher-B JET device shows negligible fast ion loss. We mention in passing that our simulations indeed reproduce this important difference, although we discuss results only for PDX-like plasmas in this report.

Physical Model To calculate the nonlinear evolution of the fishbone cycle, we begin by writing the one-sided Fourier transform of the collisionless equation of motion for bulk ions (ignoring the MHD nonlinearity)

$$-\omega(\omega - \omega_{*\mathrm{i}})\rho\,\vec{\xi} = \frac{1}{c}\left(\delta\vec{j}\times\vec{B} + \vec{j}\times\delta\vec{B}\right) - \nabla\delta p_{\mathrm{core}} - \nabla\cdot\delta\mathcal{P}_{\mathrm{hot}} \quad , \tag{1}$$

where $\omega_{*\mathrm{i}} \equiv \vec{v}_{*\mathrm{i}}\cdot\nabla\theta \sim p'_{\mathrm{core}}/\rho\omega_{\mathrm{ci}}$ is the ion diamagnetic frequency, and $\rho \equiv \mathrm{n_i m_i}$. For reference, the transform pair is

$$\vec{\xi}_\perp(\mathbf{x},t) = \frac{1}{2\pi}\int_{-\infty+i\gamma}^{\infty+i\gamma} d\omega\, e^{-i\omega t}\vec{\xi}_\perp(\mathbf{x},\omega) \quad \leftrightarrow \quad \vec{\xi}_\perp(\mathbf{x},\omega) = \int_0^\infty dt\, e^{i\omega t}\vec{\xi}_\perp(\mathbf{x},t) \quad .$$

Consider a trial solution for $\vec{\xi}_\perp$ of the form $\vec{\xi}_\perp(\mathbf{x},\omega) = d(\omega)\vec{\sigma}(\mathbf{x},\omega)$, where $\vec{\sigma}$ is independent of both position and frequency in the outer layer (*i.e.*, when q is not close to unity), but may change inside the inertial layer due to the fast particle dynamics (see Fig. 1). Outside the layer, $\vec{\xi}(\mathbf{x},t)$ changes in amplitude and phase only through the Fourier transform of $d(\omega)$ [*i.e.*, $D(t)$].

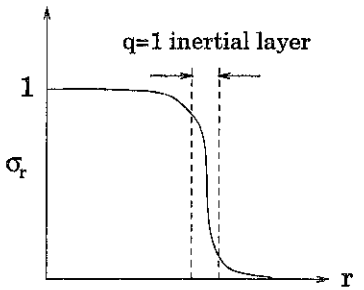

Fig. 1. Illustration of the radial component of the basis function, which changes only in the inner layer due to the nonlinear shift in frequency induced by the energetic particles.

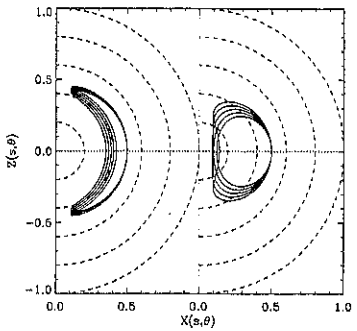

Fig. 2. Characteristic orbits for trapped beam ions in JET-like (left) and PDX-like (right) geometries. Energies range from 20 to 100 keV (JET) and from 10 to 50 keV (PDX).

Multiplying the momentum equation by $\vec{\xi}^*/d(\omega)^2$ and integrating gives

$$\underbrace{-\frac{1}{2}\int d^3x\,(1+2q^2)\omega(\omega-\omega_{*i})\rho|\vec{\sigma}|^2}_{\delta I(\omega)}\underbrace{-\frac{1}{2d}\int d^3x\left[\frac{1}{c}\vec{\sigma}^*\cdot\delta(\vec{j}\times\vec{B})-\vec{\sigma}\cdot\nabla\delta p_{\rm core}\right]}_{\delta W_{\rm core}}$$
$$\underbrace{-\frac{1}{2d}\int d^3x\,\vec{\sigma}^*\cdot\nabla\cdot\delta\mathcal{P}_{\rm hot}}_{\delta W_{\rm hot}(\omega)}=0\quad .$$

For the kinetic response of the hot particles, $\delta W_{\rm hot}(\omega)$, we take

$$\delta W_{\rm hot}(\omega)=\frac{1}{2}\int d\Gamma\,(mv_\parallel^2+\mu B)\,\frac{\delta f(\omega)}{d(\omega)}\,\vec{\kappa}\cdot\vec{\sigma}^*\quad .$$

The steep inner layer of the kink mode gives rise to two boundary layer terms which diverge as $\omega\to\omega_{*i}$:

$$\delta I(\omega)+\delta W_{\rm core}^{\rm inner}\sim-\frac{1}{2}\int d^3x\,\rho\,F(r,\omega)\left[r_0\frac{d\sigma_r}{dr}\right]^2\quad ,$$

where $q(r_0)=1$. The remaining δW integrals are insensitive to the layer structure. Now, introduce the usual layer variable $x\equiv(r-r_0)/r_0$ and expand $k_\parallel=k_\parallel(r_0)+(r-r_0)k'_\parallel=sx/R$. The Euler equation for the inner region is

$$\frac{d}{dx}F(x,\omega)\frac{d\sigma_r}{dx}=0\quad ,$$

with $F(x,\omega)=3\left[\omega(\omega-\omega_{*i})-\widetilde{\omega}_{\rm A}^2x^2\right]$ and $\widetilde{\omega}_{\rm A}=sv_{\rm A}/R$. Now, let $a^2=-\omega(\omega-\omega_{*i})/\widetilde{\omega}_{\rm A}^2$ (remember, ω is integrated **above** the real axis. The inner layer solution which matches properly to the outside is

$$\frac{d\sigma_r}{dx} = \frac{A(\omega)}{a(\omega)^2 + x^2} \qquad \text{with} \qquad A(\omega) = \frac{2R\,\delta W^{\rm out}(\omega)}{\pi (s r_0 B)^2} \quad .$$

To make contact with the literature, let $\omega_{\rm A} \equiv v_{\rm A}/sR\sqrt{3}$ and $\delta W \to (\pi/2R)(r_0 B)^2 \delta\hat{W}$. An integration through the layer then gives

$$\delta I(\omega) + \delta W^{\rm inner}_{\rm core} + \delta W^{\rm out}(\omega) = \delta W^{\rm out}(\omega)\left[\frac{\pi\omega_{\rm A}}{a}\delta\hat{W}^{\rm out}(\omega) + 1\right] = 0 \quad .$$

Now, multiply the quantity in square brackets by $d(\omega)a(\omega)/\omega_{\rm A}$, and integrate to find the sought-after complex evolution equation

$$\underbrace{\mathcal{F}\left[g(\omega)d(\omega)\right]}_{\text{propagator}} + \underbrace{\frac{1}{2}\int d\Gamma\, \delta f\, \vec{v}_{\rm Dh}\cdot\nabla(e\widehat{\Phi}^*)}_{\text{fast-ion current}} = 0 \quad , \tag{2}$$

where $\vec{v}_{\rm Dh}$ is the guiding center drift velocity, and $g(\omega)$ is just the usual dispersion relation for the kink

$$g(\omega) = -i\,\frac{\sqrt{\omega(\omega-\omega_{*\rm i})}}{\omega_{\rm A}} - \lambda_H \qquad \text{with} \qquad \lambda_H \equiv -\pi\,\delta\hat{W}^{\rm out}_{\rm core} \quad .$$

In (2), the displacement $\vec{\xi}_\perp$ is derived from the electrostatic potential Φ

$$\frac{\partial\vec{\xi}_\perp}{\partial t} = \frac{c}{B}\,\vec{b}\times\nabla\Phi(\mathbf{x},t) \quad .$$

Introducing $\Phi(\mathbf{x},t) \equiv C(t)\widehat{\Phi}(\mathbf{x})$, and recalling that $\vec{\xi}_\perp(\mathbf{x},t) \equiv D(t)\vec{\sigma}(\mathbf{x})$, it follows that $\vec{\sigma} = (c/B)\vec{b}\times\nabla\widehat{\Phi}$ and $C(t) = \dot{D}(t)$. To solve (2), δf is integrated numerically along perturbed guiding center orbits (see Fig. 2) by a toroidal particle code [4], which subsequently calculates the time-dependent fast ion current. The guiding center equations of motion depend on the vector and scalar potentials, so that the current is a functional of the quantities $D(t)$, $\dot{D}(t)$ and $\ddot{D}(t)$.

Now, it is possible to invert the transform by integrating the nonsingular part of $g(\omega)$ around the branch cut $[0,\omega_{*\rm i}]$. The result is an integro-differential operator:

$$\omega_{\rm A}\,\mathcal{F}[g(\omega)d(\omega)] = \dot{D}(t) + \left(\frac{i\,\omega_{*\rm i}}{2} - \lambda_H\right)D(t) + \left(\frac{\omega_{*\rm i}}{2}\right)^2\int_0^t d\tau\, D(\tau)K\left[\frac{\omega_{*\rm i}}{2}(t-\tau)\right] \quad ,$$

with kernel $K(x) = \exp(-ix)J_1(x)/x$. So, at each time step, the energetic particle current is computed, and the solution is then advanced in time using (2).

PDX Simulation The algorithm has been tested successfully for parameters characteristic of PDX NBI-heated plasmas: $\omega_{*\rm i} = 6\times10^4$ rad/s, $B_0 = 1$ T and $E_{\rm beam} = 50$ keV. Fig. 3 shows numerical results for the transition from the diamagnetic ($\omega < \omega_{*\rm i}$) to the precessional drift ($\omega > \omega_{*\rm i}$) branch as beam density is increased. The boundary between the two can be estimated by examination of the eigenvalue equation for the linear normal mode: $g(\omega) = \lambda_{\rm k}(\omega)$. Measuring frequency in units of $\omega_{*\rm i}$ (*e.g.*, $\hat{\omega} = \omega/\omega_{*\rm i}$) gives

$$\hat{\omega} = \frac{1}{2}\left[1 + \sqrt{1 - \left(\hat{\lambda}_H + \mathrm{Re}\,\hat{\lambda}_\mathrm{k} + i\,\mathrm{Im}\,\hat{\lambda}_\mathrm{k}\right)^2}\right] \quad .$$

When the beam density is large enough so that $\hat{\lambda}_H + \mathrm{Re}\,\hat{\lambda}_\mathrm{k} = 0$ ($\mathrm{Re}\,\lambda_\mathrm{k}$ is typically negative at low frequency), the diamagnetic root is supressed and the mode transforms smoothly into the precessional drift fishbone. Applied to the PDX scenario, this estimate gives a transition at $n_\mathrm{f}/n_\mathrm{i} \sim 0.5\%$, in rough agreement with the results in Fig. 3.

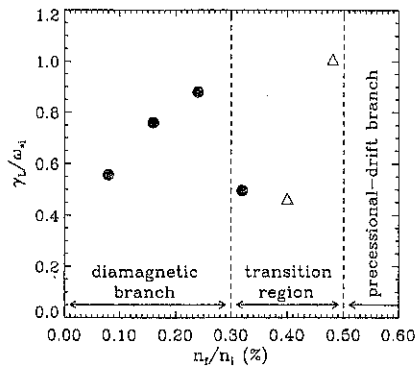

Fig. 3. Scan of linear growth rate versus beam density showing transition from diamagnetic to precessional drift fishbone in PDX.

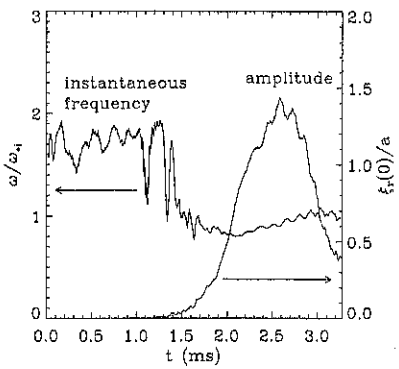

Fig. 4. Time evolution of frequency and amplitude for PDX fishbone with $n_f/n_i = 0.48$ %. The nonlinear downshift near saturation is clearly reproduced.

We have plotted the time evolution of the amplitude and instantaneous frequency for the largest beam-ion density in Fig. 4. The results – namely a burst duration of 1.5 ms, a self-consistent nonlinear frequency downshift of roughly 50% in about 0.5 ms, and substantial beam-ion losses (over 50%) – are fairly representative of typical PDX fishbone data. However, the saturated amplitude in this case is rather high, and the losses correspondingly high. This indicates that the neglect of wave-wave nonlinearity in (1) is questionable for PDX. It should be mentioned that the simulation also includes the small $m = 2$ satellite, which is intimately connected with nonresonant particle loss.

Summary A physical model of the fishbone instability has been developed which treats both the wave-particle nonlinearity and inner-layer mode dynamics self-consistently. Preliminary PDX simulations recover clearly the nonlinear downshift in frequency which accompanies mode saturation, and also the ejection of a large fraction of beam ions.

REFERENCES

[1] L. Chen, R.B. White, and M.N. Rosenbluth, Phys. Rev. Lett. **52** 1122 (1984); also B. Coppi and F. Porcelli, Phys. Rev. Lett. **57** 2272 (1986).

[2] K. Mcguire, *et al.*, Phys. Rev. Lett. **50** 891 (1983).

[3] M.F.F. Nave, *et al.*, Nucl. Fusion **31** 697 (1991).

[4] J. Candy, J. Comput. Phys. **129** 160 (1996).

Evidence for Curvature as a Source of Turbulence in the Scrape-Off Layer

William L. Rowan, X. Bonnin, Roger D. Bengtson, K. W. Gentle,
P. D. Hurwitz, D. J. Storek, D. L. Winslow and **A. J. Wootton**
Fusion Research Center, The University of Texas at Austin, USA

The toroidal curvature of the magnetic field lines may be a drive for turbulence in tokamaks [1,2]. On the open field lines in the scrape-off layer (SOL), some fluid modes may be unstable for $\kappa \bullet \nabla p > 0$ where κ is the local curvature vector and ∇p is the pressure gradient. In a tokamak, curvature is stabilizing on the high field side of the poloidal cross section and destabilizing on the low field side. Field lines can sample both stabilizing and destabilizing regions. The existence of x-points and surfaces in diverted discharges and limiting surfaces in limited discharges will determine the fraction of a field line that is susceptible to this turbulence source. Thus, in the SOL, there will be regions of varying degree of curvature which may lead to varying degrees of turbulence, that is turbulence asymmetries. Different configurations in the same device may have different levels of curvature and correspondingly different levels of turbulence.

The characteristics of the curvature drive have been identified theoretically [2,3]:

- $k_\theta \rho_s \approx 0.1$ (k_θ is the poloidal wavenumber and ρ_s is the ion poloidal gyroradius)
- Collisionality plays no role
- Large phase shift between density fluctuations $\tilde{n}$ and potential fluctuations $\tilde{\varphi}$
- Large phase velocity along the field lines
- Increased ion to electron temperature ratio T_i/T_e is stabilizing

As evidence of the drive, these and turbulence asymmetries would be sought in an ideal experiment.

In the experiment described here, the SOL profiles which are derived from Langmuir probe measurements are compared for configurations with different susceptibility to curvature drive. Turbulence asymmetries are sought in comparisons between regions of good and bad curvature in a single discharge. Because the asymmetry studies required turbulence measurements in regions that were inaccessible to probes, an optical fluctuation diagnostic was used in which fluctuations in the emission of H_α were interpreted as $\tilde{n}$. $k_\parallel$ is estimated from direct measurement of the turbulence using probes and the optical diagnostic. Magnetic reconstruction is a critical tool in assessing the results of the measurements. Field-line-following is used to determine which plasma regions are sampled and thus to estimate the turbulence due to curvature. Here, the reconstruction is done from magnetics data using a multi-filament code.

In TEXT-U, curvature drive could be studied by directly varying the fraction of an open field line that has unfavorable curvature. The three basic configurations useful for this experiment are shown schematically in Figure 1.

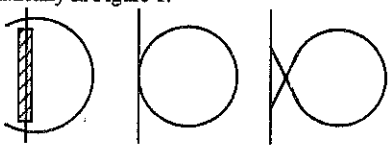

Figure 1. Schematics of the TEXT-U configurations. From left to right, double null, belt limited, equatorial single null.

The growth rate γ for the curvature instability with $k_{\parallel} = 0$ in each of the three configurations can be estimated using a simple model [2]. The results are shown in Table I.

Configuration	$\gamma \frac{R}{V_{thi}}$
double null, HFS (hatched region)	---
belt limiter	2.5
equatorial single null	2.5
double null, LFS (unhatched region)	4.0

Table I. Growth rate for different configurations: γ is growth rate, R is major radius, V_{thi} is ion thermal velocity; LFS represents low field side, and HFS represents high field side.

The configurations chosen for this experiment were those that would be expected to yield the most striking evidence for the available diagnostic set. The entries of Table I lead to the expectation of significant turbulence asymmetries in comparison of the high field side of the double null discharge, the hatched region, with the low field side of that discharge. This could only be tested with the optical fluctuation diagnostic in TEXT-U. The available Langmuir probes were in fixed locations above and below the plasma and are best used to compare belt limited discharges with the low field side of the double null discharge.

Poloidal and parallel wavenumbers

In repeated experiments, $k_{\parallel} < k_{\theta}$ (see [4], for example). This experiment has been carried out using probes at a few locations in the plasma and using the optical diagnostic on the low field and high field sides. These relative measurements of $k_{\parallel}$ are confirmed by absolute measurements in the few instances of the latter [5,6]. For the poloidal wavenumber [7,8], $k_{\theta}\rho_s \leq 0.1$.

Turbulence asymmetries

Turbulence asymmetries were sought in disconnected double null configurations. The turbulence was compared on the high and low field sides of the plasma. The turbulence was found to be higher on the low field side than on the high field side (Fig. 2). In a control experiment, these measurements were repeated for a poloidally limited discharge. There, the turbulence was found to be the same on both the low and high field sides of the plasma (Fig. 3). Further, the limited plasma was heated with ECH to vary the ratio of T_i/T_e. This resulted in no change in the turbulence. Turbulence asymmetries have also been identified in double null discharges in ASDEX [9].

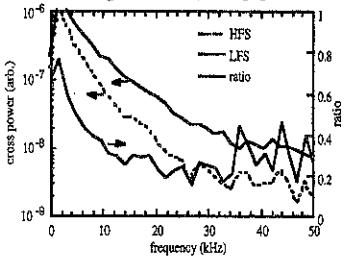

Figure 2. Turbulence cross-power levels on both sides of a double-null discharge.

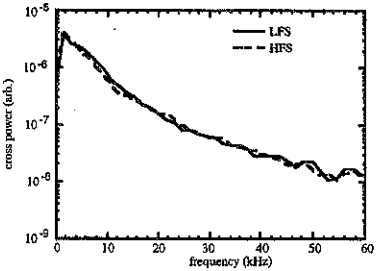

Figure 3. Turbulence cross-power levels on both sides of a poloidally limited discharge.

SOL Profiles

A purely geometrical analysis was undertaken to estimate the sensitivity of a particular plasma region to the curvature drive. The curvature drive will be present if $\kappa \bullet \nabla p > 0$. The fraction of field line arc length where this condition is satisfied is assumed to provide a measure of the strength of the curvature drive. Two discharges were compared, a disconnected (or biased) double null (BDN) and a belt limited discharge. By this measure, the low field side of the former has the larger curvature drive because the field lines do not pass through the stabilizing region on the high field side. Yet, the profiles were nearly identical in the two cases. It was not possible to measure the profiles on the high field side of the diverted discharge.

Conclusions

It is clear that curvature drive tests can be conducted in well designed experiments on existing devices. In TEXT-U, the expected turbulence asymmetries were observed when comparing one region in a double null discharge that was expected to be subject to no turbulence drive at all to a second region in the same discharge that was expected to have the largest curvature drive that could be produced. A simple geometrical analysis clearly shows that the low field side of the double-null configuration is more vulnerable to curvature-driven

instabilities than the low field side of a belt limited discharge. When comparing SOL profiles, however, there is no apparent dependence on degree of susceptibility to curvature drive. In addition, $k_\theta \rho_s$ and $k_\parallel$ are both in the expected range. The results are consistent with the drive being saturated for even modest levels of curvature drive and are summarized in Table II.

Parameter		Theory	Experiment	Parameter	
$k_\theta \rho_s$		≤ 0.1	0.04 to 0.1		
$k_\parallel$		≈ 0	≈ 0		
phase shift		60°	$\leq 90°$		
$\frac{T_i}{T_e}$		stabilizing	no effect		
$\left(\frac{\tilde{n}}{n}\right)_{LFS} \Big/ \left(\frac{\tilde{n}}{n}\right)_{HFS}$	Circular BDN	1 ∞	1 4		
γ	Belt BDN	2.5 4.0	0.12 0.12	Belt BDN	$k_\perp^2 D$
			0.3 0.3	Belt BDN	$\frac{\tilde{n}}{n}$
			1 1	Belt BDN	λ_n(cm)

Table II. Expected and measured turbulence parameters. The phase shift is between density and potential fluctuations. Since the growth rate could not be obtained experimentally, it is compared to three different measures of the turbulent transport activity on the low field side of the SOL.

References

[1] A. V. Nedospasov, Sov. J. Plasma Phys. 15, 659 (1989)

[2] X. Garbet *et al.*, Nucl. Fusion 31, 967 (1991)

[3] Ronald H. Cohen and Xueqiao Xu, "A Model for a Scrape-Off-Layer L-H Transition", January 30, 1995, URCL-JC-119821

[4] S. J. Levinson *et al.*, Nucl. Fusion 24, 527 (1984)

[5] C. P. Ritz *et al.*, Rev. Sci. Instr. 59, 1739 (1988)

[6] D. L. Winslow *et al.*, Rev. Sci. Instr. 68, 336 (1997)

[7] C. P. Ritz, D. L. Brower, T. L. Rhodes *et al.*, Nucl. Fusion 27, 1125 (1987)

[8] T. L. Rhodes, C. P. Ritz and R. D. Bengtson, Nucl. Fusion 33, 1147 (1993)

[9] M. Endler *et al.*, Nucl. Fusion 35, 1307 (1995)

Investigation of Resistive MHD Physics and High Harmonic Fast Wave Heating on CDX-U Spherical Torus

W. Choe, D. Stutman[1], J. Menard, E. Lo, T. Munsat, M. Ono, Y.S. Hwang[†], R. Majeski, J.R. Wilson, M. Finkenthal[‡], V. Gusev[*], Y. Petrov[*], T. Seki[§], R. Kaita

Plasma Physics Laboratory, Princeton University, Princeton, NJ 08543 [2]
[†]*Korea Advanced Institute of Science and Technology, Taejon, Korea*
[‡]*Johns Hopkins University, Baltimore, Maryland, USA*
[*]*Ioffe Institute, St. Petersburg, Russia*
[§]*National Institute for Fusion and Science, Nagoya, Japan*

INTRODUCTION

The CDX-U device is a spherical torus (ST) facility with $R \simeq 34\,cm$, aspect ratio $A \equiv R/a \geq 1.5$, and $B_t \leq 1.3\,kG$. Recently, STs have received increasing attention due to encouraging theoretical predictions [1] and experimental results [2,3]. Although ST plasmas thus far appear to be quite resilient to disastrous MHD activities such as disruptions in tokamaks, MHD can limit the performance and the ultimate operation window of the ST plasmas. In this context, it is important to clarify the possible effects of resistive MHD activity on ST performance, particularly for upcoming ST experiments such as NSTX. In the presence of strong MHD events in tokamaks, various large, unbalanced and non-uniform induced currents are observed in structures including the vacuum vessel. Considering its potential harmful effects on structures of the compact geometry of STs, this halo current related physics needs to be investigated in detail. Another important area of ST research topic is the non-inductive heating and current drive methods for plasma startup and sustainment. Because of the large plasma dielectric constant in a high-β ST plasma ($\omega_{pe}^2/\Omega_e^2 \gg 1$), the high harmonic ($\omega \gg \Omega_i$) fast wave is a good choice to satisfy the needs of ST plasmas considering its good accessibility and strong damping by electrons [4].

RESISTIVE MHD AND HALO CURRENT STUDY

Two MHD regimes In CDX-U, two distinct MHD regimes were observed with soft x-ray diagnostics and magnetic diagnostics. The first type (Fig. 1) is with a non-sawtoothing plasma core and a fluctuation active edge. The soft x-ray diode array shows the presence of a n=1/m=1 'hot' spot whose radius is about 20 cm rotating with a frequency of 8 – 9 kHz. Magnetic pickup coil signals indicate that the dominant edge mode is n=1/m=2,3 with the same frequency as the core modes, suggesting the presence of a rigid body rotation of plasma in the toroidal direction. More recently, with a higher B_t and higher temperature plasma, the frequency observed by both soft x-ray array and

[1] Also at Johns Hopkins University.
[2] This work was supported by the United States Department of Energy under Contract No. DE-AC02-76-CH0-3073.

magnetics increased to 12 kHz. Both internal and edge modes grow spatially and become more intense as time advances until an internal reconnection event (IRE) occurs. From this finding, our understanding of the cause of an IRE is mode coupling or magnetic island overlapping. The second type of MHD regime has a sawtoothing core and a quiescent edge (Fig. 2). As time advances, coherent modes appear (0.5 - 1 ms before IRE) which lead to an IRE. After an IRE, fluctuations appear again and the phase analysis of magnetics indicates a n=1/m=4 mode. Recently, a 75 channel ultra soft x-ray array was installed on CDX-U. Because of its good angular (1.12°), spatial (1.2 cm), and time (4 μs) resolution, a more thorough study of the MHD activity in CDX-U will be possible.

Halo Current Measurement To facilitate the halo current study, a 4-element Rogowski coil was implemented in the upper and lower areas of the center column measuring poloidal vessel currents as well as any up-down asymmetry. During the normal course of CDX-U operation, an IRE is the most serious MHD activity. The halo current measurements during an IRE indicate it is typically less than 1 % of the total plasma current. In order to simulate the disruption-like strong current termination, B_t was decreased so that the q-limit was reached before a plasma developed into a full current ST regime. Sudden loss of equilibrium caused by turning off one of the vertical field coils was also used to bring about similar rapid current termination. Even during these events, the measured halo currents were typically less than 5 % of the plasma current value, which is an order of magnitude smaller than that observed in large aspect ratio tokamaks. The plasma position monitoring showed that the plasma moved vertically rather than in major radius, possibly due to the effect of ST geometry. While this is an encouraging result for ST, more detailed and systematic study by modeling and further experimentation is warranted.

HIGH HARMONIC FAST WAVE EXPERIMENTS

CDX-U Fast Wave Antenna System The CDX-U FW antenna consists of two current straps, and can couple > 100 kW for short pulses (< 10 ms). The height, width, and center-to-center separation of straps are 27 cm, 3.8 cm, 22 cm, respectively. A maximum of 100 kW has been coupled to plasma, and it is limited by the RF source rather than the antenna power handling. The strap separation was chosen to launch toroidal mode number $n_\phi \approx 8$ with 0-π phasing. Due to its geometry, the magnetic field line pitch at the outer midplane of an ST plasma varies significantly from startup phase to full plasma current phase. Thus, it will be an important issue to investigate the effect of the angle between strap and field line. One unique feature of the CDX-U FW antenna is that the antenna straps can be rotated manually to subtend an arbitrary angle with respect to edge magnetic field lines. For the FW experiments, the RF frequency was 12MHz, which corresponds to ω/Ω_H = 5-10.

Loading Measurements Figure 3 shows the plasma loading resistance as a function of RF power and strap angle. One indication that power is coupled to propagating waves rather than dissipated in the edge comes from the fact that the plasma loading resistance becomes independent of RF power beyond a few kW for both 0-π and 0-$\pi/2$ phasings as shown in Fig. 3(a). The higher loading for 0-$\pi/2$ phasing is attributed to the shorter evanescent length of this lower $n_\parallel$ launch. In addition, plasma loading decreases as the inclination of the straps with respect to the field line becomes small (towards 90° of strap

angle in Fig. 3(b)). These results are consistent with a 1-D slab ICRF code (ANTBER [5]) simulation.

Microwave Scattering Experiment The vertical beam of the CDX-U 2mm microwave interferometer [6] was used to directly observe the HHFW density fluctuations. The microwave beam was located 90° toroidally away from antenna. The scattered signal amplitude, which is proportional to $\int n_e dz$, was measured at three different major radii (35, 40, 45 cm). R = 35 cm and 45 cm correspond to the plasma axis and $r/a \simeq 1/2$, respectively. Figure 4(a) demonstrates the presence of wave fields throughout the plasma cross-section. The profile of signals normalized to background density (proportional to wave electric field, Fig. 4(b)) indicates that the waves penetrate towards the plasma center with strap angles nearly perpendicular to field lines, which may be due to wave focusing effects. When the straps are oriented parallel to the field lines, however, the wave fields are largest at the edge, possibly because of the excitation of surface modes. Results from ray tracing simulations based on Ref. [4] at different strap angles show that most of the RF power couples to a fast wave and that the power deposition profile may depend strongly on the strap orientation.

SUMMARY

A major CDX-U research area is the physics of ST, and particularly, it has been focused on providing valuable information for the upcoming NSTX. In this paper, two main topics are addressed. It has been observed that there are two distinct MHD regimes which show different MHD behavior at the core and edge, but they both experience an IRE. The results suggest the cause of an IRE as being mode coupling or magnetic island overlap. Vacuum vessel halo current measurements were performed and indicate that the halo currents are relatively small not only for IRE but also for artificially induced disruptions. HHFW has good accessibility properties for high-β ST plasmas and will be employed in NSTX. As a testbed, CDX-U has been dedicated to this research and preliminary experiments have been performed. Plasma loading measurements show good coupling of RF power into CDX-U plasmas and the results are consistent with theory. Microwave scattering measurements suggest the presence of wave fields throughout the plasma cross-section. The RF source has been recently upgraded to provide higher power, and experiments to investigate core heating with Thomson scattering will be performed in the near future.

REFERENCES

[1] J. Menard, et al., will appear in Nucl. Fusion.
[2] M. Ono, et al., Proceedings of 16th International Conference on Plasma Physics and Controlled Nuclear Fusion (IAEA Conference, Montreal, 1996), to be published (IAEA-CN-64/C2-2).
[3] R. Akers, et al., ibid. (IAEA-CN-64/C2-1).
[4] M. Ono, Phys. Plasmas **2** 4075 (1995).
[5] M. Brambilla, Nucl. Fusion **28** 549 (1988).
[6] C. Forest, G. Greene, and M. Ono, Rev. Sci. Instrum. **61** 2888 (1990).

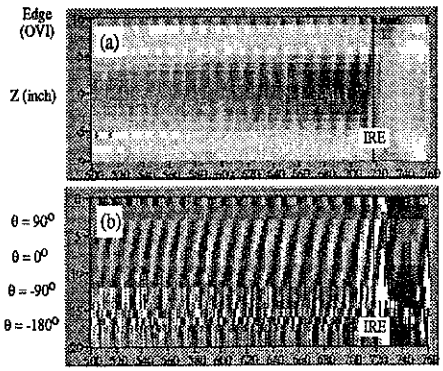

FIGURE 1. *Temporal behavior of non-sawtoothing core, active edge MHD modes. (a) Soft x-ray, and (b) magnetics data, respectively.*

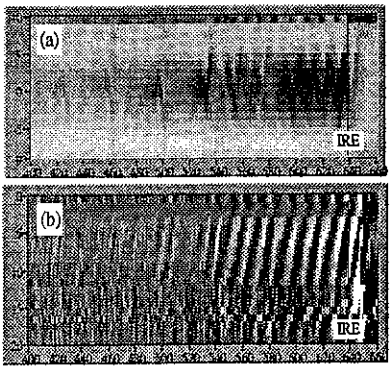

FIGURE 2. *Sawtoothing core, quiescent edge MHD modes.*

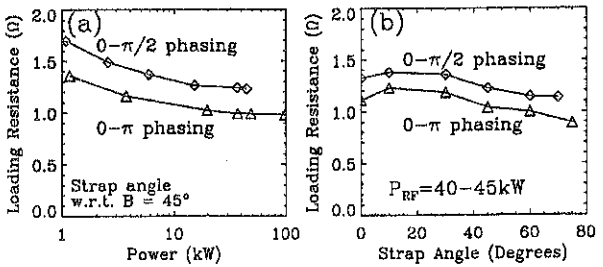

FIGURE 3. *Plasma loading vs RF power and strap angle. Strap angle 90° corresponds that straps are parallel to field lines.*

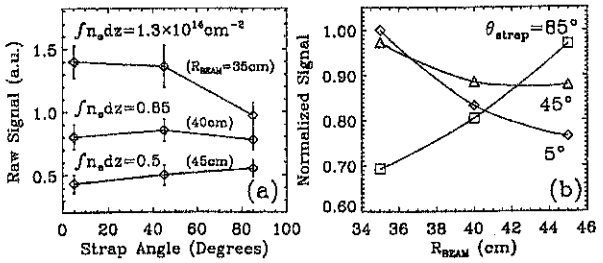

FIGURE 4. *Scattered microwave signal due to RF induced density fluctuation. Straps are parallel with angle 90°.*

Consideration on Pellet Ablation Characteristics and its Relation with Plasma Rotation in the JIPP T-IIU Tokamak

H. Sakakita[1], K. N. Sato[2], I. Nomura, Y. Hamada, K. Ida, K. Narihara, K. Toi, T. Seki, A. Ejiri, H. Kuramoto, K. Adachi, A. Fujisawa, S. Hidekuma, S. Hirokura, H. Iguchi, Y. Kano, Y. Kawasumi, M. Kojima, A. Nishizawa, S. Ohdachi, Torus Exp. Group

National Institute for Fusion Science, Chikusa, Nagoya 464-01, Japan
[1]Present address : Electrotechnical Laboratory, AIST, MITI, Umezono, Tsukuba 305, Japan
[2]Present address : Research Institute for Applied Mechanics, Kyushu University, Kasuga-Koen, Kasuga 816, Japan

1. INTRODUCTION

Consideration on pellet ablation characteristics and on the relation with plasma rotation in the JIPP T-IIU tokamak has been carried out.

Characteristics of a cloud ablated from an ice pellet has been investigated in detail by an "injection-angle controllable system"[1]. A long "helical tail" of ablation light has been observed by using CCD cameras and a high speed framing photograph[2]. In the case of an injection angle (θ) larger than a certain value ($\theta \geq 4°$), a pellet penetrates straightly through the plasma with a trace of straight ablation cloud, which has been expected from usual theoretical consideration (Case I). On the other hand, in the cases of on-axis and off-axis injections with the angle smaller than the certain value ($\theta \leq 4°$), a long helical shape ("tail") of ablation light has been observed (Case II). The direction of this helical "tail" is independent to that of the total magnetic field lines of the torus. In order to examine the tail direction, as to four conditions with the combination of two (CW and CCW) toroidal magnetic field directions and two plasma current directions, the injection-angle controllable experiments have been carried out. These results show that the "tail" poloidally rotates to the electron diamagnetic direction, and toroidally to the opposite to the plasma current direction as to almost all conditions of injection angles.

In the present paper, the "tail" phenomenon has been analyzed to find out the reason why the tail rotates to those directions, by considering both effects; i.e., the effect by collisions of hydrogen atoms/ions in a cloud with bulk ions, and the effect of $E_r \times B$ drift due to a macroscopic radial electric field.

2. EXPERIMENTAL EVIDENCES

To examine the time-dependent flow characteristics of the ablated cloud, the movement of the ablation cloud has been observed by using a high speed framing photograph[3, 4]. In cases of on-axis and of off-axis injections to the upward injection (i. e., to the inverse direction against the electron diamagnetic direction in poloidal plane), it has been observed that the ablation cloud rotates to the same direction with those of observations by CCD cameras (case II). Only in the case of off-axis injection to the downward injection (i. e., to the parallel direction against the electron diamagnetic direction in poloidal plane), it has been observed that the ablation cloud first rotates to the same direction with other cases, but at a certain time later it seems to decelerate and stay at the same location, or sometimes even flow back to the reverse direction, i. e., to the ion diamagnetic direction poloidally, and to the plasma current direction toroidally (case III).

Potential measurements of pellet-injected plasmas by using a heavy ion beam probe (HIBP) method have been carried out[5]. In the case of the upward injection in poloidal plane, the result shows that the direction of potential change is negative, and consequently the potential after the injection should be negative, because it has been measured to be negative in usual ohmic plasmas without pellet injection. Thus, the "tail" direction for case II seems to be consistent to that of the bulk plasma rotation which may be caused mainly by the effect of $E_r \times B$ drift through the plasma potential in the ohmic plasma. While the case of the downward injection in poloidal plane has exhibited the opposite result, i.e. the direction of potential change is positive, and this may be a cause of complicated behavior of ablation cloud as is described above (case III).

3. CONSIDERATION FOR "TAIL-SHAPED" PHENOMENA

In this section, it is considered why the ablation cloud rotates helically in the tokamak plasma. From the experimental results, it is shown that "tail-shaped" phenomena have a close connection with the plasma rotation through the plasma spatial potential. Therefore there is a possibility that the movement of the collisional ablation cloud is controlled mainly by the momentum transfer from the plasma rotation and the direct effect of $E_r \times B$ drift.

3-1. Derivation of an approximate equation

The phenomenon has been analyzed by considering both effects; i.e., the effect by collisions of hydrogen atoms/ions in a cloud with bulk ions, and the effect of $E_r \times B$ drift due to macroscopic radial electric field.

From the conservation of an angular momentum, (momentum of the bulk plasma rotation effect + momentum of $E_r \times B$ drift effect) = (momentum of ablation cloud on a magnetic surface of minor radius $r = l$), following relation is derived.

$$l \times m_i N_{Bi} \cdot \gamma V_{Bi} + l \times m_i N_{ci} \cdot V_{ci} = l \times (m_c N_{cn} + m_i N_{ci}) \cdot V \qquad (1)$$

The symbols mean as follows; V is the velocity of the ablation cloud, N_{Bi} the number of bulk hydrogen ions on a magnetic surface, m_i mass of a hydrogen ion, V_{Bi} the plasma rotation velocity which is caused by $E_r \times B$ drift, N_{ci} the number of hydrogen ions in the ablation cloud, V_{ci} $E_r \times B$ drift velocity in the ablation cloud, N_{cn} the number of hydrogen atoms in the ablation cloud, and m_c mass of a hydrogen atom ($m_c = m_i$), respectively. The value γ means a transfer rate of a momentum which is obtained as a result of the momentum transfer from bulk ions to hydrogen atoms/ions in the cloud due to the elastic collision. Here, it is assumed that V_{Bi}, V_{ci} are rewritten as the following equations, respectively:

$$V_{Bi} = E_r / B, \quad V_{ci} = \kappa \cdot E_r / B \quad , \qquad (2)$$

here, κ means a screening rate of a macroscopic radial electric field. From equations (1) and (2), a formula is finally obtained as

$$\mathbf{V} = \left(\frac{1}{N_{cn} + N_{ci}} \frac{E_r}{\mathbf{B}} \right) (\gamma N_{Bi} + \kappa N_{ci}) \qquad (3)$$

In right hand side of Eq. (3), the first term indicates an interaction effect with rotating bulk ions, and the second term indicates an $E_r \times B$ drift effect, respectively. For the toroidal component of **V** (V_ϕ), **B** is replaced by B_p, and for the poloidal component of **V** (V_θ), **B** is replaced by B_T.

3-2. Estimation of the value 'γ'

In this part, the bulk plasma rotation effect, that is to say, the effect by collisions of hydrogen atoms/ions in a cloud with bulk ions is considered. However the Coulomb collision time of hydrogen ions in a cloud with bulk ions (~100 μs) is longer than the elastic collision time of hydrogen atoms in a cloud with bulk ions (~1 μs) [4]. Accordingly it is assumed that bulk ions collide only with atoms (not with ions) in the ablation cloud. For the ion-atom elastic collision, two kinds of classical momentum conservation laws are applied, to obtain the particle velocities after collision.

The values of N_{cn}, $(N_{cn} + N_{ci})$, N_{ci} and N_{Bi} have been estimated as follows. From a numerical simulation using the Milora model which includes heat flux by thermal electrons, it is approximated that ablation rate (dN/dr) of a pellet (length 1.2 mm × diameter 1.1 mm) is about $(2.5 - 5.0) \times 10^{18}$ atoms/cm at the position (r~2 - 13 cm) where main pellet ablation occurs. Assuming that the ablation cloud exists on the rotating plasma column with the thickness of dr ~2 cm, the number of particles within the ablation cloud is $N_{cn} = dN/dr \times dr \sim (0.5 - 1.0) \times 10^{19}$ particles, and also $(N_{cn} + N_{ci}) \sim (0.5 - 1.0) \times 10^{19}$ particles. If we assume that $N_{ci} = (0.1 - 0.5) \times 10^{19}$ ions, the number of ions on a magnetic surface can be calculated as $N_{Bi} = n_i \cdot (\text{Volume}) \sim n_i \cdot (2\pi r \cdot dr \cdot 2\pi R_0) \sim 1.3 \times 10^{19} \cdot (2\pi\, 0.1 \cdot 0.02 \cdot 2\pi\, 0.91) \sim 10^{18}$ ions.

One method of the analysis is that, two smooth spheres (the bulk ion, the cloud atom) which have the mass $m_i N_{Bi}$, $m_i N_{cn}$, and the velocity V_{Bi}, V_2, respectively, collide with each

other from the angle θ_1 and θ_2 against for a center line, then the velocities for the bulk ion (V_{Bi}') and the cloud atom (V_2') after the elastic collision will be derived. Here, the first term of the left side in Eq.(1), $\gamma \cdot V_{Bi} = \langle V_2' \rangle$, means the averaged velocity of ablated hydrogen atoms after the elastic collision with bulk ions. From the conservation laws of momentum both for the vertical and parallel directions to the center line and from the law of the repulsion, the following relation is obtained:

$$V_2' = [V_2^2 \sin\theta_2^2 + \{2 N_{Bi} V_{Bi} \cos\theta_1 + (N_{cn} - N_{Bi}) V_2 \cos\theta_2\}^2 / (N_{Bi} + N_{cn})^2]^{1/2} . \quad (4)$$

When the velocity (V_{Bi}) of bulk ions within the region $-\pi/4 \le \theta_1 \le \pi/4$ is about 1.0×10^6 cm/s and $V_2 = 0$ at the initial stage, then $\langle V_2' \rangle$ becomes $(0.16 - 0.30) \times 10^6$ cm/s by using Eq.(4). Thus, the value γ is derived to be around 0.16 - 0.3.

Another method is as follows: It is assumed that bulk ions collide with atoms in the ablation cloud elastically, and after collisions, they are scattered to θ and ϕ directions each other with respect to the injection direction. A relation of momentum transfer between bulk ions and cloud neutrals can be expressed as the first term of the left side in Eq.(1), $m_i N_{Bi} \cdot \gamma \cdot V_{Bi} = m_i N_{Bi} (V_{Bi} - \langle V_{Bi}' \rangle)$. Here, $\langle V_{Bi}' \rangle$ means the averaged bulk plasma rotation velocity after the elastic collision with ablated hydrogen atoms. From the conservation law of momentum and energy, an averaged velocity $\langle V_{Bi}' \rangle$ of the bulk ions which are dispersed to the region $-\pi/2 \le \theta \le \pi/2$ becomes as follows:

$$\langle V_{Bi}' \rangle = \frac{1}{2\alpha} \int_{-\alpha}^{\alpha} \frac{V_{Bi}}{\left\{\cos\{\tan^{-1}(\frac{N_{cn} \sin 2\phi}{N_{Bi} - N_{cn} \cos 2\phi})\} + \sin\{\tan^{-1}(\frac{N_{cn} \sin 2\phi}{N_{Bi} - N_{cn} \cos 2\phi})\} \cos\phi/\sin\phi\right\}} d\phi \quad . (5)$$

Here, this relation, $\theta = \tan^{-1}\{(N_{cn} \sin 2\phi)/(N_{Bi} - N_{cn} \cos 2\phi)\}$ has been used. When V_{Bi} is about 1.0×10^6 cm/s and $39\pi/180 \le \alpha \le 42\pi/180$, then $\langle V_{Bi}' \rangle$ becomes $(0.72 - 0.85) \times 10^6$ cm/s by using Eq.(5). Thus, the value γ is derived to be around 0.15 - 0.28.

From the above estimations, it is considered that the momentum transfer rate γ is around 0.15 - 0.3. If the distribution functions for the velocity and for the energy have been included in the calculation of the collision effect between bulk plasma and ablated cloud, more exact value of γ will be obtained.

3-3. Estimation of the value 'κ'

In a case of a solid dielectric medium, normal screening of an electric field is caused by free electrons. In the case of torus plasmas, however, it is considered that a screening of the electric field is not induced due to the following reasons: For an ablation cloud in a toroidal plasma, if the charge separation based on the ion Larmor motion could happen, then the characteristic length of the charge separation may be defined to be almost the same size as Larmor radius (r_L). However, an electric field which screens the macroscopic radial electric field of the bulk plasma will not be induced since the Larmor radius is always much greater than the Debye length ($\lambda_D << r_L$). Here, it is assumed that temperature and density both of ions and electrons are the same with each other. Consequently, the value κ may be written as unity.

3-4. Estimation of the values "V_ϕ and V_θ"

Finally, the value of ablation cloud velocity (V) is estimated by Eq.(3). In the case of upward pellet injection (case II), the potential change is found to be negative ($\sim$-500 V) by the HIBP measurement. As a result the radial electric field after the injection should be negative because it has been measured to be negative ($\sim$-20 V/cm) in usual ohmic plasmas without pellet injection. Therefore, in this case the radial electric field is roughly estimated to be around $E_r \sim$ -20 V/cm + (-500 V)/(23 cm)$\sim$- 40 V/cm. Substituting these parameter values into Eq.(3), the cloud velocities for toroidal and poloidal directions will be obtained, respectively, as

$V_\phi \sim 1/\{(0.5\text{-}1)\times10^{19}\} \cdot \{(30\text{-}50)/0.25\} \cdot \{(0.15\text{-}0.3) \times 10^{18} + 1.0 \times (0.1\text{-}0.5) \times 10^{19}\}$
$\sim$ 2.8 - 10.6 [km/s] , and

$V_\theta \sim 1/\{(0.5\text{-}1)\times10^{19}\} \cdot \{(30\text{-}50)/2.5\} \cdot \{(0.15\text{-}0.3) \times 10^{18} + 1.0 \times (0.1\text{-}0.5) \times 10^{19}\}$
$\sim$ 0.3 - 1.1 [km/s] .

In the present case, concerning the origin of the "tail-shaped flow", the momentum transfer effect compared with $E_r \times B$ drift effect reveals ~1/10. Figure 1 shows experimental results and estimated results for the velocity of the ablation cloud. A little difference between the experimental and the estimated ones might come from the error of the calculated values and the validity of the assumption for the approximate equation etc..

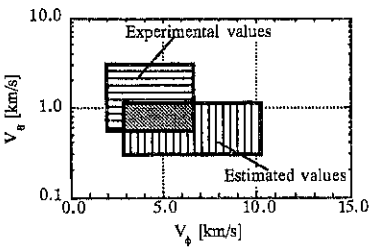

Figure 1. The regions of the ablation cloud velocity for experimental and estimated results.

On the other hand, in the case of downward injection (case III), the potential change is positive, and the plasma potential during pellet injection is not clear, because it depends on a potential depth of ohmic plasmas before injection. For example, if E_r is -20 - -10 V/cm (before injection) and the potential change by pellet injection is +500 - +800 V, then the electric field will become 0 V/cm - +10 V/cm. By using these E_r values to the Eq.(3), the cloud velocity becomes to be zero or positive. These calculation results might be a cause of complicated behavior of the ablation cloud.

4. SUMMARY

By using the "injection-angle controllable system", a long "helical tail" of ablation light has been observed in the JIPP T-IIU tokamak. Consideration on characteristics of the cloud ablated from an ice pellet and on the relation with plasma rotation has been carried out.

Based on the cloud parameters, characteristic times for various processes such as charge exchange, elastic collision, excitation, ionization and recombination are analyzed. Since the charge-exchange and the elastic-collision times are greatly shorter than the ionization time in this region, consideration on various characteristics times leads us to the conclusion that the "tail-shaped" phenomena may come from the situation of the charge exchange equilibrium of hydrogen ions and neutrals at extremely high density regime in the ablation cloud.

Also, the "tail" phenomenon has been analyzed by considering both effects; i.e., the effect by collisions of hydrogen atoms in a cloud with bulk ions, and the effect of $E_r \times B$ drift due to macroscopic radial electric field. The equation of the ablation cloud velocity is derived by the analysis, and it has been found that the momentum transfer effect is of the order of ~1/10 compared with $E_r \times B$ drift effect. Concerning the ablation cloud velocity, the calculated values have an accordance with the experimental values within the estimated parameter region.

From the experimental results and theoretical considerations, it is concluded that the "tail structure" may be caused both by the situation of charge exchange equilibrium of hydrogen ions and neutrals at extremely high density regime of the ablation cloud, and by the effect of the plasma potential and the rotation within the torus plasma.

References

[1] Sakakita H et al, *Proc. IAEA TCM on Pellet Injection*, **No. 28**, (Naka, 1993).

[2] Sato KN et al., *Int. Conf. on Plasma Phys.*, **1**-93 (Iguaccu, 1994).

[3] Sakakita H et al, *22th EPS Conf. on Controlled Fusion and Plasma Phys.*, **19C**, I-125 (Bournemouth, 1995).

[4] Sato KN et al., *23rd EPS Conf. on Controlled Fusion and Plasma Phys.*, (Kiev, 1996).

[5] Hamada Y et al., Nuclear Fusion, **Vol.36**, No.8 (1996) 1047.

Monte Carlo Simulations of Ripple-Trapped Beam Ions in the Presence of a Non-uniform Radial Electric Field

J.A. Heikkinen[1], W. Herrmann[2], and T. Kurki-Suonio[3]
[1]*VTT Energy, Euratom-TEKES Assn, P.O. Box 1604, FIN-02044 VTT, Finland*
[2]*Max-Planck-Institut für Plasmaphysik - Euratom Assn, D-85748 Garching, Germany*
[3]*Helsinki University of Technology, Department of Engineering Physics and Mathematics, Euratom-TEKES Assn, FIN-02150 Espoo, Finland*

Abstract. The increase in the neutral flux from the ripple-trapped ions at an L-H transition observed by the CX-detector at ASDEX Upgrade is reproduced by Monte Carlo simulations by turning on E_r near the plasma periphery. For E_r with large enough half-width, the rise-time of the fluxes is shorter than 100 μs, which could make this diagnostic a useful tool for time-resolved measurements of E_r.

Introduction. At an L-H transition, a sudden change in the edge radial electric field has been observed [1], but the question of causality in a spontaneous L-H transition is yet to be resolved. The time resolution of the measurements has not yet been good enough to decide whether the plasma switches to the H-mode before or after the fast changes in the E_r-field [2].

The CX-detector on ASDEX Upgrade monitors the slowing-down ions from the neutral beams that are trapped in the secondary magnetic wells near the plasma surface formed by the discrete set of magnetic coils. These ripple-trapped ions are expected to escape the plasma very fast, in about 50 μs, as a result of the ∇B-drift and, consequently, the CX-detector should receive a negligible flux under ordinary circumstances. However, as the plasma enters the H-mode, these neutral particle fluxes reach levels that are comparable to the signal from nontrapped ions. It has been suggested that the underlying reason for the increased neutral particle flux from ripple-trapped slowing-down ions is a changing E_r-field [3] and, thus, the neutral flux could be used as diagnostic tool for E_r.

We have investigated the effect of a non-uniform E_r on the ripple-trapped neutral beam ions using a Monte Carlo particle tracking code ASCOT [4] that follows the guiding center trajectories of test particles. The tokamak geometry models ASDEX Upgrade, where ∇B-drift is downward. The effects from plasma elongation, triangularity, and Grad-Shafranov shift are omitted for simplicity. The neutral density is assumed to decay rapidly as one moves inwards from the plasma boundary ($a = 50$ cm), $n_n = n_{n_0} e^{(r-a)/d_n}$ with $d_n = 2$ cm. The test particles are initialized according to ions born in the neutral injector beams. The initial energy for the test particles (deuterons) is chosen at the 1/3 power fraction of the beams (20 keV), which is dominant as far as particle source is concerned. The innermost particles are launched at $r = 41$ cm, corresponding to $\rho = r/a = 0.83$. This is well justified, because both the neutral beam flux and the neutralization

probability (relevant to the detection) drop very rapidly as the distance to the separatrix increases. The ions are followed until they either escape the plasma ($r > a$), or their energy falls below 2.5 keV.

The magnetic field ripple is modelled by $B_0\Delta(r) = B_0\Delta_0 e^{r/w_B}$, where $B_0\Delta_0$ is the ripple strength on the magnetic axis. Choosing $\Delta_0 = 0.003$ and $w_B = 16$ cm, the model fits quite well the ripple strength obtained from more detailed calculations done on ASDEX Upgrade. In ASDEX Upgrade, the number of toroidal coils is $N_c = 16$ and, thus, the magnetic ripple has a 16-fold periodicity in the toroidal coordinate. The radial electric field is given in a polynomial form $E_r = c_0 + c_1\rho + c_2\rho^2 + c_3\rho^3$, depicted in Fig. 1. The coefficients were chosen so that the profile resembles the experimental profile of E_r measured in DIII-D after an L-H transition (see Fig. 7 in Ref. [5]). We have even allowed a small region inside the separatrix where E_r turns positive (outward). This corresponds to an $E \times B$-drift that is in the same direction as the ∇B-drift and, thus, that is detrimental to the particle confinement. If the separatrix is further in, so that E_r remains always negative inside the plasma, the favorable effects presented in this paper are further magnified.

Results. In Fig. 2 we show the neutral particle flux as a function of toroidal (ϕ^*) and poloidal (θ) angle. The signal is collected on a 20×20 grid that maps the region of interest. Because of the 16-fold periodicity of the system, it is sufficient to look at just one coil period, $0 < \phi^* < \Delta\phi = \frac{2\pi}{N_c}$. The pitch, $\xi = v_{\|}/v$, of the ions contributing to the signal satisfies the condition $|\xi| < 0.07$, and their kinetic energy, $\mathcal{E}$, is between 5 and 15 keV. Here, $v_{\|}$ is the ion's velocity parallel to the magnetic field, and v is the total velocity at the moment of neutralization. With the present ripple parameters, this guarantees that the detected ions are either ripple-trapped, or they are banana particles near their turning points. Figure 2a, with $E_r = 0$, exhibits a significant depletion of particles near the bottom of the magnetic well due to the fast ∇B -drift losses. Near the coils the detector monitors banana particles for which the ripple-trapping is less probable. Therefore, this region of phase space remains reasonably densely populated, and the signal level is $10-20$ times higher. Poloidally, the signal is enhanced on the lower half due to the downward convection of the ripple-trapped ions [7].

As shown in Fig. 2b, when a non-uniform E_r is introduced to the plasma, the signal depression around the bottom of the magnetic well not only disappears but now the signal has its maximum value there. That the signal from the ripple-trapped ions now exceeds that from the banana-trapped ions can be understood as follows: In the absence of E_r, due to the very narrow neutral density profile, most of the CX-detector signal originates from the very edge of the plasma, where the drift losses efficiently deplete not only the ripple-trapped ions but also banana ions near the ripple-banana boundary. A negative E_r with wide enough profile to affect the orbits of ions residing further inside the plasma

contributes an additional drift that opposes the ∇B-drift and, consequently, bends the orbits of these ions outward and, eventually, upward. Therefore, such a radial electric field can force ions from further in to enter the line-of-sight of the detector. Because there are much more ions at these smaller radii, the signal increase due to E_r can dominate the local signal from the banana-trapped ions.

Figure 2c gives the ratio of the neutral flux in the presence of E_r to the flux in the absence of the field, *i.e.*, the ratio of flux in Fig. 2b to that in Fig. 2a. Clearly, the ions that are most sensitive to E_r, reside in the ripple-trapped part of the phase space. Therefore, the presence of a radial electric field can be best observed by monitoring ions near the bottom of the ripple well, for poloidal angles slightly below the mid-plane and, thus, the movable CX-detector on ASDEX Upgrade can monitor the optimal part of the phase space.

In Fig. 3 we show the time evolution of the neutral flux in response to an abrupt onset of E_r at $t = 1$ ms. The detector monitors ions with $|\xi| < 0.07$, $|\theta| < 0.5$ rad, 5 keV $< \mathcal{E} <$ 15 keV, and 0.25 rad$< \phi^* <$ 0.35 rad (with the magnetic well at $\phi^* \approx 0.3$ rad). According to Fig. 2, this window corresponds to ions that are most sensitive to E_r. The simulation is started well before the onset of the field to obtain stationary conditions, and new ions are born steadily throughout the simulation. Also the time evolution in the absence of E_r is shown (dotted line). Before E_r is turned on, only a weak signal is observed but, at $t = 1$ ms, a fast growth is observed for the $E_r \neq 0$ -curve, while the curve corresponding to the fieldless case remains at the low level. Constrained by the statistical accuracy of the simulation, the signal growth can be characterized by a response time of about 50 μs to the field onset. Collisional effects alone are not sufficient in explaing the fast time response to the radial electric field, and some other mechanisms must be involved. Indeed, solving the relevant Fokker-Planck equations for the ripple-blocked ion distribution [6], the fast convective drift of the ripple-blocked ions from the inner, well-filled ripple-orbits to the depletion region is found to be responsible for the fast growth of the ripple-blocked ion distribution by the onset of the radial electric field [8].

[1] R.J. Groebner, K.H. Burrell, and Seraydarian, Phys. Rev. Lett. **64**, 3015 (1990);
K. Ida, *et al.*, Phys. Rev. Lett. **65** (1990) 1364.
[2] K.H. Burrell, Plasma Phys. Control. Fusion **36** (1994) A291.
[3] W. Herrmann and Asdex Upgrade Team, Phys. Rev. Lett. **75** (1995) 4401.
[4] J.A. Heikkinen, and S.K. Sipilä, Phys. Plasmas **2** (1995) 3724.
[5] K.H. Burrell, *et al.*, Physics of Plasmas **1** (1994) 1536.
[6] A.V. Gurevich and Ya. S. Dimant, Nucl. Fusion **21** (1981) 159;
O.A. Anderson and H.P. Furth, Nucl. Fusion **12** (1972) 207.
[7] E.L. Berezovskij, *et al.*, Nucl. Fusion **23** (1983) 1575.
[8] J.A. Heikkinen, W. Herrmann, and T. Kurki-Suonio, submitted to Phys. Fluids.

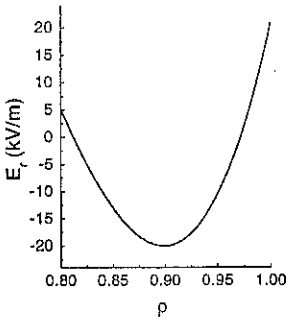

Fig. 1. The radial electric field used in the simulations.

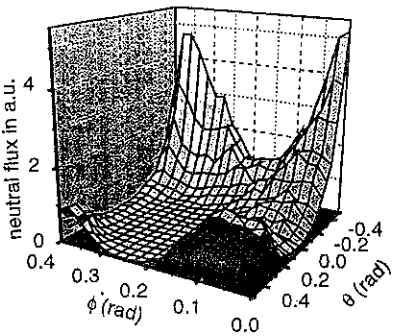

Fig. 2(a). Neutral particle flux Γ in the absence of a radial electric field.

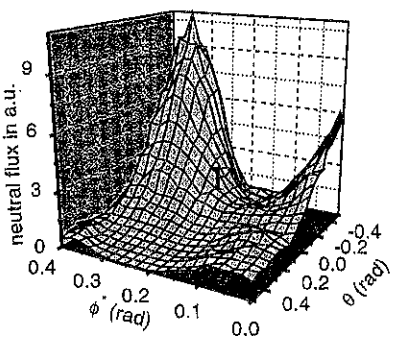

Fig. 2(b). Neutral particle flux, Γ, when the radial electric field of Fig. 1 is present.

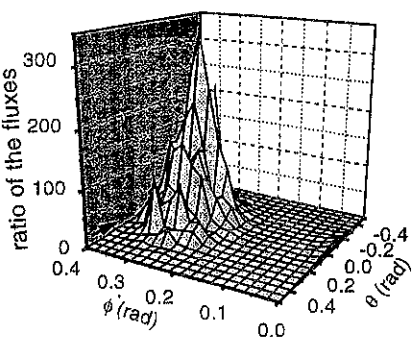

Fig. 2(c). $\Gamma(E_r < 0)/\Gamma(E_r = 0)$, i.e. ratio of the flux of Fig. 2(b) to the flux of Fig. 2(a).

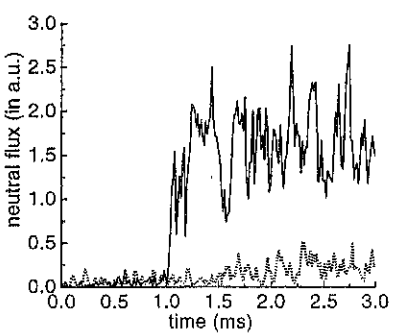

Fig. 3. The time evolution of neutral flux when E_r of Fig. 1 is turned on at t = 1ms.

Ion Orbit Loss Flux in the Presence of a Radial Electric Field

J.A.Heikkinen[1], **T.P.Kiviniemi**[2], T.Kurki-Suonio[2], S.K.Sipilä[2], W.Herrmann[3], W.Suttrop[3], H.Zohm[4]

[1] *VTT Energy, TEKES-Euratom Association, P.O. Box 1604, FIN-02044, VTT, Finland*

[2] *Helsinki University of Technology, TEKES-Euratom Association, P.O.Box 2200, FIN-02015 HUT, Finland*

[3] *Max-Planck-Institut für Plasmaphysik, Euratom Association, D-85740 Garching, Germany*

[4] *Institut für Plasmaforschung der Universität Stuttgart, D-70569 Stuttgart, Germany*

Abstract: The multivalued balance between loss of fast ions from the plasma boundary and the neoclassical return current has been proposed to be a reason for L-H transition. By fully toroidal Monte Carlo calculations it is shown that loss cone structure is remarkably modified by strong radial electric field. Effect of the collisionality and direction of the magnetic field to the bifurcation conditions are discussed.

Introduction: In tokamak plasmas, fast increase of the radial electric field E_r is observed near the plasma edge in the context of an L-H transition. The shear flow associated with E_r is believed to suppress fluctuations responsible for anomalous transport. According to one proposal, the multivalued balance between the non-ambipolar loss of fast ions from the plasma boundary and the neoclassical return current could be the reason for the spontaneous transition from low to high electric field. In this work, the ion orbit loss as a function of radial electric field in ASDEX Upgrade geometry is investigated using a fully toroidal Monte Carlo code ASCOT (3D in space and 3D in velocity) [1]. Exact guiding-center orbit trajectories are evaluated, and the loss cone is determined from the condition of intersection of the orbit with the divertor plates or wall structure. Influence of the strong radial electric field to the loss cone structure is presented for thermal and high energy tail particles. Neoclassical return current is calculated with analytical model and it is compared with the ion orbit loss flux. Analysis is done for both directions of toroidal magnetic field and for different temperatures.

Numerical model: With Monte Carlo simulations, the loss of ions of a Maxwellian distribution near the separatrix is determined as a function of E_r. In simulations, constant $E_r(\rho) = -d\phi/d\rho$ is used, to simplify the problem. Here, ϕ is electrostatic potential and ρ is the flux surface label normalized to the value on separatrix. (In tests with more realistic profiles, orbit squeezing due to negative $dE/d\rho$ [2] was found to decrease losses. However, this effect is not remarkable as already noted in [3].) Ensemble of particles with initially local thermal velocity is followed and the particles which are lost due to their orbit width are registered. The lost particles are weighted with the number which corresponds to the relative phase space volume of the initial position of the particle. From the cumulated number of lost particles, loss current density can be determined as an cumulation velocity divided by the flux surface area. Stationary background temperatures and densities are

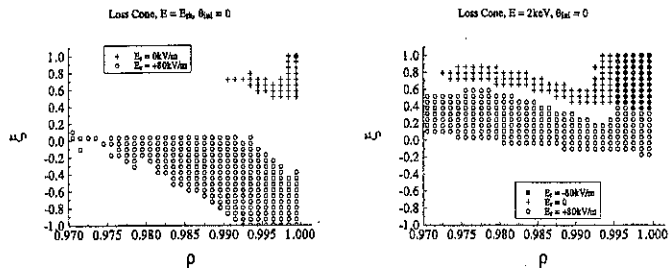

Figure 1: *Loss cone for thermal and tail particles as a function of radius and energy*

assumed. Coulomb collisions are present, including pitch angle scattering and velocity diffusion.

Neoclassical return current density is calculated using expression [4]

$$j_r = \frac{\sqrt{\pi} n T e^2}{B r v_{th} B_\theta}(E_r - \frac{T}{e}(\frac{n'}{n} + \gamma\frac{T'}{T}) - B_\theta U_{||}) e^{-(\frac{E_r}{v_{th} B_\theta})^2} \quad (1)$$

where n, T and v_{th} are local ion density, temperature and thermal velocity, respectively, r, ε B and B_θ are minor radius, inverse aspect ratio, total magnetic field and the poloidal component of the magnetic field, respectively, E_r is radial electric field, e is elementary charge, $\gamma = \frac{3}{2}$ in the plateau regime, $U_{||}$ is the mean velocity along the magnetic field and differentiation with respect to the radius is denoted by prime.

Results: Background data of Asdex Upgrade discharge 8044 is used. Near the separatrix density and temperature profiles of the background ions and electrons on equator are approximately $n, T(r) = n, T(r_{sep}) + (r - r_{sep})n', T'$ with $n_{D,e}(r_{sep}) = 1.2 \times 10^{19}$ m^{-3}, $T_{D,e}(r_{sep}) = 120$ eV, $n' \approx -4 \times 10^{20}$m^{-4} and $T' \approx -6keV/m$. Values $a = 0.5$ m, $R = 1.65$ m, $I_p = 1$ MA and $B_t = -2.5$ T are used for minor and major radius, plasma current and toroidal magnetic field on the axis, respectively. Negative B_t means that ∇B drift is downwards, which is, towards the X-point.

In Fig. 1, loss cone of thermal 120 eV, and 2 keV tail particles is presented as a function of radius and pitch angle. Analysis is done by calculating the trajectories in the absence of collisions for particles initially on outboard equator. Simulation is done in the absence and presence of constant strong radial electric field. For $E_r = 0$, loss happens for for positive pitch angles, i.e., for particles which due to ∇B drift shift outwards from the launching point. For energetic particles with larger banana width, loss cone penetrates deeper into the plasma. With $E_r = -80$ kV/m positively poloidally directed $E \times B$ drift is strong enough to turn particle first to direction where ∇B drift moves particles to inner flux surfaces. No loss orbits were observed. When $E_r = +80$ kV/m, in case of thermal particles, loss cone is shifted to particles with negative pitch angles, i.e., particles which in the absence of E_r are confined. Here again, $E \times B$ drift changes the direction of poloidal motion. Now, the particles leaving from equator with $v_{||} < 0$, are lost to outer divertor plate. For energetic particles situation is qualitatively different. For pitch angles

$\xi < -0.2$, due to their high energy, direction of poloidal motion is not reversed. However, E_r still shifts and enlarges the loss cone.

In Fig. 2, ion orbit loss flux in the presence of Coulomb collisions is calculated. Simulation is done for both directions of toroidal magnetic field $B_t = \pm 2.5$ T. To get three different collisionalities, the temperature data is multiplied by factors $k = 0.5$, 1 and 2 corresponding to edge temperatures, $T_{sep} = 60$, 120 and 240 eV, respectively. Neoclassical return current is calculated for fluid velocity $U_{\|} = 0$. At strong collisionality, the ion loss current and the neoclassical return current have their L-mode root at low electric field. Reducing the collisionality does not remove this root. In contrast, the return current increases and the loss current reduces, which implies at low collisionality a stable L-mode root even at lower electric field. This analysis was done on separatrix. When going inside the separatrix, non-ambipolar ion orbit loss flux decrease fast and, at the same time, return current obtained from Eq.(1) would increase with increasing density and temperature.

Conclusions: In this work, effect of the strong radial electric field to the loss cone structure and to the amount of the ion orbit loss current was found remarkable. An inward electric field was found to decrease ion orbit loss with both directions of B_t. It should be noted that the loss current does not fit the analytical expression of Shaing [5] (as already noted in [3]), where the loss was independent of the sign of E_r. The ambipolarity of the loss current and the neoclassical return current obtained from Eq.(1) has not been found to produce bifurcated solutions for E_r as the edge plasma becomes less collisional. In order to check the validity of this calculation, the direct calculation of the return current from the Monte Carlo simulations and with the 3D Fokker-Planck code [6] is in progress. Also, the inclusion of an anomalous radial ion diffusivity may be important for the calculation of the loss current, because the filling of the loss cone should be determined by the total diffusion of the ions in the configuration space for which the temperature dependence may be different than for the neoclassical diffusion simulated by ASCOT here.

References

[1] J.A. Heikkinen, S.K. Sipilä, Phys. Plasmas 2 (1995) 3724.

[2] K. Itoh, S. Itoh, Plasma Phys. Contr. Fusion 38 (1996) 1.

[3] A.V. Chankin, G.M. McCracken, Nucl. Fusion 33 (1993) 1459.

[4] T.E. Stringer, Nucl. Fusion 33 (1993) 1249.

[5] K.C. Shaing, E.C. Crume Jr., Phys. Rev. Lett. 63 (1989) 2369.

[6] T.P. Kiviniemi, J.A. Heikkinen, submitted to Comput. Phys. Comm.

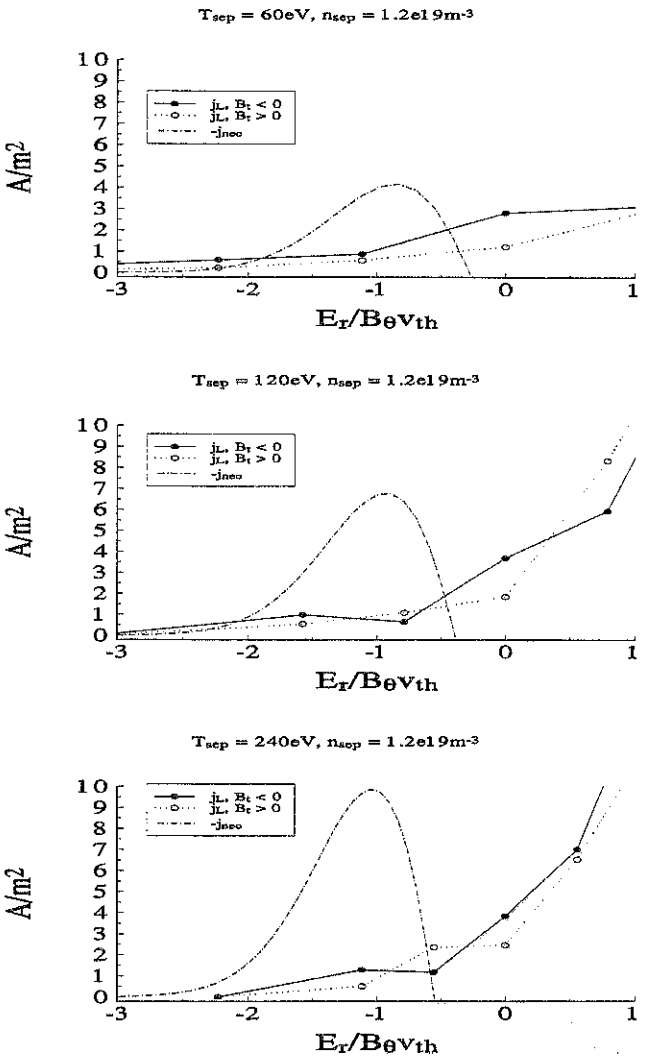

Figure 2: *The dependence of the ion orbit loss flux and the neoclassical return current on the radial electric field. Collisionality decreases from (a) to (c). Here, the numerical value of E_r is the radial electric field $E_r(r_{sep}) = -(d\phi/d\rho)\nabla\rho$ on the equator.*

Temporal Behavior of Detached Divertor Plasmas*

T.D. Rognlien,[a] M.E. Rensink,[a] G.D. Porter,[a] and F. Wising[b]
(*a*) Lawrence Livermore National Laboratory, Livermore, CA 94551 USA
(*b*) Inst. EM Field Theory, Chalmers Univ. Tech., Götburg, SWEDEN

1. Introduction and Model

In predicting the behavior of tokamak divertor plasmas in future devices such as ITER, it is common to seek steady-state solutions to simplify the parameterization and understanding of the results, and to ensure that such a divertor solution could be maintained for a long discharge pulse. A summary of recent results for ITER is given in Ref. [1,2] where it is discussed that non-steady detached plasma solutions are found with the B2/EIRENE code [3] that appear to have long timescales. However, the timestep restriction imposed by the numerically explicit coupling between the plasma and the Monte Carlo neutrals makes it difficult to follow solutions to long times ($\sim$ 1 sec). We present results for times of $\sim$ 1 sec or greater using the UEDGE transport code which couples the fluid plasma and a fluid neutral models implicitly, thereby allowing large timesteps [4]. We use these results to identify the origin of the long-time behavior, show that appropriate pumping can lead to steady states, and argue that a particle pinch term is needed to control the detached plasma solutions. At the same time, these results confirm the existence of possible detached solutions for ITER parameters via impurity injection as described in Ref. [1,2].

The 2-D UEDGE transport code is described in references given in an overview paper [4]. The code implements the two-fluid Braginskii equations for the hydrogenic plasma with classical transport parallel to the magnetic field, $\mathbf{B}$, and anomalous cross-field transport. The hydrogen gas is described by a parallel Navier-Stokes model. Impurities are represented by either a fixed-fraction (FF) model which neglects spatial transport or a multi-species (MS) model which allows spatial transport of the different impurity charge states assuming classical parallel transport and anomalous cross-field transport. Both models include charge-exchange recombination by hydrogenic gas.

The computational domain shown in Fig. 1 contains a region slightly inside the separatrix and the scrape-off layer (SOL) to the outside. Both orthogonal and vertical divertor plates have been used, and here we focus on simulations of the outer-half domain shown by the dashed line. For standard conditions, we assume 100 MW from the core to the outer–half SOL, core-edge densities of $\sim 5 \times 10^{19}$ m^{-3}, radial density diffusion of $D = 1/3$ m^{2}s^{-1} and energy diffusion of $\chi = 1/2$ m^{2}s^{-1}. Plate recycling is 100% with no pumping at the side walls unless noted.

2. Simulation Results

The effect of impurity transport is illustrated by comparing results using the FF model with those from the MS model shown in Fig. 2 with an orthogonal plate for three core-boundary concentrations of neon [levels in a) and b) differ]. Here the radiated power density is integrated radially and toroidally, and plotted versus poloidal distance. Note that the FF model shows a roughly linear increase in power with concentration and that the radiation is localized to the divertor leg ($x > 12$ m). The MS model shows a nonlinear increase of power with core-boundary concentration because of transport and requires a higher concentration to obtain the same power as the FF model.

As the neon is increased for zero core particle-flux boundary conditions, the FF model shows strong, sustained oscillations for a concentration of 0.2%, which is when

plasma detachment occurs across the plate. These oscillations are shown in Fig. 3, and have the characteristic described in Ref. [5], except that here strong impurity radiation near the x-point also plays a role (note x-point in Fig. 2). The MS model does not show similar oscillations as it passes into detachment for our parameters.

As the impurity level is increased for fixed hydrogen density at the core boundary ($n_i = 5 \times 10^{19}$ m^{-3}), here illustrated by results for the MS model with 0.8% neon and a vertical plate, the divertor plasma evolves deeply into detachment as the ionization front moves toward the x-point. This is shown in Fig. 4 by the electron temperature (T_e) contours at two times; the ionization front occurs near $T_e \approx 3$ eV. The timescale of this evolution can be understood from the fact that a nearly fixed current of 1×10^{23} particle/s flows across the core power owing to the fixed core-density boundary condition. These particles become converted to neutral gas below the ionization front, and serve to push the front toward the x-point. Given the divertor leg volume of 10 m^3, it takes about 0.4 s to fill the region with gas at the calculated density of $\sim 4 \times 10^{21}$ m^{-3}.

We have obtained a steady state by pumping the hydrogen at the input rate of 1×10^{23} particle/s. However, the large core flux cannot be sustained by neutral beam fueling. A second option is to use the zero core-flux condition, but then the core/edge density drops to lower values. We have also used a modest pinch term of ~ 3 m/s which allows the core/edge density to be maintained. This same issue arises in the modeling of SOL plasmas in present-day devices such as DIII-D. Here, the measured density profile near the core boundary is typically significantly flatter than the simulation results [6] and, correspondingly, the particle flux exceeds the neutral beam input. As for the ITER simulations, this discrepancy could be remedied by a velocity pinch term or strongly reduced D near the separatrix.

The effect of using the zero-flux core boundary conditions for a range of densities including attached and detached plasmas is shown in Fig. 5 for no impurities and a vertical plate. When neon is introduced to increase the radiation loss, the core/edge density curve decreases, thereby reducing the range of core densities where steady-state solutions with zero core particle flux can be obtained without a pinch term.

We have also performed neon and carbon detached simulations which show timescales of several seconds, even for the zero hydrogen-flux case which reaches steady state if the carbon density is fixed at the core. However, as very few carbon ions reach the plate for the detached plasma, the issue remains of how carbon gets removed from the system to balance the chemical sputtering at the carbon plate.

Finally, while hydrogenic radiation is a dominant energy loss in the detached regime for the previous cases, it is likely to be partially absorbed by the neutrals [7]. We thus reduce the hydrogenic radiation by stages (factors of 0.5, 0.25, 0.1, 0) for the MS case with 0.8% neon. The detached state is still maintained with neon radiation becoming dominant, and the ionization front widens toward the plate down to a reduction factor of 0.1. However, for no hydrogen radiation, the ionization front moves nearer the x-point.

3. Summary

A series of ITER divertor transport simulations illustrate differences between the FF and MS impurity models. Time-dependent simulations show that oscillatory solutions can arise near the attached/detached transition for the FF model and that slow time evolution occurs over the time required to fill a portion of the divertor volume with gas; the latter can be driven by excessive core particle flux. Understanding and controlling these particle balance issues is essential for stable detached divertor operation.

Acknowledgments

*This work was performed under the auspices of the US DOE by LLNL under contract No. W-7405-Eng-48 and at Chalmers University for the Swedish Natural Sci. Res. Council; part of the work of F. Wising was done at MIT, Cambridge, MA USA. We gratefully acknowledge helpful discussions with Drs. A.S. Kukushkin, D.A. Knoll, S.I. Krasheninnikov, and D.E. Post.

References

[1] A.S. Kukushkin, H. Pacher, *et al.*, Proc. 16^{th} IAEA Fusion Energy Conference, Montreal, Canada, paper FP-27, 7-11 Oct., 1996.

[2] A.S. Kukushkin, H. Pacher, *et al.*, paper at this conference.

[3] R. Schneider, D. Reiter, *et al.*, J. Nucl. Mater. **196-198**, 369 (1992).

[4] T.D. Rognlien, B.J. Braams, and D.A. Knoll, Contr. Plasma Phys. **36**, 105 (1996) and references therein.

[5] S.I. Krasheninnikov, A.S. Kukushkin, *et al.*, Nucl. Fusion **27**, 1805 (1987).

[6] G.D. Porter, T.D. Rognlien, *et al.*, paper at this conference.

[7] D.A. Knoll, P.R. McHugh, S.I. Krasheninnikov, and D.J. Sigmar, Phys. Plasmas **3**, 293 (1996).

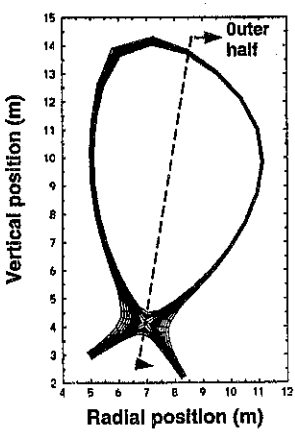

Fig. 1 Computational domain for ITER simulations; only the outer-half region is used for results reported here.

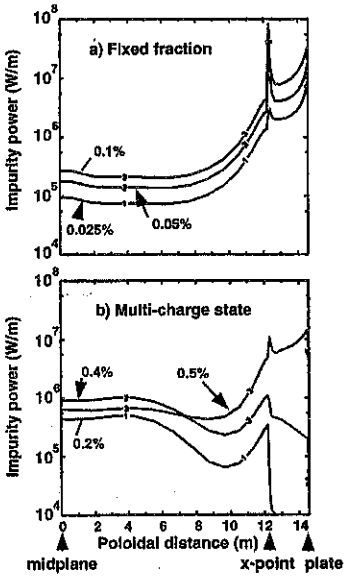

Fig. 2 Comparison of poloidal profiles of power radiated owing to neon impurities for two models. Core-boundary concentrations shown in % where total powers for case a) are 7.8, 19.4, and 39.3 MW for increasing concentration, respectively; for case b), powers are 3.7, 9.0, and 26.0 MW.

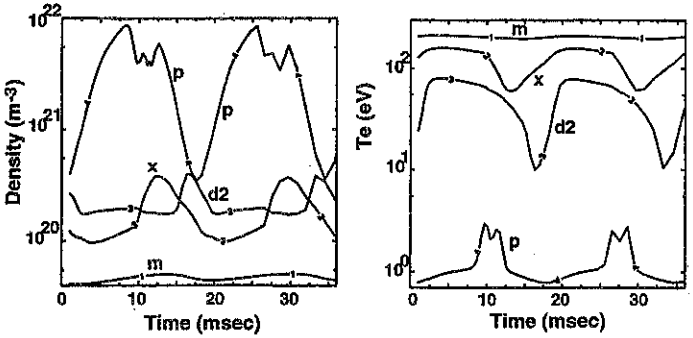

Fig.3 Sustained oscillations in the hydrogenic plasma density and electron temperature at various poloidal locations (m, midplane; x, x-point; d2, half-way between x-point and plate; and p, plate) and just beyond the separatrix in the SOL region. For fixed-fraction neon at 0.2% concentration and zero core particle flux.

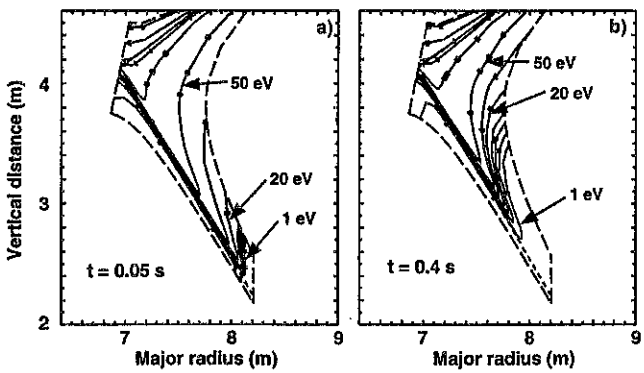

*Fig. 4. Contours of electron temperature in the outer divertor leg for the multi-species neon model with 0.8% concentration at the core boundary. The hydrogen density is fixed to 5e19 1/m**3 at the core boundary resulting in a particle flux of ~1e23 part/s; this leads to evolution to deeper detachment shown at the two times in a) and b).*

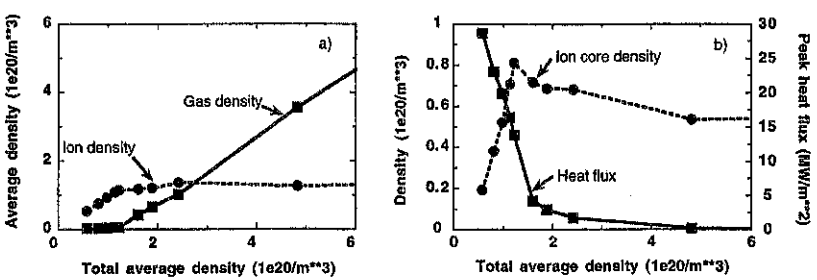

Fig. 5. Partition of density between ions and gas in a) for a series of steady-state cases without impurities for zero particle flux at core boundary, and b) corresponding core/edge density and plate peak heat flux. The transition to detachment occurs where the core/edge density peaks, and hydrogenic radiation (here assumed untrapped) is the major energy loss for the detached region.

Long Mean Free Path Electron Heat Conduction Modifications

Peter J. Catto
Massachusetts Institute of Technology, Plasma Science and Fusion Center
NW16-236, 167 Albany Street, Cambridge, MA 02139, U.S.A.

ABSTRACT

The Spitzer-Härm parallel electron heat conductivity begins to fail even at surprisingly large values of collisionality because the energy squared dependence of the mean free path results in contributions from electrons not satisfying the short mean free path expansion. Exponentially small, non-expandable modifications that cannot be retained in conventional treatments are shown to cause the departure of transport from its Spitzer-Härm value.

I. INTRODUCTION

The Braginskii [1] plasma transport coefficients begin to fail even at small values of the ratio γ defined as the mean free path of a thermal particle over the parallel temperature scale length L, $\gamma = 10^{12}T^2(eV)/N(cm^{-3})L(cm)$, where T and N the plasma temperature and density [2]. The Spitzer-Härm [3] electron heat transport coefficient, in particular, fails for $\gamma > 1/100$. The breakdown of fluid treatments occurs at these surprisingly large values of collisionality because the Coulomb collision frequency falls off as $1/v^3$ resulting in a energy weighted mean free path λ proportional to the square of the energy E ($\lambda \propto E^2$). This dependence causes the heat conduction to be dominated by electrons with energies on the order of seven times the thermal energy and energy weighted mean free paths roughly 50 times larger than those of thermal particles. The values of γ in the divertor region of current tokamaks such as Alcator C-Mod and Doublet III-D, as well as the expected values for ITER, can be as large as 1/10.

To investigate long mean free path modifications of the Spitzer electron heat conductivity the approach of Krasheninnikov [4] is adopted by seeking self-similar solutions of the model collision operator obtained from a high speed expansion of the full electron collision operator. However, to simplify the collision operator further the perpendicular distribution is assumed Maxwellian and an integration over perpendicular speeds is employed to obtain a collision operator depending only on the parallel velocity [5]. Both the physically relevant case $\lambda \propto E^2$ and the artificial, but exactly soluble, case $\lambda \propto E$ are considered. Non-expandable, exponentially small modifications to the electron heat conduction, proportional to $\exp(-1/\gamma^{1/2})$, that cannot be retained in conventional short mean free path treatments ($\gamma << 1$) are responsible for the most important departure of the parallel transport from its Spitzer value. Because self-similar variables are employed the modifications to the parallel heat conduction are local, however, they are not of the form normally employed to limit the heat flux.

II. KINETIC MODEL

Parallel electron transport in a constant magnetic field is modeled by the kinetic equation

$$v_{\|}\frac{\partial f}{\partial s}-\frac{eE_{\|}}{m}\frac{\partial f}{\partial v_{\|}}=C\{f\}=\nu_{eff}v_e^3\frac{\partial}{\partial v_{\|}}\left[\frac{1}{|v_{\|}|^3}\left(\frac{T}{m}\frac{\partial f}{\partial v_{\|}}+v_{\|}f\right)\right], \qquad (1)$$

with f the electron distribution function, $v_{\|}$ the parallel velocity, $E_{\|}$ the parallel electric field, s the distance along a magnetic field line, and e and m the magnitude of the charge and mass of an electron. To make analytic progress the full electron Fokker-Planck collision operator has been replaced by the simplified model collision operator of Ref. [5] which captures the main qualitative features of the full collision operator. The collision frequency in Eq. (1) is an effective collision frequency $\nu_{eff}=k_o 4\pi Ne^4\ell n\Lambda/m^2v_e^3$ with $k_o=k_O(Z)$ an ion charge number Z dependent factor that will eventually be determined by demanding that the parallel heat flux obtained by solving Eq. (1) recover the proper short mean free path result, $N=\int dv_{\|}f$ the electron density, and the $v_e=(T/m)^{1/2}$ electron thermal speed.

III. SELF-SIMILAR VARIABLES

Even with the simplified collision operator, Eq. (1) can not be solved analytically for general density and temperature profiles. To find analytically tractable solutions we seek self-similar solutions of the form

$$f=\frac{F_\sigma(\xi)}{T^\alpha(s)}, \qquad (2)$$

with $\sigma=v_{\|}/|v_{\|}|$ and α a constant parameterizing the family of self-similar solutions and

$$\xi=\frac{mv_{\|}^2}{2T(s)}. \qquad (3)$$

The notation F_σ denotes that $f(v_{\|}>0)=F_+(\xi)/T^\alpha$ and $f(v_{\|}<0)=F_-(\xi)/T^\alpha$. The use of self-similar variables allows the partial differential equation in s and $v_{\|}$ to be converted to a second order ordinary differential equation. As a result, what would normally be a nonlocal problem is converted into a local problem.

Defining

$$\gamma=\frac{2T}{m^2\nu_{eff}v_e^3}\frac{\partial T}{\partial s}=\text{constant}>0 \quad \text{and} \quad eE_{\|}=-\kappa\frac{\partial T}{\partial s}, \qquad (4)$$

Eq. (1) becomes

$$\frac{\partial}{\partial\xi}\left[\frac{1}{\xi}\left(\frac{\partial F_\sigma}{\partial\xi}+F_\sigma\right)\right]+\sigma\gamma\left[\alpha F_\sigma+(\xi-\kappa)\frac{\partial F_\sigma}{\partial\xi}\right]=0. \qquad (5)$$

In terms of F_σ, $N\propto 1/T^{\alpha-1/2}$ giving $\gamma\propto dT^{\alpha+3/2}/ds=$ constant. The constant κ determining the ambipolar electric field is found from the constraint that parallel electron particle flux $\Gamma_{\|}$ vanish

$$0=\Gamma_{\|}=\int_{-\infty}^{\infty}dv_{\|}v_{\|}f=\frac{1}{mT^{\alpha-1}}\sum_\sigma\sigma\int_0^\infty d\xi F_\sigma(\xi)\propto\frac{1}{T^{\alpha-1}}. \qquad (6)$$

since number conservation, $\partial\Gamma_\parallel / \partial s = 0$ must be satisfied $\Gamma_\parallel = 0$. The parallel electron heat flux $q_\parallel$ is found from

$$q_\parallel = \frac{m}{2}\int_{-\infty}^{\infty} dv_\parallel v_\parallel^3 f = \frac{1}{mT^{\alpha-2}}\sum_\sigma \sigma \int_0^\infty d\xi \xi F_\sigma(\xi). \qquad (7)$$

To obtain a finite value for $q_\parallel$, we will find that $\alpha > 2$ since F_σ always develops an algebraic tail $\propto 1/\xi^\alpha$, as might be anticipated from the streaming portion of Eq. (1) for $\xi \to \infty$.

IV. SOLUTION FOR THE ARTIFICIAL CASE $\lambda \propto E$

By letting $1/\xi \to 1$ in the collision term in Eq. (5) we obtain a differential having a solution in terms of parabolic cylinder functions [6]:

$$F_\sigma = \begin{cases} F_+ = KD_{\alpha-1}(z)\exp(-z^2/4) \\ F_- = AD_{-\alpha}(t)\exp(t^2/4) \end{cases}, \qquad (8)$$

where $z = \gamma^{1/2}\xi + \gamma^{-1/2} - \kappa\gamma^{1/2}$ and $t = \gamma^{1/2}\xi - \gamma^{-1/2} - \kappa\gamma^{1/2}$. For $\gamma << 1$ the exponentially small corrections may be neglected everywhere except in the heat flux giving (i) the constants K and A to be related by $(2\pi)^{1/2}A \approx K\Gamma(\alpha)\exp(-1/\gamma)$ for F_σ to be piecewise continuous at $\xi = 0$, (ii) the normalization from the density to be $NT^\alpha \approx \pi^{1/2}Kv_e\gamma^{1-\alpha}\exp(-1/2\gamma + \kappa)$, and (iii) the condition that particle flux vanish as $\kappa \approx -(\alpha-2) - (\alpha-2)^{1/2}$. Retaining the exponentially small terms in the heat flux where they are $O(1/\gamma)$ larger gives

$$q_\parallel = q_{SH}\left\{1 + \frac{(\cos\pi\alpha)\Gamma(\alpha-2)\exp(-1/2\gamma - \kappa)}{2(2\pi)^{1/2}[1+(\alpha-2)^{1/2}]\gamma^{7/2-\alpha}}\right\}, \qquad (9)$$

where $k_o = 2^{5/2}Z[1+(\alpha-2)^{1/2}]/3\pi\gamma_o$ recovers the Spitzer-Härm heat flux [3] q_{SH} as $\gamma \to 0$ and γ_o is the Z dependent quantity of Braginskii for a single ion species [1].

The heat flux (9) exhibits the non-expandable, exponential modification $\exp(-1/2\gamma)$ which can enhance (e.g. $\alpha \to 2$), limit (e.g. $\alpha = 3$), or not alter (e.g. $\alpha = 5/2$) the heat flux!

V. THE PHYSICAL CASE $\lambda \propto E^2$

In the actual case in which the mean free path is proportional to the energy squared, an exact analytic solution of Eq. (5) is not possible. A WKB solution is adequate for F_+, while a matched asymptotic solution must be constructed for F_- by matching WKB solutions for $0 < \xi < \gamma^{-1/2}$ and $\gamma^{-1/2} < \xi < \infty$ to a parabolic cylinder function solution about $\xi \approx \gamma^{-1/2}$. However, because the matching is asymptotic the heat flux integrals can not be evaluated accurately enough to obtain a general analytic expression for $q_\parallel$. As a result, only incomplete results can be given. In this $\lambda \propto E^2$ case $k_o = 8Z/3\pi\gamma_o$ recovers q_{SH} as $\gamma \to 0$.

As $\alpha \to 2$ no flux limiting occurs because the distribution function develops an extended tail which dominates the non-Spitzer-Härm contribution to the heat flux, giving

$$q_\parallel \xrightarrow[\alpha\to 2]{} q_{SH}\left\{1 + \frac{\exp(-2/3\gamma^{1/2})}{4(2e)^{1/2}\gamma^{5/4}(\alpha-2)}\right\}. \qquad (10)$$

For $\alpha \approx 3$ only an approximate expression for $q_\parallel$ can be discerned which is of the form

$$q_{\|} \approx q_{SH}\left\{1-\frac{\exp(-2/3\gamma^{1/2})}{8\pi^{1/2}\gamma^{5/4}}S(\gamma)\right\}, \tag{11}$$

with $S(\gamma)$ an undetermined function of γ. A choice for S that gives remarkably good agreement with the numerical results of Ref. [7], as shown by the comparison in Table I, is

$$S(\gamma)=\frac{\gamma^{1/16}}{1-\gamma^{1/8}}-\ell n\left(\frac{1+\gamma^{1/16}}{1-\gamma^{1/16}}\right). \tag{12}$$

VI. DISCUSSION

Modifications that depend exponentially on the inverse square root of the thermal mean free path and, therefore, are not possible to retain in short mean free path treatments are found to be responsible for the departure of transport from its Spitzer-Härm value.

ACKNOWLEDGMENTS

Research supported by the United States Department of Energy under grant DE-FG02-91ER-54109 at the Plasma Science and Fusion Center of the Massachusetts Institute of Technology.

TABLE I. Comparison between the numerically obtained parallel electron heat flux mormalized to the free streaming value $q_{fs}= NT(2T/m)^{1/2}$ for self-similar profiles from Ref. [7] and the approximation of Eqs. (11) and (12) with the electric field adjusted to make the particle flux vanish for $\alpha = 3$. In the table $\gamma_{num} = \gamma/k_O$.

$q_{\|}/q_{fs}$	Z=1		Z=3		Z=10	
γ_{num}	numeric	Eq. (11)	numeric	Eq. (11)	numeric	Eq. (11)
0.001	0.0041	0.0042	0.0027	0.0027	0.0012	0.0012
0.01	0.045	0.042	0.029	0.027	0.013	0.012
0.1	0.27	0.27	0.21	0.23	0.12	0.10

REFERENCES

[1] S. I. Braginskii, J. Exptl. Theoret. Phys. **33**, 459 (1957).

[2] S. I. Krasheninnikov, Phys. Fluids B **5**, 74 (1993) and references therein.

[3] L. Spitzer and R. Härm, Phys. Rev. **89**, 977 (1953).

[4] S. I. Krasheninnikov, Sov. Phys. JETP **67**, 2483 (1988).

[5] P. J. Catto, J. R. Myra, and A. J. Wootton, Phys. Plasmas **1**, 684 (1994).

[6] W. Magnus, F. Oberhettinger and R. P. Soni, *Formulas and Theorems for the Special Functions of Mathematical Physics*, 3rd ed. (Springer-Verlag, N. Y., 1966), pp. 323-327.

[7] P. Helander, S. I. Krasheninnikov, N. Kuzmicheva and A. P. Smirnov, to appear in J. Nucl. Mat. (1997).

On Structural Stability of Impurity Radiation Front

S. I. Krasheninnikov, A. A. Batishcheva, and D. J. Sigmar

MIT Plasma Science and Fusion Center, Cambridge, MA 02139, USA

Abstract. The behavior of 2D radiation front in a tokamak divertor can explain following experimental observations: a) a jump of impurity radiation region from the target to the X-point after transition to detached regime, b) easier access to detached divertor regime for vertical target (forcing the formation of V-shaped radiation front) in comparison with horizontal one (C-Mod). In addition it suggests that neutral gas bypassing in the divertor, providing increased energy dissipation in the "wings", can be very beneficial for the formation and control of V-shaped radiation front by enhancing impurity radiation loss in the core of the SOL plasma.

Introduction. Energy loss due to impurity radiation plays an important role in the physics of such interesting phenomena as: regimes with MARFE [1] and radiative and detached divertor regimes [2, 3] in tokamak plasmas. Even though the effects of energy radiation loss on tokamak plasma were investigated theoretically quite intensively, the nonlinear stages were mainly treated analytically in 1D approximation while the application of 2D codes requires a very good spatial resolution which is not always available. Here we consider both analytically and numerically the impact of 2D effects on impurity radiation fronts in a tokamak SOL plasma.

Equations. We analyze a 2D diffusion-reaction equation for a slab model of a tokamak divertor region assuming that heat conduction is the dominant mechanism of energy transport:

$$\partial_x\left(\kappa_\perp \partial_x T\right)+\partial_y\left(\kappa_p \partial_y T\right)=R(T,x), \qquad (1)$$

where T is the plasma temperature; x and y are the "radial" and "poloidal" (along the magnetic flux surface) coordinates; $\kappa_p=(B_p/B)^2\kappa_\parallel(T)$ and $\kappa_\perp(T)$ are the poloidal and radial heat conduction coefficients. The function $R(T,x)$ describes the impurity radiation and models the peaked impurity emissivity at low temperatures by assuming $R(T,x)>0$ in a small interval δT_R around the temperature T_R so that R behaves somewhat like a delta function. In Eq. (1) we neglect the influence of perpendicular heat conduction on poloidal heat flux assuming that $\kappa(T)\equiv\kappa_p(T)/\kappa_\perp(T)\gg 1$ in the temperature range of interest. However, we will see that high $\kappa_p(T)$ results in a strong poloidal extension of the front and in a sharp radial variation of the temperature within the front which can lead to a strong impact of radial transport on the radiation loss in spite of the inequality $\kappa(T)\gg 1$. We will find that the role of radial transport is sensitive to the temperature dependence of the function $\kappa(T)$.

Qualitative estimates. To begin, we make a qualitative estimate of the impact of radial and poloidal heat conduction on the radiation loss without taking into account any specific geometrical factors. Assume that the radiation function does not depend on x, and the V-shaped radiation front (defined by $T(x,y)\approx T_R$) has a poloidal length length L and a radial extent w. Assuming that the radial broadening of the SOL mainly occurs in the hot upstream region, the relation between L and w, found from Eq. (1), is $(L/w)^2\sim\kappa(T_{up})\gg 1$, where $T_{up}\gg T_R$ is the plasma temperature in that upstream hot region. The radiation loss from the front, W_R, can be written as $W_R\approx L_{tor}R(T_R)\int\Delta(\xi)d\xi$ where Δ and L_{tor} are the width and toroidal length of

the radiation front ($\Delta << w,\ L$), and we introduce the ξ coordinate to integrate along the projection of the front in the (x, y) plane. We estimate Δ and W_R for the cases when either poloidal or radial heat transport is dominant within the front and the radiation of the heat flux entering the front is nearly complete. From Eq. (1) we find the front width in the poloidal direction, $\delta_p \approx \left(\delta T_R \kappa_p(T_R)/R(T_R)\right)^{1/2}$, when $\kappa_p(T)$ is dominant; and the front width in the radial direction, $\delta_\perp \approx \left(\delta T_R \kappa_\perp(T_R)/R(T_R)\right)^{1/2}$, when $\kappa_\perp(T)$ dominates. Recall that the front is very extended along the poloidal coordinate ($L >> w$) so that it makes (on average) a small angle ~ w/L to poloidal direction and is approximately perpendicular to radial direction. Thus, we find $\Delta \to \Delta_p \sim (w/L)\delta_p$ for the case when poloidal transport is dominant within the front, and $\Delta \to \Delta_\perp \approx \delta_\perp$ for the radial case, and, finally, $W_R^{(\perp)}/W_R^{(p)} \sim \Delta_\perp/\Delta_p \sim \sqrt{\kappa(T_{up})/\kappa(T_R)}$, where $W_R^{(p)}$ ($W_R^{(\perp)}$) is the radiation loss for the case when poloidal (radial) transport is dominant within the front. Since the actual front width and radiation loss are determined by both poloidal and radial transport we can estimate $W_R \sim W_R^{(p)} + W_R^{(\perp)}$ and $\Delta \sim \Delta_p + \Delta_\perp$. Then one finds that the impact of $\kappa_p(T)$ and $\kappa_\perp(T)$ on the radiation loss and front width is determined by the function $\kappa(T) \equiv \kappa_p(T)/\kappa_\perp(T)$. When $\kappa(T)$ increases (decreases) with increasing T then both W_R and Δ are determined by radial (poloidal) heat transport. As a result of the radial conduction induced widening of the front the radiation loss is much higher [5] than the estimate from Ref. [4] where only $\kappa_p(T)$ was taken into account in the radiation front. $\kappa_p(T) \propto T^{5/2}$ and $\kappa_\perp(T) \propto T^{-1}$ ($\kappa_\perp = n\chi_\perp$, $\chi_\perp$=const. and $n \propto 1/T$) result in $\kappa(T) \propto T^{7/2}$. Then from Eq. (3) we find that for $T_{up} \sim 100$ eV and $T_R \sim 6$ eV the effect of $\kappa_\perp(T)$ on the radiation front width results in a more than 100 fold increase in the radiation loss.

2D fronts. To obtain quantitative solutions of Eq. (1) in the divertor region in a slab approximation (see Fig. 1) we use as boundary conditions fixed temperature T_t at the target (y=0), and a prescribed radial profile of the poloidal component of the heat flux, $q_y(x,y) = -\kappa_p \partial_y T$, at the upstream boundary: $q_y(x, y = L_d) = -q_L(x) \le 0$, where L_d is the poloidal extent of the divertor region. We will assume that $T_t << T_R << q_L(x) L_d/\kappa_p(T_R)$, so that the radiation region is always located within the slab $0 < y < L_d$. We analyze the case when $q_L(x)$ and $R(T,x)$ vary slowly in the radial direction, which is relevant to a divertor region, and any re-distribution of the poloidal heat flux profile due to radial heat conduction between upstream and the radiation front is weak, $q_y(x,y) \approx -q_L(x)$ which results in inequality $w/\ell_q(x) \gtrsim \left(\kappa(T_L(x))\right)^{-1/2}$, where w is the radial scale length of $q_L(x)$ and $R(T,x)$, and $\ell_q(x)$ is the distance from the front to upstream boundary.

Consider the situation when the radiation of the heat flux $q_L(x)$ is practically complete ($q_t << q_L$). Then assuming a weak radial variation of $q_L(x)$ and $R(T,x)$ we can treat the radiation front $y_R(x)$ (corresponding to the solution $T(x, y_R) = T_R$) in a local approximation as a straight line making an angle ψ to y direction as shown in Fig. 1. Notice that radial heat conduction affects re-distribution of the heat flux only at the radiation front where the radial gradients are strong. Taking into account the effects of both poloidal and radial heat conduction

and integrating Eq. (1) normal to the radiation front we find that complete radiation occurs when

$$\left(\frac{dy_R}{dx}\right)^2 = \left\{(q_L(x))^2 - (Q_p(x))^2\right\} \Big/ (Q_\perp(x))^2, \qquad (2)$$

$$(Q_p(x))^2 = 2\int_0^\infty \kappa_p(T)R(T,x)dT,\ (Q_\perp(x))^2 = 2\int_0^\infty \kappa_\perp(T)R(T,x)dT, \text{ and } \tan\psi = (dy_R/dx)^{-1}.$$

Interestingly, Eq. (2) allows a sign switch in dy_R/dx which may occur at either a maximum or minimum of $y_R(x)$. In practice such a sign switch in dy_R/dx is only possible at a minimum of $y_R(x)$. The maximum of the radiation front can only be located near the target or at the upstream boundary and corresponds to $q_L(x) \approx Q_p(x)$. The transition of Max($y_R(x)$) between these two locations occurs either as a real bifurcation (caused by radial re-distribution of the poloidal heat flux) and results in a jump of Max($y_R(x)$), or as a fast shift of Max($y_R(x)$). Below we do not distinguish between these two cases and refer to them as to a bifurcation.

We can find a constraint on the existence of the radiation front with complete radiation of the heat flux $q_L(x) > Q_p(x)$ which is imposed by the poloidal length of the divertor and because of the finite value of $(dy_R/dx)^2$:

$$\int_{x_1}^{x_2} \left\{\left[(q_L(x))^2 - (Q_p(x))^2\right] \Big/ (Q_\perp(x))^2\right\}^{1/2} dx \le 2L_d, \qquad (3)$$

where $q_L > Q_p$ for $x_1 < x < x_2$. When Eq. (3) is satisfied a V-shaped, radial heat conduction widened (even though $\kappa_\perp << \kappa_p$) front can be formed resulting in complete radiation of even high heat flux $q_L(x) >> Q_p(x)$. Notice, that in 1D case it is only possible to radiate $q_L \le Q_p$.

Front evolution. We consider the evolution of the radiation front when the magnitude, $R(T) \propto R_0$, of the radiation function increases for a smooth, periodic (in the radial direction) profile of heat flux $q_L(x)$ as shown in Fig. 2 ($q_{min} \le q_L(x) \le q_{max}$, and $q_{min} << q_{max}$). At low R_0, radiation of the heat flux is incomplete even for $q_L(x) \approx q_{min}$ and the radiation front stays very close to the target (curve a). When R_0 reaches the level where $q_{max} >> Q_p \tilde{>} q_{min}$, bifurcation of the front in the regions with $q_L(x) \approx q_{min}$ occurs and two scenarios of the subsequent front evolution are possible. The first scenario ("jump") corresponds to the case when inequality (3), written as an integral over the period of $q_L(x)$, is satisfied. Then, bifurcation in the regions with $q_L(x) \approx q_{min}$ (see Fig. 3 were the bifurcation of Max($y_R(x)$) found from numerical solution of Eq. (1) for $q_L(x)$ shown in Fig. 2.) triggers formation of a strongly shaped, radial conduction widened radiation front leading to complete radiation of the heat flux $q_L(x) \approx q_{max} >> Q_p$. As a result, the entire radiation front jumps to the upstream region (curve b). The second scenario ("gradual") corresponds to the case when inequality (3) is not satisfied. Then bifurcation of the radiation front occurs only in regions with $q_{max} >> q_L(x) \sim q_{min}$. Outside these regions the radiation is weak and $q_t \approx q_L(x)$. With a further increase of R_0 the regions with incompletely radiation shrink and gradually disappear resulting in the formation of a V shape front which radiates the heat flux $q_L(x) \approx q_{max} >> Q_p$ (curve c).

Interpretation of tokamak experiments. The experiments show that during the transition

from a radiative to a detached divertor regime the impurity radiation region shifts abruptly away from the target to the X-point [2]. Recall that near the separatrix (x=0) both $q_L(x)$ and $R_0(x)$ reach their maximum values and decrease as one moves away from the separatrix to the "wings" of the profiles, $x \sim x_w$. For typical experimental conditions the heat flux is very high near the separatrix where most of the heat flux streams to the target, $F(0)>>1$, where $F(x) \equiv q_L(x)/Q_p(R_0(x))$. This high heat flux can only be radiated by forming a V shaped radiation front with radial heat conduction setting the front width. Then, as in the preceding example, two scenarios of the front evolution can be envisioned as R_0 increases. A "jump" scenario, similar to experimental observations, occurs when inequality (3) is satisfied first and then $F(x_w) \to 1$, corresponding to relatively high heat flux at the "wings", $F(x_w)/F(0) > \left(w\sqrt{\kappa(T_R)}\right)/L_d$. Another way to assist formation of a V shaped front having strong radiation loss is to use geometrical effects due to the sidewalls and the target. The target may be turned in a such a way that it will make a grazing angle with separatrix magnetic flux surface (SMS), a so-called "vertical" target [3]. For a "vertical" target radial heat conduction enhancement of radiation loss is automatically switched on due to the grazing angle between the SMS and the target. It results in radiation loss increase and may explain the easier access to detached divertor regimes for a "vertical" target configuration as compared to a "horizontal" one as observed in experiments [3].

Acknowledgments. The authors thanks P. J. Catto for many helpful discussions and useful comments. Work is performed under the USA DOE grant DE-FG02-92ER-54109 at MIT.

References

[1] B. Lipschultz, J. Nucl. Mater. **145&147**, 15 (1987).
[2] G. D. Porter et al., Phys. Plasmas **3**, 1967 (1996).
[3] B. Lipschultz et al., 16th IAEA, Montreal, Canada, 7-11 Oct. 1996, F1-CN-64/A4-5.
[4] D. E. Post, J. Nucl. Mater. **220&222**, 143 (1995).
[5] S. I. Krasheninnikov and D. A. Knoll, Contrib. Plasma Physics **36**, 266 (1996).

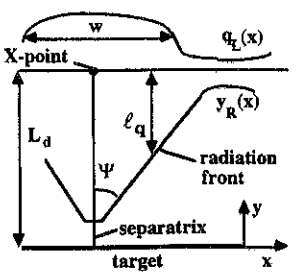

Fig. 1. *Radiation front* $y_R(x)$ *in a divertor.*

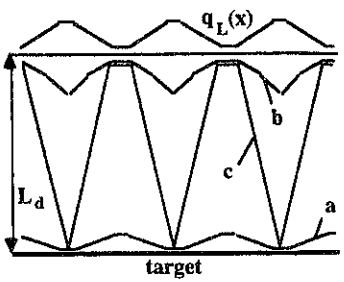

Fig. 2. *The evolution of* $y_R(x)$ *with increasing* R_0.

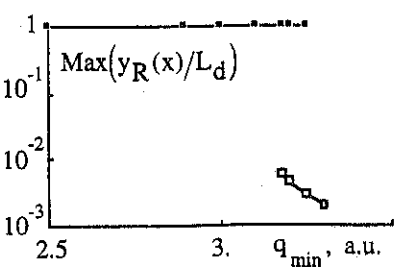

Fig. 3. *Bifurcation of* $y_R(x)$.

Studies on Plasma-Gas Interactions in Powerful High Heat Flux Plasma Device NAGDIS-II

N. Ezumi [a], N. Ohno [a], Y. Uesugi [b], J. Park [c], S. Watanabe [a], S.A. Cohen [c], S.I. Krasheninnikov [d], A.Yu. Pigarov [d], M. Takagi [a], S. Takamura [a]

[a] *Department of Energy Engineering and Science, Graduate School of Engineering,*

[b] *Center for Integrated Research in Science and Engineering,*

Nagoya University, Nagoya 464-01, Japan

[c] *Plasma Physics Laboratory, Princeton University, Princeton NJ 08543, USA*

[d] *MIT Plasma Fusion Center, Cambridge, MA, USA*

Abstract

We have constructed a new powerful high heat flux plasma device, NAGDIS-II (NAGoya university DIvertor plasma Simulator -II), to investigate edge plasma physics in fusion devices. High density plasmas generated by the powerful dc discharge with a sophisticated hot cathode assembly are heated by slow ion cyclotron wave resonance using four phased-array loop antennas coupled to the plasma column. Such a high heat flux plasma generator and strong differential pumping system make it possible to do a comprehensive investigation on plasma - gas interactions in a steady state.

1. Introduction

It is planned to employ detached plasma concept for engineering design activity (EDA) of International Thermonuclear Experimental Reactor (ITER) to reduce a peak heat load onto the divertor plate. The linear divertor simulators have been used for investigation on the fundamental physics of interactions between high heat flux plasmas and neutral gases, but their plasma parameters are not relevant to those expected in the next generation fusion devices. In order to do a comprehensive study on plasma detachment in the high heat flux plasmas, we have constructed a new linear divertor simulator, the NAGDIS-II.

Table I Plasma parameter in NAGDIS-II

Discharge Gas	Hydrogen, Helium, Argon
Plasma Length	2.8m
Plasma Radius	0.01 ~ 0.03m
Magnetic Field Strength	~ 0.25T
Plasma Density	$\lesssim 6 \times 10^{19} m^{-3}$
Ion Temperature	~ 50eV (expected)
Electron Temperature	~ 10eV
Heat Flux onto Target	~ 10MW/m^2 (expected)

Table II Specification of RF power source

Power Source	SIT Inverter
Frequency	0.5 ~ 1.5MHz
Output Power	56kW in CW
(Sum of 4 Power Supplies)	80kW in 1s Pulse
Phase Control	0 ~ 2π
Output Impedance	< 0.1Ω

Table III Diagnositc system

Scanning probes (3 sets)
Flush-mouted Langmuir probe array
Optical multichannal analyzer (OMA) Spectrometer (750mm)
Fabry-Perot interferometer
Quadruple mass analyzer with Energy analyzer

2. Divertor Plasma Simulator, NAGDIS-II

Schematic diagram of the NAGDIS-II, is shown in Fig. 1. This device consists of a DC plasma source, a RF heating assembly, a

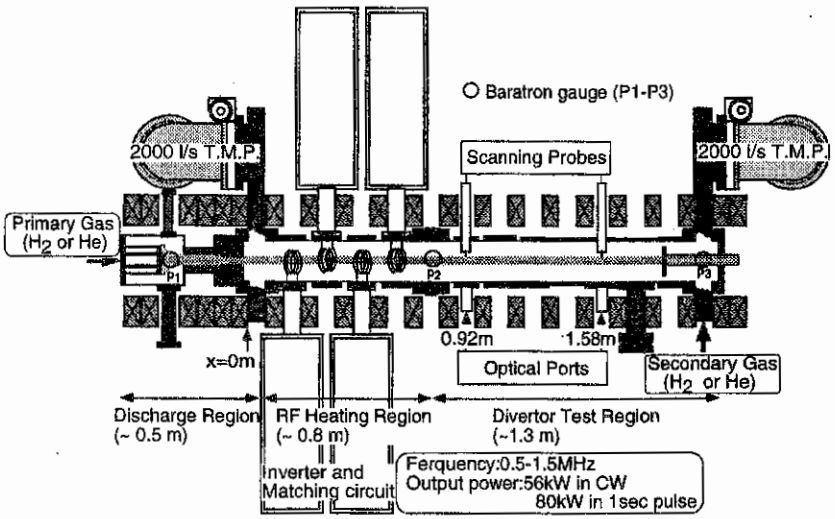

Fig. 1 Schematic of Divertor Plasma Simulator, the NAGDIS-II

differential pumping system and powerful diagnostic systems.

a) DC plasma source

Plasmas are produced in a steady state by the sophisticated dc plasma source as shown in Fig. 2, which is designed to improve the ionization efficiency using a cusp magnetic configuration and a heated LaB_6 disk cathode [1]. A generated high density plasma ($\leqq 6 \times 10^{19} m^{-3}$) is introduced into the rf heating region in the steady state magnetic field up to 0.25T. The major plasma parameters are shown in Table I.

b) RF heating system

Four phased-array loop antennas set in the rf heating regions are excited by Static Induction Transistor (SIT) inverter RF sources, providing 4x14kW in CW and 4x20kW in 1sec pulse at a frequency range from 0.5 through 1.5MHz. Slow ion cyclotron waves in the magnetic beach configuration can produce a perpendicular ion heating as

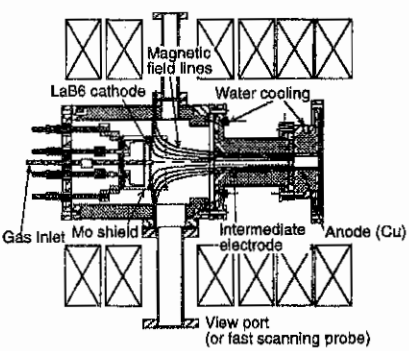

Fig. 2 Schematic diagram of plasma source region

well as a longitudinal electron heating using two power supplies for magnetic coils [2]. Specification of RF power sources is summarized in Table II.

c) Pumping system

Neutral pressure (P_n) in the divertor test region can be changed from 1mTorr to 20mTorr by controlling a pumping speed and puffing a neutral gas from the end of the chamber

independently of the pressure (~ 1Torr) in the plasma source region by the powerful differential pumping system, consisting of the orifice which divides the source and the divertor test regions, and the two turbo molecular pumps (2000 liters/sec). These pumping and fuelling systems make the stable plasma-gas interaction experiments possible.

d) Diagnostic system

Satisfactory diagnostic systems are employed in NAGDIS-II as shown in Table III. The experimental data is accumulated by CAMAC system.

3. Experimental Results of Plasma-Gas Interactions

Some interesting results obtained in detached plasma experiments have been performed by measuring the ion flux and visible light emission at two positions (upstream and downstream) along the magnetic field (See Fig. 1).

3-1 Helium plasmas with helium neutral gas puffing

Figure 3 shows a spectrum of the visible light emissions from detached plasmas in the downstream at a helium gas pressure P_n ~ 5.4mTorr by feeding helium neutral gas in the test region. Line emission from highly excited levels of helium atoms up to n=21 and continuum spectrum were clearly observed [3]. This result indicates three-body and radiative recombinations near the target with puffing helium neutral gas. The detailed analysis of the spectrum gives very low electron temperature less than 0.5eV. The electron energy loss is caused by energy transfer to the neutral through the electron-ion energy relaxation and charge exchange [4].

3-2 Helium plasmas with hydrogen molecular puffing

Importance of the molecular activated recombination (MAR) processes for plasma detachment have been pointed out by Krasheninnikov *et. al.*[5, 6]. To demonstrate the MAR effects on plasma detachment, the helium plasma in almost the same conditions as previous experiment without secondary gas puffing, but the initial helium pressure P_n is kept to be 5mTorr by adjusting the pumping speed of turbo molecular pumps. Then, the helium or hydrogen gases are puffed additionally. Figure 4 shows the spectra of visible light emissions from 310 to 370nm in wavelength observed in the downstream region with hydrogen (solid line) or helium (dashed line) gas puffing at a total pressure P_n ~ 6.5mT. For pure helium plasma, continuum and a series of visible line emission from highly excited helium neutrals due to the conventional radiative and three-body recombinations were observed as shown by the dashed line in Fig. 4. On the other hand, when hydrogen gases were introduced into the

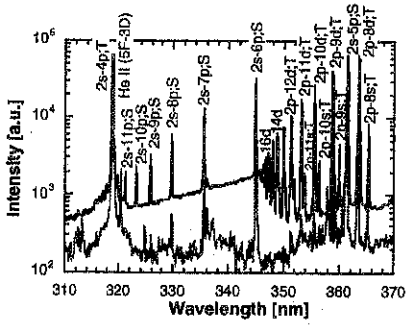

Fig. 3 Emission spectra from downstream location at 5.4mT in neutral pressure (solid line) and at 1.0mT (dashed line) on 5sec in exposure time. The downstream location lies well into the detached region at 5.4mT.

helium plasma, the spectrum is changed dramatically as shown by the solid line in Fig. 4. There are neither clear continuum nor a series of visible line emissions from highly excited levels, so that the radiative and three-body recombination processes are not dominant in this plasma condition. However, we have observed a strong reduction of the ion flux along the magnetic field line as shown in Fig. 5. Careful comparison of the observed helium Balmer spectra from the detached recombining helium and hydrogen mixture plasmas with the generalized Collisional Radiative Atomic Molecular Data (CRAMD code) [6] indicates that the population of the atomic levels with relatively low principal quantum numbers can be well explained by taking the MAR effects into account. From these results, we can conclude that the plasma volumetric recombination coming from the effective hydrogen MAR is a dominant process for the reduction of ion flux and plasma detachment in our helium and hydrogen mixture plasmas.

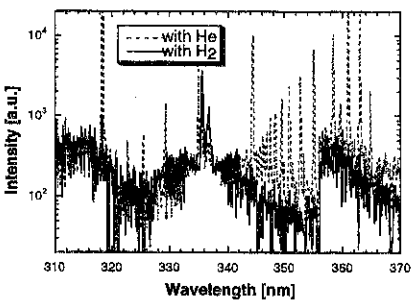

Fig. 4 Spectrum from detached helium plasma with hydrogen (solid line) and helium (dashed line) puffing at Pn ~ 6.5mT on 5sec in exposure time.

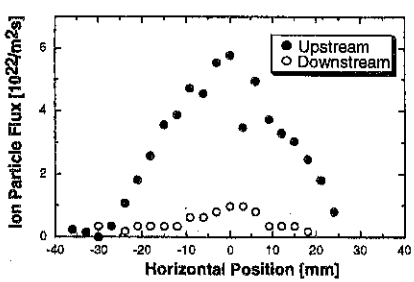

Fig. 5 Ion particle flux in detached helium plasma at Pn ~ 6.5mT in hydrogen puffing. Closed and open circles indicate upstream and downstream data, respectively.

4. Conclusion

For studies on plasma-gas interactions, a new high heat flux liner divertor plasma simulator, the NAGDIS-II, was constructed. Helium and hydrogen plasmas were generated with the sophisticated DC discharge source in steady state. In high density helium plasmas with helium gas puffing, the evidence of three-body recombination was obtained clearly in detached plasmas. Using hydrogen molecules as a target gas, the molecular activated recombination process is identified to be dominant process. In future, extensive studies on plasma-gas interactions would be expected under very high heat flux conditions in the NAGDIS-II.

References

[1] S. Narita *et. al.*, Proc. of the Int. Conf. on Plasma Physics,Nagoya,**Vol.2**,1362(1996).

[2] S. Watanabe *et. al.*, Proc. of the 12th Topical Conf. on Radio Frequency Power in Plasmas, Savannah, Georgia (1997).

[3] J. Park *et al.*, Phys. Rev. Lett. *submitted*

[4] N. Ezumi *et al.*, J. Nucl. Mater. *to be published.*

[5] S.I. Krasheninnikov *et al.* Phy. Plasmas 4 (5) (1997) 1638.

[6] A.Yu. Pigarov *et al.*, Phys. Lett. A **222** (1996) 251.

Interaction of a plasma beam with neutral hydrogen in the UMIST linear system

A. Randewich, P. K. Browning, D. A. Forder, K. Gibson, J. Hugill, M. Kay,
H. Qaosim, M. G. Rusbridge and G. Sewell.
Dept. of Physics, UMIST, PO Box 88, Manchester, U.K.

1 Introduction

The UMIST Linear System or ULS (figure 1) is a steady state linear plasma device. A Demirkhanov source injects plasma at a density of $2 \times 10^{18}\,\mathrm{m}^{-3}$ into a 0.1 Tesla axial magnetic field, which confines the discharge to a 1 cm diameter beam, consisting of a hot core of electrons at a temperature of 12 eV, and a directed beam of supersonic ions at an energy of about 70 eV. The pressure is maintained at 5×10^{-6} Torr by diffusion pumps. The physics of the gas target divertor is investigated by inserting a plate containing an aperture half way along the 1.5 m vacuum chamber, dividing it into two parts. The interaction of the plasma stream with neutral gas at variable pressure up to 8 mTorr in this "gas target" chamber has been explored.

2 Particle trajectories and throughput

The electron core of the beam has a radius of about 3 mm, and occupies a potential well about 10 V deep, originally interpreted as that required for the electrostatic confinement of ions whose Larmor radius exceeds that of the electrons. Such a beam, however, is severely attenuated by passing through a straight walled orifice (leading to the gas target chamber) of diameter 8 mm, with a maximum transmission of 34%, which increases only slowly with orifice size to reach 90% for a tapered orifice of diameter 40 mm. This effect arises because the ion trajectories extend much further from the core than expected: the transverse ion energy is large, and exceeds the height of the potential barrier so that most of the ions are confined magnetically. This explanation is supported by simulations of the ion trajectories in the observed magnetic and electric fields. Numerical integration of multiple ion paths shows that for ion energies of about 50 eV, the predicted variation of transmission with orifice radius matches the observations well, reproducing the observed difference between cylindrical and tapered apertures, see figure 2.

3 Gas Target experiment

The downstream chamber is flooded with hydrogen to a pressure of up to 8×10^{-3} Torr. Ions enter this chamber through a 14 mm diameter tapered orifice, with energies parallel to the magnetic field of approximately 70 eV. The beam is observed to be attenuated (figure 3) with a scale length inversely proportional to the gas pressure, yet no broadening of the beam can be detected (figure 4). The process is effective down to pressures of 1 mTorr, and results using argon as the target gas were similar.

Considerable difficulty has been found in interpretation of the ion saturation current to a Langmuir probe, since the ions in the gas target chamber have a two component velocity distribution due to charge exchange. A technique based on the electron equation of motion has been used to calculate that the density peaks at around $10^{19}\,\mathrm{m}^{-3}$.

Degradation of the ion beam, whether by elastic collisions or by charge exchange, is predicted to lead to a build up of ions at the neutral gas temperature. In the absence of recombination the slow ion density is governed by a balance equation of the general form:

$$n_b v_b A_b = \frac{n_s V_s}{\tau_s} = n_s v_s A_s \qquad (1)$$

where suffixes b and s refer to beam and slow ions respectively, V_s is the volume occupied by the slow ions with lifetime τ_s, and v_s is a characteristic velocity with which slow ions escape from the system through an effective area A_s. Since the slow ion mean free path is of the order of 1 cm, the slow ion loss is diffusive, and v_s is the "diffusion speed". The absence of broadening suggests that the slow ions are well confined within the beam. In this case, A_s is at most $2A_b$ as slow ions may be lost to both orifice and end plate, and it can be shown that the slow ion density should rise to a value near $10^{21}\,\mathrm{m}^{-3}$, two orders of magnitude greater than our observations, (a high slow ion density would totally outweigh the fast ion contribution, and there would be no significant ambiguity in the interpretation of the ion saturation current). Actually, three body recombination would then limit the density to around $10^{20}\,\mathrm{m}^{-3}$, but this is still too large. It can be shown that the effect of the axial electric field, which is in the sense to enhance the loss rate, would also only reduce the predicted density to about $10^{20}\,\mathrm{m}^{-3}$, and that even consideration of transverse diffusion (ignoring the lack of broadening) cannot account for the very low ion density suggested by our results. On this basis it is believed that some anomalously fast recombination process is operating.

4 Numerical model

A numerical model aimed at improving understanding of the slowing down rate of ions in the ULS gas target chamber is being developed. Radial variations of the plasma parameters are neglected leaving a one dimensional problem, although the requirement that non–Maxwellian ion velocity distributions may be considered suggests an algorithm solving a two dimensional phase space. A kinetic approach is justified since the ion–ion mean free path, $\lambda_i = v_\parallel \tau_i \sim 50\,\mathrm{m}$ is much larger than the 50 cm gas target chamber. The model assumes a sea of background neutrals unaffected by neutral–ion interactions, consistent with the large neutral density in the ULS.

A particle–in–cell (PIC) code is used, the axial length of the chamber being divided into finite spatial cells of fixed size. The range of ion velocities to be considered is similarly discretised. Short time periods, are considered during which ion populations in these phase space cells are redistributed, according to their velocities and collisional processes. This procedure is iterated over multiple time periods, until a steady state axial density distribution is reached. Collisions are implemented Monte–Carlo style, and include elastic scattering[1] and resonant and nonresonant charge exchange[2]. Greenland[3] points out that the latter process is accelerated if a significant population of vibrationally excited states, particularly $\nu = 4$ exist in the gas, and this is important since dissociative recombination $H_2^+ + e \rightarrow 2H$ is very rapid. Unfortunately, numerical results suggest a high slow ion density at equilibrium, as shown in figure 5.

5 Conclusions

Experiments in which a supersonic plasma beam in a uniform magnetic field is passed through an orifice into a target chamber where the gas pressure can be raised have been described. Characterisation of the electron and ion distributions has been achieved, leading to understanding of the flow rate through an orifice placed in the path of the plasma stream. Attenuation of the ion saturation current in the gas target chamber cannot be explained by cross field diffusion or recombination, and the size of the observed density peak can not be reconciled with analytic or numerical predictions, even taking account of nonresonant charge exchange scaling: an anomalously fast recombination process is in effect. Two stage processes e.g. involving negative ions[4] lead to a nonlinear dependence on the beam density, unless one of the steps is so rapid as to be effectively saturated.

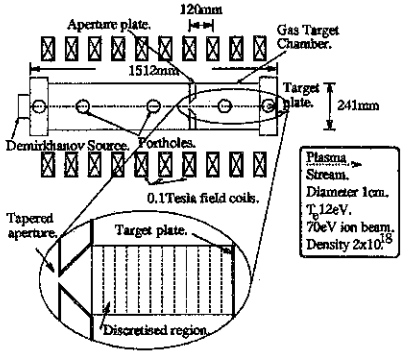

Figure 1: The ULS.

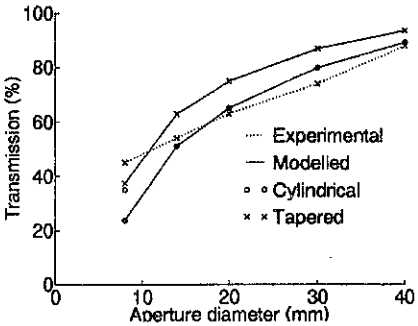

Figure 2: Experimental and modelled aperture transmissions.

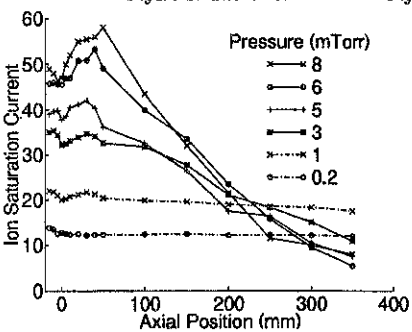

Figure 3: Axial ion saturation current at various pressures.

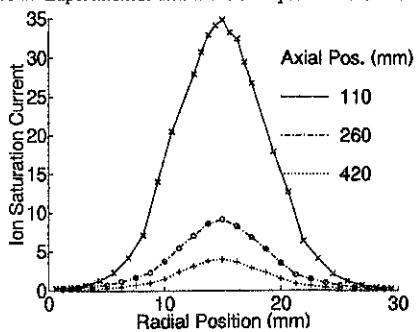

Figure 4: Radial ion saturation current profiles at 3 axial positions attenuate but do not broaden.

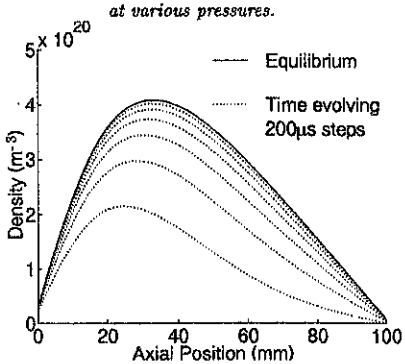

Figure 5: Axial density distribution predicted by the numerical model.

Bibliography

[1] J. H. Simons *et al.* Journal of Chemical Physics **11** pp 307–312 (1943)

[2] R. K. Janev *et al.* Elementary Processes in Hydrogen–Helium Plasmas (1987)

[3] P. T. Greenland *et al.* (ICL) unpublished (1997)

[4] Krasheninnikov *et al.* Contributions to Plasma Physics **36** pp 293–307 (1996)

AR would like to acknowledge the EPSRC for funding.

A model of hydrogen recycling and glow discharge conditioning with graphite wall.

D. Larsson, H. Bergsåker

Royal Institute of Technology, S-100 44 STOCKHOLM, Sweden
Association EURATOM/NFR

1 Introduction

The response of carbon surfaces to a transient hydrogen flux, and methods of removing hydrogen from the surfaces are decisive for the density control in plasma devices with graphite walls. One-dimensional models including trapping, detrapping, recombination and molecular reemission have been successful in describing ion beam implantation experiments [1, 2]. Zero dimensional models [2, 3] with one or more wall reservoirs exchanging particles with the plasma are more convenient for modelling the hydrogen recycling in plasma experiments. It is desirable if the zero-dimensional models can be made consistent with the more detailed knowledge acquired from well controlled beam experiments. However, it is necessary to bear in mind that the flux densities in plasma experiments are typically many orders of magnitude higher than in beam experiments. We present a zero-dimensional model designed to predict the density evolution in RFP plasma discharges, the build-up of a trapped reservoir in the wall and hydrogen removal by He glow discharge conditioning.

2 The Model

The model consists of five different reservoirs: trapped atoms N_t, mobile atoms in the wall N_a, molecules in the wall N_m, neutral molecules in the plasma N_n and plasma ions N_p. The particle exchange between the reservoirs is described by the set of equations:

$$\frac{dN_p}{dt} = -\frac{N_p}{\tau_p} + 2 \cdot \frac{N_n}{\tau_i}$$

$$\frac{dN_n}{dt} = -\frac{N_n}{\tau_i} + \frac{1-\gamma}{2}\frac{N_p}{\tau_p} + \frac{N_m}{\tau_m} - \frac{N_n}{\tau_{pump}}$$

$$\frac{dN_a}{dt} = \gamma\frac{N_p}{\tau_p} - K_t N_a(N_0 - N_t) - 2K_{r1}N_a^2 - K_{r2}N_aN_t + K_d N_t \gamma\frac{N_p}{\tau_p} + K_{He}\Phi_{He}N_t$$

$$\frac{dN_m}{dt} = K_{r1}N_a^2 + K_{r2}N_aN_t - \frac{N_m}{\tau_m}$$

$$\frac{dN_t}{dt} = K_t N_a(N_0 - N_t) - K_d N_t \gamma\frac{N_p}{\tau_p} - K_{r2}N_aN_t - K_{He}\Phi_{He}N_t$$

The particle confinement time τ_p is estimated from τ_E and probe measurements and calculated with the empirical formula $\tau_p = 20 + 100\frac{I_p}{I_0}\mu s$ where I_0 is 150 kA, the ionisation speed τ_i is

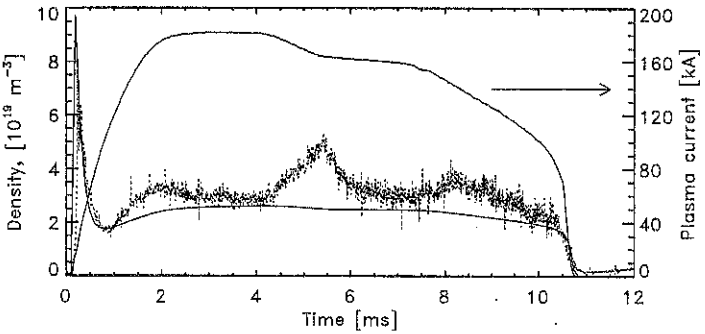

Figure 1 Density in shot nr.5155. The solid line is the simulated density and the dotted line is measured by interferometry. The plasma parameter going into the simulation, I_p, is plotted against the right axis.

estimated to $20\mu s$ from atomic data. The molecule diffusion time τ_m is set to $10\mu s$ and the pumping speed τ_{pump} is measured to 8s at $p = 1Pa$. Trapping frequency K_t, recombination frequency between mobile atoms K_{r1}, recombination between mobile and trapped atoms K_{r2}, hydrogen detrapping K_d and helium detrapping K_{He} are used as fitting parameters and are compared with constants in the literature.

For the thickness of the accessible surface layer we consider an implantation range of ~ 40Å corresponding to 60 eV implantation energy consistent with $k_B T_e(a) = 12eV$, a typical result from Langmuir probe measurements.

3 Results

The experiments have been carried out at the Extrap T2 reversed field pinch, a device with dimensions a/R=0.18 m/1.24 m. The inner wall of Extrap T2 is completely covered with tiles of high density graphite. The partial pressures are measured with two mass spectrometers, one at the main vessel and one differentially pumped for high pressure operation. The line average densities are measured by interferometry.

Figures 1-4 show simulations with choice of parameters: $K_t = 2 \cdot 10^{-19} s^{-1}$ ($2.8 \cdot 10^{-18}$[1]), $K_{r1} = 1.5 \cdot 10^{-19} s^{-1}$ ($7.5 \cdot 10^{-21}$[1]), $K_{r2} = 7 \cdot 10^{-22} s^{-1}$ ($3.9 \cdot 10^{-23}$[2]), $K_d = 3 \cdot 10^{-21}$ ($4 \cdot 10^{-22}$[4]) and $K_{He} = 4 \cdot 10^{-21}$ ($5 \cdot 10^{-22}$[4]). The difference between the fitting parameters used and those referred to can be up to a factor 20. This difference is not understood.

The discrepancy between the simulated and observed densities in figure 1 around 5 ms is due to local thermal effects. The build-up of trapped hydrogen in the wall, as can be seen in figure 2

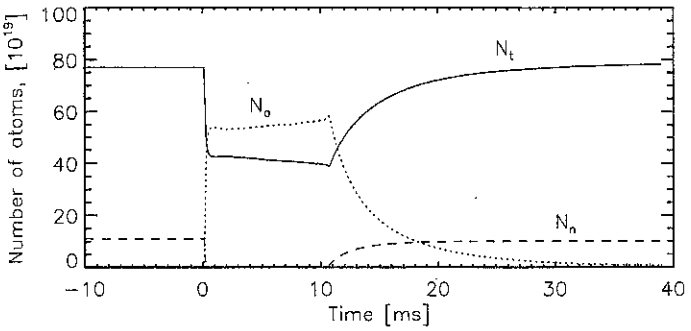

Figure 2 Simulated wall inventory around shot nr.5155 (same as in figure 1), the solid line is N_t and the dotted N_a. The dashed line shows N_n.

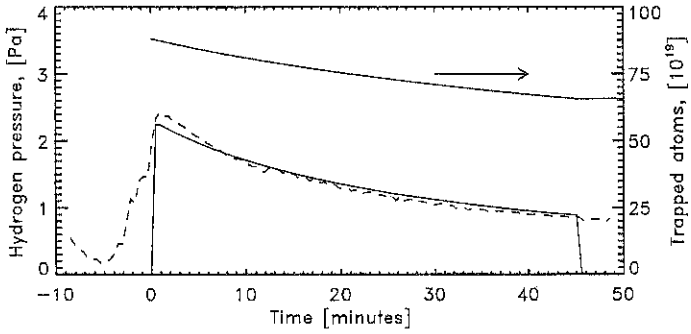

Figure 3 Partial pressure of hydrogen during He glow discharge. The solid line is the simulated pressure and the dashed line the measured. The removal of trapped hydrogen can also be seen.

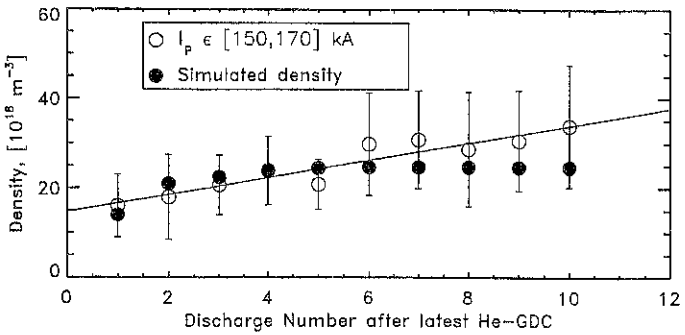

Figure 4 The loading of trapped hydrogen results in an increase of density in a series of RFP-discharges following a He GDC. The empty circles originate from experiments.

results in increased plasma density during a series of RFP-discharges. Figure 4 shows that this increase initially agrees with the increase observed. The model fails however in explaining densities above $2.5 \cdot 10^{19} m^{-3}$. The number of removed trapped hydrogen atoms during 45 minutes of helium GDC, as can be seen in figure 3, corresponds with the number of atoms implanted in a series of 10 RFP-discharges.

At the higher fluxes during RFP-discharges mobile-mobile recombination dominates whereas mobile-trapped recombination dominates at lower fluxes (GDC). This effect enables us to fix the recombination frequencies with a higher accuracy.

4 Future Plans

To further understand the thermal effects the model will be improved to deal with locally increased thermal and particle flux due to modes locking to the wall. The existence of other sets of parameters also resulting in good agreement with experimental data can not be excluded. Further investigations of the parameter space will be performed.

References

[1] W. Möller and B.M.U. Scherzer. *J. Appl. Phys*, 64(18):4860–4866, 1988.

[2] K. Morita and Y. Hasabe. *Memoirs of the school of Engeneering, Nagoya University*, 45, 1993.

[3] J. Ehrenberg, P. Andrew, and L. Horton et.al. *J. Appl. Phys*, (196-198):992–996, 1992.

[4] H. Bergsåker, S. Nagata, M. Rubel, and B. Emmoth. *E-MRS conferance proceedings, Strasbourg*, 1987.

AN EFFICIENT GAUSSIAN-BEAM POWERED QUASI-OPTICAL GRILL FOR LOWER HYBRID WAVES

V. A. Avantaggiati*, R. Borghi○, F. Frezza*, G. Gerosa*, M. Santarsiero○, and **G. Schettini***
*Dipartimento di Ingegneria Elettronica, Università "La Sapienza", Roma, Italy
○Dipartimento di Fisica, Università"Roma Tre", Roma, Italy

Abstract

The numerical analysis of a quasi-optical launcher of lower hybrid plasma waves powered by an incident Gaussian beam is presented. An experimental configuration which gives high values of the coupled power is proposed.

1. Introduction

Quasi-Optical Grills (QOG) have been introduced some years ago as a new structure for launching of LH waves in tokamaks [1]. The quite simple excitation of the structure, the enhancement of its robustness, the ability of cooling the front face of Lower Hybrid Wave couplers to withstand reactor first wall conditions are some of these attractive characteristics. The essential difficulty of these launchers is the relatively low power coupling value of the layer of conducting rods placed in proximity of the plasma surface [2]. To overcome this problem a combined version of QOG and multijunction has recently been introduced [3], which seems to give enhanced values of the aforementioned coupling, but the QOG concept is not yet fully explored.

Up to now the analysis of QOG devices has been performed in the frame of a plane wave excitation. This approach has led to a number of interesting results [2, 4, 5], but has also left some unsatisfied questions: since a plane wave cannot be really produced, what consequences does the angular spread of a (real) finite beam involve? Is it possible to find a configuration which really ensures coupling values close to total transmission? Is the Gaussian QOG less sensitive to the geometrical configuration?

In this paper we propose an efficient QOG configuration whose RF input beam is a Gaussian beam.

In Section 2 the numerical results are presented, while in Section 3 conclusions and further developments are outlined.

2. Numerical results

The theoretical analysis has been presented elsewhere [6], here it is applied to the case of a homogeneous plasma with constant density $n_0 > n_c$, where n_c is the cutoff density of the lower hybrid slow wave. The constant plasma density n_0 starts at a distance L from the first layer of the QOG (see Fig. 1). The evaluation of the reflected power and the directivity, defined as the ratio between the power

coupled for positive values of $n_{//}$ and the total coupled power, is performed in this section.

By using the Poynting vector component relevant to the diffracted field which impinges on the plasma surface, it is possible to obtain the following expression for the real part of the power flow in the x-direction per unit y-length:

$$\Phi_x = \frac{kZ_0}{4\pi}\left\{\int_{|n_{//}|<1} \left|\tilde{\mathcal{H}}_d\right|^2 \left(1-|\Gamma|^2\right) n_\perp \, dn_{//} - 2\int_{|n_{//}|>1} \left|\tilde{\mathcal{H}}_d\right|^2 \mathrm{Im}\left[\Gamma\right] |n_\perp| \, dn_{//}\right\} \quad (1)$$

where $\mathrm{Im}[\Gamma]$ is the imaginary part of the plasma reflection coefficient, and $\tilde{\mathcal{H}}_d$ is the diffracted field which impinges on the plasma surface. To evaluate the coupling efficiency, the power carried by the incident Gaussian beam has to be known. This calculation can be easily performed, leading to:

$$P_{inc} = \int_{-\infty}^{\infty} \mathrm{Re}\left[\frac{1}{2}\vec{E}_i \times \vec{\mathcal{H}}_i^* \cdot \hat{\xi}\right] d\zeta = \frac{Z_0 w_0 |\mathcal{H}_0|^2 \sqrt{\pi}}{2\sqrt{2}} \quad (2)$$

where $\mathrm{Re}[\cdot]$ denotes the real part, and $\hat{\xi}$ is the unit vector in the ξ-direction (see Fig. 1).

The following results are referred to the efficient layout proposed, sketched in Fig. 1, for an array with 40 scattering rods and $kD_3 = 10.8$, where an additional conducting wall, orthogonal to the plasma, has been introduced. The two confining walls, together with the reflecting plasma surface, form an open cavity.

In Figs. 2 and 3 the spot-size and the incidence angle are assumed as the independent variables, and variations around the optimized values ($kw_0 = 6.25$, $\varphi_0 = -45°$) are shown. In the latter figure we note a less sensitive dependence of the coupling with respect to the plane-wave case. In particular, a change of reflection from 15% to 35% is achieved in approximately ±15°, whereas for a plane-wave illumination such a coupling change occurred in ±2° [5].

In Fig. 4 the launched power spectrum, corresponding to the optimum configuration, i.e. the one yielding the minimum reflected power (12.5%), is presented. The main peak lies at $n_{//} \approx 1.7$.

To give some reference geometry, we list in Table 1 the optimized grill parameters at the nominal frequency of 5 GHz, as envisaged for ITER.

Finally, in Fig. 5 reflected power and directivity are shown as a function of the plasma density n_0/n_c for the optimized configuration reported in Table 1.

3. Conclusions and further developments

In this paper an efficient Gaussian beam powered QOG configuration, reaching about 85% of coupled power, has been proposed. The analysis could be extended to other beams having finite transverse extension: an interesting case

would be that of a beam radiated from an open-ended waveguide or from an array of waveguides radiating in a vacuum, allowing a different RF plant to be used. Moreover, a more realistic plasma density model could be considered, and the values of the electric field inside the structure could be computed to give an estimate of the incident power for a safe operation.

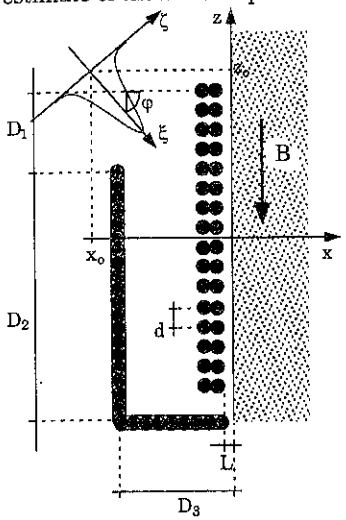

Fig. 1. The proposed configuration.

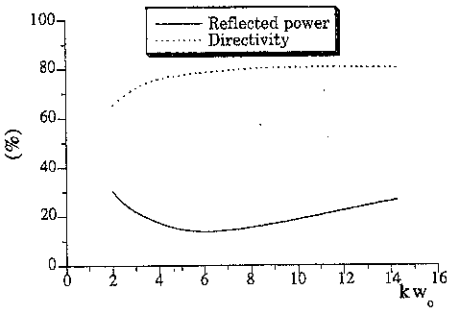

Fig. 2 Coupling parameters vs. beam spotsize at waist.

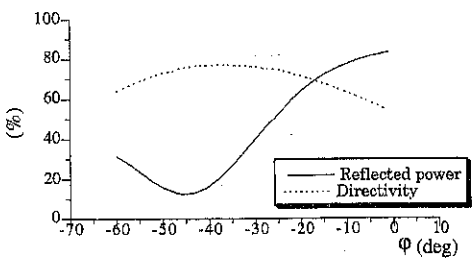

Fig. 3. Coupling parameters vs. beam angle of incidence.

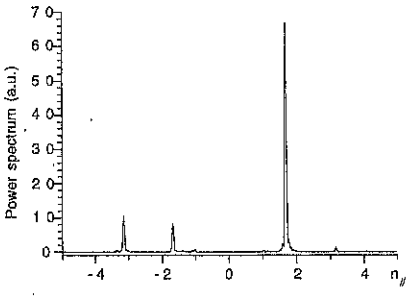

Fig. 4. The coupled spectrum.

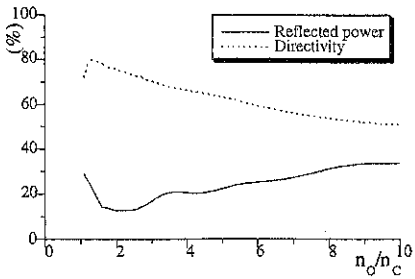

Fig. 5. Coupling parameters vs. plasma density

Table 1

QOG geometrical dimensions at 5 GHz
(All dimensions are in cm)

Array and cavity		
Scattering rod (2a x 4a)	:	1.6 x 3.2
Grating period	d :	2.5
Total array z-length	:	99.3
Cavity length	D_2 :	103.9
Cavity width	D_3 :	10.3
Structure total z-length	D_1+D_2 :	117
Beam		
Beam width at waist	w_0 :	5.7
Beam centre-plasma surface distance.	Dx_0 :	4.7
Beam centre-reflecting wall distance...	Dz_0 :	3.0

REFERENCES

[1] PETELIN, M. I., SUVOROV, E. V., Sov. Tech. Phys. Lett. **15** (1989) 882.

[2] FREZZA, F., et al., Nucl. Fusion **34** (1994) 1239.

[3] PREINHALTER, G., Nucl. Fusion **36** (1996) 593.

[4] MAZZITELLI, G., et al., Proc. of the 11th Topical Conference on Radiofrequency Power in Plasmas, Palm Springs, USA, May 1995, AIP Conference Proc. 355, printed in New York (USA), p. 421.

[5] WEGROVE, J. G., et al., Proc. of the 11th Topical Conference on Radiofrequency Power in Plasmas, Palm Springs, USA, May 1995, AIP Conference Proc. 355, printed in New York (USA), p. 429.

[6] AVANTAGGIATI, V. A., FREZZA, F., GEROSA, G., SCHETTINI,G., BORGHI, R., SANTARSIERO, M. , Nucl. Fusion **37** (1997) 699.

RADIATION CHARACTERISTICS OF WAVEGUIDE ANTENNAS FOR ICRF HEATING

J.A.Heikkinen[1], *M.A.Irzak*[2], *O.N.Shcherbinin*[2]

[1] VTT Energy, Euratom-TEKES Association, P.O.Box 1604, FIN-02044 VTT, Finland
[2] A.F.Ioffe Physico-Technical Institute, St.Petersburg, Russia

Abstract: The coupling and radiation properties of a folded waveguide (FWG) antenna and a dielectric-filled waveguide (DWG) in the ion cyclotron range of frequencies are evaluated for tokamaks with the FWGUIDE and GRILL-3D waveguide codes. For 10 MW power per unit of the FWG, the maximum voltage in the transmission line can be kept below 40 kV, and the maximum electric field inside the waveguides below 30 kV/cm. For a waveguide complex composing of eight units and fitting one ITER port, the mutual coupling between the units is found to be nonnegligible, indicating the need of tuning in the system circuit.

Introduction: The fast magnetosonic waves in the most tokamak ICRF heating experiments nowadays are excited by a set of loop antennas for which a good coupling efficiency has been widely demonstrated. In the conditions of the ITER tokamak, where high power density launchers with lower electric loads are desirable, other types of antenna construction are also considered. An antenna configuration based on a folded waveguide (FWG) principle [1] is a compact, all-metal ceramic-free construction with better input impedance matching providing high power density operation with acceptable electric field load on the antenna aperture and the transmission line. For higher power and structural rigidity, the dielectric-filled waveguide (DWG) couplers [2] may also offer a viable alternative to coil antennas, provided the DWG couplers are not posed to strong radiation.

In the present work, the power handling and coupling of a folded waveguide (FWG) antenna array (Fig. 1) in the ion cyclotron range of frequencies are analyzed numerically with the FWGUIDE code [3] for reactor plasma conditions. The fields inside the FWG unit are approximated in the model of a usual rectangular waveguide which will result from "unfolding" the FWG [1]. Reconstructing the field structure both inside the waveguides and in the vacuum layer between the coupler front and plasma, the poloidal and toroidal spectra of the waves launched into the plasma are computed. For comparison with FWG radiation properties, the

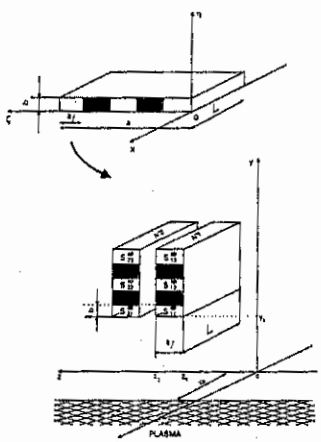

Fig. 1. Sketches of an unfolded waveguide and of a FWG units array.

radiation spectra of the DWG antenna are solved by the GRILL3D code [4] developed for simulation of complex rectangular waveguide antennas.

Inside the FWG unit we assume an external current which energizes the cavity formed by a back plate at $x = -L$ and a front polarizing plate at $x = 0$. This current is taken to be a simple, infinitely thin Hertz dipole having the height h. No external currents are applied in the DWG model. The radiation is generated by incident waves (in a TE_{10} mode) in separate waveguides stacked one over the other in one unit. Neither back plate nor polarizing plate is assumed. The plasma surface is placed at a distance x_p from the coupler mouth.

Results: We have calculated the plasma surface impedance matrix as a numerical solution of the wave equation in the plasma in FLR approximation for the ITER relevant plasma parameters: $R_0 = 810$ cm, $a_0 = 300$ cm; at the axis $B_0 = 5.7$ T, $n_{e0} = 8\times10^{13}$ cm^{-3}, $T_{e0} = 20$ keV, $T_{i0} = 20$ keV; at the separatrix ($a_S = 280$ cm) $n_{es} = 2\times10^{13}$ cm^{-3}, $T_{es} = 2$ keV, $T_{is} = 1$ keV; deuteron and triton densities $n_D = n_T = n_e/2$. Density and temperature profiles inside the separatrix were taken as a square root of parabola, the profiles in the scrape-off layer were taken exponential with the decay length 5 cm. The wave frequency $f_0 = 60$ MHz (RF absorption at the second cyclotron harmonic of tritium near the torus axis). The calculations were carried with the assumption of outward radiation at the distance 100 cm from the plasma boundary.

We choose for the ITER an array of 8 FWG units placed by 2 rows, 4 units in each row. Each FWG unit had 12 folds and 6 apertures (at every odd fold counting from the bottom), aperture width $a_f = 40$ cm and height $b = 7.8$ cm, width of a vane $b_1 = 0.2$ cm. The adjacent units were separated toroidally and poloidally by 5 cm. As a result the whole array had toroidal (z) and poloidal (y) dimensions 175 cm and 197 cm, respectively, which fits the ITER port. The basic distance between the waveguide mouth and plasma $x_p = 10$ cm. For these parameters the resonant back plate position (close to one-half of the wavelength for the fundamental TE_{10} guide mode) was $L = 288$ cm. The dipole with a driving current was placed at one-quarter of the guide wavelength from the back plate.

The power input was calculated as $P_{inp} = (1/2)\cdot\mathrm{Re}(I^*U)$, where I and U are the complex dipole current and voltage; the input impedance of the system $Z = R + iX = U/I$. The dependence of the input power on the back plate position is a typical resonance curve with the quality factor about 300. The mutual coupling between units in the array appears to be rather strong. We assumed that the array would be capable to deliver the total radiated power 32 MW, approximately 4 MW per unit. Initially the height of all dipoles was chosen equal to 1 cm and each dipole current to 400 A. Having in mind to obtain RF driven plasma currents we used the phase shift $\Delta\varphi = \pi/2$ between the neighboring units in a row. It resulted in a total radiated power 32 MW, but the power was distributed between the units unevenly. The least loaded (first in each row) units contributions to the total flux were approximately 2.3–2.4 MW per unit, while the most loaded (last in each row) units contribu-

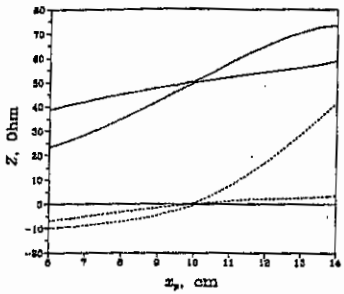

Fig. 2. Input impedances of units in a 4×2 FWG array versus wall-plasma distance.

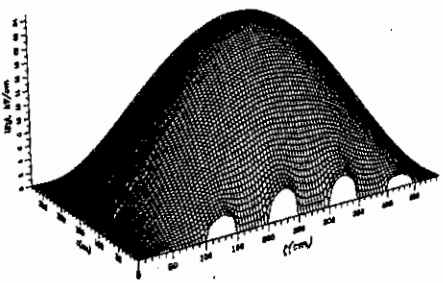

Fig. 3. Electric field inside the "unfolded" waveguide (absolute value). Single FWG unit case, P_{rad} = 10 MW.

tions were approximately 6.3–6.5 MW per unit. The input resistances were distributed in the range R = 28–81 Ω. Varying the input power in separate units (by varying the dipoles height in the range $h \approx$ 0.7–1.2 cm) we managed to get more or less even power flux distribution between the units (3.9–4.2 MW per unit) with the input resistances varying in the range R = 49–53 Ω and the input reactances $|X| < 10$ Ω. The situation could be further improved by adjusting the back plate position for each unit individually.

The shadowed areas in Fig. 2 show the range inside which the input resistances (solid lines) and reactances (dots) of the units are distributed at different x_p. Here the array was finely adjusted for x_p = 10 cm and, depending on the technical requirement for the transmission lines, we can choose the x_p range inside which input characteristics are still acceptable.

The fields structure inside a single FWG unit was calculated in the "unfolded" waveguide geometry with slightly different dimensions (10 folds, 5 apertures, a = 495 cm, a_f = 49.5 cm, b = 9.8 cm, b_1 = 0.2 cm, L = 283 cm, x_p = 10 cm). The dipole height h = 1.23 cm and current I = 630 A corresponded to the total radiated power 10 MW. The absolute value of the electric field inside the FWG unit is presented in Fig. 3. Electric field in the center (approximately at the dipole current position) attains 25.6 kV/cm and is purely real, which

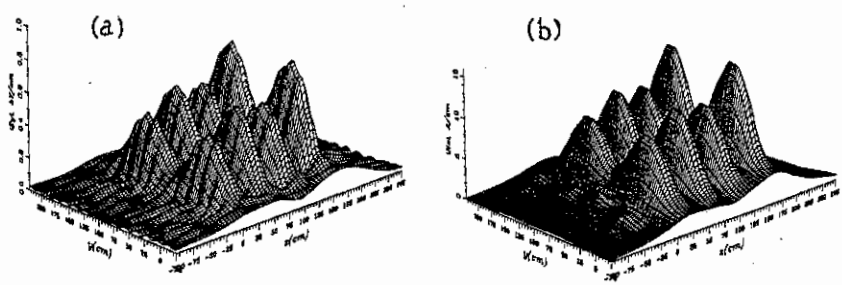

Fig. 4. Electric (a) and magnetic (b) fields at the plasma surface (x_p = 10 cm) for a 4×2 FWG array.

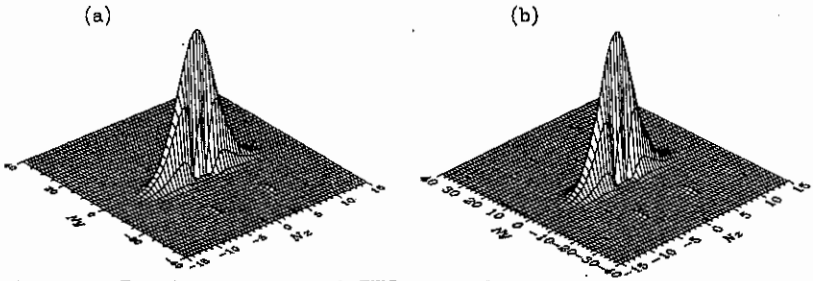

Fig. 5. Radiation spectrum of a FWG unit (a) and a DWG unit (b). x_p = 5 cm.

corresponds to the resonant conditions. The ratio of the electric field in the center to its maximum value at the apertures is approximately 5.5–6. Such a field value produces the voltage at the dipole ≈31.5 kV which in the case of ideal matching is equal to the maximum voltage in the transmission line. Here it should be noted, that a thin wire feeder used in the model may not withstand such current/voltage values, and in a real unit one may have to use a thick probe coupler which requires a more detailed input impedance modeling.

The structure of the electric and magnetic fields in the vacuum layer in front of FWG mouth was calculated for the case of 4×2 FWG array with a total radiated power of 32 MW, adjusted for x_p = 10 cm. The electric field falls off very rapidly away from the apertures. The magnetic field does not decrease so rapidly away from the apertures. The 3-*D* plots of the absolute values of the electric and magnetic fields at the plasma surface are presented in Fig. 4. In the maximums the electric field reaches the value ≈0.6 kV/cm.

Fig. 5a shows the radiated spectrum obtained from the FWG code for the 60×80 cm^2 FWG unit made of nine folds and five apertures, which corresponds to the 60×80 cm^2 DWG unit (five waveguides) used to obtain the results shown in Fig. 5b. For the FWG, the result was obtained with the backplate position at x = –283 cm and the source dipole position at x = –138 cm. For the DWG, the dielectric with ε = 25 was assumed. The spectra are found to be very similar. In fact, the DWG and FWG spectra can be modeled with a fairly good accuracy using a simplified pattern of the total electric field in the apertures which takes into account only the lowest TE_{10} incident mode for the DWG or a sinusoidal electric field amplitude distribution [1] at the apertures for the FWG. The spectra in all these cases show pronounced similarity in shape [5]. In particular, 4×2 array (both FWG and DWG) with proper phasing may excite spectra with high directivity (80–85%).

1 OWENS, T.L. IEEE Transactions on Plasma Science, PS-14 (1986) 934.
2 JOST, B.M., SCHARER, J.E., IEEE Trans. Plasma Sci. 18 (1990) 802.
3 HEIKKINEN, J.A., IRZAK, M.A., SHCHERBININ, O.N., "Modeling of Folded Waveguide Antennas", 32 pp. (1997), submitted for publication in Nucl. Fusion.
4 IRZAK, M.A., SHCHERBININ, O.N., Nuclear Fusion, 35 (1995) 1341.
5 HEIKKINEN, J.A., IRZAK, M.A., SHCHERBININ, O.N., "Radiation Properties of ICRF Waveguide Couplers", 11 pp. (1996), submitted for publication in IEEE Trans. Plasma Sci.

Nonlinear Density Profile Changes and Energy Dissipation in Helicon Wave Plasmas

V. Petržílka[a], J. A. Tataronis[b], G. G. Borg[c], I. V. Kamenski[c], L. Krlín[a] and P. Pavlo[a]

[a]Institute of Plasma Physics, P.O. Box 17, 182 11 Praha 8, Czech Republic
[b]University of Wisconsin, 1500 Engineering Dr., Madison, WI 53706, USA
[c]Australian National University, 2601 Canberra, Australia

1. Introduction

Poloidal ponderomotive forces, exerted by large-amplitude helicon waves, induce additional radial plasma transport, poloidal plasma rotation, and stationary electric fields [1, 2]. Because of these nonlinear effects, the plasma density profile is modified and thereby the helicon wave fields are altered. In this study, these nonlinear changes are estimated. In addition to effects induced by ponderomotive forces, nonlinear acceleration of electrons in the near field of the helicon wave antenna is explored. It is shown that nonlinearly accelerated electrons exhibit high dissipation rate that depends on the wave phase velocity and plasma density.

Our evaluation of the ponderomotive force effects involves three steps. (i) For a given inhomogeneous density profile, the radial and axial profiles of the wave electric fields and ponderomotive forces are computed for various antenna configurations using the coupling code FEM [3]. (ii) Because of *poloidal* ponderomotive forces, an additional transport velocity component V^{RF} is induced. This modifies the steady-state plasma density profile and introduces a new outward diffusion velocity V. (iii) Using the new radial plasma density profile, the modified helicon wave field profile and associated ponderomotive force are computed with the coupling code FEM. In addition to the new helicon wave profile, the plasma impedance and the nonlinear propagation properties of the Fourier components of the wave result from the numerical computations.

2. Helicon Waves Induced Radial Transport Velocity, Nonlinear Plasma Density Changes, and Nonlinear Helicon Wave Propagation

The initial outward radial transport velocity V_0 is given by diffusion,

$$V_0 = -D\frac{dn_0}{dr}, \tag{1}$$

where for classical diffusion $D = \eta T/B_0^2$, η is the plasma resistivity, T is the temperature and B_0 is the magnetostatic field. After the rf is switched on, an additional transport velocity V^{RF} is induced because of the effects of the ponderomotive forces. This induced transport velocity modifies the steady-state average plasma density profile, which in turn leads to a new outward diffusion velocity V,

$$V = -D\frac{dn}{dr}. \tag{2}$$

Thus the new total transport velocity is $V + V^{\mathrm{RF}}$, where

$$V^{\mathrm{RF}} = -\frac{1}{eB_0 n}\left(\frac{B_{0z}}{B_0}F_\theta^{\mathrm{P}} - \frac{B_{0\theta}}{B_0}F_z^{\mathrm{P}}\right). \tag{3}$$

In Eq. (3), $F_\theta^{\rm P}$ and $F_z^{\rm P}$ are ponderomotive forces of the helicon wave [1, 2]. The transport velocity $V^{\rm RF}$ may be positive or negative, i.e. it may have directions *into* or *from* the plasma interior. This might result in a *peaked* profile, as depicted in Fig. 1a, or a *hollow* profile, as depicted in Fig. 1b. Nonresonant helicon-wave-induced transport may result in significant changes in the plasma density radial profile. Ponderomotive forces of helicon waves change the plasma density profile from an initial profile $n_0(r)$ to a new profile $n(r)$. Before the switching on the rf field, or before the rf induced transport velocity begins to compete with the plasma transport velocity given by diffusion, the stationary profile of the plasma density is governed by the equation

$$\mathrm{div}(n_0 V_0) = \frac{1}{r}\frac{\partial}{\partial r}(r n_0 V_0) = Q_0, \tag{4}$$

where Q_0 represents plasma sources and sinks. The rf field induces a transport velocity $V^{\rm RF}$, in addition to the velocity V_0, together with a change δn in the plasma density, where δn may be comparable to n. The modified plasma density n is governed by the equations

$$n = n_0 + \delta n, \tag{5}$$

$$\frac{\partial}{\partial r}\left[r(n_0+\delta n)\left(V^{\rm RF} - D\frac{\partial(n_0+\delta n)}{\partial r}\right)\right] = Q, \tag{6}$$

where Q represents plasma sources and sinks, which might be changed by the presence of the rf field.

The radial profiles of the rf wave electric fields and associated ponderomotive forces have been computed for several antenna configurations and various inhomogeneous plasma density profiles using the coupling code FEM [3]. The computation proceeds in iterations. In each step of the computation process, the coupling code first determines the new plasma density profile. It then computes the new rf wave field profile and the ponderomotive force. Individual Fourier components of the rf field may have large radial gradients and therefore large radial derivatives at certain plasma radii. Because of the potentially large radial derivatives, the Fourier components can significantly affect the ponderomotive force and consequently the induced nonlinear changes in the plasma density profile, as depicted in Figs. 1a and 1b. Details of the nonlinear effects resulting from helicon wave propagation are found in Refs. 4 and 5.

3. Radial Electric Field and Plasma Rotation Induced by Helicon Waves

We computed the poloidal plasma rotation velocity and the associated stationary radial electric fields that the ponderomotive force of helicon waves induces. The radial electric field and the θ and z-components of the mean ion flow velocity of the ion fluid $\mathbf{U}_{\rm i}$ are given by the following equations [2],

$$E_{0\rm r} = \frac{1}{e n_0}\frac{\partial p_{\rm i}}{\partial \rm r} - \frac{B_{0z}}{m_{\rm i} r^2 n_0 U_{\rm ir}}\int_0^{\rm r} d\bar{r}\,\bar{r}^2 F_\theta^{\rm P} + \frac{B_{0\theta}}{m_{\rm i} r n_0 U_{\rm ir}}\int_0^{\rm r} d\bar{r}\,\bar{r} F_{\rm z}^{\rm P}, \tag{7}$$

$$U_{{\rm i}\theta} = \frac{1}{m_{\rm i} r^2 n_0 U_{\rm ir}}\int_0^{\rm r} d\bar{r}\,\bar{r}^2 F_\theta^{\rm P}, \tag{8}$$

$$U_{\rm iz} = \frac{1}{m_{\rm i} r n_0 U_{\rm ir}}\int_0^{\rm r} d\bar{r}\,\bar{r} F_{\rm z}^{\rm P}. \tag{9}$$

Typically, $E_{0\rm r} \simeq$ several Volts/cm, $U_{i\theta} \simeq 10^4$ m/sec, and $U_{\rm iz} \simeq$ several m/sec for a 3 kW helicon plasma source of plasma radius of about 2 cm. This value of the poloidal rotation

velocity $U_{i\theta} \simeq 10^4$ m/sec, induced by the ponderomotive forces, is significant and should be rather easily measurable.

4. Nonlinear Energy Dissipation

We study electron motion along z–coordinate in an inhomogeneous rf field $E^{\rm RF}(z)$ and an inhomogeneous stochastic electric field $E^{\rm ST}(z)$. However, in this contribution, which is to be considered as one of a series of works concerning wave particle acceleration in the near antenna rf fields, we report only computations with negligible stochastic electric field component, $E^{\rm ST}(z) \simeq 0$. Both rf and stochastic fields are directed along the z–coordinate. The equation for the coordinate z of the electron motion has the following form,

$$\frac{d^2z}{dt^2} = \frac{e}{m}[E_1^{\rm RF}(z) + E_2^{\rm RF}(z)\sin(k_1 z - \omega t + \pi\phi) + E^{\rm ST}(z)\sin(k_2 z - 2\pi R(t))] - \nu v(t), \quad (10)$$

where e is the charge and m is the mass of the electron, ω is the angular frequency of the rf field, ν is the collision frequency, $v(t)$ is the electron velocity, $R(t)$ is a random function of time t and k_1 and k_2 are wave vectors of the rf and stochastic fields, respectively, $\phi\pi$ is the wave phase for $t = 0$ and $z = 0$. The rf field profile should model the case of axially short ring type antenna, where the field in the ring region is constant, and axially on both sides of the ring there is a propagating wave, with exponentially decreasing amplitude with a scale length L. In the computations presented in Figs. 2a and 2b, we put $L = 30$ cm, electric field amplitude $E = 9$ V/cm, and we chose three values of the wave vector radiated by the antenna, (i) $k_1 = 0.21$ cm^{-1}, i.e. the wave phase velocity $v_{\rm p} = 2.01 \times 10^8$ cm/sec, (ii) $k_1 = 0.1$ cm^{-1}, i.e. the wave phase velocity $v_{\rm p} = 4.4 \times 10^8$ cm/sec, (iii) $k_1 = 1$ cm^{-1}, i.e. the wave phase velocity $v_{\rm p} = 4.4 \times 10^7$ cm/sec. Electrons are injected with the velocity $v = 1.3 \times 10^8$ cm/s, corresponding to the temperature of 5 eV, in the middle of 2 cm wide antenna ring, for the wave phase $\phi = 0.5$. The electron motion was followed for the time interval of 1.42×10^{-7} s, which is approximately one period of the rf field for the wave frequency 7 MHz, chosen in the computations.

The energy dissipated by accelerated electrons exhibits a significant maximum value that depends on the plasma density, for all three wave phase velocities considered in the computations, as Fig. 2a reveals. The peak is higher and more emphasized for higher wave phase velocities. The high dissipation rate of nonlinearly accelerated electrons, up to about 120 eV per accelerated electron in one rf field period, may be one of the reasons for the well known anomalous efficiency of helicon wave discharges. Another result, which Fig. 2b reveals, is that electrons can be accelerated in the near antenna fields to energy up to about 140 eV, depending on the wave phase velocity.

References

[1] V. Petržílka and R. L. Dewar: Australian J. of Physics **48**, (1995) 691.
[2] R. Van Nieuwenhove, V. Petržílka and J. Tataronis: J. Plasma Phys. **54**, (1995) 245.
[3] I. V. Kamenski and G. G.Borg: Phys. Plasmas **3**, (1996) 4396.
[4] V. Petržílka, J. A. Tataronis, G. G. Borg, I. V. Kamenski, L. Krlín and P. Pavlo: accepted at the 18th Symposium on Plasma Physics and Technology, 17 - 20 June 1997, Prague, Czech Republic.
[5] J. A. Tataronis, V. Petržílka, G. G. Borg and I. V. Kamenski: submitted to the GEC97 Meeting of the APS, Madison, WI, USA, 6-9 October 1997.

Acknowledgment: Supported by the grants 202/96/1355 and 1350 of the Czech Grant Agency, the U.S.-Czech grant No. 93068, and the U.S. DoE grant No. DE-FG02-97ER54398.

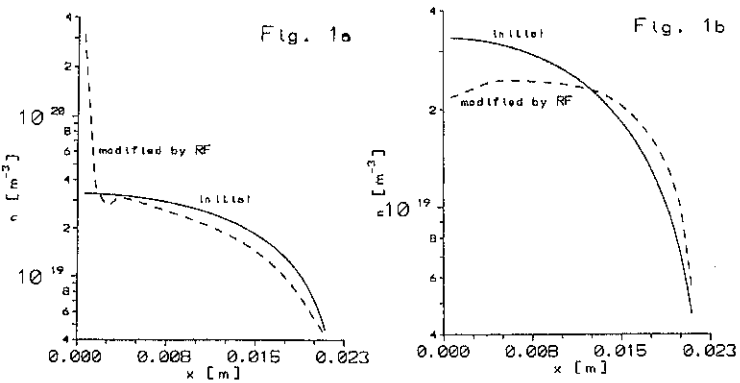

Fig. 1. *Radial dependence of the plasma density in the 3 kW helicon plasma source, the wave frequency is 7 MHz, the magnetostatic field $B_{0z} = 0.15$ T, plasma radius is $a = 2.15$ cm. Azimuthal $m = -1$ and $m = +1$ modes are considered. Solid line: The initial plasma density profile unperturbed by the RF field; Dashed line: The plasma density profile modified by the RF field. a) The rf power is launched by a helical antenna with negative helicity, b) the rf power is launched by a helical antenna with positive helicity.*

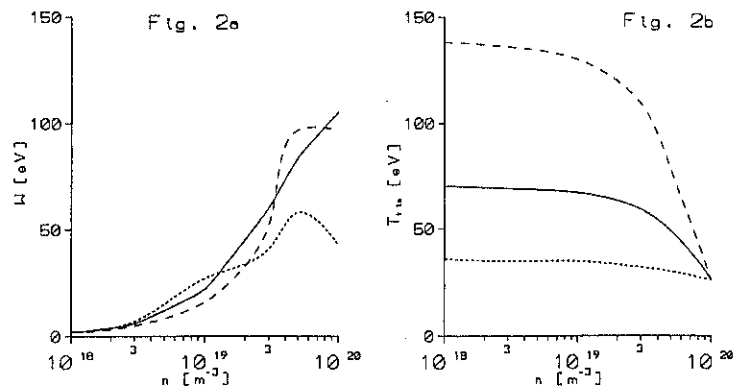

Fig. 2. *Dependency on the plasma density of a) energy W dissipated by an accelerated electron, and b) maximum electron energy $T_{\rm kin}$ of an accelerated electron, for three various wave phase velocities $v_{\rm p}$: $v_{\rm p} = 2.01 \times 10^8$ cm/sec, solid line; $v_{\rm p} = 4.4 \times 10^8$ cm/sec, dashed line; $v_{\rm p} = 4.4 \times 10^7$ cm/sec, dotted line.*

Antenna Coupling for Non-Circular Plasma

J. Källbäck and T. Hellsten
Alfven Laboratory, Royal inst. of Technology, SE-10044
Stockholm, Sweden, (EUROATOM/NFR FUSION Association)

The coupling of waves from an antenna to the plasma, in the ion cyclotron frequency range, is usually modelled by a plane plasma slab assuming complete single pass absorption. In which case there is no reflected wave. If one takes into account finite absorption the coupling resistance depends then on the amplitude and phase of the reflected wave. For geometries in which the wave equation becomes non-separable the solutions of the different poloidal Fourier modes couple. Such a coupling may lead to a wave field with a broad Fourier spectrum, broader than that obtained by Fourier decomposing the antenna current. The ray trajectories may also be stochastic. The coupling of the Fourier modes affects both the antenna coupling resistance as well as the wave field. The change in the eigenmode spectra when going towards geometries with stochastic ray trajectories have been discussed extensively in the literature in connection with solving the Schrödinger equation. Less have been discussed regarding the structure of the solutions. McDonald developed a WKE model describing the stochastic wave fields assuming the energy density in phase space to be constant [1]. However, this model did not agree well with wave field solutions of the fast magnetosonic wave in toroidal plasmas. A statistical model of the wave field was developed [2] where the wave field is expressed in terms of "eigenfunctions" for a circular cylinder, $e_m(r)$. The modulus of the wave field square is given by

$$\left\langle |E|^2 \right\rangle = C_0 \sum_m g(m) |e_m(r)|^2 \qquad (1)$$

where C_0 is a normalisation constant determined by the total absorbed power and m the poloidal Fourier number, $g(m) \approx |m|^{-\kappa}$ for $m \neq 0$ with $\kappa \approx 0.5$ and $g(0) = 1$.

1. Wave field in a cylinder with elliptic cross section

In order to understand what determines the weight function g(m), the poloidal Fourier spectra in an elliptic cylinder were studied. In this case the ray trajectories are not stochastic but form closed or periodic orbits implying the existence of regular eigenmodes. Poincaré surface of sections for rays described by the Helmholtz equation as a simplified wave equation are shown in Fig.1, where θ is the angle at the reflection point. The eigenmodes contain spectra of azimuthal Fourier modes defined by a resonating ray i.e. a ray returning to the same position in phase space with the same phase modulus 2π. The two closed regions around $\theta=0$ and $\theta=\pi$ define bouncing ball modes. These waves are reflected near the mid plane in the region with the largest radius of curvature. The separatrix is defined by rays passing through the focal

points of the ellipse. The periodic curves lying outside the separatrix define so called whispering gallery modes. The spread in m appears because of large changes in m during specular reflections at the boundary, which cannot be regarded as a diffusive process.

2. Wave field in a torus with circular cross section

By breaking the symmetry when going to a toroidal plasma the wave equation becomes also non-separable. In this case a number of islands develops around different m-numbers. As the modulus of the toroidal mode number increases more islands develop which grow in size. As they start to overlap the ray trajectory becomes stochastic as can be seen in Fig. 2 using the Helmholtz equation as a simplified wave equation. The spread in m appears because of the projection of the ray into the poloidal plane becomes a curved line incidenting at a different angle at the reflecting boundary.

3. The coupling resistance of the antenna

To analyse how the plasma shape influence the coupling we model the antenna, localised at the low field side, as a sheet current for $|\theta|<40$ and using the LION-code [3,4] to calculate the fast wave field. We first compare the antenna resistance for a circular cylinder with that of an elliptic cylinder. Thereafter we compare the antenna resistance for a JET equilibrium with the one obtained in a plane slab. The resonance peaks of the coupling resistance are determined by the phase of the reflected wave at the plasma boundary in front of the antenna. The phase is determined by the size of the plasma and the perpendicular wave number $k_\perp$ given by

$$k_\perp^2(\omega) = \frac{\omega^2}{c^2} S - k_\parallel^2 - \frac{(\omega/c)^4 |D|^2}{(\omega/c)^2 S - k_\parallel^2} \qquad (2) \qquad\qquad k_\perp^2 \approx k_r^2 + (m/r)^2 \qquad (3)$$

where S and D are the diagonal and off-diagonal components of the perpendicular part of the dielectric tensor. The perpendicular wave number $k_\perp$ increases with frequency and decreases with magnetic field. As these parameters varies the coupling resistance is expected to vary.

3.1 Antenna Resistance for a circular cylinder compared with an elliptic cylinder

The antenna resistance for a circular cylinder and for an elliptic cylinder versus frequency are compared in Fig. 3. We have used the following parameters: $n=3\cdot10^{19}m^{-3}$, T=30keV, R_0=12m, B_0=3.4T and n_φ=-15. The wave field in the resonance peaks for the circular cylinder are dominated by the m=0 Fourier mode. The antenna produce poloidal Fourier spectra with $|m| \leq 10$. Higher $|m|$-modes have smaller amplitudes because of the coupling. Only ≈ five $|m|$ -modes have significant size. About four peaks are expected to the right of the m=0 peak, but they are not resolved resulting in a broadening of the m=0 peak. Between the resonance peaks the antenna resistance is very low.

The main resonance peaks for an elliptic plasma are separated with a similar distance in frequency as for the cylinder. But these resonance peaks have much lower amplitude. This can be understood by the fact that the antenna coupling also in this case is dominated by the m=0

mode. The reflected m=0 component of the wave field is considerably smaller in the elliptic case than in the circular case, because of the elliptic coupling to higher m-modes in the plasma. Between the main peaks smaller peaks appear. The coupling resistance between the peaks is higher than for a circular cross section. This is consistent with lower amplitude of the reflected amplitude of the m=0 mode because of the elliptic coupling, although the single pass absorption is the same. Thus, the elliptic coupling results in less variation of the coupling resistance as the plasma parameters varies, but with a total averaged coupling resistance similar to that of the circular cylinder.

3.2. Antenna resistance for a plane slab compared with a JET equilibrium

The peaks of the coupling resistance can be seen in experiment and have been interpreted as standing radial modes [5]. The variation of the coupling resistance for a JET antenna when the toroidal field was ramped down from 2.6 T to 1.4 T in 10 s is shown in Fig.5. Plane slab calculation with the ISMENE code [6] predicted that the resonance peaks will be composed of eigenmodes with $k_z \approx 0$ and the distance between them in terms of B is about 0.08 T. This corresponds to a time of 0.67s between the peaks compared to 0.45s for the experiment. Calculations of the coupling resistance with the LION code show about the same separation as the ISMENE code. Thus the plane model is able to predict the separation of the peaks rather accurate, but without producing a realistic wave field or coupling resistance.

Summary

For bounded regions in which the solution to the wave equation is separable the solution can be described by quantum numbers. As the symmetry is broken such that the equations with boundary conditions are not separable an irregular wave field is obtained with a broad Fourier spectrum. In spite of the difference of the wave field in the plasma the distances between the main peaks of the coupling resistance are similar for a circular cylinder and an elliptic cylinder, which may lead to the erroneous conclusion that a plan slab describe the coupling well. The total averaged antenna resistance is similar. The variation of the coupling resistance is smaller for the elliptic cylinder and the torus because of the coupling of the poloidal Fourier modes.

ACKNOWLEDGEMENT: The authors acknowledge CRPP, Lausanne, for having made the LION code available and the Swedish National Supercomputer Center for the access of the CRAY-YMP.

References

[1] McDonald, S. W., Phys. Rep **158** (1988) 337.
[2] Hellsten, T. et al, Phys. Rev. **E 53** (1996) R3048.
[3] Villard R., Appert K., Grubes R., Vaclavik J., Comput. Phys. Reports **4** (1986) 95.
[4] Villard L., Brunner S., Vaclavik J., Nucl. Fus. **35** (1995) 1173.
[5] Heilsten, T. and Appert, K. 13th Eur. Conf. on Contr. Fusion and Plasma Physics, 1986, **II**, 129.
[6] Appert, K. et al Computer Phys. Com. **40** (1986) 73

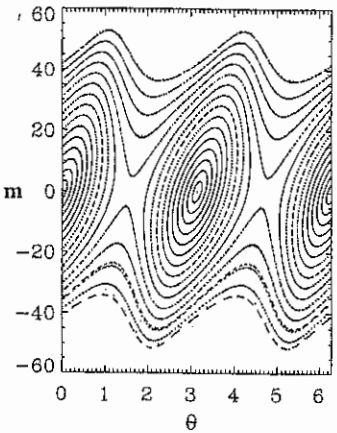

Fig. 1 Surface of section in the (m, θ)-plane of 30 rays undergoing specular reflection in an ellipse with e=1.26.

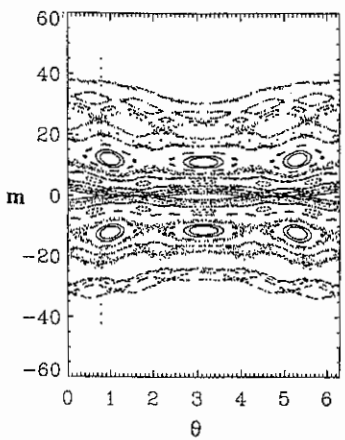

Fig. 2 Surface of section in the (m, θ)-plane for the toroidal case with circular cross section ,aspect ratio=3.0.

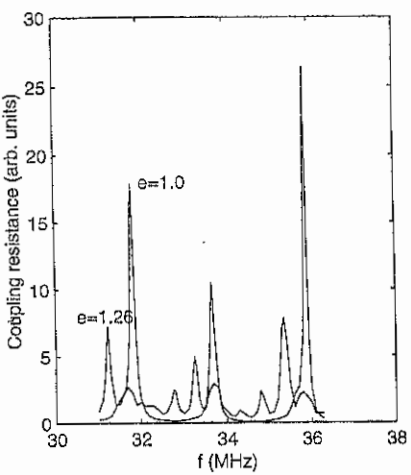

Fig. 3 Coupling resistance versus frequency for a circular cylinder, e=1.0 and for a cylinder with elliptic cross section, e=1.26.

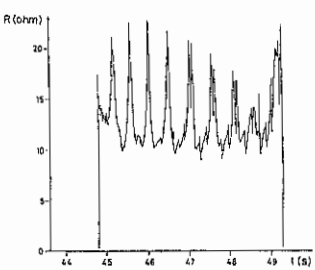

Fig. 4 Measured coupling resistance for a JET antenna during ramp down of the toroidal magnetic field. (The antenna resistance has been transformed by the short reactive stub close to the antenna.)

Parasitic Cyclotron Absorption by Fusion Born Alpha Particles

J. Hedin, J. Carlsson, T. Hellsten and A. Jaun

Division of Fusion Plasma Physics, Alfvén Laboratory, Royal Institute of Technology, SE-100 44 STOCKHOLM, Sweden, Association EURATOM/NFR

Abstract A method has been developed to calculate the dielectric tensor from a Monte Carlo distribution function in a toroidal plasma including the effect of the finite orbit widths. The procedure is here used for the calculation of parasitic α-particle absorption in JET like DT scenarios for fast wave current drive and second harmonic tritium heating.

1 Introduction

The presence of α-particles could inhibit efficient current drive or central heating with the fast wave, as previously addressed by [1, 2, 3]. In particular when $\omega \approx 2\Omega_T$ on the magnetic axis, the $\omega = 2\Omega_\alpha$ resonance appears near the plasma boundary where parasitic absorption can take place. The previous analysis of this scenario assumed Maxwellian distribution of the α-particles and an arbitrary density profile, but a more evolved model is needed since the absorption depends critically on the density and velocity distribution of the α-particles near the plasma boundary. Since the high energy particle orbits are wide, *i.e.* make large excursions from the flux surfaces, they are not only able to interact with the RF-field where they are born, but also everywhere along the orbit where the resonance condition $\omega = n\Omega + k_\parallel v_\parallel$ is satisfied. To study the effect of wide orbits, the distribution of α-particles is calculated with the Monte Carlo code FIDO [4]. The contribution of that distribution to the dielectric tensor is calculated and implemented in the toroidal full wave code LION [5, 6], which then yields consistent evaluation of the fast wave power absorption by the α-particles.

2 Physical Model

The FIDO code is first used to compute an approximative steady state α-particle distribution in toroidal geometry with a circular cross-sections without Shafranov shift. The α-particles are created in fusion reactions according to the DT fusion reaction rate of the background profiles. Self-collisions between the α-particles and wave interaction are neglected. Since the FIDO code does not model anomalous transport and the thermalised particles do not contribute to the absorption, the α-particles are removed from the simulation after one slowing down time $t_s = 1.06\,\mathrm{s}$. The dielectric tensor contribution from the resulting distribution is calculated using an expression of the tensor valid for locally homogeneous plasmas but arbitrary velocity distribution functions as given by equation 3.71 in Ref. [7]. This is done by approximating the

distribution function by

$$f(\mathbf{r},\mathbf{v}) = g(\mathbf{r},v_{\|})h(\mathbf{r},v_{\perp}) \tag{1}$$

where the two functions $g(\mathbf{r},v_{\|})$ and $h(\mathbf{r},v_{\perp})$ are obtained by assigning the orbits in a FEM representation in the radius r, the poloidal angle θ and the velocities $v_{\|}$ and $v_{\perp}$, respectively. The orbits are given by curves in the phase space $(r,\theta,v_{\|},v_{\perp})$. The dielectric tensor, including the effect of the finite orbit widths, is then calculated by numerical integration over the local distribution function and its velocity derivatives.

The global wave equation for the fast magneto-sonic wave is solved with the LION code including the contribution from the α-particles $\overleftrightarrow{\chi}_{\alpha}$ in the dielectric tensor

$$\overleftrightarrow{\varepsilon} = \overleftrightarrow{1} + \overleftrightarrow{\chi}_{e} + \overleftrightarrow{\chi}_{D} + \overleftrightarrow{\chi}_{T} + \overleftrightarrow{\chi}_{\alpha} \tag{2}$$

and using Maxwellian distributions for the other terms.

3 Results

To isolate the effect of the orbit width, two scenarios with a low and a very high plasma current are compared. The low current scenario with $I = 1\,\mathrm{MA}$ gives wide orbits, whereas the high current scenario with $I = 8\,\mathrm{MA}$ gives thin orbits. The other parameters are chosen in the range of plasma parameters obtained in JET: $B_0 = 3.4\,\mathrm{T}$, $R_0 = 3.1\,\mathrm{m}$, $n_{\varphi} = 16$, $n_D = n_T = 3\cdot 10^{19}\,\mathrm{m}^{-3}$, $T_D = T_T = 25\,\mathrm{keV}$, $T_e = 15\,\mathrm{keV}$, $r_0 = 1.35\,\mathrm{m}$, $\omega \approx 2\Omega_T$, $n = n_0\left(1-0.95(r/a)^2\right)^{1/2}$ and $T = T_0\left(1-0.95(r/a)^2\right)$. The concentration of α-particles is 0.24% for the first scenario and 0.27% for the later. The discrepancy is caused by higher orbit losses in the low current scenario. The flux surface integrated power absorption as a function of minor radius in the mid plane for $\omega/2\pi = 34, 36, 37.5\,\mathrm{MHz}$ are shown in figure 1–3. The location of the fundamental α-particle cyclotron resonance, residing on the high field side, is represented by a solid vertical line. The second harmonic tritium resonance is represented by a dotted vertical line.

For the second harmonic tritium heating scenario $\omega/2\pi = 34\,\mathrm{MHz}$, shown in figure 1, the α-particle absorption is completely dominated by the fundamental cyclotron resonance on the high field side. The bump at the edge of the absorption for the high current scenario is due to non resolved interaction with the shear Alfvén wave. The bump is not seen in the low current case, since the losses are larger and hence the α-particle density at the edge is lower.

The scenarios $\omega/2\pi = 36, 37.5\,\mathrm{MHz}$ are fast wave current drive scenarios with both $\omega = \Omega_{\alpha}$ and $\omega = 2\Omega_T$ at the high field side. A small displacement of the absorption towards the center could be observed in figure 2 as an effect of the wide orbits. Increasing the frequency results in that the second harmonic resonance of α-particles and deuterium enters the plasma from the low field side. For $\omega/2\pi = 37.5\,\mathrm{MHz}$ they are just inside the plasma represented with a dashed vertical line in figure 3. The second harmonic α-particle absorption is small compared to the second harmonic deuterium absorption due to the low α-particle density at the edge.

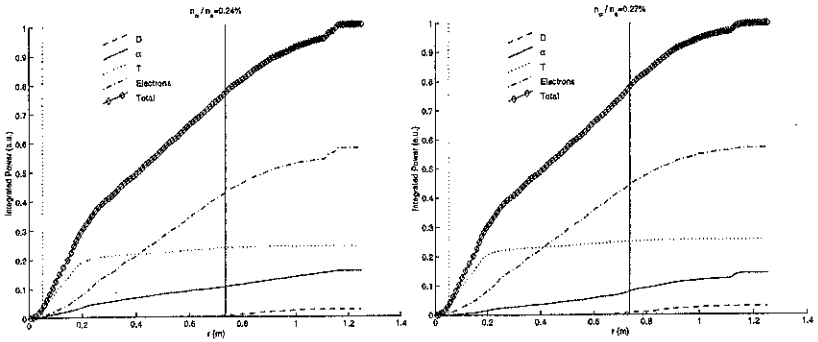

Figure 1 The integrated absorption as a function of the minor radius in the mid plane with $I = 1\,MA$ to left and $I = 8\,MA$ to the right for $\omega/2\pi = 34\,MHz$. Vertical lines for the location of $\omega = 2\Omega_T$ on the LFS (dotted) and $\omega = \Omega_\alpha$ on HFS (solid).

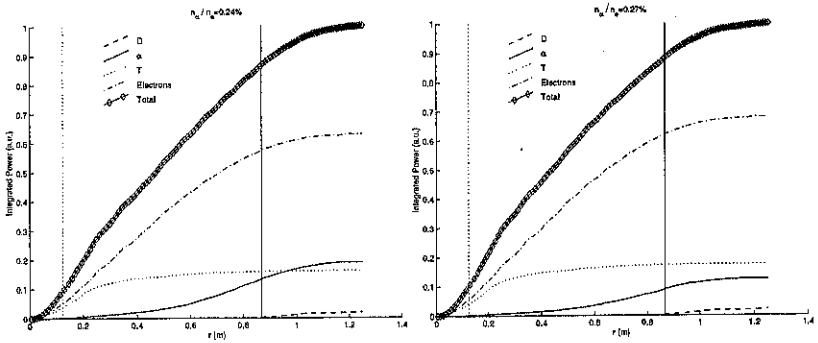

Figure 2 The integrated absorption as a function of the minor radius in the mid plane with $I = 1\,MA$ to left and $I = 8\,MA$ to the right for $\omega/2\pi = 36\,MHz$. Vertical lines for the location of $\omega = 2\Omega_T$ on the HFS (dotted) and $\omega = \Omega_\alpha$ on HFS (solid).

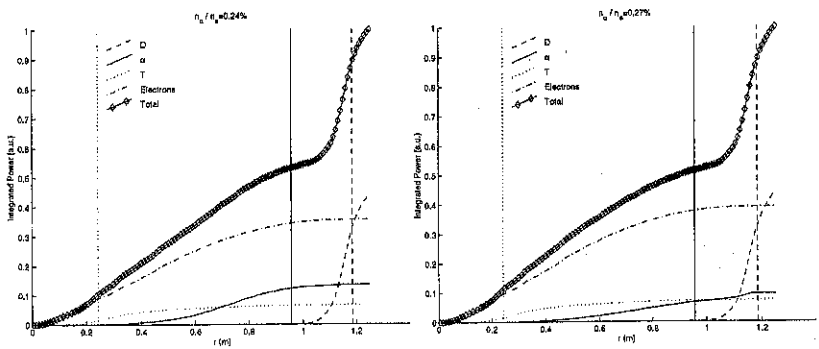

Figure 3 The integrated absorption as a function of the minor radius in the mid plane with $I = 1\,MA$ to left and $I = 8\,MA$ to the right for $\omega/2\pi = 37.5\,MHz$. Vertical lines for the location of $\omega = 2\Omega_T$ on the HFS (dotted), $\omega = \Omega_\alpha$ on HFS (solid) and $\omega = 2\Omega_\alpha$ on LFS (dashed).

4 Conclusions and Discussion

The calculations presented above is a »proof of principle« for combining the velocity distribution given by an orbit averaged Monte Carlo code with a global wave code via the dielectric tensor. Since the time scale for the evolution of the distribution function is much longer than the corresponding time scale for the wave field, the distribution function could be regarded static, while solving the wave equation. By feeding the calculated electric field into the Monte Carlo code, ultimately a self consistent calculation of RF heating will be carried out in an iterative manner.

The width of the high energy α-particle orbits does not seem to significantly increases the fast wave absorption. Due to losses, there is almost no α-particle density at the edges, and therefore almost no second harmonic absorption by the α-particles. The α-particle absorption is dominated by the fundamental cyclotron resonance. As a first study, the effect of the RF field on the distribution of α-particles has been neglected. However, this effect may be important, since the α-particle absorption will lead to formation of a high energy tail, increasing the RF absorption further.

References

[1] HELLSTEN, T., APPERT, K., VACLAVIK, J., and VILLARD, L., Nuclear Fusion **25** (1985) 99.

[2] SAUTER, O. and VACLAVIK, J., Nuclear Fusion **32** (1992) 1455.

[3] KOCH, R. and VAN-EESTER, D., Nuclear Fusion **29** (1989) 59.

[4] CARLSSON, J., ERIKSSON, L.-G., and HELLSTEN, T., in *Proceedings of the Joint Varenna-Lausanne Workshop*, p. 351, 1994.

[5] VILLARD, L., APPERT, K., GRUBER, R., and VACLAVIK, J., Computer Physics Reports **4** (1986) 95.

[6] VILLARD, L., BRUNNER, S., and VACLAVIK, J., Nuclear Fusion **35** (1995) 1173.

[7] ICHIMARU, S., *Basic Principles of Plasma Physics — A Statistical Approach*, Frontiers In Physics, Addison-Wesley Publishing Company, Inc., second edition, 1980.

SELF-CONSISTENT RAY DESCRIPTION OF ELECTRON CYCLOTRON WAVES

S.Pešić and N.Radulović

"VINČA" Institute of Nuclear Sciences, Laboratory for Nuclear and Plasma Physics, P.O.Box 522, 11001 Belgrade, Yugoslavia.

1. Introduction

Recently, there has been renewed interest in ray tracing of electron cyclotron (EC) waves in thermal plasmas [1-6]. The standard approach for EC ray tracing so far has been to determine the ray paths by neglecting the non-Hermitian part of the dielectric tensor and describing the wave properties by the cold plasma dispersion relation. The wave absorption along the ray then is calculated either using the frequency development of the thermal plasma dispersion relation about the real part of the complex circular frequency $\Omega = \omega + i\nu$, or by solving the complete thermal dispersion relation for complex $\vec{N}_\perp$. So, in the standard ray tracing approach the ray position does not depend on thermal and dissipative effects. Recently, this problem has been reconsidered in details [1-3]. It was found that thermal and dissipative effects significantly alter the ray path near and through the EC resonance (ECR), and that consequently, they affect the wave absorption (or emission). Recent experimental and theoretical results [4-6] have also confirmed the importance of thermal plasma effects near the ECR. In this paper the general properties of the ray paths and power deposition profiles obtained by using a novel, self-consistent ray tracing method in which the local plasma dispersion relation is allowed to be a complex quantity [7], are presented.

2. Plasma dispersion relation

In the ray equations (see for example [1]), the electromagnetic properties of the considered medium are completely characterized by the local dielectric tensor or more precisely, by the local plasma dispersion relation $F\left(\vec{N},\Omega,\vec{r},t\right)=0$. In general, the dielectric tensor of thermal plasma is non-Hermitian and consequently, the local plasma dispersion relation is complex. We are mainly concerned with low dissipative plasma $|\nu| << \omega$ because the wave propagation and therefrom, ray tracing are effectively possible only in these conditions. By expanding the dispersion relation about ω, one obtains

$$F\left(\vec{N},\Omega,\vec{r},t\right)=D|_{\Omega=\omega}+i\nu\left(\partial D/\partial\Omega\right)|_{\Omega=\omega}-0.5\nu^2\left(\partial^2 D/\partial\Omega^2\right)|_{\Omega=\omega}+... \qquad (1)$$

All present EC ray tracing studies are based on the assumption that the following conditions are fulfilled,

$$\left|\nu\left(\partial^2 D'/\partial\Omega^2\right)|_{\Omega=\omega}\right| << \left|\left(\partial D''/\partial\Omega\right)|_{\Omega=\omega}\right|, \quad \left|\nu\left(\partial^2 D''/\partial\Omega^2\right)|_{\Omega=\omega}\right| << \left|\left(\partial D'/\partial\Omega\right)|_{\Omega=\omega}\right| \qquad (2)$$

so that only the first two terms in the Taylor series development of F (1) are retained. Note the convention used in the paper of a prime denoting the real part and of a double prime denoting the imaginary part of the quantity as well as that $D'\left(\vec{N},\omega,\vec{r},t\right)\equiv D'$ and $D''\left(\vec{N},\omega,\vec{r},t\right)\equiv D''$.

When conditions (2) are satisfied, the complex dispersion relation can be reduced to a pair of real equations,

$$F'\left(\vec{N},\Omega,\vec{r},t\right) \approx D' - \nu\,\partial D''/\partial\omega = 0 \tag{3}$$

$$F''\left(\vec{N},\Omega,\vec{r},t\right) \approx D'' + \nu\,\partial D'/\partial\omega = 0 \tag{4}$$

In the standard ray tracing approach, equation (4) is ignored as well as the contribution of the second term in equation (3). Moreover, the ray paths are defined and traced through the ECR within the cold plasma approximation that is, using the cold plasma dispersion relation $D' \equiv D_C = 0$. By taking the real part of the weakly-relativistic plasma dispersion relation D_R (in place of D_C) recently, it has been shown [1,2] that thermal plasma corrections result in ray paths that may differ substantially from those predicted by cold plasma modeling.

In order to take into account also the non-Hermitian part of the dielectric tensor which can be very large near the ECR, we have regarded the equation

$$\Delta\left(\vec{N},\omega,\vec{r},t\right) = D'\,\partial D'/\partial\omega + D''\,\partial D''/\partial\omega = 0 \tag{5}$$

as a dispersion relation yielding the real part of the wave frequency ω while its imaginary part is determined from the expression [7],

$$\nu = D'/\left(\partial D''/\partial\omega\right) = -D''/\left(\partial D'/\partial\omega\right) \tag{6}$$

Namely, the pair of equations (3-4) is replaced by equations (5-6) which have to be solved simultaneously. In contrast to the standard ray tracing approach, this procedure includes both, thermal and dissipative effects in the ray description. So, one does not need to use the full complex ray analysis to describe properly the rays in presence of dissipative effects. As long as the rays do not propagate far from the real world, that is as long as the condition $|\nu| << \omega$ is satisfied, this self-consistent ray description provides meaningful physical informations. Its applicability for EC ray tracing has been demonstrated in [3].

3. Results

The fully 3D numerical code that we have developed is described elsewhere [1]. Throughout this paper the standard dispersion function $D\left(\vec{N},\omega,\vec{r},t\right) = 0$ is evaluated in its weakly relativistic approximation [8]. In the dielectric tensor components, finite Larmor effects are retained up to the third order. Note that the new dispersion relation $\Delta\left(\vec{N},\Omega,\vec{r},t\right) = 0$ involves the frequency derivatives of the real D' and imaginary D'' part of the standard dispersion relation so that mixed second order derivatives appear in the ray equations. This approach requires the evaluation of very high order derivatives of high-order weakly relativistic plasma dispersion functions (up to the 6^{th} order). Different evaluation methods and recursion relations are used for the calculation of these derivatives.

In the present paper we shall confine ourselves to present some general observations concerning the application of the described novel ray tracing technique. In the ECR region the variation of the quantities entering into the frequency development of F (1) is very pronounced. There are two characteristic points in the low-frequency side of the ECR: at the first point the imaginary part of F vanishes while at the second one, its real part, F' vanishes. When the electron temperature and/or the angle of incidence increase, these points move

gradually away from the resonance. Note that the imaginary part of the frequency ν remains finite in the vicinity of these points. In the numerical analysis, the smallness of the neglected second-order derivative in the frequency development of the complex dispersion relation (1) is continuously checked. In many cases of practical interest the third term in (1) can not be considered as formally small. This implies that any real ray tracing method fails to describe correctly the ray behaviour near the ECR. In this case, a full complex ray analysis has to be applied in this region.

In the outer plasma region the ray paths obtained by the novel ray tracing method practically coincide with those determined using the standard approach. Namely, at the edge of the plasma, the temperature and density are, although rapidly varying, much lower than in the bulk, causing a vanishingly small non-Hermitian part of the dielectric tensor. Indeed, in this region the ray describes one of the two familiar electromagnetic modes: the ordinary and the extraordinary mode. As the wave propagates towards the (hot) plasma core, the wave-particle interaction becomes gradually stronger and the dispersion relation becomes complex. The ray paths then starts to differ from those obtained by using the standard ray tracing approach. The deviation from the standard cold plasma ray description enlarges with increasing the electron temperature. This can also be seen from Fig.1. on which we have represented (*a*) the ray paths, (*b*) the real part $N'_{\perp o} \equiv \mathrm{Re}\{N_{\perp o}\}$ and (*c*) the imaginary part $N''_{\perp o} \equiv \mathrm{Im}\{N_{\perp o}\}$ of the ordinary wave refractive index versus the coordinate x in a one-dimensional plasma slab with parabolic plasma density and temperature distributions, magnetic field variation $B(x) = B_0/(1+1.25x)$, at an angle of incidence $\chi = 70°$, and for $X \equiv \omega_p^2/\omega^2 = 0.3$. Clearly, the ray paths through the ECR strongly depend on the electron temperature. It should be pointed out that toroidal effects additionally pronounce the deviation from the predictions of the standard approach. Since wave absorption depends on the details of the ray path, the obtained power deposition profiles differ substantially from those determined by the standard ray tracing approach.

References

[1] S.Pešić and A.Stojić, 14th Int.Conf.Plasma Physics and Controlled Nuclear Fusion Research, Wurzburg, 1992, IAEA, Vienna,Vol.2, p.273, (1993).

[2] S.Pešić and A. Stojić, J. Phys. Soc. Jpn. **62**, 2359, (1993).

[3] S.Pešić, Europhys.Lett. **35**, 349, (1996).

[4] A.Pochelon, et al., 20th EPS Conf. Controlled Fusion and Plasma Physics, Part III, p.1029, (1993).

[5] D.Vezard, et al., Phys. Plasmas **2**, 876, (1995).

[6] E.Westerhof, Proc. of the EC10 Workshop, (1997).

[7] L.Friedland and I.B.Bernstein, Phys. Rev. A **22**, 1680, (1980).

[8] I.P.Shkarofsky, Phys. Fluids **9**, 561, (1966).

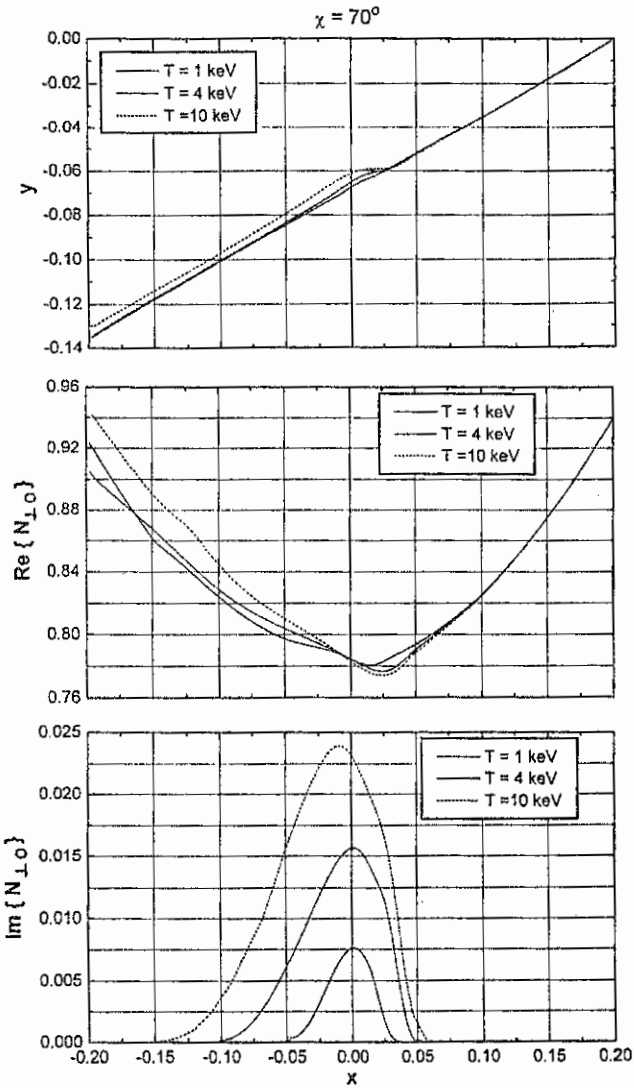

Figure 1. (a) The ray paths, (b) the real part $Re\{N_{\perp O}\}$ and (c) the imaginary part $Im\{N_{\perp O}\}$ of the ordinary wave refractive index versus the coordinate x. A plasma slab with parabolic density and temperature distributions, and $B(x) = B(0)/(1+1.25x)$ magnetic field, is assumed.

Investigation of the 5290 Å line in C^{5+} from radially resolved spectroscopy on the EXTRAP-T2 RFP.

J. Sallander, A. Hedqvist, E. Rachlew-Källne
Department of Physics I, Royal Institute of Technology, SE-100 44 Stockholm, Sweden
(EURATOM/NFR Fusion association.)

Introduction

The EXTRAP-T2 is a high aspect-ratio Reversed Field Pinch (R=1.24 m, a=0.18 m) featuring a resistive shell [1]. It has no limiters and the inside of the vacuum vessel is completely covered with graphite tiles. The choice of first wall material makes carbon and oxygen the most abundant impurities with very small levels of metals and other high-Z impurities.

The system for radially resolved spectroscopy has been developed to measure the radial dependence of line emission from impurities. Several emission lines from mainly carbon and oxygen have been studied. In the studies of carbon lines we have discovered interesting differences in the behaviour of the C^{4+} line at 2270.89 Å and the C^{5+} line at 5290.5 Å. The measured brightness profiles from C^{4+} always show that the emission mainly comes from the plasma centre. Often the C^{5+} emission show a similar radial dependence but in some discharges the emission comes from the plasma edge. This has lead us to believe that there is another excitation process than electron impact that is influencing the emission from C^{5+}.

Experimental

The light emitted by the plasma is observed in five viewing chords at one toroidal position. The lines-of-sight form a fan with 10° separation resulting in impact parameters (Shortest distance from plasma centre to viewing chord) from 0 to 128 mm. UV-grade fused silica lenses focus the light on five UV-grade optical fibres. These are coupled to the entrance slit of one 0.5m Jarrel-Ash Ebert grating spectrometer. A lens system focus the light from each fibre into five points on the slit. The separation between these spots is 3 mm to ensure minimum crosstalk. Due to the good imaging properties of the spectrometer the light from the five channels will then be imaged into five corresponding points on the exit slit. The light from the exit slit is then relayed to five PM-tubes with a lens system. The signals from the PM-tubes are amplified and recorded with transient recorders with a time resolution of 10 μs. The amplifiers include low pass filters to avoid aliasing in the signals. The whole system is absolutely calibrated against a tungsten spectral calibration lamp with integrating sphere (Optronic laboratories, OL 455).

The most obvious method for analysis of the line integrated signals would be to perform some kind of inversion to get the true emission profiles [2,3,4]. This approach has in our case produced very unpredictable results due to the small number of lines-of-sight. Instead we have used the unmanipulated radiance from the five viewing chords in combination with

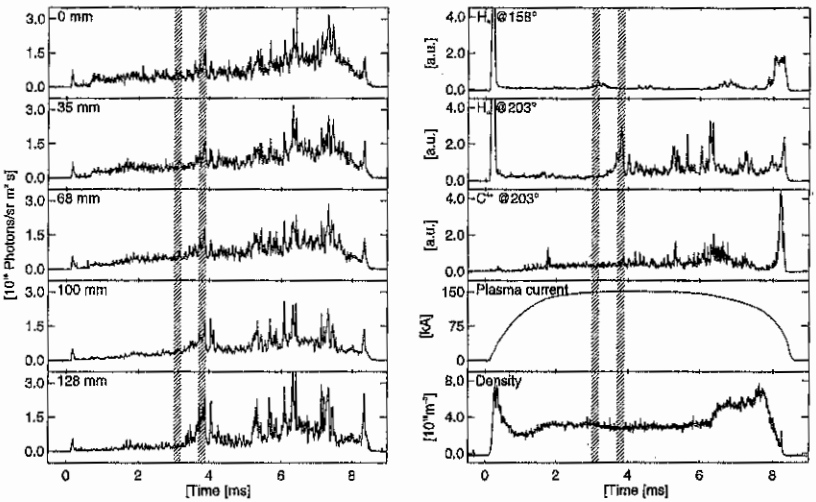

Fig. 1. Time traces from discharge #5192 showing the five chord C^{5+} brightnesses as a function of impact parameters together with H_α from two toroidal positions (203° is at the position of the five chord diagnostic), C^{4+}, plasma current and electron density. The correlation between the events in H_α and C^{5+}, which is absent in C^{4+}, is clearly seen around t=3.8 ms.

other spectroscopic diagnostics to analyse the data. The good time resolution makes it possible to follow the variation in plasma brightness for the lines-of-sight with different impact parameters.

Observations

Measurements made on C^{4+} at 2270.89 Å show that the emission is heavily peaked in the centre of the plasma. The energy required to remove one electron and go from C^{4+} to C^{5+} is high, 392 eV, since it is necessary to break the closed 1s shell. This is a higher energy than the electron temperatures of 100-200 eV measured in the centre from Thomson scattering [5]. Thus it would be expected that the emission from C^{5+} is even more centrally peaked. In many discharges this is the case but in some the observed brightness show that the emission originates from the edge of the plasma. The time evolution of the emission also departs from that of C^{4+} in these cases. While C^{4+} show a slowly increasing emission during the discharge, C^{5+} show rapid variations that are often correlated to the H_α signal at the same poloidal and toroidal position. The Doppler broadened line profiles show that the C^{5+} ions are significantly cooler than the C^{4+} ions.

The C^{5+} line at 5290.5 Å line comes from a high n transition (n=8 to n=7) that is known to have large cross-section in charge exchange reactions. In this reaction it is not the electron density but the neutral hydrogen density that determines the excitation rate and thus also the emission rate. The line emission would come from the edge of the plasma since the neutral hydrogen density is strongly peaked there. It should also follow the H_α emission in time

since this is dependent on the abundance of neutral hydrogen. The time traces from discharge #5192 (Fig. 1) show the time evolution of the C^{5+}, 5290 Å, emission from the five viewing chords, here notified by their impact parameter. Also shown are the time traces for H_α at two positions (203° is the toroidal position of the five chord spectrometer), C^{4+} at 2271 Å, plasma current and electron density. At about 3.5 ms into the discharge we can see that the H_α at 203° increases drastically. This is followed by an almost simultaneous increase in the C^{5+} emission, especially in the channels with large impact parameters. There is almost no trace at all of this event in the C^{4+} emission. The radial dependence of the C^{5+} emission shows that the increase in brightness mainly comes from the plasma edge (Fig. 2). It is interesting to notice that the event is very toroidally localised, there is no corresponding event in H_α at 158°.

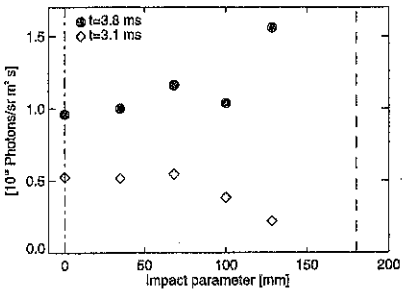

Fig. 2. Brightness as a function of radius for the two time intervals marked in fig. 1.

There have been concerns regarding the possibility that the C^{5+} line at 5290 Å is mixed with lines from neutral carbon or O^{3+}. Both of these species have lines around 5290 Å. They also have lines around 5305 Å that come from the same multiplets as their 5290 Å lines. In order to exclude the possibility of mixing a 1m spectrometer with an optical multi channel analyser was connected to the 203° position with an optical fibre. The radial dependence of the brightness from discharge #5437 shows that the C^{5+} emission comes from the plasma edge. The spectra from the wavelength regions of interest show very little trace of lines at 5305 Å while the 5290 Å line is clearly visible (Fig. 3). Since the components of the neutral carbon and O^{3+} multiplets at 5290 Å have lower statistical weight than the 5305 Å components this convinced us that there is no significant contribution from other species than C^{5+} in our case.

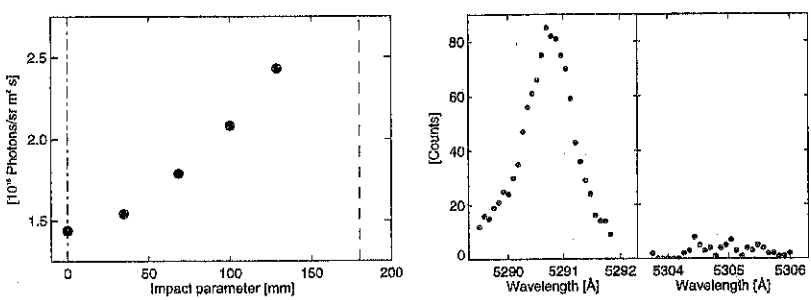

Fig. 3 Brightness profile for C^{5+} from discharge #5437 together with a spectra showing the 5290 Å line and an interval around 5305 Å where lines from the same carbon and oxygen multiplets which have components at 5290 Å occur.

The spectra show that the 5290 Å line is not actually one line but a mix of C^{5+} lines from n=8 to n=7 transitions with different l quantum numbers [6,7].

Conclusions

The results from radially resolved spectroscopic measurements on the 5290 Å line in C^{5+} have shown that there is a significant contribution from the plasma edge to the measured brightness from this transition. The correlation with sudden increases in H_α emission has lead us to the conclusion that this edge emission comes from charge exchange of C^{6+} with neutral hydrogen. The increase in H_α is likely to come from inflow of neutral hydrogen due to plasma-wall interaction. This implicates the abundance of fully stripped carbon at the edge of a plasma with a central electron temperature of less than 200 eV and an edge temperature of about 10 eV. Since the ionisation energy of C^{5+} is 490 eV this raises interesting questions concerning the heating and transport processes of electrons and ions in the EXTRAP-T2 plasmas which are yet to be answered.

References

[1] S. Hokin et. al., 23:rd EPS Conf. on Controlled Fusion and Plasma Physics, Kiev, Ukraine, II-625 (1996).

[2] A. M. Cormack, J. Applied Physics **34**, 2722 (1963).

[3] A. M. Cormack, J. Applied Physics **35**, 2908 (1964).

[4] R. S. Granetz, P. Smeulders, Nuclear Fusion **28**, 457 (1988).

[5] A. Welander, TRITA-ALF-1995-05, ISSN 1102-2051.

[6] G. W. Erickson, J. Phys. Chem. Ref. Data **6**, 831 (1977).

[7] W. R Hess, M. Mattioli, R. Guirlet, M. Druetta, EUR-CEA-FC-1477 (1993)

This work has been supported by the European Communities under an association contract between EURATOM and the Swedish Natural Science Research Council (NFR). The participation in this conference has been supported by fundings from the Royal Swedish Academy of Sciences.

Experiments with externally controlled field errors on Extrap T2

G. Hedin

Department of Fusion Plasma Physics, Alfvén Laboratory, Royal Institute of Technology, SE-100 44 STOCKHOLM, Sweden, Association EURATOM/NFR

Introduction

Toroidally localized magnetic field perturbations occur naturally in reversed-field pinches, due to phase-locking of internally resonant tearing modes with poloidal mode number of $m = 1$ and toroidal mode numbers in the range $3R/2a - 5R/2a$. These perturbations have been observed to rotate in the electron diamagnetic drift direction, but can also become stationary (locked) in the lab frame, by interaction with external field errors, mainly from eddy currents in the shell at gaps and port holes. On conducting shell reversed-field pinches, $\tau_{shell} \gg \tau_{pulse}$, this results in a growth of the radial field component of the perturbation at the shell gaps [1,2]. With a resistive shell, $\tau_{shell} \ll \tau_{pulse}$, the radial field associated with the toroidal perturbation may grow at an arbitrary position on the shell time scale, developing what is called a resistive shell mode, RSM. The advantage of the resistive shell is that it removes the restriction on the pulse length and allows penetration of magnetic fields for equilibrium control. In addition, the field errors associated with eddy current in the shell will also decay on the same time scale, thereby removing the seed for locking to the wall. However, the disadvantage is that an external feed-back system must provide the stability for the RSM, by suppressing any radial flux appearing at the edge. In this context, knowledge of how the plasma responds to an external field perturbation is crucial in order to develop a working feed-back system.

When it comes to plasma performance, wall-locking of the RSM can enhance the plasma-wall interaction, releasing particles from the wall, thereby cooling the plasma and increasing the plasma resistance. While this is a subtle effect at low currents (100-150 kA), it becomes more of an obstacle at higher currents and prevents us from operating with plasma currents above 220 kA. In order to reach higher current and improve performance at medium current, the interaction between the RSM, field errors and the wall must be understood.

Plasma response to an external field perturbation

Earlier experiments on EXTRAP T2, showed that by shifting the radial equilibrium, thereby enhancing the field error due to the gap, the perturbation could be forced to appear at the position of the gap. In order understand the interaction between of an external field perturbation and the plasma, a saddle-coil was placed on the machine. The saddle–coil has one single turn and produce a vertical $m = 1$ field error, with a toroidal extent of 25°, corresponding to toroidal mode numbers in the range $n \in [0, 25]$. A maximum amplitude of 16 mT can be applied, approximately 10% of the edge poloidal field for a standard 150 kA discharge. The coil is connected to an independent power supply and can be turned on and off during a single discharge. The vertical field produced by the coil has a measured shell penetration time of $\tau = 0.7$ ms. The plasma response to the error field was measured by internal vertical field coils and an extensive set of radial pickup-coils outside the shell. A series of experiments were made where the applied field error amplitude was varied between -15 mT to 15 mT, at three different levels of plasma current; 120 kA, 150 kA and 180 kA and at three different values of the pinch parameter, $\Theta = B_\theta(a)/\langle B_\phi \rangle$; 1.6, 1.8 and 2.0.

The results can be summarized as: (i.) The applied error field is amplified by the plasma and result in a net error field many times the originally applied value. (ii.) The induced error field in the plasma does not decay once the applied field is removed, instead it persists throughout the discharge, after which the error field decays on the shell time scale, figure 1. (iii.) The growth of the net perturbation is approximately linear and proportional to the amplitude of the applied field error, figure 3. (iv.)An initial field error at the coil position can be corrected by the applied field, however the time derivative of the field is not affected by the initial error field, figure 2. (v.) No clear pinch parameter Θ, or the plasma current dependence can be observed on the growth of the error field, however, with higher plasma current a large error field can be reached before termination of the plasma, figure 4.

Effects of wall-locking

On EXTRAP T2 the RSM appears at an arbitrary toroidal position, 1 or 2 ms into the discharge, and is observed as a stationary (locked) $m = 1, n \geq 10$ radial field perturbation with a toroidal extent of $\Delta\phi \approx 60°$ and a perturbation amplitude in the range from B =5-20 mT. In discharges where the RSM amplitude reaches a level of $B^{m=1} \geq 0.1 B_\vartheta(a)$, a plasma-wall interaction event usually occurs, with release of hydrogen and impurities from the wall. The overall effect on plasma performance is current dependent, and for plasma currents of 150 kA and below, the event is subtle and leads usually to a shorter discharge with higher density and decaying plasma current. At plasma current 180 kA - 200 kA, up to 40% of the current can be rapidly lost during the event, after which the discharge usually continues as a decaying low-current discharge. Above 220 kA the plasma always terminates rapidly with a large power load to the wall, releasing large amounts of hydrogen and impurities from the wall. After such a "hard" termination, a helium glow discharge cleaning must be performed in order to recover low resistance plasma discharges.

Since the RSM has no single prefered position on the torus and does not appear at a fixed time, quantification of wall-locking effect on the plasma have so far been difficult. With the external field error, however, we can provoke plasma-wall interaction at a particular position, at which spectroscopic diagnostics can be concentrated. With the field error temporal scan of the electron temperature and density profile was obtained using Thomson scattering, during a plasma-wall interaction event.

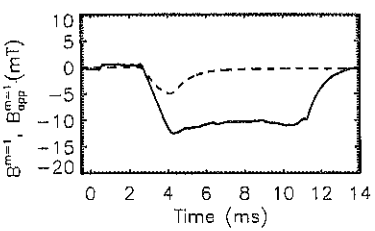

Figure 1. *The field inside the shell (—) and the applied field from the coil (– –). The that plasma responds to the external field error by amplifying it and sustaining it after the removal of the external field.*

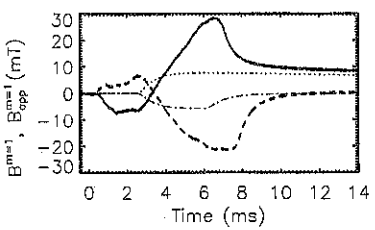

Figure 2. *Two discharges where initial field errors are corrected by the applied external perturbation. Case a, initial positive field error (—) and applied field (···). Case b, initial negative field error (- -) and field (··).*

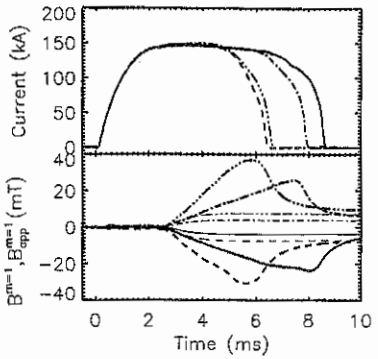

Figure 3. Top: plasma current for four discharges where external fields of -8 mT(- -), -4 mT (—), +4 mT (---) and +8 mT (-·-·-) respectively are applied. Bottom: field inside the shell, thin lines correspond to the four levels of applied field.

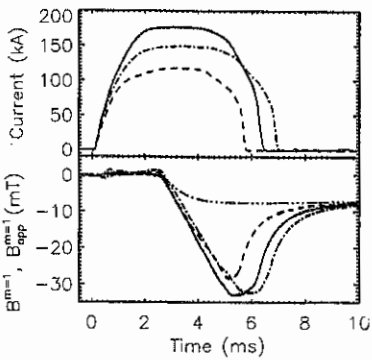

Figure 4. Top: plasma current for three discharges I_p = 120 kA (- -), I_p = 150 kA (---) and I_p = 180 kA (—). Bottom: field inside the shell for the three currents and the applied field (-·-·-).

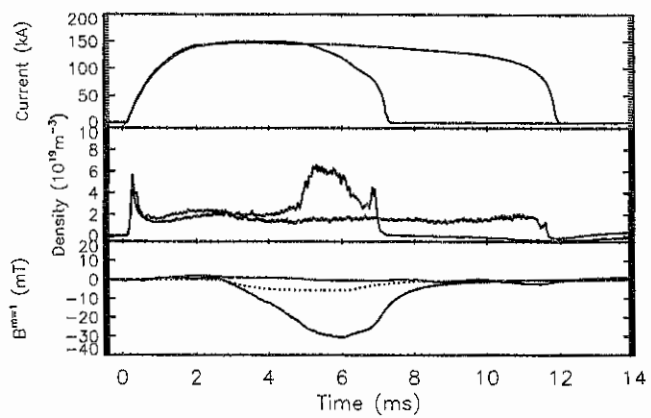

Figure 5. Comparison between two discharges; (a.) where a plasma-wall interaction event is triggered by an applied field error, (b.) no applied field. Top: plasma current. Middle: electron density. Bottom: field inside the shell (—) and the applied field for discharge (a.) The event occurs at 4.8 ms, at which the field perturbation is ≈20 mT.

[1.] Almagri *et.al.*, Phys Fluids B4 4080 (1992).

[2.] Brunsell *et.al.*, Phys Fluids B5 885 (1993).

1-D Neutral, Particle and Energy Transport Simulations for RFP Plasmas

Sam Hokin
Alfvén Laboratory Division of Fusion Plasma Physics
Association EURATOM-NFR
Royal Institute of Technology, Stockholm

Introduction. The reversed-field pinch has a very high level of magnetic fluctuations as a result of $m = 1, n \simeq 2R/a$ tearing modes. These modes are driven by the peaked current density profile resulting from strong Ohmic drive in the center where $\mathbf{E} \parallel \mathbf{J}$.

High magnetic activity is essential in the classical Ohmic RFP, as it provides the MHD dynamo motion EMF which drives poloidal current in the outer half of the plasma, maintaining the RFP magnetic topology: $\mathbf{E}_{dyn} = \langle \tilde{\mathbf{V}} \times \tilde{\mathbf{B}} \rangle$. This carrys a huge cost: magnetic fluctuation-induced transport is very large. Measurements on MST [1,2] and elsewhere indicate that it governs particle and energy transport in the inner 80% of the plasma, where the field is calculated to be stochastic [3]. Magnetic fluctuation energy is transported radially by the dynamo Poynting flux $\mathbf{S}_f = \langle \tilde{\mathbf{E}} \times \tilde{\mathbf{B}} \rangle$, which plays a major role in energy balance, transporting excess input energy from the core to the outer plasma.

This paper presents a 1-D model which simulates RFP particle, energy and neutral transport in the presence of stochastic magnetic fluctuations.

Transport Model. Conductive electron energy transport due to magnetic fluctuations [4] is very large, with heat diffusivity $\chi_e \simeq v_{te} D_m$, where D_m is the magnetic diffusivity $D_m = L_{eff} b_r^2$ and L_{eff} is the effective parallel correlation length. Convective energy transport is also large since fast electrons carry much of the electron particle flux. Measurements by Fiksel [2] show that $Q_e(r \simeq 0.8a)$ is substantially smaller than given by χ_e above and Terry has developed a theory explaining it [5]. However, in the core, one expects that Q_e is governed by χ_e above. The simulations presented here support this assertion.

Electron particle transport is reduced to the ion rate by the ambipolar potential. Harvey [6] derived the kinetic equation in the presence of E_a, from which one can obtain expressions for the ambipolar electric field

$$eE_a = -\frac{T_e}{n_e}\frac{dn_e}{dr} - \frac{1}{2}\frac{dT_e}{dr},$$

and the ambipolar particle flux

$$\Gamma_a = -D_i \left[\frac{dn_i}{dr} + \frac{n_i T_e}{n_e T_i}\frac{dn_e}{dr} + \frac{n_i}{2T_i}\left(\frac{dT_i}{dr} + \frac{dT_e}{dr} \right) \right],$$

where $D_i = \chi_i/2$. In addition, the classical particle pinch due to the inductive electric field $V_p = -E_\phi B_\theta / B^2$ has been included in runs reported here.

Another important aspect of the ambipolar potential is electrostatic energy transfer between electrons and ions: $P_a = eE_a\Gamma$ is lost by electrons as they move outward against E_a and (by ambipolarity) the same amount is gained by the ions, an important effect since $P_a \simeq P_{ei}$.

The energy flux has a similar form for both ions and electrons: $Q = 2\Gamma T - \chi n dT/dr$. The second, conductive, term dominates in these simulations.

In many runs with only magnetic fluctuation-induced transport, unreasonably high values of τ_p and low values of neutral density result. This is because edge particle transport in the RFP

is governed by *electrostatic* fluctuations and is quite large [7]. In order to simulate experimental values of τ_p and neutral density, an *ad hoc* edge diffusion term $D_{edge}(r/a)^{10}$ may be added. This has little effect on overall power balance and electron parameters, but has a large effect on the ion temperature since the neutral density and therefore charge-exchange loss is altered.

Additional Power Flow Terms. Electron dissipation $P_e = \eta J^2$ uses Spitzer resistivity and the alpha equilibrium model for $J^2(r)$, with finite pressure force balance included self-consistently.

Radiated power P_{rad} is represented by a simple function which reproduces typical experimental radiation profiles: $P_{rad} = C_{rad}(r/a)^8 P_e$, where C_{rad} is an adjustable constant.

Fluctuation ion heating may be included using a simple model: $P_{fi} = \nu_{fi} U_f$ where U_f is the local fluctuation energy density. Classical ion heating results when $\nu_{fi} = 0$.

The toroidal electric field E_ϕ is calculated by the steady-state constraint that the total power going into fluctuations is zero. The only quantity in the calculation which depends on E_ϕ is the radial pinch velocity V_p. E_ϕ is one of the key outputs of the code to be compared with experiment.

Numerical Implementation. The code RFPEQ combines the above transport model with a self-consistent calculation of the neutral hydrogen profile. This is important, since charge-exchange loss is important in ion energy balance, and the particle source term governs Γ and therefore has a large effect on all of the calculation. The code therefore has two sections:

(1) Calculate $n_H(r)$ for given profiles $n_e(r)$, $T_e(r)$ and $T_i(r)$, by solving the collisionless Boltzmann equation for neutrals in cylindrical geometry using the method of successive approximations [8]. This physically corresponds to keeping track of multiple charge-exchange generations.

(2) Calculate $n_e(r)$, $T_e(r)$, $T_i(r)$, $\Gamma(r)$, $Q_e(r)$ and $Q_i(r)$ for a given $n_H(r)$ using 4th-order Runge-Kutta integration of the particle and heat diffusion, heat flux, continuity and power balance equations with shooting from $r = 0$ and $r = a$ to a fitting point to satisfy boundary conditions $\Gamma(0) = 0$, $Q_e(0) = 0$, $Q_i(0) = 0$, n_{ea}, T_{ea} and T_{ia}.

Steps 1 and 2 are iterated until the profiles converge to fixed values.

Although the 6 first-order differential equations in step 2 are highly coupled and nonlinear, they are solved in such an order that equations requiring a particular derivative are solved after that derivative has been calculated. In order of calculation they are:

$$(r\Gamma)' = r n_e n_H \langle \sigma_i v \rangle, \tag{1}$$

$$T_e' = \frac{-Q_e + Q_e^{conv}}{\chi_e n_e}, \tag{2}$$

$$T_i' = \frac{-Q_i + Q_i^{conv}}{\chi_i n_i}, \tag{3}$$

$$n_e' = -\frac{n_e}{n_i}\frac{\Gamma - n_e V_p}{D_i(1 + T_e/T_i)} - \frac{n_e}{2}\frac{T_e' + T_i'}{T_e + T_i}, \tag{4}$$

$$(rQ_e)' = r(P_e - P_{ei} - P_{rad} - P_a), \tag{5}$$

$$(rQ_i)' = r(P_{fi} + P_{ei} - P_{cx} + P_a). \tag{6}$$

In order to simplify the equations and provide closure, a single ion impurity species of charge Ze is assumed, so that $n_i(r)/n_e(r) = (Z - Z_{eff}(r))/(Z - 1)$.

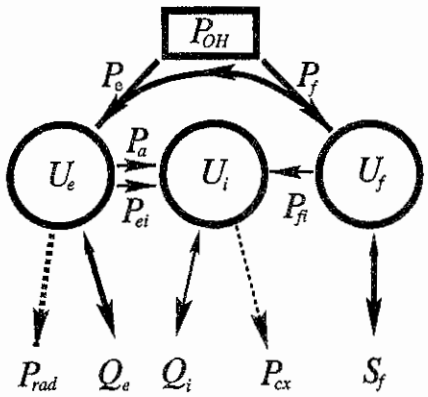

Figure 1: RFPEQ energy flow diagram.

P_{OH}	3.59
P_e	+3.59
P_{ei}	-0.13
P_a	-0.26
P_{rad}	-0.77
$Q_e(a)$	-2.41
P_{ei}	+0.13
P_a	+0.26
P_{fi}	+0.00
P_{cx}	-0.17
$Q_i(a)$	-0.22

Table 1: Volume-integrated power per toroidal length (kW/cm) from the MST 340 kA standard case shown in Fig. 2.

Fig. 1 summarizes the energy flow, almost entirely governed by electrons (P_e, Q_e, P_{rad}) and the dynamo Poynting flux S_f, indicated with thicker lines. Due to low thermal speeds, ions are well-confined and reach temperatures near the electron temperature with very little power input. Anomalous ion heating required to reach $T_i > T_e$ is a small fraction of Ohmic input. Volume-integrated power values for the MST 340 kA standard RFP simulation presented next are given in Table 1.

Simulations: MST Standard RFP and PPCD. I applied RFPEQ to standard and pulsed poloidal current drive (PPCD) MST discharges [9] to see if the observed improvement in confinement with reduced fluctuation level is reproduced. The profiles are shown in Fig. 2. For the standard RFP case, $n_H(a) = 3.8 \times 10^{10}$ cm^{-3} and $D_{edge} = 1.5 \times 10^5$ cm^2/s were set to match the experimental values of $\overline{n}_e = 1 \times 10^{13}$ cm^{-3} and $\tau_p = 4$ ms. $L_{eff} = 0.2a$ was set to match the experimental $T_{e0} = 230$ eV with the reported value of $b_r = 1.5\%$. For the PPCD case, D_{edge} and L_{eff} were fixed at the standard RFP values, $n_H(a)$ was reduced to 1.1×10^{10} cm^{-3} to hold $\overline{n}_e$ constant and other parameters were changed according to measurements, in particular $b_r = 0.8\%$. Ions were heated classically ($\nu_{fi} = 0$).

The simulated increase of T_{e0} from 230 to 350 eV and τ_E from 0.9 to 3.2 ms with application of PPCD compares favorably with the reported increase from 230 to 390 eV and 1 to 5 ms, respectively. The main discrepancy is in T_i, which remained constant at 115 eV in the experiment but increased from 113 to 221 eV in the simulation due to reduced transport and charge-exchange loss.

Simulations: Beta vs I/N Scaling. Although different RFPs exhibit different loop voltages, confinement times, etc., one trend appears to be universal: electron beta increases with increasing density. Most RFPs show a scaling close to $\beta_{pe} \propto (I/N)^{-2/3}$ (dotted lines). This can be explained as a consequence of $\chi_e \propto T_e^{1/2}$ for magnetic fluctuation-induced transport combined with power loss dominated by electron heat conduction and power input given by Spitzer resistivity in which case $\beta_{pe} \propto (ab_r T_e)^{-2}$ and, substituting for T_e in terms of β_{pe} and I/N, $\beta_{pe} \propto (aIb_r(I/N))^{-2/3}$.

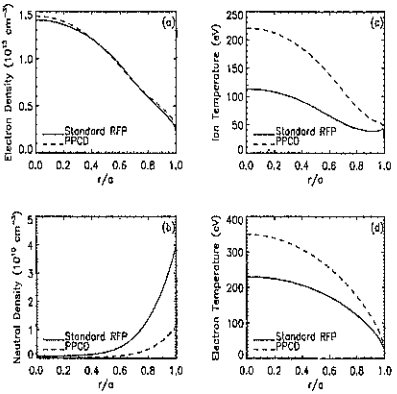

Figure 2: Simulated profiles for 340 kA MST standard RFP and PPCD conditions.

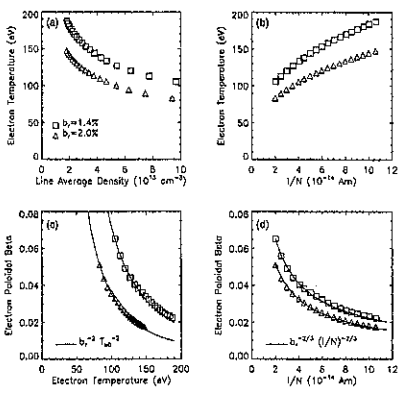

Figure 3: Density scaling simulation for two fluctuation levels in T2 at 180 kA.

I have used RFPEQ to study the scaling of β_{pe} with density (and therefore T_e and I/N) for the T2 RFP ($a = 18.3$ cm) at $I = 180$ kA and two b_r values. The results are shown in Fig. 3. $\beta_{pe} \propto (I/N)^{-2/3}$ scaling due to $\chi_e \propto T_e^{1/2}$ is reproduced in the simulations.

Summary. The 1-D neutral/particle/energy transport code RFPEQ models core magnetic fluctuation-driven transport with a self-consistent ambipolar electric field, implicit inclusion of the dynamo Poynting flux, a self-consistent neutral calculation, and a simple fluctuation ion heating model. Several conclusions may be drawn from these and other simulations: (1) Energy transport is dominated by conductive electron heat flux and dynamo Poynting flux. (2) High classical T_i results from good ion confinement and electron–ion electrostatic energy exchange. (3) Edge particle transport has a strong effect on T_i due to the strong charge-exchange dependence on neutral density. (4) Experimental τ_E values are nearly reproduced in a simulation of 340 kA MST standard RFP and PPCD discharges. (5) Experimental scaling $\beta_{pe} \propto (I/N)^{-2/3}$ is reproduced and explained as a result of dominant conductive electron heat flux with $\chi_e \propto T_e^{1/2}$.

[1] G. Fiksel *et al.*, Phys. Rev. Lett. **72**, 1028 (1994).

[2] M. Stoneking *et al.*, Phys. Rev. Lett. **73**, 549 (1994).

[3] E. Caramana, R. Nebel and D. Schnack, Phys. Fluids **26**, 1305 (1983).

[4] A. Rechester and M. Rosenbluth, Phys. Rev. Lett. **40**, 38 (1978).

[5] P. Terry, G. Fiksel and A. Ware, Phys. Plasmas **3**, 1999 (1996).

[6] R. Harvey *et al.*, Phys. Rev. Lett. **47**, 102 (1981).

[7] T. Rempel *et al.*, Phys. Rev. Lett. **67**, 1438 (1991).

[8] Y. Dnestrovskii and D. Kostomarov, *Numerical Simulation of Plasmas* (Springer-Verlag, 1986).

[9] M. Stoneking *et al.*, Phys. Plasmas **4**, 1632 (1997).

Electrostatic Fluctuations and Edge Transport in the Extrap T2

A. Möller

Division of Fusion Plasma Physics, Alfvén Laboratory, Royal Institute of Technology
SE-100 44 STOCKHOLM, Sweden, Association EURATOM/NFR

1 Introduction

Electrostatic fluctuations have been identified to be the responsible mechanism for particle transport in the edge region of reversed-field pinches (RFPs), e.g. [1, 2]. Improved edge confinement requires reduction of edge electrostatic fluctuations and it is therefore of importance to understand the underlying mechanisms driving the edge electrostatic turbulence. In this paper, we report on the characteristics of electrostatic fluctuations in Extrap T2, a mid size RFP with aspect ratio $R/a = 1.24$ m/0.183 m.

2 Experimental

A 4-pin Langmuir probe covers the region $0.9 < r/a < 1.0$ and radial profiles can be created by moving the probe from shot to shot. The four probe tips are arranged in a square with 7 mm diagonal where two toroidally separated pins measure floating potential. Data are analysed using triple probe technique giving time resolved measurement of electron temperature T_e, electron density n_e, floating potential Φ_{fl} and plasma potential Φ_{pl}. The two toroidally separated floating potentials enables the Φ_{fl} combined toroidal wave number k_ϕ and frequency f spectrum $S(k_\phi, f)$ to be estimated from two point correlation. The particle flux $\Gamma_{E\times B}$ resulting from correlated fluctuations in $E \times B$ velocity and density fluctuations is calculated. Full radial profiles were made at low plasma current $I_p = 120$ kA while measurements at larger currents, 150 and 180 kA, were made mainly at fixed position $r = 173$ mm. The pinch parameter was $\Theta = 1.8$ and the reversal parameter was $F = -0.35$.

3 Results and Discussion

Figure 1 shows radial profiles of the average and relative fluctuation levels of all measured quantities at low plasma current $I_p = 120$ kA. The decay lengths of T_e and n_e in fig 1a are $\lambda_T = 14$ mm and $\lambda_n = 13$ mm, leading to an electron diamagnetic drift velocity of about -25 km/s at $r = 173$ mm. A minimum in the plasma potential in fig 1b is found at $r \approx 170$ mm with electric fields $E_r(r < 170) \approx 6.0$ kV/m and $E_r(r > 170) \approx -4.4$ kV/m. The $E_r(r > 170)$ gives rise to an $E \times B$ velocity of about -30 km/s while $E_r(r < 170)$

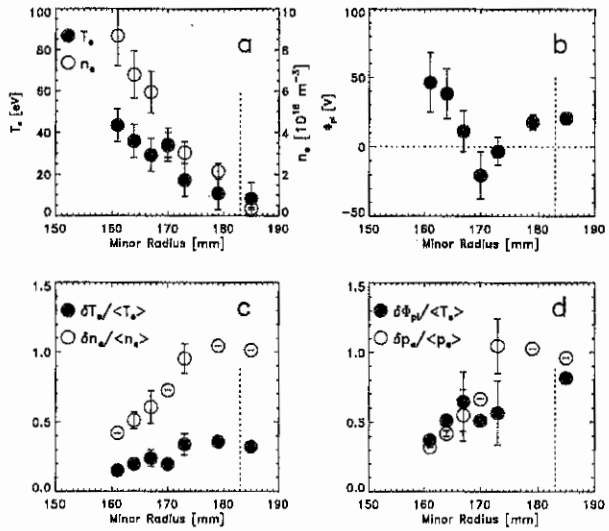

Figure 1 *Radial profiles at* $I_p = 120$ *kA*

induces a positive drift velocity of about 40 km/s. The general trend was that the decay lengths decrease and the E_r increases with increasing I_p. The relative fluctuation levels in fig 1c,d are comparable to fluctuation levels measured in other RFPs. We note here that the density and potential fluctuations approximately satisfy the Boltzman relation.

The combined toroidal wave number and frequency spectrum $S(k_\phi, f)$ is shown in figure 2a. The largest power density is found in the region $f < 50\ kHz$ and $-25 < k_\phi/\mathrm{m}^{-1} < 25$. A second peak is evident at $k_\phi \approx -40$ m^{-1} and $f \approx 140$ kHz implying a phase velocity v_ϕ of the peak of about -25 km/s. This peak is generally seen for any type of discharge parameters even though it in some cases degenerates to a plateau in the spectrum. We focus on this peak and denote the frequency and wave number of the peak f_{peak} and $k_{\phi,peak}$ respectively. The location of the peak was studied as function of global and local plasma parameters with the conclusion that the variation in $k_{\phi,peak}$ was small in the range -30--40 m^{-1} corresponding to a toroidal wave length in the range 0.21-0.16 m. The frequency f_{peak} depends mainly on I_p, and the local density n_e as shown in fig 2d where f_{peak} is plotted as function of n_e for different I_p. An increase in f_{peak} also implies an increase in the toroidal phase velocity since $k_{\phi,peak}$ is about constant. The toroidal distance traveled on an edge field line in one poloidal turn is $2\pi a \cdot |F| / \Theta = 0.22$ m, which

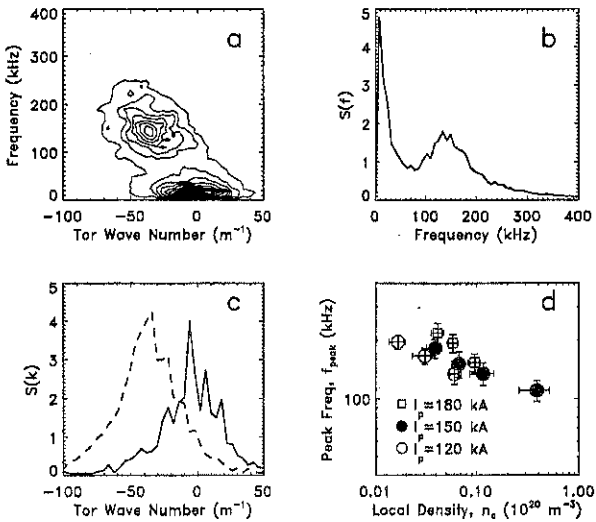

Figure 2 *Floating potential spectra averaged over 18 discharges, $r = 173$ mm: (a) $S(k_\phi, f)$, (b) $S(f)$, (c) $S(k_\phi)$ dashed line $f < 75$ kHz , solid line $f > 75$ kHz. (d) The frequency position of the second peak in the $S(k_\phi, f)$ spectrum.*

is close to the observed toroidal wave length at the peak indicating that it is resonant with the edge magnetic field. The basic structure of the spectrum with a negative $k_{\phi,peak}$ was the same for all radial positions, independent of the direction of E_r. The fluctuations have the features of a drift wave traveling with the electron diamagnetic drift velocity. The observed I_p scaling can be associated with profile steepening which leads to higher drift velocity.

The peak can also be seen in the integrated power spectrum $S(f)$ in figure 2b as a local maximum around 140 kHz. A similar peak was also reported on Extrap T1 but its frequency scaling with other plasma parameters could not be determined [3]. It is also interesting to compare with results from RFX where a plateau in $S(f)$ at $f \approx 100$ kHz has been reported [2]. This plateau may be the same feature as the peak we observe.

The global τ_p has not yet been measured on Extrap T2. However, the τ_p derived from $\Gamma_{E\times B}$ was nearly one order of magnitude larger than τ_E. The frequency spectrum of $\Gamma_{E\times B}$ is shown in figure 3a. The two curves represent ensemble averages of 4-5 discharges selected with similar values of f_{peak}. The solid line represents $100 < f_{peak}/\text{kHz} < 130$

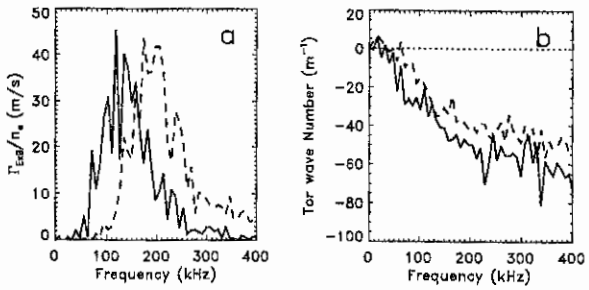

Figure 3 $\Gamma_{E\times B}$ *(a) and toroidal wave number (b) as function of frequency. The solid line represents* $100 < f_{peak}/kHz < 130$ *while the dashed line represents* $160 < f_{peak}/kHz < 190$.

while the dashed line represents $160 < f_{peak}/\mathrm{kHz} < 190$. Since different values of f_{peak} also means different values of n_e, $\Gamma_{E\times B}$ has been normalised to n_e but we mainly focus on the structure of the spectra. The maximum transport is observed approximately at f_{peak} but the interesting feature is the lack of transport at frequencies below f_{peak}. The fluctuations in the origin of the $S(k_\phi, f)$ spectrum does not seem to contribute to the particle transport which instead is dominated by the peak. The main reason for the low transport at low frequencies was the vanishing k_ϕ, as can be seen in fig 3b.

4 Conclusions

Electrostatic fluctuations and particle transport caused by coherent potential and density fluctuations have been measured in Extrap T2. The fluctuation power is concentrated in two peaks in the $S(k_\phi, f)$ spectrum. One peak appears in the origin of the spectrum while the other peak appears at $-40 < k_\phi/\mathrm{m}^{-1} < -30$, $100 < f/\mathrm{kHz} < 200$. The second peak is resonant with the edge magnetic field and has the features of a drift wave with a phase velocity equal to the electron diamagnetic drift velocity. This peak does also seem to dominate the measured particle transport.

References

[1] REMPEL, T. D., SPRAGINS, C. W., PRAGER, S. C., et al., Phys. Rev. Lett **67** (1991) 1438.

[2] ANTONI, V., BAGATIN, M., CAVAZZANA, R., et al., Poster presented at the US-EU workshop of Transport Task Force, Madison, 1997.

[3] LI, G. X., DRAKE, J. R., BERGSÅKER, H., et al., Phys. Plasmas **2** (1995) 2615.

Numerical Simulations of Induced Toroidal Rotation in the Reversed Field Pinch

H.-E. Sätherblom and J. R. Drake

Division of Fusion Plasma Physics (Association EURATOM-NFR), Alfvén Laboratory, Royal Institute of Technology, SE-100 44 Stockholm, Sweden

D. D. Schnack

Applied Physics Operation, Science Applications International Corp. 10260 Campus Point Drive, San Diego CA 92121

The phenomenon of plasma modes phase locking to some features of the stationary frame (wall-locking) has been frequently observed in many Reversed Field Pinch (RFP) experiments and is observed in the Extrap T2 device. This phenomena is a severe obstacle for good plasma performance and can cause extensive wall damage. Differential rotation has been found to decouple modes in the Tokamak [1]. A rotation induced by means of external magnetic field coils could be suitable for forcing the plasma modes to detach from the wall in an RFP experiment. The proposal is that the coils are made with a pitch and phase corresponding to a mode internal to the plasma. The coils are then fed with currents in such a way that they produce a wave resonant to the internal mode.

In this paper we present the status of an ongoing numerical study of the effects of an induced toroidal plasma rotation on the RFP performance. As the tool for this study we use the 3-dimensional, resistive, non-linear MHD code DEBS [2]. With this code it has been possible to reproduce the main features of the RFP. The DEBS-code solves the resistive MHD equations in a cylinder, periodic in the poloidal θ and toroidal ϕ directions:

$$\partial \mathbf{A}/\partial t = -\mathbf{E} = S\mathbf{V} \times \mathbf{B} - \eta \mathbf{J} \qquad (1)$$

$$\partial \mathbf{V}/\partial t = -S\mathbf{V} \cdot \nabla \mathbf{V} + S\mathbf{J} \times \mathbf{B} - \nu \nabla^2 \mathbf{V} \qquad (2)$$

The code uses a semi-implicit method which adjusts the code time step to the dynamic activity in the code. In this version of the code the pressure gradient is set to zero. For the present calculations we use 161 radial grid points. Poloidal mode numbers range from m=0 to 2 and toroidal mode numbers from n=-21 to 21. We use a Lundquist number of 10^4 and a viscosity of 1.5 in normalised units. The aspect ratio is 2.2. We use a resistivity profile of the form $\eta(r)=(1+9(r/a)^{10})^2$ where a is the minor radius. This profile is not evolved in time.

In this version of the code, named DEBS56, the toroidal current and the pinch parameter $\Theta=B_\theta(a)/\langle B_\phi\rangle$ are strictly constant in time and the toroidal loop-voltage is adjusted accordingly. This is a difference compared to the previous version of the code, named DEBS55, where the toroidal current and thus also the pinch parameter was dynamically adjusted to match a constant reference value by means of the toroidal loop-voltage. A comparison between the old code version DEBS55 and the new version DEBS56 showed the same qualitative RFP behaviour.

In DEBS56 we induce an artificial toroidal rotation in the code by means of the friction force term added to Eq. (1):

$$\partial V_z/\partial t = \cdots + \nu_f (V_0 - V_z) \qquad (3)$$

This term would, in the absence of other forces, lead to an 'spinning-up' of the plasma from $V_z=0$ to $V_z=V_0$ with a 'spinning-up' time-constant $\tau_{sp}=1/\nu_f$:

$$V_z(t) = V_0(1-e^{t/\tau_{sp}}) \qquad (4)$$

where V is normalised to the Alfvén velocity V_A and τ_s to the Alfvén time τ_A.

The code is run for 500 τ_A with a conducting shell in order to achieve the quasi-stationary state. This state is used as the initial configuration for the following simulations in this study. We simulate a case with a conducting shell at minor radius $r=a$ to be used as a reference. For this case there is no wall locking and the structure of the perturbations move slowly and apparently randomly in the toroidal direction. Next, the conducting shell case with the induced toroidal rotation is simulated. For this case, an acceleration of the perturbation pattern toroidally, up to a constant velocity, is observed.

In the next series, we introduce a resistive shell with a shell time $\tau_s=\tau_R/15$, which replaces the conducting shell at minor radius $r=a$, where τ_R is the resistive diffusion time of the plasma. A second, conducting shell is placed at $r=2a$. For this case, the observed evolution of the perturbation pattern is to lock at toroidal positions as determined by the positions of the initial perturbations in the configuration. This is shown in Fig. 1, where the radial magnetic field b_r is plotted vs. the toroidal position z (horizontal axis), and time t, normalised to τ_R (vertical axis), at $(r,\theta) = (a/2,0)$. Both V_0 and ν_f are zero for this case. It is observed that b_r in the edge region increases, compared to the conducting shell cases.

Another case examined is with a non-zero value of ν_f but with zero V_0. The toroidal locking for this case is similar to the previous case.

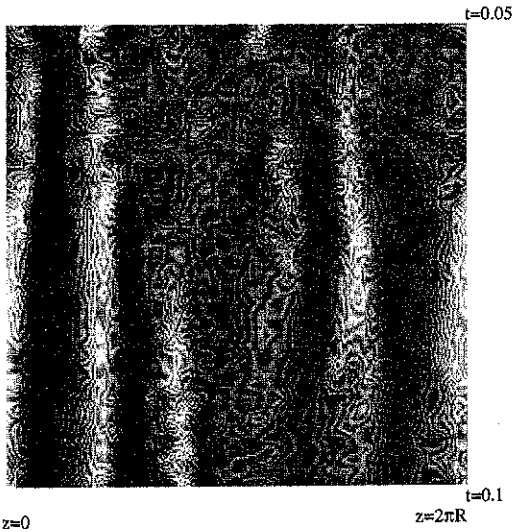

Fig 1.: The radial magnetic field b_r at $(r,\theta)=(a/2,0)$ vs. toroidal position $z=0\text{-}2\pi R$ (horizontal axis), and time $t=0.05\text{-}0.1$, normalised to τ_R (vertical axis), with resistive shell, $\tau_s=\tau_R/15$. $\nu_f=0$, $V_0=0$.

In the next series, rotation was introduced. With increasing values of ν_f and V_0 we observe a growing influence on the mode locking pattern and, beyond a threshold value of the friction force, the wall locking is suppressed and the modes start to rotate. This is illustrated in Fig. 2, where again we plot the radial magnetic field b_r vs. z and time t, normalised to τ_R, at $(r,\theta)=(a/2,0)$. For this case, $\nu_f=50$ and $V_0 = 0.25$. It is seen in Fig.2 that the plasma reaches a toroidal velocity of about $V_z=0.1$ after an acceleration time of around 200 τ_A, which is not in agreement with Eq. (4). Thus, forces exists that counteract and balance the induced toroidal rotation.

Rotation also affects the mode spectra, both for the conducting shell case and the resistive shell case. The rotation gives rise to a substantial spectrum broadening accompanied by bursts of n>0 modes.

These results indicate that the problem of RFP wall locking might be solved by inducing plasma toroidal rotation. One observation in the code simulation is that the transition from locked modes to rotation as $\nu_f V_0$ is increased has an intermediate phase where the mode locked pattern extends over only part of the z coordinate range. Similar observations have been made in the Extrap T2 experiment [3].

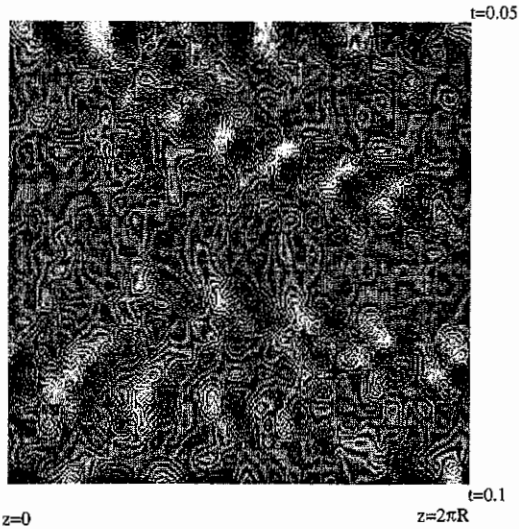

Fig 2.: The radial magnetic field b_r at $(r,\theta)=(a/2,0)$ vs. toroidal position $z=0\text{-}2\pi R$ (horizontal axis), and time $t=0.05\text{-}0.1$, normalised to τ_R (vertical axis), with resistive shell, $\tau_s=\tau_R/15$. $V_f=50$, $V_0=0.25$.

We will continue this study, starting with an investigation of the effects caused by field errors, which will be applied by means of currents in the shell. We will study field errors both in the form of single helicity modes as well as toroidally localised forms. Finally, we will try to induce the toroidal rotation by means of currents in external coils.

We believe the work presented in this paper has demonstrated the first steps towards of a possible solution of the severe problem of wall locking in the RFP.

This work was supported by the European Communities under an association contract between EURATOM and the Swedish Natural Science Research Council. NSC at Linköping is acknowledged for the access of the CRAY YMP.

[1] R. Fitzpatrick et. al., Nucl. Fusion **33**, 1533 (1993).

[2] D.D. Schnack et. al., Comput. Phys. Comm. **43**, 17 (1986).

[3] S. Hokin et. al., 23:d EPS Conf. on Controlled Fusion and Plasma Physics, Kiev, Ukraine, II-625 (1996).

Ion temperature anisotropy and toroidal rotation of impurities in Extrap-T2 RFP plasma

J.H. Brzozowski, P. Hörling[1], J. Sallander[1], G. Hedin, A. Hedqvist[1], A. Welander, P.R. Brunsell, S. Hokin and J.R. Drake

Division of Fusion Plasma Physics (Association EURATOM-NFR), Alfvén Laboratory, [1]Dept. for Physics I, Royal Institute of Technology, S-100 44 Stockholm, Sweden

Anomalous ion heating is a common phenomenon in reversed field pinch plasmas but the mechanism responsible for the heating of the ions is still not fully understood. In order to contribute to this important question a series of measurements has been undertaken at the Extrap-T2 experiment in collaboration with the Repute Group from Tokyo University. The aim was to determine if there is an anisotropy in the ion temperatures when measuring in parallel ($T_{i\parallel}$) and perpendicular ($T_{i\perp}$) directions with respect to the magnetic field. Such an anisotropy has been observed earlier in the Repute plasma when run in the ULQ mode, but never reported for RFP experiments. The observation of ion temperature anisotropy would be an important contribution to the discussion about possible ion heating scenarios in the RFP plasma. Our measurements showed a clear anisotropy with the parallel component of the ion temperature exceeding the perpendicular by up to a factor of two or more [1].

In this paper we present some recent measurements using a different experimental set-up, which allows the study of both ion temperature anisotropy and toroidal rotation of impurities simultaneously, although at lower time resolution than the previous study.

The measurements are performed with two high spectral resolution spectrometers equipped with gateable OMA detectors Fig.1a. The lines of sight are chosen in the vicinity of each other to represent the same plasma region. In the present study only low time resolution, of the order of 1.7 ms, is obtained while two spectral lines are observed (28 pixels per line) due to the readout-time requirement of the detector of about 1 ms. Gating times are varied from 200 μs to 300 μs depending on detector sensitivity and line intensities. For the O^{+4} the detectors are run in a "tandem" mode, which means that both tangential and perpendicular directions are registered simultaneously and that both directions are observed by both spectrometers on a shot to shot basis. In this way any systematic difference between the measurements obtained from different spectrometers can be accounted for. Until now the results for other species are obtained on a shot to shot basis.

The data presented here are run at about 180 kA, which until now is the highest current at which relatively long reproducible series of plasma discharges can be obtained. The time traces from a typical shot are presented in Fig.1b. The dotted vertical lines represent the time points at

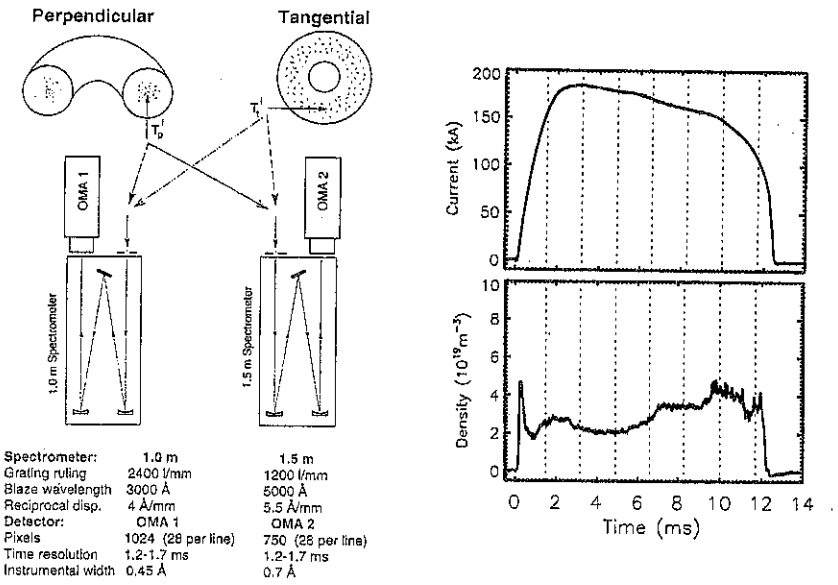

Fig.1 (a) A schematic view of the spectrometer set-up for "tandem" mode measurements, (b) Time traces from a discharge in Extrap-T2, vertical dotted lines show the data points (detectors gate-on).

which the detectors are gated on (centred at the gating time interval). The impurity ion temperature (T_i) and rotation is obtained from measurements of Doppler broadening and Doppler shift of emission lines in visible and near UV range. The measured T_{itang}/T_{iperp} (tangential / perpendicular) with respect to the minor axis is very close to the $T_{i\parallel}/T_{i\perp}$ with respect to the magnetic field, for O^{+4} and C^{+4}, according to the study reported in [1]. In this study the radial distribution of ion temperature was assumed parabolic and emissivity uniform. For lower ionisation stages with emissivity profiles close to the edge these assumptions may not apply.

The results presented in Fig.2 are obtained on shot to shot basis for all the species. Additionally the anisotropy results for O^{+4} ion are confirmed in the "tandem" runs where the direction measured is interchanged between the spectrometers typically every other shot. The relation between the measured anisotropy and plasma parameters is not clearly established yet. The lower ionisation stages are radiating from the plasma edge and O^{+4} and C^{+4} are radiating from the plasma centre. For O^{+4} and C^{+4} a clear anisotropy effect can be observed with the T_{itang} greater than the T_{iperp} by up to a factor of two. For lower ionisation stages no clear anisotropy can be observed. The range of ion temperatures in the plasma centre especially in the parallel direction exceeds the central electron temperature obtained from Thomson scattering

and/or VUV line ratios, which for this series of shots is on the average at about 120 eV level. In Fig.3 the anisotropy results for O^{+4} ion run in "tandem" mode are presented.

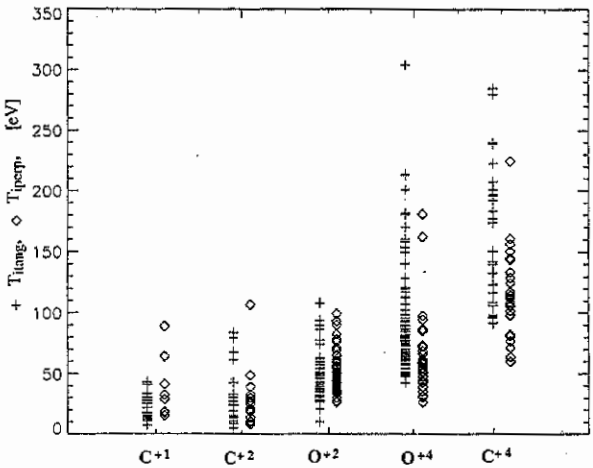

Fig.2 Anisotropy results for different ionisation stages of Carbon and Oxygen, + T_{itang} o T_{iperp}. From left to rigth: C^{+1}, C^{+2}, O^{+2}, O^{+4} and C^{+4}.

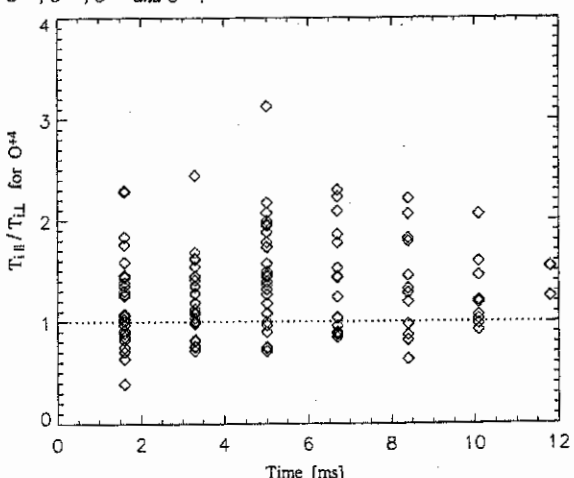

Fig.3 $T_{i\,||} / T_{i\perp}$ for O^{+4} ion run in "tandem" mode.

A model developed for taking account of both the anomalous ion heating and ion temperature anisotropy has been developed [2]. In this model a strong direct ion heating mechanism is postulated where low frequency ($<<\omega_{ci}$) magnetic fluctuations excited by global kink instability play an essential role. The instabilities excite low frequency perpendicular electric field which results in perpendicular motion of ions, and then damping of the perpendicular motion in the

parallel motion goes through the viscosity. The perpendicular motion which is equivalent to the magnetic perturbation works as a "magnetic pump" and temperature anisotropy can develop.

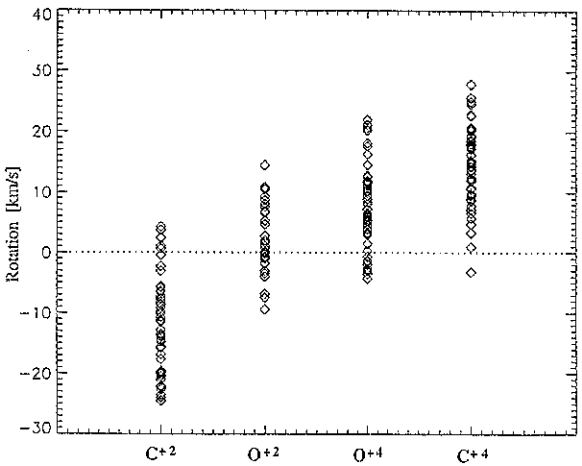

Fig.4 Toroidal rotation results, from left to right: C^{+2}, O^{+2}, O^{+4} and C^{+4}.

In Fig.4 rotation results are presented. The C^{+2} ion which is radiating from the plasma edge rotates preferentially in the direction opposite to the plasma current. The Langmuir probe measurements [3] show that the radial electric field is negative at the edge ($r > 0.93$ a, where a is the minor radius) and positive in the centre ($r < 0.93$ a). The rotation of C^{+2} ions is in the ExB drift direction. The diamagnetic drift for an ion with density profile expected for C^{+2} ion is also in the same direction. For O^{+2} ions the situation is different they behave as they were present at a minor radius in the vicinity of the point where the electric field changes sign and show the influence of both positive and negative electric field. O^{+4} and C^{+4} show almost only the influence of positive electric field which is consistent with their expected presence close to the plasma centre. The preliminary results of emissivity profiles for those ions show that C^{+4} is peaking at the centre while O^{+4} tends to show a slightly hollow profile. In such a case a contribution from diamagnetic drift would be in the positive direction for C^{+4} and in negative direction for O^{+4}. A series of measurements are planned using the "tandem" system for differential measurement of O^{+4} and C^{+4} rotation together with multi-chord viewing in order to resolve the contributions from E x B and diamagnetic drift to the observed rotation.

References:

[1] K.Sasaki et al., Plasma Physics and Controlled Fusion, **39**, 333-338, 1997.

[2] Z. Yoshida, Journal of Plasma and Fusion Research, **72**, 688-691, 1996.

[3] A. Möller, "Electrostatic fluctuations and edge transport in the Extrap T2", this conference.

Results from Thomson scattering measurements in the Extrap T2

A. Welander

Division of Fusion Plasma Physics, (Association EURATOM-NFR), Alfvén Laboratory, Royal Institute of Technology, S-100 44 Stockholm, Sweden

1. Introduction

Extrap T2 is a reversed field pinch (RFP) experiment with an aspect ratio (R/a = 1.24 m / 0.183 m). Plasma currents can be varied in the range from 60 to 220 kA and the line-averaged electron density from interferometry is in the range from below 10^{19} m^{-3} to 10^{20} m^{-3}. A Thomson scattering (TS) system is used to measure electron density and temperature at one selected time into the discharge at three minor radii (r/a = 0, 0.28, 0.56). The three spatial points have been used to define profile peaking factors for density, temperature and pressure. These peaking factors are in turn included in a data base in order to study the scaling with relevant parameters. The observed peaking factors correspond to a range of profiles from parabolic to hollow. There is substantial scatter in the data believed to be related to profile non axisymmetry due to a large internal mode structure also observed with magnetic diagnostics. The most apparent correlations for the density peaking factor are with the plasma current and the absolute value of the density. These quantities together with the temperature profile are also important for the empirical scaling of plasma confinement parameters.

2. Experimental

The TS profile data is very limited. However two peaking factors have been defined in order to gain some insight into possible dependencies of parameters on profile shapes. The first peaking parameter is defined in terms of TS data only and is given by $q(0)/\langle q_{TS}\rangle$ where $\langle q_{TS}\rangle$ is defined by $\langle q_{TS}\rangle=(q(0)+q(0.28)+q(0.56))/3$ and is the average of the three TS points. Here $q(r/a)$ signifies one of the measured quantities density (n_e), temperature (T_e) or pressure (p_e) at minor radius (r/a). This parameter characterises profile peaking in the inner region of the plasma. Since this factor is defined in terms of TS data alone, problems related to changes in absolute calibration do not affect the interpretation of the results. The second parameter $\langle n_{TS}\rangle/\langle n_e\rangle$ compares the average density of the inner region as measured by TS to the line-averaged density ($\langle n_e\rangle$) measured by interferometry. This parameter could give information on the steepness of the gradient in the edge region where there is no TS data (r/a>0.56). Since an average value for the central region is used to define the peaking factor, this method is less sensitive to small changes in the global equilibrium position of the plasma. On the other hand the TS data is compared with interferometer data, so changes in the TS calibration need to be accounted for which introduces an additional error.

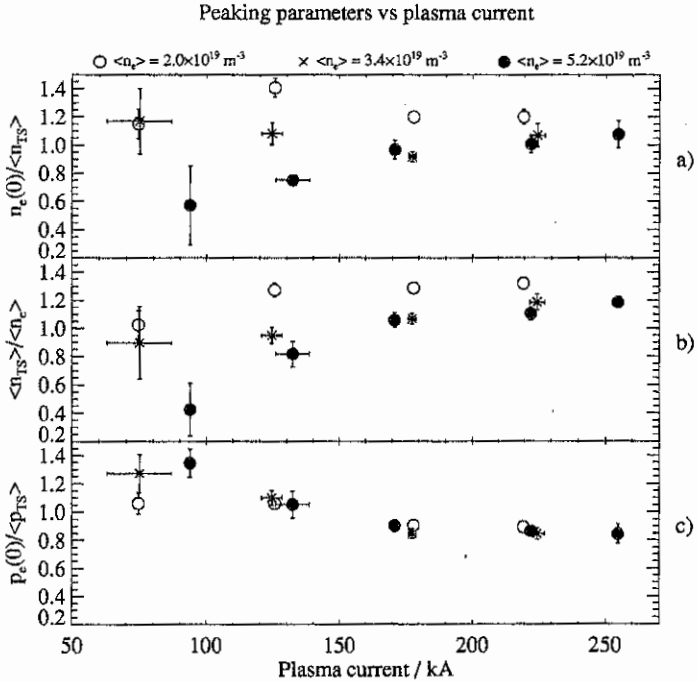

Fig. 1 Different peaking parameters are plotted versus discharge current. In a) the peaking of the density profile in the inner region, in b) the peaking of the density profile in the outer region and in c) the peaking of the pressure profile is indicated. Different symbols are used to denote measurements made with the line-averaged density in the intervals 0-3, 3-4 and 4-7×10^19 m^-3.

One common phenomenon in Extrap T2 discharges is the occurrence of a large localised mode structure at one toroidal position which is followed by an increase in density brought on by increased release of hydrogen from the wall due to intensive plasma wall loads. The data points studied here were all taken at early times into the discharge before these non reproducible and non axisymmetric effects occur. The error bars included represent three times the standard deviation of the ensemble-average values.

The two different density profile peaking parameters are plotted for a range of densities versus plasma current (I_p) in fig. 1. The high density series shows a clear tendency for hollow density profiles, whereas the lower density cases have more peaked profiles. For values of $\langle n_e \rangle$ below 3×10^{19} m^{-3}, both peaking parameters decrease with increasing $\langle n_e \rangle$ and are independent I_p. For values of $\langle n_e \rangle$ above 4×10^{19} m^{-3}, the situation changes and the peaking parameters instead depend on I_p only and increase with it. The pressure profile is always quite flat but is slightly more peaked for low plasma currents for the full range of densities.

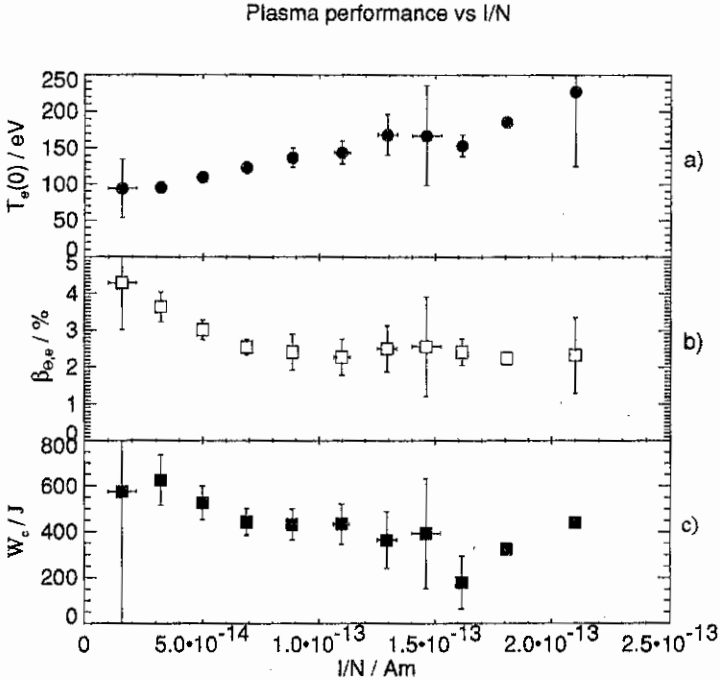

Fig. 2 The scaling of a) the central electron temperature, b) the poloidal electron β value and c) the electron energy content in the plasma with I/N.

The TS profile data has also been used to estimate the poloidal electron β value ($\beta_{\Theta,\varepsilon}$) and the electron energy content (W_e) in Extrap T2. In doing this, the edge electron density and temperature is modelled based on measurements by electrostatic probes [1]. Fig. 2 shows T_e, $\beta_{\Theta,\varepsilon}$ and W_e plotted versus I/N ($I/N \propto I_p/\langle n_e \rangle$). The central electron temperature ranges from 100-300 eV and the poloidal electron β is around 3 %. A regression analysis yields that very roughly $W_e \propto I_p^{1.0} \langle n_e \rangle^{0.35}$, $\beta_{\Theta,e} \propto I_p^{-0.25} \langle n_e \rangle^{0.15}$ and $T_e(0) \propto I_p^{1.2} \langle n_e \rangle^{-0.5}$.

The effect of the temperature profile on the electron energy content is shown in fig. 3. A peaking of the temperature profile resulting from an increased central temperature does not lead to a decrease of the plasma loop resistance (R_p) and a clear decrease of W_e is seen for peaked T_e profiles. Dividing W_e in fig. 3c by power input to the plasma (P_{in}) does not affect the observed trend but improves the correlation for the individual measurements. The trend is caused either by a degradation of the energy confinement time for electrons with higher T_e profile peaking or by a change in the fraction of P_{in} that heats the electrons. In fig. 3c it appears that W_e decreases

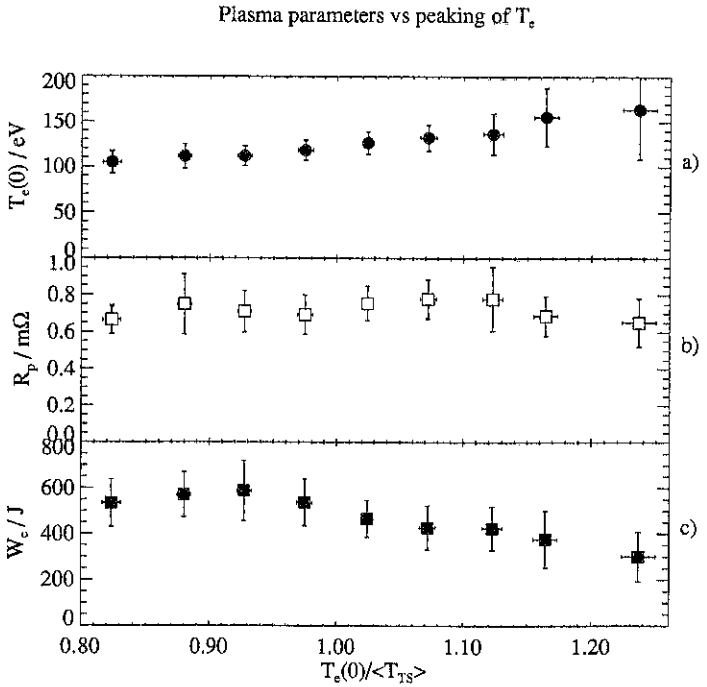

Fig. 3 Various parameters are plotted versus the temperature peaking parameter: in a) the central temperature, in b) the plasma loop resistance and in c) the electron energy content of the plasma.

with the global electron temperature gradient (the peaking parameter). However it is also the case that this peaking factor increases with increasing $T_e(0)$ and it is not determined what the important parameter is. A data base is being accumulated and this will be a subject for further study. One possible caveat here is that the trend in fig. 3c would be sensitive to random errors in the measured value of $T_e(0.56)$. However, plotting $p_e(0.56)$ vs $T_e(0)/T_e(0.28)$ reveals the same clear trend. Since the TS values from the three different points are measurements which are essentially independent of each other, the observed trend should be significant.

3. Summary

The TS system in operation on the Extrap T2 has been used to study the effect of changes in profiles on the global plasma behaviour and to estimate confinement parameters.

References

[1] Möller A., These proceedings.

MAGNETIC FIELD FLUCTUATIONS IN TURBULENT PLASMA

I.F. Goutych, A.G. Sitenko and A.G. Zagorodny

Bogolyubov Institute for Theoretical Physics
14B Metrologichna str., Kiev 252143, Ukraine

1. Introduction

Theoretical studies of magnetic field fluctuation spectra are of great importance both for the theory and applications. However, the detailed analysis of magnetic fluctuations have not been carried out up to now. This concerns both plasmas with stationary macroscopic parameters and plasmas with large-scale random motions (turbulent plasmas).

The purpose of the present paper is to generalize the theory of electromagnetic fluctuations in a stable stationary plasma to the case of a plasma with fluid-like random perturbations and to study magnetic field fluctuation spectra. To provide the generalization, the Green's functions taking into account large-scale random perturbations are used [1-4].

2. Basic set of equations

Let us consider a plasma with macroscopic random motion of volume elements. We assume the statistical dependence of both individual particle motions and stochastic motion of volume elements to be weak.

Averaging equation for microscopic phase density

$$\mathcal{F}_\sigma(x,t) = \sum_{i=1}^{N} \delta(x - x_{i\sigma}(t)),\ x \equiv (\mathbf{r},\mathbf{v}),$$

over the ensemble of turbulent perturbations one obtains

$$\left\{\frac{\partial}{\partial t} + \mathbf{v}\frac{\partial}{\partial \mathbf{r}} + \frac{1}{m}\left(\mathbf{F}^{\rm ext} + \tilde{\mathbf{F}}\right)\frac{\partial}{\partial \mathbf{v}}\right\}\tilde{\mathcal{F}}(x,t) = \left(\frac{\partial \tilde{\mathcal{F}}}{\partial t}\right)_T, \tag{1}$$

where $\tilde{\mathcal{F}}(x,t) \equiv <\mathcal{F}(x,t)>_T$ and $\tilde{\mathbf{F}} \equiv <\mathbf{F}^{\rm int}>_T$ are the microscopic phase density and intrinsic force averaged over the ensemble of large-scale chaotic motion, $(\frac{\delta\tilde{\mathcal{F}}}{\delta t})_T$ is the change of averaged microscopic density per unit time under the action of turbulent force $\mathbf{F}_T = \mathbf{F}^{\rm int} - <\mathbf{F}^{\rm int}>_T$.

If the relaxation of $\tilde{\mathcal{F}}(x,t)$ can be treated as the Gaussian process the equations for the microscopic phase density takes the form [1,4]

$$\left\{\frac{\partial}{\partial t} + \mathbf{v}\frac{\partial}{\partial \mathbf{r}} + \frac{1}{m}\left(\mathbf{F}^{\rm ext} + \tilde{\mathbf{F}}\right)\frac{\partial}{\partial \mathbf{v}}\right\}\tilde{\mathcal{F}}(x,t) = \frac{\partial}{\partial \mathbf{r}}\left[D\frac{\partial}{\partial \mathbf{r}} - \mathbf{U}_d\right]\tilde{\mathcal{F}}(x,t), \tag{2}$$

where D and $\mathbf{U}$ are the diffusion coefficient and drift velocity for large-scale volume element.

Performing the statistical averaging of Eq. (2) over the Gibbs ensemble related to the particles involved in the volume of large-scale perturbation and subtracting the averaged equation from Eq. (2) one obtains in the polarization approximation the following equation for smoothened microscopic fluctuations

$$\left\{\frac{\partial}{\partial t} + \mathbf{v}\frac{\partial}{\partial \mathbf{r}} + \frac{e}{m}\left[\mathbf{E}^{\rm ext} + \frac{\mathbf{v}}{c}\times\mathbf{B}^{\rm ext}\right]\frac{\partial}{\partial \mathbf{v}}\right\}\delta f(x,t) + \tag{3}$$
$$+\frac{e}{m}\left[\delta\mathbf{E}(\mathbf{r},t) + \frac{\mathbf{v}}{c}\times\delta\mathbf{B}(\mathbf{r},t)\right]\frac{\partial f(\mathbf{v})}{\partial \mathbf{v}} = \frac{\partial}{\partial \mathbf{r}}\left[D\frac{\partial}{\partial \mathbf{r}} - \mathbf{U}_d\right]\delta f(x,t).$$

Here $f(v) \equiv <\tilde{\mathcal{F}}(x,t)> \equiv << \mathcal{F}(x,t)>_T>$ is the distribution function smoothened over large-scale perturbations.

The formal solution of Eq. (3) is given by

$$\delta f(x,t) = \delta f^{(0)}(x,t) - \frac{e}{m}\int_{-\infty}^{t} dt' \int dx' W(x,x',t-t') \times \tag{4}$$
$$\times \left[\delta \mathbf{E}(\mathrm{r}',t') + \frac{\mathbf{v}}{c} \times \delta \mathbf{B}(\mathrm{r}',t')\right] \frac{\partial f(\mathbf{v}')}{\partial \mathbf{v}'}.$$

Here $\delta f^{(0)}(x,t)$ is the fluctuation in the system without self-consistent electromagnetic interactions, $W(x,x',t-t')$ is the probability of particle transition from x to x' during $\tau = t - t'$. The latter satisfies the equation

$$\left\{\frac{\partial}{\partial t} + \mathbf{v}\frac{\partial}{\partial \mathrm{r}} + \frac{e}{m}\left[\mathbf{E}^{\mathrm{ext}} + \frac{\mathbf{v}}{c} \times \mathbf{B}^{\mathrm{ext}}\right]\frac{\partial}{\partial \mathbf{v}}\right\} W(x,x',\tau) = \frac{\partial}{\partial \mathrm{r}}\left[D\frac{\partial}{\partial \mathrm{r}} - \mathbf{U}_d\right] W(x,x',\tau) \tag{5}$$

with the initial condition $W(x,x',0) = \delta(x-x')$.

The fluctuation fields are governed by the Maxwell equations

$$\begin{aligned}
&\mathrm{rot}\delta\mathbf{E}(\mathrm{r},t) = -\frac{1}{c}\frac{\partial}{\partial t}\delta\mathbf{B}(\mathrm{r},t)\\
&\mathrm{dev}\delta\mathbf{B} = 0\\
&\mathrm{rot}\delta\mathbf{B}(\mathrm{r},t) = \frac{1}{c}\frac{\partial}{\partial t}\delta\mathbf{E}(\mathrm{r},t) + \frac{4\pi}{c}\delta\mathbf{J}^{\mathrm{ind}}(\mathrm{r},t) + \frac{4\pi}{c}\delta\mathbf{J}^{(0)}(\mathrm{r},t)\\
&\mathrm{div}\delta\mathbf{E}(\mathrm{r},t) = 4\pi\delta\rho^{\mathrm{ind}}(\mathrm{r},t) + 4\pi\delta\rho^{(0)}(\mathrm{r},t),
\end{aligned} \tag{6}$$

where

$$\delta\mathbf{J}^{\mathrm{ind}}(\mathrm{r},t) = \sum e\int_{-\infty}^{t} dt' \int d\mathbf{v} \int dx' \cdot \tag{7}$$
$$\left(\mathbf{v} + \mathbf{U}_d - D\frac{\partial}{\partial \mathrm{r}}\right) W(x,x',t-t')\left[\delta\mathbf{E}(\mathrm{r}',t') + \frac{\mathbf{v}'}{c} \times \delta\mathbf{B}(\mathrm{r}',t')\right]\frac{\partial f(v')}{\partial \mathbf{v}'},$$
$$\delta\mathbf{J}^{(0)}(\mathrm{r},t) = \sum e\int d\mathbf{v}\left(\mathbf{v} + \mathbf{U}_d - D\frac{\partial}{\partial \mathrm{r}}\right)\delta f^{(0)}(x,t).$$

The correlation functions of fluctuation sources are given by

$$< \delta J_i^{(0)}(\mathrm{r},t)\delta J_j^{(0)}(\mathrm{r}',t') >= \sum e^2 \int d\mathbf{v} \int d\mathbf{v}' \left(v_1 + U_{di} - D\frac{\partial}{\partial r_i}\right) \cdot$$
$$\cdot \left(v_j' + U_{dj} - D\frac{\partial}{\partial r_j'}\right) W(x,x',t-t')f(\mathbf{v}'). \tag{8}$$

3. Fluctuation spectra in turbulent plasmas

Eqs. (6) – (8) make it possible to calculate the fluctuation quantities in the same manner as in the case of ordinary plasmas. For example,

$$< \delta E_i \delta E_j >_{\mathrm{k}\omega} = \frac{16\pi}{\omega^2}\Lambda_{ik}^{-1}(k,\omega)\Lambda_{jl}^{-1}(\mathrm{k},\omega) < \delta J_k^{(0)}\delta J_l^{(0)} >_{\mathrm{k}\omega}, \tag{9}$$

$$< \delta B_i \delta B_j >_{\mathrm{k}\omega} = \frac{16\pi^2 c^2}{\omega^4} k_k k_n e_{ikl} e_{jnm}\Lambda_{il}^{-1}(\mathrm{k},\omega)\Lambda_{mm_1}^{-1*}(\mathrm{k},\omega) < \delta J_{l_1}^{(0)}\delta J_{m_1}^{(0)} >_{\mathrm{k}\omega}, \tag{10}$$

where

$$\Lambda_{ij}(\mathrm{k},\omega) = \varepsilon_{ij}(k,\omega) - \frac{k^2c^2}{\omega^2}\left(\delta_{ij} - \frac{k_i k_j}{k^2}\right),$$

$$\varepsilon_{ij}(k,\omega) = \delta_{ij} + \sum_{\sigma} \chi_{ij}(k,\omega) \tag{11}$$

$$\chi_{ij}(k,\omega) = -\frac{e^2}{m\omega^2} \int d\mathbf{v} \int d\mathbf{v}'(v_i + U_{id} - ik_i D) \cdot$$

$$\cdot G_{k\omega}(\mathbf{v},\mathbf{v}') \left\{ \delta_{jk}(\omega - \mathbf{kv}') - ik_k v_j' \right\} \frac{\partial f(\mathbf{v}')}{\partial v_j'},$$

$$G_{\mathbf{k}\omega}(\mathbf{v},\mathbf{v}') = \int_0^{\infty} d\tau \int d\mathbf{R} e^{-i\mathbf{k}\mathbf{R} + i\omega\tau} W(x,x',\tau),$$

$$< \delta J_i^{(0)} \delta J_j^{(0)} >_{\mathbf{k}\omega} = \sum e^2 \int d\mathbf{v} \int d\mathbf{v}'(v_i + U_{id} - ik_i D)(v_j' + U_{id} - ik_j D) \cdot$$

$$\cdot \{ G_{\mathbf{k}\omega}(\mathbf{v},\mathbf{v}') f(\mathbf{v}') + G^*_{\mathbf{k}\omega}(\mathbf{v},\mathbf{v}') f(\mathbf{v}) \}.$$

Now, let us specify $W(x,x',\tau)$ for the case of plasma in external magnetic field $\mathbf{B}^{\mathrm{ext}} = (0,0,B_0)$. If the large-scale motions are well pronounced only in the directions perpendicular to z-axis, the solution of Eq.(5) with the appropriate initial condition is

$$W(x,x',\tau) = \frac{1}{(4\pi D\tau)} e^{-\frac{(\mathbf{r}_\perp - \mathbf{r}_\perp - \Delta\mathbf{r}_\perp(\mathbf{v}',\tau))^2}{4D\tau}} \delta(z - z' - v_z\tau) \cdot \tag{12}$$

$$\cdot \delta(v_x - v_x' \cos\Omega\tau - v_y \sin\Omega\tau)\delta(v_y' + v_x' \sin\Omega\tau - v_y' \cos\Omega\tau)\delta(v_z - v_z').$$

Substituting Eq.(12) into Eqs.(11) one obtains explicite expressions for the dielectric permittivity tensors and correlation functions of Langeven sources [5].

4. Numerical analysis

Since the detailed studies of magnetic fluctuation spectra have not been performed up to now, in the present paper we consider the simplest case of a regular plasmas. For the sake of simplicity we restrict ourselves by the calculation of the quantity

$$\langle \delta B^2 \rangle_{\mathbf{k}\omega} = \frac{16\pi^2 c^2 k^2}{\omega^4} \left(\delta_{ij} - \frac{k_i k_j}{k^2} \right) \Lambda_{ik}^{-1}(\mathbf{k},\omega) \Lambda_{jl}^{-1*}(k,\omega) \langle \delta J_k^{(0)} \delta J_l^{(0)} \rangle_{\mathbf{k}\omega}. \tag{13}$$

Calculations were performed for the case of hydrogen isothermic plasmas at the following value of plasma parameters $\omega_{pe}/|\Omega_e| = 1$, $c/s_e = 10$. At the figures below the quantity (13) in arbitrary units $I = n\omega_{pe} \frac{< \delta B^2 >_{k\omega}}{B_0^2}$ is presented as a function of dimensionless frequency $x = \omega/\omega_{pe}$ at various values of $y = k/k_{De}^2$ (Fig. $1 - y = 10^{-3}$, Fig. $2 - y = 5 \cdot 10^{-3}$; $k_{De}^2 = \frac{4\pi e^2 n_e}{T}$) and φ which is the angle between k and $\mathbf{z}_0$ ($1 - \varphi = 89°$, $2 - \varphi = 88°$, $3 - \varphi = 87°$, $4 - \varphi = 86°$ at Fig. 1a,2a and $1 - \varphi = 75°$, $2 - \varphi = 60°$, $3 - \varphi = 45°$, $4 - \varphi = 30°$ at Figs. 1b,2b).

Numerical analysis shows that in the low-frequency domain magnetic fluctuation spectra consists of incoherent maximum in the withinity of zero frequency and more, or less pronounced two resonances, associated with excitation of the Alfven and fast magnetosound waves. Intensity of both incoherent and resonance maxima is considerably dependent on the wavelength and the direction of fluctuation field propagation.

References

1. A.G. Sitenko, A.G. Zagorodny, Ukr.Journ.Phys. (1995) **40** 390
2. P. Sosenko, N. Maafa, D. Gresillon, Phys.Scr. **51** (1995) 647
3. P. Sosenko, N. Maafa, D. Gresillon, J. Atmosph. Terrestrial Phys. **50** (1996) 1047
4. A.G. Sitenko, A.G. Zagorodny, P.P.J.M. Schram, Physica B (1996) **228** 125
5. A.G. Sitenko, A.G. Zagorodny, *Magnetic Field Fluctuations in a Plasma with Large-Scale Random Motions* (to be published)

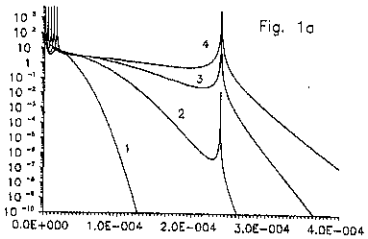

Fig. 1a

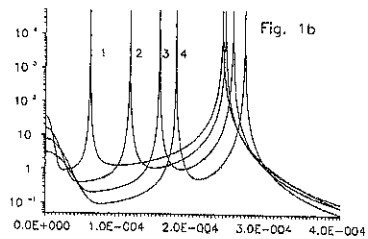

Fig. 1b

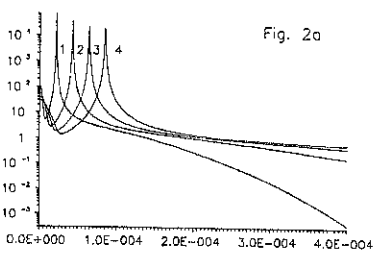

Fig. 2a

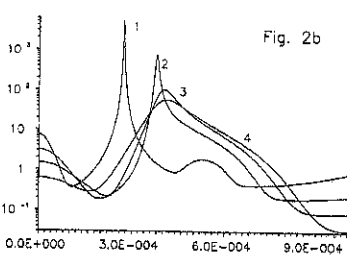

Fig. 2b

Chaotic dynamics and structure formation in the plasma diode with virtual cathode

Vasiliy G.Anfinogentov
College of Applied Science, Saratov State University,
Astrakhanskaya 83 Saratov 410026 RUSSIA, e-mail:vga@cas.ssu.runnet.ru

One of the simplist models of collisionless plasma is the plasma diode. It consists of diode region filled by neutralising ion background. The electron beam propagates through the region. The control parameter of the system is the Pierce parameter [1] $\alpha = \omega_p L/v_b$ for full neutralisation. Here $\omega_p = \sqrt{e\rho_b/\varepsilon m}$; ρ_b, v_b are the charge density and velocity on the input grid, L is the length of the system. Pierce parameter is the ratio between transit time $T = L/v_b$ and the plasma oscillation period $T_p = 2\pi/\omega_p$. This model takes into account collective phenomena as well as boundary effects. The growth of the electrostatic instability leads to the appearance of the virtual cathode (VC) for $\alpha > \pi$. VC is the region with the space charge potential almost equal to the cathode potential. Plasma diode with VC is the simplest model of such devices as plasma implantation devices, ICF and microwave devices (see [2] and cited refs for review). Complex behaviour of the plasma diodes attracts widespread interest in the recent years [3-6].

In the present paper we consider complex behaviour and structure formation in the partially neutralised diode region. This assumption leads to the new parameter $n_o = n_i/n_b$. Here n_i is the concentration of ion background and $n_b = \rho_b/e$ is the beam concentration.

The system behaviour was simulated with the help of PIC method. Considerable influence of the neutralisation degree on the VC oscillation was observed. As known [6] three regimes of complex VC oscillation exist for full neutralisation. Strong chaotic regime appears for small supercritical value of $\alpha(\alpha < 1.3\pi)$. Power spectrum has noise-like form and the phase trajectory fills whole region in the phase space (Fig.1a). The leading Lapunov exponent is positive ($\lambda = 0.045$) and attractor dimension has the value 2.5 in the scaling region. The increasing of α leads to the almost regular oscillations (ribbon chaos). The strong chaos arises again for $\alpha > 1.7\pi$ (Fig.1b). The phase trajectory moves on the attractor during main time and sometimes walks around the attractor sheet (intermittence regime).

Decreasing of the neutralisation degree produces the breaking of chaotic regimes and regular VC oscillations appear. The breaking occurs through ribbon chaos for small values of α. Attractors have the narrow ribbon in these regions. For large α suddenly destroying of the chaotic state was observed.

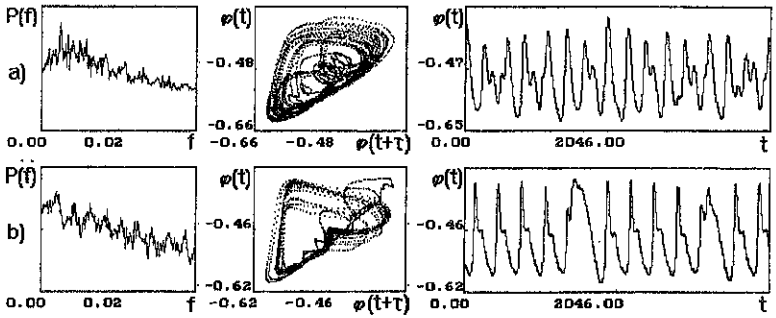

Fig.1. Power spectrum, phase portraits and time histories of strong chaos regimes for full neutralisation: (a) $\alpha=1.05\pi$, (b)$\alpha=1.7\pi$

For small neutralisation the quasiperiodical behaviour with two independent frequencies was founded. The growth of α leads to the breaking of this state and complex dynamics arises. Leading Lapunov exponent is positive, that proves the chaotic behaviour of the beam. Attractor dimension has small value 1.2. This value of dimension justifies exiting the small number of modes. Therefore in the strong nonlinear regime the mode coupling plays the main role.

The typical structures were extracted from spatio-temporal data of the potential with the help of proper orthogonal decomposition [6]. In this method the typical structure F_k is the solution of the Fredholm integral equation

$$\int K(x,y)F_k(x)dx = \lambda_k F_k(y) \qquad (1)$$

where $K(x,y) = \frac{1}{T}\int_0^T u(x,t)u(y,t)dt$ is the mutual correlation function. The value of $E_k = \lambda_k / \sum \lambda_j$ is the measure of energy of mode F_k. In all regimes of the complex VC oscillations the irregular behaviour appears as a result of interaction between small number of modes, because more than 98% energy of beam oscillation accumulated in the three higher modes.

The typical structures with $E_k > 0.01$ are shown in Fig.2 for strong neutralisation. Three modes are exited in the chaotic regime. The highest mode demonstrates strong nonuniform potential distribution with one maximum. This distribution is typical for formation of VC in the diode. The spatial structure of other modes proves existence of additional bunches in the beam. The energy of second mode is maximal for chaotic behaviour.

If neutralisation degree decreases then the energy of highest mode remains constant and energy of third mode decreases from 0.05 for $n_0 = 1$ to 0.01 for $n_0 = 0.7$. Third mode disappeares for small neutralisation and only two modes were observed in the regular VC oscillations.

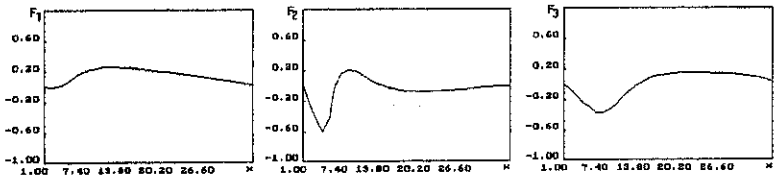

Fig.2. Typical structures for strong chaos in the neutralised beam. The energy of the first mode is 0.82, second mode - 0.11 and the third mode - 0.05.

Two specific structures are exited in the regular quasiperiodical regime. Exiting of third structure accompanies transition to chaos for small neutralisation. Phase projection, power spectrum and time histories for oscillation of mode amplitudes are shown in the Fig.3. Mode amplitude is $a_k(t) = \int u(x,t)F_k(x)dx$. As clearly shown in Fig.3, the complex behaviour in nonneutralised beam is connected with oscillation of third structure and other modes demonstrate quasiperiodical oscillation.

Analysis of the physical processes in the system shows that the highest mode coincides with the potential distribution during VC formation. Other modes are bound up with formation of the bunch during VC disappearing for strong neutralisation. This bunch is marked on the spatio-temporal diagram (Fig.4a). For complex regime increasing of energy E_2 is connected with increasing of the charge density in this structure. Reflection of the beam from second bunch appears for large charge density. It provides strong feedback required for chaotic behaviour. This feedback influences during all times in the first regime of strong chaos. In the second one the reflection starts the turbulence bursts. If neutralisation degree decreases then second bunch breaks, that explains decreasing of energy of the low modes and appearance of regular oscillation.

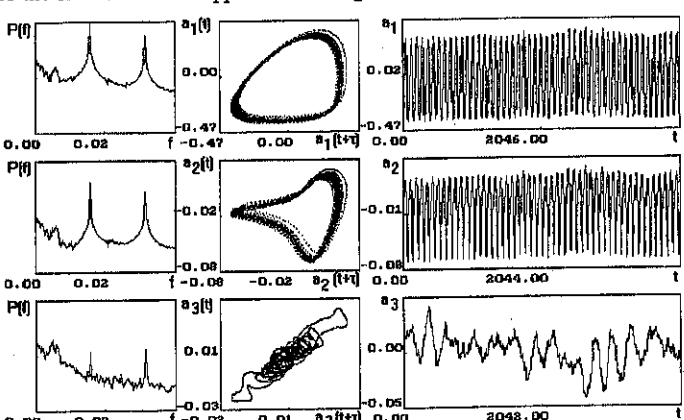

Fig.3. Power spectrum, phase portraits and time histories of mode amplitude oscillations for chaotic regime in the noneutrolised beam

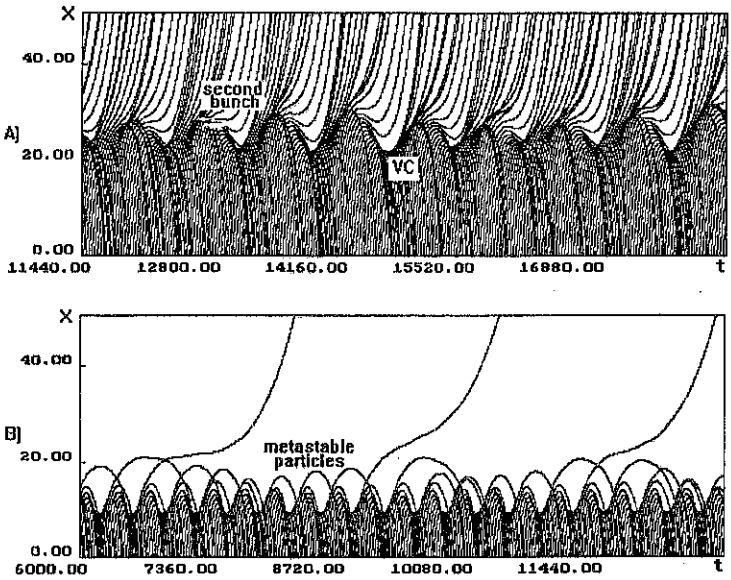

Fig.4. Spatio-temporal diagram for chaotic regimes: a)-neutralised and b)-noneutralised beam

Second and third structures are connected with metastable particles for nonneutralised beam (Fig.4b). These particles exist long time (some periods) in the VC region. Existence of metastable particles provides internal feedback required for chaotic behaviour. The greater charge density of the metastable bunch produces nonlinear action of feedback and leads to the chaotic behaviour. Increasing of the charge density in the metastable bunch explains increasing of the mode energy E_3. The peculiarity of power spectrum of $a_3(t)$ is connected with slow modulation of the charge density in the metastable bunch. Recognising of the typical structures gives a possibility of effective influence on the system behaviour by managing the structure formation.

This work is supported by the Ministry of Common and Professional Education of Russia (Grant N2-33) and Russian Fund of Basic Research (Grant N96-02-16753).

1.J.Pierce. J.Appl.Phys., v.15, p.721, 1944.
2.S.Kuhn, Phys.Fluids, v.27, p.1834, 1984.
3.B.B.Godfrey, Phys.Fluids, v.30, p.1553, 1987.
4.X.Chen, P.A.Lindsay, SPIE vol.2557, p.88, 1995.
5. F.Bauer, H.Shamel. Physica D, v.54, p.235, 1992.
6.V.G.Anfinogentov, Tech.Phys.Lett., v.21, p.310, 1995.
7.J.L.Lumley in Atmospheric Turbulence and Radio Wave Propagation, ed. by A.M.Yaglom and V.I.Tatarski, Nauka, Moscow, 1967.

BISTABLE UPPER HYBRID SOLITONS

T.A.Davydova, A.I.Fishchuk

Institute for Nuclear Research,
pr.Nauki-47, Kiev, Ukraine.

A number of experiments shows the possibility of formation of coherent wave structures near the upper hybrid resonance (UHR) where the frequency of an incident extraordinary wave ω_0 is close to $(\omega_{pe}^2+\Omega_e^2)^{1/2}$ (ω_{pe} and Ω_e are the electron plasma and cyclotron frequencies, respectively). Above some threshold a wave propagating across the magnetic field is "trapped" near the resonance and a density well is formed near the peak of the field [1].

Soliton formation in the nonlinear stage of the modulational instability of electrostatic UH waves in many cases may be described by the following modified nonlinear Schrödinger equation [2-4]:

$$i\frac{\partial\psi}{\partial\tau}+D\frac{\partial^2\psi}{\partial\xi^2}+\psi\left(B+C\frac{\partial^2}{\partial\xi^2}\right)|\psi|^2+P\frac{\partial^4\psi}{\partial\xi^4}=0. \tag{1}$$

Here $\psi=E/B_0$ is the dimensionless electric field envelope, $\tau=\omega_0 t/2$ is the dimensionless time and $\xi=x/\rho_e$ is the dimensionless space coordinate, ρ_e is the electron Larmor radius. The constants D and P describe the linear dispersion of UH waves. Coefficients B and C depend on the dominant nonlinear process in the particular plasma system.

According to the theory [2-4], the dependence between the density perturbations and the field intensity is often nonlocal. For example in interaction of UH waves with slow, short scale ($L\ll c/\omega_{pe}$) magnetosonic perturbations the density variation has the form

$$\frac{\delta n}{n_0}\approx\frac{c^2}{\omega_{pe}^2B_0^2}\frac{d^2}{dx^2}|E|^2+\frac{\delta B}{B_0}.$$

Simultaneously a magnetic field well is created near the pump peak under the action of the ponderomotive force $\delta B/B_0\sim-|E|^2/B_0$. In this case $C\approx c^2/v_{Te}^2$, $B\approx 1$.

According to theory [2,3], "cusp solitons" appear when the nonlocal nonlinear coupling is dominant. But they have been proven to be unstable [5]. However the predictions of Refs.[2,3,5] were based on treating only the lowest order dispersive effects, which is insufficient in case of a nonlocal coupling [4].

One particular regular exact solution of Eq.(1) was found in [4] for the case

$$B=0, D>0, P<0, C<0. \tag{2}$$

It has the *sech*-form:

$$\psi=\left(\frac{2D}{|C|}\right)^{1/2}\operatorname{sech}\left(\sqrt{\frac{D}{2|P|}}\xi\right)e^{i\lambda\tau},\quad \lambda=-\frac{D^2}{4P}. \tag{3}$$

Stationary soliton - solutions of Eq.(1) in the case (2) of the type

$$\psi = U(\xi)\exp(\mathrm{i}\lambda\tau) \tag{4}$$

with different values of λ have been found numerically in Ref.[6].

In this report we study the general properties of UH solutions and their stability. We suppose that the function $U(\xi)$ in Eq.(4) is real and that the invariants $N = \int\limits_{-\infty}^{+\infty} |\psi|^2 d\xi$, the plasmon number, and

$$H = \int\limits_{-\infty}^{+\infty} \left(D\left|\frac{d\psi}{d\xi}\right|^2 - P\left|\frac{d^2\psi}{d\xi^2}\right|^2 + \frac{C}{2}\left(\frac{d|\psi|^2}{d\xi}\right)^2 - \frac{B|\psi|^4}{2}\right) d\xi, \tag{5}$$

the Hamiltonian, have finite values. The function $U(\xi)$ satisfies the ordinary differential equation

$$-\lambda U + D\frac{d^2U}{d\xi^2} + BU^3 + CU\frac{d^2U^2}{d\xi^2} + P\frac{d^4U}{d\xi^4} = 0, \tag{6}$$

which has an integral

$$J = -\lambda U^2 + D\left(\frac{dU}{d\xi}\right)^2 - P\left(\frac{d^2U}{d\xi^2}\right)^2 + 2P\frac{dU}{d\xi}\frac{d^3U}{d\xi^3} + \frac{BU^4}{2} + \frac{C}{2}\left(\frac{dU^2}{d\xi}\right)^2,$$

which is a constant for all ξ. For any soliton solution $J = 0$, since U vanishes on infinity and the following identity is valid:

$$\lambda U^2(\xi_e) = \frac{B}{2}U^4(\xi_e) - P\left(\frac{d^2U(\xi_e)}{d\xi^2}\right)^2, \tag{7}$$

where ξ_e is a extremum. From Eq.(6) two integral identities may be obtained [7]. These identities give a rather simple expression for λ :

$$\lambda = \frac{1}{3N}\int\limits_{-\infty}^{+\infty} \left(D\left(\frac{dU}{d\xi}\right)^2 - 5P\left(\frac{d^2U}{d\xi^2}\right)^2 + 2BU^4\right) d\xi. \tag{8}$$

To obtain the asymptotic behaviour of soliton solutions on infinity it is sufficient to consider the linear part of Eq.(6). For $U(\xi) \sim \exp(-\kappa\xi)$ this gives

$$\kappa^2 = -\frac{D}{2P} \pm \sqrt{\frac{D^2}{4P^2} + \frac{\lambda}{P}}$$

In the case $D > 0$, $P < 0$ the solution decays monotonically toward infinity if $0 < \lambda < D^2/4|P|$. If $\lambda > D^2/4|P|$, solitons have oscillating tails which do not influence essentially the integral properties of solitons.

A rather good analytical approximation to numerical solutions [6] may be obtained using the variational method with a trial function of the type (4) with

$$U(\xi) = h\,\mathrm{sech}(\mu\xi). \tag{9}$$

The soliton amplitude h and its characteristic size μ^{-1} are found from the requirement that the function $U(\xi)$ (9) gives an extremum to the Hamiltonian (5) at fixed number N. The last condition gives $h = (N\mu/2)^{1/2}$ and

$$N = 4\mu\left(\frac{D - 2.8\,P\mu^2}{B - 2.4\,C\mu^2}\right). \tag{10}$$

Below we consider the case $D > 0, P < 0, B > 0, C < 0$. Then the right hand side of Eq.(10) is a monotonic function of μ if

$$\frac{D}{7|P|} < \frac{B}{2|C|} + \left(\frac{DB}{21|PC|}\right)^{1/2}. \tag{11}$$

In this case Eq.(10) has only one positive root μ corresponding to one stable soliton solution. When the opposite inequality is valid, $N(\mu)$ has two extrema. The latter case will be considered below.

In the problem of UH solitons the linear and nonlinear spatial scales are strongly different, i.e.,

$$L_{lin} \sim \left|\frac{D}{P}\right| \gg \left|\frac{B}{C}\right| \sim L_{nl}, \tag{12}$$

and the extremal values of the plasmon number N are

$$N_{max} = N(\mu_-) = \left(\frac{5}{3}\frac{D^2}{B|C|}\right)^{1/2}, \quad N_{min} = N(\mu_+) = \left(\frac{280}{9}\frac{D|P|}{C^2}\right)^{1/2}.$$

Thus we find that for $N < N_{min}$ and $N > N_{max}$ Eq.(10) has one positive root but in the region $N_{min} < N < N_{max}$ this equation has three positive roots μ corresponding to three possible soliton solutions. The exact solution (3) belongs to the branch $\mu > \mu_+$.

Soliton stability may be established by the Kolokolov- Vakhitov criterion [5]. This criterion states that a soliton is stable if $dN/d\lambda$ is positive and that a soliton is unstable in the opposite case. Calculation of λ using Eq.(8) gives $\lambda = (D\mu^2 + 7|P|\mu^4 + 2BN\mu)/9$. This function increases monotonically with μ. Thus the qualitative dependence $N(\lambda)$

for soliton solutions is similar to the dependence $N(\mu)$. A sketch of the curve $N(\lambda)$ is shown in Fig.1 for the case considered.

According to the stability criterion long scale solitons ($\mu < \mu_-, \lambda < \lambda(\mu_-), N < N_{max}$) and short scale solitons ($\mu > \mu_+, \lambda > \lambda(\mu_+), N > N_{min}$) are stable. Solitons of intermediate scale are unstable. Cusped solutions belong to this unstable branch (even after their smoothing by the fourth order dispersive effects). In the range $N_{min} < N < N_{max}$ there are two stable soliton solutions of Eq.(1). This is a kind of bistability phenomenon. Such a possibility was suggested in [8] for a different nonlinear system. The mechanism leading to this phenomenon is a competition between focusing and defocussing forces which behave differently on different spatial scales.

References

1. T.Cho and S.Tanaka, Phys.Rev.Lett, **45**, 1403(1980).
2. M.Porkolab and M.V.Goldman, Phys.Fluids, **19**, 872(1976).
3. K.P.Sharma and P.K.Shukla, Phys.Fluids, **26**, 87(1983).
4. T.A.Davydova and A.Yu.Kargin, Fiz.Plazmy, **19**, 233(1993).
5. A.G.Litvak.and A.M.Sergeev, Pis'ma Z E T F, **27**, 549(1978).
6. T.A.Davydova and A.I.Fishchuk, 23 EPS Conf CFPF, Kiev, 1996, pg004.
7. T.A.Davydova and A.I.Fishchuk, accepted for publication in Phys.Scripta (1997).
8. I.A.Kol'chugina, A.G.Litvak and A.M.Sergeev, Pis'ma Zn. Eksp. Teor. Fiz., **35**, 510 (1982).

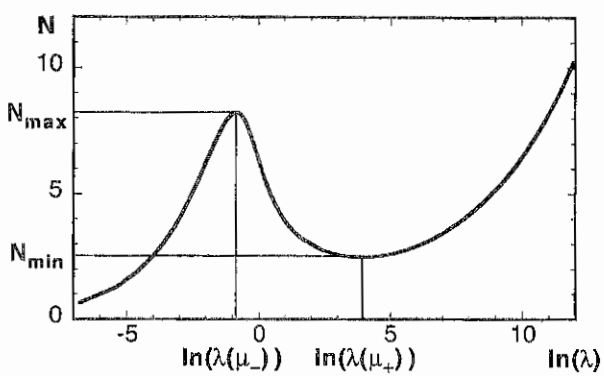

Figure 1. Dependence of number of quanta N on inverse scale length $\ln\lambda$ with parameters $D = 2$, $P = -1$, $C = -1$, $B = 0.1$

Wave Mode Conversion Due to the Linear Plasma Echo in Non-Uniform Magnetic Fields

Sergei V. Kasilov

Institute of Plasma Physics, National Science Center "Kharkov Institute of Physics and Technology", Ul. Akademicheskaya 1, 310108 Kharkov, Ukraine

Introduction

Since the prediction of electromagnetic wave absorption in plasmas due to multiple electron cyclotron resonance [1], this mechanism has been shown to be responsible for various phenomena in laboratory and space plasmas. The important feature of cyclotron absorption in non-uniform magnetic fields is the existence of various linear echo effects such as transillumination of wave barriers as well as ballistic wave reflection and wave conversion [2-5]. Up to now, the ballistic reflection has been mainly studied in the case when the magnetic field gradient is parallel to the magnetic field direction (see, e.g., Refs. [6, 7]). In the case when the angle α between the magnetic field gradient and its direction is finite, in addition to reflection into the mode of the same type, also reflection and conversion into modes of different type occurs. The prime factors which seriously affect wave reflection and conversion include the relativistic cyclotron frequency dependence on energy and the variation of the parallel particle velocity during its motion in the non-uniform magnetic field [6]. Together with these effects, even the rare Coulomb collisions can effectively destroy the wave-particle phase memory and the corresponding echo phenomena [8]. In the present paper, electromagnetic wave conversion and wave reflection effects are studied for the case of multiple electron cyclotron resonance in a weakly relativistic plasma for arbitrary angle α taking into account all three features mentioned above which may reduce the ballistic effects.

RF Current Density

We consider the 1D problem with linearly increasing magnetic field module along the x-axis, $B = B_0(1 + x/L_x)$ and straight magnetic filed lines in the xz-plane declined by an angle α with respect to z-axis. The unperturbed distribution of plasma particles is assumed homogeneous. The plasma temperature is assumed nonrelativistic and thus the only important relativistic effect to be taken into account is the dependence of the electron cyclotron frequency ω_{ce} on energy. We consider the case of multiple electron cyclotron resonance $n\omega_c(x) = -\omega$ at $x = 0$, ω_c is the cyclotron frequency of nonrelativistic electrons. In this case, the resonant particles provide only a small correction to the rf plasma current and cannot change the polarization of the electromagnetic waves significantly. Because of the narrow resonance zone, the magnetic field inhomogeneity needs to be retained in the current density of resonant electrons only and one may look for the electric field of the electromagnetic waves in the form $\vec{E}(\vec{r},t) = \vec{\mathcal{E}}(x)\exp(i\vec{k}\vec{r} - i\omega t)$ where $\vec{k}$ is the wave vector satisfying the cold plasma dispersion equation and $\vec{\mathcal{E}}(x)$ is an amplitude slowly varying due to resonant interaction. The right-polarized components of the resonant particles rf current density and the electric field are linked in the short wave limit $k_\parallel^2 \gg \omega \sin\alpha/v_T L_x$ by the following relation,

$$j^- = \sigma_{loc}\exp(i\vec{k}\vec{r} - i\omega t)\mathcal{E}^-(x) + \sigma_{ech}\exp\left(i\vec{k}\vec{r} - i\omega t - 2ik_\parallel x/\sin\alpha\right)\mathcal{E}^-(-x). \quad (1)$$

Here, the conductivity kernels which are slowly varying in space are given by

$$\sigma_{loc}\left(x;\vec{k}\right) = \frac{\omega_{pe}^2 n^2 a^{n-1}}{4\sqrt{2\pi}\, n!|k_\parallel|v_T} w(z_n), \tag{2}$$

$$\sigma_{ech}\left(x;\vec{k}\right) = \frac{2\omega_{pe}^2 n^2 a^{n-1}\Theta(k_\parallel)}{4\sqrt{2\pi}\, n!|k_\parallel|v_T(1-i\vartheta_1)^{n+1}} \exp\left(-(1-i\vartheta_2)z_n^2+\delta\Phi\right), \tag{3}$$

where $a = k_\perp^2 v_T^2/(2\omega_c^2(0))$, $k_\parallel$ and $k_\perp$ are parallel and perpendicular wave numbers, $v_T = \sqrt{T_e/m_e}$ is the electron thermal velocity, $w(z_n)$ is the probability integral of complex argument, $z_n = -\omega x/(\sqrt{2}|k_\parallel|v_T L_x)$, and $\Theta(k_\parallel)$ is the Heaviside step function.

The first term on the rhs of Eq. (1) corresponds to the usual local plasma response leading to cyclotron absorption of waves. The second term is the "echo" current which is responsible for the generation of reflected and converted waves. The following effects which limit the value of the current are taken into account: the variation of the parallel electron velocity due to adiabatic invariance, the relativistic dependence of frequency on the energy represented by $\vartheta_1 = 2k_\parallel L_x(1-N_\parallel^2/3)v_T^2/(c^2\sin\alpha)$ and $\vartheta_2 = k_\parallel L_x v_T^2/(c^2\sin\alpha)$ respectively, and the wave-particle phase decorrelation due to Coulomb collisions described by $\delta\Phi = -4D_\parallel k_\parallel^5 L_x^3/(15\omega^3\sin^3\alpha)$. Here $N_\parallel$ is the parallel refraction index and $D_\parallel$ is the coefficient of Coulomb diffusion with respect to parallel velocity.

Generation of Converted Modes

The fast spatial variation of the "echo" current given by the exponent in the second term on the rhs of (1) can be characterized by an effective wave vector which has the same values of k_y and k_z as the electric field wave vector but a different value of the x-component, $k^{(e)} = -k_x - 2k_z\mathrm{ctg}\alpha$. If $k^{(e)}$ is close to one of the solutions of the cold plasma dispersion equation solved with respect to x-component of the wave vector k_m, $m = 1,\ldots,4$, the generation of reflected or converted waves occurs. In the case of weak wave absorption after one passing of the wave through the resonance zone, the power conversion coefficients are given by the expression $\Gamma = p_{M_0}\, p_M\, \rho_m^2/(4N_M^2)$, where

$$\rho_m = \frac{\pi n^2\omega_{pe}^2 a^{n-1} L_x}{\omega c n!\,(1+\vartheta_1^2)^{(n+1)/2}(1+\vartheta_2^2)^{1/4}} \exp\left\{-\frac{k_\parallel^2 v_T^2 L_x^2\left(k^{(e)}-k_m\right)^2}{2\omega^2(1+\vartheta_2^2)}+\delta\Phi\right\}. \tag{4}$$

Here subscripts M_0 and M denote the modes of propagation of incident and converted waves ($M = O$ for ordinary and $M = X$ for extraordinary). For small angles α it is sufficient to consider the case of wave propagation almost perpendicular to the magnetic field. In this case, the polarization factors p_M and refraction indices N_M can be approximated by

$$N_O^2 \approx \varepsilon_3, \quad N_X^2 \approx \frac{\varepsilon_+\varepsilon_-}{\varepsilon_1}, \quad p_O = \left(\frac{\beta\varepsilon_3(\varepsilon_3-\varepsilon_+)}{\varepsilon_1\varepsilon_3-\varepsilon_+\varepsilon_-}\right)^2, \quad p_X = \frac{\varepsilon_+^2}{\varepsilon_1^2}, \tag{5}$$

where ε_1, ε_2, ε_3 are the components of the cold plasma dielectric tensor, $\varepsilon_\pm = \varepsilon_1 \pm \varepsilon_2$, $\beta = \pi/2-\theta$, and θ is the angle between the magnetic field and the wave vector.

The conversion coefficient takes its maximum value for $k^{(e)} - k_m = 0$. In the particular case $N_y = 0$, i.e. wave incidence in xz-plane, this condition restricts the angle ϕ between the wave vector of the incident mode and x-axis. The N_x and $N_\parallel$ components of the refraction index as functions of the incidence angle ϕ are shown in Figure 1. Also shown

are the effective refraction index $N_x = ck^{(e)}/\omega$ of the "echo" current and the effective parallel refraction index of this current.

It can be seen that the refraction index of the particular converted mode matches the effective refraction index of the "echo" current at some specific values of incidence angle ϕ. In these points the conversion is maximum. These matching points are marked in Figure 1 with **A**, **B** and **C**.

Point **A** corresponds to the generation of a reflected mode of the same type as the incident one. For perpendicular incidence, this occurs at $\phi = \phi_A = 0$. Point **B** corresponds to the generation of a reflected mode of different type. This occurs for incidence from the low field side at $\phi = \phi_B < 0$ for the ordinary and at $\phi = \phi_B > 0$ for the extraordinary mode. Point **C** corresponds to the generation of a mode of different type which travels through the resonance zone in the same direction as the incident mode (wave splitting). This occurs for incidence of the ordinary mode into the cyclotron resonance zone from the low field side or for incidence of the extraordinary mode incidence from the high field side with $k_{\|} > 0$.

Example

As a numerical example we consider the case of an extraordinary mode incident on the second harmonic $n = 2$ resonance layer in a tokamak with big radius $R = L_x = 200$ cm, magnetic field $B = 30$ kG, electron density $n_e = 10^{13}$ cm^{-3} and temperature $T_e = 500$ eV. The analysis shows that for arbitrary α relativistic effects and Coulomb collisions will reduce significantly the value of the conversion coefficient. On the other hand, taking $N_{\|} \approx \alpha = 0.1$ and $D_{\|} = \nu v_T^2$ where $\nu \approx 2 \cdot 10^5 s^{-1}$, we estimate $|\delta\Phi| \sim 10\alpha^2 = 0.1$. This shows that for small α the collisional decorrelation is small and also the modification of the parallel velocity due the adiabatic invariance and the relativistic cyclotron frequency dependence on energy described by $\vartheta_1 \approx \vartheta_2 \approx 12\alpha = 1.2$ do not reduce the ballistic effect significantly. The power conversion coefficient in this case is estimated to be $\Gamma \approx 0.05$. That means that there should be a possibility to observe reflected modes in a plasma with parameters close to a tokamak plasma. In this way one could obtain the information about the value of the angle α from a comparison of the reflected power of different wave modes. This effect may provide an additional tool to measure the poloidal magnetic field component in the core plasma of tokamaks.

References

[1] Sitenko, A. G. and Stepanov, K. N., *Soviet Phys. JETP*, **4**, 512 (1957).

[2] Vodyanitskij, A. A., Erokhin, N. S., and Moiseev, S. S., *Soviet Phys. JETP*, **34**, 336 (1974).

[3] Vodyanitskij, A. A., et al., *Nuclear Fusion*, **14**, 267 (1974).

[4] Marsh, J., *Phys. Fluids*, **15**, 647 (1972).

[5] Erokhin, N. S. and Moiseev, S. S., *Reviews of Plasma Physics* (Consultants Bureau, New York), Vol. 7, pp. 181–256 (1979).

[6] Zvonkov, A. V. and Chulkov, G. N., *Soviet Phys. JETP*, **57**, 35 (1983).

[7] Kasilov, S. V., et al., *Physica Scripta*, **45**, 373 (1992).

[8] Kasilov, S. V., Pyatak, A.I., and Stepanov, K. N., *Nuclear Fusion*, **30**, 2467 (1990).

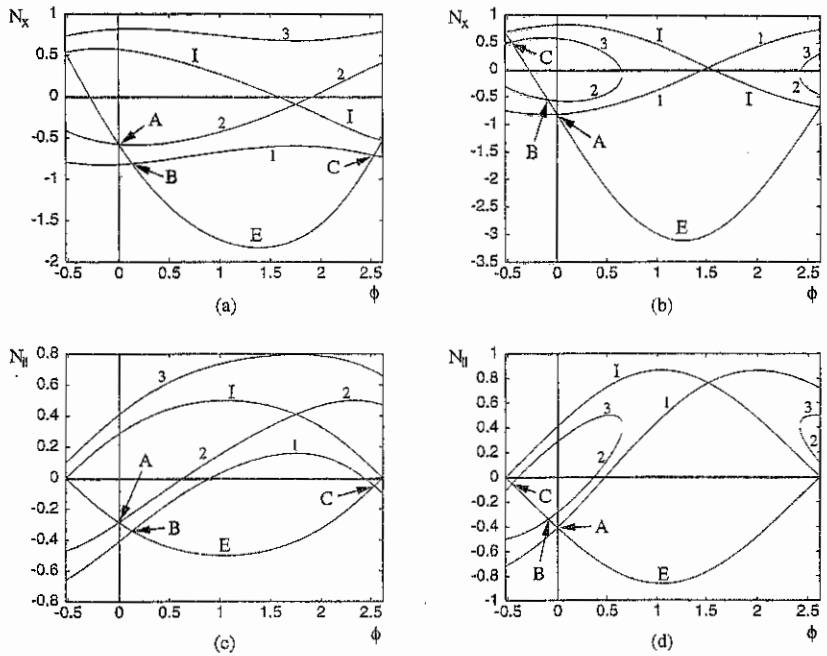

Figure 1. *Refraction indices of the incident (**I**) and generated modes (**1,2,3**) and effective refraction index of the "echo" current (**E**) are shown as functions of ϕ, the angle between the incident mode wave vector and the normal to the cyclotron resonance zone. In the case of extraordinary mode incidence ((a) and (c)) 1 and 3 correspond to the generated ordinary modes and 2 corresponds to the generated extraordinary mode. In the case of ordinary mode incidence ((b) and (d)) 1 corresponds to the generated ordinary mode, 2 and 3 correspond to the generated extraordinary modes. The points where the effective refraction index of the "echo" current matches the refraction index of one of the generated modes are marked by **A**, **B** and **C**. These points correspond to maximum energy conversion into the particular mode.*

Dissipative Saturation Structure and Transport Effects of Self-Excited Microislands in Tokamaks

E.Minardi, E. Lazzaro.

Istituto di Fisica del Plasma, Assoc. EURATOM-ENEA-CNR, Via R.Cozzi 53, Milan, Italy

1-Introduction

The possibility of self-excitation in tokamaks of microislands (whose width is much smaller than the ion gyroradius and the mode numbers m and n are large) by pumping energy from the plasma through the interaction of the ions with densely packed island chains has been suggested in recent years by Kadomtsev [1]. The interaction with the random electrostatic poloidal field generated by the system of incoherent island chains may cause a net slow radial drift of ions in the outward direction of the major radius R through the toroidal nonlinear terms of the equation of motion [2] quadratic in the electric field. The adiabatic conservation of the magnetic moment $\mu = m_i v_\perp^2/2B \propto v_\perp^2 R$ during the slow motion toward increasing R implies a loss of plasma kinetic energy that is pumped into the islands. In view of discussing the conditions for reaching a stationary situation where the pumping term is balanced by an appropriate damping we reformulate and solve numerically in the stationary case the nonlinear partial differential equation describing the structure of the microislands and elucidate how the topology of the islands is affected by the nonlinearity. In presence of densely packed incoherent island chains the ion may experience a nonvanishing poloidal electrostatic field while crossing a single chain during a single Larmor gyration and exchange of momentum may occur between the ions and the island chains [1]. Under this assumption we develop a model of island sustainment considering that the pumping term is balanced by a damping term arising from a resistive-like anomalous dissipation related to the interaction between the islands and marginally stochastic electrons .

The saturated island width is expressed in terms of the physical and geometrical parameters of the tokamak. The consequences on plasma transport and the scaling of the energy confinement time with respect to these parameters are presented.

2.- Nonlinear Stationary Solutions

We start from the continuity equation for the electrons

$$\frac{\partial n_e}{\partial t} + c\frac{\vec{E}\times\vec{B}}{B^2}\cdot\nabla n_e = \frac{1}{e}\nabla_{//} J_{//} \qquad (1)$$

and the equilibrium equation (neglecting inertia) along $\vec{B}$

$$(1/en_e)\vec{B}\cdot\nabla(n_e T_e) + \vec{E}\cdot\vec{B} - \eta\vec{J}\cdot\vec{B} = 0 \quad (2)$$

where $\vec{B}\cdot\nabla T_e = 0$ is assumed. The density of ions, treated as adiabatic is fixed by quasi-neutrality. In slab geometry and in stationary conditions the independent variables for a

single helicity mode with n,m>>1 are $x = r - r_s$, $y = r(\theta - n\phi/m) - uv_* t$ where $v_* = cT_e/eBL$, $L^{-1} = -dn_e/n_e dx$ and u is a quantity to be determined. Combining the equations above with Maxwell's equations in a tokamak like slab geometry one obtains the following equation for the normalized helical flux function Ψ and the electrostatic potential Φ [1]:

$$\Delta\Psi = \begin{cases} \Gamma\left[1 - x/\left[2(\Psi_s - \Psi)\right]^{1/2}\right] - 1 & \text{for } \Psi \le \Psi_s \\ G(\Psi) - 1 \quad \text{for } \Psi > \Psi_s \end{cases}; \Phi = \begin{cases} (1-u)\left[2(\Psi_s - \Psi)\right]^{1/2} - x\right] & \Psi \le \Psi_s \\ (u-1)x & \Psi > \Psi_s \end{cases} \quad (3)$$

where Ψ_s is the separatrix label and $\Psi \le \Psi_s$ corresponds to the region outside the separatrix. $G(\Psi)$ is an arbitrary function that here we choose to be linear, i.e. $G(\Psi) = -k^2\Psi$, with $k = m/r_s$ and $\Gamma = \gamma_0(u+\tau)(u-1)$ where $\gamma_0 = 4\pi n_e T_e (1+\tau)^{-1}\left(r_s/LB_\theta S\right)^2$, $\tau = T_i/T_e$ and S is the magnetic shear. In the linear approximation ($kw << 1$) one has $\Gamma = kw$ as follows from the appropriate matching conditions. The nonlinear partial differential equation (3) is solved numerically as a boundary value problem for Ψ by a finite elements solver using the Galerkin method with quadratic basis functions on an adaptive grid. Four cases are considered: 1) $\Gamma = 0$, $G(\Psi) = 0$: the magnetic energy of the island $W = (1/8\pi)\int\left(\nabla\tilde{\Psi}\right)^2 dV$ (where $\tilde{\Psi}$ is the helical part of Ψ) is minimum (Dirichlet principle); 2) $\Gamma = 0$, $G(\Psi) = -k^2\Psi$: W is minimum only in the volume *outside* the separatrix; 3) $\Gamma = kw$, $G(\Psi) = 0$: W is minimum only *inside* the separatrix and nonlinear effects are introduced outside; 4) $\Gamma = kw$, $G(\Psi) = -k^2\Psi$: W is *not* minimum and the problem is nonlinear. The nonlinearity introduces a new harmonic content producing ridges and corrugations of the island shape but at critical values of Γ well shaped islands are formed (Fig.1). By increasing Γ a sudden collapse occurs with subsequent formation of two islands. Fig.1 to 5 capture this phase (for 1/k=1cm). When Γ increases further the two islands tend to coalesce partially and to form again a ridged island. The same general pattern is reproduced (at least up to Γ=0.5). In the case of densely packed islands one cannot have diffuse current outside the separatrix and only cases 1) and 2) are possible. Case 1) cannot be stable (although W is minimum) when pumping is present, because pumping cannot be balanced by resistive damping in the absence of diffuse current. We shall assume that saturation corresponds to minimum W outside the separatrix, i.e. case 2).

3- Model of Island Pumping

Fig.6 presents the behaviour of the poloidal electric field and shows that the poloidal component of the electric field is antisymmetric around x=0 and vanishes inside the island. However when the plasma is filled with densely packed but not overlapping incoherent island chains, the poloidal electric field inside the islands is a superposition of the incoherent electric field created by the adjacent chains and exchange of momentum between the field and the ion can occur in each single crossing during a Larmor gyration. In this case, as a consequence of the ion equation of motion, also a net slow ion drift appears in the outward

R direction, after averaging over the electric field, over many gyrations and over a magnetic surface [2]. The net outward shift follows [2] from the nonlinear toroidal term in the magnetic force $\bar{f} = \bar{V} \times B_{0\phi}\bar{e}_{\phi}\left(1-(r_s+x)\cos\theta(t)/R_0\right)$ (this is the term involving x and the components $\dot{x}, \dot{y}$ of $\bar{V}$) which after a time iteration turns out to be *quadratic* in the electric field amplitude) and is accompanied by an electron shift due to ambipolarity. Conservation of the magnetic moment $\mu = mv_{\perp}^2/2B \propto v_{\perp}^2 R$ during the slow motion toward increasing R implies a loss of plasma kinetic energy at a rate $\dot{T} = -Trv\left(e\Phi\cos\theta/TR_0\right)^2$ where Φ is the electrostatic potential , v is related to the radial outward flow and $T = T_i$ or T_e. The effect of this flow must be taken into account by a sink term $-\hat{S} = -nv\cos\theta\left(e\Phi/TR_0\right)$ on the r.h.s of the continuity equation(1). This leads to the following energy integral:

$$\frac{1}{4\pi}\int\frac{\partial\Psi}{\partial t}\left(\bar{e}_{\phi}\times\bar{B}\right)\cdot d\bar{S} + \frac{\partial}{\partial t}\int\left[\frac{(\nabla\Psi)^2}{8\pi} + \frac{n(T_i+T_e)}{2}\left(\frac{e\Phi}{T_i}\right)^2\right]dV = P_+ - P_- \qquad (4)$$

where $P_+ = \int\left(T_i+T_e\right)\frac{e\Phi\hat{S}}{T_i}dV$ and $P_- = \int\eta\tilde{j}^2 dV$. The comparison between $\dot{T}$ and P_+ shows that the energy lost by the plasma is converted completely into the pumping term P_+.

4. Energy Balance, Saturation Width and Transport

A linear time dependent solution with effective pumping and damping can be obtained in the form $\exp(iuv_*k+\omega-\gamma)t$ where $\omega = v\cos\theta/R, \gamma = \eta(ck/(1+\tau))^2/\gamma_0\pi^3$ and $u = -\tau$ (rotation in the ion diamagnetic direction). The quantity v can be estimated [2] assuming, as an example, that the root mean square value of the electric field of the collection of chains is of the same order as that of a single chain. One obtains $v \approx kw^2\omega_{ci}L/r_s$. For typical values $\omega \approx 10^3 s^{-1}$ [2] ,w~ 0.1 cm and one finds that *classical resistivity* is insufficient for balancing ω with γ. Thus following Kadomtsev [1], we consider an anomalous resistivity to be ascribed to a resonant interaction between quasi-stochastic electrons and island waves with parallel phase velocity $v_*k\tau/k_{//} \approx v_e$. As shown by eq.(4) $P_+ = P_-$ is a necessary condition for saturation, independent of linear approximation. In case 2) this condition gives :

$$w = 2.8\cdot 10^5\frac{n_{13}^2 T_e^{1/2}(1+\tau)\tau Rq^3}{BLA_i k^4 S^3} \qquad (CGS; n_{13} = n\cdot 10^{-13}) \qquad (5)$$

The consistency with $w << \rho_i$ and $v_*k\tau/k_{//} \le v_e$ for x<w (resonance in the interior of the island) imposes a lower and an upper limit to the quantity k^4/n_{13}^2. Proceeding on purely dimensional grounds let us assume a diffusivity $\chi_e \propto |k_{//}|v_e w^2 = w^3 kSv_e/qR$ in the confinement region, where q is limited in the range 1<q<2. Consequently the energy confinement time in a regime of sustained microislands turns out to scale as $\tau_E \propto P^{-0.66}ILRQ$ where I is the total current, P is the power and Q is bracketed within the strong limits:

$$2\cdot 10^{-2}q^{1/3}\left[S(1+\tau)\tau^{1/2}R/L\right]^{2/3} << \frac{Q}{k} < 0.35q^{-1/3}S^2(1+\tau)^{2/3}A_i^{1/3} \qquad (6)$$

References

[1] B.B.Kadomtsev , Nucl. Fus. **31** 1301 (1991) ; Plasma Phys. Contr. Fus. **34** 1931 (1992)
[2] E. Minardi, Nucl. Fus. **34** 1561 (1994)

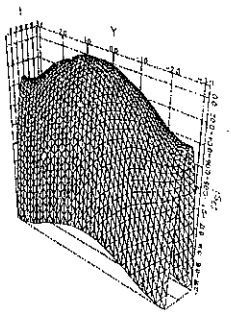

Fig1. Γ=0.24, W=0.24

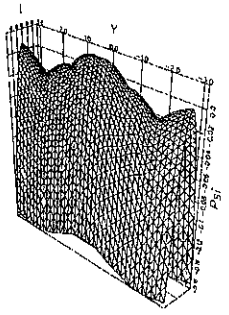

Fig2. Γ=0.24204, W=0.24204

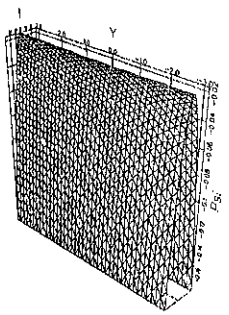

Fig3. Γ=0.245, W=0.245

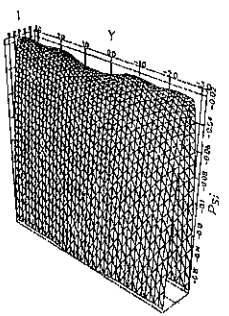

Fig4. Γ=0.249, W=0.249

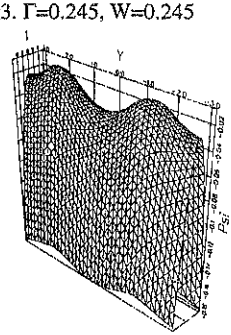

Fig5. Γ=0.25, W=0.25

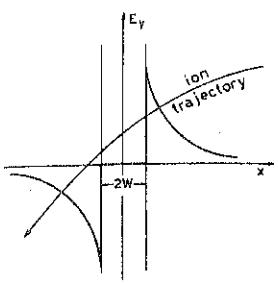

Fig6. Poloidal electric field

Ponderomotive coupling of lower hybrid waves with low frequency plasma oscillations

M. Lontano, C. Castaldo, E. Lazzaro, and A.M. Sergeev[1]

Istituto di Fisica del Plasma "Piero Caldirola"
Consiglio Nazionale delle Ricerche
EURATOM-ENEA-CNR Association
Via R. Cozzi, 53 - 20125 Milano, Italy
(lontano@ifp.mi.cnr.it)

Abstract

The propagation of large amplitude lower hybrid (LH) waves in a nonuniform plasma is computed in the slowly varying envelope (SVE) approximation. It is shown that the ponderomotive force produced by the radiofrequency (RF) field drives strong density perturbations whose amplitude grows untill the LH energy density distribution in space developes a small scale structure.

Introduction

Several experiments and theoretical investigations have been carried out in the past and in more recent times on the ponderomotive effects which are likely to occur during the propagation of finite amplitude LH waves in a magnetized plasma (see for example Refs.1,2). Besides the principle interest arisen from the observation in small scale experiments of wave-induced robust density perturbations and of the formation of "traces" along the resonant cones, along which the RF energy flows, a strong impact of such nonlinearities is expected in RF heating (H) and current drive (CD) operations in tokamak devices for fusion research [3].

One of the most important issues of the nonlinear behaviour of LH waves in plasmas is the coupling of the RF power, as it appears at the mouth of the transmission line, in the form of an electromagnetic field, with the low density edge plasma. Moreover, beyond the slow-mode cutoff, a large amplitude field is continuously fed in a finite density, low temperature plasma. Here the RF pressure ($\propto \nabla|E|^2$) is particularly effective in modifying the background density distribution, as it can be argued by looking at the simple relationship

$$\frac{\delta n}{n} \cong -\frac{|E|^2}{16\pi n(T_e+T_i)} \cong 1.4\times10^5 \frac{|E(V/cm)|^2}{n(cm^{-3})[T_e(eV)+T_i(eV)]}, \qquad (1)$$

valid in a steady state. Here, $\delta n/n$ is the ratio between the perturbed and the background densities, T_e and T_i are the electron and ion temperatures, $|E|^2/8\pi$ is the electrostatic energy density associated with the LH waves. Indeed, by inspection of Eq.(1) it is seen that for a peripheral plasma with $n = 10^{12}cm^{-3}$ and $T_e = T_i = 10eV$, a LH field of amplitude $E = 10kV$ produces approximately a density perturbation of the order of 50%.

Electric fields of the order of few kilovolts can actually occur in present day LHH and CD experiments, where MW-level powers are fed into the plasma. Then, a renewed interest for the nonlinearities occurring during LH wave propagation has led us to reconsider the problem trying to model in a realistic way the wave-plasma interaction [4].

In the frame of the SVE approximation, we have solved numerically the nonlinearly coupled equations for the complex electric field envelope of the LH vave (with frequency ω_0), and for the plasma density perturbation. The model is two-dimensional in space,

allowing for a constant background density gradient in the direction perpendicular to the external magnetic field $\mathbf{B}_0 = B_0 \hat{\mathbf{e}}_z$, and describes the time evolution of an initial LH energy density distribution over the time scale T longer than ω_0^{-1}.

Relevant equations in the SVE approximation

In the LH frequency range, i.e. for $\Omega_i << \omega << |\Omega_e|$, in the low density limit, i.e. for $|\Omega_e| >> \omega_{p,e}$, the dispersion relation for the slow mode takes the following approximate form:

$$\omega^2 \cong \omega_{p,e}^2 \frac{k_{//}^2}{k_\perp^2}\left(1+3k^2\lambda_{D,e}^2\right); \tag{2}$$

here, the following parameters have been introduced: $\Omega_\alpha = q_\alpha B_0/m_\alpha c$, $\omega_{p,\alpha} = \sqrt{4\pi q_\alpha^2 n_\alpha / m_\alpha}$, n_α, m_α, q_α are the cyclotron frequency, the plasma frequency, the density, the mass and the electric charge of the species α ($\alpha = e,i$), respectively; $\lambda_{D,e} = \sqrt{T_e/4\pi e^2 n_e}$ is the electron Debye length, and c is the speed of light. In order to derive Eq.(2) it is assumed that the LH electric field is of the form $\mathbf{E}(x,z,t) = E\exp\left(-i\omega t + ik_\perp x + ik_{//} z\right)$, $k_\perp$ and $k_{//}$ being the projections of the wavevector $\mathbf{k}$ normally and along $\mathbf{B}_0$, respectively.

Two main physical hypothesis are introduced in order to obtain the relevant equations: *i)* it is assumed that the dynamics of the wave-plasma takes place over two different time scales; a fast oscillation of the electric field, with characteristic time $\tau = f^{-1} = 2\pi/\omega$, and a slower evolution of its amplitude and of the plasma macroscopic parameters (like the density), over the time scale T. *ii)* the background plasma density is allowed to increase with a linear law along the x-direction, over a typical length L. Then, we can introduce in Eq.(2) the following relationships: $\omega = \omega_0 + \delta\omega$ (from *i*, with $|\delta\omega| << \omega_0$), and $\omega_{p,e}^2 = \omega_{p0,e}^2\left(1+\delta n/n + x/L\right)$ (from *ii*), where $\delta n(x,y,\tau)$ is the plasma density perturbation induced by the waves, n is the background density at $x = 0$. With the above positions, Eq.(2) can the be transformed into:

$$\begin{aligned}\left(k_\perp^2 + k_{//}^2\right)2\omega_0\delta\omega - k_{//}^2\left(\omega_{p0,e}^2 - \omega_0^2\right) - k_{//}^2\omega_{p0,e}^2\left(\delta n/n + x/L\right) - \\ -3\omega_{p0,e}^2\lambda_{D0,e}^2 k_{//}^2\left(k_\perp^2 + k_{//}^2\right) \cong -\omega_0^2 k_\perp^2.\end{aligned} \tag{3}$$

Let us introduce the following transformations:

$$\delta\omega \to i\frac{\partial}{\partial\tau}\ ,\ k_\perp \to -i\frac{\partial}{\partial x}\ ,\ k_{//} \to -i\frac{\partial}{\partial z}. \tag{4}$$

Then, the corresponding differential form in the physical space $(\mathbf{r},\tau)$ of Eq.(3) reads

$$\frac{2i}{\omega_0}\nabla^2\frac{\partial E_z}{\partial\tau} - \left[\left(\frac{\omega_{p0,e}^2}{\omega_0^2} - 1\right) + \frac{\omega_{p0,e}^2}{\omega_0^2}\left(\frac{x}{L} + \frac{\delta n}{n}\right)\right]\frac{\partial^2 E_z}{\partial z^2} + 3\frac{v_{th,e}^2}{\omega_0^2}\nabla^2\frac{\partial^2 E_z}{\partial z^2} \cong -\frac{\partial^2 E_z}{\partial x^2}, \tag{5}$$

where $v_{th,e} = \sqrt{T_e/m_e}$ is the electron thermal velocity. Eq.(5) represents the evolution equation for the SV complex amplitude E_z, the LH electric field along $\mathbf{B}_0$. It is coupled to the density perturbation *via* the nonlinear term $\propto \delta n\left(\partial^2 E_z/\partial z^2\right)$. $\delta n(x,y,\tau)$ evolves according to the fluid equation for magnetized sound waves which reads:

$$\frac{\partial^2\delta n}{\partial\tau^2} - v_s^2\frac{\partial^2\delta n}{\partial z^2} = \frac{1}{16\pi M}\frac{\partial^2|E_z|^2}{\partial z^2}, \tag{6}$$

where the r.h.s. represents the effect of the ponderomotive force ($F_{pm} \propto -\partial|E_z|^2/\partial z$), and $v_s = \sqrt{(T_e + T_i)/M}$ is the sound velocity. Finally, Eqs.(5) and (6) have been put in dimensioless form

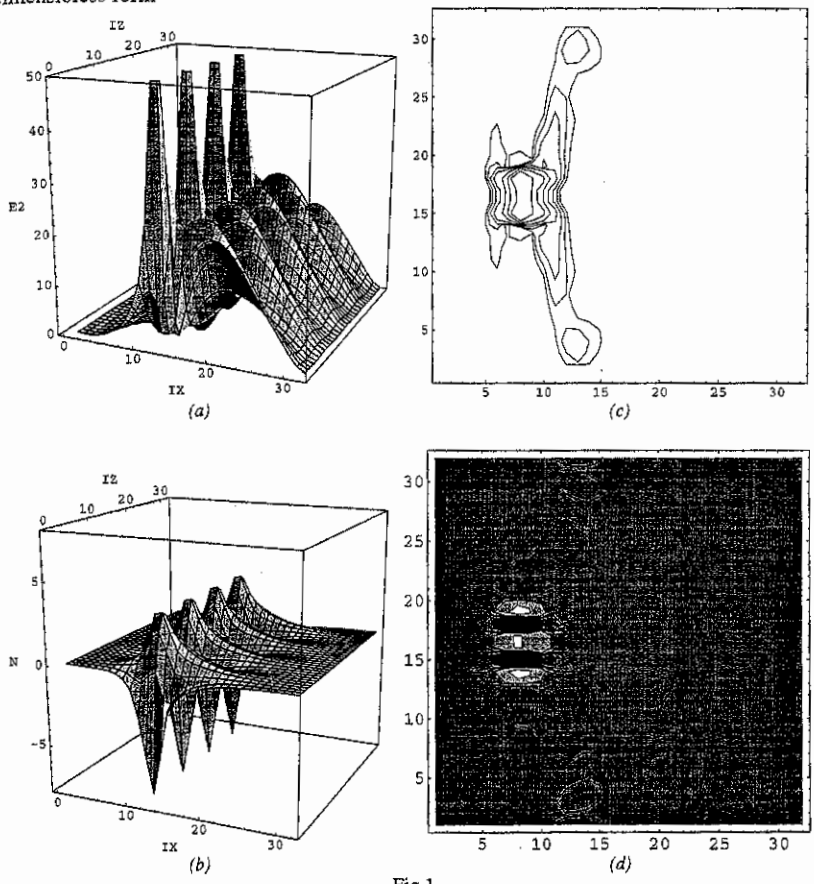

Fig.1

$$\frac{\partial^2}{\partial z^2}\left[i\frac{\partial E}{\partial \tau} + \frac{\partial^2 E}{\partial z^2} - \varepsilon x E - \delta n E + i\gamma_{th} E \right] = -\frac{\partial^2 E}{\partial x^2}, \tag{7}$$

$$\frac{\partial^2 \delta n}{\partial \tau^2} - \frac{\partial^2 \delta n}{\partial z^2} + 2\gamma_s \frac{\partial \delta n}{\partial \tau} = \frac{\partial^2 |E|^2}{\partial z^2}, \tag{8}$$

where the following normalized variables have been defined:

$$x_n = \frac{3^{3/2}}{4}\Lambda \frac{\lambda_{D0,e}}{1+\beta}\,,\quad z_n = \frac{3}{2}\Lambda^{1/2}\frac{\lambda_{D0,e}}{\sqrt{1+\beta}}\,,\quad \tau_n = \frac{3}{2}\frac{\Lambda}{\omega_0}\frac{1}{1+\beta}\,,$$

$$E_n^2 = \frac{64\pi}{3}\frac{n_{cr}T_e}{\Lambda}(1+\beta)^2 \ , \ n_n = \frac{4}{3}\frac{n_{cr}}{\Lambda}(1+\beta),$$

and $\Lambda = M/m >> 1$, $\beta = T_i/T_e$, $n_{cr} = m_e\omega_0^2/4\pi e^2$.

Numerical results

Eqs.(7) and (8) have been solved giving the LH field envelope versus x and z, at $\tau = 0$,

$$E(x,z,\tau=0) = E_0(z)\exp\left[-\frac{(x+4.95)^2}{4}\right]\cdot\left\{e^{i2\Delta k_{//}z} + \lambda e^{-i2\Delta k_{//}z}\right\}, \qquad (9)$$

with $\delta n(x,z,\tau=0) = 0$. Here, $\Delta k_{//} = 2$, $\lambda = 0.1$, and $E_0(z) = A = \text{const.}$ for the case of uniform illumination of the plasma (see Fig.1*a,b*), and $E_0(z) = A\cdot z$ to simulate the irradiation from a finite-width grill. In Fig.1 the field intensity distribution $|E(x,z,\tau)|^2$ (in *a* and *c*) and the corresponding density perturbation $\delta n(x,z,\tau)$ (in *b* and *d*) are shown for a uniform illumination (*a* and *b*, for $A = 11$, $\varepsilon = 1$, $\tau = 1.2$) and for the grill-like model (*c* and *d*, for $A = 7$, $\varepsilon = 1$, $\tau = 1.8$). In the former case, it is seen (*a*) that while a part of the initial distribution of RF energy propagates towards increasing density (i.e., to the right), an appreciable portion is "trapped" inside deep density holes (*b*) which have been produced by LH-ponderomotive forces. In the latter case, the contour lines of the field intensity (*c*) show that actually the propagation of the energy towards increasing x-values (to the right) takes place along the "resonant cones", predicted by the linear theory. However, it is seen (*d*) that a "trace" is left by the RF on the backgroud plasma density. In Figs.1*c* and *d* the $x(z)$-coordinate is the horizontal (vertical) axis, and they are measured in arbitrary units.

An important issue in nonlinear LH wave propagation is the modification of the injected $k_{//}$-spectrum due to the coupling with the low-frequency plasma motion. The study of the evolution of $|E_{k_{//}}(x,\tau)|^2$ beyond the x-position where the LH energy is deposited initially shows that an appreciable modification of the LH spectra do occur, which can be responsible of a reduced coupling with the electron population in the plasma core.

Conclusions

We have discussed the results of the 2-dim code which has been implemented in order to describe the nonlinear propagation of LH waves in a nonuniform plasma. It is found that for LH power levels typical of fusion relevant LHH and LHCD experiments the coupling of the injected RF with the slow plasma motions leads to appreciable modifications of LH $k_{//}$-spectra which can affect the energy deposition in the core plasma.

References

[1]Institute of Applied Physics, Russian Academy of Sciences, Nizhny Novgorod, Russia

[1] - W. Gekelman and R.L. Stenzel, *Phys. Rev. Lett.* **35**, 1708 (1975);
R.L. Stenzel and W. Gekelman, *Phys. Fl.* **20**, 108 (1977).
[2] - G.J. Morales and Y.C. Lee, *Phys. Rev. Lett.* **35**, 1544 (1975).
[3] - R. Cesario, *et al.*, Nucl. Fusion **32**, 2127 (1992).
[4] - C. Castaldo, E. Lazzaro, M. Lontano, and A. Sergeev, *Phys. Lett. A* (1997), in press.

Propagation of femtosecond laser pulses in gases and the ionization induced self-guiding effect

M. Lontano, A.V. Kim[1], and A.M. Sergeev[1]

Istituto di Fisica del Plasma "Piero Caldirola"
Consiglio Nazionale delle Ricerche
EURATOM-ENEA-CNR Association
Via R. Cozzi, 53 - 20125 Milano, Italy
(lontano@ifp.mi.cnr.it)

Abstract

The dominant process which takes place when a short and intense laser pulse interacts with a neutral gas is the quick ionization of the atoms which are acted upon by the electric field (with intensity higher than 10^9 V/cm). Although the ionization nonlinearity is usually expected to be a defocusing one, here we show that there are particular regimes of laser-gas interaction, characterized by the ionization saturation, in which the laser pulse is partially channeled overal several Rayleigh lengths. The self-channeling driven by the gas ionization is accompanied by the leaking of part of the energy of the laser pulse (*leaking modes*).

Introduction

Several plasma-based advanced technologies involving the use of ultrashort $\left(\tau_p \approx 10-100\,\mathrm{fs}\right)$ and higly intense $\left(I > 10^{15}\,\mathrm{W/cm^2}\right)$ laser pulses rely on the interaction of the radiation with an almost uniform and dense plasma target, and on the possibility of inhibiting the diffraction broadening over several Rayleigh lengths. It is the case, for example, of the compact electron accelerator concept based on the laser wakefield acceleration (LWFA) [1]: here a relativistically intense short laser pulse should produce a large amplitude electrostatic plasma wave which in its turn is able to accelerate electrons to relativistic energies over a distance of the order of one meter. Then, the channeling of the pulse is required in order to maintain its relativistic amplitude and, as a consequence, to guarantee the efficiency of the ponderomotive drive of the longitudinal accelerating electric field.

Self-channeling regimes have been recently experimentally observed [2,3], and have been attributed to the focusing nature of both the relativistic and Kerr-type nonlinearities. In fact they cause a radially dependent increase of the laser refractive index and the consequent deviation of light rays toward regions of stronger field intensity. Moreover, it is expected that the ionization nonlinearity leads to radiation defocusing, since the higher plasma density at higher field intensity produces a refractive index pattern opposite to that of the previous cases.

Here we show that the regime of laser-gas interaction characterized by a sharp dependence of the ionization rate on the electric field amplitude and by an effective ionization saturation leads to the partial self-channeling of the laser pulse over many Rayleigh lengths [4].

Ionization-induced self-channeling

The numerical investigation of the propagation of a femtosecond laser pulse in an initially neutral gas has been performed in the frame of the *quasi-optical approximation*. The laser electric field is assumed to be characterized by two space-time scales: a rapidly oscillating carrier, with frequency ω and wavevector $\mathbf{k}$, and a slowly varying envelope (SVE), i.e.

$$\boldsymbol{E}(\mathbf{r},t)=\mathbf{E}(\mathbf{r},t)\exp\left[-i(\omega t-\mathbf{k}\cdot\mathbf{r})\right]+\text{c.c.} \tag{1}$$

In general, $\mathbf{E}(\mathbf{r},t)$ is a complex function of its arguments, and "c.c." stays for "complex conjugate". Let $T\approx|\mathbf{E}|/|\partial\mathbf{E}/\partial t|$ and $L\approx|\mathbf{E}|/|\nabla\mathbf{E}|$ be respectively the characteristic time and space scales over which $\mathbf{E}(\mathbf{r},t)$ varies appreciably. Then it is assumed that the following inequalities hold: $2\pi/\omega<<T$, $\lambda\equiv 2\pi/|\mathbf{k}|<<L$. Under these conditions, the evolution equation for the complex SVE $E(\mathbf{r},t)$ takes the form:

$$2ik_0\frac{\partial E}{\partial z}+\frac{\partial^2 E}{\partial x^2}+\frac{\partial^2 E}{\partial y^2}-\frac{4\pi e^2}{mc^2}NE+ik_0\Gamma E\approx 0, \tag{2}$$

which is obtained from the Maxwell equations once Eq.(1) is assumed and an expansion in the smallness parameters $1/kL$ and $1/\omega T$ is performed, retaining terms up to the second order. Moreover, in Eq.(2) linear polarization, $\mathbf{E}(\mathbf{r},t)=E(\mathbf{r},t)\hat{\mathbf{e}}_\perp$, and propagation along the z-axis, $\mathbf{k}=k\hat{\mathbf{e}}_z$ are assumed. Finally, the new "local time" $\tau=t-z/v_{gr}$, measured from the pulse arrival at a given z position, has been introduced.

By inspection of Eq.(2) we can recognize the ingredients which determine the evolution of the SVE $E(\mathbf{r},\tau)$. The first term in the l.h.s. describes the propagation of the envelope with the group velocity v_{gr}; the second and the third terms contains the effects of the transverse (with respect to $\mathbf{k}$) diffraction of the pulse; the fourth term represents the ionization nonlinearity; the fifth contribution describes the energy dissipation due to the plasma production and to other damping mechanisms. The electron density $N(\mathbf{r},\tau)$ is produced and evolves according to the following equation:

$$\frac{\partial N}{\partial\tau}=\left[N_0-N(\mathbf{r},\tau)\right]f(|E|), \tag{3}$$

which describes the gas ionization characterized by the field-dependent rate $f(|E|)$, with a saturation at the constant value N_0. In the case of tunneling ionization the rate $f(|E|)$ takes the following form:

$$f(|E|)=\frac{4\nu}{|E/E_{at}|^{2n-3/2}}\exp\left(-\frac{E_{at}}{|E|}\right), \tag{4}$$

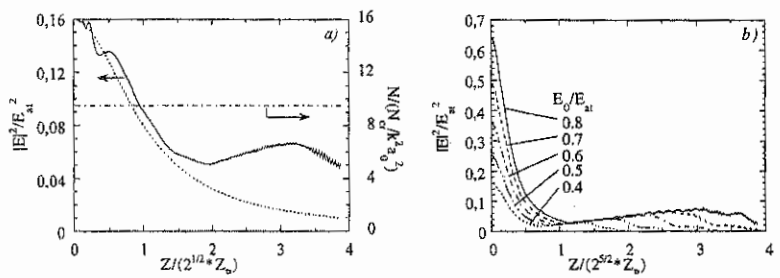

Fig.1

where $\nu\approx me^4/\hbar^3\approx 4.1\times10^{16}s^{-1}$, $E_{at}\equiv\left(m^2e^5\right)/\hbar^4\cong 5\times10^9\,\text{Volt/cm}$, and n is the principal quantum number of the electron involved in the ionization. For the sake of simplicity, we have related the ionization saturation to the detachment of all optical electrons. For a H target

gas, the saturation density N_0 is then simply obtained from the initial gas pressure p through the relationship $N_0(cm^{-3}) \approx 2.7\times10^{19}\,p(atm)$. We notice that for a Ti:Sa laser ($\lambda = 0.8\mu m$) the corresponding critical electron density is $N_{cr} \equiv m\omega^2/4\pi e^2 \approx 1.7\times10^{21}\,cm^{-3}$.

Eqs.(2) and (3) have been solved giving the laser envelope at $z = 0$, and requiring that the field distribution remains localized both in the transverse direction, and in the "local time" domain. Moreover the laser pulse is assumed Gaussian in x, y, and τ directions, and focused in vacuum at the beginning of the interaction with the gas (at $z = 0$), that is

$$E(x,y,z=0,\tau) = E_0 \exp\left[-\frac{x^2+y^2}{a_p^2} - \frac{\tau^2}{\tau_p^2}\right], \qquad (5)$$

with $\tau_p = 30\,fs$, $a_p = 20\mu m$ (corresponding to a waist in intensity of $w_0 \approx 14\mu m$), and a Rayleigh length $Z_R = \pi w_0^2/\lambda \cong 770\,\mu m$. The integration box (X,Y,Z) of Eqs.(2) and (3) has dimensions $(16\times a_p, 16\times a_p, 5.3\times Z_R)$, corresponding to $(320\mu m\times320\mu m\times4083\mu m)$.

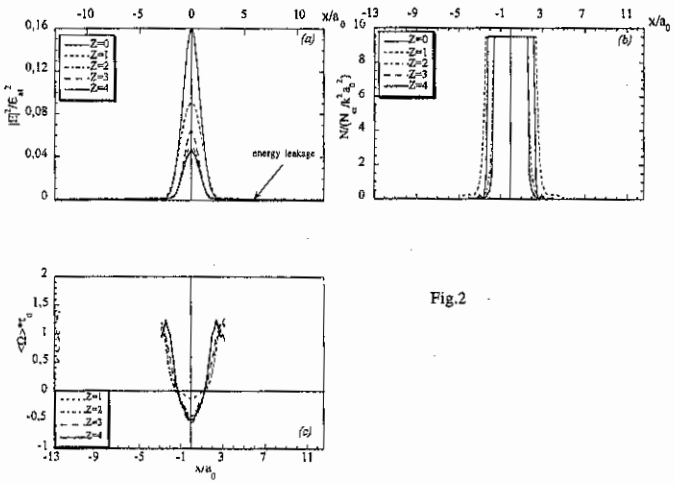

Fig.2

Eqs.(2) and (3) have been integrated for a laser field of initial amplitude $E_0 = 0.4\,E_{at}$ gas presssure of $p = 80\,Torr$, and principal quantum number $n = 3$ (e.g., in Ar). In Fig.1*a* the field intensity (full line) and the electron density (dash-dotted line) distributions are plotted versus z, at $x = 0$ and $y = 0$. For the sake of comparison, the vacuum filed intensity is also shown (dotted line). Here, $a_0 = 10\mu m$ is a reference value of the pulse radius, and $a_p = 2a_0$. The electric field and the density values are taken at the "local time" τ values where the former is maximum. It is seen that immediately after the pulse injection into the gas the diffraction spreading dominates. At a later stage of the interaction, however, a partial channeling of the radiation takes place which persists over several Rayleigh lengths. In Fig.1*b* the axial profile of the field intensity distribution is shown for a narrower initial (at $z = 0$) laser pulse, i.e. $a_p = a_0 = 10\mu m$, and for different laser intensities $E_0/E_{at} = 0.4 - 0.8$. It is shown that the partial self-guiding occurs over a longer distance for higher field amplitudes, while by comparison with Fig.1*a*, it seems that the fractional amount of electromagnetic energy which

is trapped is larger for broader field distributions. In Fig.2 the transverse field intensity (*a*) and the produced electron density (*b*) distributions are plotted against x for $y = 0$, at several axial positions. Finally, in Fig.3 the contour surfaces of the 3-dim field intensity (*a*) and electron density (*b*) distributions are shown for $|E(x,y,z,\tau_{max})|^2 = 3\times10^{-2}E_{at}^2$ and $N(x,y,z,\tau_{max}) = 5\times N_{cr}/k^2a_0^2$, respectively. The z-interval covered in the plots is the same as in Fig.1*a*, that is $0 < z < 4\times\sqrt{2}\times Z_R$. The pulse enters the gas region from the right, and is focused at the boundary ($z = 0$). The effective self-guiding of the radiation and the production of a long dense plasma channel is demonstrated.

It has been shown that the interaction conditions under which the laser self-guiding induced by the ionization is effective are characterized by a laser spot of radial dimension a_p appreciably smaller than the radius a of the plasma channel produced by ionization (see Fig.2*a* and *b*), i.e. $a_p << a$. By assuming that $(k_0 a)^{-2} << N_0/N_{cr} << 1$, the typical distance over which the trapped laser energy decreases appreciably (*leakage distance*) can be estimated as $Z_L \approx k_0^2 a^3 (N_0/N_{cr})^{1/2}/6$. Here, $k_0 = \omega_0/c$. Then, in order to have efficient channeling the following inequality should be satisfied [4]:

$$\frac{Z_L}{Z_R} \approx \frac{k_0 a^3}{3a_0^2}\left(\frac{N_0}{N_{cr}}\right)^{1/2} >> 1 \qquad (6)$$

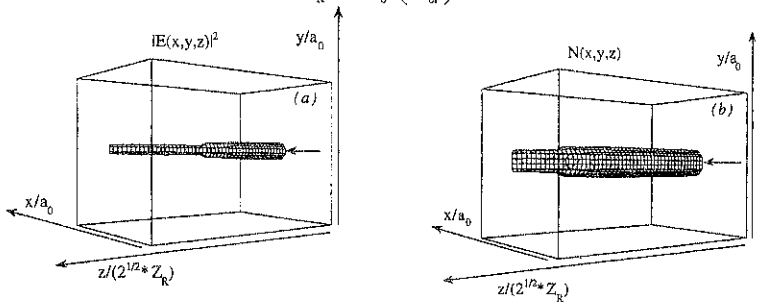

Fig.3

Conclusions

The possibility of creating a high density plasma channel by the interaction of an ultrashort laser pulse with a gas target has been investigated. It has been shown that an effective self-guiding of the laser is achievable when the ionization process is saturated over an appreciable radial extension of the electric field distribution. A very sensitive dependence of the ionization rate on the electric field amplitude together with the ionization saturation creates a hollow radial profile of the laser frequency which acts as a waveguide.

References

[1]Institute of Applied Physics, Russian Academy of Sciences, Nizhny Novgorod, Russia

[1] - T. Tajima and J.M. Dawson, *Phys. Rev. Lett.* **43**, 267 (1979).

[2] - A. Sullivan, *et al.*, *Optics Lett.* **19**, 1544 (1994).

[3] - E.T.J. Nibbering, *et al.*, *Optics Lett.* **21**, 62 (1996).

[4] - A. Sergeev, *et al.*, *Application of High Field and Short Wavelength Sources VII*, Vol.7, 1997 OSA Technical Digest Series (Optical Society of America, Washington DC, 1997).

Control of the chaotic regimes of nonlinear drift waves in a magnetized plasma

Th. Pierre, A. Latten†, Th. Klinger†, E. Gravier, X. Caron, G. Bonhomme, Th. Mausbach†, and A. Piel†

L.P.M.I., URA 835 du CNRS, Université Nancy I, BP 239, 54506 Vandœuvre Cedex, France
†*Institut für Experimentalphysik, C.A.U. Kiel, Olshausenstr. 40-60, D-24098 Kiel, Germany*

There is a growing interest in understanding the detailed nonlinear dynamics of waves in spatially extended systems. The existence of universal routes to temporal chaos has now been clearly established [1,2]. Furthermore, simple and efficient methods of dynamical control of these regimes have been recently developped [3, 4, 5]. All these control algorithms take into account the intrinsic sensitivity to initial conditions (S.I.C) of chaotic systems. The regular states of the chaotic system are recovered through the application of weak proper signals. This can be obtained even without a-priori knowledge about the exact dynamical system. The control of temporal chaos can be achieved by relatively simple control strategies. Technically convenient is the is the so-called time-delay autosynchronization (TDAS) [4] and we present here an experimental study of the efficiency of TDAS for an extended plasma system exhibiting spatiotemporal chaos.

I. EXPERIMENTAL SET-UP

The experiments are performed in a magnetized triple-plasma device. A detailed description may be found in [6]. A multipolar plasma discharge is operated in one end-chamber (argon, 10^{-4} torr). The anode voltage can be varied leading to the change of the plasma potential. An isolated high transparency stainless steel mesh grid separates the source chamber from the central magnetized plasma. The bias of the source plasma can induce an electron drift along the plasma column. At the other end, the target chamber is collecting the drifting plasma and the electron beam. The magnetized pasma exhibits a radial density profile (half widht -half maximum 12 cm) with a sharp density gradient on the plasma edge. In this region, collisional drift waves [7,8] are strongly excited, with an azimuthal phase velocity close to the electron diamagnetic drift velocity. A rigid-body rotation of the plasma column is induced when the electron beam is injected, due to the radial electric field established between the core magnetized plasma column and the outer edge. This, combined with the presence of a radial density gradient, leads to the excitation of strongly nonlinear azimuthal drift waves with a relative fluctuation up to 50%. The frequency selection is given by the density gradient length, the magnetic field, the axial electron drift, and the rotation of the column. Two essentially equivalent control parameters for the drift waves destabilization can be chosen, the source chamber bias, and the grid bias.

II. ROUTE TO DRIFT WAVE CHAOS AND TURBULENCE

Starting from the equi-potential situation, the plasma potential of the source chamber is slightly decreased. After a first Hopf bifurcation, nonlinear drift waves are established, with a peaked frequency spectrum around 7 kHz. The phase-space attractor is a limit

circle. For a critical control parameter, the drift waves perform successive bifurcations towards low-dimensional chaos. The spatiotemporal diagnostics are performed using an array of azimuthally arranged Langmuir probes [9] allowing to determine the mode number spectrum of the unstable waves, using the real-time display of the spatiotemporal pattern on the screen of the monitor of the acquisition system (VXI standard operated with a fast multichannel digitizer). In fact, an azimuthal m=3 mode is propagating along the plasma column at the onset of the unstable regime. Decreasing the control parameter, a second Hopf bifurcation, correlated with a Doppler shift of the most unstable frequency, introduces an additional drift mode (m=1) at lower frequency. After a mode-locked state, the chaotic regime is obtained after dissolution of this later state, and turbulence is finally observed. A detailed analysis of this scenario may be found in [10]. The chaotic regime under investigation here is obtained just after the destabilization of the mode-locked state. Figure 1 depicts a typical frequency spectrum and the corresponding attractor with the corresponding time-series. The detailed analysis of the data obtained with the probe array shows that this extended system exhibits spatio-temporal chaos.

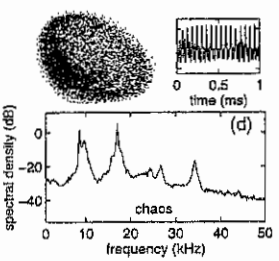

FIG. 1. *Time series of chaotic density fluctuations, its power spectrum, and phase space contour (delay time embedding in three dimensions).*

III. CONTROLLING DRIFT WAVES CHAOS

The problem of controlling these regimes of spatio-temporal chaos is not yet solved. In fact, recent results indicate that, under certain conditions, spatiotemporal chaos can be controlled using only local probing but extended action [11]. We are reporting here the control of chaotic regimes of drift waves in a laboratory magnetized plasma using the TDAS method. This method has been recently used successfully in controlling the chaotic regime of ionization waves in a discharge tube. The control of the chaotic state was achieved using the TDAS, i.e., the chaotic signal of single probe is digitized, delayed by a variable delay circuit (analog to digital conversion and propagation in FIFO memories) and is applied to the control parameter. Along Pyragas method, the appropriate adjustment of the delay time, close to the period duration of the most unstable frequency, leads to a significant reduction of the broad band component in the power spectrum while selecting the targeted frequency. A careful analysis of the efficiency of this method has been recently published [13] based on the topological characteristics of the attractor. The same method is used here in the case of this extended system : one probe gives a real-time signal which is delayed of the period of the targeted frequency and subtracted to the real-time signal. This control signal is applayed to the biasing supply of the source anode allowing to obtain a fast influence inside the magnetized column through the injected fast electron beam. Adjusting the level of the control signal, a significant reduction of the broad band component in the spectrum is obtained. Figure 2 depicts the transient signal

obtained just before and after switching on the control system. Clearly, a mode with lower erratic fluctuations is obtain after control, but the existence of a non-vanishing control signal indicate that the efficiency is far to be optimum. Nevertheless, such a reduction in the dimensionality of the chaotic system obtained using TDAS will require further investigations on the efficiency of the theoretical and numerical point of view.

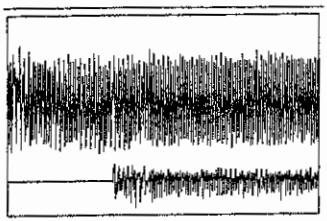

FIG. 2. *Time series of the probe signal (upper trace) before and after switching on the control process using TDAS. With a different vertical scale, the applied control signal is the lower trace, exhibiting non-vanishing mean value.*

IV. SPATIAL CONTROL OF THE CHAOTIC REGIMES

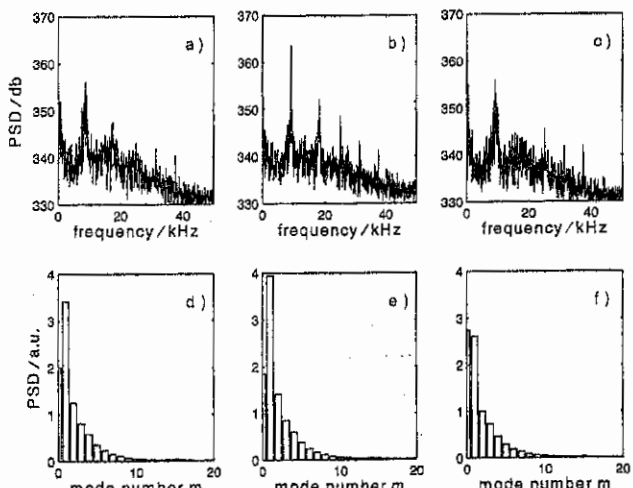

FIG. 3. *Frequency (top row) and mode number (bottom row) spectra of a destabilized $m = 1$ mode. Left side: without exciter, middle: with co-circulating external field, right side: with counter-circulating field.*

Improved efficiency of the dynamical control is expected from the application of spatially structured control signals [11]. The high efficiency of this approach has been demonstrated numerically for the nonlinear drift-wave equation [14]. In the experimental approach, the synchronization of drift waves is achieved using an azimuthally segmented hexapole electrode. By applying an appropriately phase-shifted signal with the frequency of the drift mode, an azimuthal electric field is produced that synchronizes spatially the corresponding drift mode. In fig. 3 the frequency and mode number spectra for a destabilized $m = 1$ mode are shown. In fig. 3 (a) the frequency spectrum of a destabilized

$m = 1$ mode is shown. There is still a remaining (but broadened) peak corresponding to the prior mode. The situation is similar in the mode number spectrum (fig. 3 (d)). There is also a remaining dominant peak at $m = 1$ with contributions from higher mode numbers. For the case of the co–circulating external wave field there is a strong increase of the $m = 1$ mode in the frequency and mode number spectrum, either (figures 3 (b), (e)). This yields to an increase in the radial anomalous transport [15]. In contrast, for the counter–circulating external field (figures 3 (c), (f)), the energy of the mode is reduced yielding also in a reduced transport.

V. CONCLUSION

The experimental study of the spatiotemporal chaotic regimes of collisionnal drift waves has been performed using a probe array. These chaotic regimes have been partially controlled using a time-delay autosynchronization method, using only one probe. The control information is obtained locally, but the action is distributed along the column through the fast electron beam. Until now, such a situation has not been studied experimentally, and this new result will have to be be comforted using a theoretical or a numerical investigation. However, it was also the first time that turbulent drift waves were synchronized by a spatiotemporal travelling field pattern. The influence on the turbulent transport is in this way that the co–circulating wave increases and the counter–circulating field decreases the radial transport.

REFERENCES

[1] P. Manneville, Dissipative Structures and Weak Turbulence (Academic Press, San Diego, 1990)
[2] A. J. Lichtenberg and M. A. Libermann, Regular and Chaotic Dynamics, 2nd ed. (Springer, New York, 1992)
[3] E. Ott, C. Grebogi and J. A. Yorke, Phys. Rev. Lett. **64**, 1196 (1990)
[4] K. Pyragas, Phys. Lett. A **170**, 421 (1992)
[5] T. Shinbrot, C. Grebogi, E. Ott, J. Yorke, Nature **363**, 411 (1993)
[6] Th. Pierre, G. Leclert and F. Braun, Rev. Sci. Instrum. **58**, 6 (1987)
[7] H. Lashinski, Phys. Rev. Lett. **12**, 121 (1964)
[8] S. S. Moiseev and R. Z. Sagdeev, Sov. Phys.-JETP **17**, 513 (1963)
[9] A. Latten, T. Klinger, A. Piel and T. Pierre, Rev. Sci. Instrum. **66**, 3254 (1995)
[10] T. Klinger, A. Latten, A. Piel, G. Bonhomme, Th. Pierre and Th. Dudok de Wit, submitted to Phys. Rev. Lett.
[11] D. Auerbach, Phys. Rev. Lett. **72**, 1184 (1994)
[12] Th. Pierre, G. Bonhomme and A. Atipo, Phys. Rev. Lett. **76**, 2290 (1996)
[13] W. Just , T. Bernard, M. Ostheimer, E. Reibold and H. Benner, Phys. Rev. Lett. **78**, 203 (1997)
[14] K. He and G. Hu, Phys. Rev. E **53**, 2271 (1996)
[15] A. Latten, T. Mausbach, T. Klinger and A. Piel, to be published.

Non-linear condensation of the KAWs spectra and the origin of gyro-Bohm transport in tokamaks

Yu. M. Voitenko

Department of Space Plasma Physics, Main Astronomical Observatory,

Holosiiv, Kyiv, 252650, Ukraine (voitenko@mao.kiev.ua)

1. Introduction

Recent experiments on ρ_i/a (ion gyro-radius/minor machine radius) scaling, together with experimental results on plasma turbulence, show gyro-Bohm-(GB-) like plasma transport in tokamaks [1, 2].

Dominant turbulence, determining thermal diffusivity and energy confinement time, contains sufficient power in electromagnetic fluctuations and/or coherent structures) with correlation lengths of the order of ρ_i. To proceed the way of better confinement of future tokamaks, the knowledge of the nature and origin of this turbulence is of great importance.

In the present paper we consider the non-linear spectral energy transfer in the turbulence of kinetic Alfven waves (KAWs), a very feasible candidate to produce GB transport in tokamaks.

2. Kinetic Alfven Turbulence

Depending on the values of the perpendicular wave-numbers, $k_\perp$, the Alfven spectrum in tokamaks can take on two distinct forms. The waves with long wavelengths, $k_\perp\rho_i<<1$, are toroidicity-induced Alfven eigenmodes (TAEs), and the waves with $k_\perp\rho_i\sim1$, are finite Larmor radius-induced kinetic Alfven waves (KAW), which are only weakly affected by the geometry of the magnetic field and by non-zero resistivity. The finite ion gyroradius and electron inertia effects produce E_z in KAWs, which brings about collisionless wave-particle resonant interaction, resulting in the enhanced plasma heating and anomalous transport.

As linear kinetic theory shows, KAWs can be easily excited in tokamaks by various destabilising factors, including field-aligned currents, parallel electric fields, particles beams, and unstable particles velocity distributions. Although each of these

mechanisms gives rise to wave growth in its own $k_\perp$-domain, often lying far from $k_\perp=\rho_i^{-1}$, the wave energy is transferred in wave-number space via non-linear wave-wave interaction. Contrary to MHD Alfven waves, three KAWs can effectively interact among themselves. Three-wave resonant interaction among KAWs have been studied in the past by a number of authors (see, e.g. [3]), but the common approach so far was two-fluid MHD-type theory in the limit of weak wave dispersion, i.e., $k_\perp\rho_i<<1$. In fact, even linear dispersion of $k_\perp\rho_i<<1$ Alfven waves, known from the kinetic theory, cannot be obtained from two-fluid MHD. Therefore, the results of the non-linear theory cannot also be considered as exact even in $k_\perp\rho_i<<1$ limit. Moreover, KAWs with $k_\perp\rho_i\geq 1$ are often excited, for which previous results are not applicable. To study non-linear KAWs interaction in that case one should turn to kinetic plasma theory using Maxwell-Vlasov set of equations. In the present paper the kinetic Vlasov equations are used to derive coupling coefficients (matrix elements) of the three-wave resonant interaction of KAWs with arbitrary dispersion. Our consideration is restricted to the plasma β lying in the range $m_e/m_i<\beta<1$, typical for many cases of laboratory and space plasma. Some implications regarding parametric decay instability of pump KAW and weak KAW turbulence are also discussed.

2.1. Coupling coefficients of the three-wave resonant interaction. Let us analyse three-wave resonant (TWR-) interaction, lowest in order of wave amplitudes. Contrary to the MHD Alfven waves, KAWs undergoes strong TWR-interaction, which in many cases is a most efficient mechanism of the non-linear saturation of plasma instabilities and non-linear wave spectrum modification.

We calculate coupling coefficients of the TWR-interaction by use of kinetic equations for all plasma components. Canonical equations for wave amplitudes are derived from the quasineutrality equation and Ampere's law in the z-direction, with second-order current density and particles number density calculated by use of second-order particles velocity distribution functions. The equation for Fourier amplitudes $\tilde{A}_1$ of the KAWs magnetic potential, describing three-mode couplings, reads as

$$i\left(\frac{\partial}{\partial t}-\gamma_1\right)\tilde{A}_1=\sum_{2,3}\delta(1-2-3)U_{1,2,3}\tilde{A}_2\tilde{A}_3\,. \qquad (1)$$

Here subscripts **3, 2, 1** mean wave-vectors $\mathbf{k}_3$, $\mathbf{k}_2$, $\mathbf{k}_1 = \mathbf{k}_3 + \mathbf{k}_2$ correspondingly, and matrix elements of three-wave interaction ($\kappa = k_\perp \rho_i$)

$$U_{1,2,3} = i\frac{V_A}{4B_0}(K_2 - K_3)\left(\frac{K_1}{\kappa_1^2}\right)\left(\frac{\kappa_1^2}{K_1} + \frac{\kappa_2^2}{K_2} + \frac{\kappa_3^2}{K_3}\right)[\mathbf{k}_2 \times \mathbf{k}_3]_z . \qquad (2)$$

Linear growth/damping rate, γ , and dispersion function, K, are given elsewhere [4]

2.2. Inverse energy cascade and spectra of KAW turbulence. The coupling coefficients and linear dispersion of KAWs have such mathematical structure that TWR-interaction of KAWs leads to inverse turbulent cascade, transporting energy towards lower $k_\perp$. Indeed, from above equations one can get increment of parametric decay instability as (B is wave magnetic field):

$$\gamma_{NL}^2 = \Omega_i^2\left(\frac{V_A}{4V_{Ti}}\right)^2 (K_2 - K)(K - K_1)\left(\frac{K}{\kappa^2}\right)\left(\frac{\kappa^2}{K} + \frac{\kappa_2^2}{K_2} + \frac{\kappa_1^2}{K_1}\right)^2 [\mathbf{k}_1 \times \mathbf{k}_2]_z^2 \rho_i^2 \left(\frac{B}{B_0}\right)^2 . \qquad (3)$$

Since K is monotonous function of k, the wave-numbers of decay products k_1 and k_2 should satisfy the following instability condition: $k_1 < k < k_2$. In this case, the conservation of energy and enstrophy throughout consequent decay processes should lead to the formation of the inverse cascade like in two-dimensional Navier-Stokes turbulence [5]. The rate of TWR non-linear interaction and wave-numbers of decay products growing faster may be found by maximizing equation (3):

$$\gamma_{NL} \approx \Omega_i \kappa^3 \frac{B}{B_0}, \qquad (k_2 \approx 1.4k,\ k_1 \approx 0.64k) \text{ for } \kappa < 1, \text{ and}$$

$$\gamma_{NL} \approx 0.7\Omega_i \kappa^2 \frac{B}{B_0}, \qquad (k_2 \approx 1.46k,\ k_1 \approx 0.73k) \text{ for } \kappa > 1. \qquad (4)$$

By use of expression (2) for coupling coefficients we found Kolmogorov-type spectra of the weak KAW turbulence, one for energy cascade,

$$W_k = W_0 k_z^{-1/2} k_\perp^{-5} \ , \ (k_\perp < \rho^{-1}) \text{ and } W_k = W_0 k_z^{-1/2} k_\perp^{-3} \ (k_\perp > \rho^{-1}), \qquad (5)$$

and another for enstrophy cascade:

$$W_k = W_0 k_z^{-1/2} k_\perp^{-4} \ , \ (k_\perp < \rho^{-1}) \text{ and } W_k = W_0 k_z^{-1/2} k_\perp^{-3.5} \ (k_\perp > \rho^{-1}) \qquad (6)$$

3. Condensation of KAW turbulence

In small-$k_\perp$-domain, the ion Compton scattering of weakly dispersing KAWs comes into play. Since ion Compton scattering transports energy towards larger $k_\perp$ [6], it can balance inverse TWR-induced energy cascade. Therefore, independently on

the source positions in wave-number space, the energy of KAW turbulence is caught near $k_\perp\rho_i \sim 1$ by the co-operative action of oppositely directed TWR-interaction and ion Compton scattering of KAWs. The inverse/direct cascade turning point $k_\perp^*$, where condensation of KAWs spectra happens, may be found by equating TWR rate and ion Compton scattering rate. The result is:

$$k_\perp^* \rho_i = C_s (R/a)^2 \beta (\rho_i / a)^{-1}, \qquad (7)$$

where C_s is constant determined by the source of turbulence. Typical values for C_s are 0.1 - 0.01, resulting with ITER-like parameters in the following values for that point: $k_\perp^* = (0.24 - 2.4)\rho_i^{-1}$.

4. Conclusion

The growth of coherent vortex structures with typical transversal sizes of the order of ρ_i is quite possible, provided sufficient amount of energy is supplied by sources. In any case, we expect that despite the action of various KAW sources, a universal character of the turbulent energy condensation due to counter-directed TWR-interaction and ion Compton scattering of KAWs should result in enhanced fluctuations around $k_\perp$ close to ρ^{-1}. As a diagnostic tool to determine dominant instability, the spectra of broad-band turbulence may be used, with cut-offs indicating sources positions in wave-number space.

References

[1] Cordey J.G., Balet B., Campbell D. et al, *Plasma Phys. Control. Fusion*, **38,** A67-A75 (1996)

[2] Petty C.C., Luce T.C., Burrell K.H. et al, *Phys. Plasmas*, **2,** 2342 (1995)

[3] Shukla P.K., and Stenflo L., *Physica Scripta*, **T60**, 32 (1995)

[4] Voitenko Yu.M., in: *Control. Fusion and Plasma Phys.* (Ed. D. Gressilon, A. Sitenko and A. Zagorodny). EPS Conf. Series, **20C**, Part III, p.1293 (1996)

[5] Hasegawa A., *Advances in Physics*, **34**, 1 (1984)

[6] Gang F., *Phys.Fluids*, **B4**, 3152 (1992)

Composite Transport Coefficients for Well Confined Plasmas

B. Coppi, W. Daughton
Massachusetts Institute of Technology
Cambridge, MA 02139

1 Introduction

A confinement scaling and associated transport coefficient originally proposed for ohmic and ICRF heated L-mode discharges in Alcator C-Mod [1] has been generalized for the observed confinement in other machines. The thermal transport coefficient involves the difference of two terms. One term represents the normal outward diffusion of thermal energy while the other corresponds to a process which reduces the outward flux. This reduction term degrades as the the heating power increases above the characteristic ohmic level. There are in fact theoretical arguments [2] in support of a composite transport coefficient based on the symmetry properties of a transport matrix. The coefficient includes the constraint of profile consistency and is inspired by the properties of the so-called "ubiquitous" modes [3]. The confinement scaling consistent with the composite transport coefficient is not a simple power law, but is also composed of two terms. The experimental database assembled for the ITER project is used to compare D3D, JET, JT60, PDX, TFTR, FTU and Alcator C-Mod with this analysis. The comparison is quite favorable.

2 L-Mode Scaling for Alcator C-Mod

The proposed scaling was originally developed from observations of ohmic and ICRF heated discharges in Alcator C-Mod [1]. For ohmic discharges, it was observed that $\beta_p/q_E^{2/3}$ is roughly constant where $q_E = 2\pi a^2 \kappa B_T/(\mu_o I_p R)$. Drawing inspiration from this observation a more general dimensionless relationship for auxiliary heated plasmas was developed in terms of the relevant dimensionless parameters. Since one expects β_p to increases with the heating power, a natural dimensionless parameter to consider is the ratio of the total heating power P_H to some characteristic power scale. An obvious choice for this is the product of the plasma current I_p and a characteristic voltage scale $\mathcal{V}_o$. For ohmic plasmas, the loop voltage is a reasonable choice for this scale since the ohmic loop voltage does not vary greatly between different discharges and between different machines. For auxiliary heated plasmas, the loop voltage can vary significantly and one must look for another appropriate voltage scale. One possible choice for this scale is in terms of a dimensionless parameter introduced originally in connection with the CMG diffusion coefficient for ohmic plasmas [4]

$$\mathcal{V}_o = \alpha_v \frac{T_e}{e}\left(\omega_{pi}\frac{c^2}{\omega_{pe}^2}\frac{\nu_e}{v_{the}^2}\right)^{2/5} , \tag{1}$$

where α_v is a dimensionless constant chosen such that $\mathcal{V}_o \approx 1$ for typical tokamak parameters. Notice that $\mathcal{V}_o \propto n^{1/5}$ is a weakly increasing function of density.

Examining data from Alcator C-Mod, it was found that the relationship between $\beta_p/q_E^{2/3}$ and $P_H/I_p\mathcal{V}_o$ is well represented by a linear function of the form

$$\frac{\beta_p}{q_E^{2/3}} \approx \gamma_1 \frac{P_H}{I_p \mathcal{V}_o} + \gamma_2 , \tag{2}$$

where γ_1 and γ_2 are numerical constants. For ohmic plasmas, the two contributions to β_p are roughly equal.

3 Extension to Other Experiments

To extend this idea to other machines, a more general form was proposed

$$\frac{\beta_p}{q_E^{2/3}} \approx f_1 \frac{P_H}{I_p \mathcal{V}_o^o} + f_2 \,, \tag{3}$$

where f_1 and f_2 are functions of other dimensionless parameters involving geometry and weaker dependences on other plasma parameters. For any particular machine, f_1 and f_2 vary weakly. Thus, it is only possible to determine f_1 and f_2 from examining data from a range of machines.

Using the L-mode database assembled for the ITER project, possible forms for the functions f_1 and f_2 where identified. A primary purpose of transport scalings is to extrapolate the confinement characteristic of machines envisioned to operate at or near ignition conditions. Thus, relatively clean thermal plasmas close to equilibrium are the most relevant. Ohmic and L-Mode discharges where selected based on the following criteria : $Z_{eff} < 2.0$, $0.7 < W_i/W_e < 1.3$ and $[dW/dt]/P_H < 0.1$. Discharges from D3D, JET, JT60, PDX, TFTR, FTU and Alcator C-mod where considered.

In performing the analysis, a weak density dependence was found which is convenient to group with the density dependence already present in Eq. (1) by defining a modified $\mathcal{V}_o^o$

$$\mathcal{V}_o^o \approx \alpha_v \frac{T_e}{e} \left(\omega_{pi} \frac{c^2}{\omega_{pe}^2} \frac{\nu_e}{V_{the}^2} \right)^{2/5} \left[\frac{\nu_*}{1+\nu_*} + \left(\frac{n_o^o}{n} \right)^{1/3} \right] \,, \tag{4}$$

where $\alpha_v \approx 0.18$ and

$$\left(\frac{n_o^o}{n} \right)^{1/3} \equiv C_1 \left(\frac{\omega_{pi}}{\nu_e} \right)^{2/3} \left(\frac{c}{4\pi V_{the}} \right)^2 \frac{m_e}{m_p} \,, \tag{5}$$

with $C_1 \approx 0.24$ corresponding to $n_o^o \approx 0.7 \times 10^{20}$ m^{-3}. Thus $\mathcal{V}_o^o$ decreases weakly with density when $\nu_{*e} \ll 1$.

A power law form for f_1 and f_2 was identified in terms of dimensionless parameters involving geometry and other weakly varying quantities. As shown in Fig. 1, the selected discharges are well described by Eq. (3) using f_1 and f_2 of the form

$$f_1 \approx 0.11 \left(\frac{d_i}{a} \right)^{1/3} A_i^{1/4} \left(\frac{\omega_{pe}}{\Omega_{ce}} \right)^{1/3} \qquad f_2 \approx 0.15 \, \frac{R}{10a} A_i^{1/2} \left(\frac{\omega_{pe}}{\Omega_{ce}} \right)^{1/3} \,, \tag{6}$$

where A_i is the average mass number and $d_i \equiv c/\omega_{pi}$ evaluated with the line average electron density.

An important result of this work is that the confinement scaling for the stored energy is not a simple power law. The scaling in Eq. (3) can be re-written in terms of the stored energy as

$$\begin{aligned} W &\approx 0.11 \frac{3 V_a \mu_o}{4 \mathcal{L}^2 \mathcal{V}_o^o} I_p q_E^{2/3} P_H \left(1 + f_3 \frac{I_p \mathcal{V}_o^o}{P_H} \right) \left(\frac{d_i}{a} \right)^{1/2} \left(\frac{\omega_{pe}}{\Omega_{ce}} \right)^{1/3} A_i^{1/4} \,, \\ f_3 &\approx 1.4 \left(\frac{R}{5a} \right)^{1/2} \left(\frac{R}{20 d_i} \right)^{1/2} A_i^{1/4} \,, \end{aligned} \tag{7}$$

where $\mathcal{L}$ is the poloidal length around the outermost flux surface and V_a is the plasma volume. In simplified form, the energy confinement time $\tau_E = W/P_H$ from Eq. (7) is

$$\tau_E \approx 0.031 R q_E^{2/3} I_p \left(1 + f_3 \frac{I_p \mathcal{V}_o^o}{P_H} \right) \left(\frac{d_i}{a} \right)^{1/2} \left(\frac{\omega_{pe}}{\Omega_{ce}} \right)^{1/3} A_i^{1/4} \,, \tag{8}$$

with R in meters, I_p in MA, P_H in MW and τ_E in seconds. In the thermal diffusion coefficient consistent with this scaling, the second term is related to a process which reduces the outward flux of energy. The degradation in confinement observed with increased heating power is attributed to the decreased importance of this term. In contrast with a typical L-mode power law scaling, this analysis indicates that the confinement time will saturate for large heating power. As shown in Fig. 1, this scaling compares quite favorably with the selected discharges.

4 Associated Diffusion Coefficient

Consider a toroidal geometry where ξ is the square root of the normalized toroidal flux and ϕ, θ are the toroidal and poloidal angles. We assume that the electron thermal conductivity is the main form of power loss and write the surface averaged electron energy equation as

$$\langle \nabla \cdot \vec{q}_e \rangle = \langle S_H \rangle, \tag{9}$$

where $\vec{q}_e$ is the heat flux and S_H is the heating power per unit volume and $\langle\rangle$ represent a flux surface average.

Assuming that the electron thermal transport coefficient D_e^{th} is a function of the flux surface variable, the heat flux can be written as

$$\langle \vec{q}_e \cdot \nabla \xi \rangle = -n D_e^{th} \frac{\partial T_e}{\partial \xi} \langle |\nabla \xi|^2 \rangle. \tag{10}$$

Combining Eq. (9) and (10) and integrating from the magnetic axis to a given flux surface gives D_e^{th} of the form,

$$D_e^{th} = -\frac{\mathcal{P}_H}{n \frac{\partial T_e}{\partial \xi} V' \langle |\nabla \xi|^2 \rangle} \qquad \mathcal{P}_H \equiv \int_0^\xi V' \langle S_H \rangle d\xi, \tag{11}$$

where $\mathcal{P}_H$ is the heating power within a flux surface ξ. Although the heating profile can vary dramatically in a tokamak plasma, the resulting temperature profile is usually of a well defined canonical form. Therefore it is assumed the temperature profile is represented by $T_e = T_{e_0}\ exp\left[-\alpha(\xi) V(\xi)/V_a\right]$ where T_{e_0} is a constant, V_a is the total plasma volume and α is a weak function of ξ to allow greater flexibility in the canonical form. Using this form for T_e Eq. (11) becomes

$$D_e^{th} = \frac{1}{n T_e} \frac{V_a}{\langle |\nabla V|^2 \rangle} \frac{\mathcal{P}_H}{\alpha}. \tag{12}$$

In order to derive a transport coefficient which is dependent only the plasma parameters, it is desirable to relate the heating power to the local and global plasma parameters. Referring to the the dimensionless scaling in Eq. (3) we assume $\mathcal{P}_H/\alpha \propto I(\xi)$ where $I(\xi)$ is the plasma current within flux surface ξ and write, on the basis of Eq. (12),

$$D_e^{th}(\xi) \approx \mathcal{V}_o^o \frac{I(\xi)}{n(\xi) T_e(\xi)} \frac{V_a}{\langle |\nabla V|^2 \rangle} \left[\frac{\beta_p}{q_E^{2/3}} - f_2 \right] \frac{1}{f_1}. \tag{13}$$

Motivated by the properties of the "ubiquitous" modes [3] it is assumed that the underlying collective modes responsible for the energy transport are driven by the electron pressure gradient. Therefore, instead of β_p we have introduced

$$\beta_{p*} \equiv \frac{8\pi p_{e*}}{\langle B_\theta^2 \rangle}, \qquad \text{where} \qquad p_{e*} \equiv \left| \frac{dp_e}{d\xi} \langle |\nabla \xi| \rangle \right|_{max} a, \tag{14}$$

and a is the half width of the flux surface with maximum $dp_e/d\xi$. The form we adopt then is

$$D_e^{th}(\xi) \approx \mathcal{V}_o^o \frac{I(\xi)}{n(\xi)T_e(\xi)} \frac{V_a}{\langle|\nabla V|^2\rangle} A_i^{1/4} \mathcal{F}_D \,, \tag{15}$$

$$\mathcal{F}_D \approx \begin{cases} C_2 \left(\frac{a}{d_i}\right)^{1/3} \left[C_3 \frac{10\beta_{p*}}{q_E^{2/3}} \left(\frac{\Omega_{ce}}{\omega_{pe}}\right)^{1/3} \frac{1}{A_i^{1/2}} - \frac{R}{4a}\right] & \text{if } C_3 \frac{10\beta_{p*}}{q_E^{2/3}} \left(\frac{\Omega_{ce}}{\omega_{pe}}\right)^{1/3} \frac{1}{A_i^{1/2}} - \frac{R}{4a} \gtrsim 0.25 \\ 0.25 C_2 \left(\frac{a}{d_i}\right)^{1/3} & \text{otherwise,} \end{cases}$$

where $\mathcal{V}_o^o$ is given by Eq. (4) and $C_3 \approx 1.7$, $C_2\alpha_v \approx 0.02$ are dimensionless numerical coefficients. Note that, in practice, there are only *two* numerical coefficients to be fitted since for nearly all discharges considered $\nu_* << 1$.

The function $\mathcal{F}_D$ contains two terms. The first corresponds to the standard diffusive outflow of thermal energy while the second represents a process which reduces this outward flux. For discharges with β_{p*} below the minimum criteria stated in Eq. (15) (typically in the range $\beta_p \sim 0.1 - 0.15$), we take an alternate form for $\mathcal{F}_D$ obtained by selecting out ohmic discharges from a number of machines and assuming that the minimum transport corresponds to the typical level of ohmic confinement observed. For typical tokamak parameters, the minimum β_p is in the range

A series of numerical simulations for plasmas from Alcator C-Mod have been carried out using the diffusion coefficient in Eq. (15) for the electron thermal diffusivity and neoclassical diffusion for the ions. Good agreement has been obtained between the simulated and experimentally measured electron temperature profiles in nearly two dozen ohmic and ICRF heated discharges.

The authors gratefully acknowledge the Alcator C-Mod group and the ITER group for providing transport data. This work was supported in part by the U.S. Department of Energy.

References

[1] B. Coppi A. Airoldi, F. Bombarda et al., IAEA Conference, **F1-CN-64/BP-14** (1996)

[2] B. Coppi and F. Pegoraro, *Phys. Fluids B* **3** 2582 (1991)

[3] B. Coppi and G. Rewoldt, *Phys. Rev. Letters* **33** 1320 (1974) and B. Coppi and F. Pegoraro, *Nucl. Fusion* **17**, 963 (1977).

[4] B. Coppi and E. Mazzucato, *Phys. Letters* **71A** 337 (1979)

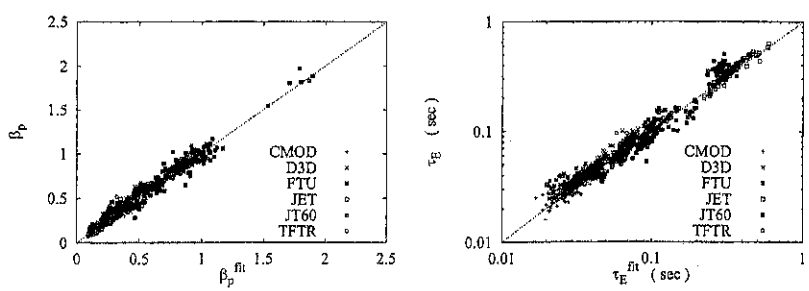

Figure 1: Comparison of β_p scaling in Eq. (3) and τ_E scaling in Eq. (8) with ITER L-mode database

The Weibel instability in inhomogeneous plasmas

F.Califano[1], F.Pegoraro[2] and S.V.Bulanov[3]

[1] Dept. of Astromy, University of Florence, Italy and
Scuola Normale Superiore and INFM, Pisa, Italy

[2] Dept. of Theoretical Physics and INFM, University of Turin,
and Dept. of Physics, University of Pisa, Italy

[3] General Physics Institute, RAS, Moscow, Russia

Abstract

Magnetic fields play a fundamental role in the dynamics of laboratory and astrophysical plasmas. In most cases, the understanding of the mechanism able to build up magnetic energy in a natural plasma is a very difficult and unresolved problem. Here we present an efficient mechanism of magnetic field generation which comes into play when two (relativistic) compenetrating counter-streaming electron beams are present into the plasma. This process, known as the Weibel instability, is capable to convert part of the initial anisotropic kinetic energy into magnetic energy. In an inhomogeneous plasma, we show, both analytically and numerically, that, due to the occurrence of a spatial "resonant"-type singularity, the magnetic field generated by this instability is strongly non uniform with opposite polarities around the singularity.

1 Introduction

Magnetic fields can be generated in plasmas with temperature anisotropy by an instability known as the Weibel instability [1]. The same physical mechanism can produce magnetic fields also in cold plasmas where the initial anisotropy is given by two beams of electrons streaming in the opposite direction. These electron beams, which can be symmetric or non-symmetric, are initially compenetrating such that the total current is zero everywhere. In this system, the free kinetic energy stored into the electron streams can be partly transferred into magnetic energy as follows. Let us assume that the initial electron beams, directed along the x-axis, are perturbed by a transversal infinitesimal disturbance along the axis y. Then, since two opposite directed currents repulse each other, the initial transversal displacement is reinforced and a magnetic field, perpendicular to the plane of the streams and of the perturbation, grows exponentially in time.

2 The two-fluid relativistic equations

The physical mechanism which drives the evolution of the Weibel instability is an high frequency process which develops at the electron (fast) time scale. Therefore, at least to a first approximation, the ions can be taken to be at rest, simply providing a uniform neutralizing background.

To study the Weibel instability in the linear phase, i.e. before non-linear interactions generate scales comparable to the kinetic relevant scales, we use the (relativistic) two-electron-

fluid equations. Using, as characteristic quantities, the density $\bar{n}$, the speed of the light c and the electron plasma frequency, the equations, in dimensionless form, read:

$$\frac{\partial \mathbf{p}_a}{\partial t} = -\mathbf{v}_a \cdot \nabla \mathbf{p}_a - (\mathbf{E} + \mathbf{v}_a \times \mathbf{B}), \quad \frac{\partial n_a}{\partial t} = \nabla \cdot \mathbf{j}_a, \tag{1}$$

$$\frac{\partial \mathbf{B}}{\partial t} = -\nabla \times \mathbf{E}, \quad \frac{\partial \mathbf{E}}{\partial t} = \nabla \times \mathbf{B} - \sum_a \mathbf{j}_a, \tag{2}$$

$$\mathbf{v}_a = \frac{\mathbf{p}_a}{(1+p_a^2)^{1/2}}, \quad \mathbf{j}_a = -n_a \mathbf{v}_a, \quad a = 1, 2. \tag{3}$$

Notice that in dimensionless units, the electron skin depth is equal to one.

We consider an homogeneous plasma with initial velocities $v_{0,a}$ of the beams of the two electron populations parallel to the x-axis with zero net current density, $n_{0,1}v_{0,1} + n_{0,2}v_{0,2} = 0$. This is the only preferred axis at the initial time and, without loss of generality, we chose the y-axis such that the wavevector of the initial perturbation lies in the plane (x, y). We linearize the system of Eqs. (1)-(2) using small amplitude perturbations of the form $exp[i(k_x x + k_y y - \omega t)]$ with the velocity and electric field laying in the plane (x, y) and the magnetic field directed along the z-axis. This is the most general case where the Weibel instability (limit for $k_x \to 0$) is coupled, for wavevectors forming an arbitrary angle with the stream direction, with the two-streams instability (limit for $k_y \to 0$). The dispersion relation was given in [2]. Here we limit ourselves to the 1D limit, $k_x = 0$, [3] in order to focus the discussion on the Weibel instability alone. In this case, by defining $\Gamma_a = (1 - v_{0,a}^2)^{-1/2}$, the dispersion relation is given by:

$$\omega^2(1 - \Omega_2^{-2})(1 - \Omega_1^{-2}) - k_y^2 \left[(1 - \Omega_1^{-2})(1 + \Omega_4^{-2}) + \Omega_3^{-4}\right] = 0, \tag{4}$$

$$\Omega_1^{-2} = \sum_a \frac{n_{0,a}}{\Gamma_a \omega^2}, \quad \Omega_2^{-2} = \sum_a \frac{n_{0,a}}{\Gamma_a^3 \omega^2},$$

$$\Omega_3^{-2} = \sum_a \frac{n_{0,a} v_{0,a}}{\Gamma_a \omega^2}, \quad \Omega_4^{-2} = \sum_a \frac{n_{0,a} v_{0,a}^2}{\Gamma_a \omega^2}.$$

By defining $\gamma = Im(\omega)$ the growth rate of the instability, the main results contained in Eq. (4) can be summarized as follows.

The Weibel mode is a non-propagating mode with zero frequency, $Real(\omega) = 0$, both in the symmetric ($n_1 = n_2$) and non-symmetric ($n_1 \neq n_2$) case as well as in the relativistic limit. The growth rate increases both in the symmetric and non-symmetric case with the intensity of the stream velocities and increases linearly with the wavenumber k_y in the range $0 < k_y < 1$. Saturation occurs at wavenumbers $k_y = O(1)$ corresponding to wavelengths comparable to the electron skin depth. In the relativistic limit, due to the relativistic increase of the effective electron skin depth, the instability saturates at lower and lower values of wavenumber ($k_y \approx (\Gamma_a)^{-1/2}$).

Finally, in the linear homogeneous approximation, the electrostatic component E_y of the electric field is zero.

3 Non-homogeneous plasma

When the initial electron streams are inhomogeneous, for example when the transversal width of the beams is comparable to or smaller than the wavelength of the perturbation, the equations become singular and the magnetic field is strongly localized around the singularity, regardless the spatial scale of the initial perturbation. To show the appearance of this singularity analytically, we limit ourselves to the case of an equal and homogeneous mean electron density distributions $n_{0,1} = n_{0,2} = 1$. We assume that the inhomogeneity can be described as one-dimensional along the y-axis in the symmetric limit of two equal opposite "equilibrium" velocity streams $v_{0,1}(y) = -v_{0,2}(y)$. Under these conditions, at the initial time the total net current is zero in any point y. Assuming all perturbed quantities in the form $F(y,t) = f(y)e^{\gamma t}$, in the non-relativistic limit the linearized system of Eqs. (1)-(2) can be cast in a second order differential equation [2] for the inductive electric field E_x:

$$\frac{\partial}{\partial y}\left\{ \left[2v_0^2(y) - \gamma^2\right] \frac{\partial}{\partial y} E_x \right\} + \gamma^2\left(\gamma^2 + 2\right) E_x = 0, \tag{5}$$

where $v_0(y) = v_{0,1}(y)$.

Eq. (5) shows that for non-propagating mode, the second order derivative term vanishes at the point $\bar{y}$ where $2v_0(\bar{y})^2 = \gamma^2$. In this point, a local Frobenius analysis [4] of Eq. (5) shows that the solution is singular with the following behaviour for the electric and magnetic field:

$$E_x \sim \ln|y - \bar{y}|, \quad B_z \sim (y - \bar{y})^{-1}. \tag{6}$$

This logarithmic singularity in E_x is a standard one encountered for general oscillations in inhomogeneous flows, [5]. Eq. (6) indicates that the magnetic field B_z is strongly inhomogeneous and localized in the neighborhood of the resonant point. Around this point the field reverses its polarity which corresponds to the formation of a current sheet.

In Fig. 1 we show, as an example, the evolution of the Weibel "resonance" in a nonuniform plasma by plotting the magnetic field at four different time instants. The results showed in this figure are obtained by integrating numerically Eqs. (1)-(2) (for details on the numerical algorithm, see [2], [6]) with the following initial conditions:

$$\mathbf{v}_{0,1}(y) = v_\infty + \frac{\delta}{2}\left[1 + tanh(y)\right]\mathbf{e}_x, \quad \mathbf{v}_{0,2} = -\mathbf{v}_{0,1},$$

$$B_z(y, t = 0) = -10^{-6} exp[-y^2/\sigma] cos(k_0 y), \quad k_0 = 0.01,$$

where $\delta = 0.25$, $\sigma = 80$ and $\partial/\partial y = 0$ for all the variables at $y = \pm L_y$.

A detailed investigation of the "resonant" Weibel mode can be found in [2]. The main results can be summarized as follows.

First of all, the formation of a strong peak of the magnetic field in the central inhomogeneous region develops on a characteristic time independent from the initial wavenumber k_0 and much shorter than the inverse of the homogeneous growth rate at wavenumbers of the order of k_0. Eventually the typical scale length of the perturbation becomes comparable to the electron skin depth and the resonant process rapidly slows down. Then, the exponential

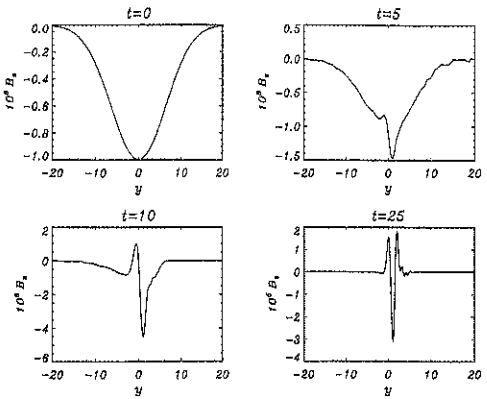

Figure 1: The evolution of the magnetic field in a inhomogeneous plasma.

growth of the magnetic field is independent on the initial conditions. No significant propagation of this mode is observed. In the relativistic regime the qualitative behaviour of the "resonant" mode remains the same.

The development of the resonance is observed also in the 2D case, leading to the formation of a chain of oppositely polarized magnetic domains and to current density vortices. In this case, we expect that magnetic reconnection induced by electron inertia [7] may play a fundamental role in the evolution of the X-points produced by the 2D "resonant" instability.

Acknowledgement

We are pleased to acknowledge the Scuola Normale Superiore (Pisa), Institut de Physique du Globe (Paris) and the supercomputing center of Cineca (Bologna) for the use of their CM200, CM5 and Cray T3D, respectively.

References

[1] Weibel, E.W., 1959, *Phys. Rev. Lett.* **2**, 83.

[2] Califano F., Pegoraro F. and Bulanov S.V., 1997, *Phys. Rew. E, in press.*.

[3] Pegoraro F., Bulanov S.V., Califano F. and Lontano M., 1996, *Physica Scripta*, T **63**, 262.

[4] Bender C.M. and Orszag S.A., 1978, *Advanced Mathematical Metods for Scientist and Engineering, MCGRAW-HILL, NY*, pag. 70

[5] Timofeev A.V., 1970, *Usp. Fiz. Nauk* **102**, 185, [*Sov. Phys. Uspekhi* 1971, **13**, 632].

[6] Califano F., 1996: *Comp. Phys. Comm.*, **99/1**, 29.

[7] Bulanov S.V., Sakharov A.S. and Pegoraro F., 1992, *Physics of Fluids*, B **4**, 1.

COMPUTER MODELLING OF EXPANDING PLASMAS WITH DUST PARTICLES

Yu. I. Chutov, A.Yu. Kravchenko, P. Schram*

Department of Physical Electronics, Taras Shevchenko Kiev University,
Volodymyrs'ka Str. 64, 252017 Kiev, Ukraine
* Department of Physics, Eindhoven University of Technology, Postbox 513, 5600 MB Eindhoven The Netherlands

Introduction

Expanding plasmas with dust particles have been intensely investigated in recent years [1-7] including investigations of relaxation phenomena in such plasmas [5-7]. However these investigations have been carried out under an assumption of an equilibrium initial state although non-equilibrium plasmas can be realized in many cases, for example, by an interaction of laser radiation with solid state surfaces, in particular in laser fusion.

The aim of this work is the computer modeling of an expansion of bounded plasma layers with dust particles and with two groups of electrons with different temperatures which can be realized by an interaction of laser radiation with solid state surfaces.

Model

Uniform quasi-neutral plasma layers with the initial size L and sharp boundaries consist of two groups (cold and hot) of electrons with initial densities n_{eo}^c and n_{eo}^b as well as with different initial temperatures T_{eo}^c and T_{eo}^b, respectively, as well as ions with density n_{io} and temperature T_{io}. The quasi-neutrality condition gives the following relation between densities of electrons and ions: $n_{io} = n_{eo} = n_{eo}^c + n_{eo}^b$.

This plasma layer can expand into a vacuum due to the self-consistent electric field. Non-charged dust particles with radius R_d and density n_d appear in this plasma layer at the initial time. Therefore the plasma relaxation takes place both by this plasma expansion and by the collection of electrons and ions from the plasma on dust particles. The plasma is considered to be collisionless because the plasma relaxation time is much less than the electron-ion collision time due to a choice of plasma parameters and non-changed dust particles.

Various parameters of this relaxing plasma have been numerically simulated using the PIC method and taking into account the dynamics of the dust particle charge in the framework of the orbit-limited-probe theory without the assumption about equilibrium of electrons and ions. Coulomb collisions of electrons and ions with dust particles are taken into account in the framework of the method of

stochastic differential equations. In some cases, the electron and ion collection by dust particles and the Coulomb collisions have been also simulated by the Monte Carlo method.

3. Results

Typical results of the computer modeling are plotted in Fig. 1 - 3 for different numbers $N_d = n_d L_\delta^3$ of dust particles in the Debye cube at $R_d = 0.32$, $(T_{eo}^e / T_{eo}^x) = 10$, $T_{io} = T_{eo}^x$ and $m_i / m_e = 256$ which last value is taken to obtain higher simulation precision. Here R_d and the spatial coordinates X are divided by the initial Debye length L_δ of the cold electrons, the time t is multiplied by the initial ion plasma frequency ϖ_{oi}.

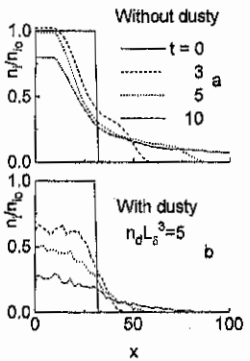

Fig. 1

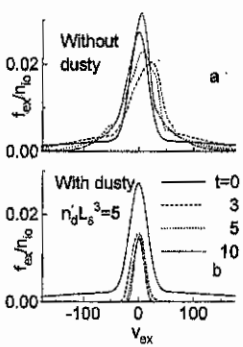

Fig. 2

The influence of dust particles on the plasma expansion is clearly seen from Fig. 1 in which the spatial distributions of the ion density n_i divided by the initial ion density n_{io} are shown for various times after the start of the plasma expansion in case of the plasma expansion without dust particles (upper part) and in case of the plasma expansion with dust particles (lower part). In the first case, we have the usual plasma expansion with a rarefaction wave propagating into the central part of the plasma layer. Therefore the decrease of the ion density in the same layer point starts only after this point has been reached by the rarefaction wave. In case of plasma expansion with dust particles (lower part of Fig. 1) the decrease of the ion density starts in all points of the plasma layer simultaneously due to the ion collection by dust particles. Besides, this decrease is faster than in the case of the plasma expansion without dust particles.

The influence of dust particles on electrons is clearly seen from Fig. 2 in which the X-components of the mean (for positive values of the spatial X-axis) electron velocity distribution function are shown for various cases corresponding to Fig. 1.

As can be seen from Fig. 2, this function is non-equilibrium initially because the plasma layers consist of two groups of electrons. In the case of plasma without dust particles, this function evolves due to a transfer of the electron energy to ions by the self consistent electric field during the plasma acceleration. All electrons participate in this energy transfer and therefore the non-equilibrium of this function as well as the special properties of this non-equilibrium are preserved during the plasma expansion without dust particles (Fig. 2a). However in the case of plasma with dust particles, fast electrons can only be collected by dust particles due to their negative electric charge. Therefore these fast electrons vanish just after the start of the plasma expansion and the electron velocity distribution function is like Maxwellian.

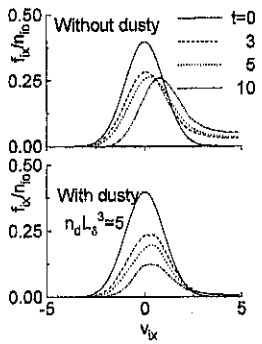

Fig. 3

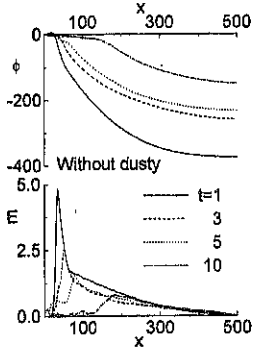

Fig. 4

As can be seen from Fig. 3, there is also some difference between the evolution of the mean ion velocity distribution function during the plasma expansion for these two cases. In case without dust particles, the ion acceleration takes place due to the self consistent electric field along the X-axis during the plasma expansion. Therefore there is some shift of the mean (for positive values of the spatial X-axis) ion velocity distribution function to the right. In the case of plasma without dust particles, this shift is smaller because fast electrons are just collected by dust particles and their contribution to the ion acceleration is smaller than in the case of plasma without dust particles.

It is of interest to investigate especially the influence of dust particles on potential structures which are created during the plasma layer expansion. Such potential structures are plotted in Fig. 4 in the case of plasma without dust particles as well as in Fig. 5 - 6 for different numbers of dust particles in the Debye cube. Electric fields E and potentials ϕ are divided in these figures by characteristic values kT_{eo}^e/eL_δ and kT_{eo}^e/e, respectively.

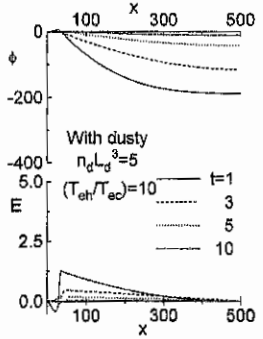

Fig. 5

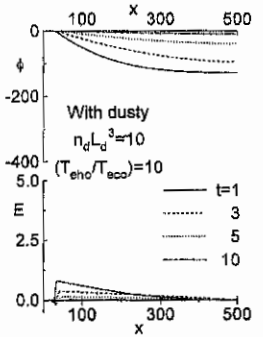

Fig. 6

Comparison of these figures shows that dust particles essentially decrease electric fields and electric potentials created by the plasma expansion. This change corresponds to the influence of dust particles on electron and ion velocity distribution functions during plasma expansions.

4. Conclusion

Computer modeling of expanding non-equilibrium plasma layers with dust particles show that dust particles can strongly influence different phenomena accompanying this expansion. This influence is caused by the selective collection of electrons and ions by dust particles with self-consistent negative electric charge. First of all, these particles can change the initial energy distribution functions of electrons and ions due to the selective collection of electrons and ions.

Acknowledgment

This work was partially supported by INTAS in the framework of contract No 94-2959 and by a grant from the Ukrainian Committee of Science and Technology

References

[1] Lonngren K.E. Planet Space Sci. 1990. V.38, N 11. P.1457-1459
[2] Luo H., Yu M.Y. Phys. Fluids. 1992. V. B4. - P.1122-1125
[3] Yu M.Y., Luo H. Physics Letters. 1992. V.A161. P.506-509
[4] Yu M.Y., Luo H. // Phys. Plasmas. - 1995 - V.2, No 3. - P. 591-593
[5] Chutov Yu., Kravchenko A., Schram P. // Physica.- 1996.- V.B128. - P.11-20
[6] Chutov Yu.I., Kravchenko A.Yu, Schram P. / J. Plasma Phys. -1996 - V.55. P. 87-94
[7]. Chutov Yu.I. at al. Invited papers of PFNL'96 September 17-19, 1996, Sendai, Japan. Abstracts of PFNL'96, p.71

NON-LINEAR SHEATHS WITH DUST PARTICLES

Yu. I. Chutov, A. Yu. Kravchenko, V. S. Yakovetsky

Department of Physical Electronics, Faculty of Radiophysics, Taras Shevchenko Kiev University, Volodymyrs'ka Str. 64, 252017 Kiev, Ukraine

Introduction

Non-linear sheaths are existing on all cold walls which the plasma is in a contact. These sheaths determine an interaction of plasmas with wall surfaces including flows of charged particles from plasmas to these walls. In much practical important cases, for example at an interaction of a laser radiation with a pellet, dust particles can be created close to a surface. These particles can strongly influence various plasma properties, including sheaths, due to a selective collection of electrons and ions from plasmas.

The aim of this work is to study non-linear sheathes in plasmas with dust particles in order to investigate an influence of these particles on sheaths.

Model

An one-dimensional slab plasma consisting of equilibrium electrons and ions with densities $n_{eo} = n_{io} = n_o$ and temperatures T_e and T_i creates an equilibrium sheath in front of an electrode to which a large negative potential ϕ_o is applied. According to the Bohm sheath criterion [1], an drift ion velocity u_o has to satisfy the well known condition $u_o \geq (kT_e / M)^{1/2}$ close to a sheath boundary with a plasma. Here M is the ion mass. Dust particles with a density n_d and a radius r_d appear in this sheath at some initial time $t = 0$ and both a collection and scattering starts of electrons and ions by these dust particles here. These processes cause an evolution of a sheath.

The PIC method is used for computer modelling of sheaths, taking into account the dynamics of dust particle charge in plasmas with self-consistent energy distribution functions of electrons and ions [2-4]. The Coulomb scattering of electrons and ions are taken into account in the framework of the Monte-Carlo method.

A case of a sheath without dust particles is used as a test of computer programs created according to these methods. In this case, spatial distributions of plasma parameters for a usual steady-state sheath [1] are

used as initial conditions for a computer simulation of their evolution. These simulations show that initial equilibrium distributions are conserved during simulation times. In case of some deviations of initial distributions from the equilibrium case, these non-equilibrium distributions evolve to equilibrium one during several ion plasma cycles. These results confirm an adequation of computer programs.

Results

Obtained results show that an influence of dust particles on sheaths strongly depend from relations between some characteristic times, namely: time τ_p of an ion penetration through a sheath, an ion collection time τ_a, and an ion scattering time τ_s. Of course, this influence is very small in the case of $\tau_p << \tau_a, \tau_s$. In the opposite case of $\tau_p >> \tau_a, \tau_s$, dust particles create some barrier between a plasma and an electrode due to a strong collection and scattering of electrons and ions by a sharp boundary of dust particles so that electrons and ions can not reach an electrode at all. In this last case, there is not a space electric charge close to an electrode and a sheath vanish.

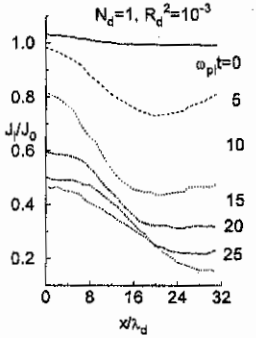

Fig. 1

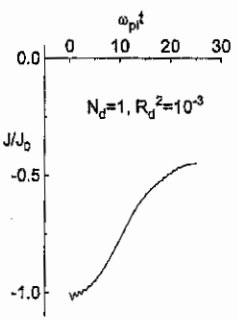

Fig. 2

The most interesting phenomena are realized in the case $\tau_p \sim \tau_a + \tau_s$. Typical results of computer simulations are shown for this case in Fig. 1 - 6 where spatial distributions of various plasma parameters are plotted for various times t after a start of their evolution from initial equilibrium distributions for $\phi_o = 10$ due to an appearance of dusty particles in a sheath. In these figures, the spatial coordinate x is divided by the initial Debye

length $\lambda_d = (kT_e / 4\pi n_o e^2)^{1/2}$, a time t is multiplied by the initial ion plasma frequence $\omega_{pi} = (4\pi n_o e^2 / M)$, a potential ϕ is divided by a characteristic value kT_e / e, N_d is the number of dust particles in the Debye cube, R_d is the radius of a dust particle divided by the initial Debye length λ_d.

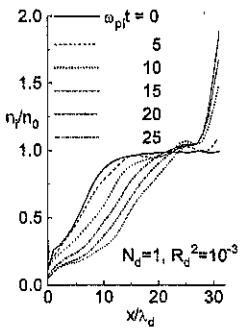

Fig. 3

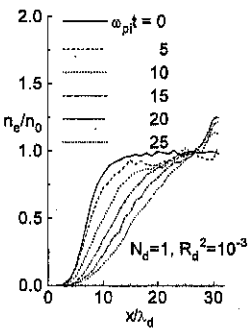

Fig. 4

As can be seen from these figures, all plasma parameters evolve essentially due to an influence of dust particles in a sheath. This influence is seen especially clear from an evolution of an ion flux J_i shown in Fig. 1. Initially, this flux is uniform because it is a case of steady-state sheaths without dust particles [1]. However dust particles decrease this flux and cause its essential heterogeneity due to a different collection and scattering of ions in different places of a sheath . Corresponding changes of an electric current J take place in an external circuit (Fig. 2).

A sheath evolution is accompanied by a decrease of ion n_i and electron n_e densities in a sheath (Fig. 3-4) due to their collection and scattering by dust particles. However some sharp increase of these densities takes place close to a boundary of a sheath with a plasma. This increase is caused by a sharp scattering of ions by dust particles due to a sharp boundary between dust particles and a plasma. This sharp region coordinates an preliminary ion flux from a non-disturbed plasma [1] with a new sheath although it is not obviously a necessity to conserve this flux in the case of a sheath with dust particles.

Of course, distributions of an electric potential ϕ (Fig. 5) evolve according to an evolution of electron and ion densities. These distributions

can be non-monotonous during their evolution times but a final distribution is monotonous always. Note, the Child-Langmuir law [1] is not valid for sheathes with dust particles because an ion flux does not conserve in this case (Fig. 1).

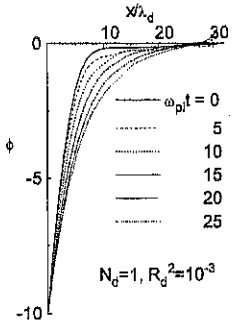

Fig. 5

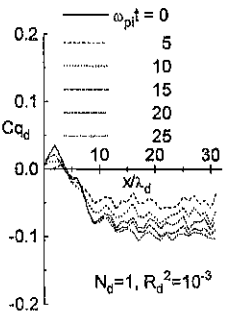

Fig. 6

Finally, spatial distributions of a dust particle charge q_d (Fig. 6) show a various sign of these charges in various regions of a sheath according to spatial distributions of electrons and ions. Note that Fig. 6 allows to determine q_d for various cases using $C = en_o / n_d$.

4. Conclusion

Computer modeling of sheaths with dust particles show that dust particles can strongly influence properties of these sheaths. This influence is caused by a collection and a scattering of electrons and ions by dust particles with self-consistent negative electric charge. First of all, these particles can strongly change an ion flux in a sheath that causes other change of sheath parameters.

References

1. Chen F.F. Introduction to plasma physics. - New York and London: Plenum Press, 1985.- Ch. 8.
2. Chutov Yu.I. et al // J. Plasma Phys.- 1996.- V. 55, part 1.- P. 87-94.
3. Sytenko O.G.et al //Plasma Phys. and Contr. Fusion. - 1996.-V.38, No 12a.- P.A105-A120.
4. Chutov Yu. et al // Physica. - 1996. - V.B128. - P.11-20.

Measurement of Anomalous Transport Produced by Electrostatic Fluctuations in a Plasma

C.Riccardi, L.Gamberale, L.Fattorini, **G.Chiodini** and M.Fontanesi

Dipartimento di Fisica, Università di Milano,INFM

Via Celoria 16, 20133- Milano, Italy

It is well known that the particle transport phenomenon is the main cause of degeneration of a confined plasma. The analysis of the anomalous fluxes, i.e. fluxes produced by micro-fluctuations, is of great interest in elucidating the dynamics of such phenomenon. For this reason it is important to know how such a particle flux is distributed in space and how it behaves under different plasma conditions. In this work we have measured the local particle flux produced by electrostatic fluctuations in the toroidal magnetoplasma Thorello. The data are analysed by using the digital correlation techniques.

The local particle flux is defined by

$$\underline{\Gamma}(\underline{x},t)=<n(\underline{x},t)\underline{v}(\underline{x},t)> \qquad (1)$$

where $n(\underline{x},t)$ is the instantaneous local plasma density, $\underline{v}(\underline{x},t)$ is the instantaneous mean velocity of the plasma particles and $< >$ is a well suited temporal average.

It is customary to decompose $n(\underline{x},t)$ and $\underline{v}(\underline{x},t)$ into a slow varying part and in a fluctuating part

$$n(\underline{x},t)=n_0(\underline{x},t)+n'(\underline{x},t)\ ,\ \underline{v}(\underline{x},t)=\underline{v}_0(\underline{x},t)+\underline{v}'(\underline{x},t) \qquad (2)$$

where $\underline{v}_0(\underline{x},t) = < \underline{v}(\underline{x},t) >$ and $n_0(\underline{x},t) = < n(\underline{x},t) >$ so that

$$\underline{\Gamma}(\underline{x},t) = \underline{\Gamma}_0(\underline{x},t) + \underline{\Gamma}'(\underline{x},t) \qquad (3)$$

with $\underline{\Gamma}_0(\underline{x},t)=<n_0(\underline{x},t)\underline{v}_0(\underline{x},t)>$ called *normal particle transport flux* and $\underline{\Gamma}'(\underline{x},t)=<n'(\underline{x},t)\underline{v}'(\underline{x},t)>$ called *anomalous* or *fluctuation-induced particle transport flux.*

If we consider a steady-state plasma the flux is independent of time and we can evaluate the anomalous part by an average on different intervals of time:

$$\underline{\Gamma}'(\underline{x}) = \lim_{M\to\infty} \sum_{i=1}^{M} \frac{1}{MT} \int_{-T/2}^{T/2} dt \cdot n'(\underline{x}, \frac{iT}{2} + t)\underline{v}'(\underline{x}, \frac{iT}{2} + t) \qquad (4)$$

Since we are interested to the flux induced by the electrostatic fluctuations we identify $\underline{v}'(\underline{x},t)$ as the fluctuating drift velocity and than it can be written as

$$\underline{v}'(\underline{x},t) = \frac{\underline{E}'(\underline{x},t) \times \underline{B}}{B^2} \cdot 10^8 \qquad (5)$$

where $\underline{E}'$ is the fluctuating part of the electric field and $\underline{B}$ is the axial magnetic field.

The anomalous flux can be written [1]:

$$\Gamma'_{\omega,d\omega}(x) = \lim_{M\to\infty} \sum_{i=1}^{M} \frac{2\cdot 10^8}{MTB} \int_0^\infty \frac{d\omega}{2\pi} \underline{k}(\omega) \times \frac{\underline{B}}{B} \cdot \mathrm{Im}[n_i^{*'}(\underline{x},\omega)\phi_i'(\underline{x},\omega)] \qquad (6)$$

where $n(\underline{x},\omega)$ and $\phi(\underline{x},\omega)$ are the Fourier transforms of density and plasma potential respectively and $\underline{k}(\omega)$ is the dispersion relation.

The quantity integrated in frequency can be viewed as the contribution to the anomalous flux of the fluctuations with frequency comprised between $\omega/2\pi$ and $(\omega+d\omega)/2\pi$.

It is the radial component of the flux that causes the lost of the particles on the wall so from now we consider only the radial component of the flux.

The measurement is performed by synchronous acquisition on a digital oscilloscope of the signals coming from three pins (that we label 1, 2, 3) such that pins 1 and 2 are disposed along the poloidal direction and pins 1 and 3 in the $\underline{B}$-direction. Pins 1 and 2 are floating potential probes whereas pin 3 is negatively biased to -18V and measures the ion saturation current I^+.

It is possible to evaluate the fluctuating plasma potential with the fluctuating floating potential

$$\tilde{\Phi}_p = \tilde{\Phi}_f \qquad (7)$$

and the relative density fluctuations with the relative ion saturation current fluctuations

$$\tilde{n} = <n> \frac{I^+}{<I^+>} \qquad (8)$$

The direct evaluation of the time average is affected by an aliasing in $k_\theta(\omega)$ effect. In fact the electric field of the modes that have a k_ϑ value larger than $\frac{\pi}{\Delta x}$ (where Δx=0.6cm is the separation between the pins 1 and 2) will be systematically underestimated, leading to an overall underestimate of the flux.

The experiment is carried out in the toroidal device Thorello (whose major and minor radii are R= 40 cm and r= 8 cm respectively) which produces magnetised hydrogen plasma in steady-state conditions.

Typically obtained plasma parameters for a toroidal magnetic field of 1kG are: $T_e \cong 1$ eV, $T_i \cong$ 0.3 eV, edge plasma density$\cong 10^9$ cm^{-3}, centre plasma density$\cong 10^{11}$ cm^{-3}, neutral gas pressure P=10^{-4} mbar.

The data are composed by 32768 samples with a base time of τ = 20 μsec and each sample contains the readouts of the three pins. In the analysis we have subdivided the data in N=128 records each one containing M=256 samples.

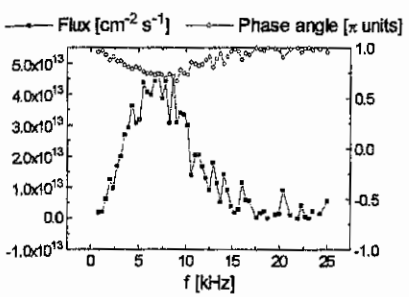

Fig.1: Spectral distribution of the anomalous flux and averaged phase angle in units of π at 3.5 cm from the wall.

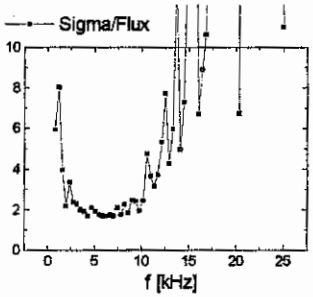

Fig.2: The normalised standard deviation of the flux in fig.1 as a function of the frequency.

Fig.1 shows a typical flux spectrum together with the averaged phase angle between $\phi'(\underline{x},t)$ and $n'(\underline{x},t)$ in units of π measured at a distance from the wall of 2.5cm. The main contribution to the flux is in the frequency range below 12.5 kHz and is directed outward. It also shows that in the frequency range where the flux is significant the phase angle ranges between 0.7 π and 0.9 π, indicating the presence of dissipative effects (a value of 0.5 is expected when the drift-type electrostatic fluctuations are collisionless [2]).

In Fig.2 the normalised standard deviation of the flux as a function of the frequency shows that in the frequency range below 12.5kHz the measurement is statistically meaningful. On the contrary, when the frequency is above 12.5kHz, $\phi'(\underline{x},t)$ and $n'(\underline{x},t)$ are completely uncorrelated and the signal has to be considered as statistical noise.

Fig.3 shows the frequency integrated anomalous flux and the frequency averaged phase angle as a functions of the distance from the wall chamber.

The change in sign of the flux profile around r=3.5cm is in correspondence with the shear ExB velocity layer and is probably due to the strong variation of the phase velocity fluctuations in a scale of length comparable to the probe separation.

Such a behaviour in this region will be the argument of a future work.

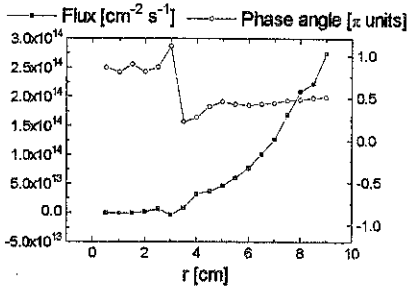

Fig.3: Integrated anomalous flux and averaged phase angle for different distance from the wall.

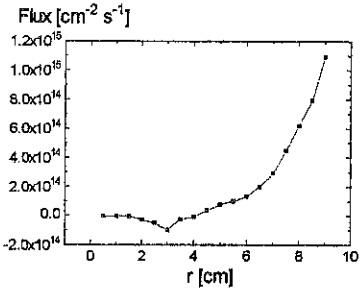

Fig.4: Anomalous flux measured as a time average of the fluctuations

The data analysed are in substantial agreement with the results of other groups[3,4].

If we compute the anomalous flux simply as a time average of the fluctuations of n and E we find the result depicted in Fig.4. The difference between the two methods lies on the fact that in the former case the electric field is found by means of the fitted statistical dispersion relation whereas in the latter the "instantaneous" value of $k_\theta(\omega)$ is usedor, in other words, in this case the correlation between $k_\theta(\omega)$ and $\Phi(\omega)$ is taken into account. This observation may be relevant for a critical review of the definition of the anomalous flux (eq.6).

References

1. Rowan, C.C. Klepper, C.P. Ritz, R.D. Bengston, K.W. Gentle, P.E. Phillips, T.L. Rhodes, B. Richards and A.J. Wootton, *Nucl. Fus.* **27** n. 7 (1987)
2. Riccardi, D. Caspani, L. Gamberale, G. Chiodini and M.Fontanesi, contribution at this Conference.
3. Ch. P. Ritz, Roger D. Bengston, S.J. Levinson and E. J. Powers *Phys. Fluids* **27** (12) 1984
4. Hidalgo *et al.*, *Nucl. Fus.* **31** n. 8 (1991), and references therein.

Dependence of the Electrostatic fluctuations on a static radial electric field

C.Riccardi, **G.Chiodini**, L.Gamberale, L.Fattorini and M.Fontanesi
Dipartimento di Fisica, Universita' di Milano - INFM
Via Celoria 16, 20133 Milano - ITALY

This work concerns the characterisation of the low frequency spontaneously excited electrostatic fluctuations driven by the radial density gradient, in presence of a radial electric field. The radial electric field produces a macroscopic poloidal rotation of the plasma which modifies some important aspects of the electrostatic plasma fluctuations. A static radial electric field in a plasma column can produce cinematic effects on the fluctuation propagation, for instance the modification of the wave spectra and spatial coherence, as well as dynamic effects, like generation of wave instabilities [1-4]. In this research we analyse the main cinematic phenomena induced by the electric field.

The experiment is carried out in the toroidal device Thorello (whose major and minor radii are R= 40cm and r= 8cm respectively) which produces magnetised hydrogen plasma in steady-state conditions. In our experiment the electrostatic fluctuations are, in the plasma edge, quasi-coherent drift modes [1] at low magnetic field but they destabilise and become turbulent when the magnetic field is increased up to 2kG. The relevant wave spectra and spatial coherence have been measured by means of double electrostatic probes applying the digital correlation techniques to the ion saturation current and to the floating potential.

The profile of the radial electric field has been obtained by Langmuir probes and is plotted in fig.1. It can be seen that in x=3.5 cm the electric field reverses its direction (E_r=0) and in the plasma edge it is directed outward while in the plasma inner after the shear (x=3.5 cm) is inward directed.

Being the poloidal plasma rotation velocity $v_{E\times B}$ proportional to the electric field, it also changes its direction: in the edge has the same versus of the ion diamagnetic velocity while in the inner has the electron diamagnetic velocity versus. In fig.2 the vorticity obtained from the following formula :

$$vor = \frac{dv_{E\times B}(r)}{dr} \qquad (1)$$

is plotted for different distance from the wall chamber.

An high value of the vorticity around the shear, indicate a possible presence of an instability produced by the poloidal plasma rotation. This dynamic effect has been analysed theoretically in previous works [2,4]. As concerns the cinematic effects, we analysed the wave parameter along the plasma radius.

The frequency and wave number power spectra of the fluctuations have been measured in the laboratory reference frame [3].

This means that if ω and k_p are respectively the frequency and poloidal wavevector in the laboratory frame, the same quantities in the plasma frame ω', k_p' are correlated by the following relations :

$$k_p'=k_p \qquad (2)$$
$$\omega'=\omega-k_p v_{E\times B}$$

It results that the wave frequency is Doppler-shifted by the $v_{E\times B}$ plasma rotation, while the wavenumber is not affected from it.

To analyse better the modification of the frequency spectra we have considered measured frequency $S(\omega)$ and wavenumber $S(k_p)$ spectra obtained in the laboratory frame (figs.3,4) and we have numerically evaluated the same spectra in the plasma frame considering the experimentally estimated poloidal plasma velocity. As can be seen in figs.3,4 the wavevector spectrum does not change with respect to the frame while the frequency autospectrum is modified.

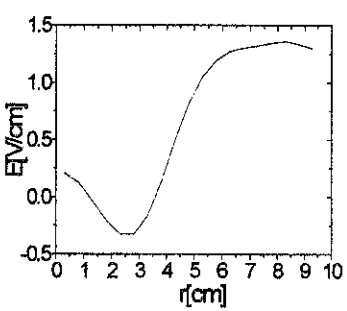

fig.1 Radial electric field profile for B=1kG ; r=0 corresponds to the plasma edge.

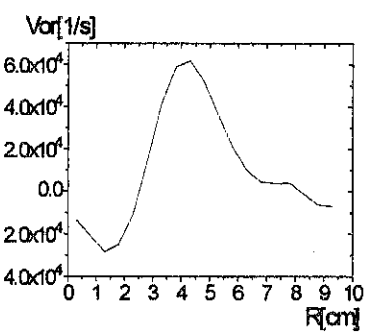

fig.2 Vorticity profile for B=1kG ; r=0 corresponds to the plasma edge.

In particular the power law $S(f) \approx \frac{1}{f^b}$ of the frequency autospectra are modified so that its spectral index b changes. It turns out that the power laws are mainly dependent on the Doppler shift effect rather than on the kind of instability.

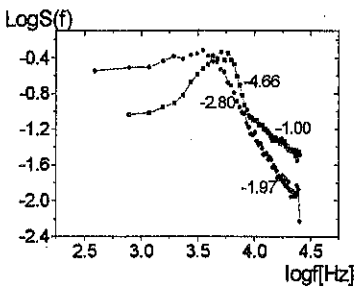

fig.3 Autospectra: the spectral index are indicated in figure; (■) lab. frame, (+) plasma frame.

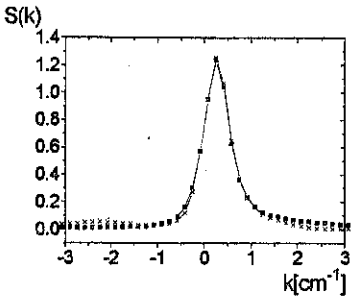

fig.4 Wavenumber poloidal spectra: (■) lab. frame, (+) plasma frame.

Other measurements show that the frequency spectral index (relevant to the frequency spectra) depends on the electric field in a way to increase with increasing of the electric field, while the wave number spectral index (relevant to the wave number spectra) is quite independent on the electric field.

Another cinematic effect is represented by the modification of the spatial wave coherence.

In general we can observe that if the density fluctuations are quite localised in f- k_p space, the effect of the ExB poloidal drift on the evaluation of the drift waves coherence coefficient can be considered negligible this can be directly seen if we represent the coherent modes as single plane waves with frequency shifted by the Doppler effect (eq.2)

On the contrary, when the fluctuations are delocalised in f- k_p space, the ExB poloidal rotation can affect the spatial drift waves coherence.

The effect of the electric field on the wave coherence can be observed in fig.5 where the total integrated coherence is shown for the poloidal and parallel wavenumber as a function of the radial coordinate for a magnetic field value of 1kG. It can be noticed that when the ExB drift velocity and the drift wave phase velocity have opposite signs, the coherence is smaller than the coherence evaluated in the shear; whereas when they have the same sign the electric field increases the wave coherence.

In general data show an increase of the spatial coherence coefficient for high ExB plasma rotation. This means that a radial electric field can be imposed in order to increase the wave spatial coherence, diminishing the turbulence.

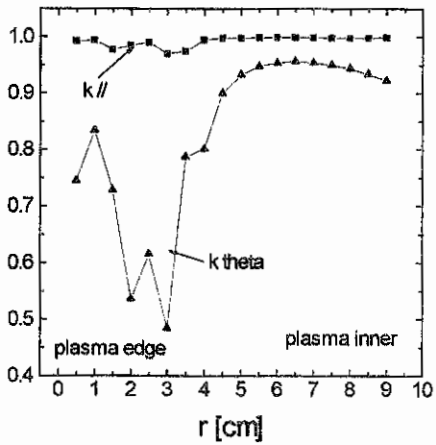

fig.5 Wave spatial coherence for the poloidal and parallel wavevector

References:

1. C. Riccardi, D. Xuantong*, M. Salierno, L. Gamberale and M. Fontanesi, accepted on Phys.Plasmas (1997)

2. Wemdel Horton, Jixing Liu, Phys. Fluids **27**, 2067 (1984)

3. Prasad, D. Bora, Y. C. Saxena, S. D. Verma Phys. Plasmas **1**, 1832 (1994)

4. Ch. P. Ritz, E. J. Powers and R. D. Bengtson, Phys. Fluids B **1**, 153 (1989)

Forced Magnetic Field Line Reconnection in Electron Magnetohydrodynamics.

K. Avinash[1], S.V. Bulanov[2], T. Esirkepov[3],
P. Kaw[1], F. Pegoraro[4], P.V.Sasorov[5], A. Sen[1],

1. Institute for Plasma Study, Ghandinagar, India,
2. Geneneral Physics Institute – RAS, Moscow, Russia,
3. Moscow Institute for Physics and Technology, Russia,
4. Physics Department, University of Pisa and INFM, Pisa, Italy,
5. Institute for Theoretical and Experimental Physics, Moscow, Russia

Abstract

Electron Magnetohydrodynamic[1] (EMHD) equations provide a convenient model for studying collisionless magnetic reconnection. In 2-D configurations, they take the well known form

$$\partial_t \vartheta - \{b, \vartheta\} = 0, \qquad \partial_t \beta - \{b, \beta\} = -\{\psi, \vartheta\}, \tag{1}$$

where $\vartheta = \psi - \Delta\psi$, $\psi(x, y, t)$ is the z-component of the vector potential, $\beta = b - \Delta b$, and b the z-component of the magnetic field. We present[2] explicit equilibrium solutions of the 2-D EMHD equations with scalelengths as small as the electron skin depth and with cross field motions. Then we investigate the time evolution of perturbations imposed from the boundary of a high conductivity plasma slab. The initial magnetic field has a null surface. The perturbations cause a change in the topology of the magnetic field. The plasma and the magnetic field evolve with the time scale of the linear tearing mode. However, the Hamiltonian nature of the EMHD equations, where magnetic field reconnection is caused by electron inertia, changes the long time evolution of the current layer from algebraic, as in the case of the resistive tearing mode, to exponential.

Introduction

An important similarity between ordinary magnetohydrodynamics, MHD, and EMHD arises from the fact that in both theories the magnetic flux is conserved when "non-ideal" effects are neglected. The whistler mode

in EMHD plays a role that corresponds to that of the Alfvén mode in MHD. However the basic spatial symmetry of the EMHD equations is not equivalent to that of the MHD equations. The frequency range of validity of EMHD is bounded on the low-frequency side by the ion cyclotron frequency $\omega_{Bi} = Z_i eB/m_i c$ and, on the high-frequency side, by the electron cyclotron frequency $\omega_{Be} = eB/m_e c$. Here, m_i and m_e are the ion and electron masses and Z_i is the ion charge number. In this frequency range the plasma is described as a single electron fluid where ions are assumed to be at rest, and electrons behave in such a way as to keep the plasma quasineutral under the condition $\omega_{Be} \ll \omega_{pe}$, where ω_{pe} is the Langmuir wave frequency.

In the case of two-dimensional configurations, where the magnetic field depends on two spatial coordinates x and y and on time t, Eq.(1) implies that the topology of $\vartheta(x,y,t) = const$ lines cannot change. However the topology of the lines $\psi(x,y,t) = const$ can change. This means that, despite the conservation of the topology of $\vartheta(x,y,t)$, the topology of the magnetic field lines can change and thus that magnetic reconnection can occur[3,4].

Stationary Solutions

For $\partial_t = 0$, we obtain from Eqs.(1)

$$\{b, \vartheta\} = 0, \qquad \{b, \Delta b\} = \{\psi, \Delta\psi\}. \tag{2}$$

The term $\{b, \Delta b\}$ arises from electron inertia and is important for stationary configurations with spatial variations on the d_e scale. For such configurations we obtain

$$b = b(\vartheta), \qquad \psi + G(\vartheta) = \left[\frac{db}{d\vartheta}\right]^2 \Delta\vartheta + \left[\frac{db}{d\vartheta}\right]\left[\frac{d^2b}{d\vartheta^2}\right](\nabla\vartheta)^2. \tag{3}$$

In the case of solutions that do not vary on the d_e scale, the r.h.s. of the second equation is negligible and we recover the standard relationship $\Delta\psi = I(\psi)$. Here G and I are arbitrary functions. In order to describe a richer class of equilibria that incorporate cross field motions, we introduce an external irrotational and divergence-free electric field and analyze configurations with

$$\psi = -Et + \tilde{\psi}(x,y), \tag{4}$$

i.e., $\vartheta = -Et + \tilde{\vartheta}(x,y)$, where the electric field E is directed along the z-axis and is supposed to be uniform. In this case, instead of the first equation in (2), we have

$$E + \{b, \tilde{\vartheta}\} = 0. \tag{5}$$

Special solutions that incorporate the effect of electron inertia can be obtained by an expansion in powers of E assuming that, to lowest order in E, only ϑ, or only β, does not vanish.

Taylor's Problem

We consider a slab geometry configuration in the region $-a < x < a$ with a neutral plane of the magnetic field at $x = 0$. The unperturbed magnetic field is taken to be a linear function of x, i.e., $\psi_0 = -x^2/2$ and $b_0 = 0$, which gives $\mathbf{B}_0 = B_0 \mathbf{e}_y = x\mathbf{e}_y$. Assuming as boundary conditions that both ψ_1 and b_1 vanish at $x = \pm a$, this configuration is stable against perturbations which depend on x, y and t. We perturb the boundaries of the configuration as follows:

$$x = \pm a \left[1 - \xi(t)/(a \cos ky)\right], \tag{6}$$

where ξ is the perturbation amplitude and k its wavenumber, and assume the ratio ξ/a to be small, $\xi/a \ll 1$. We divide the slab into two subregions: an external region where we can set $\partial_t = 0$ and an internal region where we must take into account electron inertia. The magnetic field perturbation in the external region is described by $x\left(\psi'' - k^2\psi\right) = 0$. The solution in the external region is the same as in the Hahm and Kulsrud paper[5].

The dependence of $\psi(0)$ on time in the ψ =const approximation can be obtained by matching the solutions in the internal and the external regions. Following Hahm and Kulsrud, we write the relationship between $\psi(0,\gamma)$, the amplitude of the perturbation ξ, and the function Δ' which gives the jump of the logarithmic derivative of ψ through the internal region, as

$$\psi(0,\gamma) = \frac{2k\xi}{\gamma\left(2k \cosh ka + \Delta'(\gamma) \sinh ka\right)}, \tag{7}$$

where γ is the variable in the Laplace transform with respect to time. The factor γ in the denominator of Eq.(7) is due to the fact that ξ is taken to be zero for $t < 0$. In Eq.(7), the function $\Delta'(\gamma)$ is a function of γ, that must be found matching the solutions in the internal and external regions. In order to obtain the long time behaviour of the magnetic configuration under the perturbation imposed from the boundary, we must invert the Laplace transform. Thus we must first determine the dependence of Δ' on γ all over the complex γ-plane. In the case of oscillatory EMHD modes, $Re\gamma = 0$, contrary to the case of standard resistive MHD and to the case of EMHD instabilities growing exponentially in time, this analysis is complicated by the mode behavior in the short wavelength limit. To describe these modes properly we must take into account the effects that can regularize their short wavelength limit. Spitzer resistivity does not regularize this limit, while electron viscosity does. As a result, close to the negative/positive real γ-axis we find

$$\Delta'(\gamma) = \frac{(\mp\gamma)^{1/2}}{|k|^{1/2}} \frac{2\pi\Gamma(3/4)}{\Gamma(1/4)}. \tag{8}$$

Eq. (8) gives the limiting expressions, respectively along the negative and the positive real γ axis, of a function regular over the complex γ-plane outside a small viscosity region near the origin which is neglected in the following. Renormalizing variables, we can write the inverse Laplace transform as

$$\bar{\Psi}(0,t) = \frac{1}{2\pi i}\int_C \frac{\exp(pt)\,dp}{p(1+(-p)^{1/2})}, \tag{9}$$

where the integration contour C has been chosen such that the form of Δ' given by Eq.(8) holds. We have neglected the contribution of the region near the origin. The integrand has two poles at $p = 0$ and $p = -1$. Calculating the residues we find

$$\bar{\psi}(0,t) = [1 - \exp(-t)]. \tag{10}$$

Numerical simulations

The equilibrium magnetic configuration is forced at $|y| = 1$ with an x-dependent perturbation with amplitudes that decay exponentially in time. The isolines of b, $b - \Delta b$, ψ, $\psi - \Delta\psi$ show that $\psi = const$ curves, reconnect while $\psi - \Delta\psi$ is conserved and its field lines do not reconnect.

In a Hamiltonian system, the memory of the initial perturbation is preserved at all times. This is evident in the evolution of $\psi - \Delta\psi$ which shows that the effect of the perturbation imposed from the boundary does not decay with time and develops increasingly small spatial scales. On the contrary, the effect of the perturbation on the "integrated" quantity ψ tends to saturate with time.

[1] A.S. Kingsep, K.V. Chukbar, and V.V. Yan'kov, in *Reviews of Plasma Physics*, edited by B. Kadomtsev (Consultant Bureau, New York, 1990), Vol. 16, p. 243.

[2] K. Avinash, S.V. Bulanov, T. Esirkepov P. Kaw, F. Pegoraro, P.V. Sasorov, A. Sen, Forced Magnetic Field Line Reconnection in Electron Magnetohydrodynamics., submitted to .....(1997)

[3] S.V. Bulanov, F. Pegoraro, and A.S. Sakharov, *Phys. Fluids B* **4**, 2499 (1992).

[4] S.V. Bulanov, G.I. Dudnikova, T.Zh. Esirkepov, V.P. Zhukov, I.N. Inovenkov, F.F. Kamenets, N.M. Naumova, L. Nocera, F. Pegoraro, V.V. Pichushkin, R. Pozzoli, D. Farina, *Plasma Physics Reports* **22**,867 (1996).

[5] T.S. Hahm, and R.M. Kulsrud, *Phys. Fluids* **28**, 2412 (1985).

Finite temperature effects on collisionless magnetic reconnection

E.Cafaro[1], **D.Grasso**[1,2], F.Pegoraro[2,3],
F.Porcelli[1], A.Saluzzi[1]

1. Energetics Dept., Polytechnic of Torino, Italy
2. Physics Dept., University of Torino, INFM Torino,
3. Physics Dept., University of Pisa, Italy

Plasmas produced in magnetic fusion experiments such as JET exhibit relaxation oscillations and self-organisation processes on time scales that are shorter than the average electron-ion collision time. In collisionless regimes, electron inertia replaces resistivity in allowing for transition of the magnetic field topology. The first nonlinear simulations [1] of electron inertia reconnection neglected the electron pressure gradient in the generalized Ohm law. This term was considered in subsequent contributions [2, 5], which indicated a further enhancement of the reconnection rate, although the physical interpretation of the simulation results remain unclear.

A related problem is the role played by the invariants (Casimir) of the collisionless plasma evolution. It can be shown that collisionless models of the type adopted in [6, 5, 3] admit an Hamiltonian structure. Clearly, while magnetic flux is reconnected in the course of plasma evolution, the invariant fields preserve their initial topology. The nature of collisionless reconnection under these circumstances is entirely different form that of resistive (dissipative) reconnection.

The aim of the present letter is twofold. First we present new numerical results in the regimes where both electron inertia and the electron pressure tensor are important. We confirm that the nonlinear growth of magnetic islands is even faster than in the case where the electron pressure is neglected, and that this fast growth is accompanied by the formation of microscales below the electron inertia skin depth, as in the purely inertial case [6]. A significant finding [7] is the splitting of the current and vorticity sheets, forming near the neutral line of the sheared component of the equilibrium magnetic field, in two branches crossing at the stagnation point of the plasma flow. A similar behavior was also observed in [2] in the context of resistive reconnection with electron pressure effects. Secondly, we interpret these results on the basis of the Hamiltonian structure of the adopted plasma model. In particular, we show that the resulting structure of the current and vorticity sheets is the consequence of the presence of Casimirs advected by effective velocity fields.

Our investigation considers an exthension of reduced MHD on a two dimensional slab, where electron inertia, proportional to the square of the inertial skin depth, $d_e = c/\omega_{pe}$, with ω_{pe} the plasma frequency, and the elctron pressure term are retained in the generalized Ohm law. Diamagnetic effects are neglected here. Thus, the pressure effect we consider, has to do with electron pressure perturbations, which cause an electron space charge along the field lines, balanced by ions streaming across the field lines in order to preserve quasineutrality. This process is associated with the characteristic scale length, $\varrho_s = \sqrt{T_e/m_i}/\omega_{ci}$. In addition, we consider the cold ion limit. The equation we solve are

$$\partial F/\partial t + [\varphi, F] = \varrho_s^2 [U, \Psi] \tag{1}$$

$$\partial U/\partial t + [\varphi, U] = [J, \Psi] \tag{2}$$

The quantities appearing in these equations are dimensionless, the normalization being based on the Alfvèn time, τ_A, and L_z. The magnetic field is $\mathbf{B} = B_0\mathbf{e}_z + \nabla\Psi \times \mathbf{e}_z$, with B_0 a constant component along the ignorable z-direction. The $\mathbf{E} \times \mathbf{B}$ drift on the normal plane is $\mathbf{v}_\perp = \mathbf{e}_z \times \nabla\varphi$, where φ is the stream function. $U = \nabla^2\varphi$ is the vorticity, $J = -\nabla^2\Psi$ is the current density and $F = \Psi + d_e^2 J$ is the generalized average momentum [6] along z. The Poisson brackets are defined as $[A, B] = \mathbf{e}_z \cdot \nabla A \times \nabla B$. Note that $[\varphi, A] = \mathbf{v} \cdot \nabla A$, thus the l.h.s of Eqs. (1,2) represent the total time derivatives of the scalar field U and F. This system of equations can be written in a convective form for the quantities

$$G_\pm \equiv F \pm d_e \varrho_s U \tag{3}$$

Defining the generalized stream functions

$$\varphi_\pm = \varphi - \varrho_s^2 U^2 \mp d_e \varrho_s J \tag{4}$$

we obtain the alternative form for the model equations

$$\partial G_\pm / \partial t + [\varphi_\pm, G_\pm] = 0 \tag{5}$$

Thus, the quantities $G_\pm$, advected by the effective velocity fields $\mathbf{v}_\pm = \mathbf{e}_z \times \nabla\varphi_\pm$, are conserved, so their topology remains "frozen" during time evolution.

It can be shown [5, 3] that Eqs. (1,2) can be cast in Hamiltonian from. The Hamiltonian is

$$H = \frac{1}{2}\int d^2x \left(|\nabla\Psi|^2 + d_e^2 J^2 + +(\nabla\varphi)^2 + \varrho_s^2 U^2\right) \tag{6}$$

The associated generalized Poisson brackets admit two infinite sets of Casimirs

$$C_\pm = \int d^2x h_\pm(\xi_1 \pm \xi_2) = \int d^2x h_\pm(G\pm) \tag{7}$$

with $h_\pm$ arbitrary functions. In the limit of vanishing ϱ_s, upon expanding $h_\pm$ to first order, we find the Casimirs of the purely inertial case, $C_1 = \int d^2x h_1(F)$ and $C_2 = \int d^2x U h_2(F)$. Thus, for $\varrho_s = 0$, the generalized momentum F is conserved and its topological structure is preserved in time. When $\varrho_s \neq 0$, the fields $G_\pm$ are topologically invariant, while F can undergo reconnection.

In this paper, we present the numerical solution of the nonlinear model (1,2) obtained on the basis of a finite difference scheme with nonuniform grid. We assuned double periodic boundary conditions at the frontier of a rectangular slab with aspect ratio $\epsilon = L_x/L_y$ and equilibrium magnetic flux $\Psi_{eq} = \cos x$, $\varphi_{eq} = U_{eq} = 0$ In Figs. 1-7 we present the solution for a case with $\epsilon = 1/2$, $d_e = 0.08$ and $\varrho_s = d_e/2$. In particular, Figs. 1-4 show the contour plots at $t = 80\tau_A$ of the fields φ, Ψ, J and U. Figs. 5-7 show the contour plots of G_+, φ_+ and F.

We note that the mode structure develops a microscale rapidly shrinking in time. As in the case $\varrho_s = 0$ [6], we attribute this behavior to the presence of the conserved quantities $G_\pm$. When $\varrho_s \neq 0$, the generalized momentum F is no longer conserved, indeed F changes topology , with an O-point forming at $x = y = 0$ and four Y-points forming symmetrically around the origin, as shown in Fig. 7. On the other hand, the initial topology of the $G_\pm$ fields is preserved, as expected.

The most striking difference between $\varrho_s = 0$ and $\varrho_s \neq 0$ is the formation, in the latter case, of cross shaped current density and vorticity layers. This structure is clearly visible when $\varrho_s > d_e$, as shown in Figs. 8-9, where contour plots of J and U are presented for a

case with $\varrho_s = 3d_e$, d_e and ϵ as in the previous simulation. The contour plots of $G_\pm$, $\varphi_\pm$ for $\varrho_s = d_e$ are similar to those in Fig. 4, with the contour lines near the origin following closely the two branches of the current and vorticity layers.

We can establish a link between the Casimirs and the spatial structures that form nonlinearly. This link can clarify an important difference between Hamiltonian and dissipative reconnection. Both these processes require the localized violation of the topological constraints that involve the magnetic flux Ψ. However, electron inertia (and the electron stress tensor) make field line reconnection possible, but do not eliminate these topological constraints. Simply they now involve different fields (F, or $G_\pm$ when $\varrho_s \neq 0$, instead of Ψ). The difference between the newly locally conserved fields and Ψ consists of a current density and of a plasma vorticity term. Thus, reconnection of Ψ can only proceed unimpeded by the conservation of F (or of $G_\pm$) if current (and vorticity) layers are formed. In the presence of dissipation there are no fields conserved locally and thus these layers have a minimum diffusive width. On the contrary, in Hamiltonian reconnection the presence of the locally conserved fields makes these layers increasingly sharper and leads to a cascade towards smaller and smaller microscales. Eventually, this cascade must be limited by kinetic and dissipative effects. In this sense, the collisionless model is incomplete from a physics point of view. One can draw an analogy with Landau damping and phase mixing, where smaller and smaller scale lengths are produced that are eventually wiped out by collisions.

The cross-shaped structure of the current and vorticity layers can be interpreted on the basis of the advection of the invariants $G_\pm$. At equilibrium, $G_\pm = G_\pm(x)$. As the instability evolves, G_+ and G_- rotate in opposite directions, advected by the effective velocities $\mathbf{v}_\pm$. Note that these velocities introduce a rotation, as the corresponding stream functions, $\varphi_\pm$, add terms with mixed parity with respect to x and y (by contrast, the potential $\varphi(x,y)$ is odd in x and even in y: indeed, the convection cells in Fig. 1 do not exhibits any rotation). Since the instability evolution is slow, the potentials $\varphi_\pm$ remain largely aligned with $G_\pm$. The structure of J, U and F follows that of $G_\pm$ and $\varphi_\pm$, as $2\varrho_s d_e J = \varphi_+ - \varphi_-$. $2\varrho_s d_e U = G_+ - G_-$ and $2F = G_+ + G_-$.

In conclusion we have established a link between the topological constraints of the collisionless model and the spatial structure that are formed nonlinearly. This link can clarify important differences between Hamiltonian and dissipative reconnection.

References

[1] Aydemir,A.Y. *Phys. Fluids* bf 4 (11), 3469 (1992)

[2] Kleva,R.G. *et al. Phys. Plasmas* **2**, 23 (1995)

[3] Schep,T. *et al. Phys. Plasmas* **1**, 2843 (1994).

[4] Kuvshinov,B.N. *et al. Physics Letters A* **191**, 296 (1994)

[5] Morrison,P.J. *Phys. Fluids* **27** (4), 886 (1984)

[6] Ottaviani,M. *et al. Phys. Plasmas* **2**, 4104 (1995)

[7] Cafaro,E., *et al. Joint Varenna-Lausanne International Workshop on Theory of Fusion Plasmas.* Varenna (1996) SIF Conference Proceedings ISPP-16, Bologna, (1996)

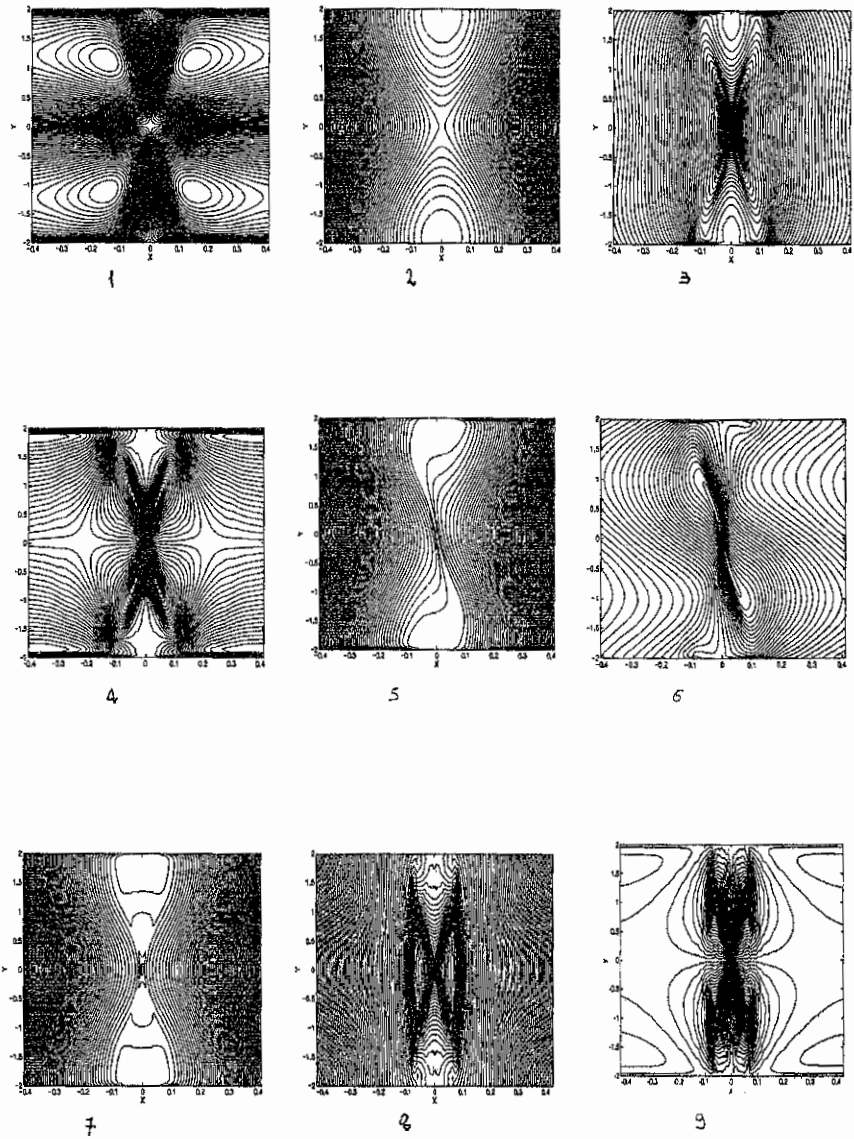

Figure 1: fig.1-7: φ, Ψ, J, U, G_+, φ_+ and F for $\varrho_s = d_e/2$; fig.8-9: J and U for $\varrho_s = 3d_e$

Debye Length in a Neutral-beam-heated Plasma

B. Wolle
Institut für Angewandte Physik, Universität Heidelberg, D-69120 Heidelberg, Germany

1. Introduction

One of the major auxiliary heating methods for tokamak fusion plasmas is neutral beam injection (NBI). The fast injected neutrals become ionized and slow down to thermal energy through Coulomb collisions with the background plasma. As a consequence of the injection, the velocity distribution of the injected ion species consists of a Maxwellian part and a non-Maxwellian high-energy part. The evolution of the velocity distribution f of the neutral-beam-injected ions can be described by the following kinetic equation:

$$\frac{\partial f}{\partial t} + \boldsymbol{v} \cdot \nabla_r f + \frac{eZ}{m} \nabla\Phi \cdot \nabla_v f = C(f) + S - L, \tag{1}$$

where ∇_r and ∇_v are the gradients with respect to coordinate and velocity, respectively, $C(f)$ is the collision operator, S is the fast ion source term and L is a loss term for ions. Furthermore, $eZ\nabla\Phi/m$ is the acceleration of a particle due to electrostatic collisions in a quasi-neutral multi-species plasma, where Z and m are the charge and the mass of the particle and Φ is the resulting potential of the macroscopic field.

If a test charge Q is placed at the origin in the plasma, its effect is to attract particles of opposite sign and to repel charges of the same sign. The resulting modifications of the ion and electron velocity distributions are simply positive and negative shifts of energy $E_\Phi = eZ\Phi$. The potential Φ follows from the Poisson equation

$$\nabla^2\Phi = -\frac{e}{\epsilon_0}\left[\sum_i Z_i \int f_i(\boldsymbol{v}, \Phi)\ \mathrm{d}^3v - \int f_e(\boldsymbol{v}, \Phi)\ \mathrm{d}^3v + Q\delta(\boldsymbol{r})\right], \tag{2}$$

where Z_i and n_i are the charge and density of the ith ion species and f_e and f_i are the electron and ion velocity distributions normalized to the density $n_{e,i}$ as $\int f_{e,i}(\boldsymbol{v})\mathrm{d}^3v = n_{e,i}$. The Poisson equation in the general form given above is impracticable to solve analytically. In deriving the expression for the Debye length in a plasma it is therefore commonly assumed that the velocity distributions of the plasma ions and electrons are isotropic Maxwellians with temperatures T_i and T_e, respectively. Thus, effects of plasma heating due to fast particle injection (and other mechanisms leading to highly non-Maxwellian velocity distributions) are neglected. The resulting Poisson equation

$$\nabla^2\Phi = -\frac{e}{\epsilon_0}\left[\sum_i n_i Z_i \exp\left(-\frac{eZ_i\Phi}{kT_i}\right) - n_e \exp\left(\frac{e\Phi}{kT_e}\right) + Q\delta(\boldsymbol{r})\right], \tag{3}$$

where k is the Boltzmann constant, can be linearized if the perturbation is small, i.e. if $eZ_i\Phi \ll kT_i$ and $e\Phi \ll kT_e$. From the spherically symmetric solution of equation (3), one obtains for the Debye length: $\lambda_D = (\sum_i k_i^2 + k_e^2)^{-1/2}$, where $k_i^2 = e^2Z_i^2 n_i/\epsilon_0 kT_i$ and $k_e^2 = e^2 n_e/\epsilon_0 kT_e$ are the Debye constants for Maxwellian ions and electrons, respectively.

2. Debye Length for a Plasma with Neutral-Beam-Injected Ions

In deriving an expression for the effective Debye length in a plasma with NBI slowing-down distributions, it is reasonable to assume that the electron and background ion velocity distributions are Maxwellians. Since the main effect in the calculation of the effective Debye length is the existence of a high-energy tail and the result does not markedly depend on whether the velocity distribution is isotropic or anisotropic, the non-Maxwellian velocity distribution of the injected ions is assumed to be isotropic. Furthermore, for simplicity, the effective screening length will be derived for steady-state conditions. If the subscript '0' refers to the injected ion species and f_0 is the corresponding isotropic non-Maxwellian velocity distribution, the Poisson equation can be written as:

$$\nabla^2\Phi = -\frac{e}{\epsilon_0}\left[Z_0\int f_0(v,\Phi)\,\mathrm{d}^3v + \sum_{i\neq 0} n_i Z_i \exp\left(-\frac{eZ_i\Phi}{kT_i}\right) - n_e\exp\left(\frac{e\Phi}{kT_e}\right) + Q\delta(\boldsymbol{r})\right]. \quad (4)$$

An appropriate non-thermal velocity distribution of the injected ion species can approximately be obtained from the steady-state kinetic equation with the Fokker-Planck collision operator in its high-energy approximation neglecting diffusive terms and loss terms [1]. The complete solution for the velocity distribution of the injected ion species (which is normalized to the density n_0) is the sum of the Maxwellian homogenious solution f_{th} of the kinetic equation and the approximate particular (non-Maxwellian) solution f_{b}:

$$f_0(v) = f_{\mathrm{th}}(v) + f_{\mathrm{b}}(v) \approx \frac{n_0 - n_{\mathrm{b}}}{\pi^{3/2}v_{\mathrm{th}}^3}\exp(-v^2/v_{\mathrm{th}}^2) + \frac{s_0\tau_{\mathrm{s}}}{4\pi}\frac{\sigma(v_0 - v)}{v^3 + v_\alpha^3}, \quad (5)$$

where the non-thermal density n_{b} and the slowing-down time τ_{s} of ions on electrons are given by:

$$n_{\mathrm{b}} = s_0\tau_{\mathrm{s}}\frac{1}{3}\log\left(1 + \frac{v_0^3}{v_\alpha^3}\right), \qquad \tau_{\mathrm{s}} = \frac{3}{2}\pi^{1/2}\frac{m_e}{m_0 C_e}\left(\frac{2kT_e}{m_e}\right)^{3/2}, \quad (6)$$

with $C_e = 8\pi n_e Z_0^2 e^4 m_0^{-2}\log\Lambda$ and v_α is given by:

$$E_\alpha \equiv \frac{1}{2}m_0 v_\alpha^2 = 14.8kT_e\left[\frac{A_0^{3/2}}{n_e}\sum_i \frac{n_i Z_i^2}{A_i}\right]^{2/3}. \quad (7)$$

Furthermore, v_0 and s_0 are the injection velocity and source rate, respectively, v_{th} is the thermal velocity, σ is the unit step function, $\log\Lambda$ is the Coulomb logarithm and A denotes atomic masses. Again, the effect of the test charge on the velocity distribution of the injected ion species results in a positive shift of energy $E_\Phi = eZ_0\Phi = \frac{1}{2}m_0 v_\Phi^2$:

$$f_0(v,\Phi) = \frac{n_0 - n_{\mathrm{b}}}{\pi^{3/2}v_{\mathrm{th}}^3}\exp\left(-\frac{v^2}{v_{\mathrm{th}}^2}\right)\exp\left(-\frac{eZ_0\Phi}{kT_0}\right) + \frac{s_0\tau_{\mathrm{s}}}{4\pi}\frac{\sigma(v_0 - v_\Phi - v)}{(v^2 + v_\Phi^2)^{3/2} + v_\alpha^3}. \quad (8)$$

For small perturbations, $(v^2 + v_\Phi^2)^{3/2} \approx v^3 + \frac{3}{2}v_\Phi^2 v$ and the denominator can be expanded. One obtains an approximate expression for f_0 which can be introduced into the Poisson equation (4). After linearization and integration over the velocity domains one obtains a

simplified Poisson equation. Neglecting the term $3^{-1/2}\tan^{-1}3^{-1/2}$ in that equation, the Debye constant k_b^2 which accounts for the fast particle contribution due to NBI heating can be written as:

$$k_b^2 = \frac{e^2}{\epsilon_0}\frac{Z_0 s_0 \tau_s}{2m_0 v_\alpha^2}\left[\frac{2Z_0 m_0 v_\alpha^2}{3kT_0}\log\left(1+\frac{v_0^3}{v_\alpha^3}\right)+\frac{v_0 v_\alpha^2}{v_0^3+v_\alpha^3}-\frac{1}{6}\log\frac{(v_0+v_\alpha)^3}{v_0^3+v_\alpha^3}+\right.$$
$$\left.-\frac{1}{\sqrt{3}}\tan^{-1}\frac{2v_0-v_\alpha}{v_\alpha\sqrt{3}}\right]. \qquad (9)$$

The Debye screening length for a neutral-beam heated plasma can, in parallel with the above, be written as:

$$\lambda_{NBI} = \left(\sum_i k_i^2 + k_e^2 - k_b^2\right)^{-1/2}. \qquad (10)$$

This equation is, however, only valid for completely static screening. In reality, the ions are moving very slowly. Therefore they are completely screened by the fast moving electrons, but they are only partially screened by surrounding ions. In order to discuss effects of dynamical screening one can use the results given in [2] for a Maxwellian plasma. Generalizing the expression for the effective screening length given in [2] to NBI heated plasmas, one obtains:

$$\lambda_{NBI}^{eff} = \left[k_e^2 \exp\left(\frac{\sum k_i^2 + k_e^2 - k_b^2}{\sum k_i^2 - k_b^2}\log\frac{\sum k_i^2 + k_e^2 - k_b^2}{k_e^2} - 1\right)\right]^{-1/2}, \qquad (11)$$

where the summation is over all ion species. This effective Debye length is inbetween the total Debye length for static screening in a Maxwellian plasma λ_D and the one for static screening of Maxwellian electrons $\lambda_e = 1/k_e$.

3. Results and Conclusions

In order to illustrate the effects of a non-Maxwellian NBI slowing-down distribution on the screening distance, a pure deuterium plasma with temperatures $T_i = T_e$ ranging from 5 keV to 8 keV and D^0-injection with varying source rates and injection velocities is considered. To be independent of the densities, only the ratios of the Debye lengths, viz λ_{NBI}/λ_D and $\lambda_{NBI}^{eff}/\lambda_D$, are calculated as functions of the fast particle fraction. The results are shown in figure 1 for a plasma with 80 keV injection energy and temperatures of 5 keV and 8 keV, respectively. It can be seen that for reasonable plasma parameters with fast particle fractions below about 40%, the Debye lengths for completely static screening differ by up to about 12%. For more extreme plasma parameters differences by up to 20% can occur. In addition, the effect of dynamical screening is also shown in figure 1. For the same plasma parameters and fractional fast particle densities below 40%, the differences to the Maxwellian case with static screening are about 17-25% while for more extreme plasmas differences around 30% can occur. Generally, the differences are somewhat increasing with increasing temperatures. The dependence on the injection energy is logarithmically weak and with increasing injection velocity, the ratios of

the Debye lengths are slightly decreasing. (This is because the fast particle fraction is kept constant and therefore with increasing injection velocity, the Maxwellian part of the velocity distribution extends to higher velocities.) As described in [3], the Coulomb logarithm for the interaction of a test particle with a background particle is in the classical limit $\log \Lambda = \log \lambda_D - \log \rho_\perp$, where $\rho_\perp$ is the impact parameter. Therefore, although the improved Debye length differs by about 20% from the Debye length for static screening in a Maxwellian plasma, the final effect on the Coulomb logarithm is small. For parameters relevant for fusion plasmas, where the Coulomb logarithm is in the order of 20, the modifications are only in the order of 1%. In conclusion, the effects of non-Maxwellian slowing-down velocity distributions on the Debye length and, in particular, on the Coulomb logarithm may be neglected in many cases without substantial loss of accuracy.

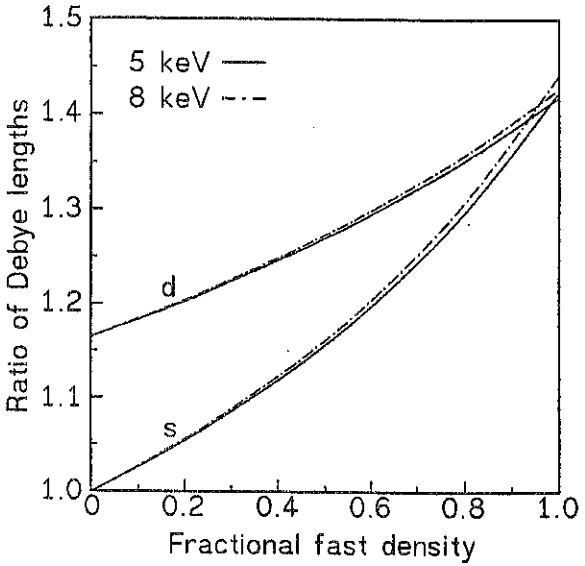

Figure 1. *Ratios of the NBI Debye lengths for completely static (s) and for dynamical screening (d) to the Maxwellian Debye lengths (λ_{NBI}/λ_D and $\lambda^{eff}_{NBI}/\lambda_D$) as functions of the fractional fast particle density for a deuterium plasma with 80 keV deuterium injection and temperatures of 5 keV (——) and 8 keV (– · – ·).*

References

[1] Cordey J G and Houghton M J, *Nucl. Fusion* **13** 215 (1973)

[2] Kihara T, Aono O and Itzikawa Y, *J. Phys. Soc. Japan* **18** 1043 (1963)

[3] Sivukhin D V, Coulomb Collisions in a fully ionized Plasma, in Reviews of Plasma Physics, vol. 4, (Consultants bureau, New York, 1966)

Generally Covariant Plasma Equations

K. Elsässer[(a)] and **S. Popel**[(b)]
(a) Institut für Theoretische Physik, Ruhr–Universität Bochum,
D–44780 Bochum, Germany
(b) Institute for Dynamics of Geospheres, Leninsky pr. 38, Building 6,
117979 Moscow, Russia

1. Introduction

Plasma equations and general relativity are usually not considered together. However, for certain astronomical objects like galactic nuclei or black holes the mean gravitational field may be strong, and the observation of magnetic fields indicates that a combination of general relativity and plasma physics at least on the level of a fluid description is appropriate. A microscopic plasma description on the basis of a classical one–particle distribution function is then a good starting point; all fluid quantities are then defined by corresponding averages in velocity space. Here we discuss the basic equations in two extreme situations: First we consider the plasma to be collisionless and formulate the Vlasov equation in a manifestly covariant form. Secondly we derive the covariant multifluid equations from the corresponding moment equations, assuming an isotropic distribution function for each species in the corresponding inertial system of a locally co–moving observer. Then on the basis of Vlasov equation we derive the dispersion relation for weakly damped Langmuir waves and investigate it.

2. The Covariant Vlasov Equation

Let (x,u) denote the 8–dimensional phase space, with $(x) = (x^0, x^1, x^2, x^3)$ the coordinates of an event in space–time ($x^0 \equiv ct$, where c is the velocity of light), and $(u) = (u^0, u^1, u^2, u^3)$ the four–velocity of a particle, with a normalization given by

$$u^\mu u_\mu = c^2. \tag{1}$$

If we consider a general coordinate transformation, it is well–known that the four–velocity transforms like the differentials of the coordinates, and each of the formal volume elements d^4x, d^4u transforms by multiplying it with the Jacobian of the transformation. Using the transformation rule for the metric tensor $g_{\mu\nu}$, one can easily obtain the invariant volume element in (x,u)–space as the product of the separately invariant volume elements, namely: $\sqrt{g}\ d^4x =$ invariant; $\sqrt{g}\ d^4u =$ invariant. Here g is the modulus of the determinant of $g_{\mu\nu}$. Let us then introduce a scalar function $f(x,u)$ for each particle species, denoting formally the number of particles per (invariant) cell in phase space. It is nonzero only on the hypersurface given by the normalization condition (1). To determine the number of particles we have then to count the number of world lines crossing a spatial hypersurface with normal unit vector (u^μ/c) at (x,u), as has been observed by Synge [1]. The result is proportional to a 7–dimensional volume element:

$$d^7N = \frac{u^0}{c} f(x,u)\ \sqrt{g}\ d^3x\ \sqrt{g}\ d^4u.$$

Let $\lambda^{(a)}(x)$ be four independent functions of x, with $a = 0, 1, 2, 3$; they define a local coordinate system ("tetrade") by their partial derivatives: $V_\varrho^{(a)} = \partial\lambda^{(a)}/\partial x^\varrho$. Any four-vector $A^\mu(x)$ may then be represented by four scalar functions $A^{(a)}(x)$, the projections of $A^\mu(x)$ onto the local coordinate system: $A^{(a)}(x) = A^\mu(x)V_\mu^{(a)}$. Let us then represent $f(x,u)$ as a function F of x and $u^{(a)}$, the invariant parts of u^μ: $f(x,u) = F(x,u^{(a)})$. This operation has the advantage that the gradient of F in (x,u)-space, $(\partial F/\partial x, \partial F/\partial u)$, is composed of two four-vectors. The vector character of $\partial F/\partial x^\mu$ (at constant scalars $u^{(a)}$) is obvious since F itself is a scalar; the gradient with respect to u^μ (at constant x) is then

$$\frac{\partial F}{\partial u^\mu} = \sum_a \frac{\partial u^{(a)}}{\partial u^\mu}\bigg|_x \frac{\partial F}{\partial u^{(a)}} = \sum_a V_\mu^{(a)} \frac{\partial F}{\partial u^{(a)}},$$

where the last term is a superposition of the four-vectors $V_\mu^{(a)}$ with scalar factors, i.e., again a four-vector. Let us now choose $\lambda^{(a)}(x)$ to be a local inertial coordinate system $x'^{(a)}$ with Minkowskian metric at x; $u^{(a)}$ is then the corresponding four-velocity u' in this system, and the volume element in velocity space is simplified considerably (since $det(V_\varrho^{(a)}) = \sqrt{g}$ in this case), namely: $\sqrt{g}\ d^4u = d^4u'$. Then we can immediately write down the covariant form of Vlasov equation in any coordinate system, using also the four-vector $a^\mu(x)$ of the acceleration:

$$u^\mu \frac{\partial F}{\partial x^\mu} + a^\mu \frac{\partial F}{\partial u^\mu} = 0. \tag{2}$$

This equation is valid by the equivalence principle: Since Eq. (2) is true in a locally Minkowskian metric (i.e., within special relativity), and since it is generally covariant, it must be true in any coordinate system with or without a gravitational field. We are here interested in the electromagnetic force on a particle of charge e and rest mass m, therefore we have:

$$a^\mu = \frac{e}{mc} u_\nu F^{\mu\nu} \quad ; \quad F_{\mu\nu} \equiv A_{\nu,\mu} - A_{\mu,\nu}, \tag{3}$$

where A_ν is the covariant four-vector of the electromagnetic potential, and $(\ )_{,\mu}$ denotes the partial derivative of $(\ )$ with respect to x^μ.

Eq. (2) is particularly convenient to derive the set of moment equations. One can demonstrate [2] that the following tensor quantity

$$M^{\varrho\sigma\cdots\mu\nu}(x) \equiv \int d^4u\ \sqrt{g}\ u^\varrho u^\sigma \cdots u^\mu u^\nu F(x, u^{(a)})$$

obeys the relationship

$$M^{\varrho\sigma\cdots\mu\nu}{}_{;\nu} = \int d^4u\ \sqrt{g}\ u^\varrho u^\sigma \cdots u^\mu u^\nu F_{,\nu}, \tag{4}$$

with the usual formula for the left-hand side (involving the affine connection or Christoffel symbol $\Gamma^\varrho_{\alpha\nu}$):

$$\begin{aligned} M^{\varrho\sigma\cdots\mu\nu}{}_{;\nu} \ \equiv\ & M^{\varrho\sigma\cdots\mu\nu}{}_{,\nu} + \Gamma^\varrho_{\alpha\nu} M^{\alpha\sigma\cdots\mu\nu} + \Gamma^\sigma_{\alpha\nu} M^{\varrho\alpha\cdots\mu\nu} \\ & + \cdots + \Gamma^\mu_{\alpha\nu} M^{\varrho\sigma\cdots\alpha\nu} + \Gamma^\nu_{\alpha\nu} M^{\varrho\sigma\cdots\mu\alpha}. \end{aligned}$$

The covariant moment equations are then as follows:

$$M^{\varrho\sigma\cdots\mu\nu}{}_{;\nu} = \frac{e}{mc}(F^{\varrho}{}_{\alpha}M^{\alpha\sigma\cdots\mu} + F^{\sigma}{}_{\alpha}M^{\varrho\alpha\cdots\mu} + \cdots + F^{\mu}{}_{\alpha}M^{\varrho\sigma\cdots\alpha}). \tag{5}$$

Several other forms of Eq. (2) are possible [2]. Here we present only the Vlasov equation for $f(x,u)$ which reads as follows:

$$u^{\nu}\frac{\partial f}{\partial x^{\nu}} + (a^{\nu} - \Gamma^{\nu}_{\alpha\beta}u^{\alpha}u^{\beta})\frac{\partial f}{\partial u^{\nu}} = 0. \tag{6}$$

This is the equation of Walker [3] in the case of a neutral gas ($a^{\nu} = 0$).

One can show [2] the validity of Liouville's theorem for the phase space associated with the distribution function $F(x,u^{(a)})$: $\sqrt{g}\,d^4x\,d^4u^{(a)} =$ constant along a particle path.

3. The Covariant Fluid Equations

The covariant form of the fluid equations for a locally isotropic fluid can be derived [2] from the moment equations (5). We can define a covariant Eulerian four–velocity $U^{\nu}(x)$ in any frame of reference, with a norm c^2:

$$U^{\nu}(x) \equiv \frac{1}{n_0(x)}\int d^4u\,\sqrt{g}\,u^{\nu}f(x,u), \quad U^{\nu}U_{\nu} = c^2.$$

The scalar $n_0(x)$ is the particle density in the local inertial rest frame (where the $\Gamma^{\mu}_{\alpha\beta}$ are zero, and $g_{\mu\nu} = \eta_{\mu\nu}$ is a Minkowskian metric with $\sqrt{g} = 1$), and n_0U^{ν} is the particle flux in x–space. Its conservation law follows from Eq. (5) for the lowest moment $M^{\nu} \equiv n_0U^{\nu}$, replacing the right–hand side of Eq. (5) by zero: $(n_0U^{\nu})_{;\nu} = 0$. The second moment is related to the energy–momentum–stress tensor $T^{\mu\nu}$ defined as follows: $T^{\mu\nu} = m\int d^4u\ \sqrt{g}\ u^{\mu}u^{\nu}f(x,u)$. Its projection w onto the local Eulerian velocity is the total relativistic energy per volume element in the local inertial rest frame: $w = U_{\mu}\,T^{\mu\nu}\,U_{\nu}/c^2$. It is this quantity that was used by Eckart [4]. The value of w can be related to the mean internal energy per mass ε in the local inertial rest frame: $w = mn_0c^2\,(1 + \varepsilon/c^2)$. Another scalar is defined by the trace of $T^{\mu\nu}$. This quantity is related to the scalar local pressure p: $p = (w - T^{\nu}_{\nu})/3$. For a locally isotropic distribution function no other scalars exist, and we obtain a covariant representation of $T^{\mu\nu}$ as in the case of a perfect fluid (see, e.g., [5]):

$$T^{\mu\nu} = \sigma\,U^{\mu}U^{\nu} - p\,g^{\mu\nu}, \tag{7}$$

where $\sigma \equiv (w + p)/c^2 = \varrho\,(1 + h/c^2)$ is the total relativistic enthalpy per volume element in the local inertial rest frame, divided by c^2, $h \equiv \varepsilon + p/\varrho$ is the local enthalpy per mass, and $\varrho \equiv mn_0$ is the rest mass density. From Eq. (5) we obtain then, with $T^{\mu\nu} = m\,M^{\mu\nu}$, the corresponding equation of motion for the fluid component:

$$(\sigma U^{\mu}U^{\nu})_{;\nu} - p_{,\nu}g^{\mu\nu} = \frac{e}{mc}\varrho\,U_{\nu}F^{\mu\nu}.$$

Using the mass conservation, the product rule for the covariant derivative, and the relationships between h, ϱ, p, and ε, one can obtain from the above equation:

$$\left(1 + \frac{h}{c^2}\right)U^{\nu}U_{\mu;\nu} + \frac{p_{,\nu}}{\varrho}\left(\frac{U_{\mu}U^{\nu}}{c^2} - \delta^{\nu}_{\mu}\right) = \frac{e}{mc}U^{\nu}F_{\mu\nu}. \tag{8}$$

This is exactly the equation of motion for an adiabatic fluid in special relativity, if the covariant derivative is again replaced by the partial derivative (compare, e.g., Eq. (18) of [6] with $U^\mu \to cu^\mu$).

A solution of Vlasov equation will in general not be locally isotropic; this property, however, may approximately be established if particle collisions lead to a local thermodynamic equilibrium; then additional (small) terms appear in Eqs. (7) and (8) due to these "kinetic terms" which are neglected here.

4. Electrostatic Oscillations in a Gravitational Field

The simplest application is to find the dispersion equation describing electrostatic waves in a gravitational field. For this we have to couple the linearized Vlasov equation with Maxwell's equations presented in covariant form [7]. We assume that the wave electric field is not very strong (so that one can neglect variations of the gravitational field caused by the wave), the perturbations in the wave are rapid (compared with the variations of $g_{\mu\nu}(x)$), and the perturbations in the wave are proportional to $\exp(-i\psi)$, where $(\psi_{,\mu}) \equiv (k_\mu) \equiv (\omega/c, -\mathrm{k})$. The dispersion equation takes the form [2]: $\varepsilon(\mathrm{k},\omega) = 0$ with the following expression for the plasma dispersion function (with $\omega \equiv ck_0, (\mathrm{k}) \equiv -(k_i)$):

$$\varepsilon(\mathrm{k},\omega) \equiv 1 + (k^i k_i)^{-1} \frac{\omega_{pe}^2}{n_0 c^2} \int d^4u \, \sqrt{g} \, \frac{u_0}{k_\nu u^\nu} (k_j u^i g^{e0} - k_j u^0 g^{ej}) \frac{\partial f^{(0)}}{\partial u^e}. \tag{9}$$

where $\omega_{pe}^2 \equiv 4\pi n_0 e^2/m$, $f^{(0)}$ is the unperturbed distribution function, and the Latin indices denote the spatial components.

The analysis of the dispersion equation has been carried out in [2]. The frequency of Langmuir oscillations for long wavelengths (compared to the Debye length) is the invariant electron plasma frequency ω_{pe} multiplied by two factors. For a cold plasma, the first factor is $\sqrt{g_{00}}$, the redshift factor or "lapse function" [8]; it measures the lapsed time of a clock in the local inertial rest frame at x during the unit time interval of a clock in the local "laboratory" rest frame at x where the gravitational field is present. The second factor is invariant; its square is the trace of the energy–momentum–stress tensor in units of the invariant rest energy density; it becomes smaller with increasing temperature, and both factors lead typically to a stronger Landau damping than in the non-relativistic limit.

One of the authors (S. I. Popel) would like to thank the Alexander von Humboldt Foundation for supporting this work.

References

[1] J. L. Synge, *Relativity: The General Theory* (North-Holland, Amsterdam, 1960).

[2] K. Elsässer and S. Popel, *"Plasma Equations in General Relativity"*, *Phys. Plasmas* **4** (1997), in press.

[3] A. G. Walker, *Proc. Edinburgh Math. Soc.* **4** 238 (1936).

[4] C. Eckart, *Phys. Rev.* **58** 919 (1940).

[5] A. H. Taub, *Arch. Rat. Mech. Anal.* **3** 312 (1959).

[6] K. Elsässer and S. Popel, *Phys. Plasmas* **3** 482 (1996).

[7] L. D. Landau and E. M. Lifshitz, *The Classical Theory of Fields* (Addison-Wesley, Reading, 1960).

[8] V. Buzzi, K. C. Hines, and R. A. Treumann, *Phys. Rev. D* **51** 6663 (1995).

New Theory of Transition from Weak to Strong Turbulent Plasma State

S. Popel
Institute for Dynamics of Geospheres, Leninsky pr. 38, Building 6,
117979 Moscow, Russia

1. Introduction

The weak turbulent plasma state is characterized by random wave phases. The arbitrary wave motion in this state can be represented as a linear superposition of oscillation modes, and the wave amplitudes change slowly in time owing to interaction with other waves and the particles of a plasma. In the strong turbulent plasma state the regular fields in the plasma are growing in importance, that results in formation of many coherent structures (e.g., solitons, filaments, and nonlinearly self-contracting wave packets). Within these structures, the phases of the modes are strongly correlated, while the structures themselves interact chaotically with each other. Thus it is the presence of the regular fields in the plasma that differs the strong turbulent state from the weak turbulent one. Previously some *scenarios* of the strong plasma turbulence have been proposed (see, e.g., [1]). The problem of the validity limits of the theory of weak plasma turbulence was raised in [2]. However, a theory including a mathematical formalism and demonstrating clearly physical processes in transition from the weak turbulent plasma state to the strong turbulent one has not been constructed yet. Here we propose such a theory. The modulational interaction is the key one in the transition [3]. It is the modulational interaction that results in the generation of the regular fields. We can use the concept of the transition from the weak turbulence state to the strong turbulent one only in the case when both these states can exist *separately*. This is possible only if there are thresholds of the modulational interaction. Otherwise, in a plasma there are both regular fields appearing due to the modulational interaction and the random ones. Such a state is a strong turbulent one, by definition. Furthermore, it is useful to apply to the transition the concept of entropy [4] which allows us to consider the transition as the process of self-organization. Thus the following items should be included in the theory:

1) development of the general nonlinear formalism for description of the modulational interaction in a plasma system consisting of random and regular fields;

2) investigation of the modulational instability of wave spectra, study of the thresholds of the instability;

3) verification of the validity of S-theorem and the principle of minimum entropy production [4] in processes of self-organization in application to the transition considered; demonstration that the plasma system is more ordered in the strong turbulent state and the transition from the weak turbulent state to the strong turbulent one can be considered as a nonequilibrium phase transition.

2. General Nonlinear Formalism

The general nonlinear formalism for description of the modulational interaction in a plasma system consisting of random and regular wave fields is developed for the case of a

plasma without magnetic field in [5] and generalized to the case of a plasma in the presence of an external magnetic field in [6]. This formalism takes into account the stochastic properties of the modulational interactions [7, 8].

The main steps of the formalism are the following: We separate random and regular components of the electric field and the distribution function of plasma particles. Averaging the kinetic equation over a statistical ensemble we obtain separate equations for the random and regular quantities. We distinguish (see [3]) the positive- and negative-frequency harmonics of the fields. Taking into account interactions via low-frequency "virtual" (beat) fields we obtain equations both for these fields and for the high-frequency wave fields. The (nonlinear) spectrum of the weak turbulence is the solution of the corresponding unperturbed (nonlinear) equation. Equations describing the modulational instability can be written for the correlation functions $G^{\pm}_{k,k'} = \left\langle \delta' E^{\pm}_{\pm k+k'} \delta E^{\mp(0)}_{\mp k} \right\rangle$, where $k = \{\omega, \mathrm{k}\}$, the angular brackets $\langle\rangle$ denote the averaging over statistical ensemble, $\delta' E$ is the random field perturbation due to modulational interaction, and $\delta E^{\pm(0)}$ is the initial random field. For a general case these equations take the form:

$$\begin{aligned}
\varepsilon_{\pm k+k'} G^{\pm}_{k,k'} = &-2 \int \Sigma^{\mathrm{eff}}_{\pm k+k', \pm k_1, \mp k_1} G^{\pm}_{k,k'} |E^{+(0)}|^2_{k_1} \, dk_1 \\
&-2 \int \Sigma^{\mathrm{eff}}_{\pm k_1, \pm k+k', \mp k_1} G^{\pm}_{k,k'} |E^{+(0)}|^2_{k_1} \, dk_1 \\
-2|E^{+(0)}|^2_k \int G^{\pm}_{k_1,k'} &(\Sigma^{\mathrm{eff}}_{\pm k_1+k', \pm k, \mp k_1} + \Sigma^{\mathrm{eff}}_{\pm k, \pm k_1+k', \mp k_1}) dk_1 \\
-2|E^{+(0)}|^2_k \int G^{\mp}_{k_1,k'} &(\Sigma^{\mathrm{eff}}_{\pm k, \pm k_1, k' \mp k_1} + \Sigma^{\mathrm{eff}}_{\pm k_1, \pm k, k' \mp k_1}) dk_1 ,
\end{aligned} \tag{1}$$

where $\Sigma^{\mathrm{eff}}_{k_1,k_2,k_3}$ is the effective third-order (in the wave field) response [3, 9], ε_k is the dielectric function, $\left\langle \delta E^{+(0)}_k \delta E^{-(0)}_{k_1} \right\rangle = -|E^{+(0)}|^2_{k_1} \delta(k + k_1)$. The concrete form of these equations for the case of the Langmuir waves is represented in [5]. Here we represent these equations for the case of a lower-hybrid (LH) wave spectrum consisting of waves propagating under the same angle with respect to the magnetic field (this assumption does not concern the modulational perturbations):

$$\begin{aligned}
(\varepsilon_{\pm k+k'} + \varepsilon^N_{\pm k+k'}) G^{\pm}_{k,k'} = |E^{+(0)}|^2_k \left(\frac{\omega_{pe}}{\omega}\right)^2 \left(\frac{\omega_{pe}}{\omega_{Be}}\right)^2 \int dk_1 \frac{[\mathbf{k}'_\perp \times \mathbf{k}_\perp]_\parallel [\mathbf{k}'_\perp \times \mathbf{k}_{1\perp}]_\parallel}{|\mathbf{k}||\mathbf{k}_1|} \\
\times \left\{ \alpha_{k'} \left(\frac{G^{+}_{k_1,k'}}{|\mathbf{k} \pm \mathbf{k}'||\mathbf{k}_1 + \mathbf{k}'|} + \frac{G^{-}_{k_1,k'}}{|\mathbf{k} \pm \mathbf{k}'||\mathbf{k}_1 - \mathbf{k}'|} \right) + \alpha_{k-k_1 \pm k'} \frac{G^{\mp}_{k_1,k'}}{|\mathbf{k} \pm \mathbf{k}'||\mathbf{k}_1 \mp \mathbf{k}'|} \right\},
\end{aligned} \tag{2}$$

where ε^N_k is the nonlinear dielectric function, ω_{pe} is the electron plasma frequency, ω_{Be} is the electron gyrofrequency,

$$\alpha_k \approx \frac{1}{4\pi n_0 T_e} \begin{cases} \mathbf{k}^2 v_s^2/(\omega^2 - \mathbf{k}^2 v_s^2) & \text{if } |\mathbf{k}| v_{Ti} \ll \omega \ll |k_\parallel| v_{Te} \\ -T_e/(T_e + T_i) & \text{if } \omega \ll |\mathbf{k}| v_{Ti}, \end{cases} \tag{3}$$

n_0 is the electron density, T_e is the electron temperature, and $v_{Te(i)}$ is the thermal electron (ion) velocity, v_s is the ion sound velocity, the subscript $\parallel$ denotes the vector component parallel to the external magnetic field.

3. Modulational Instability

The modulational instability of the Langmuir wave spectra has been investigated in [5, 10, 11], while that of the LH wave spectra in [6]. LH waves have been supposed in [6] to

have the frequency exceeding the frequency of the LH resonance. The main conclusions, which are important for the description of the transition considered, are the following:
a) The "long–scale" modulational instability of the wave spectra (when the length of the waves in the spectrum is less significantly than the wave length of the modulational perturbations $2\pi/|\mathbf{k}'|$, and the width in $\mathbf{k}$–space of the wave spectrum δk is larger than $|\mathbf{k}'|$) is suppressed compared with that of a monochromatic (with fixed frequency and wave vector) pump wave.
b) The instability thresholds appear only for very broad spectra when their width δk exceeds the wave vector of any modulational perturbation, i.e. for spectra containing all possible (for the waves) magnitudes of $\mathbf{k}$ ($\omega/|\mathbf{k}| > (2-3)v_{Te}$ for the Langmuir waves, and $\omega/k_{\|} > (2-3)v_{Te}$ for the LH waves). For example, for sufficiently wide LH wave spectra in ω–space so that $\delta\omega \gg \delta k v_s$ the threshold is determined by the following condition of the modulational instability development:

$$\int \frac{d\mathbf{k} W_{\mathbf{k}}^{LH}}{n_0 T_e \mathbf{k}^2 \lambda_{De}^2} \gg \frac{m_e}{m_i}\left(1+\frac{\omega_{pe}^2}{\omega_{Be}^2}\right)^2\left(\frac{\omega_{Be}}{\omega_{pe}}\right)^2, \qquad (4)$$

where $W^{LH} = \int W_{\mathbf{k}}^{LH} d\mathbf{k}$ is the energy density of the random waves, $m_{e(i)}$ is the electron (ion) mass, and λ_{De} is the electron Debye length. The thresholds of the modulational instability of the spectra of the Langmuir waves are given in [10].

We emphasize also the conclusion which concerns the case of the "short–scale" modulational instability of the LH wave spectra (when the length of the waves in the spectrum exceeds significantly the wave length of the modulational perturbations $2\pi/|\mathbf{k}'|$ and the width (in $\mathbf{k}$–space) of the wave spectrum δk is less than $|\mathbf{k}'|$). As shown in [6], the instability in this case develops analogously to the case of monochromatic pumping. Since in most cases, when the "short–scale" modulational instability of the LH waves is important, the LH waves constitute broad spectra, the above conclusion shows the validity of application of approximation of monochromatic pumping to description of real plasma phenomena (LH current drive, etc.) [9]. The characteristic feature of this case is the absence of the instability thresholds [6].

Thus we can use the concept of the transition from the weak turbulence state to the strong turbulent one only in the case b) when both these states can exist *separately*. Otherwise, in a plasma there are both regular fields appearing due to the modulational interaction and the random ones, and from the outset the system is in the strong turbulent state. Analogously, in the case of a monochromatic pumping there is no threshold of the modulational instability (see, e.g., [3, 9]), and the system is in the strong turbulent plasma state from the outset.

4. The Relative Degree of Order

To recognize whether the transition considered can be treated as a self–organization process we have to determine which state is more ordered. In the weak turbulent ("old") state there are only random fields, while in the strong turbulent ("new") one there are both random and regular fields. It is natural to choose the function which depends on the spectral density of the waves and determines the threshold of the modulational interaction as the control parameter [4] which characterizes the transition. We introduce the notion of the extended "old" state which means a hypothetical situation when the

system is in the weak turbulent state (the regular fields are absent) but the energy density of the random waves exceeds the threshold value. Considering only the near–threshold situation, one can show [12] that the difference in the entropy $S_{\rm old} - S_{\rm new}$ of the system in the extended "old" and "new" states (under the assumptions of the same magnitudes of the control parameter and of the same values of the mean effective energy in these states) is positive:

$$S_{\rm old} - S_{\rm new} \approx \frac{\delta W}{T_e} > 0, \tag{5}$$

where $\delta W > 0$ denotes the difference between the energy of the random waves in the strong turbulent state and their energy, corresponding to the threshold. In accordance with S–theorem [4], this means that the strong turbulent state is the more ordered one than the weak turbulent state. This allows us to consider the transition as a self–organization process. Furthermore, one can demonstrate that under the above assumptions the entropy production $\sigma = dS/dt$ in the extended "old" state is higher than in the "new" state. This means the validity of the principle of minimum entropy production in processes of self–organization [4] and gives us the possibility to treat the transition from the weak turbulent state to the strong turbulent one as a *nonequilibrium* phase transition.

5. Conclusions

Thus, the concept of the transition from the weak turbulence state to the strong turbulent one can be introduced only in the case when the random wave spectra are very broad, and the tresholds of the modulational instability of the wave spectra exist. Otherwise, there is no threshold of the instability, and the system is in the strong turbulent plasma state from the outset. The transition from the weak turbulent state to the strong turbulent one can be treated as a nonequilibrium phase transition.

One of the authors (S. I. Popel) would like to thank the Alexander von Humboldt Foundation for supporting his participation in the Conference.

References

[1] V.D. Shapiro and V.I. Shevchenko, in *Basic Plasma Physics*, Vol. 2 (North–Holland, Amsterdam, 1984).

[2] J. Krommes, in *Basic Plasma Physics*, Vol. 2 (North–Holland, Amsterdam, 1984).

[3] S.V. Vladimirov, V.N. Tsytovich, S.I. Popel, and F.Kh. Khakimov, *Modulational Interactions in Plasmas* (Kluwer, Dordrecht, 1995).

[4] Yu.L. Klimontovich, *Turbulent Motion and Structure of Chaos* (Kluwer, Dordrecht, 1991).

[5] S.I. Popel, V.N. Tsytovich, and S.V. Vladimirov, Phys. Plasmas, **1** 2176 (1994).

[6] S.I. Popel, Preprint *No.* 4, General Physics Institute, Moscow, 1997.

[7] S.I. Popel and S.V. Vladimirov, Phys. Lett. A, **200** 156 (1995).

[8] S.I. Popel, J. Plasma Phys., **57** 363 (1997).

[9] S.I. Popel, S.V. Vladimirov, and V.N. Tsytovich, Phys. Reports C, **259** 327 (1995).

[10] S.V. Vladimirov and S.I. Popel, Phys. Rev. E, **51** 2390 (1995).

[11] S.I. Popel, Bulletin of the Lebedev Physics Institute, *No.* 7–8 (1997), in press.

[12] S.I. Popel, Bulletin of the Lebedev Physics Institute, *No.* 12 (1996).

Radiative transfer in anisotropic, weakly inhomogeneous media with internal sources

U. Bellotti† and **M. Bornatici**†‡

†*INFM, Department of Physics "A. Volta", University of Pavia, Pavia 27100, Italy*

‡*Department of Physics, University of Ferrara, Ferrara 44100, Italy*

The transport of radiation in anisotropic, weakly inhomogeneous and spatially dispersive media with internal sources is investigated on the basis of the relevant geometric optics far-field as a function of position and frequency. The second rank radiation intensity tensor is obtained directly from the autocorrelation of the electric far-field in terms of a second rank emissivity tensor. Both the Faraday rotation and the change of ellipticity due to the Cotton-Mouton effect are discussed in some detail.

Introduction. A full description of the transport of radiation in anisotropic media with sources requires a second rank radiation intensity tensor for which a few equations have been established which are valid in the weak anisotropy limit and for incoherent radiation sources [1-4]. Here an approach is adopted which consists in obtaining the radiation intensity tensor directly on evaluating the autocorrelation of the electric field on the basis of the geometric optics far-field solution of the inhomogeneous wave equation, the result thus obtained applying to media with an arbitrary degree of anisotropy and to incoherent as well as coherent sources [5].

The radiation intensity tensor. With reference to a given orthonormal basis $\mathbf{e}_1, \mathbf{e}_2, \mathbf{e}_3$, such that one of the axes, e.g., $\mathbf{e}_3$, is locally along the direction of propagation of the radiation, the relevant radiation intensity tensor can be expressed in the form

$$I_{\alpha\beta}(\mathbf{r},\omega) \cong \frac{c}{4\pi^2 \overline{T}} (\mathbf{e}_\alpha)_i \left\langle E_i(\mathbf{r},\omega) E_j^*(\mathbf{r},\omega) \right\rangle (\mathbf{e}_\beta)_j \quad , \quad \alpha,\beta = 1,2 , \tag{1}$$

the dyad occurring within the angle brackets, which denote an ensemble average, being the (time-averaged, with $\overline{T}$ the time scale connected with such an average) autocorrelation of the electric field, taken as a function of position and (positive) frequency. The trace of $I_{\alpha\beta}$ is just equal, *in vacuo*, to the modulus of the (time and ensemble-averaged) Poynting vector, i.e., the power emitted per unit area and unit frequency. On making use of the geometric optics far-field solution of the inhomogeneous wave equation, one obtains the radiation intensity tensor (1) in the form of an integral over the effective volume connected with the radiation source

[5]. As part of the integrand one has an oscillating exponential factor which accounts for the relative phase between the X and O mode, namely,

$$e^{i\frac{\omega}{c}\left[l^{\sigma}(\mathbf{r},\rho)-l^{\sigma'}(\mathbf{r},\rho)\right]} \cong e^{i\frac{\omega}{c}R\left(n^{\sigma}-n^{\sigma'}\right)}, \tag{2}$$

where $l^{\sigma}(\mathbf{r},\rho) \equiv \frac{1}{2}\left(\int_{s^{O}(\mathbf{r})}^{s^{O}(\rho)} ds + \int_{s^{X}(\mathbf{r})}^{s^{X}(\rho)} ds\right) n^{\sigma}(s)\hat{\mathbf{v}}_{g}^{\sigma}(s)\cdot\hat{\mathbf{k}}^{\sigma}(s)$, the integration being along the ray paths, $\mathbf{r}$ and ρ denoting, respectively, some generic point where $I_{\alpha\beta}$ is evaluated, cf. Eq. (1), and the source point; also, n^{σ} and $\hat{\mathbf{v}}_{g}^{\sigma}\cdot\hat{\mathbf{k}}^{\sigma}$ denote, respectively, the refractive index and the cosine of the angle between the group velocity and the direction $\mathbf{k}$ of propagation of mode σ. In the weak-anisotropy limit, for which $\hat{\mathbf{v}}_{g}\cdot\hat{\mathbf{k}}\cong 1$, and disregarding inhomogeneity, it is $l^{\sigma}(\mathbf{r},\rho)\cong Rn^{\sigma}$, with $R\equiv|\mathbf{r}-\rho|$, and approximation (2) then applies. The phase factor (2) describes polarization changes of the radiation as it propagates from the source point ρ to some generic point $\mathbf{r}$. The polarization of the radiation near the source can be taken to be (approximately) the same as the polarization of the source itself, described by the second rank polarization tensor $p_{\alpha\beta}^{(\text{source})} \equiv \left(\mathbf{e}_{\alpha}\cdot\left\langle\mathbf{j}\mathbf{j}^{*}\right\rangle\cdot\mathbf{e}_{\beta}\right)\Big/\mathrm{Tr}\left\{\mathbf{e}_{\alpha}\cdot\left\langle\mathbf{j}\mathbf{j}^{*}\right\rangle\cdot\mathbf{e}_{\beta}\right\}$, $\left\langle\mathbf{j}\mathbf{j}^{*}\right\rangle$ being the (ensemble-averaged) Fourier transform (in space) of the autocorrelation of the (time Fourier transform of the) source current density. Let us consider specifically the case of radiation generated by a linearly polarized source propagating in a magnetoactive medium, such as a magnetized plasma.

Faraday rotation. For propagation (observation) along the axis of symmetry, the ambient magnetic field, say, the two propagating modes, to be labeled + and −, are circularly polarized, the corresponding polarization vectors being $\mathbf{e}^{+}=\left(1/\sqrt{2}\right)\left(\hat{\mathbf{t}}+i\hat{\mathbf{a}}\right)$ and $\mathbf{e}^{-}=\left(1/\sqrt{2}\right)\left(i\hat{\mathbf{t}}+\hat{\mathbf{a}}\right)$, with $\hat{\mathbf{t}}$ and $\hat{\mathbf{a}}$ mutually orthogonal (to $\mathbf{k}$) vectors. The source polarization matrix, equal to $p_{\alpha\beta}^{(\text{source})}=\begin{pmatrix}1 & 0\\ 0 & 0\end{pmatrix}$ in a suitable basis $\left(\mathbf{e}_1,\mathbf{e}_2\right)$, is $p_{\sigma\sigma'}^{(\text{source})}=\frac{1}{2}\begin{pmatrix}1 & -i\\ i & 1\end{pmatrix}$, with $\sigma=+,-$, in the basis $\left(\mathbf{e}^{+},\mathbf{e}^{-}\right)$. As the radiation propagates, $p_{\sigma\sigma'}$ varies along the ray due to the fact that the + and − modes get out of phase, according to Eq. (2), with the result that

$$\begin{aligned} p_{\sigma\sigma'}(\mathbf{r}) &= e^{i\frac{\omega}{c}\left[l^{\sigma}(\mathbf{r},\rho)-l^{\sigma'}(\mathbf{r},\rho)\right]} p_{\sigma\sigma'}^{(\text{source})} \\ &\cong \frac{1}{2}\begin{pmatrix} 1 & \sin\left[\frac{\omega}{c}\left(l^{+}-l^{-}\right)\right]-i\cos\left[\frac{\omega}{c}\left(l^{+}-l^{-}\right)\right] \\ \sin\left[\frac{\omega}{c}\left(l^{+}-l^{-}\right)\right]+i\cos\left[\frac{\omega}{c}\left(l^{+}-l^{-}\right)\right] & 1 \end{pmatrix}\cdot \end{aligned} \tag{3a}$$

Note that the diagonal terms of $p_{\sigma\sigma'}$ are constant. Re-expressing the polarization matrix (3a) in the basis $(\mathbf{e}_1, \mathbf{e}_2)$ yields

$$p_{\alpha\beta}(\mathbf{r}) = \begin{pmatrix} \cos^2\left[\frac{\omega}{2c}\left(l^+ - l^-\right)\right] & \sin\left[\frac{\omega}{2c}\left(l^+ - l^-\right)\right]\cos\left[\frac{\omega}{2c}\left(l^+ - l^-\right)\right] \\ \sin\left[\frac{\omega}{2c}\left(l^+ - l^-\right)\right]\cos\left[\frac{\omega}{2c}\left(l^+ - l^-\right)\right] & \sin^2\left[\frac{\omega}{2c}\left(l^+ - l^-\right)\right] \end{pmatrix}, \quad (3b)$$

which describes radiation linearly polarized along the direction at an angle $\psi = \frac{\omega}{2c}\left(l^+ - l^-\right)$ with respect to $\mathbf{e}_1$. Hence, during the propagation, the polarization direction rotates (Faraday rotation) at a rate given by

$$\frac{d\psi}{ds} = -\frac{\omega}{2c}\left[\left(n\left(\hat{\mathbf{v}}_g \cdot \hat{\mathbf{k}}\right)\right)^+ - \left(n\left(\hat{\mathbf{v}}_g \cdot \hat{\mathbf{k}}\right)\right)^-\right] \cong -\frac{\omega}{2c}\left(n^+ - n^-\right), \quad (3c)$$

the approximation being valid in the limit of weak anisotropy.

Cotton-Mouton effect. Let us consider propagation in the plane perpendicular to the ambient magnetic field, for which the polarization unit vectors $\mathbf{e}^X$ and $\mathbf{e}^O$ of the two natural modes, X and O-mode, are mutually orthogonal. On identifying the basis $(\mathbf{e}_1, \mathbf{e}_2)$ with $(\mathbf{e}^X, \mathbf{e}^O)$, one can express the source polarization matrix in the form

$$p_{\alpha\beta}^{(\text{source})} = \begin{pmatrix} \cos^2\psi_o & \sin\psi_o\cos\psi_o \\ \sin\psi_o\cos\psi_o & \sin^2\psi_o \end{pmatrix}, \quad (4)$$

ψ_o being the angle between the direction of polarization of the source and $\mathbf{e}^X$. On the basis of Eq. (2), the polarization matrix at the generic point $\mathbf{r}$ is

$$p_{\alpha\beta}(\mathbf{r}) = \begin{pmatrix} \cos^2\psi_o & \sin\psi_o\cos\psi_o\left[\cos\left(\frac{\omega}{c}\Delta l\right) - i\sin\left(\frac{\omega}{c}\Delta l\right)\right] \\ \sin\psi_o\cos\psi_o\left[\cos\left(\frac{\omega}{c}\Delta l\right) + i\sin\left(\frac{\omega}{c}\Delta l\right)\right] & \sin^2\psi_o \end{pmatrix}, \quad (5)$$

with $\Delta l \equiv \left(l^O - l^X\right)(\mathbf{r}, \rho)$. As known [4], to the polarization matrix (5) can be given a geometrical representation, namely, the polarization ellipse, characterized by the ellipticity T, that is, the axial ratio, and the angle ψ of orientation. On comparing the general expression of the polarization matrix in terms of T and ψ with expression (5), one obtains

$$T = \frac{1 - \sqrt{1 - 4A^2}}{2A}, \qquad A \equiv \sin\psi_o\cos\psi_o\sin\left(\frac{\omega}{c}\Delta l\right) \quad (6a)$$

and

$$\sin^2\psi = \frac{\left(1 + T^2\right)\sin^2\psi_o - T^2}{1 - T^2}. \quad (6b)$$

In particular, Eq. (6b) admits the solution $\sin\psi = \sin\psi_0$, i.e., the angle ψ is constant during the propagation, for $\psi = \pi/4$, independently of the value of the ellipticity. Correspondingly, from Eq. (6a), one has

$$T(\psi = \pi/4) = \frac{1 - \left|\cos\left(\frac{\omega}{c}\Delta l\right)\right|}{\sin\left(\frac{\omega}{c}\Delta l\right)} \tag{7}$$

Eq. (7) describes the ray evolution of the ellipticity in the Cotton-Mouton effect [6]. More specifically, at distances from the source for which $\sin\left(\frac{\omega}{c}\Delta l\right) = 0$, i.e. for $R \cong \pi m \frac{c}{\left|\left(n^{\mathrm{O}} - n^{\mathrm{X}}\right)\omega\right|}$ (m is a positive integer), the radiation is linearly polarized at an angle $\psi = \pi/4$, whereas for $\cos\left(\frac{\omega}{c}\Delta l\right) = 0$, i.e. for $R \cong \left(m + \frac{1}{2}\right)\pi \frac{c}{\left|\left(n^{\mathrm{O}} - n^{\mathrm{X}}\right)\omega\right|}$, the radiation is in turn left-hand and right-hand circularly polarized. In general, the radiation is elliptically polarized: the polarization ellipse has major axis of constant length at an angle $\psi = \pi/4$ and minor axis of oscillating length with distance. For source polarizations along the two mode polarization vectors the effect obviously does not occur, while, for intermediate angles, the maximum value of the ellipticity is, cf. Eq. (6a), $T_{\max} = \frac{1 - \left|\cos 2\psi_0\right|}{\sin 2\psi_0}$ and, during the propagation, the orientation of the major axis is no longer constant, its evolution being described by Eq. (6b).

Acknowledgments. This work was supported by the Italian National Research Council (CNR) and by the Italian Ministry of University, Scientific Research and Technology (MURST).

[1] V. V. Zheleznyakov, V. V. Kocharovskiĭ, and Vl. V. Kocharovskiĭ, Sov. Phys. Usp. **26**, 877 (1983).

[2] V. L. Ginzburg, *Applications of Electrodynamics in Theoretical Physics and Astrophysics* (Gordon and Breach, New York, 1989), Chap. 10.

[3] D. B. Melrose, *Plasma Astrophysics Vol. I Emission, Absorption and Transfer of Waves in Plasmas* (Gordon and Breach, New York, 1980), Chap. 6.

[4] D. B. Melrose and R. C. McPhedran, *Electromagnetic Processes in Dispersive Media* (Cambridge University Press, Cambridge, 1991), Chap. 14.

[5] U. Bellotti and M. Bornatici, Phys. Plasmas **6** (August issue), 1997.

[6] Yu. A. Kravtsov, O. N. Naĭda, and A. A. Fuki, Physics-Uspekhi **39**, 129 (1996).

Role of ion dynamics on magnetic electron drift vortex modes

Arshad M. Mirza[1] and P. K. Shukla
Institut für Theoretische Physik IV, Ruhr-Universität Bochum
D-44780 Bochum, Germany

Abstract- A new dispersion relation for low-frequency magnetic electron drift modes (MEDV) in a nonuniform plasma is derived, by incorporating the ion dynamics. It is shown that the ion dynamics introduces new classes of instabilities when the wave frequency either lies between the electron and ion plasmas frequencies or is close to the ion plasma frequency. The modified MEDV modes involving the ion motion can cause nonthermal particle as well as electron heat transports.

Recently, Yu and Stenflo[1] discovered the magnetic electron drift (MEDV) modes in an electron plasma, by assuming that the ions form the neutralizing background.

Our objective here is to re-examine the MEDV mode with the ion dynamics in a plasma with both the density and electron temperature inhomogeneities. It is shown that the inclusion of the ion motion renders a non-zero value for the electron and ion number density perturbations when the equilibrium density gradient and the ion flow velocity are finite. Consequently, the dispersion relation of the MEDV mode is significantly altered. Conditions under which the MEDV mode exists are presented. Furthermore, we have identified two new instabilities of the MEDV mode involving the ion motion in plasmas containing the equilibrium density and magnetic field inhomogeneities. It is found that, in addition to anomalous electron energy transport, nonthermal MEDV modes involving ion motion can also cause the particle transport due to finite density fluctuations.

We consider a nonuniform electron-ion plasma in the presence of electromagnetic disturbances. The equilibrium density and temperature inhomogeneities, which are maintained either by some external sources or by gravitational forces, are along the x-axis.

---

[1]Permanent address: Department of Physics, Quaid-i-Azam University, Islamabad 45320, Pakistan

Subtracting the ion momentum equaion from the electron and taking the curl of the resulting equation, we obtain

$$(1-\lambda_e^2\nabla_\perp^2)\partial_t \mathbf{B} = \frac{c}{e}\left(\nabla T_{e1}\times\nabla \ln n_0 + \frac{1}{n_0}\nabla T_{e0}\times\nabla n_{e1}\right), \tag{1}$$

where $\lambda_e = c/\omega_{pe}$ is the collisionless electron skin depth, $\omega_{pe} = (4\pi n_0 e^2/m_e)^{1/2}$ is the electron plasma frequency, and $T_{e1}(= T_e - T_{e0} << T_{e0})$, $n_{e1} = n_e - n_{e0} << n_{e0}$ and $\mathbf{B}$ are the electron temperature and electron number density and magnetic field perturbations, respectively.

The electron temperature perturbation is obtained from

$$\partial_t T_{e1} + \left[\left(\mathbf{v}_i - \frac{c}{4\pi e n_0}\nabla\times\mathbf{B}\right)\cdot\nabla\right]T_{e0} + \frac{2}{3}T_{e0}\nabla\cdot\left(\mathbf{v}_i - \frac{c}{4\pi e n_0}\nabla\times\mathbf{B}\right) = 0, \tag{2}$$

whereas the electron number density perturbation obeys

$$\partial_t n_{e1} + \nabla\cdot\left(n_0\mathbf{v}_i - \frac{c}{4\pi e}\nabla\times\mathbf{B}\right) = 0. \tag{3}$$

Equations (1) to (3) together with $\nabla\times\mathbf{B} = 4\pi e n_0/c(\mathbf{v}_i - \mathbf{v}_e)$, are the desired equations for the study of the MEDV mode with the ion dynamics. Here $n_j, \mathbf{v}_j, m_j$ and T_j are the number density, the fluid velocity, the mass, and the temperature of the particle species j (j equals e for the electrons and i for the ions), respectively. Furthermore, γ_j is the adiabatic index.

Let us assume that the MEDV mode magnetic field $\mathbf{B}$ is of the form $\hat{\mathbf{z}}B_1$, where $\hat{\mathbf{z}}$ is the unit vector along the z-axis. Supposing that B_1 is proportional to $\exp(iky - i\omega t)$, where k is the wave number along the y axis and ω is the wave frequency, we Fourier transform our basic system of equations and combine them to obtain[2]

$$\omega^2\left[(\omega^2-\omega_{pi}^2)(\omega^2-3k^2v_{te}^2) - \omega^2\omega_{pe}^2\right](1+k^2\lambda_e^2) = \left[-k^2c^2\lambda_{De}^2\left\{(\omega^2-\omega_{pi}^2)\right.\right.$$
$$\left.\left.\times(\omega^2-3k^2v_{te}^2) - \omega^2\omega_{pe}^2\right\} + c_s^2\left\{\omega_{pi}^2(\omega^2-3k^2v_{te}^2) + \omega^2\omega_{pe}^2\right\}\right]\left(\eta - \frac{2}{3}\right)L_n^{-2}. \tag{4}$$

Several comments are in order. First, when the wave frequency (wave phase velocity) is much larger than $\omega_{pe}(v_{te})$, then (4) yields $\omega^2 = -k^2c^2\lambda_{De}^2(\eta - 2/3)$ $/L_n^2(1+k^2\lambda_e^2)$, which is the dispersion relation of the MEDV mode that has been obtained in Ref. 1 for a nonuniform unmagnetized plasma. Here, on a very short time scale, the ion motion is unimportant as the ions do not have time to respond

to high-frequency purely magnetic oscillations. When $\eta > 2/3$ the MEDV mode becomes purely growing[1]. Second, some new interesting results emerge in two limiting cases, as described below.

Consider that the wave frequency is close to the ion plasma frequency and that the wave phase velocity is much smaller than the electron thermal velocity. In this case, (4) reduces to

$$\omega^2 \approx -\frac{(k^2\lambda_{De}^2 c^2 + c_s^2)}{(1+k^2\lambda_e^2)L_n^2}\left(\eta - \frac{2}{3}\right). \tag{5}$$

where $\lambda_{De}(= v_{te}/\omega_{pe})$ is the electron Debye length. Equation (5) predicts an instability when $\eta > 2/3$.

Furthermore, in the hydrodynamic approximation in which the electron inertial forces dominate over the pressure gradient force, we obtain from (4) for $\omega < \omega_{pe}$

$$\omega^2 = -\frac{c_s^2(1+k^2\lambda_i^2)}{L_n^2(1+k^2\lambda_e^2)}\left(\eta - \frac{2}{3}\right), \tag{6}$$

where $\lambda_i = c/\omega_{pi}$ is the collisionless ion skin depth. Equation (6) exhibits a purely growing instability provided that $\eta > 2/3$.

The electron temperature gradient driven MEDV involving the ion motion can cause nonthermal particle as well as electron heat transports, because the mode contains finite density perturbations. The particle flux is given by $\Gamma_x = \langle n_1 V_x \rangle + compl.conj.$, where the angular bracket denotes the sum over k. The electron density fluctuations for low-frequency ($kv_{te} \ll \omega \ll \omega_{pe}, \omega_{pi}$) and for purely growing mode is given by $n_{e1} = -in_0 e\gamma_k L_n^{-1} B_{\mathbf{k}}/m_i\omega_{pe}^2 kc$, and consequently Γ_x becomes

$$\Gamma_x = -\frac{1}{2\pi m_i L_n \omega_{pe}^2}\sum_{\mathbf{k}} \frac{\gamma_k(1+k_\perp^2\lambda_i^2)}{k_\perp^2\lambda_i^2}|B_{\mathbf{k}}|^2. \tag{7}$$

Similarly, a straightforward calculation yields the heat flux

$$\begin{aligned} Q_x &= \langle T_1 V_x \rangle + compl.conj. \\ &= \frac{(\eta - \frac{2}{3})}{2\pi n_0 L_n \lambda_i^2}\sum_{\mathbf{k}} \frac{(1+k_\perp^2\lambda_i^2)(c_s^2 + k_\perp^2\lambda_{De}^2 c^2)}{k_\perp^2\gamma_k}|B_{\mathbf{k}}|^2. \end{aligned} \tag{8}$$

It is evident from (8) that the heat flow could be inward or outward direction depending on the direction of density and temperature gradients. Clearly, for a given magnetic field spectrum of the MEDV mode the particle and heat fluxes are completely determined.

To summarize, we have derived a new dispersion relation for the MEDV mode, taking into account the ion dynamics. It is found that the role of the latter is unimportant so long the MEDV mode frequency is much larger than the electron plasma frequency. On the other hand, we have identified new classes of purely growing instabilities that occur on the time scale of the ion plasma period. Here, the ion motion plays a crucial role. Furthermore, we have presented quasilinear calculations of nonthermal particle and electron energy transports that are caused by enhanced MEDV modes involving ion dynamics.

In conclusion, we stress that the results of the present investigation should help us to a better understanding of the MEDV modes which plays an important role in laser produced plasmas as well as in plasma switches[2].

Acknowledgments One of us (A. M. Mirza) acknowledges the benefit of very useful discussions with Dr. M. Y. Yu and L. Stenflo. Furthermore, this work was partially supported by the Alexander von Humboldt Foundation.

References

[1] M. Y. Yu and L. Stenflo, Phys. Fluids **28**, 3447, (1985); L. Stenflo and M. Y. Yu, *ibid.* **29**, 2335 (1986).

[2] A. M. Mirza and P. K. Shukla, Phys. Plasmas **6**, (1997).

Electrical Conductivity of Strongly Coupled Model Plasmas

I.M. Tkachenko, P. Fernández de Córdoba, B. Solís, P. Zubía

Department of Applied Mathematics,
Polytechnic University of Valencia,
Valencia E-46071, Spain
e-mail: imtk@iqn.upv.es

1. The theory of electrical conductivity of dense cold fully-ionized hydrogen plasmas based on the concept of self-consistent field, and the generalized random-phase approximation (RPA) [1],[2] is applied to the determination of electrical conductivity of model Coulomb systems [3].

The basic idea considered in [1],[2] is that each electron (carrier) moves in a self-consistent field generated by all other free charges in the system. The finite values of the transport coefficients result from the electron's scattering on the self-consistent field fluctuations.

This approach was first outlined and applied in [1]. This work was based on the paper [4] by S.F. Edwards, which related the Lorentz-model expression for the fully-ionized plasma electrical conductivity to the strict quantum-statistical calculation involving the Green's function formalism with the self-consistent field potential.

The starting point for the conductivity calculation is thus the Lorentz formula

$$\sigma = -\frac{4e^2}{3m}\int_0^\infty EdE\frac{d\omega(E)}{dE}\rho(E)\tau(E), \tag{1}$$

where $\rho(E) = (2m^3E)^{1/2}/(2\pi^2\hbar^3)$ is the density of one-electron states in the energy space. and $\omega(E)$ is the Fermi-Dirac distribution.

Generally speaking, the mean relaxation time $\tau(E)$ of Eq. (1) is determined by the exact pairwise scattering cross-section, and we express it in terms of the self-consistent field correlation function,

$$\tau^{-1}(E) = \frac{me^2}{4\pi(2mE)^{3/2}}\int_0^Q q^3dq\int_{-\infty}^{\infty} < |\hat{V}(\vec{q},\omega)|^2 > d\omega. \tag{2}$$

Here $Q = (8mE/\hbar^2)^{1/2}$, momentum $\hbar Q$ being the maximum possible variation of the electronic momentum as a result of the scattering process; and

$$\hat{V}(\vec{q},\omega) = \frac{4\pi e}{q^2\varepsilon(q,\omega)}\sum_{a=e,i} Z_a\,\hat{\rho}_a(\vec{q},\omega) \tag{3}$$

is the field potential operator complete Fourier transform, $\hat{\rho}_a(\vec{q},\omega)$ being the a-species density operator in the $(\vec{q},\omega)$-space, and $\varepsilon^{-1}(q,\omega)$ - the plasma dynamic screening function. The system is presumed to contain electrons (e) and protons (i), the charge number of electrons and ions are $Z_e = -1$, $Z_i = 1$. The field potential correlation function thus equals

$$< |\hat{V}(\vec{q},\omega)|^2 >= (\frac{4\pi e}{q^2\varepsilon(q,\omega)})^2\sum_{a,b} Z_aZ_bS_{ab}(\vec{q},\omega). \tag{4}$$

The dynamic structure factor of the species a and b, $S_{ab}(\vec{q},\omega)$ was determined in [2] in terms of the system polarization operators:

$$\tau^{-1}(E) = \frac{4\pi m e^4}{\beta(2mE)^{3/2}} \int_0^Q \frac{dq}{q} \sum_{a,l} \frac{\Pi_a(q,l)}{\varepsilon^3(q,l)} , \tag{5}$$

β^{-1} being the system temperature in energy units.

The l-summation in Eq. (5) is spread over the poles $2\pi l/\beta\hbar$, $(l = 0, \pm 1, \pm 2, \ldots)$ of $coth(\beta\hbar z/2)$ on the imaginary z-axis.

Eq. (5) together with Eq. (1) form a general algorithm of conductivity calculation, as soon as specific approximate expressions are used for the density-response functions and the polarization operators.

2. In our computations we evaluated the real part $\Pi_a(q,l)$ of the a-species polarization operator beyond the standart RPA, using the temperature dependent electronic static local-field correction $G_e(q)$ [2] parametrized to satisfy both the compressibility sum rule (with the electronic subsystem compressibility determined from the one component plasma (OCP) excess interaction energy determined by the Monte Carlo (MC) simulation [5]), and the long-wavelength limiting condition of Kimball [6]:

$$G_e(q) = G_e(z) = (b + a/(2z)^2)^{-1}. \tag{6}$$

Here $b = (1 - g_e(0))^{-1}$, and a was estimated as in [8]:

$$a = -(12\pi^2)^{-1/3} \left(\frac{U_{OCP}(\Gamma)}{12\Gamma} + \frac{U'_{OCP}(\Gamma)}{36} \right)^{-1} \tag{7}$$

with

$$U_{OCP}(\Gamma) = -0.89937495\Gamma - 0.2244699 - 0.017874675\Gamma^{-1/3} + 0.5175753\Gamma^{1/3} \tag{8}$$

being the MC-simulated classical OCP Coulomb energy normalized to β^{-1} [5].

Here $\Gamma = \beta e^2 (4\pi n/3)^{1/3}$ measures the rate of Coulomb coupling in the system with electronic concentration n, $z = q/k_F$, $k_F = (3\pi^2 n)^{1/3}$ is the Fermi wavevector. Notice that the Brueckner parameter $r_s = \Gamma\Theta/0.534$, where $\Theta = 2m/(\beta\hbar^2 k_F^2)$ is another dimensionless parameter measuring the plasma degeneracy rate.

The electronic radial distribution function, $g_e(r)$, was determined by a self-consistent procedure, which is a simple generalization of that proposed and elaborated in [7, 2, 8] for the calculation of its zero-separation value $g_e(0)$, i.e., $g_e(r)$ was computed *via* a simultaneous solution of two integral equations:

$$S_e(z) = \frac{1}{\beta n} \sum_l \frac{\Pi_e(z,l)}{1 + (e/k_F z)^2 \Pi_e(z,l)} , \tag{9}$$

$$g_e(r) = 1 + \frac{6}{r k_F} \int_0^\infty z \sin(2k_F r z)(S_e(z) - 1)\, dz. \tag{10}$$

Thus putting

$$\Pi_e(z,l) = \Pi_e^0(z,l)\left(1 - \frac{\Gamma}{(12\pi^2)^{1/3}} \frac{G_e(z)\Pi_e^0(z,l)}{\beta n z^2}\right)^{-1} ,$$

$$\Pi_i(z,l) = \beta n \delta_{l,0}\left(1 - \frac{\Gamma}{(12\pi^2)^{1/3}} \frac{G_i(z)}{z^2}\right)^{-1}$$

with

$$G_i(z) = \left(b(1 + (e/k_F z)^2 \Pi_e(z,0)) + a/(2z)^2\right) ,$$

we obtain a closed expression for the conductivity coefficient.

$\Pi_e^0(q,\omega)$ is the RPA electronic polarization operator real part[9].

In addition, we calculated the excess Coulomb interaction energy normalized to β^{-1}:

$$U = \frac{1}{8}\frac{k_D^2}{k_F^2}\int_0^\infty (g_e(r) - 1)\; r\; dr, \tag{11}$$

with $k_D^2 = 4\pi n e^2 \beta$. The results are given in Table 1, where we also provided the corresponding values of $U_{OCP}(\Gamma)$.

Both estimates are closer in less degenerate electronic liquids.

3. Fully ionized strongly coupled hydrogen plasmas were simulated using the method of molecular dynamics (MD) in well-known studies by J.P. Hansen et al. [3]. Quantum effects were taken into account in these simulations through the use of effective pair potentials; at short distances these differed significantly from the bare Coulomb potential.

The *"dynamical"* results of [3] were successfully considered in [10].

The static conductivity of model plasmas was first obtained in [3] on the basis of the Nernst-Einstein law in terms of electronic and ionic diffusion coefficients directly estimated by MD simulations:

$$\sigma_D = \frac{n_e e^2}{k_B T}(D_i + D_e). \tag{12}$$

In addition, σ was determined, at least for $\Gamma = 2$ and $r_s = 1$, through the electric current autocorrelation function in the relaxation time approximation [3].

We computed the conductivity of strongly coupled hydrogen plasma for all three cases considered in [3], and using the static local field correction (Eq. (6)) suggested in [7] and studied in [2, 8]. The results are presented in Table 2 for the dimensionless conductivity $\sigma^* = \sigma/\omega_{pe}$ (ω_{pe} being the electronic plasma frequency). Notice that the simulation data for $\Gamma = 2$ and $r_s = 1$ were obtained in [3] by MD calculations, in this case the value σ_D^* was calculated as

$$\sigma_D^* = \frac{3\Gamma}{4\pi}(\frac{m}{M})D_i^* + D_e^*, \tag{13}$$

D_e^* and D_i^* being the dimensionless diffusion coefficients determined in [3]; other results were found in [3] by extrapolation, in these cases D_i^* was put to be zero (not determined in [3]). The value of σ_L^* was obtained in [3] by a limiting procedure over the dynamic conductivity $\sigma(k,\omega)$,

$$\sigma_L = \lim_{\omega \longrightarrow 0}\lim_{k \longrightarrow 0} Re\sigma(k,\omega) , \tag{14}$$

and thus related via the fluctuation-dissipation theorem to the dynamic structure factor *"charge-charge"*. The limiting value of (14) could be found in [3] only by extrapolation of long-wavelength MD data (see Table IV of [3]). We thus consider $\sigma_L^* = \sigma_L/\omega_{pe}$ (characterized in [3] as the *"true"* value) to be less reliable then σ_D^*.

We conclude that a good level of agreement with plasma-simulation data is achieved.

$n\ (10^{24}\ cm^{-3})$	$T\ (10^5\ K)$	Γ	Θ	U	U_{OCP}
0.258	1.715	1.00	1.00	-0.54	-0.62
1.610	6.315	0.5	1.09	-0.24	-0.29
1.611	1.579	2.0	0.27	-1.11	-1.38
$2.579 \cdot 10^5$	$1.715 \cdot 10^3$	0.10	0.10	-0.044	-0.11

Table1. The excess Coulomb interaction energy (normalised to temperature) U, calculated using the self-consistent model [6] (see Sect.2) and the results of the electronic liquid MC-simulation, U_{OCP} [7].

$n\ (10^{24}\ cm^{-3})$	$T\ (10^5\ K)$	Γ	r_s	σ^*	$\sigma_D{}^*$	$\sigma_L{}^*$
1.611	1.579	2.0	1.00	0.59	0.60	1.1
1.610	6.315	0.5	1.00	1.00	0.86	2.15
25.170	15.79	0.5	0.40	1.80	1.47	3.6

Table 2. Electrical conductivity of model hydrogen plasmas (normalised to the plasma frequency) σ^* calculated according to the present algorithm, the values of $\sigma_D{}^*$ were calculated in terms of the diffusion coefficients, as explained in Sect.3; $\sigma_L{}^*$ are the results of the extrapolation procedure according to Eq. (15).

References

[1] V.M. Adamjan et al., High Temp. (USA), **18**, 186 (1980).

[2] Z. Djuric, A.A. Mihajlov, V.A. Nastasyuk, M. Popovic and I.M. Tkachenko, Phys. Lett., **A155**, 415 (1991).

[3] J.P. Hansen, I.R. McDonald, Phys. Rev. A, **23**, 2041 (1981).

[4] S.F. Edwards, Philos.Mag., **3**, 1020 (1958).

[5] G.S. Stringfellow, H.E. DeWitt, W.L.S. Slattery, Phys. Rev. A, **41**, 1105 (1990).

[6] J.C. Kimball, Phys. Rev. A, 7, 1648 (1973).
J.C. Kimball, Phys. Rev. A, **14**, 2371 (1976).

[7] I.M. Tkachenko, Europhys. Lett., **9**, 351 (1989).

[8] I.M. Tkachenko, P. Fernández de Córdoba and M. Urrea, J.Phys.A, **29**, 2599(1980).

[9] N.R. Arista and W. Brandt, Phys. Rev. A, 29, 1471 (1981).

[10] S.V. Adamyan, I.M. Tkachenko, J.L. Muñoz-Cobo González and G. Verdú Martín, Phys.Rev.E, **48**, 2067 (1993).

On the Theory of Microfields and Fusion Rates for Dense Plasmas

M.Yu.Romanovsky and W.Ebeling

Institute of Physics, Humboldt-University Berlin, Invalidenstr. 110, D-10115 Berlin, Germany

Abstract

The microscopic dynamics and the influence of microfields is studied. New expressions for the rates of fusion reactions are obtained, which include the effect of average forces and of random fields.

The rates of nuclear rections R in plasmas are determined by the Coulomb interaction between the charged plasma particles [1,2]. Assuming that the decay rates behave ideally, we get in some approximation [3]

$$R = R_{id} \exp\left(\frac{\Delta\mu}{k_B T}\right) \tag{1}$$

where T is plasma temperature and $\Delta\mu$ is the potential on mean force. We are interested here in the investigation of the influence of the microfields on the fusion process. Since fusion is a process of relative motion of two bodies, we need now relative microfields.

We have to find out, what fields are really acting during the two-body fusion process in plasmas. The actual force between nucleus 1 with the charge q_1, mass m_1 and a nucleus 2 with q_2, m_2 in a microfield $\delta E(r)$ is given by

$$\vec{F_{av}} + Q_{eff}(\delta\vec{E}(\vec{r_1}) + \delta\vec{E}(\vec{r_2})) + q_{eff}(\delta\vec{E}(\vec{r_1}) - \delta\vec{E}(\vec{r_2})).$$

where $\vec{F_{av}}$ is the mean force and

$$Q_{eff} = \mu(\frac{q_1}{m_1} - \frac{q_2}{m_2}); q_{eff} = \mu(\frac{q_1}{m_1} + \frac{q_2}{m_2})$$

(μ is the reduced mass). In spite of the fact that the distances between the two nuclei which are going to react is very small, it is still finite and therefore the correlation length of the random field will play an essential role. The second important effect which we have to study is the dynamic resolution of the microfield, since the fusion process occurs in a small, but finite time.

The Fourier decomposition of static Coulomb field is given by [4]:

$$(\vec{k}\vec{E}_{\vec{k},\omega}) = \frac{iq}{2\pi^2\epsilon(\omega,\vec{k})} \cdot \delta[\omega - (\vec{k}\cdot\vec{v})].$$

Here i is the imaginary unit, $\delta(x)$ is the Dirac delta-function and $\epsilon(\omega, \vec{k})$ is the dielectric function. In order to receive the total average spectra, we have to take the mean value over the velocity distribution. For a Maxwell distributions with $v_T = (2T/m)^{1/2}$ we get:

$$(\vec{k}\vec{E}_{k\omega})_v = -\frac{iq \cdot \exp(-\omega^2/k^2 v_T^2)}{2\pi^{3/2} k v_T \cdot \epsilon(\omega, k)}, \tag{2}$$

The long wavelengths are (practically) absent in eq. (2) if $k < \omega/2v_T$. This means that $\vec{E}(\vec{r}_1)$ and $\vec{E}(\vec{r}_2)$ are independent, and their difference is principally non-zero; the sum of $\vec{E}(\vec{r}_1)$ and $\vec{E}(\vec{r}_2)$ is also the random value which is not equal to twice the field amplitude; because the thermal electron velocities are much higher than the ion velocities, the same k-values in (2) can be provided for electrons for much more frequencies ω than for ions. Thus we have a strongly oscillating electron random field during the elementary fusion process and we can suppose that this field is averaged during it: the electron component of the random field is not active in the fusion processes.

The normalized field-field correlation function is about 1 [5] up to the time $\tau = \mu/4\pi ne^2$ (n is ion density and e is electron charge), which is much more than the time of a barrier penetration (fusion time). Consequently, we can suppose that the ion component of random field is stationary during the fusion process, therefore the values $\delta\vec{E}(\vec{r}_1) - \delta\vec{E}(\vec{r}_2)$ and $\delta\vec{E}(\vec{r}_1) + \delta\vec{E}(\vec{r}_2)$ can be considered as time-independent.

How to determine the distribution of random values $\Delta\vec{E} = \delta\vec{E}(\vec{r}_1) - \vec{E}(\vec{r}_2)$ and $\Sigma\vec{E} = \delta\vec{E}(\vec{r}_1) + \vec{E}(\vec{r}_2)$? At first, we should determine the distribution of projections E_x, E_y, E_z, then the distributions of each difference $\Delta E_x, \Delta E_y, \Delta E_z$, and then the distributions of the full vector $\Delta\vec{E}$ and $\Sigma\vec{E}$.

The natural system of coordinates in the problem under consideration is a spherical one with the polar axis given by vector $\vec{r}$. Thus we should write the distributions of $\Delta\vec{E}$ and $\Sigma\vec{E}$ in this spherical coordinate system. The distributions with respect to the angles are uniform; therefore, the angle distribution function F_{ang} is uniform:

$$F_{ang} \sin\theta d\theta d\varphi = \frac{1}{4\pi} \sin\theta d\theta d\varphi \tag{3}$$

here θ and φ are the polar and azimutal angles respectively.

In case of ideal plasma, the distribution of δE is the Holtsmark distribution. The distribution of vector random field E is:

$$W(\vec{E}) = (2\pi)^{-3} \int_{-\infty}^{+\infty} \exp(-i\vec{K}\vec{E}) F(\vec{K}) d^3K,$$

Let us make the following trick to clarify the (semi-quantitative) shape of the $\Delta\vec{E}$ and $\Sigma\vec{E}$ distributions: we replace $F(\vec{K})$ by $\exp(-\beta K)$. In this case we get

$$W(E) = W_{\text{mod}}(E) = 4\beta E^2/(\beta^2 + E^2)^2,$$

and the integral over E from zero to infinity is equal to 1, thus β is a good adjustment parameter. This model distribution provides the correct asymptotics at the point zero: all distributions are proportional to E^2, and the wrong one in the infinity E^{-2} (Holtsmark's distribution gives $\sim E^{-5/2}$). The value $E = \beta$ corresponds to the maximum $W_{\mathrm{mod}}(E) = 1/\pi\beta$. In this case we get

$$W_{\mathrm{mod}}(\Delta E_x) = W_{\mathrm{mod}}(\Sigma E_x) = W_{\mathrm{mod}}(E_x/2) \tag{4}$$

Thus the model distributions $W_{\mathrm{mod}}(\Delta E), W_{\mathrm{mod}}(\Sigma E)$ coincide with $W_{\mathrm{mod}}(\delta E/2)$, and we can suppose that the real distribution of ΔE and ΣE have - at least semi-quantitatively - the same character as $W(\delta E/2)$.

The Gamov's formula for the rate of two-body fusion even if has been obtained in the framework of Schrödinger equations for nonrelativistic inelastic scattering (see, for example [6]). In presence of weak microfield we get the enhanced fusion probability:

$$W_{GU} \simeq \exp[-3(\pi/2)^{2/3}({q_{eff}}^4/2\mu\hbar^2T)^{1/3}]{W^*}_s{W^*}_d = W_T{W^*}_s{W^*}_d \tag{5}$$

The first factor corresponds to the rate obtained by Thompson [2]. Further ${W^*}_s, {W^*}_d$ are the static and dynamic enhancement factors respectively. The corresponding formula for the fusion rate is

$$R = R_{id}{W^*}_s{W^*}_d \tag{6}$$

The static enhancement is given by the potential of mean force and coincides with (1) (see also [3]) . The dynamic enhancement factor ${W^*}_d$ averaged over angles and random field distributions is given by

$${W^*}_{dE\theta} = \frac{2\beta 2^{1/3}{q_{eff}}^{8/3}n^{2/3}\hbar^{2/3}}{36\pi^{2/3}\mu^{1/3}(T)^{5/3}} = \frac{2A\beta}{3} \tag{7}$$

It is easy to show that the same dynamic enhancement factor for the strong random field ${W^{**}}_{dE\theta}$:

$${W^{**}}_{dE\theta} \simeq W_T\exp(B\beta^{-1/4}) \tag{8}$$

where

$$B = 8K(2^{1/2}/2)({q_{eff}}^4n^{-2/3}\mu^2)^{1/4}/3\hbar$$

if $B\beta^{-1/4} >> 1$.

Let us do now some estimations of the enhancement factors. First, let us estimate the influence of the proposed effect in solar interior for proton-proton fusion reaction. Here the density is $n = 3.3 \cdot 10^{25}$ per cubic cm, the plasma temperature is about $T \simeq 1.3$ keV [3]. We find

$$W^*_r \simeq 0.02; W^*_{dE\theta} = \exp(2.6 \cdot 10^{-5}) \simeq 0.000026$$

Therefore the dynamic enhancement is about 0.0026% in comparison with the static enhancement which has been obtained already by Ichimaru ([3]).

For white dwarfs (WD), let us estimate the enhancement for the carbon-carbon reaction [3]. Here the density is $n \simeq 10^{32}$ per cubic cm, and the temperature is $T \simeq 4.5$ keV. We find: $lnW^{**}_{dE\theta} = 88.5$ (to be compared with the logarithm from the static enhancement factor = 23.5 given by Ichimaru [3]).

For He-He reactions in white dwarfs we get $n = 1,47 \cdot 10^{31}$ per cubic cm and $T \simeq 0,9$ keV, $\alpha >> 1$, $\ln W^{**}_{dE\theta} = 28.6$.

We have considered so far only plasmas under astrophysical conditions. Let us now discuss the question, whether the enhancement of fusion rates due to nonideality may play a role under the conditions of laboratory plasmas. The deuterium-tritium reaction has the additional term Q_{eff} as for different nuclei. Its influence is comparably less since here $q_{eff} = e, Q_{eff} = e/5$. For deuterium-thritium plasma compressed 350-times under laser driving (e.g. by a ICF process for deuterium-tritium reaction), the characteristic densities are $n = 0,7 \cdot 10^{25}$ per cubic cm and the plasma temperature $T \simeq 5$ keV and $W^*_{dE\theta} = \exp(0.38 \cdot 10^{-5})$, i.e. the enhancement is about 0,00038% (to be compared with the static enhancement factor 0,4% obtained by Ichimaru [3] and by (1)).

Thus, the considered enhancements due to the action of a zero-average microfield are about three orders less than obtained by the corrected two-body interaction for plasmas close to ideal one. The influence of dynamic enhancement on fusion rates is in general rather weak, except under the conditions of astrophysical objects. For the fusion in the sun the dynamic enhancement by random fields gives only a small corresction, but for white dwarfs it gives the main enhancement effect.

REFERENCES

[1] G. Gamov, Z.Phys. 51 204 (1928)

[2] W.B. Thompson, Proc.Phys.Soc.London Sect. B 70 1 (1957)

[3] S. Ichimaru, Rev.Mod.Phys. 65 255 (1993)

[4] V.P. Silin, A.A. Rukhadse, Electromagnetic Properties of Plasmas and Plasma-like Media (in Russ.) (Gosatomizdat, Moscow, 1964)

[5] M.A.Berkovsky *et al*, Phys.Rev.E 54 (1996) 4087.

[6] L.D. Landau and E.M.Lifshitz, Quantum Mechanics. (Pergamon Press, London, 1959)

MONTE-CARLO SIMULATIONS OF STRONGLY COUPLED PLASMAS

O.Bystrenko and A.Zagorodny
Bogolyubov Institute for Theoretical Physics, 252143, Kiev, Ukraine

In this work we present the results of Monte- Carlo (MC) simulations of strongly coupled asymmetric Coulombic systems. Our interest in this subject is connected, first of all, with a possibility to explain spatial ordering phenomena (such as existence of liquid and crystalline phase in colloidal component) in dusty plasmas (DP) recently observed in experiments [1,2]. Besides, the conclusions obtained may be applicable to charged colloidal suspensions, which can also form Coulomb lattices or liquids. Numerical simulations of above phenomena performed up to date are mostly based on a concept of effective pair interaction between colloidal particles and seem to be semi-phenomenological. The present work is an attempt to study the subject microscopically, in particular, focusing on the effects resulting from the discrete nature of plasma components.

In all the simulations we regarded two-component plasma as a set of two sorts of hard spheres of opposite charge interacting with Coulombic forces. In the case of infinite systems, an accurate account of long-range Coulomb forces was possible due to utilization of Ewald's summation procedure. MC simulations were carried out for NVT ensemble using conventional Metropolis algorythm.

Three types of models were investigated:

a). Finite system consisting of several immobile colloidal particles (grains) in neutralizing plasma background closed in a single box;

b). Infinite systems with periodical boundary conditions with various charge asymmetry;

c). For the sake of comparison, a series of runs were carried out for one-component plasma (OCP) consisting of charged hard spheres in uniform background.

Below we use conventional plasma parameters and notations:

Z - relative charge of a colloidal particle,

z - relative charge of plasma particle (i.e. belonging to the second, opposite to colloidal component),

N, n - numbers of particles of colloidal and plasma component, respectively,

$P = (N\pi\sigma^3)/(6V)$ - packing coefficient for colloidal component,

$p = (n\pi\sigma_{pl}^3)/(6V)$ - packing coefficient for plasma component,

$q = (2Zze^2)/(k_BT(\sigma + \sigma_{pl}))$ -coupling constant of one component to the other,

$G = G_{cc} = (Z^2e^2)/(k_BTa)$ - coupling constant for colloidal component,

$a = (4N\pi/3V)^{-1/3}$ - average distance between grains.

Here T is temperature, σ is the diameter of a grain, k_B -Boltzmann's constant, e - charge of electron. Subscript c denotes colloidal component, and pl - plasma (second, opposite to colloidal) component.

MC simulations in the model a) were performed for parameters $P = 10^{-3}$, $p = 10^{-12}$, $N = 2$, $n = 128$, $q = 2...64$; with the two colloidal particles fixed near the centre of the box at the distance $a = 0.5L$; where L - the length of the box.

The results confirm the conclusions obtained by the authors in the previos work [3] about a critical behavior of the system near the point $q = 8 - 12$, which manifests itself, specifically, as a peak in heat capacity in that region. In addition, a screened force (taking into account plasma surrounding) of interaction between grains $< F >$ averaged over the ensemble of accepted configurations was examined. As can be seen from the Fig.2, the character of screening changes abruptly near the point $q = 6 - 8$: the relative amplitude of force reduces stepwise from 0.65 at $q = 6.$ to zero at $q > 8$.

MC simulations for the model b) performed for various parameters of plasma indicate that that sort of critical behavior with the critical value $q = 8 - 12$ is characteristic of two-component plasmas. In particular, the simulations for the case of symmetric system for $N = n = 32$, $P = p = 0.01$ evidence in favour of that assumption. Let us note, that the existence of gas-liquid phase transition with the same critical parameter $q = 12$ in such system was reported before in Ref.[4]. The results presented in Figs.1,3,4 indicate an apparent resemblance of these phenomena in both (symmetric infinite and asymmetric finite systems) cases. It suggests that the accumulation of particles on the surface of grains at $q > 8$ (similarly to formation of clusters in the symmetric case, see Figs. 3,4) may represent a condensation of liquid plasma phase, and separate plasma particles distributed in volume - gas phase being in thermal equilibrium with liquid.

In any event, critical behavior of screened forces between charged colloidal particles at the point $q = 6 - 8$ may have important consequences for a possibility of spatial ordering phenomena in colloidal component. Namely, to make such phenomena possible, the potential energy between grains must considerably exceed their kinetic energy, i.e. the relationship $G_{cc} >> 1$ must fulfil. It means that q should not exceed the value $q = 6$, and that, in turn, imposes a restriction on a charge asymmetry of the system. Really, if we assume, that for formation of Coulomb lattice some minimal critical value G must be attained, say, $G_0 = 180$ similarily to OCP, it means that two conditions, $G > 180$, and $q < 6$ must be simultaneosly satisfied. From it follows immediately, that the relationship

$$P^{1/3} Z/z > 30 \qquad (1)$$

must fulfil, and the value of Z/z should not be less than 30.

The connection between above mentioned phase transition and formation of Coulomb lattices in colloidal component can be interpreted in the other way. Namely, with the beginning of condensation on grain surfaces the bulk of plasma is concentrating in the vicinity of grains. The potential energy plasma-grain considerably exceeds grain-grain energy in this case, and it disrupts the formation of lattice.

It is interesting to note, that a similar, but much more severe condition on minimal asymmetry based on Lindeman criterion was obtained in Ref.[6] for the case of weak interaction between colloidal and plasma component (i.e. $q << 1$). Thus, the condition

(1) may happen to be necessary but not sufficient for possibility of Coulomb lattices.

To observe a liquid phase in colloidal component, MC simulations were performed in the model b). To make the restriction on the asymmetry less severe, a large value $P = 0.125$ was chosen, which is not characteristic of real physical systems. In this case the asymmetry 40 is sufficient to reach the value $G = 100$. The numbers of particles was $N = 16$, $n = 640$. The results (radial distribution fuction) are represented in Fig.6. For the sake of comparison, the same distribution function for OCP with hard spheres and the same packing coefficient $P = 0.125$ and $G = 100$ is given in Fig.5.

CONCLUSIONS

1. In two-component plasmas within the wide range of parameters a critical behavior with the critical coupling parameter $q = 8 - 12$ is observed. Presumably it may be connected with a liquid-gas phase transition.

2. Critical behavior of screened forces between colloidal particles gives rise to a restriction on the minimal charge asymmetry, necessary for formation of Coulomb lattices in colloidal component.

REFERENCES

[1] J.H.Chu and Lin I. Coulomb lattice in a weakly ionized colloidal plasma. Physica A 205, 1994, p. 183-190.

[2] R.L.Merlino et al. Laboratory experiments on Dusty Plasma. International Conference on Plasma Physics, Foz Iguacu, 1994, p. 295-302.

[3] O.Bystrenko, A.Zagorodny. Monte-Carlo simulation of effective interaction in dusty plasmas. Proc. Int. Conf. on the Physycs of Dusty Plasmas, Goa, India, 1996.

[4] P.Vorontsov-Vel'yaminov et al. High Temp. 8, 1970, p.261.

[5] P.Schramm, S.Trigger. Minimal charge of microions for crystallization of colloidal suspensions. Workshop on complex fluids and plasmas, Eindhoven, 1995.

FIGURE CAPTIONS

1. Heat capacities vs. temperature $T^* = 1/q$ for finite asymmetric (A: $N = 2, n = 128, P = 10^{-3}, p = 10^{-12}$) and infinite symmetric (B: $N = n = 32, P = p = 0.01$) plasmas.

2. Average relative screened force F of interaction between grains vs. temperature $T^* = 1/q$; units are chosen so that $F = 1$. in the absence of screening.

3. Equilibrium configuration of particles for finite asymmetric ($N = 2, n = 128, P = 10^{-3}, p = 10^{-12}$) plasma, $q = 64$.

4. Equilibrium configuration of particles for infinite symmetric ($N = n = 32, P = p = 0.01$) plasma, $q = 64$.

5. Radial distribution functions for OCP with hard spheres, $P = 0.125, G = 100, N = 16$.

6. Radial distribution function (grain-grain) for asymmetric two-component plasma, $N = 16, n = 640, P = 0.125, p = 10^{-12}, q = 5, G = 100$.

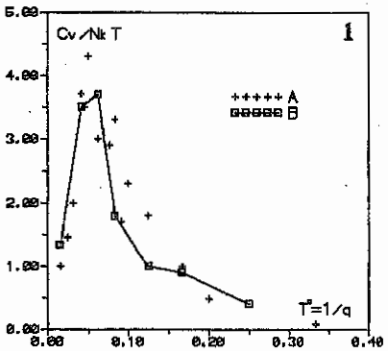
Cv/Nk T
1
+++++ A
BBBBB B
T*=1/q

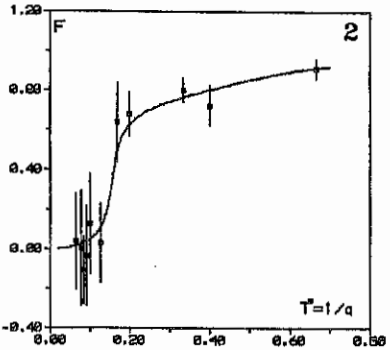
F
2
T*=1/q

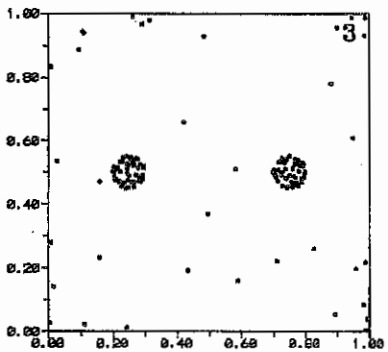
3

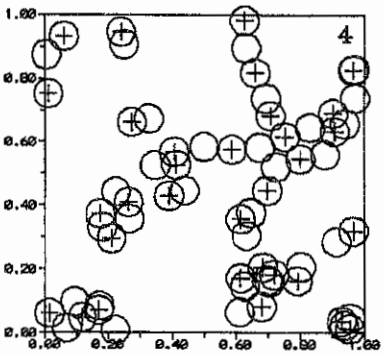
4

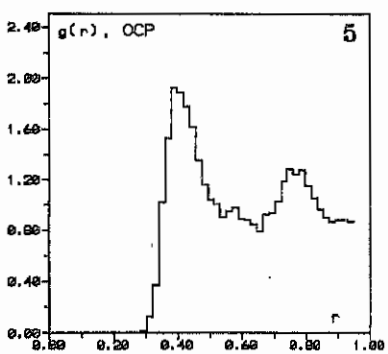
g(r), OCP
5
r

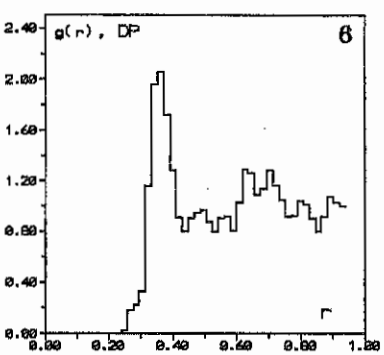
g(r), DP
6
r

Author Index

Author Index

Author Index

Author Index

Author Index

Author Index

Author Index

Author Index

Author Index

Author Index

Author Index

Author Index

Author Index

Author Index

Author Index

Author Index

Author Index

Author Index

Author Index

Author Index